MEALOR II Damage Mechanics and Local Approach to Fracture

Jacques Besson, Jérémy Bleyer, Sylvia Feld-Payet, Anne-Françoise Gourgues-Lorenzon, Florent Hannard, Thomas Helfer, Jeremy Hure, Djimedo Kondo, Veronique Lazarus, Christophe Le Bourlot, et al.

MEALOR II

Damage Mechanics and Local Approach to Fracture

A collective work by J. Besson, J. Bleyer, S. Feld-Payet, A. Gourgues-Lorenzon, F. Hannard, T. Helfer, J. Hure, D. Kondo, V. Lazarus, C. Le Bourlot, H. Maitournam, C. Maurini, N. Moës, T. Morgeneyer, L. Morin, T. Petit, & A. Simar

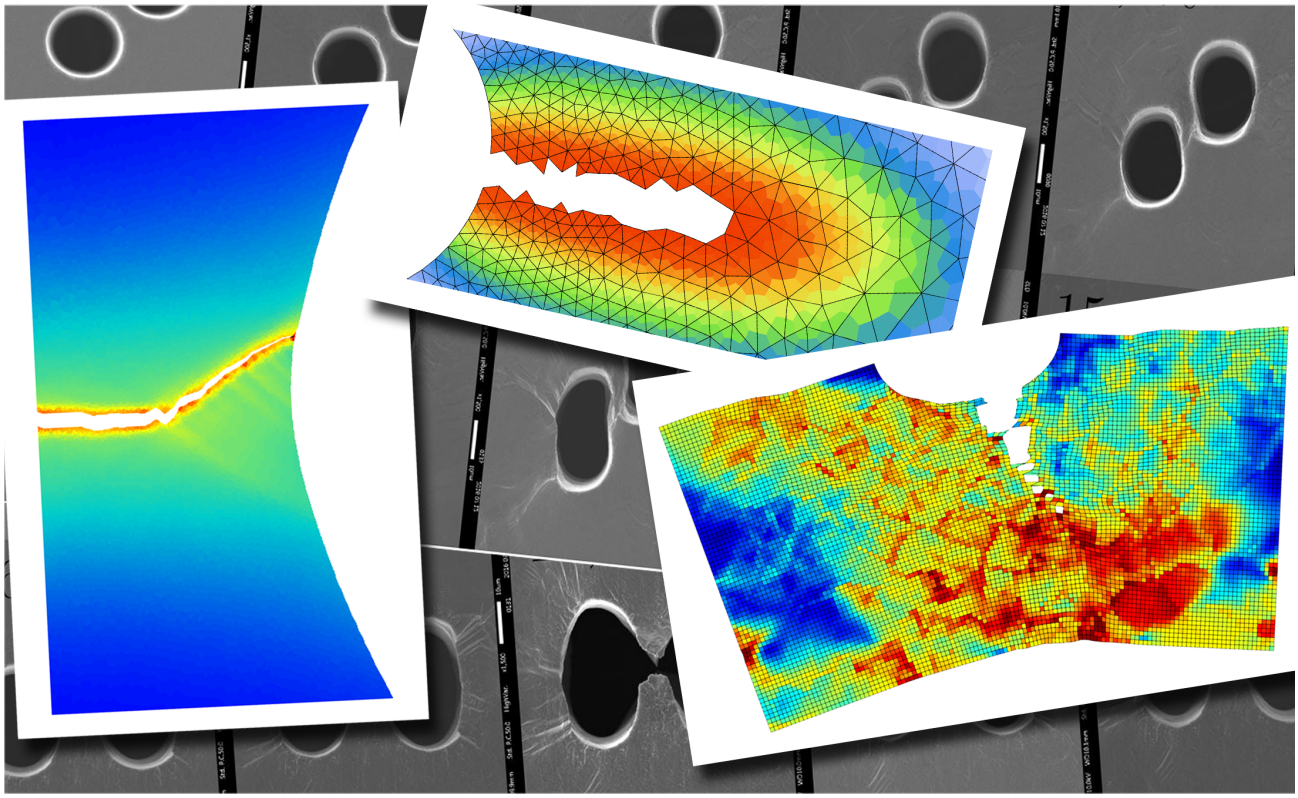

August 2023

https://doi.org/10.5281/zenodo.10125170

MEALOR II

Damage Mechanics and Local Approach to Fracture

J. Besson, J. Bleyer, S. Feld-Payet, A. Gourgues-Lorenzon, F. Hannard, T. Helfer, J. Hure, D. Kondo, V. Lazarus, C. Le Bourlot, H. Maitournam, C. Maurini, N. Moës, T. Morgeneyer, L. Morin, T. Petit, & A. Simar

Contents

Contributors

Jacques Besson	Mines Paris - PSL	France
Jérémy Bleyer	Ecole des Ponts ParisTech	France
Florent Hannard	Université catholique de Louvain	Belgium
Thomas Helfer	CEA	France
Jérémy Hure	CEA	France
Sylvia Feld-Payet	ONERA	France
Anne-Françoise Gourgues-Lorenzon	Mines Paris - PSL	France
Djimédo Kondo	Sorbonne Université	France
Véronique Lazarus	ENSTA Paris	France
Habibou Maitournam	ENSTA Paris	France
Corrado Maurini	Sorbonne Université	France
Nicolas Moës	Centrale Nantes	France
Thilo Morgeneyer	Mines Paris - PSL	France
Léo Morin	University of Bordeaux	France
Thomas Pardoen	Université catholique de Louvain	Belgium
Tom Petit	CEA	France
Aude Simar	Université catholique de Louvain	Belgium

Nomenclature

Acronyms

BDWTT Battelle Drop Weight Tear Test

CT Computed Tomography

CTOD Crack Tip Opening Displacement

DBT Ductile Brittle Transition

DIC Digital Image Correlation

EBSD Electron BackScatter Diffraction

FEM Finite Element Method

GB Grain Boundary

GTN Gurson-Tvergaard-Needleman

LD Longitudinal Direction

LEFM Linear Elastic Fracture Mechanics

ND Normal Direction

NLFM Non Linear Fracture Mechanics

PFZ Precipitate Free Zone

RD Rolling Direction

RVE Representative Volume Element

SEM Scanning Electron Microscope

SIF Stress Intensity Factor

TEM Transmission Electron Microscope

TLS Thick Level Set

X-FEM eXtended Finite Element Method

Fracture mechanics variables

α damage

ℓ, a crack length

ϵ_c, ϵ_f fracture strain

σ_c, σ_f fracture stress

f porosity

G_c critical energy release rate

J J-integral

K	stress intensity factor	Q_σ	Q-stress
K_c	fracture toughness	T_σ	T-stress

Geometrical and kinematical variables

Γ	crack path	W, L	length
$\mathcal{S}$	surface	W_{void}, χ, λ	void distribution descriptors
ω, Ω	volume	$\boldsymbol{u}$	displacement
B	width	$\boldsymbol{v}$	velocity
h	thickness	$\boldsymbol{x}$	position
R	radius		

General mechanical variables

$\bar{\theta}$	Lode Angle	$\boldsymbol{D}$	deformation rate tensor
ϵ_0, ϵ_Y	yield strain	$\boldsymbol{M}$	Mandel stress tensor
ϵ_{eq}	norm of the strain tensor	$\boldsymbol{P}$	first Piola-Kirchhoff stress tensor
η	stress triaxiality	$\boldsymbol{S}$	second Piola-Kirchhoff stress tensor
Λ	plastic multiplier	$\boldsymbol{T}$	Hencky stress tensor
σ_0, σ_Y	yield stress	$\boldsymbol{\epsilon}^{\mathrm{el}}$	elastic strain
σ_I, Σ_I	maximal principal stress	$\boldsymbol{\epsilon}^{\mathrm{p}}$	plastic strain
σ_m, Σ_m	hydrostatic stress	$\boldsymbol{\epsilon}^{\mathrm{th}}$	thermal strain
d_{eq}	norm of the strain rate tensor	$\boldsymbol{\epsilon}^{\mathrm{to}}$, $\boldsymbol{\epsilon}$	linearized total strain
J_F	determinant of deformation gradient tensor	$\boldsymbol{\epsilon}^{\mathrm{vis}}$	viscoplastic strain
$\boldsymbol{F}$	deformation gradient tensor	$\mathbb{K}$	Hooke fourth order tensor
σ_{eq}, Σ_{eq}	von Mises norm of the Cauchy stress	$\boldsymbol{\sigma}$, $\boldsymbol{\Sigma}$	Cauchy stress
		$\boldsymbol{U}$	stretch tensor

Mathematical notations

Div(.)	divergence operator in the reference configuration
div(.)	divergence operator in the current configuration
$\dot{(.)}$	time derivative
Grad(.)	gradient operator in the reference configuration
grad(.)	gradient operator in the current configuration
$\boldsymbol{a}^{-\mathrm{T}}$	inverse of the transpose of a matrix (also applies to tensors)
$\boldsymbol{a}^{-1}$	inverse of a matrix (also applies to tensors)
$\boldsymbol{a}$	first order tensor (lower case Latin letter)
$\boldsymbol{A}$, $\boldsymbol{\sigma}$	second order tensor (upper case or Greek letter)
$\mathbb{A}$	fourth order tensor
$\mathrm{tr}(\boldsymbol{a})$	trace of a matrix
$\boldsymbol{a}^{\mathrm{T}}$	transpose of a matrix (also applies to tensors)

General physical quantities

γ	surface fracture energy
λ	Lamé first parameter
μ	Lamé second parameter
ν	Poisson ratio
E	Young's modulus
P_f	fracture probability
ρ	mass density

Specimen geometry

C(T)	Compact Tension
DCB	Double Cantilever Beam
N(T)	Notch Tension
PCCV	Pre Cracked Charpy V-notch
SEN(B)	Single Edge Notch Bending
SEN(T)	Single Edge Notch Tension

Thermodynamical variables

$\mathcal{E}$	total energy
$\mathcal{G}$	energy release rate

$\mathcal{P}$	potential energy	Φ	dissipation potential
$\mathcal{W}$	work	Ψ	free energy
ϕ	yield / strength criterion	s	entropy
w	energy density	T	temperature

1

Preamble

Thomas Pardoen
Institute of Mechanics Materials and Civil Engineering (iMMC), Université catholique de Louvain, Belgium

1.1 About MEALOR II

MEALOR is the french abbreviation for « Mécanique de l'Endommagement et Approche Locale de la Rupture ». This translates in english into « Damage Mechanics and Local Approach of Fracture ». The "II" means that there has been a first magnificent edition of this summer school in Roscoff, France in 2004. The pressure for MEALOR II is extreme in view of the success of the first version MEALOR I, almost 20 years ago !

During 10 days, young and less young scientists will be exposed to the science of damage and fracture, taught by a series of top experts from Europe, mainly from France, and with a few outsiders. This is not a surprize as the Local Approach to Fracture has been originally promoted in France under this terminology by the pioneers: André Pineau, Dominique François and André Zaoui. Similar approaches were following the same path in the rest of the international community, under the umbrella of the "micromechanics of fracture" paradigm. The dogma of the local approach is to address the physical micromechanisms of damage and fracture in direct link with the microstructure of materials and in the context of rigorous solid mechanics theory and models. Over time, numerical modelling has become the third main pillar of the approach which thus relies on: I. Materials microstructure and characterization – II. Solid mechanics theory and mechanical testing – III. Numerical methods. The coverage of the relevant experimental methods at the scales of interest, of the material microstructure aspects, of the advanced solid mechanics theoretical concepts and of the appropriate numerical methods is a challenge and justifies why 10 days are indeed needed for the School.

Maybe, one can see this subject as an old topic. But, is it so ? Long term operation of nuclear reactors to 60 years and possibly to 80 years will essentially rely on fracture mechanics, microstructure evolution and local approach considerations. The development of novel and safe large pressurized hydrogen tanks will require advances in local approach of fracture combined with hydrogen embrittlement. The extensive use of additive manufacturing of complex metal components keep facing problems of premature damage and cracking events connected to the processing and specific microstructures. The so much hoped success of future fusion reactors is very much tied to meeting severe requirements in terms of cracking resistance under ultra severe environment. Although, much of the school is focused on metals, many polymer-based applications also face similar issues which can be handled using local approach of fracture borrowed often from the metal field. The subject in thus timely and th impact is major, not only on safety, but also on economy and on durability. Making progresses in all these challenging problems, and on many others, require a constant dialog between mechanics, materials (and processing) and numerical methods.

Crack or no crack, that's the question ? First, let us assume there is no crack in the material, component, or structure of interest. Many modern materials are indeed produced immune of pre-cracks owing to excellent control of the thermomechanical processes. This is the "no crack" case. If the application is not critical, the failure assessment analysis can be addressed starting from a virgin system. A loading is applied. If during loading the stress is large enough to trigger cleavage either because the yield stress is very large and that locally one can create a stress concentration to reach the theoretical cleavage stress with no option for relaxing the stress by plasticity, or if there is some chemical poisoning or internal oxydation, fast fracture occurs giving rise to the typical faceted surface. This is essentially the curse of trans- or intergranular cleavage. In metals, this is observed essentially only for BCC or HCP crystalline structures, and especially at low T°. Cleavage is by nature a statistical process very much connected to the distribution of crack initiators in the microstructure. Fortunately, most often metals fail by a ductile mechanism, voids nucleate mostly on second phase particles, grow by plastic deformation and finally coalesce leading to failure. This sequence of mechanisms, same as for brittle fracture, have been unravelled in the context of the local approach and then modelled using micromechanics theory. The local approach is able to predict the fracture strain in the ductile regime ideally for any loading condition and stress state.

In the alternative scenario, a macroscopic crack is present. This (pre)crack may result from poor manufacturing, from cyclic/fatigue loading during operation or from corrosion. Sometimes, there is no crack but one cannot take any risk and the safety assessment procedures impose to assume there is a crack. This potential crack is either taken at the limit of detection of non-destructive methods or much larger such as for nuclear pressure vessels. In this case "with crack", fracture mechanics is the preferred paradigm. In fracture mechanics, a driving force expressed in terms of the energy available for cracking (G or J) or, equivalently, stress intensity factor K, is compared to the fracture toughness G_c, J_c or K_c, as measured on laboratory specimens. However, fracture mechanics has limits. In particular, J_c or K_c are not always transferable due to constraint effects and there is no convincing remedy within the fracture mechanics framework. Furthermore, J_c or K_c is a black box telling nothing about the underlying mechanisms and about the links with the microstructure. The local approach of fracture complements and solves for these limitations by modelling the failure mechanisms in the fracture process zone either by cleavage initiation or by nucleation, growth and coalescence of voids with the crack. It does not mean that fracture mechanics is not useful anymore, it is. It will remain the paradigm for structural integrity assessment as well as to compare materials among one another by comparing their fracture toughness.

This short story sets the journey for the School. Fracture is by essence an irreversible process often associated with a lot of dissipation – which is good to make tough materials – requiring some background on the thermodynamics of irreversible processes, covered by D. Kondo and H. Maitournam in Chapter 2. When things go well, materials deform with a lot of plasticity before fracturing making unavoidable the use of a finite strain formalism of plasticity, the topic of Chapter 3 presented by T. Helfer. The survivors of this challenging start will have the right to enter Chapter 4 with T. Petit and J. Hure and be exposed to the experimental methods used in fracture mechanics to determine the fracture toughness of materials. The rigorous basis on linear elastic fracture mechanics is then introduced in Chapter 5 by V. Lazarus. Linear elastic fracture mechanics is sufficient for treating brittle fracture as well materials with limited toughness, but elastoplastic fracture mechanics is mandatory for tough metals. This will be the subject of Chapter 6 by J. Besson, indicating also the limits of the approach. Basically, this ends the presentation of the macroscopic or global approach to fracture, with no appraisal yet of the physics of damage and fracture as connected to the material microstructure.

What could be seen as a second part of the School and of the book really

enters into the local approach of fracture. It starts with the brittle cleavage fracture by A.F. Gourgues in Chapter 7. After the Yin, comes the Yang with Chapter 8 on the mechanism of ductile fracture covered by F. Hannard, T. Morgeneyer, and A. Simar. This is immediately followed in Chapter 9, by D. Kondo and L. Morin, with a classic topic of the French solid mechanics school who is certainly the most active in the world these days: the micromechanical modelling of the nucleation, growth and coalescence of voids leading to ductile fracture. As a transition to the third part of the school, Chapter 12 by T. Helfer and J. Hure, presents the key theoretical issues and good practices that must be followed when simulating numerically fracture problems based on local damage models.

In the third part of the book, the attention is put on numerical methods. One, if not the most complicated problem when simulating fracture with damage models, is the need to introduce one or several internal lengths. This length scale sets the thickness of the fracture process zone and, from there, the magnitude of the energy dissipated in the near crack tip region. J. Bleyer and S. Feld-Payet discuss in Chapter 10 the so called "non local" methods that introduce such internal length and regularize the numerical problem. Without non local formulation, a finite element simulation leads to a mesh sensitive response associated to the loss of ellipticity of the underlying equations. Chapter 11 by C. Maurini gives an introduction to the variational approaches and to their advantages. Chapter 13 written by N. Moës contemplates the question of simulating a crack in a diffuse or sharp way with pro and cons. Finally, the question to move, in terms of numerical formulation, from a diffuse description of damage to a discrete representation of a crack is addressed in Chapter 14 by Sylvia Feld-Payet.

Long life to local approach of fracture – enjoy the school !

Thomas Pardoen

UCLouvain

2

Thermodynamics of Irreversible Processes : formulation of constitutive models

Djimedo Kondo

Sorbonne Université, IJLRDA

Habibou Maitournam

Ensta, Imsia

Thermodynamics of Irreversible Processes (TIP) with internal variables constitutes a powerful method for the formulation of constitutive models of mechanical systems. In this chapter, after a brief recall on some basic concepts of continuum mechanics, we begin by briefly presenting the two principles of thermodynamics. Then, we present the derivation of the state laws and complementary equations. Next, the introduction of the Generalized Standard Materials (GSM) framework allows to formulate in a unified way the different classes of standard dissipative constitutive laws, namely elastoplasticity with or without hardening, elasticity coupled with damage.

2.1 Mass balance et equation and conservation of momentum

Let us first emphasize that there are several papers (see for instance [Halphen and Nguyen, 1975], [Germain et al., 1983], [G.A. Maugin, 1994], [Collins and Houlsby, 1997]) and many books devoted to the subject of thermodynamics-based formulation of standard dissipative laws. The reader may also refer to [Ziegler, 1983], [Lemaître and Chaboche, 1990], [Maugin, 1992], [Maugin, 1999], [Houlsby and Puzrin, 2006], [Nguyen, 2000], [Maitournam, 2012].
Concerning the basic concepts of Continuum Mechanics, the reader can also refer for instance to [Salençon, 2001] and references cited herein.

Continuum mechanics deals with a macroscopic representation of the continuum in which the particles represent an infinitesimal volume of matter. In this framework, and from a geometrical point of view, the particles are considered as material points which are characterized by their position (and

then velocity and acceleration) during the motion. This description and the resulting concepts of deformation (or rate of deformation) is classically done by means of two different formalisms which are known as the Lagrangian and the Eulerian ones. A brief summary of such descriptions can be found in chapter 2. Let us just recall that the deformation and the rate of deformation are characterized by:

- the Green-Lagrange deformation in the Lagrangian description

$$\boldsymbol{e}(\boldsymbol{X},t) = \frac{1}{2}\left(\boldsymbol{Grad}\,\boldsymbol{\xi} + (\boldsymbol{Grad}\,\boldsymbol{\xi})^{\mathrm{T}} + (\boldsymbol{Grad}\,\boldsymbol{\xi})^{\mathrm{T}} \cdot \boldsymbol{Grad}\,\boldsymbol{\xi}\right) \tag{2.1}$$

  in which $\boldsymbol{\xi}(\boldsymbol{X},t)$ represents the displacement vector field which is function of the Lagrangian variables $(\boldsymbol{X},t)$.
  Under the classical assumption of small perturbations this finite strain tensor reduces to a linearized strain tensor $\boldsymbol{\varepsilon}$, obtained as the symmetric part of the gradient of the displacement vector field:

$$\boldsymbol{\varepsilon}(\boldsymbol{X},t) = \frac{1}{2}\left(\boldsymbol{Grad}\,\boldsymbol{\xi} + (\boldsymbol{Grad}\,\boldsymbol{\xi})^{\mathrm{T}}\right) \tag{2.2}$$

- the Eulerian rate of the deformation (function of the eulerian variables $(\boldsymbol{x},t)$):

$$\boldsymbol{d}(\boldsymbol{x},t) = \frac{1}{2}\left(\boldsymbol{grad}\,\boldsymbol{v} + (\boldsymbol{grad}\,\boldsymbol{v})^{\mathrm{T}}\right) \tag{2.3}$$

  which turns out to be the symmetric part of the gradient of the Eulerian velocity field $\boldsymbol{v}(\boldsymbol{x},t)$.

Note that under small perturbation hypothesis the Eulerian strain rate tensor d is equal to the rate of linearized strain tensor:

$$\boldsymbol{d} = \frac{d\boldsymbol{\varepsilon}}{dt} = \dot{\boldsymbol{\varepsilon}} \tag{2.4}$$

Note also that the following presentation of conservation laws of mass and of momentum is done here considering the current configuration, that is by means of eulerian quantities (see chapter 3 for the corresponding Lagrangian formalism).

2.1.1 Mass balance equation

With the Eulerian description in hand, we are now able to present the mass conservation equation at time t. By definition the mass of the system occupying the domain Ω_t at time t is given by

$$\mathcal{M}(t) = \int_{\Omega_t} dm = \int_{\Omega_t} \rho d\Omega_t \tag{2.5}$$

in which ρ is the mass per unit volume, with for an infinitesimal domain $d\Omega_t$ the corresponding mass $dm = \rho d\Omega_t$.
The global form of the mass conservation equation reads then:

$$\frac{d\mathcal{M}(t)}{dt} = \int_{\Omega_t} \frac{d}{dt}(\rho d\Omega_t) = \int_{\Omega_t} (\frac{d\rho}{dt} + \rho \,\mathrm{div}(\boldsymbol{v}))d\Omega_t = 0 \tag{2.6}$$

This results in the local form of the mass conservation law:

$$\frac{d\rho}{dt} + \rho \mathrm{div}(\boldsymbol{v}) = 0 \tag{2.7}$$

or equivalently:

$$\frac{\partial\rho}{\partial t} + \mathrm{div}(\rho\boldsymbol{v}) = 0 \tag{2.8}$$

(2.7) and (2.8) are known as continuity equation.

2.1.2 Conservation of momentum - the Cauchy stress tensor

Without searching to provide here a method of construction, we follow here a very classical approach[1] which consists in:

- starting from the fundamental principle of dynamics, extended to a continuous medium. Such fundamentals principles correspond to the conservation of momentum and is expressed for a subdomain Ω'_t (included in Ω_t) at time t :

$$\boldsymbol{\mathcal{F}}' = \frac{d}{dt}\left(\int_{\Omega'_t} \rho\boldsymbol{v}\; d\Omega_t\right) = \int_{\Omega'_t} \rho\boldsymbol{\gamma}\; d\Omega_t \tag{2.9}$$

  $\boldsymbol{\gamma} = \frac{d\boldsymbol{v}}{dt}$ being the Eulerian acceleration vector field.

$$\boldsymbol{\mathcal{M}}'_O = \frac{d}{dt}\left(\int_{\Omega'_t} \boldsymbol{x} \wedge \rho\boldsymbol{v}\; d\Omega_t\right) = \int_{\Omega'_t} \boldsymbol{x} \wedge \rho\boldsymbol{\gamma}\; d\Omega_t \tag{2.10}$$

  in which $\boldsymbol{\mathcal{F}}'$ and $\boldsymbol{\mathcal{M}}'_O$ represent the exterior forces and their moment with respect to a point O, respectively.

  Remark 1: *Interestingly, one may note that the final writing of the above equations has required the consideration of the mass conservation law.*

- proposing a schematization of internal forces for which it is postulated that in addition to body forces $\rho\boldsymbol{f}$, the part of forces $\boldsymbol{\mathcal{F}}'$ exerted on the subsystem occupying Ω'_t by the rest of the domain $(\Omega_t - \Omega'_t)$ are due to contact interactions. The latter are in the form of surface forces which depend linearly (and only) on the exterior unit normal $\boldsymbol{n}$ to the considered

[1] *The alternative view is that provided by the Principle of Virtual Powers (PVP) (see again a presentation in [Salençon, 2001]*

surface element.

The linear application between $\boldsymbol{n}$ and $\boldsymbol{T}$ corresponds to a bilinear form, the Cauchy stress second order tensor $\boldsymbol{\sigma}$ (an Eulerian tensor), such that :

$$\boldsymbol{T}(\boldsymbol{x}, t, \boldsymbol{n}) = \boldsymbol{\sigma}(\boldsymbol{x}, t).\boldsymbol{n} \tag{2.11}$$

known as the Cauchy's postulate.

Consideration of (2.11) in (2.9) yields the equations of motion, valid in all the domain Ω_t:

$$(\Omega_t) \qquad div\, \boldsymbol{\sigma} + \rho \boldsymbol{f} = \rho \boldsymbol{\gamma} \tag{2.12}$$

while introducing (2.11) in (2.10) yields the symmetry of the Cauchy stress tensor. In components, one has $\sigma_{ji} = \sigma_{ij}$.

Remark 2: By dualization of (2.12) (multiplication by the velocity field $\boldsymbol{v}$), it appears that a direct consequence of the momentum conservation is the well-known kinetics energy theorem (mechanical energy balance):

$$\dot{\mathcal{K}} = \mathcal{P}_{\text{ext}} + \mathcal{P}_{\text{int}}, \tag{2.13}$$

for which it is recalled that $\dot{\mathcal{K}}$ represents the material derivative of $\mathcal{K}$, and

- $\mathcal{K} = \int_{\Omega_t} \frac{\rho}{2} \boldsymbol{v}.\boldsymbol{v}\, d\Omega_t$ is the kinetic energy of the system
- $\mathcal{P}_{\text{int}}$ is the power of internal forces, given by:

$$\mathcal{P}_{\text{int}} = -\int_{\Omega(t)} \boldsymbol{\sigma} : \boldsymbol{d}\, d\Omega, \tag{2.14}$$

- $\mathcal{P}_{\text{ext}}$, defined by

$$\mathcal{P}_{\text{ext}} = \int_{\Omega(t)} \rho \boldsymbol{f}.\boldsymbol{v}\, d\Omega + \int_{\partial\Omega(t)} \boldsymbol{T}.\boldsymbol{v}\, da, \tag{2.15}$$

  is the power of the external forces.

It will be seen in the following that the objective formulation of the energy conservation (the first principle of thermodynamics) will require the consideration of the kinetic energy theorem, built itself from the conservation of momentum.

2.2 The two principles of continuum thermodynamics and the Clausius-Duhem inequality

This section is devoted to a brief presentation of the two principles of thermodynamics for continuous media, and of the resulting Clausius-Duhem inequality. To this end, it is convenient to recall first the local state postulate

which stands that the considered systems are made up of sub-systems whose evolution is sufficiently slow so that each sub-system can be considered as almost in thermodynamic equilibrium at any time t. This will notably allow to define a temperature T, a specific (per unit mass) internal energy e and a specific entropy s.

2.2.1 The first principle : energy conservation law

This principle which expresses an energy balance for the studied system postulates that the variation of the total energy (internal energy + kinetics energy) of a system is equal to the energy that it received by exchange with the outside (in the form of work and heat) :

$$\frac{d}{dt}(E + \mathcal{K}) = \mathcal{P}_{\text{ext}} + \mathcal{P}_{\text{cal}}, \tag{2.16}$$

E is the internal energy of the system. As mentioned before, $\mathcal{P}_{\text{ext}}$ represents the power of the external forces. $\mathcal{P}_{\text{cal}}$ is the calorific power, that is the received quantity of heat.
Since the kinetics energy $\mathcal{K}$ and $\mathcal{P}_{\text{cal}}$ which appear in (2.16) are non objective quantities (they depend on the observer), it is more appropriate to rewrite the energy conservation by referring to the already presented kinetics energy theorem (see Eq. (2.13)). It follows that the global and objective form of the first thermodynamics principle reads:

$$\dot{E} = -\mathcal{P}_{\text{int}} + \mathcal{P}_{\text{cal}}. \tag{2.17}$$

Aiming at expressing the above conservation law in a local form, it is assumed by taking advantage of the local state postulate that, as an additive quantity, the internal energy of the system, E, can be put in the form:

$$E = \int_{\Omega(t)} \rho e \, d\Omega, \tag{2.18}$$

where, as mentioned before, e represents the specific internal energy (energy per unit mass). Taking into account the continuity equation ((2.7) or (2.8)), one gets:[2]

$$\dot{\boldsymbol{E}} = \frac{d}{dt}\int_{\Omega(t)} \rho e \, d\Omega = \int_{\Omega(t)} \rho \dot{e} \, d\Omega. \tag{2.19}$$

Moreover, the calorific power $\mathcal{P}_{\text{cal}}$ consists of two terms :

$$\mathcal{P}_{\text{cal}} = \int_{\Omega(t)} r \, d\Omega - \int_{\partial\Omega(t)} q \, da, \tag{2.20}$$

[2] *From now, to simplify the writing, the material time derivative will be denoted as* $\frac{dy}{dt} = \dot{y}$ *for any quantity* y.

in which r and q represent respectively the volumetric power and imposed heat flux.
Taking into account the above expressions, one gets the local form of the first principle :

$$\rho\dot{e} = \boldsymbol{\sigma} : \boldsymbol{d} + r - \mathrm{div}(\boldsymbol{q}) \tag{2.21}$$

This clearly shows that the variation of the internal energy of a particle is only due to the power of internal forces imposed by the exterior to the particle ($\boldsymbol{\sigma} : \boldsymbol{d}$), the heat source ($r$) and to the heat exchange by conduction ($-\mathrm{div}(\boldsymbol{q})$).

2.2.2 The second principle of thermodynamics

The second principle concerns the irreversible aspects of the system during its evolution. To this end, it is postulated that the production of entropy within the system is always positive. More precisely, such entropy production is strictly positive for irreversible processes and null in the case of reversible evolutions of the system. It is equal to the difference between the total entropy variation and the sum of the elementary quantities of heat received divided by the temperature.
In its global form, this principle is expressed as:

$$\dot{S} - \left(\int_{\Omega(t)} \frac{r}{T}\, d\Omega - \int_{\partial\Omega(t)} \frac{\boldsymbol{q}\cdot\boldsymbol{n}}{T}\, da \right) \geq 0, \tag{2.22}$$

The entropy S of the system being an extensive quantity, a specific entropy s can be introduced such that :

$$S = \int_{\Omega(t)} \rho s\, d\Omega, \tag{2.23}$$

The local form of the second principle follows then :

$$\rho\dot{s} + \frac{1}{T}\mathrm{div}(\boldsymbol{q}) - \frac{r}{T} - \frac{\boldsymbol{q}.\mathbf{grad}(T)}{T^2} \geq 0. \tag{2.24}$$

Dissipations

By multiplying the local production of entropy (see (2.24)) by the absolute (positive) temperature, one gets an energetic quantity, called total local dissipation. The second principle then amounts to saying that this dissipation, $\mathcal{D}$, is always positive:

$$\mathcal{D} = \rho T\dot{s} + \mathrm{div}(\boldsymbol{q}) - r - \frac{\boldsymbol{q}}{T}.\mathbf{grad}(T) \geq 0.$$

By combining this result with the local equation of the energy conservation (2.21), the total dissipation can be rewritten as :

$$\mathcal{D} = \rho T\dot{s} - \rho\dot{\boldsymbol{e}} + \boldsymbol{\sigma} : \boldsymbol{d} - \frac{\boldsymbol{q}}{T}.\mathbf{grad}(T) \geq 0 \tag{2.25}$$

known as the Clausius-Duhem inequality.

The total dissipation $\mathcal{D}$ is constituted of two parts :

- $\mathcal{D}_1$ called intrinsic dissipation, is defined by :

$$\mathcal{D}_1 = \rho T\dot{s} - \rho\dot{\boldsymbol{e}} + \boldsymbol{\sigma} : \boldsymbol{d} = \rho T\dot{s} + \mathrm{div}(\boldsymbol{q}) - r. \tag{2.26}$$

- $\mathcal{D}_2$ called thermal dissipation, reads :

$$\mathcal{D}_2 = -\frac{\boldsymbol{q}}{T}.\mathbf{grad}(T). \tag{2.27}$$

The Clausius-Duhem inequality, (2.25), implies that the total dissipation $\mathcal{D}$ must be positive or null, that is $\mathcal{D} = \mathcal{D}_1 + \mathcal{D}_2 \geq 0$. A more restrictive condition, often assumed, consists to admit that the intrinsic and thermal dissipations are separated and are each positive:

$$\begin{cases} \mathcal{D}_1 \geq 0 \\ \mathcal{D}_2 \geq 0 \end{cases} \tag{2.28}$$

Obviously, this assumption guarantees the positivity of $\mathcal{D}$, but is not equivalent to the Clausius-Duhem inequality.

2.3 State laws and evolution equations

In this section we aim at summarizing here the main procedure to obtain the state laws from the thermodynamics potential.

2.3.1 State laws and intrinsic dissipation

A first step consists in establishing expressions of the reversible thermodynamics forces from the knowledge of the thermodynamic potential, here the specific internal energy e. Restricting ourselves to small perturbations assumption, e is a function of the state variables: the linearized strain tensor $\boldsymbol{\varepsilon}$, the specific entropy s and the internal variables $\boldsymbol{\alpha}$ the physical signification of which depends on the type of the considered behavior.
From the expression of the intrinsic dissipation (2.26), it follows that :

$$\rho\dot{\boldsymbol{e}} = (\boldsymbol{\sigma} : \dot{\boldsymbol{\varepsilon}} - \mathcal{D}_1) + \rho T\dot{s}. \tag{2.29}$$

As ($\boldsymbol{\varepsilon}$, s $\boldsymbol{\alpha}$) are independent state variables for the state function e, one gets:

$$\rho\frac{\partial e}{\partial \boldsymbol{\varepsilon}} : \dot{\boldsymbol{\varepsilon}} + \rho\frac{\partial e}{\partial \boldsymbol{\alpha}}\dot{\boldsymbol{\alpha}} + \rho\frac{\partial e}{\partial s}\dot{s} = (\boldsymbol{\sigma} : \dot{\boldsymbol{\varepsilon}} - \mathcal{D}_1) + \rho T\dot{s}. \tag{2.30}$$

By identification, one deduce the following relations :

$$T = \frac{\partial e}{\partial s} \tag{2.31}$$

$$\rho\frac{\partial e}{\partial \boldsymbol{\varepsilon}} : \dot{\boldsymbol{\varepsilon}} + \rho\frac{\partial e}{\partial \boldsymbol{\alpha}}\dot{\boldsymbol{\alpha}} = \boldsymbol{\sigma} : \dot{\boldsymbol{\varepsilon}} - \mathcal{D}_1. \tag{2.32}$$

Noting that Equation (2.32) expresses equality between the non dissipated part of the mechanical power and the rate of the internal energy at fixed entropy, the reversible part of the thermodynamic forces associated with $\boldsymbol{\varepsilon}$ and $\boldsymbol{\alpha}$ are defined by

$$\begin{cases} \boldsymbol{\sigma}^{rev} = \rho\dfrac{\partial e}{\partial \boldsymbol{\varepsilon}} \\ \\ \mathcal{A}^{rev} = \rho\dfrac{\partial e}{\partial \boldsymbol{\alpha}} \end{cases}, \tag{2.33}$$

These equations together with equation (2.32) constitute the state laws of the system and allow to deduce from the internal energy $e(\boldsymbol{\varepsilon}, s, \boldsymbol{\alpha})$ the conjugated forces in a reversible process.
Entropy being a less "measurable" variable, it can be appropriate to replace it by the temperature T as state variable which is more common to be observable. Moreover, many processes are assumed to be isothermal. For this reason, it can be preferable to consider instead of the internal energy $e(\boldsymbol{\varepsilon}, s, \boldsymbol{\alpha})$, the Helmholtz free energy $\Psi(\boldsymbol{\varepsilon}, T, \boldsymbol{\alpha})$ as the thermodynamic potential. The opposite of this potential Ψ is defined as the partial Legendre transform (with respect to s)[3] of the internal energy e, that is :

$$-\Psi(\boldsymbol{\varepsilon}, T, \boldsymbol{\alpha}) = Ts - e(\boldsymbol{\varepsilon}, s, \boldsymbol{\alpha}), \tag{2.34}$$

Note that, as the internal energy e, the potential $\Psi(\boldsymbol{\varepsilon}, T, \boldsymbol{\alpha}) = e - Ts$ is a state function. With this potential in hand, the total dissipation (see Eq. 2.25) can be rewritten as :

$$\mathcal{D} = \boldsymbol{\sigma} : \dot{\boldsymbol{\varepsilon}} - \rho s\dot{T} - \rho\dot{\Psi} - \frac{\boldsymbol{q}}{T}.\mathbf{grad}(T) \geq 0 \tag{2.35}$$

and then for the intrinsic dissipation

$$\mathcal{D}_1 = \boldsymbol{\sigma} : \dot{\boldsymbol{\varepsilon}} - \rho s\dot{T} - \rho\dot{\Psi}. \tag{2.36}$$

[3]The Legendre transform (not to be confused with a Legendre-Fenchel one) of a function g is defined by $g^*(k) = kx_k - g(x_k)$ where x_k is determined by solving $g'(x_k) = k$

Moreover, the state laws, which provide the reversible part of the forces, read now:

$$\left\{\begin{array}{rcl} s & = & -\dfrac{\partial \Psi}{\partial T} \\ \boldsymbol{\sigma}^{rev} & = & \rho\dfrac{\partial \Psi}{\partial \boldsymbol{\varepsilon}} \\ \mathcal{A}^{rev} & = & \rho\dfrac{\partial \Psi}{\partial \boldsymbol{\alpha}} \end{array}\right. . \tag{2.37}$$

It follows then from (2.36) that

$$\mathcal{D}_1 = \left(\boldsymbol{\sigma} - \rho\frac{\partial \Psi}{\partial \boldsymbol{\varepsilon}}\right) : \dot{\boldsymbol{\varepsilon}} - \rho\frac{\partial \Psi}{\partial \boldsymbol{\alpha}} : \dot{\boldsymbol{\alpha}} \tag{2.38}$$

and must be positive according to the Clausius-Duhem inequality which becomes:

$$\mathcal{D}_1 = (\boldsymbol{\sigma} - \boldsymbol{\sigma}^{rev}) : \dot{\boldsymbol{\varepsilon}} - \mathcal{A}^{rev} : \dot{\boldsymbol{\alpha}} \geq 0. \tag{2.39}$$

In summary, one has

$$\mathcal{D}_1 = \boldsymbol{\sigma}^{irr} : \dot{\boldsymbol{\varepsilon}} + \mathcal{A}^{irr}.\dot{\boldsymbol{\alpha}} \geq 0 \quad \text{and} \quad \mathcal{D}_2 = -\frac{\boldsymbol{q}.\mathbf{grad}(T)}{T} \geq 0. \tag{2.40}$$

in which the irreversible forces $\boldsymbol{\sigma}^{irr}$ associated with the strain $\boldsymbol{\varepsilon}$ and $\mathcal{A}^{irr}$ to the internal variable $\boldsymbol{\alpha}$ are

$$\boldsymbol{\sigma}^{irr} = \boldsymbol{\sigma} - \boldsymbol{\sigma}^{rev} \quad ; \quad \mathcal{A}^{irr} = -\mathcal{A}^{rev} = -\rho\frac{\partial \Psi}{\partial \boldsymbol{\alpha}}, \tag{2.41}$$

Remark 3: In the case where the deformation $\boldsymbol{\varepsilon}$ is non dissipative (this is for instance the case of rate-independent models), $\boldsymbol{\sigma}^{irr} = 0$ and then

$$\boldsymbol{\sigma} = \boldsymbol{\sigma}^{rev} = \rho\frac{\partial \Psi}{\partial \boldsymbol{\varepsilon}} \tag{2.42}$$

For completeness, it must be mentioned that for a viscoelastic model such as the Kelvin-Voigt one for which $\boldsymbol{\varepsilon}$ is the unique variable, $\boldsymbol{\sigma}^{irr}$ is not null but given by (2.41).
The above formulations have mainly focused on the consideration of the internal energy $e(\boldsymbol{\varepsilon}, s, \alpha)$ or of the Helmholtz free energy $\Psi(\boldsymbol{\varepsilon}, T, \alpha)$. However, depending on the context of loadings imposed to the system (for instance stress-controlled loading), other state potentials can be considered.
A summary of the most usual potentials are given in the following table.

Internal energy	Helmholtz free energy	Enthalpy	Gibbs free energy
$e = e(\boldsymbol{\varepsilon}, s, \alpha)$	$\Psi = \Psi(\boldsymbol{\varepsilon}, T, \alpha)$	$h = h(\boldsymbol{\sigma}, s, \alpha)$	$g = g(\boldsymbol{\sigma}, T, \alpha)$
	$\Psi = e - Ts$	$h = e - \frac{1}{\rho}\boldsymbol{\sigma} : \boldsymbol{\varepsilon}$	$g = h - Ts$ $= \Psi - \frac{1}{\rho}\boldsymbol{\sigma} : \boldsymbol{\varepsilon}$
$\boldsymbol{\sigma}^{rev} = \rho\frac{\partial e}{\partial \boldsymbol{\varepsilon}}$	$\boldsymbol{\sigma}^{rev} = \rho\frac{\partial \Psi}{\partial \boldsymbol{\varepsilon}}$	$\boldsymbol{\varepsilon} = -\rho\frac{\partial h}{\partial \boldsymbol{\sigma}}$	$\boldsymbol{\varepsilon} = -\rho\frac{\partial g}{\partial \boldsymbol{\sigma}}$
$T = \frac{\partial e}{\partial s}$	$s = -\frac{\partial \Psi}{\partial T}$	$T = \frac{\partial h}{\partial s}$	$s = -\frac{\partial h}{\partial T}$
$\mathcal{A}_\alpha^{rev} = \rho\frac{\partial e}{\partial \alpha}$	$\mathcal{A}_\alpha^{rev} = \rho\frac{\partial \Psi}{\partial \alpha}$	$\mathcal{A}_\alpha^{rev} = \rho\frac{\partial h}{\partial \alpha}$	$\mathcal{A}_\alpha^{rev} = \rho\frac{\partial h}{\partial \alpha}$

Different energies and of their links through the Legendre transform.

Enthalpy $h = e - \frac{\partial e}{\partial \boldsymbol{\varepsilon}} : \boldsymbol{\varepsilon}$ is the partial Legendre transform of $-e$ with respect to $\boldsymbol{\varepsilon}$ while the Gibbs free energy g is that of h with respect to s or of Ψ with respect to $\boldsymbol{\varepsilon}$.

2.3.2 Complementary evolution laws

The matter presented in (2.3.1) does not provide any information about the evolution of the internal variables. This calls for the search of complementary laws. In fact, such question goes back to Lord Rayleigh (1873, 1877) who introduced a concept of dissipation function for problems involving viscous fluids. Later, and for systems fluctuating near equilibrium, Lars Onsager [L., 1931] postulates linear relationships between thermodynamics irreversible forces and fluxes (of state variables)[4]:

$$\mathcal{F} = \boldsymbol{L}\dot{\boldsymbol{\chi}} \tag{2.43}$$

Satisfaction of the celebrated Onsager's symmetry (reciprocity) relations by $\boldsymbol{L}$ allows to comply with the Clausius-Duhem inequality. Relation (2.43) can be also expressed by means of the notion of quadratic dissipation potential D as introduced by Thomson, such that:

$$\mathcal{F} = \frac{\partial D}{\partial \dot{\boldsymbol{\chi}}} \qquad with \qquad D = \frac{1}{2}\dot{\boldsymbol{\chi}}.\boldsymbol{L}.\dot{\boldsymbol{\chi}} \tag{2.44}$$

Fourier law for heat conduction constitutes an example of such a linear relation.

[4] *In the context presented here,* $\dot{\boldsymbol{\chi}}$ *represents* $(\boldsymbol{\varepsilon}, T, \alpha)$

It is clear that in a general context, the evolution of the internal variables will rather require the introduction of a non quadratic dissipation potential instead of linear relations.
A more general approach consists in introducing the hypothesis of normal dissipativity (see [Moreau, 1970] [Germain, 1973]) which assumes that there exists a dissipation potential $\Phi(\dot{\chi})$ which is convex, positive scalar-valued and minimal for $\dot{\boldsymbol{\chi}} = 0$, such that:

$$\mathcal{F} = \frac{\partial \Phi}{\partial \dot{\boldsymbol{\chi}}} \tag{2.45}$$

Such definition of irreversible forces with the properties required for Φ automatically guarantees the satisfaction of the Clausius-Duhem inequality.

2.4 Thermoelasticity as a first basic example

Linear thermoelasticity can be viewed as a first example of a constitutive law which couples elasticity to thermal dissipation. Energetic formulation of the coupled theory of thermoelasticity goes back to Biot [Biot, 1956] based on the Thermodynamics of Irreversible Processes (see the comprehensive textbook of W. Nowacki [Nowacki, 1986]).
The main purpose of this section is to present in a classical manner the coupled thermoelastic behaviour according to the thermodynamics-based formalism introduced before. Infinitesimal transformations around a natural initial state will be considered, by focusing on the case of small variations temperature.

2.4.1 Linear thermoelastic behaviour

Thermal conduction constitutes the unique source of dissipation in thermoelastic materials. This class of materials is therefore entirely characterised by a free energy for the reversible behavior and a heat dissipation potential which may account for the conduction law.
Starting from $\Psi(\boldsymbol{\varepsilon}, T)$ the state laws reduce to :

$$\boldsymbol{\sigma}^{rev} = \rho_0 \frac{\partial \Psi(\boldsymbol{\varepsilon}, T)}{\partial \boldsymbol{\varepsilon}} \qquad \text{et} \qquad s = -\frac{\partial \Psi(\boldsymbol{\varepsilon}, T)}{\partial T} \tag{2.46}$$

The intrinsic dissipation $\mathcal{D} = (\boldsymbol{\sigma} - \boldsymbol{\sigma}^{rev}) : \dot{\boldsymbol{\varepsilon}}$ being null for any $\dot{\boldsymbol{\varepsilon}}$, one readily gets :

$$\boldsymbol{\sigma} = \boldsymbol{\sigma}^{rev} \tag{2.47}$$

The formulation of linear thermoelasticity under small perturbations (including small variation of temperature) requires a classical linearization procedure which consists in expressing the state laws in the vicinity of the initial state

by replacing equations (2.46) by their first-order expansion with respect to the deformation ((**ε** = 0) and to ($\tau = T - T0$). One gets then:

$$\left\{ \begin{array}{rcl} \boldsymbol{\sigma}(\boldsymbol{\varepsilon}, T) & = & \rho_0 \frac{\partial \Psi(0,T_0)}{\partial \boldsymbol{\varepsilon}} + \rho_0 \frac{\partial^2 \Psi(0,T_0)}{\partial \boldsymbol{\varepsilon} \partial \boldsymbol{\varepsilon}} : \boldsymbol{\varepsilon} + \rho_0 \frac{\partial^2 Psi(0,T_0)}{\partial \boldsymbol{\varepsilon} \partial T} \tau \\ \\ s & = & -\rho_0 \frac{\partial \Psi(0,T_0)}{\partial T} - \rho_0 \frac{\partial^2 \Psi(0,T_0)}{\partial T \partial \boldsymbol{\varepsilon}} : \boldsymbol{\varepsilon} - \rho_0 \frac{\partial^2 \Psi(0,T_0)}{\partial T^2} \tau \end{array} \right. \tag{2.48}$$

which reads

$$\left\{ \begin{array}{rcl} \boldsymbol{\sigma}(\boldsymbol{\varepsilon}, T) & = & \boldsymbol{\sigma}_0 + \mathbb{C} : \boldsymbol{\varepsilon} - \boldsymbol{\beta} \tau \\ \\ s & = & s_0 + \frac{\boldsymbol{\beta}}{\rho} : \boldsymbol{\varepsilon} + \rho_0 c_\epsilon \tau \end{array} \right. \tag{2.49}$$

for which the following notations are adopted:

$$\rho_0 \frac{\partial \Psi(0,T_0)}{\partial \boldsymbol{\varepsilon}} = \boldsymbol{\sigma}_0 \qquad \text{and} \qquad -\rho_0 \frac{\partial \Psi(0,T_0)}{\partial T} = s_0$$

as well as :

$$\mathbb{C} = \rho_0 \frac{\partial^2 \Psi(0,T_0)}{\partial \boldsymbol{\varepsilon} \partial \boldsymbol{\varepsilon}}, \quad \boldsymbol{\beta} = -\rho_0 \frac{\partial^2 \Psi(0,T_0)}{\partial T \partial \boldsymbol{\varepsilon}} \qquad \text{and} \quad \rho_0 c_\epsilon = -T_0 \frac{\partial^2 \Psi(0,T_0)}{\partial T^2}$$

$\mathbb{C}$ is the elasticity tensor, c_ϵ is the specific heat capacity, $\boldsymbol{\beta}$ is the thermoelastic coefficient tensor.
The above set of equations must be completed by a thermal conduction law which characterizes the thermal dissipation. The Fourier's law is generally adopted:

$$\boldsymbol{q} = -\boldsymbol{K}.\boldsymbol{\nabla T} \tag{2.50}$$

where $\boldsymbol{K}$ is the thermal conductivity tensor specific to the material under consideration and dependent on the initial state. It is non-negative and symmetric,

$$K_{ij} = K_{ji} \tag{2.51}$$

It can be easily verified that these state laws (Eq. (2.49)) derive from the following Helmholtz free energy[5]:

$$\rho Psi\left(\boldsymbol{\varepsilon}, T\right) = \frac{1}{2} \boldsymbol{\varepsilon} : \mathbb{C} : \boldsymbol{\varepsilon} - \boldsymbol{\beta} : \boldsymbol{\varepsilon} (T - T_0) - \frac{\rho c_\epsilon}{2T_0} (T - T_0)^2 \tag{2.52}$$

In the usual case of isotropic thermoelastic materials, this energy potential is expressed as:

$$\rho_0 \Psi\left(\boldsymbol{\varepsilon}, T\right) = \frac{1}{2} \lambda (tr\ \boldsymbol{\varepsilon})^2 + \mu \boldsymbol{\varepsilon} : \boldsymbol{\varepsilon} - \beta (T - T_0)(tr \boldsymbol{\varepsilon}) - \frac{\rho_0 c_\epsilon}{2T_0} (T - T_0)^2 \tag{2.53}$$

[5]This free energy density (2.52) can be also rewritten as

$$\rho_0 \Psi\left(\boldsymbol{\varepsilon}, T\right) = \frac{1}{2} \left(\boldsymbol{\varepsilon} - \boldsymbol{\alpha}(T - T_0)\right) : \mathbb{C} : \left(\boldsymbol{\varepsilon} - \boldsymbol{\alpha}(T - T_0)\right) - \frac{\rho_0 c_\epsilon}{2T_0} (1 + \chi)(T - T_0)^2$$

in which $\boldsymbol{\alpha} = \mathbb{C}^{-1} : \boldsymbol{\beta}$ *and* $\chi = \frac{\boldsymbol{\alpha} : \mathbb{C} : \boldsymbol{\alpha}}{\rho_0 c_\epsilon} T_0 = \frac{\boldsymbol{\alpha} : \boldsymbol{\beta}}{\rho_0 c_\epsilon} T_0$

which provides the following state laws.

$$\left\{\begin{array}{rcl} \boldsymbol{\sigma} & = & \lambda(tr\,\boldsymbol{\varepsilon})\mathbf{1} + 2\mu\boldsymbol{\varepsilon} - \beta(T-T_0)\mathbf{1} \\ s & = & \frac{\beta}{\rho_0}(tr\boldsymbol{\varepsilon}) + \frac{c_\epsilon}{T_0}(T-T_0) \end{array}\right. \tag{2.54}$$

where $\boldsymbol{\beta} = \beta\mathbf{1}$ for the isotropic ma terial.
The above linearized thermoelastic theory can be directly extended to the context of finite variations of temperature. In this case, the free energy, generalizing (2.53) reads (see for instance [Maitournam, 2012]:

$$\rho_0\Psi(\boldsymbol{\varepsilon},T) = \frac{1}{2}\lambda(tr\boldsymbol{\varepsilon})^2 + \mu\boldsymbol{\varepsilon}:\boldsymbol{\varepsilon} - \beta(T-T_0)(tr\boldsymbol{\varepsilon}) - \frac{\rho_0 c_\epsilon}{T}(ln\frac{T}{T_0} - 1 + \frac{T_0}{T}) \tag{2.55}$$

which only leads to the modification of the second state law in (2.54)

2.4.2 Heat equations - Thermoelastic evolution

The field equations of the thermoelastic evolution problem include the conservation laws and the constitutive relations. We aim at establishing here the heat equations.
In the context of small perturbations, the mass conservation equation reads :

$$\rho = \rho_0(1 - div\,\boldsymbol{\xi}) \tag{2.56}$$

where $\boldsymbol{\xi}$ is the displacement field. In the following, we will take $\rho \approx \rho_0$.
The starting point for the derivation of the heat equation here is Eq. (2.26) in which one may consider that in the thermoelasticity case the intrinsic dissipation ($\mathcal{D}_1$) is null. Applying the Fourier law $\boldsymbol{q} = -\boldsymbol{K}.\boldsymbol{\nabla T}$ (in which $\boldsymbol{K}$ is the thermal conductivity tensor), it follows that:

$$\underline{div}\,(-\boldsymbol{K}.\boldsymbol{\nabla T}) + \rho_0 T\dot{s} = r \tag{2.57}$$

Taking advantage of the expression (2.49)b for entropy, one gets:

$$\underline{div}\,(-\boldsymbol{K}.\boldsymbol{\nabla T}) + T_0\boldsymbol{\beta}:\dot{\boldsymbol{\varepsilon}} + \rho_0 c_\epsilon\dot{T} = r \tag{2.58}$$

which is known as the heat equation and can be also put in the form:

$$\underline{div}\,(\boldsymbol{K}.\boldsymbol{\nabla T}) + r = T_0\boldsymbol{\beta}:\dot{\boldsymbol{\varepsilon}} + \rho_0 c_\epsilon\dot{T} \tag{2.59}$$

In addition to these equations, there are the compatibility equations (relations between deformations and displacements), the thermoelastic constitutive law, the initial and boundary conditions. Denoting $\tau = T - T_0$, the resulting equations to be solved read in the homogeneous isotropic case:

$$(\lambda+\mu)\mathrm{grad}(\mathrm{div}\,\boldsymbol{\xi}) + \mu\Delta\boldsymbol{\xi} + \rho\boldsymbol{f} - \beta\mathrm{grad}\,\tau = \rho_0\frac{\partial^2\boldsymbol{\xi}}{\partial t^2} \tag{2.60}$$

together with

$$k\Delta T - \rho_0 c_\epsilon \dot{T} - T_0 \beta div\dot{\boldsymbol{\xi}} = -r \tag{2.61}$$

For completeness, mention must be made of variational formulation of coupled thermoelasticity problems. Some early references in this field are [Biot, 1955], [Ben-Amoz, 1965], [Herrmann, 1963]. More recently [Yang et al., 2006], [Stainier, 2013] established variationnal principles for more general thermomechanical couplings.

2.5 Generalized Standard Materials framework

A constitutive model of generalized standard material (GSM) is defined by means of two potentials, the thermodynamics state potential and the dissipation potential. The thermodynamics potential is a function of state variables, while the dissipation potential is a convex function of their fluxes[6].

In addition to the identification of the appropriate state variables, one may

- **identify an energy potential**. Classically, an Helmholtz free energy $\Psi(\boldsymbol{\varepsilon}, T, \alpha)$ furnishes the state laws (2.37) which define the reversible forces associated to the state variables $(\boldsymbol{\varepsilon}, T, \alpha)$. This step allow to proceed to an analysis of dissipation, and then to identify the dissipative (irreversible) forces associated to each variable.

- **identify a dissipation potential** $\Phi(\dot{\boldsymbol{\varepsilon}}, \dot{\boldsymbol{\alpha}})$ which may allow to retrieve the irreversible forces through the complementary relations. For instance for the internal variables, one has:

$$\mathcal{A}_\alpha \;=\; \frac{\partial \Phi}{\partial \dot{\boldsymbol{\alpha}}}(\dot{\boldsymbol{\varepsilon}}, \dot{\boldsymbol{\alpha}}) \tag{2.62}$$

  In the case where the potential Φ is not differentiable (in this case Φ is denoted as a pseudo potential), one should refer to the notion of subdifferential $\partial\Phi$.
  The evolution laws then take the form :

$$\mathcal{A}_\alpha \;\in\; \partial\Phi(\dot{\boldsymbol{\varepsilon}}, \dot{\boldsymbol{\alpha}}) \tag{2.63}$$

  $\mathcal{A}_\alpha$ is said to belong to the sub-gradient of Φ at the considered point.

[6] *An extended version of this GSM framework consists in possibly including state variables in the dissipation potential as parameters (and not arguments) accounting for the present state.*

In general, by definition, the irreversible forces $\boldsymbol{\sigma}^{irr}$ and $\mathcal{A}_\alpha$ belong to the sub-gradient of Φ at $(\dot{\boldsymbol{\varepsilon}}, \dot{\boldsymbol{\alpha}})$ if for any rate $\boldsymbol{\varepsilon}^*$ and one has:

$$\Phi(\dot{\boldsymbol{\varepsilon}}, \dot{\boldsymbol{\alpha}}) - \Phi(\boldsymbol{\varepsilon}^*, \boldsymbol{\alpha}^*) + \boldsymbol{\sigma}^{irr} : (\boldsymbol{\varepsilon}^* - \dot{\boldsymbol{\varepsilon}}) + \mathcal{A}_\alpha(\boldsymbol{\alpha}^* - \dot{\boldsymbol{\alpha}}) \leq 0 \tag{2.64}$$

This is the so-called normality rule.

Equivalently, and coming back to the case where the deformation is not a dissipative variable, the evolution law (2.63) can be obtained by means of the dual potential $\Phi^*(\mathcal{A}_\alpha)$, through the normality rule:

$$\dot{\boldsymbol{\alpha}} \in \partial\Phi^*(\mathcal{A}_\alpha) \tag{2.65}$$

The dual potential $\Phi^*(\mathcal{A}_\alpha) = \sup_{\dot{\boldsymbol{\alpha}}>0} \{\mathcal{A}_\alpha \dot{\boldsymbol{\alpha}} - \Phi(\dot{\boldsymbol{\alpha}})\}$ is the Legendre–Fenchel transform of Φ.

For rate-independent models, it is classically shown that a convex function f exists such that :

$$\Phi^*(\mathcal{A}_\alpha) = \begin{cases} 0 & \text{if} \quad f(\mathcal{A}_\alpha) \leq 0 \\ \infty & \text{otherwise} \end{cases} \tag{2.66}$$

which is the indicator function of a convex domain $\mathcal{C}$ defined by :

$$\mathcal{C} = \{\mathcal{A}_\alpha / f(\mathcal{A}_\alpha) \leq 0\} \tag{2.67}$$

$f(\mathcal{A}) \leq 0$ defines the domain of elasticity.

From (2.37) and (2.62), in the case where the deformation is non dissipative, the constitutive equations of the GSM, can be summarized as:

$$\boldsymbol{\sigma} = \frac{\partial \Psi}{\partial \boldsymbol{\varepsilon}}(\boldsymbol{\varepsilon}, \boldsymbol{\alpha}), \qquad \frac{\partial \Psi}{\partial \boldsymbol{\alpha}}(\boldsymbol{\varepsilon}, \boldsymbol{\alpha}) + \frac{\partial \Phi}{\partial \dot{\boldsymbol{\alpha}}}(\dot{\boldsymbol{\alpha}}) = 0 \tag{2.68}$$

The second equation in (2.68) is known as the Biot equation (see [Biot, 1965] well quoted in chapter 15 of [Nguyen, 2000], or in [Stolz, 2004])[7] in reference to a series of works conducted by Biot including viscoelasticity. The reader can also found in [Biot, 1970] the use of such type of mathematical structure for the derivation of variationnal principles in heat transfer problems.

Equation (2.68) constitutes a set of equations which, together with the normality rule (see Eq. (2.64)), allow to establish a variational formulation for problems involving standard dissipative models (see Section (2.8)).

[7] An interesting study of Biot equation in link with quasi-static stability analysis can be found in [Abed-Meraim and Nguyen, 2007]

2.6 Rate-independent elastoplasticity

We aim here at formulating elastoplastic models as well as coupled elasticity-damage laws by taking advantage of GSM framework. Although the corresponding constitutive laws are different in nature, they can be essentialy described by means of a phenomenological approach based on thermodynamics with internal variables. These constitutive laws are generally based on experimental mechanical tests which make it possible to identify and characterize the appropriate deformation mechanisms and the relevant physical quantities. The procedure already presented in section (2.5) will be systematically followed and, as already stated, will mainly consists in identification of the relevant state variables, of the thermodynamics potential for the reversible part of the constitutive law and of the dissipation potential (or equivalently the dual potential) for the evolution laws. For simplicity, and as before, assumption of small perturbations and isothermal conditions are adopted.

2.6.1 Formulation of perfect elastoplastic models

Although the presentation will concern 3D formulation of elastoplastic models, in order to fix ideas, consider a quasi-static uniaxial test consisting of tension followed by compression. The resulting tension-compression curve is shown on figure (2.1). In the case of perfect elastoplastic behavior, a remarkable point is that the absolute value of the applied uniaxial stress σ cannot exceed a characteristic constant σ_0. Moreover, an unloading of the material exhibits a linear behavior (BD) with a permanent (plastic) strain at $\sigma = 0$ Such type of observations applies also for multiaxial tests conditions (e.g. tension-torsion): existence of a plastic strain and of an elasticity domain.

In agreement with the above comments, the mechanical state variables are therefore the total deformation $\boldsymbol{\varepsilon}$ and the plastic deformation $\boldsymbol{\varepsilon}^p$ which will allow to describe the inelastic and irreversible phenomena. The following partition holds

$$\boldsymbol{\varepsilon} = \boldsymbol{\varepsilon}^e + \boldsymbol{\varepsilon}^p$$

The thermodynamics potential
It is in the form of a Helmholtz free energy, given by :

$$\rho_0 \Psi(\boldsymbol{\varepsilon}, \boldsymbol{\varepsilon}^p) = \frac{1}{2}(\boldsymbol{\varepsilon} - \boldsymbol{\varepsilon}^p) : \mathbb{C} : (\boldsymbol{\varepsilon} - \boldsymbol{\varepsilon}^p)$$

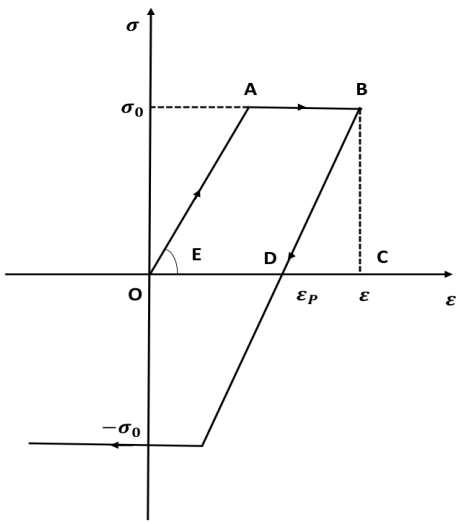

FIGURE 2.1: Response of an elastic-perfectly plastic material under tension followed by a compression

from which one deduces the state laws:

$$\begin{cases} \boldsymbol{\sigma}^{rev} = \rho_0 \frac{\partial \Psi(\boldsymbol{\varepsilon},\boldsymbol{\varepsilon}^p)}{\partial \boldsymbol{\varepsilon}} = \mathbb{C} : (\boldsymbol{\varepsilon} - \boldsymbol{\varepsilon}^p) \\ \mathcal{A}^{rev} = -\rho_0 \frac{\partial \Psi(\boldsymbol{\varepsilon},\boldsymbol{\varepsilon}^p)}{\partial \boldsymbol{\varepsilon}^p} = -\mathbb{C} : (\boldsymbol{\varepsilon} - \boldsymbol{\varepsilon}^p) \end{cases} \tag{2.69}$$

$\mathcal{A}^{rev}$ represents the reversible part associated to the plastic deformation.
Analysis of the intrinsic dissipation, as described in Section (2.3.1), allows to obtain the irreversible forces associated with the total deformation and with the plastic strain, respectively

$$\boldsymbol{\sigma}^{irr} = 0; \qquad \mathbf{A} = \mathbf{A}^{irr} = -\mathbf{A}^{rev} = \mathbb{C} : (\boldsymbol{\varepsilon} - \boldsymbol{\varepsilon}^p) = \boldsymbol{\sigma}$$

.
Interestingly, $\boldsymbol{\sigma}$ appears as the thermodynamics irreversible forces associated with the plastic strain tensor $\boldsymbol{\varepsilon}^p$. Therefore, evolution of the plastic strain tensor will depend on $\boldsymbol{\sigma}$.

The plastic dissipation potential $\Phi(\dot{\boldsymbol{\varepsilon}}^p)$
First of all, let us recall, as already stated, that the evolution law is equivalently given by a plastic dissipation potential $\Phi(\dot{\boldsymbol{\varepsilon}}^p)$ or by its dual $\Phi^*(\boldsymbol{\sigma})$ which is obtained as its Legendre-Fenchel transform. Starting with the dissipation potential, it must be chosen convex, scalar positive-valued and minimum (in fact null) for $\dot{\boldsymbol{\varepsilon}}^p = 0$. The so-called normality rule (see Eq. (2.63)) is then expressed as

$$\boldsymbol{\sigma} \in \partial\Phi(\dot{\boldsymbol{\varepsilon}}^p). \tag{2.70}$$

Alternatively, the dual dissipation potential is given by :

$$\Phi^*(\boldsymbol{\sigma}) = \sup_{\dot{\boldsymbol{\varepsilon}}^p}(\boldsymbol{\sigma} : \dot{\boldsymbol{\varepsilon}}^p - \Phi(\dot{\boldsymbol{\varepsilon}}^p))$$

Following (2.71), the plastic strain rate, obtained by normality rule reads then

$$\dot{\boldsymbol{\varepsilon}}^p \in \partial\Phi^*(\boldsymbol{\sigma}) \tag{2.71}$$

that is $\dot{\boldsymbol{\varepsilon}}^p$ belongs to the sub-gradient of $\Phi^*(\boldsymbol{\sigma})$.

For rate-independent models, such us the one studied here for perfect elasto-plasticity, a general result is that the dual potential $\Phi^*(\boldsymbol{\sigma})$ is the indicator function of a convex admissible domain

$$\mathcal{C} = \{\boldsymbol{\sigma} \qquad \text{such that} \qquad f(\boldsymbol{\sigma}) \leq 0\}$$

$f(\boldsymbol{\sigma})$, called yield function, defines the elastic domain. Therefore, one has

$$\Phi^*(\boldsymbol{\sigma}) = I_C(\boldsymbol{\sigma}) = \left\{ \begin{array}{ccc} 0 & \text{if} & \boldsymbol{\sigma} \in \mathcal{C} \\ +\infty & \text{if} & \boldsymbol{\sigma} \notin \mathcal{C} \end{array} \right. \tag{2.72}$$

For the detailed computation of the plastic strain rate $\dot{\boldsymbol{\varepsilon}}^p$ (see Eq. (2.71)), a classical mathematical result for the indicator function is

$$\partial\Phi^* = \left\{ \begin{array}{lll} \emptyset & \text{if} & \boldsymbol{\sigma} \notin \mathcal{C} \\ \{0\} & \text{if} & \boldsymbol{\sigma} \in \mathring{\mathcal{C}} \quad \text{(inside of } \mathcal{C}\text{)} \\ \mathcal{N}_{\mathcal{C}}(\boldsymbol{\sigma}) & \text{if} & \boldsymbol{\sigma} \in \partial\mathcal{C} \quad \text{(at the boundary of } \mathcal{C}\text{)} \end{array} \right. \tag{2.73}$$

The cone of normals is defined, at a regular point on the boundary, by :

$$\mathcal{N}_{\mathcal{C}}(\boldsymbol{\sigma}) = \left\{ \dot{\boldsymbol{\varepsilon}}^p \quad \text{such as} \quad \dot{\boldsymbol{\varepsilon}}^p = \dot{\lambda}\frac{\partial f}{\partial \boldsymbol{\sigma}}, \dot{\lambda} \geq 0 \right\} \tag{2.74}$$

in which $\dot{\lambda}$ is a positive scalar called plastic multiplier. At a singular point, one has:

$$\mathcal{N}_{\mathcal{C}}(\boldsymbol{\sigma}) = \{\dot{\boldsymbol{\varepsilon}}^p \quad \text{such as} \quad \dot{\boldsymbol{\varepsilon}}^p : (\boldsymbol{\sigma}^* - \boldsymbol{\sigma}) \leq 0, \forall \boldsymbol{\sigma}^* \in \mathcal{C}\}\,. \tag{2.75}$$

Brief summary: The perfect elastoplastic model is entirely defined by means of the two potentials:

- the Helmholtz free energy $\rho_0\Psi(\boldsymbol{\varepsilon}, \boldsymbol{\varepsilon}^p)$
- and the dissipation potential $\Phi(\dot{\boldsymbol{\varepsilon}}^p)$ or equivalently its dual $\Phi^*(\boldsymbol{\sigma})$ or the corresponding yield function $f(\boldsymbol{\sigma})$

Taking advantage of the partition of the deformation (see (2.6.1)), the perfect elastoplastic constitutive law is expressed as:

$$\dot{\boldsymbol{\varepsilon}} = \dot{\boldsymbol{\varepsilon}^e} + \dot{\boldsymbol{\varepsilon}^p} = \mathbb{S} : \dot{\boldsymbol{\sigma}} + \dot{\boldsymbol{\varepsilon}}^p. \tag{2.76}$$

for which $\dot{\boldsymbol{\varepsilon}}^p$ is given by the evolution equations, that is (2.74) together with (2.75).

2.6.2 Case of a Drucker-Prager elastoplastic material

As an illustration, let us consider the case of elastoplastic materials whose plastic regime is described by means of the so-called Drucker-Prager criterion [Drucker and Prager, 1952]

$$f(\boldsymbol{\sigma}) = \sigma_{eq} + \alpha tr(\boldsymbol{\sigma}) - \sigma_0 \leq 0 \tag{2.77}$$

The equivalent von Mises stress $\sigma_{eq} = \sqrt{\frac{3}{2}\boldsymbol{s} : \boldsymbol{s}}$ is defined by means of the deviatoric part of the stress tensor $\boldsymbol{s} = \boldsymbol{\sigma} - \frac{1}{3}tr(\boldsymbol{\sigma})\mathbf{1}$.
(2.77) defines a domain of reversibility

$$\mathcal{C} = \{\boldsymbol{\sigma} \quad \text{such as} \quad f(\boldsymbol{\sigma}) \leq 0\}$$

whose indicator function

$$\Phi^*(\boldsymbol{\sigma}) = \begin{cases} 0 & \text{if} \quad \boldsymbol{\sigma} \in \mathcal{C} \\ \\ \infty & otherwise \end{cases} \tag{2.78}$$

corresponds to the dual potential.
Since the Drucker-Prager criterion (Eq. (2.77)) depends on the hydrostatic part of the stress tensor, it is usually considered for materials which exhibit plastic volume changes such us geomaterials (rocks, concrete), powders, polymers, and even some metals (see for instance [Wilson, 2002]), etc..
In addition to its own interest, the Drucker-Prager criterion constitutes also a generalization of the well-known von Mises criterion which is retrieved (including for the dual potential and the dissipation potential) as a limiting case when $\alpha \to 0$.
In order to build the dissipation potential corresponding to the Drucker-Prager material, $\Phi(\dot{\boldsymbol{\varepsilon}}^p)$, one may start from the dual potential $\Phi^*(\boldsymbol{\sigma})$ and compute its Legendre Fenchel transform:

$$\Phi(\dot{\boldsymbol{\varepsilon}}^p) = \sup_{\boldsymbol{\xi}\sigma \in \mathcal{C}} \{\boldsymbol{\sigma} : \dot{\boldsymbol{\varepsilon}}^p - \Phi^*(\boldsymbol{\sigma})\} = \sup_{\boldsymbol{\sigma} \in \mathcal{C}} \{\boldsymbol{\sigma} : \dot{\boldsymbol{\varepsilon}}^p\}$$

Based on (2.77), and denoting

$$\dot{\varepsilon}^p_m = \frac{1}{3} tr\, \dot{\boldsymbol{\varepsilon}}^p, \quad and \quad \dot{\varepsilon^p}_{eq} = \sqrt{\frac{2}{3}\dot{\boldsymbol{\varepsilon}}^p_d : \dot{\boldsymbol{\varepsilon}}^p_d}$$

with $\boldsymbol{\varepsilon}^p_d$ the deviatoric part of $\boldsymbol{\varepsilon}^p$, it can be shown that (see proof in Appendix)

$$\Phi(\dot{\boldsymbol{\varepsilon}}^p) = \begin{cases} \frac{\sigma_0}{\alpha}\dot{\varepsilon}^p_m & \text{if} \quad \alpha\dot{\varepsilon}^p_{eq} - \dot{\varepsilon}^p_m \leq 0 \\ \\ \infty & otherwise \end{cases} \tag{2.79}$$

The condition $\alpha\dot{\varepsilon}^p_{eq} - \dot{\varepsilon}^p_m \leq 0$ is called the admissibility condition. $\dot{\varepsilon^p}_{eq}$ is known in metal plasticity as the equivalent plastic strain rate, while $\dot{\boldsymbol{\varepsilon}}^p_m$ represents

the volumetric plastic strain rate.
For completeness, one may express the normality rule which can be equivalently deduced from the dissipation potential (see Eq. (2.79)) or from the plasticity criterion. From the latter, (expressed by (2.77)), and on its regular part, one has:

$$\dot{\boldsymbol{\varepsilon}}^p = \dot{\lambda}\left(\frac{3}{2}\frac{\boldsymbol{s}}{\sigma_{eq}} + \alpha\mathbf{1}\right), \tag{2.80}$$

which clearly shows the existence of plastic dilatancy (plastic volume change) when $\alpha \neq 0$.
It is interesting to examine now the specialization of the above presentation to the particular case of perfect elastoplastic materials obeying to the well-known von Mises criterion. This corresponds to the case $\alpha \to 0$ for which (2.77) takes the form

$$f(\boldsymbol{\sigma}) = \sigma_{eq} - \sigma_0 \leq 0 \tag{2.81}$$

This leads to the usual flow rule in metal plasticity:

$$\dot{\boldsymbol{\varepsilon}}^p = \frac{3}{2}\dot{\lambda}\frac{\boldsymbol{s}}{\sigma_{eq}}, \qquad \dot{\lambda} \geq 0 \tag{2.82}$$

Interestingly, it can be shown (see also appendix) that the dissipation potential given by (2.79) reduces in the limit $\alpha \to 0$ to:

$$\Phi(\dot{\boldsymbol{\varepsilon}}^p) = \begin{cases} \sigma_0 \dot{\varepsilon}^p_{eq} & \text{if} \quad \dot{\varepsilon}^p_m = 0 \\ \\ \infty & \text{if} \quad \dot{\varepsilon}^p_m \neq 0 \end{cases} \tag{2.83}$$

which is a classical result in agreement with the plastic incompressibility of materials obeying to von Mises criterion.

2.6.3 Elastoplasticity with isotropic and linear kinematics hardening

For the formulation of elastoplastic constitutive models with hardening, we consider both isotropic and kinematic hardening. Restricting ourselves to Generalized Standard Materials (GSM), the latter is chosen in the form of a linear kinematic rule (Prager law), the non linear kinematics hardening law of Armstrong-Fredericks [Armstrong and Frederick, 1966] being excluded[8].

2.6.3.1 General formulation

We consider again an isothermal, quasi-static uniaxial test of tension followed by compression. The resulting tension-compression curve is shown on Figure 2.2 on which the yield stress depends on the plastic strain level. Response

[8] *For a brief discussion concerning this point, the reader can refer to [Bouby et al., 2015].*

of the elastoplastic material with isotropic hardening is schematized on Figure 2.2a, while Figure 2.2b corresponds to materials with linear kinematic hardening. In both cases, $\boldsymbol{\varepsilon}$ and $\boldsymbol{\varepsilon}^p$ are no longer sufficient to characterize the mechanical state and one may consider a new variable describing the hardening which results from specific microscopic mechanisms.

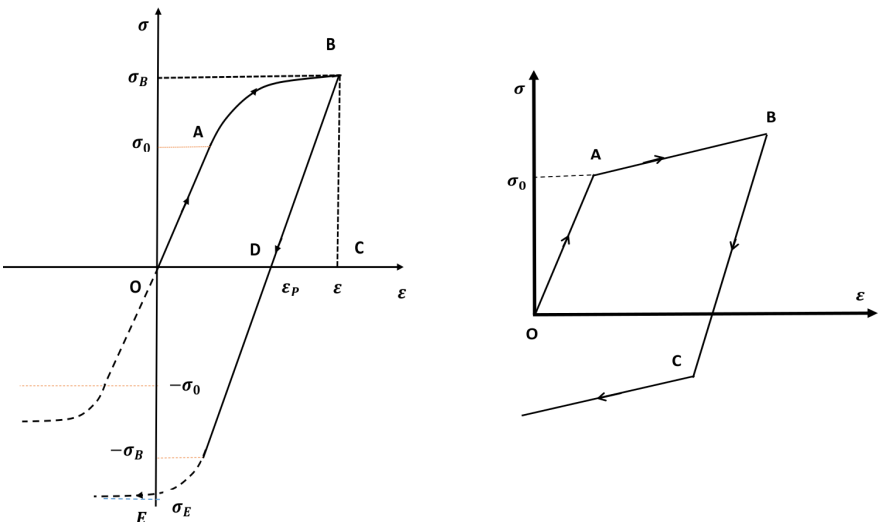

FIGURE 2.2: Elastoplastic material under uniaxial tension followed by compression : a) case of an isotropic hardening; b) case of a linear kinematic strain hardening

For isotropic hardening, the elasticity domain increases in size while remaining symmetric with respect to the origin. This will be therefore accounted for by means a single scalar variable, denoted β and whose mechanical signification will be given below (see Eq.(2.93)).
In the case of kinematic hardening, the elasticity domain exhibits a translation phenomenon without change of shape (as also confirmed by experiments for multiaxial loadings state) which depends on the plastic strain. Roughly speaking, the material is said to have linear kinematic strain hardening when the elastoplastic part of the uniaxial tensile curve is linear.
Having in mind the above hardening phenomena, the state variables are chosen without loss of generality as ($\boldsymbol{\varepsilon}$, $\boldsymbol{\varepsilon}^p$, β).

Therefore, the thermodynamic potential (Helmholtz free energy) reads :

$$\rho_0 \Psi(\boldsymbol{\varepsilon}, \boldsymbol{\varepsilon}^p, \beta) = \frac{1}{2}(\boldsymbol{\varepsilon} - \boldsymbol{\varepsilon}^p) : \mathbb{C} : (\boldsymbol{\varepsilon} - \boldsymbol{\varepsilon}^p) + \rho_0 \Psi^s(\boldsymbol{\varepsilon}^p, \beta) \tag{2.84}$$

in which $\rho_0\Psi^s(\boldsymbol{\varepsilon}^p,\beta)$ represents the stored energy due to hardening, while $\frac{1}{2}(\boldsymbol{\varepsilon}-\boldsymbol{\varepsilon}^p):\mathbb{C}:(\boldsymbol{\varepsilon}-\boldsymbol{\varepsilon}^p)$ is the part of the free energy which is recoverable by an elastic unloading.
From this potential, the state laws, delivering the reversible forces, read:

$$\left\{\begin{array}{lcl} \boldsymbol{\sigma}^{rev} &=& \rho_0\frac{\partial\Psi(\boldsymbol{\varepsilon},\boldsymbol{\varepsilon}^p,\beta)}{\partial\boldsymbol{\varepsilon}} = \mathbb{C}:(\boldsymbol{\varepsilon}-\boldsymbol{\varepsilon}^p) \\ \boldsymbol{A}^{rev}_{\boldsymbol{\varepsilon}^p} &=& \rho_0\frac{\partial\Psi(\boldsymbol{\varepsilon},\boldsymbol{\varepsilon}^p)}{\partial\boldsymbol{\varepsilon}^p} = -\mathbb{C}:(\boldsymbol{\varepsilon}-\boldsymbol{\varepsilon}^p)+\frac{\partial\Psi^s(\boldsymbol{\varepsilon}^p,\beta)}{\partial\boldsymbol{\varepsilon}^p} \\ \mathcal{A}^{rev}_{\beta} &=& \rho_0\frac{\partial\Psi(\boldsymbol{\varepsilon},\boldsymbol{\varepsilon}^p,\beta)}{\partial p} = \frac{\partial\Psi^s(\boldsymbol{\varepsilon}^p,\beta)}{\partial\beta} \end{array}\right. \tag{2.85}$$

Analysis of the intrinsic dissipation, and considering that $\boldsymbol{\varepsilon}$ is not a dissipative variable, leads to

$$\boldsymbol{\sigma}=\boldsymbol{\sigma}^{rev}=\mathbb{C}:(\boldsymbol{\varepsilon}-\boldsymbol{\varepsilon}^p)$$

and then to the following expression of the intrinsic dissipation

$$\mathcal{D}_1(\dot{\boldsymbol{\varepsilon}}^p,\dot{\beta})=\boldsymbol{A}_{\boldsymbol{\varepsilon}^p}:\dot{\boldsymbol{\varepsilon}}^p+\mathcal{A}_\beta\dot{\beta}$$

in which the irreversible forces are

$$\left\{\begin{array}{lcl} \boldsymbol{A}^{irr}_{\boldsymbol{\varepsilon}^p} &=& -\boldsymbol{A}^{rev}_{\boldsymbol{\varepsilon}^p} = \mathbb{C}:(\boldsymbol{\varepsilon}-\boldsymbol{\varepsilon}^p)-\boldsymbol{X} = \boldsymbol{\sigma}-\boldsymbol{X} \\ \mathbf{A}^{irr}_{\beta} &=& -\mathbf{A}^{rev}_{\beta} = -\frac{\partial\Psi^s(\boldsymbol{\varepsilon}^p,\beta)}{\partial\beta} \end{array}\right. \tag{2.86}$$

with the notation $\boldsymbol{X}=\frac{\partial\Psi^s(\boldsymbol{\varepsilon}^p,\beta)}{\partial\boldsymbol{\varepsilon}^p}$ which is known as the back stress.
Again, to simplify the writing, the two irreversible forces will be denoted $\boldsymbol{A}_{\boldsymbol{\varepsilon}^p}$ and $\mathbf{A}_\beta$. Now, for the determination of the complementary laws, a dual potential can be introduced as the indicator function of the elasticity domain

$$\mathcal{C}=\{(\boldsymbol{A}_{\boldsymbol{\varepsilon}^p},\mathbf{A}_\beta) \quad \text{such as} \quad f(\boldsymbol{A}_{\boldsymbol{\varepsilon}^p},\mathbf{A}_\beta)\leq 0\}$$

$f(\boldsymbol{A}_{\boldsymbol{\varepsilon}^p},\mathbf{A}_\beta)=f(\boldsymbol{\sigma}-\boldsymbol{X},\mathbf{A}_\beta)$ being the yield function in presence of the combined isotropic and kinematic hardening.
The complementary laws read then :

$$\left\{\begin{array}{lcl} \dot{\boldsymbol{\varepsilon}}^p &=& \dot{\lambda}\frac{\partial f(\boldsymbol{A}_{\boldsymbol{\varepsilon}^p},\mathbf{A}_\beta)}{\partial\boldsymbol{A}_{\boldsymbol{\varepsilon}^p}} \\ \dot{\beta} &=& \dot{\lambda}\frac{\partial f(\boldsymbol{A}_{\boldsymbol{\varepsilon}^p},\mathbf{A}_\beta)}{\partial\mathbf{A}_\beta} \end{array}\right. , \qquad \dot{\lambda}\geq 0 \tag{2.87}$$

2.6.3.2 An elastoplastic model with combined isotropic and linear kinematics hardenings

We briefly present here an example for which we still consider as state variables $(\boldsymbol{\varepsilon},\boldsymbol{\varepsilon}^p,\beta)$.

- **The thermodynamic potential and the state laws**
  It has now the form

$$\rho_0\Psi(\boldsymbol{\varepsilon},\boldsymbol{\varepsilon}^p,\beta)=\frac{1}{2}(\boldsymbol{\varepsilon}-\boldsymbol{\varepsilon}^p):\mathbb{C}:(\boldsymbol{\varepsilon}-\boldsymbol{\varepsilon}^p)+\frac{1}{2}\boldsymbol{\varepsilon}^p:\mathbb{H}:\boldsymbol{\varepsilon}^p+\Psi^{st}(\beta) \quad (2.88)$$

  in which $\mathbb{H}$ is a hardening moduli tensor[9] and Ψ^{st} the contribution of isotropic hardening to the stored energy.
  Based on (2.86), the irreversible forces read

$$\left\{\begin{array}{lcl} \boldsymbol{A}_{\boldsymbol{\varepsilon}^p} & = & \boldsymbol{\sigma}-\boldsymbol{X} \\ \\ \mathbf{A}_\beta & = & -\frac{\partial\Psi^{st}(\beta)}{\partial\beta}=R(\beta) \end{array}\right. \quad (2.89)$$

  $\boldsymbol{X}=\mathbb{H}:\boldsymbol{\varepsilon}^p$ being the relation between the back stress and the plastic strain tensor. $R(\beta)=-\frac{\partial\Psi^{st}(\beta)}{\partial\beta}$

- **The plasticity criterion and the flow rule**
  Generalizing the von Mises criterion, the plasticity criterion in presence of the two types of hardening is taken in the form:

$$f(\boldsymbol{A}_{\boldsymbol{\varepsilon}^p},\mathbf{A}_\beta)=(\boldsymbol{A}_{\boldsymbol{\varepsilon}^p})_{eq}+\mathbf{A}_\beta-\sigma_0 \quad (2.90)$$

  which also reads

$$f(\boldsymbol{A}_{\boldsymbol{\varepsilon}^p},\mathbf{A}_\beta)=(\boldsymbol{\sigma}-\boldsymbol{X})_{eq}+\mathbf{A}_\beta-\sigma_0 \quad (2.91)$$

  The normality rule gives then

$$\left\{\begin{array}{lcl} \dot{\boldsymbol{\varepsilon}}^p & = & \frac{3}{2}\dot{\lambda}\frac{\boldsymbol{s}-\boldsymbol{X}}{(\boldsymbol{s}-\boldsymbol{X})_{eq}} \\ \\ \dot{\beta} & = & \dot{\lambda}\frac{\partial f(\boldsymbol{s},\mathbf{A}_p)}{\partial\mathbf{A}_\beta} \quad = \quad \dot{\lambda} \end{array}\right. , \qquad \dot{\lambda}\geq 0 \quad (2.92)$$

  from which it is readily seen that $\dot{\beta}=\dot{\lambda}=\dot{\varepsilon}^p_{eq}=\sqrt{\frac{2}{3}\dot{\boldsymbol{\varepsilon}}^p_d:\dot{\boldsymbol{\varepsilon}}^p_d}$. It is then concluded that the isotropic hardening state variable β is the cumulated equivalent plastic strain.

$$p=\int_0^t\sqrt{\frac{2}{3}\dot{\boldsymbol{\varepsilon}}^p_d:\dot{\boldsymbol{\varepsilon}}^p_d}d\tau \quad (2.93)$$

  Note that $R(p)$ (defined in (2.89)) can be estimated from experiments.

[9] *Based on an assumption of the constitutive behaviour, the tensor $\mathbb{H}$ is often taken in the form : $\mathbb{H}=H\mathbb{I}$ with $\mathbb{I}$ the symmetric fourth order identity tensor. Notation $H=\frac{2}{3}C$ where C is called the strain hardening modulus is also often used.*

2.7 Local elastic damage laws for quasi brittle materials

Under various loading conditions, the main mechanisms of quasi brittle engineering materials involve degradation phenomena due to nucleation and growth of defects such as microvoids and microcracks. Such deterioration phenomena induce irreversible processes and the damage localization stage can lead to fracture occurrence.
A typical stress-strain behavior of quasi brittle materials exhibiting an elastic behavior coupled with damage is depicted on Figure 2.3. A notable aspect of this behavior is the existence of a softening regime due to damage. Moreover, the damage phenomenon induces degradation of elastic property which is observed during an unloading of the material.
Continuum damage mechanics (CDM) has been introduced in the 60 s and consolidated in the 80 s by taking advantage of thermodynamics-based studies which followed the newly introduced framework of Generalized Standard Materials [Halphen and Nguyen, 1975]. Despite the occurence of a softening regime, such procedure guarantees the models to be consistent with the Clausius-Duhem inequality. Among several contributions, mention can be made of [Marigo, 1981; Lemaître and Chaboche, 1985]. The theoretical framework of CDM has been progressively enriched, for instance by improving the description of damage-induced anisotropy related to microcracks orientation. To this end, second-order tensors as well as higher-order tensors have been considered as internal variables [Chaboche, 1992]. A related important issue has been the modeling of unilateral effects due to microcracks closure in presence of compression-like loadings.
In what follows, and for simplicity, the internal damage variable of the material point will be represented by a positive scalar variable α, which may correspond to microcracks density parameter as earlier introduced by [Budiansky and O'Connel, 1976].

2.7.1 A standard isotropic elastic damage model formulation

As already indicated, the GSM-based approach provides a suitable modeling framework which allows to automatically comply with the Clausius-Duhem inequality (2.25). In this framework, the first step consists in a suitable choice of state variables. Owing to arguments already mentioned, the infinitesimal strain tensor $\boldsymbol{\varepsilon}$ and a positive scalar α are chosen as the state variables. Again, α may represent a first-order isotropic approximation of the microcracks density parameter distribution (see for instance [Krajcinovic, 1996] or [Welemane and Goidescu, 2010] for analysis and discussion of this point). Modeling of the nonlinear behavior of this class of materials in the context of GSM requires two potentials.

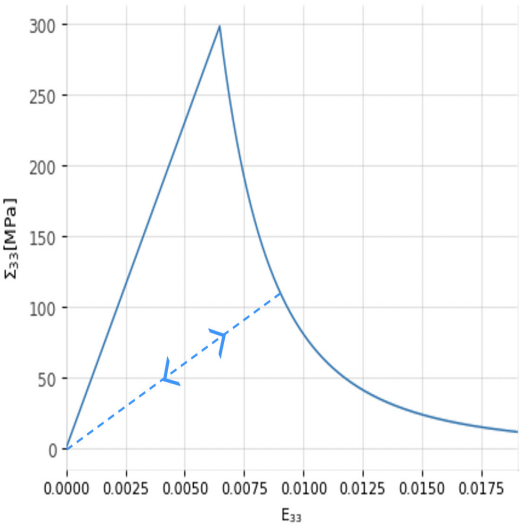

FIGURE 2.3: Typical response of an elastic-damage material under tensile loading

The first potential corresponds to the free energy

$$\rho\Psi(\boldsymbol{\varepsilon},\alpha) \;=\; \frac{1}{2}\,\boldsymbol{\varepsilon} : \mathbb{C}(\alpha) : \boldsymbol{\varepsilon} \tag{2.94}$$

From the analysis performed in subsection (2.3.1), it readily follows that the Cauchy stress tensor $\boldsymbol{\sigma}$ and the irreversible force $\mathcal{Y}$ associated to the damage α reads :

$$\begin{cases} \boldsymbol{\sigma} \;=\; \rho\dfrac{\partial\Psi}{\partial\boldsymbol{\varepsilon}}(\boldsymbol{\varepsilon},\alpha) \\ \mathcal{Y} \;=\; -\rho\dfrac{\partial\Psi}{\partial\alpha}(\boldsymbol{\varepsilon},\alpha) \end{cases} \tag{2.95}$$

while the intrinsic dissipation takes the form

$$\mathcal{D}_1 \;=\; \mathcal{Y}\dot{\alpha} \tag{2.96}$$

$\mathcal{Y}$ (whose unit is $N/mm^2 = MPa$ represents the damage energy release which, in spite of the similitude, must not be confused with the fracture energy release $\mathcal{G}$ (whose unit is $N/mm = MPa.mm$) usually considered in Fracture Mechanics.
For the complementary law, a simple choice of the dissipation potential, positive scalar-valued, convex with $\dot{d}$ and null at $\dot{d} = 0$ is :

$$\Phi(\dot{\alpha}) \;=\; \mathcal{Y}_c\,\dot{\alpha} \tag{2.97}$$

where $\mathcal{Y}_c$ is a critical damage energy release, characteristic of the elasto-damageable material. A priori, $\mathcal{Y}_c$ may be obtained from experimental data

concerning the elastic damage behavior of the material. Again, note that $\mathcal{Y}_c$ must not be confused with the fracture energy $\mathcal{G}_c$. A further remark is that the GSM authorizes a dependence of the dissipation potential with the damage state, that is $\mathcal{Y}_c$ can be replaced by $\mathcal{Y}_c(\alpha)$
With this dissipation potential in hand, and since it is not differentiable, one should refer to the notion of subdifferential $\partial\Phi$. The complementary law reads then :

$$\mathcal{Y} \in \partial\Phi(\dot{\alpha}) \tag{2.98}$$

The irreversible force $\mathcal{Y}$ is said to belong to the sub-gradient of Φ at the considered point.
Alternatively, the dual potential $\Phi^*(\mathcal{Y})$ of Φ, defined as its Legendre–Fenchel transform, takes the form of an indicator function of a convex domain $\mathcal{C}$ which is defined by

$$\mathcal{C} = \{\mathcal{Y}/f(\mathcal{Y}) = \mathcal{Y} - \mathcal{Y}_c \leq 0\} \tag{2.99}$$

This damage criterion, based on the damage energy release rate, reads then

$$f(\mathcal{Y}) = -\frac{1}{2}\,\boldsymbol{\varepsilon} : \mathbb{C}'(\alpha) : \boldsymbol{\varepsilon} - \mathcal{Y}_c(\alpha) \leq 0 \tag{2.100}$$

With the help of Φ^* and the above corresponding damage criterion, the normality rule, $\dot{\alpha} \in \partial\Phi^*(\mathcal{Y})$, which provides the irreversible damage evolution law, reads on the regular part:

$$\dot{\alpha} = \dot{\lambda}\frac{\partial f}{\partial \mathcal{Y}} \tag{2.101}$$

The damage multiplier $\dot{\lambda}$ is determined by the classical Karush-Kuhn-Tucker conditions.
This allows to build a rate formulation of the damage model by means of a symmetric multi-branch tangent operator and paves the way for specific numerical implementations.
Note that the general form of the isotropic elasticity stiffness tensor of the damaged material, based on a scalar variable d takes the form

$$\mathbb{C}(\alpha) = 3k(\alpha)\mathbb{J} + 2\mu(\alpha)\mathbb{K} \tag{2.102}$$

where $\mathbb{J} = \frac{1}{3}\mathbf{1} \otimes \mathbf{1}$ and $\mathbb{K} = \mathbb{I} - \mathbb{J}$ are the two isotropic projectors of fourth-order tensors with the symmetries of a stiffness tensor. $\mathbb{I}$ is the symmetric fourth-order identity tensor.
$k(\alpha)$ is the bulk modulus of the damaged material, while $\mu(\alpha)$ represents its shear modulus. In the recent literature, a common choice of simplification consists in

$$\mathbb{C}(\alpha) = g(\alpha)\mathbb{C}_s = g(\alpha)(3k_s\mathbb{J} + 2\mu_s\mathbb{K}) \tag{2.103}$$

$\mathbb{C}_s$ being the stiffness of the isotropic sound material, and $g(\alpha)$ a degradation function.

2.7.2 Modelling damage-induced unilateral effects

Modeling elasticity coupled with unilateral damage introduce difficulties that are widely recognized in several publications including those devoted to the modeling of gradient damage models [Amor et al., 2009]. This concern is still debated in terms of different energy decompositions.

We focus here on the context of bimodular elastic behaviors (then with the distinction of two domains in strain space). Clearly enough, the case of more than two domains of separation of strain space is excluded in the present discussion. In such context, and for isotropic behaviors, the formulation generally attributed to [Amor et al., 2009; Lancioni and Royer-Carfagni, 2009] can be rigorously established as a special case by following a constructive method initially introduced by [Wesolowski, 1969] and developed by [He and Curnier, 1995] based on the argument that the elastic energy must be continuously differentiable while a jump in the elastic stiffness (or compliance) tensor is allowed. This approach has been followed by several authors among which [Cormery and Welemane, 2010] and [Kondo et al., 2007], to cite very few.
The main result of application of the theory by Curnier et al. [He and Curnier, 1995] in the context of an isotropic model is the following expression of the free energy $w(\boldsymbol{\varepsilon}, \alpha)$:

$$\rho\Psi(\boldsymbol{\varepsilon}, \alpha) = \begin{cases} \dfrac{1}{2}k(\alpha)\left(\mathrm{tr}\left(\boldsymbol{\varepsilon}\right)\right)^2 + \mu(\alpha)\boldsymbol{\varepsilon}^d : \boldsymbol{\varepsilon}^d \quad \text{if} \quad \mathrm{tr}\left(\boldsymbol{\varepsilon}\right) \geq 0 \\ \dfrac{1}{2}k_s\left(\mathrm{tr}\left(\boldsymbol{\varepsilon}\right)\right)^2 + \mu(\alpha)\boldsymbol{\varepsilon}^d : \boldsymbol{\varepsilon}^d \quad \text{if} \quad \mathrm{tr}\left(\boldsymbol{\varepsilon}\right) \leq 0 \end{cases} \tag{2.104}$$

which is well-known as that of Amor et a. [Amor et al., 2009].
In summary, the isotropic elastic damage behavior in the presence of unilateral damage, will require in addition to the bulk and shear moduli of the sound material, two degradation functions, namely that defining $k(d)$ and $\mu(d)$ which are the same needed for the model withouting account for the unilateral effect.

2.8 Variational formulations related to the GSM framework

This section is devoted to a brief presentation of variational principles relying on the structure of models which describe GSM behaviors. Its main objective is to present a general structure of the variational structure of problems involving GSM for which we rely for instance to recent study by [Nguyen, 2016] and introduce he condensed notation:

$$U = (\boldsymbol{u}, \alpha), \tag{2.105}$$

in which we follow a classical notation $\boldsymbol{u}$ (instead of $\boldsymbol{\xi}$) for the displacement vector field and α the field of internal variables, both defined on the considered structure Ω. Then, the overall counterpart of the free energy $\rho\Psi\big(\boldsymbol{\varepsilon},\alpha\big)$ and of the dissipation potential $\Phi\big(\dot{\boldsymbol{\varepsilon}},\dot{\alpha}\big)$, previously considered in the GSM framework are defined as:

$$\boldsymbol{W}(U) = \int_\Omega \rho\Psi\big(\boldsymbol{\varepsilon},\alpha\big)d\Omega, \tag{2.106}$$

and

$$\boldsymbol{D}(\dot{U}) = \int_\Omega \Phi\big(\dot{\boldsymbol{\varepsilon}},\dot{\alpha}\big)d\Omega, \tag{2.107}$$

in which we recall that $\Phi\big(\dot{\boldsymbol{\varepsilon}},\dot{\alpha}\big)$ is possibly non-differentiable.
In order to establish the variational formulation, and based on (2.68), we rely on

- **the normality rule** in its global form :

$$\forall \dot{U}^*, \quad -\partial \boldsymbol{D}_{,\dot{U}} \cdot (\dot{U}^* - \dot{U}) + \boldsymbol{D}(\dot{U}^*) - \boldsymbol{D}(\dot{U}) \geqslant 0. \tag{2.108}$$

- **the Biot equation** in its global form

$$\boldsymbol{W}_{,U} + \partial \boldsymbol{D}_{,\dot{U}} = F, \tag{2.109}$$

  in which F corresponds to the power of external forces.

It follows from (2.109) in (2.108) that:

$$\forall \dot{U}^*, \quad \Big(\boldsymbol{W}_{,U} - F\Big) \cdot (\dot{U}^* - \dot{U}) + \boldsymbol{D}(\dot{U}^*) - \boldsymbol{D}(\dot{U}) \geqslant 0. \tag{2.110}$$

This structure can be linked to a class of variational constitutive updates that has been proposed by Ortiz and Stainier [Ortiz and Stainier, 1999] in the form of rate variational principles (see also Mielke [Mielke, 2005]). We follow here a recent summarize of this principle by [Bleyer, 2022]. Considering a time increment $[t_n; t_{n+1}]$, for which the mechanical quantities are known at time t_n, it can be shown that the solution at time t_{n+1} of the mechanical problem is that of the following minimization principle (here the dissipation potential is taken in a general form $\Phi(\dot{\boldsymbol{\varepsilon}},\dot{\alpha})$:

$$(u_{n+1},\boldsymbol{\varepsilon}_{n+1},\alpha_{n+1}) \;=\; \underset{(u,\boldsymbol{\varepsilon},\alpha)}{\operatorname{argmin}} \int_{t_n}^{t_{n+1}} \int_\Omega \Big(\dot{\Psi}(\boldsymbol{\varepsilon},\alpha) \;+\; \Phi(\dot{\boldsymbol{\varepsilon}},\dot{\alpha})\Big)\, d\Omega dt - \mathcal{W}_{ext}(\dot{u}) \tag{2.111}$$

where $\mathcal{P}_{ext}(\dot{u})$ is the power of external loads. Coming back to the variational principle (2.111), by applying an implicit Euler discretization for the state variables, their rate can be approximated by :

$$\dot{\boldsymbol{\varepsilon}}(t) \;\approx\; \frac{\boldsymbol{\varepsilon} - \boldsymbol{\varepsilon}_n}{\Delta t} \quad ; \quad \dot{\alpha}(t) \;\approx\; \frac{\alpha - \alpha_n}{\Delta t} \tag{2.112}$$

where $\Delta t = t_{n+1} - t_n$. One can then write :

$$\int_\Omega \int_{t_n}^{t_{n+1}} \Phi(\dot{\boldsymbol{\varepsilon}}, \dot{\alpha}) d\Omega \, dt \approx \int_\Omega \Delta t \Phi \left(\frac{\boldsymbol{\varepsilon} - \boldsymbol{\varepsilon}_n}{\Delta t}, \frac{\alpha - \alpha_n}{\Delta t} \right) d\Omega \tag{2.113}$$

from which is established the following incremental variational principle:

$$\begin{aligned} (u_{n+1}, \boldsymbol{\varepsilon}_{n+1}, \alpha_{n+1}) = & \underset{(u,\boldsymbol{\varepsilon},\alpha)}{\operatorname{argmin}} \int_\Omega (\Psi(\boldsymbol{\varepsilon}, \alpha)) \, d\Omega \\ & + \int_\Omega \Delta t \, \Phi \left(\frac{\boldsymbol{\varepsilon} - \boldsymbol{\varepsilon}_n}{\Delta t}, \frac{\alpha - \alpha_n}{\Delta t} \right) d\Omega \end{aligned} \tag{2.114}$$

which can be put in the form:

$$(u_{n+1}, \boldsymbol{\varepsilon}_{n+1}, \alpha_{n+1}) = \underset{(u,\boldsymbol{\varepsilon},\alpha)}{\operatorname{argmin}} \int_{\substack{\Omega \\ (u,\boldsymbol{\varepsilon}) \in \mathcal{K}(E)}} J(\boldsymbol{\varepsilon}, \alpha) \, d\Omega \tag{2.115}$$

where the incremental pseudo-potential $J(\boldsymbol{\varepsilon}, \alpha)$ takes the following form for the rate-dependant materials :

$$J(\boldsymbol{\varepsilon}, \alpha) = \Psi(\boldsymbol{\varepsilon}, \alpha) + \Delta t \Phi \left(\frac{\boldsymbol{\varepsilon} - \boldsymbol{\varepsilon}_n}{\Delta t}, \frac{\alpha - \alpha_n}{\Delta t} \right) \tag{2.116}$$

and for rate-independent materials:

$$J(\boldsymbol{\varepsilon}, \alpha) = \Psi(\boldsymbol{\varepsilon}, \alpha) + \Phi \left(\boldsymbol{\varepsilon} - \boldsymbol{\varepsilon}_n, \alpha - \alpha_n \right) \tag{2.117}$$

Extension of this type of incremental variational approach to gradient plasticity and to gradient damage models are presented in chapter 11.
For completeness, note also that the incremental variational formulation has been already considered by [Lorentz and Andrieux, 1999] for damage mechanics problems. A detailed presentation in the case of classical elastoplasticity can be also found in [Maitournam, 2012].

Appendix: Dissipation potential for the Drucker-Prager criterion

$$\Phi(\dot{\boldsymbol{\varepsilon}}^p) = \sup_{\boldsymbol{\sigma} \in \mathcal{C}} \{ \boldsymbol{s} : \dot{\varepsilon}_d^p + 3\sigma_m \dot{\varepsilon}_m^p \}$$

for which it is recalled that $\dot{\varepsilon}_m^p = \frac{1}{3} tr \, \dot{\varepsilon}^p$ and

$$\Phi(\dot{\boldsymbol{\varepsilon}}^p) = \sup_{\boldsymbol{\sigma} \in \mathcal{C}} \left\{ \sigma_{eq} \dot{\varepsilon}_{eq}^p + 3\sigma_m \dot{\varepsilon}_m^p \right\}$$

Since the criterion is defined by

$$\sigma_{eq} + 3\alpha\sigma_m - \sigma_0 \leq 0,$$

one has

$$3\sigma_m \leq \frac{\sigma_0 - \sigma_{eq}}{\alpha}$$

from which it is deduced that

$$\Phi(\dot{\boldsymbol{\varepsilon}}^p) = \sup_{\sigma_{eq}} \left\{ \sigma_{eq}\dot{\varepsilon}^p_{eq} + \frac{\sigma_0 - \sigma_{eq}}{\alpha}\dot{\varepsilon}^p_m \right\} \tag{2.118}$$

which can be put in the form

$$\Phi(\dot{\boldsymbol{\varepsilon}}^p) = \sup_{\sigma_{eq}} \left\{ \frac{\sigma_0}{\alpha}\dot{\varepsilon}^p_m + \frac{\sigma_{eq}}{\alpha}(\alpha\dot{\varepsilon}^p_{eq} - \dot{\varepsilon}^p_m) \right\}$$

It follows that if $\alpha\dot{\varepsilon}^p_{eq} - \dot{\varepsilon}^p_m \leq 0$ then $\Phi(\dot{\boldsymbol{\varepsilon}}^p) = \frac{\sigma_0}{\alpha}\dot{\varepsilon}^P_m$; otherwise (if $\alpha\dot{\varepsilon}^p_{eq} - \dot{\varepsilon}^p_m > 0$), $\Phi(\dot{\boldsymbol{\varepsilon}}^p) = \infty$
The dissipation potential reads then :

$$\Phi(\dot{\boldsymbol{\varepsilon}}^p) = \begin{cases} \frac{\sigma_0}{\alpha}\dot{\varepsilon}^p_m & \text{if} \quad \dot{\varepsilon}^p_m \geq \alpha\dot{\varepsilon}^p_{eq} \\ \\ \infty & \text{if} \quad \dot{\varepsilon}^p_m < \alpha\dot{\varepsilon}^p_{eq} \end{cases} \tag{2.119}$$

Now, let us examine the case where $\lim_{\alpha\to 0} \Phi(\dot{\boldsymbol{\varepsilon}}^p)$. To this end we expand the above result in three parts:

$$\Phi(\dot{\boldsymbol{\varepsilon}}^p) = \begin{cases} \frac{\sigma_0}{\alpha}(\alpha\dot{\varepsilon}^p_{eq}) & \text{if} \quad \dot{\varepsilon}^p_m = \alpha\dot{\varepsilon}^p_{eq} \\ \\ \frac{\sigma_0}{\alpha}\dot{\varepsilon}^p_m & \text{if} \quad \dot{\varepsilon}^p_m > \alpha\dot{\varepsilon}^p_{eq} \\ \\ \infty & \text{if} \quad \dot{\varepsilon}^p_m < \alpha\dot{\varepsilon}^p_{eq} \end{cases} \tag{2.120}$$

At the limit $\alpha \longrightarrow 0$, one has then:

$$\Phi(\dot{\boldsymbol{\varepsilon}}^p) = \begin{cases} \sigma_0\dot{\varepsilon}^p_{eq} & \text{if} \quad \dot{\varepsilon}^p_m = \alpha\dot{\varepsilon}^p_{eq} \\ \\ \infty & \text{if} \quad \dot{\varepsilon}^p_m > \alpha\dot{\varepsilon}^p_{eq} \longrightarrow 0 \quad \text{or} \quad \dot{\varepsilon}^p_m < \alpha\dot{\varepsilon}^p_{eq} \end{cases} \tag{2.121}$$

Bibliography

[Abed-Meraim and Nguyen 2007] Abed-Meraim, F. ; Nguyen, Q.S.: A quasi-static stability analysis for Biot's equation and standard dissipative systems. In: *European Journal of Mechanics-A/Solids* 26 (2007), Nr. 3, p. 383–393

[Amor et al. 2009] Amor, H. ; Marigo, J.J. ; Maurini, C.: Regularized formulation of the variational brittle fracture with unilateral contact: Numerical experiments. In: *Journal of the Mechanics and Physics of Solids* 57 (2009), Nr. 8, p. 1209–1229

[Armstrong and Frederick 1966] Armstrong, P.-J. ; Frederick, C.-O: A Mathematical Representation of the Multiaxial Baushinger Effect / C.E.G.B. Report No. RD/B/N731. 1966. – Technical repport

[Ben-Amoz 1965] Ben-Amoz, M: On a variational theorem in coupled thermoelasticity. (1965)

[Biot 1956] Biot, M. A.: Thermoelasticity and irreversible thermodynamics. In: *Journal of applied physics* 27 (1956), Nr. 3, p. 240–253

[Biot 1955] Biot, M.A.: Variational principles in irreversible thermodynamics with application to viscoelasticity. In: *Physical Review* 97 (1955), Nr. 6, p. 1463

[Biot 1965] Biot, M.A.: *Mechanics of incremental deformations*. 1965

[Biot 1970] Biot, M.A.: Variational principles in heat transfer: a unified Lagrangian analysis of dissipative phenomena / New York. 1970. – Technical repport

[Bleyer 2022] Bleyer, J.: Applications of conic programming in non-smooth mechanics. In: *Journal of Optimization Theory and Applications* (2022), p. 1–33

[Bouby et al. 2015] Bouby, C. ; Kondo, D. ; Saxcé, G. de: A comparative analysis of two formulations for non linear hardening plasticity models: Application to shakedown analysis. In: *European Journal of Mechanics. A/Solids* 26 (2015), Nr. 53, p. 48–61

[Budiansky and O'Connel 1976] Budiansky, B. ; O'Connel, J.R.: Elastic moduli of a cracked solid. In: *International Journal of Solids and Structures* 12 (1976), p. 81–97

[Chaboche 1992] Chaboche, J.L.: Damage induced anisotropy: on the difficulties associated with the active/passive unilateral condition. In: *International Journal of Damage Mechanics* 1 (1992), Nr. 2, p. 148–171

[Collins and Houlsby 1997] Collins, I.F. ; Houlsby, G.T.: Application of thermomechanical principles to the modelling of geotechnical materials. In: *Proceedings of the Royal Society A* 453 (1997), Nr. 1964, p. 1975–2001

[Cormery and Welemane 2010] Cormery, F. ; Welemane, H.: A stress-based macroscopic approach for microcracks unilateral effect. In: *Computational materials science* 47 (2010), Nr. 3, p. 727–738

[Drucker and Prager 1952] Drucker, D. C. ; Prager, W.: Soil mechanics and plastic analysis for limit design. In: *Quarterly of Applied Mathematics* 10 (1952), p. 157–165

[G.A. Maugin 1994] G.A. Maugin, W. M.: Thermodynamics with internal variables, I. General concepts. In: *J. Non-equilib. Thermodyn.* 19 (1994), p. 217–249

[Germain 1973] Germain, P.: *TCours de Mécanique des Milieux Continus - Volume 1.* Masson , Paris, 1973

[Germain et al. 1983] Germain, P. ; Suquet, P. ; Nguyen, Q.S.: Continuum thermodynamics. In: *ASME Journal of Applied Mechanics* 50 (1983), p. 1010–1020

[Halphen and Nguyen 1975] Halphen, B. ; Nguyen, Q.: Sur les matériaux standard généralisés. In: *Journal de Mécanique* (1975), Nr. 14, p. 39–63

[He and Curnier 1995] He, Q.C. ; Curnier, A.: A more fundamental approach to damaged elastic stress-strain relations. In: *International Journal of Solids and Structures* 32 (1995), Nr. 10, p. 1433–1457

[Herrmann 1963] Herrmann, G.: On variational principles in thermoelasticity and heat conduction. In: *Quarterly of Applied Mathematics* 21 (1963), Nr. 2, p. 151–155

[Houlsby and Puzrin 2006] Houlsby, G.T. ; Puzrin, A.M. ; Springer (Hrsg.): *Principles of Hyperplasticity. An Approach to Plasticity Theory based on Thermodynamic Principles.* 2006

[Kondo et al. 2007] Kondo, D. ; Welemane, H. ; Cormery, F.: Basic concepts and models in continuum damage mechanics. In: *Revue européenne de génie civil* 11 (2007), Nr. 7-8, p. 927–943

[Krajcinovic 1996] Krajcinovic, D.: *Damage mechanics.* Elsevier, 1996

[L. 1931] L., Onsager: Reciprocal relations in irreversible processes. I. In: *Phys Rev.* 37 (1931), p. 405–426

[Lancioni and Royer-Carfagni 2009] Lancioni, G. ; Royer-Carfagni, G.: The variational approach to fracture mechanics. A practical application to the French Panthéon in Paris. In: *Journal of elasticity* 95 (2009), p. 1–30

[Lemaître and Chaboche 1985] Lemaître, J. ; Chaboche, J.: Mécanique des matériaux solides. In: *Dunod, Paris* (1985)

[Lemaître and Chaboche 1990] Lemaître, J. ; Chaboche, J.: Mechanics of Solid Materials. In: *Cambridge University Press,* (1990)

[Lorentz and Andrieux 1999] Lorentz, E. ; Andrieux, S.: A variational formulation for nonlocal damage models. In: *International journal of plasticity* 15 (1999), Nr. 2, p. 119–138

[Maitournam 2012] Maitournam, H.: *Matériaux et structures anélastiques*. Presse de l'Ecole Polytechnique, 2012

[Marigo 1981] Marigo, J.-J.: Formulation de l'endommagement d'un matériau élastique. In: *C. R. Acad. Sci. Paris Sér. II* 292 (1981), Nr. 19, p. 1309–1312

[Maugin 1992] Maugin, G.: *The thermomechanics of plasticity and fracture*. Cambridge University Press, 1992

[Maugin 1999] Maugin, G.A.: *The thermomechanics of nonlinear irreversible behaviours*. Bd. 27. World scientific, 1999

[Mielke 2005] Mielke, A.: Evolution of rate-independent systems. In: *Evolutionary equations* 2 (2005), p. 461–559

[Moreau 1970] Moreau, JJ: Sur les lois de frottement, de viscosité et de plasticité. In: *CR Acad. Sci. Paris Sér. II Méc. Phys. Chim. Sci. Univers Sci. Terre* 271 (1970), p. 608–611

[Nguyen 2000] Nguyen, Q.S.: *Stability and nonlinear solid mechanics*. Wiley, 2000

[Nguyen 2016] Nguyen, Q.S.: Quasi-static response, implicit scheme and incremental problem in gradient plasticity. In: *J. Mech. Phys. Solids* 97 (2016), p. 156–167

[Nowacki 1986] Nowacki, W.: *Thermoelasticity. Second edition*. Pergamon Press, 1986

[Ortiz and Stainier 1999] Ortiz, M. ; Stainier, L.: The variational formulation of viscoplastic constitutive updates. In: *Computer Methods in Applied Mechanics and Engineering* (1999), Nr. 171, p. 419–444

[Salençon 2001] Salençon, J.: *Handbook of Continuum Mechanics : Basic concepts and thermoelasticity*. World scientific, 2001

[Stainier 2013] Stainier, L.: A variational approach to modeling coupled thermo-mechanical nonlinear dissipative behaviors. In: *Advances in Applied Mechanics* 46 (2013), p. 69–126

[Stolz 2004] Stolz, C. ; WARSAW (Hrsg.): *Energy Methods in Non-Linear Mechanics*. 2004

[Welemane and Goidescu 2010] Welemane, H. ; Goidescu, C.: Isotropic brittle damage and unilateral effect. In: *Comptes Rendus Mécanique* 338 (2010), Nr. 5, p. 271–276

[Wesolowski 1969] Wesolowski, Z.: Elastic material with different elastic constants in two regions of variability of deformation(Energy balance relations for elastic material with different elastic moduli in two regions of deformation space). In: *Archivum Mechaniki Stosowanej* 21 (1969), Nr. 4, p. 449–468

[Wilson 2002] Wilson, C. D.: A Critical Reexamination of Classical Metal Plasticity. In: *Journal of Applied Mechanics* 69 (2002), p. 63–68

[Yang et al. 2006] Yang, Q. ; Stainier, L. ; Ortiz, M.: A variational formulation of the coupled thermo-mechanical boundary-value problem for general dissipative solids. In: *Journal of the Mechanics and Physics of Solids* 54 (2006), Nr. 2, p. 401–424

[Ziegler 1983] Ziegler, H.: *An introduction to Thermomechanics*. North-Holland, 1983

3

Compendium of finite strain (visco-)plasticity

Thomas Helfer

CEA, DES/IRESNE/DEC/SESC/LSC, Département d'Études des Combustibles, Cadarache, France

Ductile failure generally involves large strains and, more generally, failure in practical applications may involve small strain but large rotations. For those reasons, a finite strain analysis is often required. However, most theories and courses (including the chapters of the present textbook) describe constitutive equations written in the framework of infinitesimal strain theory. This chapter aims at bridging this gap.

Introduction

Constitutive equations written in the framework of infinitesimal strain theory are commonly based on an additive split of the total strain into an elastic and (visco-)plastic part and must satisfy constraints imposed by thermodynamics, namely the positivity of the dissipation, expressed by the Clausius-Duhem inequality. The class of standard generalized constitutive equations, discussed in depth in Chapter 2 of this textbook, is particularly interesting, both physically and numerically. For the following discussion, it is worth emphasizing the link between the trace of the strain and the change of volume, the description of which plays a central role in (visco-)plasticity, either to ensure the incompressibility of the (visco-)plastic flow prior to damage or to describe the growth of voids associated with a ductile failure (see Equation (3.3) below).

In contrast, finite strain constitutive equations are more diverse and must ensure an additional condition named objectivity which guarantees that the results do not depend of the referential used to perform the computations. Following most classical textbooks [Simo and Hughes; Doghri; Belytschko; Lemaitre and Desmorat; de Souza Neto et al.], three main classes of constitutive equations in finite strain [Sidoroff, 1981] emerges.

Constitutive equations written in rate form based on an additive split of the deformation rate $\boldsymbol{D}$ into an elastic and plastic part

This class of constitutive equations can be introduced as approximations of the $\boldsymbol{F}_e \cdot \boldsymbol{F}_p$ framework described below and allows an almost directly reuse of constitutive equations written in the infinitesimal strain formalism. In particular, the rate of change of volume is directly related to the trace of $\boldsymbol{D}$. However, constitutive equations written in rate form suffers from various theoretical and practical drawbacks [Simo and Hughes; Doghri], such as spurious energy dissipation, the restriction to isotropy (in most cases) and the non intuitive introduction of objective derivatives to transport the stress and the internal state variables to ensure the objectivity constraint. In particular, there is an infinite choice of objective derivatives and none is more advantageous than the others in our opinion, although this point has been a subject of fierce debates. However those approaches are still used in many popular academic and commercial solvers.

Constitutive equations written using lagrangian strain measures and conjugated stresses

Once a strain measure is choosen, the reuse of constitutive equations written in the small strain formalism is possible. Those approaches are sound thermodynamically and automatically objective. In particular, the standard generalized character is preserved when transposing constitutive equations in this framework. The main drawbacks of this approach are as follows:

- There is an infinite number of strain measures.
- There is generally no link between the change of volume and the trace of the strain measures except in the small strain limit.
- The conjugated stresses are defined by energetic considerations and thus are difficult to interpret physically. In particular, there is generally no link between those conjugated stresses and the forces (contrary to the Cauchy stress for instance). Hence, this framework is generally not suitable to build micromechanical models.

One noticable variant of this approach is the logarithmic strain framework [Miehe et al.] which, in the author's opinion, is currently one of the most interesting option for the macroscopic behaviors.

Constitutive equations based on the multiplicative decomposition of the deformation gradient into an elastic and a (visco-)plastic part

.

This decomposition, generally refered to by the $\boldsymbol{F}_e \cdot \boldsymbol{F}_p$ framework has been introduced by Lee [Lee, 1969; Mandel]. This approach is well established, thermodynamically sound and objective, and suited to build micro-mechanical

models, notably for single crystals. However, the constitutive equations written in the small strain formalism can't be reused. Furthermore, constitutive equations written with this framework are less intuitive than those written in the small strain framework. For instance, multiplication replaces addition and most tensors are unsymmetric which is uncommon in the infinitesimal strain theory.

Outline

Hence, each of the previous approaches has its advantages and its drawbacks and this diversity of approaches partially explains why accounting for finite strain in constitutive equations is generally considered difficult to address. Another reason is that most solvers imposes their own strategy, adding to theoretical issues, numerical and practical issues.

This chapter aims at providing an overview of those different approaches and at highlighting the link between constitutive equations written in the small strain framework and the constitutive equations written in the finite strain framework. It proceeds as follows:

- Section 3.1 describes the kinematics and the mechanical equilibrium in finite strain theory. It also recalls the basics of thermodynamics and discusses the notion of objectivity.
- Section 3.2 recalls the basics of visco-plastic behaviors in the infinitesimal strain theory and discusses the limit of this framework is recalled.
- Section 3.3 discusses how lagrangian strain measures can be used to build constitutive equations.
- Section 3.4 discusses the $\boldsymbol{F}_e \cdot \boldsymbol{F}_p$ framework.
- Section 3.5 discusses constitutive equations written in rate form for their practical importance, despite their theoretical flows.

3.1 Kinematics, mechanical equilibrium and mechanical power in the finite strain theory

This section starts by describing two aspects of the finite strain theory: the kinematics and the mechanical equilibrium. Those two aspects are then linked by the principle of virtual power which leads to the definition of the mechanical power and the thermodynamics basis used to build the constitutive equations exposed in Sections 3.3, 3.4 and 3.5.

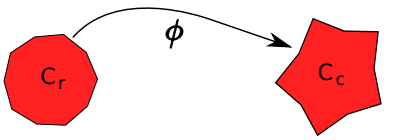

FIGURE 3.1: The deformation mapping

3.1.1 Kinematics

Kinematics describes the change of geometry of the considered structure.

Deformation

Let $\vec{x}_c$ be the current position of a point in the current configuration $\mathcal{C}_c$ and $\vec{X}_r$ its position in the reference configuration $\mathcal{C}_r$ (see Figure 3.1). The mapping $\phi_{r\to c}$ transforming $\vec{X}_r$ in $\vec{x}_c$ is called the deformation:

$$\vec{x}_c = \phi_{r\to c}\Big(\vec{X}_r\Big)$$

For the sake of simplicity, the indices $_c$ and $_r$ will generally be omitted, the tensors associated with the current configuration being noted using lowercase letters and the tensors in the reference configuration in capital letters. The previous equation is thus equivalent to:

$$\vec{x} = \phi\Big(\vec{X}\Big)$$

Displacement

The displacement of this point is denoted $\vec{u}$:

$$\vec{u} = \vec{x} - \vec{X} = \phi\Big(\vec{X}\Big) - \vec{X}$$

First order theory

The deformation ϕ can be expanded using a Taylor series as follows:

$$\vec{x} + \delta\,\vec{x} = \vec{x} + \frac{\partial \phi}{\partial \vec{X}} \cdot \delta\,\vec{X} + \cdots = \vec{x} + \boldsymbol{F} \cdot \delta\,\vec{X} + \ldots$$

where $\boldsymbol{F}$ denotes the deformation gradient. In this document, higher order terms are not considered. The deformation gradient $\boldsymbol{F}$ satisfies:

$$\boldsymbol{F} = \frac{\partial \phi}{\partial \vec{X}} = \frac{\partial \vec{x}}{\partial \vec{X}} = \boldsymbol{I} + \frac{\partial \vec{u}}{\partial \vec{X}} \tag{3.1}$$

Change of volume

The integral of a function $f(\vec{x})$ over the current configuration is related to the integral over the reference configuration by the following classical relation:

$$\int_{\Omega_c} f(\vec{x})\,\mathrm{d}\,v = \int_{\Omega_r} f\left(\vec{X}\right) J\,\mathrm{d}\,V \tag{3.2}$$

where J is the determinant of the deformation gradient:

$$J = \det\left(\boldsymbol{F}\right)$$

Applying Equation (3.2) to the special case $f\left(\vec{X}\right) = 1$ show that J can be interpreted as a the local measure of the change of volume.‘

By conservation of mass, it is also possible to show that J is also equal to the ratio of the mass density ρ_c in the current configuration and the mass density ρ_r in the reference configuration:

$$J = \det\left(\boldsymbol{F}\right) = \frac{\rho_c}{\rho_r}$$

Growth of cavities, porosity evolution

Let us consider the case of a elementary cell containing an incompressible matrix and cavities.

The porosity f is the ratio between the volume of void V_f and the total volume V:

$$f = \frac{V_f}{V} = 1 - \frac{V_m}{V}$$

where V_m is the volume of the matrix.

Taking the incompressibility of the matrix into account, i.e. $\dot{V_m} = 0$, the porosity evolution is thus given by:

$$\dot{f} = (1-f)\,\frac{\dot{V}}{V} \tag{3.3}$$

From a macroscopic point of view, one finds:

$$\dot{f} = (1-f)\,\frac{\dot{J}}{J}$$

Composition

Let us consider an intermediate configuration $\mathcal{C}_i$ between the reference configuration and the current configuration. The following composition rule holds:

$$\vec{x}_c = \phi_{i\to c}(X_c) = \phi_{i\to c}\Big(\phi_{r\to i}\Big(\vec{X}_r\Big)\Big)$$

The chain rule leads to the following multiplicative composition rule of the deformation gradients:

$$\boldsymbol{F}_{r\to c} = \boldsymbol{F}_{i\to c}\,\cdot\,\boldsymbol{F}_{r\to i} \tag{3.4}$$

3.1.2 Velocity gradient, deformation gradient

The velocity of a point is defined as:

$$\vec{v} = \frac{\mathrm{d}\vec{x}}{\mathrm{d}t}$$

The principle of virtual power (see Section (3.1.4)) naturally introduces the gradient of the velocity in the current configuration, denoted $\boldsymbol{L}$:

$$\boldsymbol{L} = \mathbf{grad}(\vec{v}) = \frac{\partial \vec{v}}{\partial \vec{x}}$$

$\boldsymbol{L}$ is expressed in the current configuration.

Rate of deformation

The symmetric part of the velocity gradient is the rate of deformation, denoted $\boldsymbol{D}$:

$$\boldsymbol{D} = \frac{1}{2}\Big(\boldsymbol{L}^{\mathrm{T}} + \boldsymbol{L}\Big)$$

Rate of change of volume

The time derivative of the change of volume, $\dot{J}$, is given by[1]:

$$\dot{J} = J\,\mathrm{tr}(\boldsymbol{D}) \quad \Leftrightarrow \quad \frac{\mathrm{d}\ln(J)}{\mathrm{d}t} = \mathrm{tr}(\boldsymbol{D}) = \mathrm{tr}(\boldsymbol{L}) \tag{3.5}$$

This relation shows that there is no change of volume if the trace of the rate of deformation $\boldsymbol{D}$ is null.

3.1.3 Stretch tensor, right Cauchy tensor, Green-Lagrange strain

Polar decomposition

The theorem of polar decomposition of the deformation gradient states that it exists a unique rotation $\boldsymbol{R}$ and a unique symmetric tensor $\boldsymbol{U}$ such that:

$$\boldsymbol{F} = \boldsymbol{R} \cdot \boldsymbol{U} \tag{3.6}$$

$\boldsymbol{U}$ is called the stretch tensor. Equation (3.4) allows a simple interpretation of the Polar Decomposition (3.6).

[1] Equation (3.5) can be established by computing the following first order development of the determinant of the deformation gradient:

$$\begin{aligned} J|_{t+\Delta t} &= \det\Big(\boldsymbol{F}|_{t+\Delta t}\Big) = \det\big(\boldsymbol{F}|_t + \Delta\boldsymbol{F}\big) = \det\big(\boldsymbol{F}|_t + \Delta t\,\boldsymbol{L}\cdot\boldsymbol{F}|_t\big) \\ &\approx \det\big(\boldsymbol{F}|_t\big)\,\det\left(\boldsymbol{I} + \Delta t\,\boldsymbol{L}\right) \approx J|_t\,(1 + \Delta t\,\mathrm{tr}(\boldsymbol{D})) \end{aligned}$$

$\boldsymbol{U}$ is expressed in the reference configuration and is invariant by change of observer. Such a tensor is called lagrangian.

As the determinant of a rotation matrix is 1, the change of volume can be related to the determinant of the stretch tensor:

$$J = \det(\boldsymbol{F}) = \det(\boldsymbol{U})$$

The right Cauchy tensor and the Green-Lagrange strain

The computation of the stretch tensor is cumbersome in practice, but the square of it exhibits the following simple expression:

$$\boldsymbol{C} = \boldsymbol{U}^2 = \boldsymbol{F}^{\mathrm{T}} \cdot \boldsymbol{F}$$

The symmetric tensor $\boldsymbol{C}$ is called the right Cauchy tensor. This tensor and functions of this tensor plays a major role in finite strain theory.

$\boldsymbol{C}$ has a simple interpretation. Let $\mathrm{d}\vec{X}$ denote a vector joining two points infinitely close in the reference configuration. The vector $\mathrm{d}\vec{x}$ joining those points in the current configuration is given by $\boldsymbol{F} \cdot \mathrm{d}\vec{X}$. The square of the euclidian norm $\|\mathrm{d}\vec{x}\|^2$ is given by:

$$\|\mathrm{d}\vec{x}\|^2 = \mathrm{d}\vec{x} \cdot \mathrm{d}\vec{x} = \mathrm{d}\vec{X} \cdot \boldsymbol{F}^{\mathrm{T}} \cdot \boldsymbol{F} \cdot \mathrm{d}\vec{X} = \mathrm{d}\vec{X} \cdot \boldsymbol{C} \cdot \mathrm{d}\vec{X}$$

The right Cauchy tensor is directly related the so-called Green-Lagrange strain $\boldsymbol{E}^{GL}$, defined as follows:

$$\boldsymbol{E}^{GL} = \frac{1}{2}(\boldsymbol{C} - \boldsymbol{I}) = \frac{1}{2}\Big(\boldsymbol{F}^{\mathrm{T}} \cdot \boldsymbol{F} - \boldsymbol{I}\Big) = \frac{1}{2}\big(\boldsymbol{U}^2 - \boldsymbol{I}\big)$$

$\boldsymbol{C}$ and $\boldsymbol{E}^{GL}$ are two examples of an isotropic function of the stretch tensor as:

$$\boldsymbol{C} = \sum_{i=1}^{3} U_i^2 \, \boldsymbol{n}_i^{\boldsymbol{U}} \quad \text{and} \quad \boldsymbol{E}^{GL} = \sum_{i=1}^{3} \left(U_i^2 - 1\right) \boldsymbol{n}_i^{\boldsymbol{U}}$$

where U_i and $\boldsymbol{n}_i^{\boldsymbol{U}}$ are respectively the eigenvalues and the eigen tensors of the stretch tensor.

Green-Lagrange strain is the first example of a strain measure, i.e. an isotropic function of the stretch tensor that tends linearized strain when the assumptions of the infinitesimal strain theory (see Section (3.2))

3.1.4 Mechanical equilibrium, principle of virtual power

Equilibrium in the current configuration: the Cauchy stress

In this document, we admit the existence of a second order tensor named the Cauchy stress, denoted $\boldsymbol{\sigma}$, such that:

- the conservation of the linear momentum can be expressed by the following partial differential equation:

$$\vec{\mathrm{div}}(\boldsymbol{\sigma}) + \rho\,\vec{b} = \vec{0} \quad \Leftrightarrow \quad \frac{\partial \sigma_{ij}}{\partial x_i} + \rho_c\, b_j = 0 \tag{3.7}$$

  where $\vec{b}$ denotes the body forces by unit of mass and div is the divergence operator in the current configuration.

- the conservation of angular momentum implies that the Cauchy stress is symmetric:

$$\boldsymbol{\sigma} = \boldsymbol{\sigma}^{\mathrm{T}} \tag{3.8}$$

Principle of virtual power

The principle of virtual power is obtained by contracting Equation (3.7) with the velocity $\vec{v}^\star$ of any kinematically admissible displacement $\vec{u}^\star$ and integrating over Ω:

$$\int_\Omega \vec{\mathrm{div}}(\boldsymbol{\sigma}) \cdot \vec{v}^\star \,\mathrm{d}v + \int_\Omega \rho\,\vec{b} \cdot \vec{v}^\star \,\mathrm{d}v = 0$$

Using the Gauss theorem, the first integral can be expressed as follows:

$$\int_{\Omega_c} \vec{\mathrm{div}}(\boldsymbol{\sigma}) \cdot \vec{v}^\star \,\mathrm{d}v = \int_{\partial\Omega_{c,\vec{t}}} \vec{t} \cdot \vec{v}^\star \,\mathrm{d} - \int_{\Omega_c} \boldsymbol{\sigma} : \mathbf{grad}(\vec{v}^\star)\,\mathrm{d}v$$

where $\mathbf{grad}(\cdot)$ denotes the gradient operator with respect to the current configuration. The traction force $\vec{t}$ satifies:

$$\vec{t} = \boldsymbol{\sigma} \cdot \vec{n} \tag{3.9}$$

where $\vec{n}$ denotes the outer normal. Finally, the principal of virtual work reads:

$$\int_{\Omega_c} \boldsymbol{\sigma} : \mathbf{grad}(\vec{v}^\star)\,\mathrm{d}v = \int_{\Omega_c} \rho\,\vec{b} \cdot \vec{v}^\star \,\mathrm{d}v + \int_{\partial\Omega_{\vec{t}}} \vec{t} \cdot \vec{v}^\star \,\mathrm{d}s \tag{3.10}$$

The virtual velocity gradient $\mathbf{grad}(\vec{v}^\star)$ is generally denoted $\boldsymbol{L}^\star$.

Mechanical power density

Applied to real velocity, the Principle of Virtual Power (3.10) leads to the following definition of the mechanical power density in the current configuration w_c:

$$w_c = \boldsymbol{\sigma} : \boldsymbol{L} = \boldsymbol{\sigma} : \mathbf{grad}(\vec{v}) = \boldsymbol{\sigma} : \boldsymbol{D}$$

where the rate of deformation can be introduced thanks to the symmetry of the Cauchy stress (Equation (3.8)).

Equilibrium in the reference configuration: the first Piola-Kirchhoff stress

The virtual power of the inner forces can be rewritten in the current configuration, as follows:

$$\int_{\Omega} \boldsymbol{\sigma} : \mathbf{grad}(\vec{v}^{\star})\,\mathrm{d}v = \int_{\Omega_r} J\boldsymbol{\sigma} : \mathbf{grad}(\vec{v}^{\star})\,\mathrm{d}V \int_{\Omega_r} \boldsymbol{\tau} : \mathbf{grad}(\vec{v}^{\star})\,\mathrm{d}V \quad (3.11)$$

where $\boldsymbol{\tau} = J\,\boldsymbol{\sigma}$ denotes the Kirchhoff stress.

Equation (3.11) still contains the gradient of the virtual velocity in the current configuration, which can be related to the gradient of the virtual velocity in the reference configuration, denoted $\mathbf{Grad}(\vec{v}^{\star})$, as follows:

$$\mathbf{grad}(\vec{v}^{\star}) = \frac{\partial \vec{v}^{\star}}{\partial \vec{x}} = \frac{\partial \vec{v}^{\star}}{\partial \vec{X}} \cdot \frac{\partial \vec{X}}{\partial \vec{x}} = \mathbf{Grad}(\vec{v}^{\star}) \cdot \boldsymbol{F}^{-1}$$

Using the similarity invariance of the trace[2], the virtual mechanical power in the reference configuration, i.e. the integrand of the last integral, can be rewritten as follows:

$$\begin{aligned} J\,\boldsymbol{\sigma} : \mathbf{grad}(\vec{v}^{\star}) &= J\,\mathrm{tr}\big(\boldsymbol{\sigma}^{\mathrm{T}} \cdot \mathbf{grad}(\vec{v}^{\star})\big) \\ &= J\,\mathrm{tr}\big(\boldsymbol{F}^{-1} \cdot \boldsymbol{\sigma}^{\mathrm{T}} \cdot \mathbf{grad}(\vec{v}^{\star}) \cdot \boldsymbol{F}\big) \\ &= J\,\mathrm{tr}\Big(\Big(\boldsymbol{\sigma} \cdot \boldsymbol{F}^{-\mathrm{T}}\Big)^{\mathrm{T}} \cdot \mathbf{Grad}(\vec{v}^{\star})\Big) \\ &= \boldsymbol{P} : \mathbf{Grad}(\vec{v}^{\star}) \end{aligned}$$

The tensor $\boldsymbol{P} = J\,\boldsymbol{\sigma} \cdot \boldsymbol{F}^{-T} = \boldsymbol{\tau} \cdot \boldsymbol{F}^{-T}$ is the first Piola-Kirchhoff stress, also called the Boussinesq stress.

Using the Gauss theorem, the first Piola-Kirchhoff stress statisfies the following balance equations:

$$\vec{\mathrm{Div}}(\boldsymbol{P}) + \rho_r\,\vec{b}_r = \vec{0} \quad (3.12)$$

The first Piola-Kirchhoff stress is related to the traction forces using the Nanson's formula as follows:

$$\vec{t} = \boldsymbol{\sigma} \cdot \vec{n} = \boldsymbol{P} \cdot \vec{N} \quad (3.13)$$

where $\vec{N}$ is the outer unit normal in the reference configuration.

Expressing the equilibrium in the reference configuration can be useful numerically. In particular, Equation (3.12) is widely used in solvers based on the fast-Fourier transform (microstructure computations with periodic boundary conditions).

[2]For a given matrix $\boldsymbol{A}$ and an invertible matrix $\boldsymbol{B}$, the following identity holds:

$$\mathrm{tr}(\boldsymbol{A}) = \mathrm{tr}\big(\boldsymbol{B} \cdot \boldsymbol{A} \cdot \boldsymbol{B}^{-1}\big)$$

This property is denoted as the similarity invariance of the trace.

Second Piola-Kirchhoff stress

As the Cauchy stress is assumed symmetric, this expression can be further developped to introduce another useful stress measure as follows:

$$\begin{aligned} J\,\boldsymbol{\sigma} :\, \mathbf{grad}(\vec{v}^{\star}) &= J\,\mathrm{tr}\big(\boldsymbol{F}^{-1} \cdot \boldsymbol{\sigma}^{\mathrm{T}} \cdot \mathbf{Grad}(\vec{v}^{\star})\big) \\ &= J\,\mathrm{tr}\Big(\boldsymbol{F}^{-1} \cdot \boldsymbol{\sigma}^{\mathrm{T}}\,\boldsymbol{F}^{-\mathrm{T}} \cdot \boldsymbol{F}^{\mathrm{T}} \cdot \mathbf{Grad}(\vec{v}^{\star})\Big) \\ &= \boldsymbol{S} :\, \Big(\boldsymbol{F}^{\mathrm{T}} \cdot \mathbf{Grad}(\vec{v}^{\star})\Big) \end{aligned}$$

where $\boldsymbol{S} = J\,\boldsymbol{F}^{-1} \cdot \boldsymbol{\sigma}\,\boldsymbol{F}^{-\mathrm{T}}$ is the second Piola-Kirchhoff stress (also called the Piola stress). This tensor is symmetric if the Cauchy stress is symmetric. Using this property, one can write:

$$\begin{aligned} J\,\boldsymbol{\sigma} :\, \mathbf{grad}(\vec{v}^{\star}) &= \frac{1}{2}\,\boldsymbol{S} :\, \Big(\boldsymbol{F}^{\mathrm{T}} \cdot \mathbf{Grad}(\vec{v}^{\star}) + \mathbf{Grad}(\vec{v}^{\star})^{\mathrm{T}} \cdot \boldsymbol{F}\Big) \\ &= \frac{1}{2}\,\boldsymbol{S} :\, \dot{\boldsymbol{C}}^{\star} = \boldsymbol{S} :\, \dot{\boldsymbol{E}}^{GL\,\star} \end{aligned} \tag{3.14}$$

where $\dot{\boldsymbol{C}}^{\star}$ is the virtual rate of the right-Cauchy tensor and the $\dot{\boldsymbol{E}}^{GL\,\star}$ is the virtual rate of Green-Lagrange strain.

Equation (3.14) shows that the second Piola-Kirchhoff stress is the power conjugate of the Green-Lagrange strain.

Four equivalent forms of the virtual power of the inner forces

Finally, the following expression of the virtual power of inner forces in the reference configuration yields:

$$\begin{aligned} \int_{\Omega} \boldsymbol{\sigma} :\, \mathbf{grad}(\vec{v}^{\star})\,\mathrm{d}v &= \int_{\Omega_r} \boldsymbol{\tau} :\, \mathbf{grad}(\vec{v}^{\star})\,\mathrm{d}v \\ &= \int_{\Omega_r} \boldsymbol{P} \colon\, \dot{\boldsymbol{F}}^{\star}\,\mathrm{d}V \\ &= \int_{\Omega_r} \boldsymbol{S} :\, \dot{\boldsymbol{E}}^{GL\,\star}\,\mathrm{d}V \end{aligned} \tag{3.15}$$

Those equivalent expressions of the principle of virtual power leads to (at least) three different numerical schemes in finite element solvers.

3.1.5 Thermodynamics in finite strain

Mechanical power in the reference configuration

Following Equation (3.15), the density of mechanical power in the reference configuration w_r is given by:

$$w_r = J\,\boldsymbol{\sigma} :\, \boldsymbol{D} = J\,w_c = \boldsymbol{\tau} :\, \boldsymbol{D} = \boldsymbol{P} \colon\, \dot{\boldsymbol{F}} = \boldsymbol{S} :\, \dot{\boldsymbol{E}}^{GL} \tag{3.16}$$

where $\boldsymbol{\tau}$ denotes the Kirchhoff stress.

First and second principles, Clausius-Duhem inequality

Let e be the specific energy (energy per unit of mass). The first principle, written in the current configuration, states that:

$$\rho\,\dot{e} = \boldsymbol{\sigma} :\ \boldsymbol{D} + \rho\,q - \vec{\mathrm{div}}\left(\vec{j}\right)$$

where q is the specific heat source and $\vec{j}$ the heat flux.

Let s be the specific entropy. The second principle, written in the current configuration, reads:

$$\rho\,\dot{s} + \vec{\mathrm{div}}\left(\frac{\vec{j}}{T}\right) - \frac{\rho\,q}{T} \geqslant 0$$

where T denotes the temperature.

Combining those two principles leads to the Clausius-Duhem inequality:

$$-\rho(\dot{e} - T\,\dot{s}) + \boldsymbol{\sigma} :\ \boldsymbol{D} - \frac{\vec{q}}{T} \cdot \vec{\mathrm{grad}}(T) \geqslant 0$$

This expression can be further simplified by introducing the specific free energy $\Psi = e - T\,s$:

$$-\rho\left(\dot{\Psi} - s\,\dot{T}\right) + \boldsymbol{\sigma} :\ \boldsymbol{D} - \frac{\vec{q}}{T} \cdot \vec{\mathrm{grad}}(T) \geqslant 0 \tag{3.17}$$

Finally, this expression can be written in the reference configuration as follows:

$$-\rho_r\left(\dot{\Psi} - s\,\dot{T}\right) + \boldsymbol{\tau} :\ \boldsymbol{D} - \frac{\vec{Q}}{T} \cdot \vec{\mathrm{Grad}}(T) \geqslant 0 \tag{3.18}$$

3.1.6 Objectivity

Objectivity refers to the invariance of the physical description by a change of observer, also referred to as *frame invariance*.

The descriptions of the motions by two observers are related by a rigid body motion:

$$\vec{x}^{(2)} = y_{1\to 2}(t) + \boldsymbol{Q}_{1\to 2}(t)\left(\vec{x}^{(1)} - \vec{x}_{1\to 2}\right) \tag{3.19}$$

where:

- $\vec{x}^{(1)}$ and $\vec{x}^{(2)}$ are the current positions of a given point for the first and second observers respectively.
- $y_{1\to 2}(t)$ describes the translation between the two observers.
- $\boldsymbol{Q}_{1\to 2}(t)$ describes the rotation between the two observers.
- $x_{1\to 2}$ is an arbitrary origin.

With this definition, the deformation gradients computed by the two observers, denoted respectively $\boldsymbol{F}^{(1)}$ and $\boldsymbol{F}^{(2)}$ are related by:

$$\boldsymbol{F}^{(2)} = \boldsymbol{Q}_{1\to 2}(t)\,\boldsymbol{F}^{(1)}$$

This relation is a simple application of the chain rule.

Quantities associated with the current configuration (the Cauchy stress $\boldsymbol{\sigma}$, the Kirchhoff stress $\boldsymbol{\tau}$, the rate of deformation $\boldsymbol{D}$) are affected by the rotation $\boldsymbol{Q}_{1\to 2}$ as follows:

$$\begin{cases} \boldsymbol{D}^{(2)} = \boldsymbol{Q}_{1\to 2} \cdot \boldsymbol{D}^{(1)} \cdot {\boldsymbol{Q}^{\mathrm{T}}}_{1\to 2} \\ \boldsymbol{\sigma}^{(2)} = \boldsymbol{Q}_{1\to 2} \cdot \boldsymbol{\sigma}^{(1)} \cdot {\boldsymbol{Q}^{\mathrm{T}}}_{1\to 2} \\ \boldsymbol{\tau}^{(2)} = \boldsymbol{Q}_{1\to 2} \cdot \boldsymbol{\tau}^{(1)} \cdot {\boldsymbol{Q}^{\mathrm{T}}}_{1\to 2} \end{cases} \tag{3.20}$$

The Relation (3.20) for the rate of deformation $\boldsymbol{D}$ can be obtained by a direct application of the chain rule. It is worth highlighting that Relation (3.20) for the Cauchy stress $\boldsymbol{\sigma}$ can be obtained in two ways:

1. One may use the chain rule on the Equilibrium Equation (3.7).
2. One may invoke the invariance of the power density $\boldsymbol{\sigma} : \boldsymbol{D}$ by change of observer and the transformation rule for the rate of deformation.

Tensors that transforms according to Relation (3.20) are associated with the current configuration and are called Eulerian tensors.

The transformation rule of the deformation gradient $\boldsymbol{F}$ can be used to show that tensors associated with the reference configuration (stretch tensor $\boldsymbol{U}$, right Cauchy tensor $\boldsymbol{C}$, Green-Lagrange strain $\boldsymbol{C}$, second Piola-Kirchhoff stress $\boldsymbol{S}$) are invariant by change of observers. Such tensors are called lagrangian.

It is worth emphasizing the fact that objectivity is not a physical principle: it is a constraint of the constitutive equations. Constitutive equations that does not comply with the Transformation Rules (3.20) for every change of observer given by Relation (3.19) are inconsistent.

3.2 (Visco-)plasticity in the infinitesimal strain theory

3.2.1 Kinematics and mechanical equilibrium in the infinitesimal strain theory

The infinitesimal strain theory can be introduced by considering an small perturbations of the rotation matrix and the stretch tensor as follows:

$$\boldsymbol{R} = \boldsymbol{I} + \delta\,\boldsymbol{R}$$
$$\boldsymbol{U} = \boldsymbol{I} + \delta\,\boldsymbol{U}$$

where $\delta\,\boldsymbol{R}$ is a skew symmetric tensor (this classical result is admitted here) and $\delta\,\boldsymbol{U}$ is a symmetric tensor.

The deformation gradient can be expanded as follows:

$$\boldsymbol{F} = (\boldsymbol{I} + \delta\,\boldsymbol{R}) \cdot (\boldsymbol{I} + \delta\,\boldsymbol{U}) \approx \boldsymbol{I} + \delta\,\boldsymbol{R} + \delta\,\boldsymbol{U}$$

This expression shows that the $\delta\,\boldsymbol{U}$ is the symmetric part of $\boldsymbol{F} - \boldsymbol{I}$ and $\delta\,\boldsymbol{R}$ its skew symmetric part. Taking Equation (3.1) into account, the following relations holds:

$$\delta\,\boldsymbol{U} \approx \frac{1}{2}\left(\frac{\partial \vec{u}}{\partial \vec{X}} + \frac{\partial \vec{u}}{\partial \vec{X}}^{\mathrm{T}}\right)$$
$$\delta\,\boldsymbol{R} \approx \frac{1}{2}\left(\frac{\partial \vec{u}}{\partial \vec{X}} - \frac{\partial \vec{u}}{\partial \vec{X}}^{\mathrm{T}}\right)$$

where $^{\mathrm{T}}$ denotes the transposition of a tensor

The linearised strain tensor $\boldsymbol{\epsilon}^{\mathrm{to}}$ is defined as the first order approximation of the stretch tensor, i.e. the symmetric part of the displacement gradient:

$$\boldsymbol{\epsilon}^{\mathrm{to}} = \frac{1}{2}\left(\frac{\partial \vec{u}}{\partial \vec{X}} + \frac{\partial \vec{u}}{\partial \vec{X}}^{\mathrm{T}}\right) \tag{3.21}$$

Using the Polar Decomposition (3.6), an alternate expression of the linearised strain tensor $\boldsymbol{\epsilon}^{\mathrm{to}}$ can be established:

$$\boldsymbol{\epsilon}^{\mathrm{to}} = \frac{1}{2}\Big(\boldsymbol{F} + \boldsymbol{F}^{\mathrm{T}}\Big) - \boldsymbol{I} = \frac{1}{2}\Big(\boldsymbol{R} \cdot \boldsymbol{U} + \boldsymbol{U} \cdot \boldsymbol{R}^{\mathrm{T}}\Big) - \boldsymbol{I} \tag{3.22}$$

Change of volume

A first order approximation relates the change of volume J to the trace of the strain tensor as follows:

$$J \approx 1 + \mathrm{tr}(\delta\,\boldsymbol{U}) \approx 1 + \mathrm{tr}\big(\boldsymbol{\epsilon}^{\mathrm{to}}\big) \tag{3.23}$$

Equilibrium

In the initial configuration, the mechanical equilibrium is given by:

$$\vec{\mathrm{div}}(\boldsymbol{\sigma}) + \rho\,\vec{b} = \vec{0} \quad \Leftrightarrow \quad \frac{\partial \sigma_{ij}}{\partial x_i} + \rho\,b_j = 0 \tag{3.24}$$

where $\vec{b}$ are the unit force by unit of mass.

3.2.2 Main ingredients of (visco-)plastic behaviors in the infinitesimal strain theory

Under the assumptions of the infinitesimal strain theory, incompressible (visco-)plastic behaviors are based on the following ingredients:

- The strain tensor is splitted additively in an elastic $\boldsymbol{\epsilon}^{\text{el}}$ and a (visco-)plastic $\boldsymbol{\epsilon}^{\text{in}}$ part as follows:

$$\boldsymbol{\epsilon}^{\text{to}} = \boldsymbol{\epsilon}^{\text{el}} + \boldsymbol{\epsilon}^{\text{in}}$$

- The stress tensor is given by the Hooke Law:

$$\boldsymbol{\sigma} = \mathbb{D} : \boldsymbol{\epsilon}^{\text{el}} \tag{3.25}$$

- The inelastic strain evolution has the following general form:

$$\dot{\boldsymbol{\epsilon}}^{\text{in}} = \dot{\lambda}\, \boldsymbol{n} \tag{3.26}$$

  where $\dot{\lambda}$ is either a plastic multiplier enforcing that the material remains on the yield surface (plasticity) or an explicit fonction of the stress (viscoplasticity) and where $\boldsymbol{n}$ describes the direction of the inelastic flow.

- Following Equation (3.23), the *plastic incompressibility* is enforced by requiring that the trace of the inelastic strain to be null:

$$J = \frac{\rho_c}{\rho_r} = 1 \underset{\approx}{\implies} \operatorname{tr}\left(\boldsymbol{\epsilon}^{\text{in}}\right) = 0 \implies \operatorname{tr}(\boldsymbol{n}) = 0$$

- Following Equation 3.3, the porosity evolution is given by:

$$\dot{f} = (1-f)\operatorname{tr}\left(\dot{\boldsymbol{\epsilon}}^{\text{to}}\right) \approx (1-f)\operatorname{tr}\left(\dot{\boldsymbol{\epsilon}}^{\text{in}}\right) \tag{3.27}$$

- Last but not least, sound behaviors are based on energetic considerations. The *mechanical power density* w is the contracted product of the total strain $\boldsymbol{\epsilon}^{\text{to}}$ and the stress tensor $\boldsymbol{\sigma}$:

$$w = \boldsymbol{\sigma} : \dot{\boldsymbol{\epsilon}}^{\text{to}} \tag{3.28}$$

3.2.3 Limitations in finite strain

Before introducing a rigorous description of visco-plastic behaviors at finite strain, it is interesting to point out the limitations of the small strain framework described in the previous paragraph, from the point of view of the behavior:

- The first limitation comes to the fact that the total strain is a mix of stretch and rotation (See Equation (3.22)).

- The second limitation to the notion of *objectivity* which is the requirement stating that behavior must yield to same results whatever the observer, as detailled in Section 3.1.6. The total strain is not objective (this is indeed a consequence of the first limitation): hence the behaviors build on top of it are not objective.

- The third limitation is related to the approximate nature of the Relation (3.23). Hence, using a small strain viscoplastic behavior does not guarantee to preserve the (visco-)plastic incompressibility.
- The last point is that the mechanical power density is not given by Equation (3.28), whatever the choice of the stress measure[3].

3.3 Lagrangian stress and strain measures

So far, four stress tensors have introduced: the Cauchy stress $\boldsymbol{\sigma}$, the Kirchhoff stress $\boldsymbol{\tau}$, the first and second Piola-Kirchhoff stresses, denoted respectively $\boldsymbol{P}$ and $\boldsymbol{S}$.

$\boldsymbol{P}$ and $\boldsymbol{\sigma}$ can be related to forces acting on the body, as stated by Equations (3.9) and (3.13), and equilibrium equations in strong form, as stated by Equations (3.7) and (3.11).

This is not the case for the the Kirchhoff stress $\boldsymbol{\tau}$ and the second Piola-Kirchhoff stress $\boldsymbol{S}$ which have been introduced through equivalent expression of the mechanical power in the reference configuration (see Equation (3.16)) as the conjugate of the rate of deformation $\boldsymbol{D}$ and the rate of the Green-Lagrange strain $\dot{\boldsymbol{\varepsilon}}^{GL}$ respectively.

The Green-Lagrange strain $\boldsymbol{\varepsilon}^{GL}$ and the second Piola-Kirchhoff stress $\boldsymbol{S}$ are example of lagrangian tensors (see Section (3.1.6)). It is worth highlighting the fact that constitutive equations written in terms of lagrangian tensors are automatically objective.

This section shows that an infinite number of strain measures can be defined and, by duality, an infinite number of stress measures.

3.3.1 Lagrangian strain measures and conjugated strain measures

Lagrangian strain measures can be defined as functions of the stretch tensors which tends to the linearized strain $\boldsymbol{\epsilon}^{\text{to}}$ when the assumptions of the infinitesimal strain theory holds.

An important example of lagrangian strain measures is given by the Seth-Hill strain measures $\boldsymbol{E}^{(m)}$ defined as follows:

$$\boldsymbol{E}^{(m)} = \begin{cases} \dfrac{1}{m}(\boldsymbol{U}^m - \boldsymbol{I}) & m \neq 0 \\ \ln U & m = 0 \end{cases}$$

The special case $\boldsymbol{E}^{(2)}$ corresponds to the Green-Lagrange strain, while

[3]Indeed, in finite strain, there are an infinite number of stress measures.

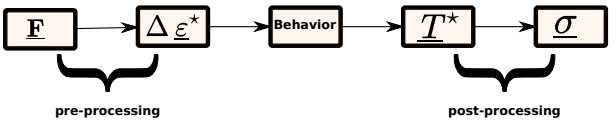

FIGURE 3.2: A general framework to reuse constitutive equations written in the infinitesimal strain framework

$\boldsymbol{E}^{(0)}$ corresponds to the Hencky strain that will be discussed in depth in Section 3.3.3.

Given a lagrangian strain measure $\boldsymbol{E}^\star$, a conjugated stress tensor $\boldsymbol{S}^\star$ can be defined by duality as follows:

$$w_r = \boldsymbol{S} : \dot{\boldsymbol{E}}^{GL} = \boldsymbol{S}^\star : \dot{\boldsymbol{E}}^\star \tag{3.29}$$

Due to this duality, the Clausius-Duhem Inequality (3.18) can be written as follows:

$$-\rho_r \left(\dot{\Psi} - s\dot{T}\right) + \boldsymbol{S}^\star : \dot{\boldsymbol{E}}^\star - \frac{\vec{Q}}{T} \cdot \vec{\mathrm{Grad}}(T) \geqslant 0$$

where $\vec{Q}$ is the lagrangian counterpart of $\vec{q}$.

This inequality has a strong similitude with its counterpart in the infinitesimal strain framework: $\boldsymbol{E}^\star$ replaces the linearised strain $\boldsymbol{\epsilon}^{\mathrm{to}}$ and $\boldsymbol{S}^\star$ replaces the stress tensor.

In particular, classical arguments leads to the following relationship:

$$\boldsymbol{S}^\star = \rho_r \frac{\partial \Psi}{\partial \boldsymbol{E}^\star} \quad \text{and} \quad s = \frac{\partial \Psi}{\partial T}$$

3.3.2 A general framework to reuse constitutive equations written in the infinitesimal strain framework

Valid finite strain constitutive equations can be obtained by selecting a lagrangian strain measure, reusing constitutive equations written in the infinitesimal strain framework and interpreting the result as the conjugated of the selected strain measure (see Figure 3.2).

This strategy has several advantages:

- Objectivity is ensured by construction.
- If the constitutive equations written in the infinitesimal strain framework satisfies the Clausius-Duhem inequality, the finite strain constitutive equations will also satisfies the Clausius-Duhem inequality.

However, this strategy has a strong limitation due to the lack of link between the change of volume and the trace of the strain measure. As stated in

Section 3.2.2, this link is crucial for most (visco-)plastic behaviors. Hence, the proposed strategy is often limited to small strain but finite rotations, except for the Hencky strain which is detailed in Section 3.3.3.

The Saint-Venant Kirchhoff hyperelastic behavior

As a trivial example of this strategy, the Saint-Venant Kirchhoff hyperelastic behavior generalizes the Hooke law using the Green-Lagrange strain as follows:

$$\boldsymbol{S} = \mathbb{D} : \boldsymbol{E}^{GL}$$

where $\boldsymbol{D}$ is the elastic stiffness matrix.

The Saint-Venant Kirchhoff hyperelastic behavior derives from the following free-energy:

$$\Psi = \frac{1}{2\,\rho_r} \boldsymbol{\varepsilon}^{GL} : \mathbb{D} : \boldsymbol{\varepsilon}^{GL}$$

3.3.3 The logarithmic strain framework

Another approach, popularized by Miehe et al. [Miehe et al.], is based on the lagrangian Hencky strain, also called the logarithmic strain, defined as the logarithm of the stretch tensor:

$$\boldsymbol{\varepsilon}^{\mathrm{to}}_{\log} = \ln(\boldsymbol{U}) = \frac{1}{2} \ln(\boldsymbol{C})$$

where $\boldsymbol{C}$ denotes the right Cauchy tensor in the reference configuration. Following Equation (3.29), the dual stress $\boldsymbol{T}$ of the Hencky strain is defined by the following equality:

$$\boldsymbol{S} : \dot{\boldsymbol{\varepsilon}}^{GL} = \boldsymbol{T} : \dot{\boldsymbol{\varepsilon}}^{\mathrm{to}}_{\log}$$

Change of volume

The fundamental property of the Hencky logarithmic strain measure is that its trace is related to the change of volume as follows:

$$J = \exp\left(\mathrm{tr}\left(\boldsymbol{\varepsilon}^{\mathrm{to}}_{\log}\right)\right)$$

This equation shows that if the trace of the strain is null, no change of volume may occur. With this property, the strategy exposed in Section 3.3.2 for large strain and large rotations.

Interpretation in 1D

Another nice property of the logarithmic strain framework is that if in absence of material rotation, it can be shown that $\boldsymbol{T}$ is equal to the Kirchhoff stress $\boldsymbol{\tau}$, which, for most metals, is almost equal to the Cauchy stress $\boldsymbol{\sigma}$.

Hence, for uniaxial tensile tests, the logarithmic strain is the so-called "true strain" and its dual is almost the so-called "true stress".

3.4 Multiplicative decomposition of the deformation gradient

The reference configuration has a special role in the framework described in Section 3.3.2, a fact depicted as undesirable by some authors [Sidoroff, 1981].

An alternative approach, widely used in the litterature, is the so-called $\boldsymbol{F}_e \cdot \boldsymbol{F}_p$ framework introduced by Lee [Lee, 1969; Mandel].

This framework is based on the following multiplicative decomposition of the deformation gradient into an elastic part, denoted $\boldsymbol{F}_e$ and a (visco-)plastic part, denoted $\boldsymbol{F}_p$:

$$\boldsymbol{F} = \boldsymbol{F}_e \cdot \boldsymbol{F}_p \tag{3.30}$$

Based on Equation (3.4), $\boldsymbol{F}_p$ is interpreted as the deformation gradient into an intermediate configuration. The main idea of this decomposition is that the stress tensor shall only be a function of the elastic part of the deformation gradient. This allows to interpret the intermediate configuration as a *relaxed* configuration, i.e. the stress is null if $\boldsymbol{F}$ and $\boldsymbol{F}_p$ coincide.

3.4.1 Decomposition of velocity gradient

The velocity gradient $\mathbf{grad}(\vec{v})$ can be related to the deformation gradient $\boldsymbol{F}$ as follows:

$$\begin{aligned}\mathbf{grad}(\vec{v}) = \frac{\partial \vec{v}}{\partial \vec{x}} &= \frac{\partial \vec{v}}{\partial \vec{X}} \cdot \frac{\partial \vec{X}}{\partial \vec{x}} = \frac{\partial}{\partial \vec{X}}\left(\frac{\partial \vec{u}}{\partial t}\right) \cdot \boldsymbol{F}^{-1} \\ &= \frac{\partial}{\partial t}\left(\frac{\partial \vec{u}}{\partial \vec{X}}\right) \cdot \boldsymbol{F}^{-1} = \dot{\boldsymbol{F}} \cdot \boldsymbol{F}^{-1}\end{aligned}$$

Using Equation (3.30), the velocity gradient $\boldsymbol{L}$ can be decomposed as follows:

$$\begin{aligned}\boldsymbol{L} = \dot{\boldsymbol{F}} \cdot \boldsymbol{F}^{-1} &= \left(\dot{\boldsymbol{F}}_e \cdot \boldsymbol{F}_p + \boldsymbol{F}_e \cdot \dot{\boldsymbol{F}}_p\right) \cdot \boldsymbol{F}^{-1} \\ &= \left(\dot{\boldsymbol{F}}_e \cdot \boldsymbol{F}_p + \boldsymbol{F}_e \cdot \dot{\boldsymbol{F}}_p\right) \cdot \boldsymbol{F}_p^{-1} \cdot \boldsymbol{F}_e^{-1} \\ &= \dot{\boldsymbol{F}}_e \cdot \boldsymbol{F}_e^{-1} + \boldsymbol{F}_e \cdot \dot{\boldsymbol{F}}_p \cdot \boldsymbol{F}_p^{-1} \cdot \boldsymbol{F}_e^{-1} \\ &= \boldsymbol{L}_e + \boldsymbol{F}_e \cdot \boldsymbol{L}_p \cdot \boldsymbol{F}_e^{-1}\end{aligned} \tag{3.31}$$

where:

- The elastic part $\boldsymbol{L}_e = \dot{\boldsymbol{F}}_e \cdot \boldsymbol{F}_e^{-1}$ of the velocity gradient is defined in the current configuration C.
- The plastic part of the velocity gradient $\boldsymbol{L}_p = \dot{\boldsymbol{F}}_p \cdot \boldsymbol{F}_p^{-1}$ in the intermediate configuration C_i.

3.4.2 Expression of the mechanical power

The mechanical power per unit of volume in the current configuration p_v is given by the contracted product of the Cauchy stress and the deformation gradient.

Assuming the symmetry of the Cauchy stress, p_v can be developped as follows:

$$\boldsymbol{\sigma} : \boldsymbol{D} = \boldsymbol{\sigma} : \boldsymbol{L} = \boldsymbol{\sigma} : \boldsymbol{L}_e + \boldsymbol{\sigma} : \left(\boldsymbol{F}_e \cdot \boldsymbol{L}_p \cdot \boldsymbol{F}_e^{-1}\right)$$

The term $\boldsymbol{\sigma} : \boldsymbol{L}_e$ is assumed to be reversible and must derive from an convex free energy Ψ, as developped in Section 3.3.2, such that:

$$\boldsymbol{\sigma} : \boldsymbol{L}_e = \frac{1}{J_e} \boldsymbol{S}_e : \dot{\boldsymbol{E}}^{GL} \quad \text{with} \quad \boldsymbol{S}_e = \rho_e \frac{\partial \Psi_e}{\partial \boldsymbol{E}^{GL}}$$

where $\boldsymbol{S}_e$ is the second Piola-Kirchhoff stress, $\boldsymbol{E}^{GL}$ is the Green-Lagrange strain, J_e is the determinant of the elastic part of the deformation gradient and ρ_e the mass density in the intermediate configuration.

The second term will be associated with the plastic dissipation in Section 3.4.2 which introduces the Mandel stress M such that:

$$\boldsymbol{\sigma} : \boldsymbol{D} = \boldsymbol{\sigma} : \boldsymbol{L}_e + \frac{1}{J_e} \boldsymbol{M} : \boldsymbol{L}_p \tag{3.32}$$

Plastic dissipation and Mandel stress

The Mandel stress $\boldsymbol{M}$ is defined as the dual of the plastic velocity gradient $\boldsymbol{L}_p$, i.e. as the stress measure which satisfies:

$$\boldsymbol{\sigma} : \left(\boldsymbol{F}_e \cdot \boldsymbol{L}_p \cdot \boldsymbol{F}_e^{-1}\right) = \frac{1}{J_e} \boldsymbol{M} : \boldsymbol{L}_p$$

The Mandel stress $\boldsymbol{M}$ is equal to:

$$\boldsymbol{M} = \boldsymbol{C}_e \cdot \boldsymbol{S}_e = \left(2\,\boldsymbol{E}^{GL} + \boldsymbol{I}\right) \cdot \boldsymbol{S}_e \tag{3.33}$$

Note that the Mandel stress is not symmetric.

Clausius-Duhem inequality

The Clausius-Duhem inequality, as given by Equation (3.17) can be combined with Equation (3.32) as follows:

$$-\rho \left(\frac{\partial \Psi}{\partial \boldsymbol{E}^{GL}} : \dot{\boldsymbol{E}}^{GL} + \frac{\partial \Phi}{\partial \vec{y}} \cdot \vec{\dot{y}} \right) + \boldsymbol{\sigma} : \boldsymbol{D} \geqslant 0$$

$$-\rho \left(\left(\frac{\partial \Psi}{\partial \boldsymbol{E}^{GL}} - \frac{1}{\rho\, J_e} \boldsymbol{S}_e \right) : \dot{\boldsymbol{E}}^{GL} \right) - \rho \frac{\partial \Phi}{\partial \vec{y}} \cdot \vec{\dot{y}} + \frac{1}{J_e} \boldsymbol{M} : \boldsymbol{L}_p \geqslant 0$$

where, for the sake of simplicity, terms related to heat transfer has been omitted.

Classical arguments (considering a reversible process), leads to:

$$\boldsymbol{S}_e = \rho_e \frac{\partial \Psi}{\partial \boldsymbol{E}^{GL}} \quad \text{and}$$

where ρ_e is the density in the intermediate configuration ($\rho_e = \rho\, J_e$).

The dissipation can then be re-written by introducing the thermodynamic forces $\vec{Y} = -\rho_e \dfrac{\partial \Phi}{\partial \vec{y}}$ associated to the internal state variables $\vec{y}$:

$$\vec{Y} \cdot \dot{\vec{y}} + \boldsymbol{M} : \boldsymbol{L}_p \geqslant 0$$

The dissipation is automatically positive if we introduce a convex dissipation potential ϕ minimal at zero such that:

$$\boldsymbol{L}_p = \frac{\partial \phi}{\partial \boldsymbol{M}} \quad \text{and} \quad \dot{\vec{y}} = \frac{\partial \phi}{\partial \vec{Y}}$$

This expression of the plastic rate is now used to devise two examples of constitutive equations:

- Isotropic viscoplasticity and plasticity.
- Single crystal (visco-)plasticity.

3.4.3 Isotropic viscoplasticity and plasticity

This section is devoted to describe a class of isotropic finite strain constitutive equations associated to viscoplasticity and plasticity which is derived in a way quite similar to the small strain theory.

Choice of the stress criterion

Du to isotropy, the dissipation potential must be a function of the invariants of the Mandel stress:

- the trace of the Mandel stress, I_1.
- the von Mises norm of the Mandel stress, M_{eq}:

$$M_{\text{eq}} = \sqrt{\frac{3}{2}\, \boldsymbol{M}_{\text{dev}} : \boldsymbol{M}_{\text{dev}}}.$$

  where $\boldsymbol{M}_{\text{dev}}$ is the deviatoric part of the Mandel stress.
- the determinant of the deviatoric part of the Mandel stress.

Since the plastic flow is assumed to be isochoric, L_p must be traceless according to Equation (3.5), so the dissipation potential can't be a function of I_1.

In this section, we assume that the behavior oly depends on M_{eq}. Thus,

$$\boldsymbol{L}_p = \frac{\partial \phi}{\partial M_{\text{eq}}} \frac{\partial M_{\text{eq}}}{\partial \boldsymbol{M}} = \frac{\partial \phi}{\partial M_{\text{eq}}} \left(\frac{3}{2\, M_{\text{eq}}} \boldsymbol{M}_{\text{dev}} \right) = \frac{\partial \phi}{\partial M_{\text{eq}}} \boldsymbol{N}$$

where $\boldsymbol{N} = \dfrac{3\, \boldsymbol{M}_{\text{dev}}}{2\, M_{\text{eq}}}$ is the normal.

Isotropic incompressible viscoplasticty

$$\phi = \frac{M_0\, \dot{\varepsilon}_0}{n+1} \left(\frac{M_{\text{eq}}}{M_0} \right)^{n+1}$$

Isotropic incompressible plasticity

The yield surface of a plastic behavior with linear isotropic hardening is given by:

$$f = M_{\text{eq}} - M_0 - H\,(p)$$

where p is the equivalent plastic strain, M_0 is the yield stress and H is the hardening slope.

3.4.4 Single crystal

It is assumed that the crystal deforms by gliding of dislocations on a set of N_s prescribed crystallographic planes called *slip planes*, also called *slip systems* or *gliding systems*.

A slip plane is characterized by its normal $\vec{n}_s$ and a slip direction $\vec{m}_s$ in the plane ($s \in [1, N_s]$). By definition, the vectors are $\vec{n}_s$ and $\vec{m}_s$ are orthogonal. A slip plane is also characterized by its orientation tensor $\boldsymbol{N}_s$ such that:

$$\boldsymbol{N}_s = \vec{m}_s \otimes \vec{n}_s$$

The gliding of dislocations leave the crystal orientations unchanged, so the orientation tensors are the same in the initial configuration C_0 and in the intermediate configuration C_i.

Finally, the plastic part of the velocity gradient is given by the sum of the glidings on all gliding planes, as follows:

$$\boldsymbol{L}_p = \sum_{s}^{N_s} \dot{\gamma}_s\, \boldsymbol{N}_s$$

where $\dot{\gamma}_s$ is the slip rate of the s^{th} plane.

This plastic flow is isochoric, as:

$$\mathrm{tr}(\boldsymbol{L}_p) = \sum_s^{N_s} \dot{\gamma}_s \,\mathrm{tr}(\boldsymbol{N}_s) = \sum_s^{N_s} \dot{\gamma}_s \,\vec{m}_s \,\cdot\, \vec{n}_s = 0$$

The expression of the plastic dissipation naturally introduces the resolved shear stresses τ^s:

$$\boldsymbol{M} : \boldsymbol{L}_p = \sum_s^{N_s} \dot{\gamma}_s \,\tau^s$$

with $\tau^s = \boldsymbol{M} : \boldsymbol{N}_s$.

A simple dissipation potential for crystal plasticity

A simple dissipation potential for the single crystal can be defined as follows:

$$\phi(\boldsymbol{M}) = \sum_s^{N_s} \phi^s(|\tau^s|)$$

where each function ϕ^s is assumed to be convex and minimal at zero.

This dissipation potential leads to:

$$\boldsymbol{L}_p = \sum_s^{N_s} \frac{\partial \phi^s}{\partial\,|\tau^s|} \frac{\partial\,|\tau^s|}{\partial \tau^s} \frac{\partial \tau^s}{\partial \boldsymbol{M}} = \sum_s^{N_s} sgn\,(\tau^s) \frac{\partial \phi^s}{\partial\,|\tau^s|} \frac{\partial \tau^s}{\partial \boldsymbol{M}} = \sum_s^{N_s} sgn\,(\tau^s) \frac{\partial \phi^s}{\partial\,|\tau^s|} \boldsymbol{N}_s$$

where $sgn\,(\tau^s)$ denotes the sign function:

$$sgn\,(x) = \begin{cases} 1 & \text{if } x \geq 0 \\ -1 & \text{if } x < 0 \end{cases}$$

A classical choice for ϕ^s is a power-law:

$$\phi^s(|\tau^s|) = \frac{A}{n+1} \,|\tau^s|^{n+1}$$

3.5 Rate form constitutive equations

Another attempt to resuse implementations of behaviors written in the infinitesimal strain formalism is to write constitutive equations in rate form. Even if this approach suffers from various theoretical and practical drawbacks [Simo and Hughes; Doghri], it is still used in many popular academic and commercial solvers.

The departure point is the Decomposition (3.31) of the velocity gradient:

$$\boldsymbol{L} = \boldsymbol{L}_e + \boldsymbol{F}_e \cdot \boldsymbol{L}_p \cdot \boldsymbol{F}_e^{-1}$$

which, if the elastic part of the deformation gradient is small can be simplified as follows:

$$\boldsymbol{L} \approx \boldsymbol{L}_e + \boldsymbol{L}_p$$

Under this assumption, the rate of deformation can also be decomposed additatively as follows:

$$\boldsymbol{D} \approx \boldsymbol{D}_e + \boldsymbol{D}_p$$

3.5.1 Hypoelasticity, objective stress derivatives

Assuming constant elastic material properties, the Hooke Law (3.25) can be written in rate form as follows:

$$\dot{\boldsymbol{\sigma}} = \mathbb{D} : \dot{\boldsymbol{\epsilon}}^{\mathrm{el}}$$

which would naturally lead to the following constitutive equations when transposed in the finite strain framework

$$\dot{\boldsymbol{\sigma}} = \mathbb{D} : \boldsymbol{D}_e$$

However, such a constitutive equation would be physically dubious as the time derivative of the Cauchy stress $\dot{\boldsymbol{\sigma}}$ is not objective. Objective stress rates were introduced to avoid this issue and allows to rewrite the previous equations as follows:

$$\overset{\nabla}{\boldsymbol{\sigma}} = \mathbb{D} : \boldsymbol{D}_e$$

There is an infinite number of objective stress rates. The most popular ones are:

- Truesdell rate of the Cauchy stress: $\overset{\nabla}{\boldsymbol{\sigma}} = \frac{1}{J}\left(\boldsymbol{F} \cdot \dot{\boldsymbol{S}} \cdot \boldsymbol{F}^{\mathrm{T}}\right)$
- Green-Naghdi rate of the Cauchy stress: $\overset{\nabla}{\boldsymbol{\sigma}} = \dot{\boldsymbol{\sigma}} + \boldsymbol{\sigma} \cdot \boldsymbol{\Omega} - \boldsymbol{\Omega} \cdot \boldsymbol{\sigma}$ where $\boldsymbol{\Omega} = \dot{\boldsymbol{R}} \cdot \boldsymbol{R}$ is the angular velocity.
- Zaremba-Jaumann rate of the Cauchy stress: $\overset{\nabla}{\boldsymbol{\sigma}} = \dot{\boldsymbol{\sigma}} + \boldsymbol{\sigma} \cdot \boldsymbol{\omega} - \boldsymbol{\omega} \cdot \boldsymbol{\sigma}$

At this stage, it is important to highlight that most of those objective stress rates are only limited to isotropic constitutive equations.

3.5.2 Rate form constitutive equations

Similar to hypoelasticity, most constitutive equation written in the infinitesimal strain theory can be reused by replacing time derivatives by objective derivatives.

3.6 Conclusions

This chapter introduced three approaches to finite strain constitutive equations:

- A first approach based on the lagrangian strain measures.
- A second approach based on the multiplicative decomposition of the deformation gradient.
- A third approach based on the objective derivatives.

This chapter highlighted the link of such constitutive equations with the ones written in the infinitesimal strain theory.

Bibliography

[Belytschko] Belytschko, T.: *Nonlinear Finite Elements for Continua and Structures*. Wiley-Blackwell. – ISBN 978–0–471–98774–1

[Doghri] Doghri, I.: *Mechanics of deformable solids: linear, nonlinear, analytical, and computational aspects*. Springer. – ISBN 3–540–66960–4 978–3–540–66960–9 3–642–08629–2 978–3–642–08629–8

[Lee 1969] Lee, E.H.: Elastic-Plastic Deformation at Finite Strains. In: *Journal of Applied Mechanics* 36 (1969), 03, Nr. 1, p. 1–6. – 10.1115/1.3564580 . – ISSN 0021–8936

[Lemaitre and Desmorat] Lemaitre, J. ; Desmorat, R.: *Engineering Damage Mechanics: Ductile, Creep, Fatigue and Brittle Failures*. Springer-Verlag. – ISBN 978–3–540–21503–5

[Mandel] Mandel, J.: Equations constitutives et directeurs dans les milieux plastiques et viscoplastiques. 9, Nr. 6, p. 725–740. – 10.1016/0020-7683(73)90120-0 . – ISSN 0020–7683

[Miehe et al.] Miehe, C. ; Apel, N. ; Lambrecht, M.: Anisotropic additive plasticity in the logarithmic strain space: modular kinematic formulation and implementation based on incremental minimization principles for standard materials. 191, Nr. 47, p. 5383–5425. – 10.1016/S0045-7825(02)00438-3 . – ISSN 0045–7825

[Sidoroff 1981] Sidoroff, F.: *Formulations élasto-plastiques en grandes déformations*. Version: 1981. `http://perso.ec-lyon.fr/francois.sidoroff/coursGD/EcEte.html`

[Simo and Hughes] Simo, J.C. ; Hughes, T.J.R.: *Computational inelasticity*. Springer. – ISBN 0–387–97520–9 978–0–387–97520–7

[de Souza Neto et al.] Souza Neto, E.A. de ; Perić, D. ; Owen, D.R.J.: *Computational methods for plasticity: theory and applications*. Wiley. – ISBN 978–0–470–69452–7 0–470–69452–1 978–0–470–69462–6 0–470–69462–9

4

Experimental fracture mechanics

Tom Petit

Université Paris-Saclay, CEA, Service d'Étude des Matériaux Irradiés, Gif-sur-Yvette, 91191, France

Jérémy Hure

Université Paris-Saclay, CEA, Service d'Étude des Matériaux Irradiés, Gif-sur-Yvette, 91191, France

This chapter is an introduction to fracture mechanics from an experimental point of view. After an overview of the experimental observations of failure modes and fracture mechanisms in metal alloys, the properties relevant to predict the initiation and propagation of brittle and ductile cracks are presented based on experimental results. Some conventional and micromechanical tests used to measure these properties are finally detailed along with the effects of testing conditions.

4.1 Introduction

Fracture mechanics is omnipresent in our daily life, from **breaking** bread for breakfast or **tearing** a food package, to (fortunately) more exceptional situations such as breaking one's leg or **damaging** a car during an accident. If all these situations correspond to experimental observations of the initiation and propagation of cracks, the different words available - breaking, tearing, damaging - to describe them reflect notable differences between these cases.

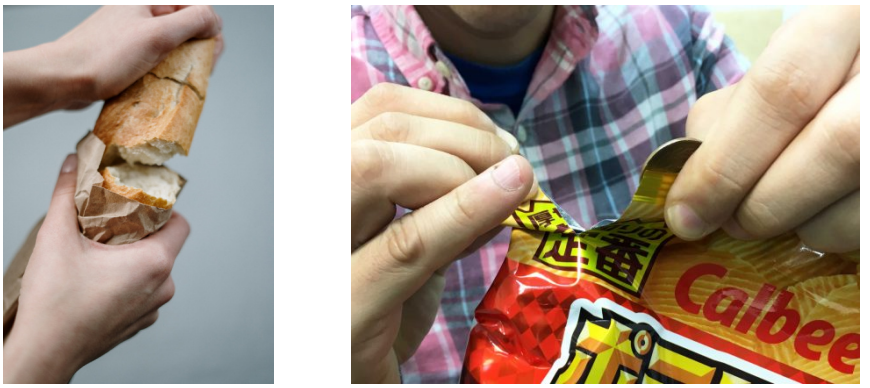

(a) (b)

FIGURE 4.1: Two examples of experimental fracture mechanics: (a) breaking bread, and (b) tearing food packaging.

Let's have a closer look at each of these examples. For the case of the breakage of a fresh bread stick (Fig. 4.1a), it is necessary to bend it sufficiently before seeing a sudden crack appear in the crust which will then propagate slowly in the crumb. After complete breakage, the two pieces cannot stick together exactly, which indicates that the material has been strongly deformed locally. A completely different phenomenology can be observed in the case of the opening of some plastic packaging (Fig. 4.1b). When pulling on it, the material does not seem to deform until a crack appears and propagates over a long distance (and incidentally all the contents of the package end up on the ground). Contrary to the case of the bread stick, the two pieces of the package can be assembled in a puzzle-like fashion, indicating the absence of significant strain locally.

(a) (b)

FIGURE 4.2: Two other examples of experimental fracture mechanics: (a) breaking your leg, and (b) damaging your car

Let's now turn to more exceptional situations. The breakage of a bone (Fig. 4.2a) is most often the result of an impact that leads to sudden cracking. As in the case of the packaging, the two fragments have the same geometry, *i.e.*, little strain is visible locally, and it is sufficient to replace the pieces face to face and wait for the reconstitution of the bone. Finally, a car accident (Fig. 4.2b) leads to strain and damage of metallic structures both at the scale of the car and more locally at the scale of crack propagation. These examples from everyday life highlight the diversity of situations encountered when one is interested in fracture mechanics. It is already possible to identify some differences:

- **Initiation *vs.* Propagation**

The objects shown in Figs. 4.1, 4.2 have no cracks / defects in the initial state - at least at the scale considered - and the failure is the result of two different stages. The first one corresponds to the appearance of a crack-like defect which is called **initiation phase**. This crack then propagates in the structure in the propagation phase. This propagation can be **stable** - increasing the loading a little makes the crack advances a little - or **unstable** when sudden macroscopic crack propagation occurs just after the initiation.

- **Quasi-static *vs.* Dynamic**

By defining the speed of loading as slow when it is less than the speed of crack initiation and propagation, and fast in the opposite case, the examples of bread and packaging correspond to cases of slow loading, whereas bone fracture and car accident are to be classified as fast loading. In the first case, the loading is said to be **static** or **quasi-static** while in the second it is said to be **dynamic**.

- **Environmental effect**

All the examples described above take place in ambient air, and a natural question is whether there is an **environmental effect**, *i.e.*, whether these phenomena would occur in the same way in another environment (vacuum, water, acid, high/low temperatures, low/high pressures). In the bread example, the common experience tells us that waiting a few days would change the result radically, with a brutal crack propagation without having to strongly deform the bread stick.

- **Strain at the structural scale**

Another important difference between the examples is the level of strain at the scale of the object under study that is required to lead to failure. In the case of the bread and the car accident, the geometry of the objects is different at the time of failure compared to the initial geometry, and the failure is said to be **macroscopically ductile**. In the two other cases, the geometries appear unchanged and fracture is said to be **macroscopically brittle**.

- **Strain at the crack scale**

Regardless of what is observed at the scale of the objects, the material may also deform - or not - along the path followed by the crack. In the case of packing and bone, the strains remain small at the crack scale and the failure is therefore **microscopically brittle**. On the contrary, it would be impossible to reassemble the two edges of the crack for the bread and the damaged car, the failure being **microscopically ductile**.

- **Fracture mechanisms**

Again, regardless of the above categories, two experimental observations of failure that would fit the same categories may differ in their **microscopic fracture mechanisms**. For example, it is unlikely that the fractures of a piece of glass and of the steel of the Titanic's hull would proceed from the same mechanisms. The difference is important especially when it comes to developing physically based fracture models.

Beyond the categories of failure sketched with the help of these examples, the question arises of the **relevant parameters** to predict **crack initiation and propagation**, parameters that may be different depending on the type of failure studied. The parameters allowing to completely describe the initiation of a crack in plastic packaging do not have reasons to be the same as those allowing to predict the propagation of a crack in a metal sheet. Finally, these parameters being known for each situation of interest, the question arises of determining them by means of **dedicated mechanical tests**.

The **objectives of this chapter** are therefore the following:

- **to present an overview** of failure modes and fracture mechanisms observed in metal alloys used in industrial applications;
- **to highlight** from experimental results the relevant parameters to describe the initiation and propagation of cracks;
- **to present the mechanical tests** recommended in the standards as well as some micromechanical tests to determine these parameters.

This chapter is an introduction to fracture mechanics from an experimental point of view. Thus, the different notions are introduced on the basis of experimental results using only the concepts of stresses (force per unit area) and strains (elongation per unit length of reference). Moreover, the emphasis is especially put on introducing the **vocabulary** and the **keywords** related to fracture mechanics that will be further developed in this book. A selection of key references is also given along the way.

4.2 Overview of failure modes in metal alloys

In order to complete the examples of daily life presented in the introduction, situations from industrial applications, mainly nuclear, are detailed in this part. These examples correspond to cases of crack initiation and propagation in metallic alloys under quasi-static loading conditions excluding environmental effects. In particular, the objective of this section is to shed light on the different macroscopic and microscopic behaviors. Brittle and ductile fracture mechanisms commonly observed in metal alloys are then presented. This section is not intended to be exhaustive: for further examples of experimental observations of brittle and ductile fracture of metal alloys, the reader is referred to Chapters 7 & 8 of this book and to comprehensive reviews on the topic (see, *e.g.*, [Pineau et al., 2016]).

4.2.1 Macroscopic vs. Microscopic behaviors

All the examples presented in this section correspond to steels, alloys widely used in a large number of industrial applications. The addition of minor alloying elements and the different loading conditions lead to different failure modes detailed in this section.

4.2.1.1 A very versatile steel

Austenitic stainless steels are alloyed with chromium and nickel. They are omnipresent around us: knives, forks, cookware, cars, boats all use this material known for its good mechanical properties and resistance to corrosion. For the same reasons, it is also used in nuclear reactors. Fig. 4.3a shows the typical result of a tensile test at room temperature. This material has the ability to deform very significantly - here more than 50% strain - which leads to classify it as macroscopically ductile.

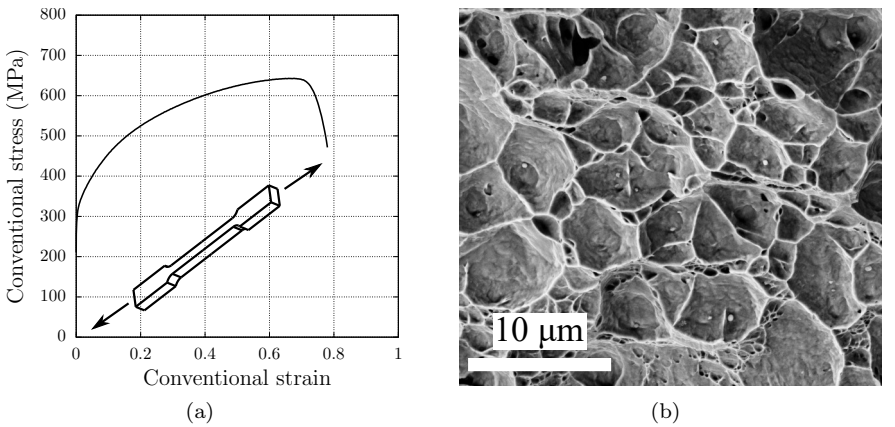

(a) (b)

FIGURE 4.3: (a) Typical tensile curve of an austenitic stainless steel at room temperature (b) SEM observation of the fracture surface (Courtesy of LM2E lab, CEA Saclay) [Hure et al., 2018]

What about the strain level at the crack scale? Fig. 4.3b shows an image of the fracture surface, *i.e.*, the location where the crack has separated the two pieces of the specimen, obtained using a Scanning Electron Microscope (SEM). The image shows the presence of craters, called dimples, most often with particles in the center of them. This observation is characteristic of the fracture mechanism by initiation, growth and coalescence of internal voids: under mechanical loading, cavities appear in the material from inclusions, then grow and eventually coalesce leading to fracture (see [Benzerga and Leblond, 2010] and references therein). This fracture mechanism will be further detailed in Chapters 8 & 9. Clearly, the material is highly deformed at the crack scale,

and thus the mode of failure is microscopically ductile.

This first example shows a ductile macroscopic behavior associated with a ductile fracture mechanism. If the concordance between what happens at the two scales may seem natural, it is not, as illustrated in the following (counter-)example.

4.2.1.2 A steel with holes

Let's take the same class of material as in the previous section, the variant of which has been specially studied for use in fast neutron nuclear reactors. In these reactors, the material is subjected to extreme conditions - a temperature between 450 °C and 650 °C and an intense flux of high energy neutrons - which leads to changes in the microstructure of the material.

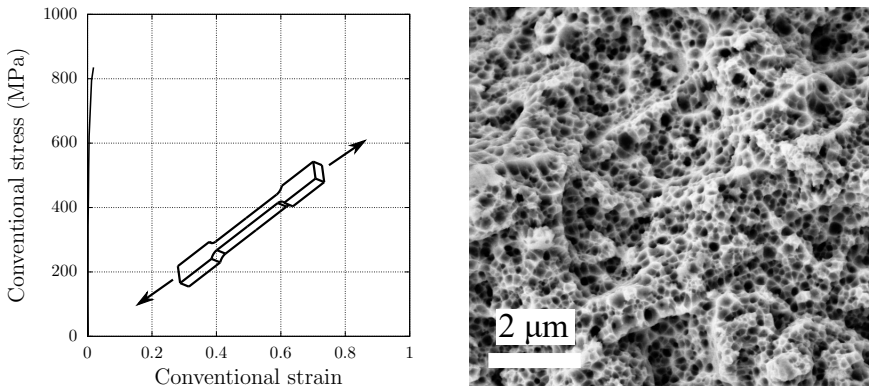

(a) (b)

FIGURE 4.4: (a) Typical tensile curve of a highly irradiated austenitic stainless steel at room temperature (b) SEM observation of the fracture surface (Courtesy of LM2E lab, CEA Saclay) [Hure et al., 2022]

In particular, nanocavities appear, ranging from 10 to 100nm in diameter with porosity levels that can exceed 10%. Fig. 4.4a shows the typical result of a room temperature tensile test. The material deforms slightly, elastically, and then breaks abruptly. It is therefore a macroscopically brittle case, where failure occurs without significant strain at the specimen scale.

Let's now look at what happens at the crack scale. Here again, the SEM observation of the fracture surface provides answers as to the mechanisms at work. Surprisingly, the fracture surface is very similar to the one shown in Fig. 4.3b, *i.e.*, with dimples, the essential difference being the size of these dimples which is of the order of hundreds of nanometers. The mechanism is therefore the same, with growth and coalescence of cavities, and involves large

strain at the local scale. The fracture mechanism is therefore microscopically ductile even though at the scale of the structure a brittle behavior - almost without strain - is observed.

These first two examples show that the terminology of brittle and ductile failure must be used with caution, and that it is necessary to specify the scale to which one is referring. What these examples have in common is that the fracture mechanism is ductile, but the same difficulties are encountered when the fracture mechanism is brittle as we will see in the next two examples.

4.2.1.3 A rather hot steel

Let's continue to look at the steels used in nuclear power plants. The example shown in Fig. 4.5 concerns a low-alloy steel currently used for French power plants pressure vessels. This is a fracture toughness test on a precracked Compact Tension C(T) specimen, performed at relatively high temperature: on the load-opening curve in Fig. 4.5a, after a yielding phase and then a transition, there is a relatively long phase where the load seems to saturate, which corresponds to a significant development of plasticity, before the specimen suddenly fails. Here there is no stable crack propagation phase strictly speaking: the crack propagates almost instantaneously as soon as the initiation appears.

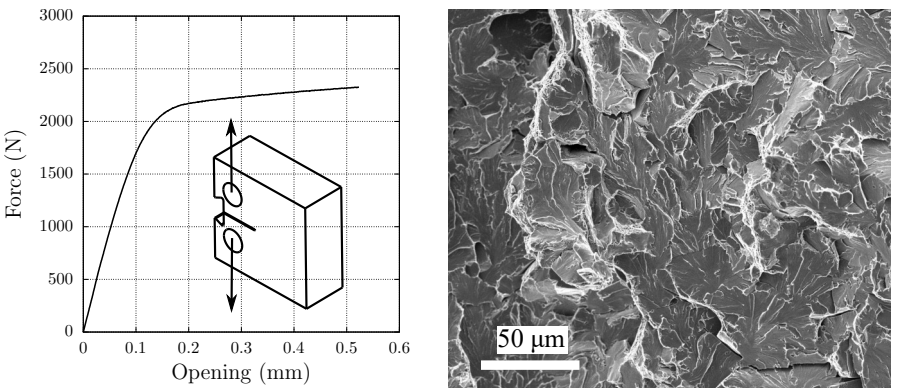

(a) (b)

FIGURE 4.5: (a) Typical load-opening curve of a precracked C(T) specimen of a low-alloy steel at high temperature (b) SEM observation of the fracture surface [Petit et al., 2022]

When looking at the fracture mechanisms, it is clear that the fracture surface corresponds to cleavage fracture, as shown in the SEM image in Fig. 4.5b. This type of cleavage fracture corresponds to brittle fracture, which is of the transgranular type, and results in this surface type with no real evidence of

plastic strain, with a flat, shiny surface where planes and rivers of cleavage can be identified.

Again, this example highlights the not necessarily trivial correlation between the macroscopic and microscopic behaviors.

4.2.1.4 A rather cold steel

Let's continue the study of the steel from the previous paragraph. By testing the same steel, but at a lower temperature, one obtains the load-opening curve shown in Fig. 4.6a. The curve is linear, and no plasticity seems to appear macroscopically. Unsurprisingly, the fracture surface in Fig. 4.6b corresponds well to what is observed macroscopically: the fracture is typically brittle, again corresponding to transgranular cleavage.

What may appear more surprising is the complete correspondence between the fracture surfaces of Fig. 4.5b and 4.6b: although these mechanisms are totally similar, we have seen that they do not result in the same macroscopic behavior. In addition to the essential characterization of the fracture mechanisms, it therefore appears necessary to develop relevant analytical methods to correctly quantify the multitude of existing fracture behaviors.

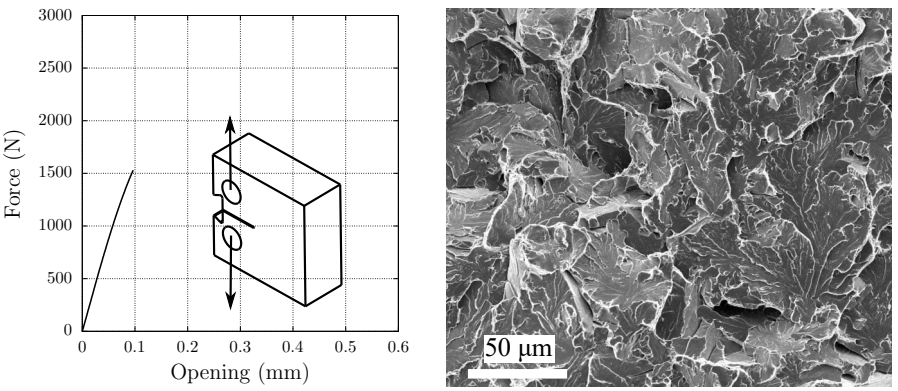

(a) (b)

FIGURE 4.6: (a) Typical load-opening curve of a precracked C(T) specimen of a low-alloy steel at low temperature (b) SEM observation of the fracture surface [Petit et al., 2022]

The various examples presented hereabove show that, for a given material and microscopic fracture mechanism - qualified as brittle or ductile - different macroscopic behaviors can be observed. The situation is in fact more complex as different brittle and ductile fracture mechanisms are observed.

4.2.2 Ductile vs. Brittle fracture mechanisms

4.2.2.1 Brittle fracture mechanisms

Different kind of brittle fracture mechanism exist. One may think of course of the case of amorphous materials, such as the silica glass, but as shown previously this phenomenon is also involved in the fracture of metal alloys at very low temperatures, as in the Titanic accident for example. This type of fracture generally starts on an inclusion present in the material, which will break when a critical stress is reached, and which will lead to an abrupt crack propagation from one grain to another, separating planes in the crystal structure. This is what we observed above in Fig. 4.5b or here in Fig. 4.7a. This brittle fracture mechanism is called **transgranular cleavage**.

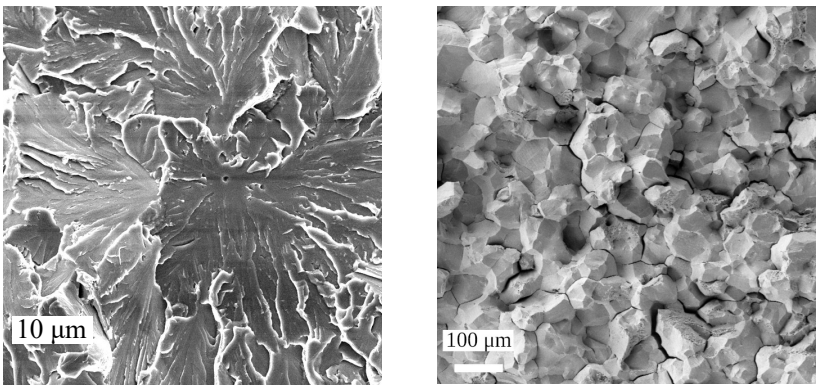

(a) (b)

FIGURE 4.7: Two different brittle fracture mechanisms observed in metal alloys: (a) transgranular cleavage in a low-alloy steel, and (b) intergranular decohesion in a stainless steel (Courtesy of LM2E lab, CEA Saclay) [Hure et al., 2018]

Brittle fracture can also result solely from a weakness in the grain boundary. This is known as **intergranular decohesion**, an example of which is shown in Fig. 4.7b. These fracture surfaces have a generally planar appearance and it is difficult to identify a macroscopic zone of initiation or a direction of propagation. At the microscopic scale, they show juxtaposed polyhedra, corresponding to the surface of the grains defining the fracture surface. Embrittling phases may appear at the fracture surface. Often, secondary cracks can be observed.

An important point to keep in mind is that a given material may exhibit these two fracture mechanisms depending on the conditions. One may for example think of the **segregation of some chemical species** and / or

precipitation at grain boundaries promoting intergranular decohesion. These brittle fracture mechanisms are detailed in Chapter 7.

4.2.2.2 Ductile fracture mechanisms

Different kind of ductile fracture mechanisms do also exist. As shown in the examples detailed in the previous sections, metal alloys are not totally homogeneous: they contain secondary phases, such as impurities, precipitates or dispersoids.

The ductile fracture of these alloys may originate in these secondary phases, which will give origin to cavities under the effect of a mechanical loading. These cavities will enlarge and then merge, leading to the macroscopic failure of the material. To describe this gradual damage phase, we speak of **nucleation, growth, and coalescence of cavities**, which leave characteristic marks on the fracture surfaces, called **dimples**. These fractures, driven by the location of secondary phases, often located within the grains, are often **transgranular** (Fig. 4.8a). The crack therefore preferentially follows these secondary phases, which are generally randomly distributed in the material, leading to tortuous crack paths, which distinguish them from the flat surfaces of brittle fracture. In some materials, voids are already present, and fracture mechanism proceeds directly by growth and coalescence (Fig. 4.8b). This fracture mechanism can also be **intergranular** when second phases / inclusions are located at the grain boundaries (Fig. 4.8c).

It is also observed that these mechanisms can be affected by the nature of the applied loading (tensile, shear, multi-axial,...) which can be quantified by a parameter called **stress triaxiality**. This quantity is all the higher (and all the more harmful to failure) the more the three principal stresses are of the same order of magnitude. At low triaxiality, **ductile shearing** is observed as shown on Fig. 4.8d. Failure occurs in an extremely progressive way with extensive strain. In this case, rotation and elongation of voids finally lead to fracture. This mechanism is close to what is observed in pure, or near-pure, metals where necking occurs until the strain is too high, which leads to the separation of the two halves of the specimen. These ductile fracture mechanisms are further detailed in Chapter 8. Finally, some materials may exhibit a **ductile-brittle transition (DBT)** as for the nuclear reactor pressure vessel steel described in the section 4.2.1.3, where the fracture mechanism is brittle at low temperature and ductile at high temperature.

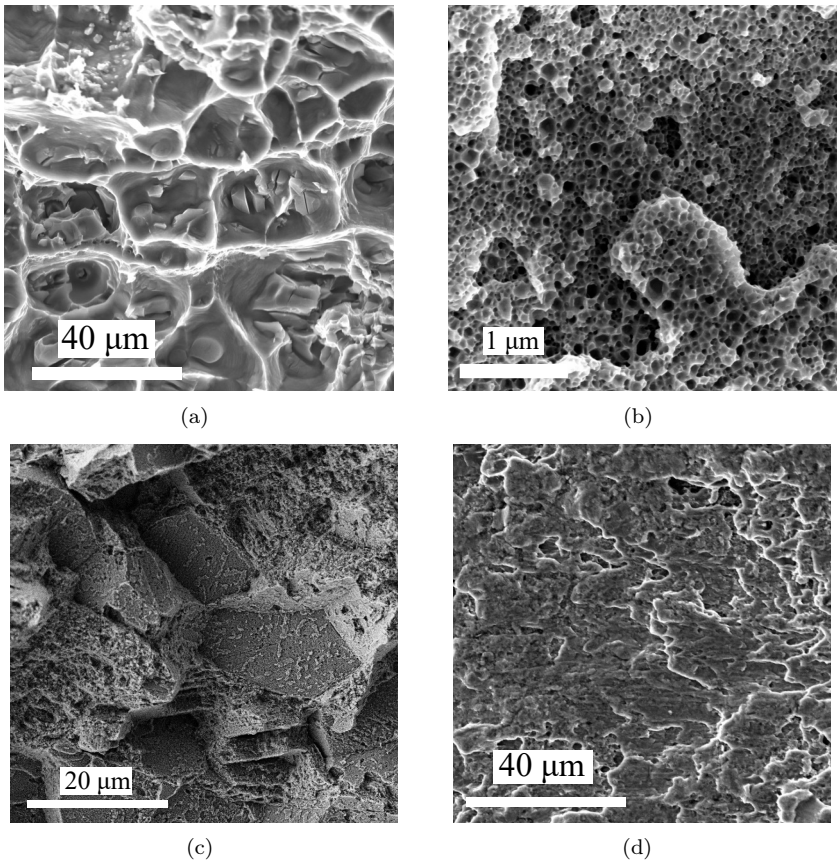

(a) (b) (c) (d)

FIGURE 4.8: Four different ductile fracture mechanisms in metal alloys: (a) Transgranular void nucleation, growth and coalescence in an aluminum alloy [Petit et al., 2019], (b) Transgranular void growth and coalescence and (c) intergranular void nucleation, growth and coalescence in an austenitic stainless steel [Hure et al., 2022], (d) Ductile shearing in a low-alloy steel (Courtesy of LM2E lab, CEA Saclay)

After this short introductory overview of macroscopic *vs.* microscopic behaviors and ductile *vs.* brittle fracture mechanisms, let's now have a look at the properties controlling crack initiation and propagation.

4.3 Searching for fracture invariants

The aim of this part is to highlight experimentally the relevant parameters to characterize the initiation and propagation of cracks according to local fracture mode. Hence, the terms brittle and ductile are used to describe the fracture mechanisms and not the behavior at the structural scale.

4.3.1 From brittle fracture...

Let's take the example of PolyMethyl MethAcrylate (PMMA), often referred to as Plexiglas. This material is known to have a brittle fracture mechanism. What are the relevant parameters to describe the initiation of cracks in this material?

4.3.1.1 Crack initiation

In order to characterize crack initiation, a simple experiment consists in pulling on notched flat specimens (Fig. 4.9a). The geometrical parameters of this type of specimen are the radius of the notches R, the distance between the notches ℓ and the thickness h.

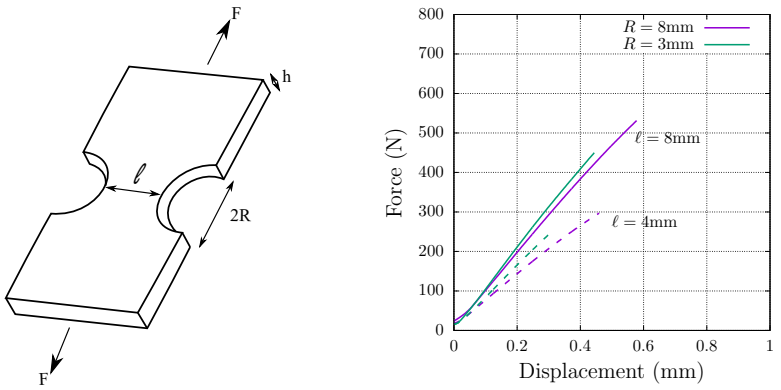

FIGURE 4.9: (a) Notched flat specimen used to characterize crack initiation (b) Force-displacement curves for different notch radius R / distance between notches ℓ, for a thickness $h = 1.58$mm

Typical force-displacement curves are shown in Fig. 4.9b. A linear elastic behavior is obtained until the initiation (and propagation) of a crack at the minimum section of the specimen, for a critical value of the force F_c. What is the invariant of these experiments, *i.e.*, the parameter that is constant for all

these results?

Fig. 4.10 shows that, for $R \gtrsim \ell$ (corresponding to the largest notch radius $R = 8\,\text{mm}$ and smallest ligament for $R = 3\,\text{mm}$), the critical force F_c evolves linearly with the minimum section of the specimen, and that the effect of the notch diameter is relatively weak. This experiment thus shows the existence of a **critical stress** σ_c - the slope of the line in Fig. 4.10 - for which a crack initiates in PMMA:

$$\sigma = \sigma_c \Rightarrow \text{Crack initiation} \tag{4.1}$$

Eq. 4.1 is therefore a crack initiation criterion for brittle materials. It should be noted that the definition used here of the stress - average at the minimum section - is not completely satisfactory because of the non-uniformity of the stresses at the notch. A more detailed analysis would be necessary to extract the true critical stress of the material, for example based on the work of [Inglis, 1913]. Nevertheless, Eq. 4.1 constitutes the first pillar of fracture mechanics of brittle materials. The determination of this critical stress σ_c and its physical origin will be discussed in Chapter 7. It is already possible to imagine that this critical stress depends, for example, on the temperature, the orientation of the material if it is not isotropic:

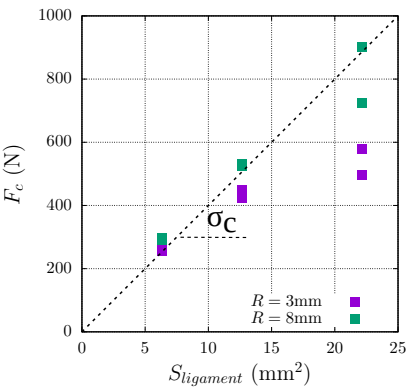

FIGURE 4.10: Critical force as a function of the minimum cross-section of the specimen

$$\sigma_c = \mathcal{F}\,(T, \text{orientation}, \text{loading conditions...}) \tag{4.2}$$

Another interesting feature shown on Fig. 4.10 is that, for a given notch radius, the critical force appears to saturate when the ligament size increases. This regime corresponds to the case $R \ll \ell$, *i.e.*, the notch is in fact a crack, which is studied in the next section.

4.3.1.2 Crack propagation

In order to characterize crack propagation in brittle materials, another simple experiment consists in pulling on a cracked specimen, *i.e.*, a notched specimen whose notch radius is very small compared to all the other dimensions (Fig. 4.11a). The notch radius is then no longer a relevant geometrical parameter, and only the length of the crack ℓ, the width L and the thickness h of the specimen remain. When these PMMA specimens are mechanically loaded, the force increases almost linearly with the applied displacement (Fig. 4.11b)

until a critical force F_c for which the crack propagates in an unstable manner and the specimen is broken in two. Fig. 4.11b also shows that the shorter the crack, the higher the maximum force.

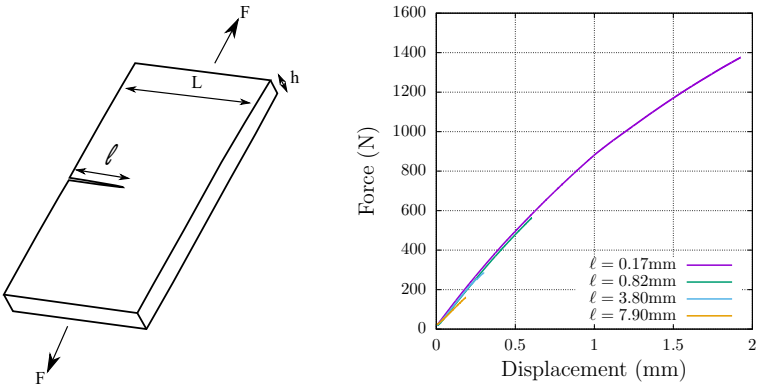

(a) (b)

FIGURE 4.11: (a) Cracked flat specimen used to characterize crack propagation (b) Force-displacement curves for different crack lengths ℓ, for a thickness $h = 1.58\,\text{mm}$

What is the invariant of these experiments, *i.e.*, the parameter that is constant for all these results? Let's have a look first at the results obtained at 20 °C.

Fig. 4.12 shows that the critical force F_c normalized by the nominal cross-section $S_0 = L\,h$ of the specimen actually varies linearly with $\ell^{-1/2}$. The slope, noted K_{Ic} in the following, is thus the invariant we are looking for:

$$K_{Ic} = \Sigma_c \sqrt{\ell} \tag{4.3}$$

where $\Sigma_c = F_c/S_0$. For all these experiments performed at a given temperature, this parameter K_{Ic} is therefore constant and is equal to about $0.5\,\text{MPa}\sqrt{\text{m}}$ for this particular material at 20 °C. Additional experiments would show that in fact this parameter is also independent, to some extent, of the thickness h and the width L. It is therefore a property of the material that characterizes its resistance to crack propagation. Let's reformulate Eq. 4.3:

$$\begin{aligned} \Sigma\sqrt{\ell} < K_{Ic} &\Rightarrow \text{no propagation} \\ \Sigma\sqrt{\ell} = K_{Ic} &\Rightarrow \text{propagation} \end{aligned} \tag{4.4}$$

The product $\Sigma\sqrt{\ell}$ and the quantity K_{Ic} are called **stress intensity factor** and **fracture toughness**, respectively. The former characterizes the intensity of crack loading while the latter describes the resistance of the material

to crack propagation. Eq. 4.4 thus states that the crack propagates when the stress intensity factor reaches a critical value which is the toughness of the material.

What is the physical origin of this quantity K_{Ic}? Its unit ($\mathrm{MPa}\sqrt{\mathrm{m}}$) hardly helps us. Some insights can be obtained from Fig. 4.12 by comparing the tests performed at two temperatures. The higher the temperature, the lower the slope, hence the lower the fracture toughness. The effect of temperature is to decrease the Young's modulus E. An analysis of these results indicates a new invariant noted γ_c and such that:

$$\gamma_c = \frac{K_{Ic}^2}{E} \tag{4.5}$$

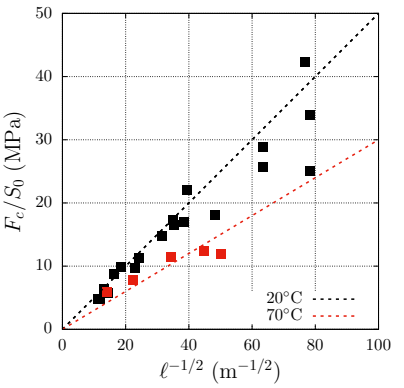

FIGURE 4.12: Critical force as a function of the square root of the initial crack length

The unit of γ_c ($\mathrm{J\,m^{-2}}$) is simpler to understand from a physical point of view. It is an energy per unit area that can be interpreted as the energy necessary for the propagation of the crack. In order to validate this hypothesis, a last experiment consists in measuring the energy necessary to break a specimen of given section S_0. To do this, we drop weights of different heights on a cracked specimen (Fig. 4.13a). The failure energy is estimated from the initial potential energy of the weights used.

Fig. 4.13b shows that sufficient energy must be supplied to break the bar. The critical energy is, to a first approximation, proportional to the breaking surface: the larger the surface, the more energy must be supplied. More interestingly, the order of magnitude of the surface energy that can be extracted from Fig. 4.13b - $\gamma_c \sim 1\,\mathrm{kJ\,m^{-2}}$ - is consistent with Eq. 4.5 with $K_{Ic} \sim 1\,\mathrm{MPa}\sqrt{\mathrm{m}}$ and $E \sim 1\,\mathrm{GPa}$. Obviously, and as in the previous paragraph, this simplified analysis neglects many aspects - and in practice all the prefactors of the equations! - but it has allowed us to highlight the second pillar of the mechanics of brittle fracture, namely the concepts of stress intensity factor and fracture toughness K_{Ic} which form Griffith's theory of fracture [Griffith, 1921]. The origin of these concepts will be detailed in Chapter 5, and their limitations discussed in Chapter 6. In the same way as for the critical stress, it is also possible to imagine that the fracture toughness depends on temperature, on the orientation of the material if it is not isotropic, and that there may be several values of toughness depending on the loading mode:

$$K_{Ic} = \mathcal{F}\left(T, \text{anisotropy}, \text{loading conditions}, ...\right) \tag{4.6}$$

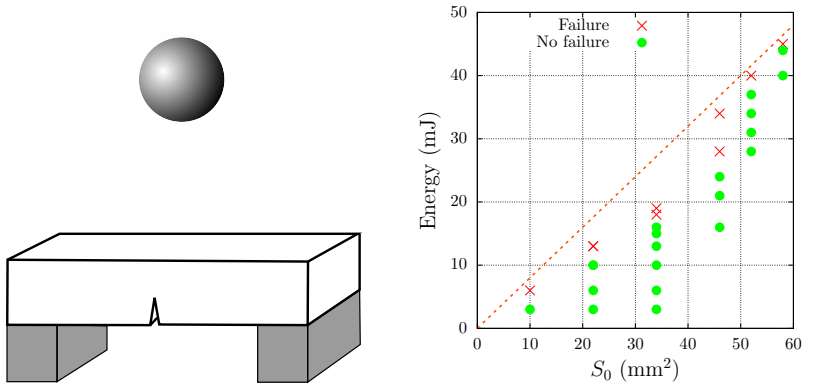

(a) (b)

FIGURE 4.13: (a) Notched bar subjected to an impact to characterize the energy required for fracture (b) Potential energy of the weights leading (or not) to fracture as a function of the ligament surface

This part has allowed to highlight the relevant parameters to characterize the crack initiation and propagation, namely critical stress σ_c, fracture toughness K_{Ic} and fracture energy γ_c, in the case of brittle fracture. The objective of the next section is now to evaluate if these parameters remain relevant in the case of ductile fracture.

4.3.2 ... to ductile fracture

Let's take this time the example of an austenitic stainless steel, more precisely type 304, the same one presented in section 4.2.1.1, and resume the experiment of Fig. 4.11a with two initial crack lengths. The phenomenology is completely different compared to PMMA. Looking first at the force-displacement curves (Fig. 4.14a), continuous evolutions are observed, with a work hardening phase followed by a softening phase. The characteristic quantities of this test - maximum force, displacement at failure - depend on the initial crack length. Looking at the evolution of the crack (Fig. 4.14b), a first phase corresponds to the blunting of the crack tip - which is thus transformed into a notch of finite radius - then by the initiation of a new crack from the notch and its propagation. An important point to note in this particular case is that the work hardening part of the load curve is related to the blunting of the crack, and the softening part to the crack propagation.

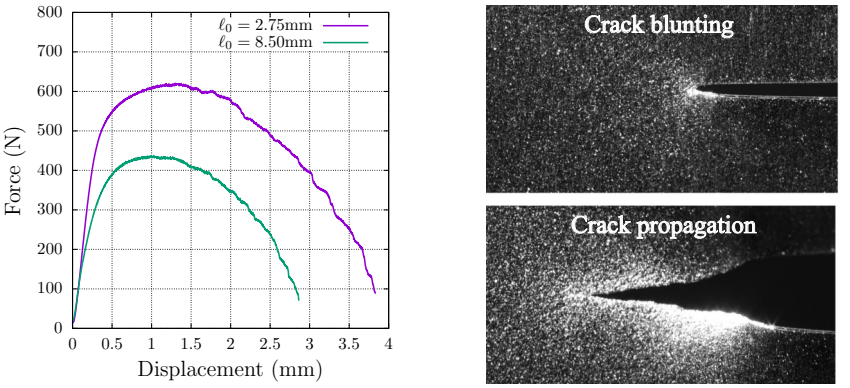

(a) (b)

FIGURE 4.14: (a) Force-displacement curves for different initial crack lengths ℓ_0, for a thickness $h = 0.1$ mm (b) Crack evolution: blunting then propagation

These experiments are analyzed in more detail in the following sections, distinguishing between crack initiation and crack propagation, searching for the invariants characterizing these two phases.

4.3.2.1 Crack initiation

One way to characterize the crack initiation is to look at the evolution of the crack edge shape. Fig. 4.14b shows that in a first phase called blunting the edges of the crack spread, the crack becomes a notch with a finite radius of curvature before the appearance and propagation of a new crack. Specifically, Fig. 4.15 shows the crack shapes of the two tests - corresponding to the two initial crack lengths - at the time of initiation of a new crack. For both tests, the shapes are identical, both for the crack opening and for the radius of curvature of the crack tip.

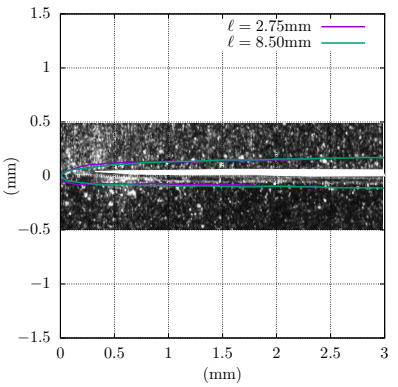

FIGURE 4.15: Crack shape at the end of the blunting phase. Inset: initial crack

This shape is therefore an invariant to describe the crack initiation. Since this invariant is a deformed geometry, it shows the existence of a critical strain ε_c for which a sufficient damage has occurred at the crack tip to lead to the

appearance of a new crack:

$$\varepsilon = \varepsilon_c \Rightarrow \text{Crack initiation} \tag{4.7}$$

The situation is very different from the crack initiation observed for brittle materials. In this last case, a criterion in critical stress was obtained whereas a criterion in critical strain is observed for the ductile material. The physical origin is in this case related to the fracture mechanism that will be detailed in Chapter 8: the damage of the material is gradual by growth and coalescence of internal cavities, explaining the choice of a criterion in strain, and early models can be traced back to the work of Rice & Tracey [Rice and Tracey, 1969].

The extension of the initiation criterion (Eq. 4.7) to more complex cases is still an active research topic, both from a theoretical and an experimental point of view, because the critical equivalent (for multi-axial loading) strain can depend on the stress state σ, on the loading path, on the temperature for a given material:

$$\varepsilon_c^{eq} = \mathcal{F}\left(\sigma, T, \text{anisotropy}, ...\right) \tag{4.8}$$

In some cases, the criterion defined by Eq. 4.8 can be sufficient, at least in first approximation, to describe the failure of a material if the following propagation phase is short and/or unstable. In other cases, it is necessary to describe the propagation phase as well. Note finally that Eq. 4.8 requires also a proper definition in the finite strain context, as discussed in Chapter 3.

4.3.2.2 Crack propagation

To characterize the crack propagation phase, two quantities are extracted from the results presented in Fig. 4.14. The first one is the crack advance - noted $\Delta\ell$ - and the second quantity is the energy supplied to the specimen $\mathcal{E}$. The crack advance is estimated from the optical tracking of the crack tip on the surface of the specimen, and the energy is simply obtained by the area under the force-displacement curve.

Fig. 4.16 shows the evolution of this surface energy - normalized by the cross-section of the specimen - as a function of the crack advance. For both tests, this evolution is identical (and additional experiments would show that it remains true at first approximation by varying the thickness). This curve corresponds to an invariant of the ductile crack propagation, and can be characterized by two quantities. The first is the energy per unit surface that is required to lead to crack propagation:

$$\begin{aligned} \frac{\mathcal{E}}{S_0} = J < J_{Ic} &\Rightarrow \text{no propagation} \\ \frac{\mathcal{E}}{S_0} = J = J_{Ic} &\Rightarrow \text{propagation} \end{aligned} \tag{4.9}$$

This critical value of the energy per unit surface is noted J_{Ic} because of its link with the integral J [Rice, 1968] which will be discussed in Chapter 6.

What is the physical interpretation of this quantity? Considering two specimens of which the second one has a longer initial crack length $\Delta\ell_0$ than the first one, the difference of stored energy $\Delta\mathcal{E}$ at the time of the crack propagation is by definition $J_{Ic}h\Delta\ell_0$, that is to say $J_{Ic} = \Delta\mathcal{E}/h\Delta\ell_0$. It is therefore tempting to interpret J_{Ic} as the energy that must be supplied to the crack for propagation, as in the case of brittle failure (Eq. 4.5). The second characteristic quantity in Fig. 4.16 is the evolution of the energy as the crack advances:

$$\frac{dJ}{d\Delta\ell} = T_\sigma \tag{4.10}$$

This quantity is called **tearing modulus** and quantifies the increase in energy required as the crack propagates.

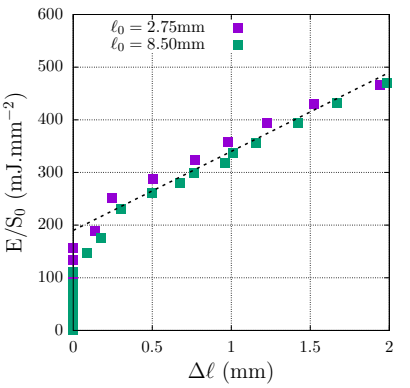

FIGURE 4.16: Evolution of the energy $\mathcal{E}$ normalized by the section S_0 of the ligament as a function of the crack advance

As in the previous sections, this simplified analysis of the experimental results needs to be refined, but as in the case of brittle fracture, it has allowed us to highlight the notions of critical value of the integral J and of ductile tearing modulus T_σ. Again, the origin of these concepts and their precise mathematical definitions will be detailed in Chapter 6. As for the critical strain, these two quantities are obviously dependent on the stress state σ, the temperature and the anisotropy:

$$\{J_{Ic}, T_\sigma\} = \mathcal{F}\left(\sigma, T, \text{anisotropy}, ...\right) \tag{4.11}$$

4.3.3 Concluding remarks

The experiments presented in this section have allowed us to highlight the invariants related to brittle fracture - critical stress σ_c, fracture toughness K_{Ic} and fracture energy γ_c - and ductile fracture - critical strain ε_c, initiation toughness J_{Ic} and tearing modulus T_σ. These quantities that appear naturally in experiments can also be recovered more rigorously from the mathematical analysis of the equations of mechanics (see, *e.g.*, [Leblond, 2003]) as detailed in Chapters 5 & 6. Once known for a given material, these values can be used to predict crack initiation and propagation. The objective of the following section is to present mechanical tests to determine these fracture properties.

4.4 Mechanical tests to quantify fracture properties

The purpose of this section is to provide a short - and non exhaustive - overview of conventional and non-conventional tests to investigate brittle and ductile fracture phenomena and above all to quantify the properties in fracture introduced in section 4.3. But first, the importance of testing conditions are stressed in the next paragraph.

4.4.1 On the importance of the testing conditions

In order to characterize the fracture properties of materials, some specimen geometry and test condition have to be chosen. However, these choices may have a strong impact on the results of the tests, as shown by the two examples given below.

4.4.1.1 Round vs. Plate samples

Let's take this time a material having low hardening capability such as an aluminum alloy or a cold worked austenitic stainless steel. Various samples can be chosen to characterize the fracture properties of such materials under tensile loading conditions. This could be cylindrical tensile specimen (Fig. 4.17a) or plate-like tensile specimen (Fig. 4.17b). Often the choice is dictated by the material available.

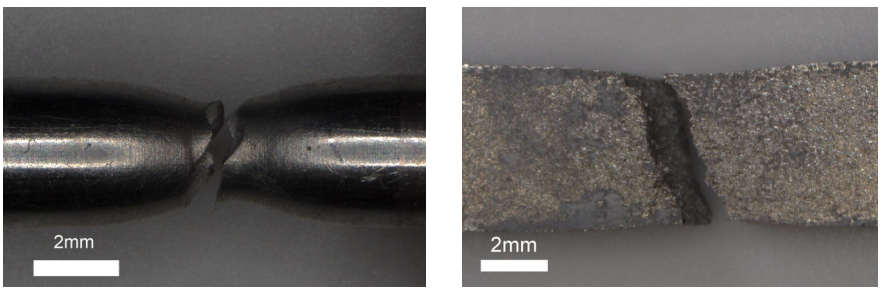

(a) (b)

FIGURE 4.17: Failure of aluminum alloy tensile samples: (a) necking / cup-cone fracture on a cylindrical specimen, (b) shear band fracture on a plate-like specimen

As shown in Fig. 4.17, for the same material, the result of the tensile test can be different. For the cylindrical specimen, **necking** - localization inside a given volume - first occurs, and then strain gradually increases inside the neck up to the so-called **cup-cone** failure. For the plate-like specimen, strain is rapidly concentrated along a particular plane, called **shear band**, slanted with respect to the loading direction. At the macroscopic scale, the second case leads to lower measured ductility. Necking and shear band formation are two examples of **mechanical instabilities**: in each case an homogeneous deformation mode is possible, but unstable, and a **bifurcation** is observed towards an inhomogeneous deformation mode. Theoretical models exists to predict such instabilities [Rudnicki and Rice, 1975].

The previous example makes clear that the failure modes observed experimentally may be the result of the coupling between material behavior and specimen geometry used, which is very important to keep in mind when analyzing the experimental results. But other effects related to the test conditions may also affect the results.

4.4.1.2 Stiff vs. soft tensile machine

To perform the tests described in the previous section, a tensile machine - or something similar - is obviously required. This is not without effect on the test result as shown by the following example. Fig. 4.18 shows the load-opening curves obtained with C(T) specimens (see inset Fig. 4.5a) of aluminum alloy obtained with a stiff and a soft tensile machine, respectively.

With the stiff machine, the curve is continuous, with a hardening regime followed by a softening regime corresponding to the stable propagation of the crack. With the soft machine, the curve is similar, except for a missing part in the softening regime corresponding to an unstable crack propagation, at least too fast to be recorded by the extensometer.

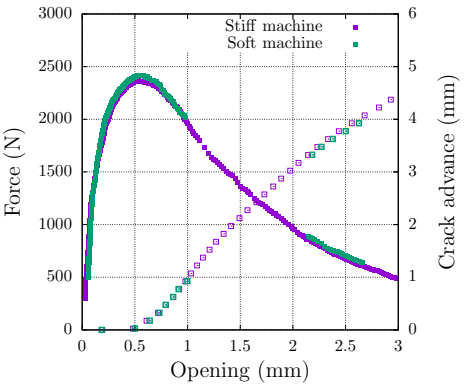

FIGURE 4.18: (a) Typical load - opening curve (solid symbols) and crack propagation - opening (hollow symbols) of a precracked aluminum C(T) specimen

What happens is that, at some point during the crack propagation, the energy stored in the machine - inside the bars used to pull on the sample - is enough for the crack to propagate *without additional energy supplied by the tensile machine*. This leads to the un-

stable crack propagation that look like a brittle event. In a nutshell, the effect of test conditions in fracture mechanics tests is somehow like the observer effect in quantum mechanics, which is a keypoint to be reminded when analyzing fracture mechanics experiments.

Let's now have a look of mechanical tests often used to measure fracture properties.

4.4.2 Conventional and standard tests

First of all, let's look at the tests classically performed in mechanical testing laboratories, or even standardized tests, developed specifically for the damage and fracture study.

4.4.2.1 Quantifying fracture strain / stress

Mechanical tests to investigate the fracture behavior of a material do not necessarily require the very damaging case of a real crack. A first step can be to quantify **stress or strain values at failure** for a sample free of defects, as discussed in Sections 4.3.1.1, 4.3.2.1. A tensile test, for example, can already be used to measure some properties such as ultimate elongation, or the value of the necking at break. By filming the tests, Bridgman-type corrections or image correlation - detailed below and in Chapter 8 - can be used to determine **local strain** (Fig. 4.21a); by coupling these tests to finite element simulations, **local stress values** can also be calculated.

Other geometries allow the investigation of more complex and representative loadings than the uniaxial case. This involves introducing **notches** with very precise radii of curvature, such as the Flat U notch (Fig. 4.19b) or axisymmetric notched tensile (Fig. 4.19d) specimens. These tests make it possible to improve the **material behavior laws**, by making them more representative of what can occur at a potential crack tip. Due to the increase in the stress triaxiality ratio, this type of specimen allows to reach locally level of stresses much higher than the yield stress of the tested material. Such property is important to study the effect of the stress level on the ductile and brittle fracture mechanisms. Tensile and compressive directions are not always the privileged loading in a given structure, and not necessarily the most critical for some specific materials. If it is shear that is the loading of interest, there are dedicated geometries like the one in Fig. 4.19a. For all these geometries, evaluation of local strain is required, either experimentally through digital image correlation or numerically through finite element simulations. Testing these different geometries finally allows to obtain fracture criteria (see, *e.g.*, [Roth and Mohr, 2016]).

The Kahn specimens, described in [ASTM B871-01, 2013] and illustrated in Fig. 4.19c, introduce an even more severe defect by machining an **acute notch**. Three parameters are extracted from these tests, namely the crack initiation energy, the crack propagation energy and the tearing stress. Although these tests do not provide an absolute value of the fracture toughness in the sense of fracture mechanics, there are empirical relationships between these three parameters and the evolution of the toughness. These tests therefore allow relative changes in fracture properties to be compared quite easily.

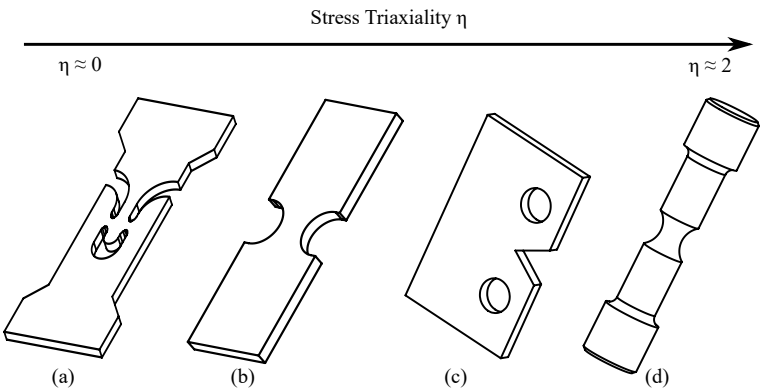

FIGURE 4.19: Some examples of samples used to study fracture properties: (a) Smiley shear (b) Flat Notched, (c) Kahn specimens (d) axisymmetric Notched Tensile N(T)

Application to ductile fracture: Fracture strain ε_c^{eq}

Different experimental techniques may be used to evaluate fracture strains on the specimens described previously. One of them consists in monitoring the evolution of the shape of the specimens with a digital camera. Using a retro-lightning to have a strong contrast between the specimen and the background allows to measure precisely the edge of the sample. An example of such technique is shown in the inset of Fig. 4.20a for axisymmetric notched samples (Fig. 4.19d). In this example, an aluminum alloy is tested with different N(T) specimens, and the minimal radius is used to compute an equivalent plastic strain in the notch region using the Bridgman formula [Bridgman, 1964]:

$$\varepsilon^{eq} = 2 \ln \frac{d_0}{d} \tag{4.12}$$

in which the factor 2 shows that the deformation corresponds to the ratio of the surface before and after the test. Fig. 4.20a shows that the critical strain - taken at the abrupt change of slope - depends on the specimen geometry, and more precisely on the ratio of the initial minimal diameter d_0 to the initial radius of the notch R.

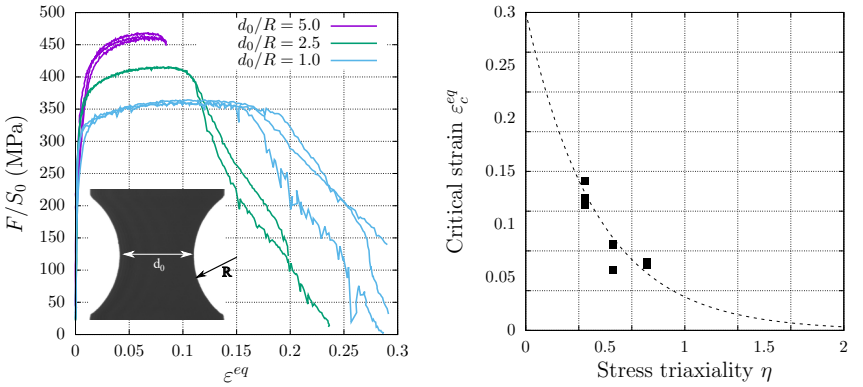

(a) (b)

FIGURE 4.20: (a) Force as a function of equivalent plastic strain measured through the Bridgman formula for an aluminum alloy, for different N(T) specimen geometries. Inset: optical measurement of the minimal diameter (b) Evolution of the equivalent fracture strain as a function of stress triaxiality [Shokeir et al., 2022]

Changing the geometry of the samples is in fact a way to change the stress conditions prevailing in the notch region that can be described by the **stress triaxiality** defined as [Bridgman, 1964]:

$$\eta = \frac{\sigma_m}{\sigma_{eq}} \approx \frac{1}{3} + \ln\left(1 + \frac{d_0}{4R}\right) \tag{4.13}$$

Stress triaxiality quantifies the ratio of pressure over shear, and is an important parameter for ductile fracture as detailed in Chapters 8 & 9. Fig. 4.20b shows that the fracture equivalent strain depends exponentially on the stress triaxiality, in agreement with the Rice & Tracey model [Rice and Tracey, 1969] that will be detailed in Chapter 8.

Another technique, called Digital Image Correlation (DIC) and also presented in Chapter 8, allows evaluating more precisely strains. This technique relies on measuring the displacement of markers attached to the material. These markers could be already present on the material or added. Once the displacement field is known, strains can be computed. A typical example is shown in Fig. 4.21 on the Smiley shear specimen (Fig. 4.19a) covered with black and white paint.

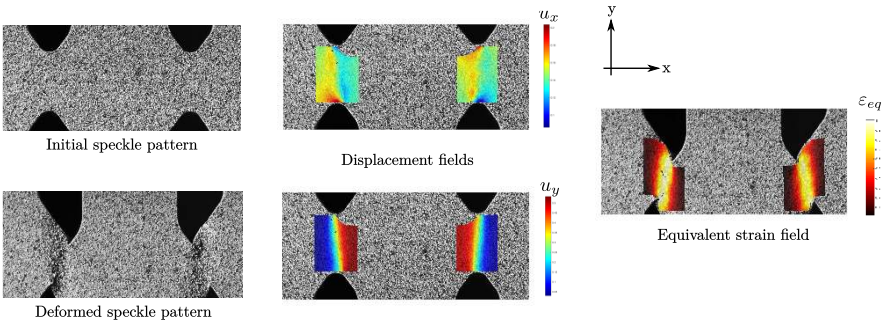

FIGURE 4.21: Example of DIC on the Smiley shear specimen where the speckle pattern has been obtained with black and white paint

DIC is widely used nowadays, either to measure in-plane displacements and strain fields at the surface of samples, but also out-of plane displacement by using two or more cameras (stereo-correlation), and even to volume fields through X-ray imaging. More details can be found in dedicate reviews on DIC [Sutton et al., 2017].

4.4.2.2 Quantifying fracture toughness

To adequately measure the fracture toughness of a material, the previous notches are not sufficient. In order to place oneself in the theoretical framework of fracture mechanics, and to study the material in an unfavorable setting, it is necessary to study **real cracks**, generating a singularity of the mechanical fields at the crack tip. **Precracked specimens** are used, usually obtained following fatigue testing of notched samples.

Standards give several types of precracked specimens for which the stress intensity factor K_I values are given as a function of the crack length. The most commonly used are the Compact Tension - C(T) specimen (Fig. 4.22a and Fig. 4.22c), and the three point bending tests performed on Single Edge Notched Bending - SEN(B) specimen (Fig. 4.22b). The Pre Cracked Charpy V-notch - PCCV (*e.g.* SEN(B) with $10\,\mathrm{mm}^2$ cross section) is also often used; however this geometry loses his load carrying capacity very early in the load history and should be used preferentially for brittle materials [ASTM E399-22, 2022].

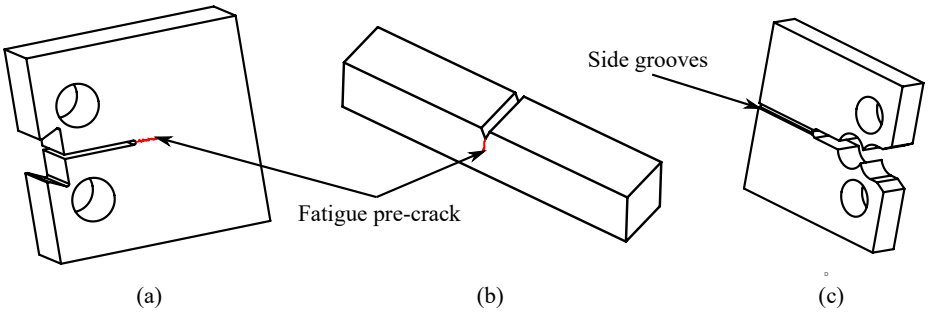

FIGURE 4.22: Some examples of precracked samples used to quantify fracture toughness: (a) Thick Compact Tension - C(T) specimen without side grooves, (b) Single Edge Notched Bending - SEN(B) specimen, (c) Thin C(T) specimen with side grooves

The [ASTM E1820-18, 2018] standard combines several approaches into a single document, so that with a single testing procedure the results are analyzed in a manner that is appropriate to the material behavior (for brittle material, for ductile tearing initiation or for ductile tearing resistance).

Fracture toughness measurement requires to precrack the specimen before testing. Contrary to polymers for which a crack is made with a razor blade, metallic materials need to be fatigue precracked. Precracking requirements are set in order to ensure that test results are not affected by precracking and to ensure a reasonable number of fatigue cycles.

C(T) and SEN(B) specimens are loaded in tension and in bending, respectively. If any stable tearing response occurs, the amount of slow-stable crack extension shall be measured. After test, it is necessary to measure the initial crack length. Standards provides the formulas to convert load-opening curves to fracture toughness (see, *e.g.*, [Zhu and Joyce, 2012]).

It is important to emphasize here that the specimen thickness has a major influence on the state of the mechanical fields at the crack tip. On a very thin specimen, such as the one in Fig. 4.22c, stresses related to the thickness direction are almost zero due to the free surface effect: the specimen is said to be in a state of **plane stress**. On the contrary, on a very thick specimen, such as the one shown in Fig. 4.22a, it is the deformation close to the crack tip in the direction of the thickness which is almost zero: the specimen is said to be in a state of **plane strain**. Note that this is mainly true at the specimen's centre: the outer surfaces remain in a state of plane stress. It can be seen that the fracture toughness measured experimentally is not totally intrinsic to the material: the toughness value is necessarily influenced by this size of the specimen.

Application to brittle fracture: Plane strain fracture toughness, K_{Ic} or K_{Jc} The plane-strain fracture toughness, K_{Ic}, is obtained when some practical conditions, detailed in the standards, are fulfilled. Examples include the fact that the specimen precrack front must respect conditions of straightness, or that the ligament and the thickness must have sufficient size to maintain a condition of high crack-front constraint at fracture. These later requirements ensure a particular state, called the condition of **small scale yielding** (SSY), meaning that the crack front is mainly under plane strain conditions, and that plasticity can not release ahead or behind the precrack. Indeed, plasticity always develops at the crack tip during loading. If the size of this plastic zone remains limited, linear elastic fracture mechanics can be applied, as explained in Chapter 5.

But this ideal linear elastic case is relatively seldomly obtained, in particular for metallic materials. Macroscopically, the load-displacement curve shows a non-linear section before fracture, reflecting locally a significant increase in the plastic zone size compared to the typical size of the sample. In this case, called **large scale yielding** (LSY), the elasto-plastic fracture mechanics has to be used to determine the fracture toughness, as explained in Chapter 6. This determination relies on the Rice J-integral properties. The standard gives the formulas to determine J, which can be converted to equivalent K values. The toughness is therefore noted K_{Jc}.

An example of an industrial application of these tests is shown in Fig. 4.23a, which plots the evolution of the fracture toughness K_{Jc} as a function of the test temperature (each point represents a specimen). The objective of this approach, described in the standard [ASTM E1921-22a, 2022], is to determine the macroscopic fracture toughness for ferritic steels in the lower ductile–brittle transition range. An intrinsic scatter is observed as well as an increasing evolution of the fracture toughness values as a function of the temperature. It can be observed that these phenomena, whose driving mechanisms are described in Chapter 7, are common to all ferritic steels; the only notable difference is a temperature shift, but otherwise they all follow the same type of distribution. This has given the method its name: the Master-Curve approach.

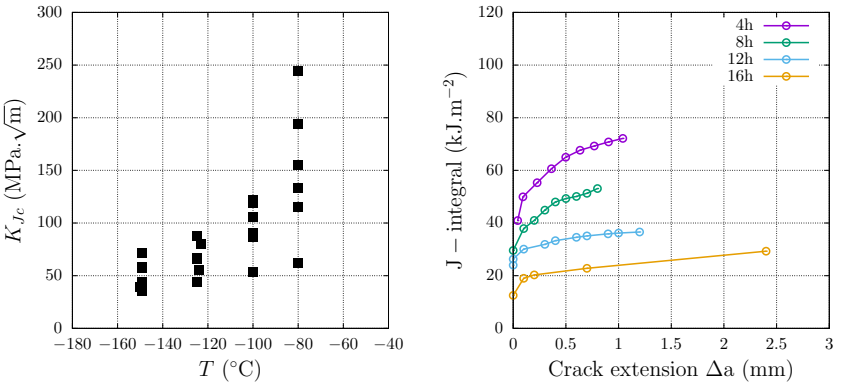

(a) (b)

FIGURE 4.23: Examples of experimental campaigns using C(T) specimens: (a) Brittle approach: K_{Jc} values of the fracture toughness as function of temperature, for a reactor pressure vessel steel [Hure et al., 2015]. (b) Ductile approach: R-curves of an aluminum alloy, after several heat treatment times [Petit et al., 2018].

Application to ductile fracture: J-R curves determination

In a precracked specimen, a stable crack propagation can occur due to the increase of tearing resistance with the crack propagation. Test specimens should be side grooved in order to avoid tunneling and maintain a straight crack front. The tearing resistance variation as a function of crack propagation is called the J-R curve (or R-curve). The determination of the J-R curve relies on the measurement of the crack length variation during the test.

The J-R curve for J_{Ic} determination can be generated either by a multispecimen technique, requiring comparatively more material, or a single specimen technique, requiring dedicated test equipment. With the multiple specimen technique, a serie of nominally identical specimens are loaded to various levels and then unloaded: each specimen is then broken open and the various crack extension lenghts are measured. The most common single specimen test technique is the unloading compliance method: the crack length is computed at regular intervals during the test by partially unloading the specimen and measuring the compliance; an alternative single specimen test method is the potential drop procedure in which crack growth is monitored through the change in electrical resistance which accompanies a loss in cross sectional area. When the entire R-curve is of interest, only single unloading compliance tests are allowed by the standard. Illustrations of this method can be found in Chapter 6.

Once the R-curve is constructed, two main parameters can be extracted:

- The fracture toughness J_{Ic} [J/m^2](generally defined as the value of J for 0.2 mm of propagation), quantifying the crack initiation resistance of the material and which can be converted into K_{Jc}.
- The tearing modulus T_σ [MPa] (generally defined as the slope of the R-curve between 0.2 and 1.5 mm of propagation), quantifying the crack propagation resistance of the material.

An example of an industrial application of these tests is shown in Fig. 4.23b, which compiles the R-curves of an aluminum alloy that has been subjected to 4 different heat treatments. It can be seen that these heat treatments have a significant role both on the J_{Ic} (higher or lower curves on the graph) and on T (steeper or shallower curves).

4.4.2.3 Quantifying fracture energy

The resilience test, or Charpy test, is probably one of the most performed test all around the world. The test itself, the specimen geometry, and the post-processing are defined by various standards, for example [ASTM E23-18, 2018]. These tests aim to quantify the ability of a material to absorb energy before failure. They consist of measuring the energy required to break a notched bar (geometry in Fig. 4.24a), by a fast impact caused by the falling of a rotating hammer. More details can be found in Chapter 7. Initially, the Charpy test has been developed as a comparative test: the only information was the absorbed energy during the test. Due to its low cost and convenience, there is a growing interest in using the test to obtain more sophisticated fracture mechanics related material information.

Application to the characterization of ductile-brittle transition

An example of an industrial application of this test is shown in Fig. 4.24b, which plots the evolution of the fracture energy as a function of the test temperature (each point represents a specimen) for a ferritic steel. The objective of this approach is to determine the transition temperature between macroscopic brittle and ductile failure behavior. For ferritic steels, these curves show three main characteristic domains: the brittle behavior (low fracture energy), the ductile behavior (high fracture energy), and the transition domain. As for fracture toughness (Fig. 4.23a), an intrinsic scatter is observed, and thus an average evolution of fracture energy with temperature is first computed, and then used to determine the ductile to brittle transition temperature (DBTT) and the upper shelf energy (USE) values. These indexes are often used in fracture safety analysis to estimate the material embrittlement due to aging (index DBTT) or to determine correlation with fracture toughness parameter (index USE).

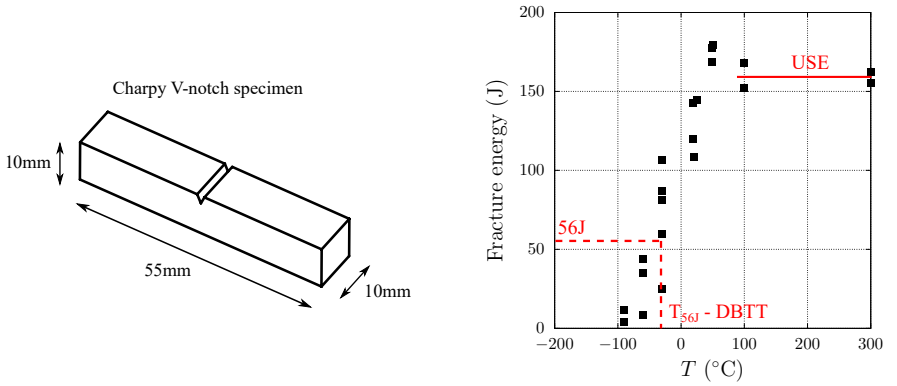

(a) (b)

FIGURE 4.24: (a) Standard Charpy specimen (b) Evolution of fracture energy obtained by the Charpy test as a function of temperature, for a ferritic steel, and determination of fracture indexes [Hure et al., 2015]

The tests described here above are widely used to obtain the fracture properties of metallic alloys. These data can then be used to assess structural integrity in engineering applications. Other tests, developed more recently, aim at investigating fracture at a lower scale. These tests are referred to as micro-mechanical fracture tests. Some examples of specimen geometries and applications are given in the next section. Again, this section is not intended to be exhaustive, the reader can find state of the art review *e.g.* in [Dehm et al., 2018]

4.4.3 Micro-mechanical tests

Similarly to the tests described in the standards, micro-mechanical tests have been developed to measure fracture strain / stress and fracture toughness, but at a lower scale. This is particularly relevant to assess fracture at the scale of the microstructure.

4.4.3.1 Quantifying fracture strain / stress

In order to improve our understanding of the phenomena at the origin of failure, and to be able to model the damage kinetics more finely, an ideal solution is to conduct experiments allowing measurements of critical stress and strain at extremely local levels.

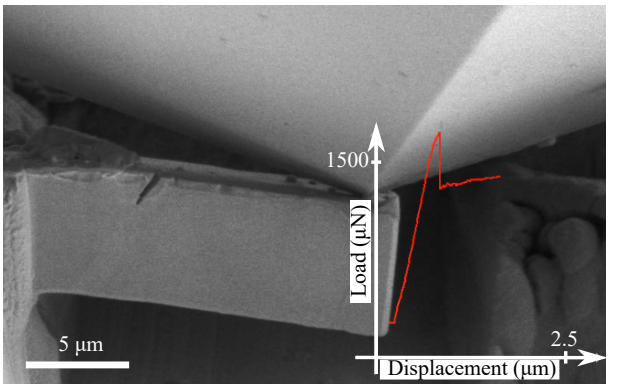

FIGURE 4.25: Bending test on a micrometric cantilever beam leading to the failure of a brittle grain boundary (Courtesy of R. Azihari, CEA) [Azihari, 2023]

To measure a **local critical stress**, micro-beam bending tests can be performed, for example, as shown in Fig. 4.25. This consists of machining micron-scale cantilever beams (via Focused Ion Beam technique) directly in the regions of interest, here a steel with an oxidized grain boundary. These micro-beams can then be mechanically loaded in a SEM, using a nanoindenter: the load required to initiate a crack is then measured, and fracture properties can be extracted. In this example, using both the force at the onset of failure and the force drop due to crack propagation (Inset Fig. 4.25) allows to measure fracture stress and fracture surface energy.

Local strain measurements can also be very valuable. For example, notched specimens can be mechanically loaded in a SEM via an in situ tensile device, as illustrated in Fig. 4.26. The objective of this experiment was to study the role of particles on void nucleation in an aluminum alloy, in order to improve the nucleation laws used in ductile fracture models. Using 2D digital image correlations (DIC), associated with finite element simulations, the strain values required to break these precipitates, or to break the interface between the precipitate and the aluminum matrix, are precisely quantified.

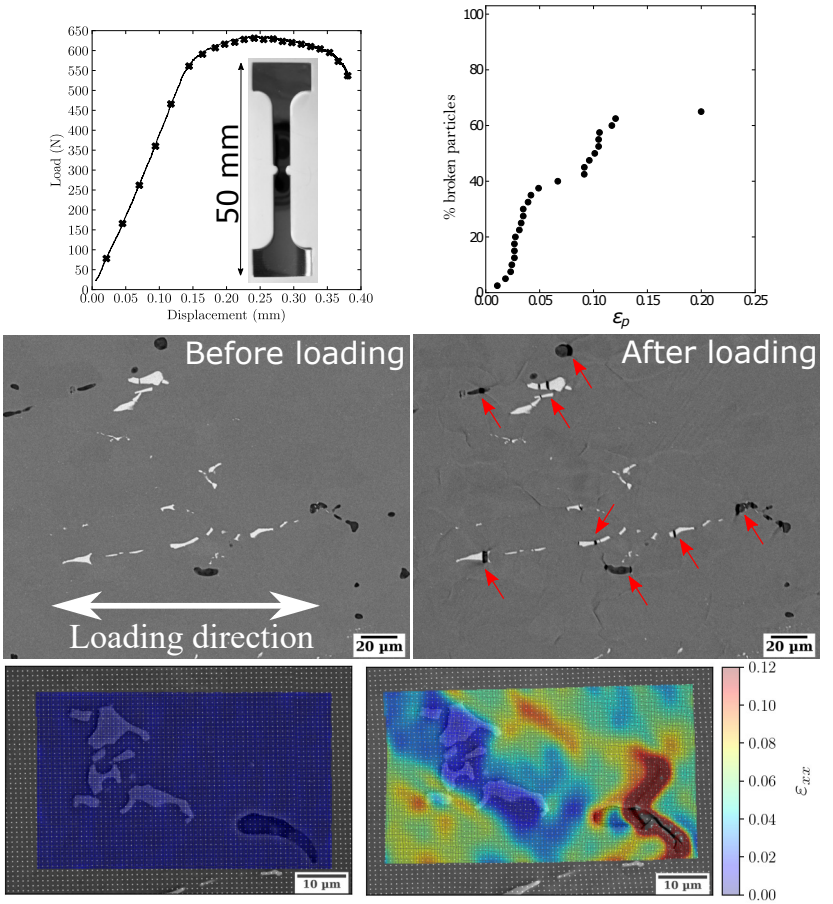

FIGURE 4.26: SEM in-situ test on notched specimen to identify nucleation kinetics based on local strain values (measured by DIC) in an aluminum alloy [Shokeir, 2022]

The limitation of this type of experiment is that investigations can only be completed on the surface of the sample, where the mechanical fields are in a state of plane stress, which is not necessarily representative of an industrial component. One solution is to carry out the same type of in situ experiment in a laboratory tomograph or, even better, in a synchrotron: the high flux make it possible to image the sample through its thickness, and thus to process 3D DIC. This technique, called DVC for Digital Volume Correlation, is described in detail in Chapter 8. This allows to assess triaxial stress states. But today it is still difficult to image a real state of plane strain: the thicknesses must be limited to maintain good spatial and temporal resolutions (especially in the case of metals). In order to finely characterize the damage kinetics in a thick

specimen, it is then necessary to carry out interrupted tests: the specimens are then cut and polished in order to be expertised.

4.4.3.2 Quantifying fracture toughness

Micromechanical tests have also been developed to quantify fracture toughness. These tests are even more challenging than the ones described previously as they require to machine an initial crack in addition to the samples themselves. Moreover, the conditions for which fracture toughness concept is relevant mainly restrain these tests to brittle fracture. Typically, these tests require simulations to design the samples as well as to analyze the results.

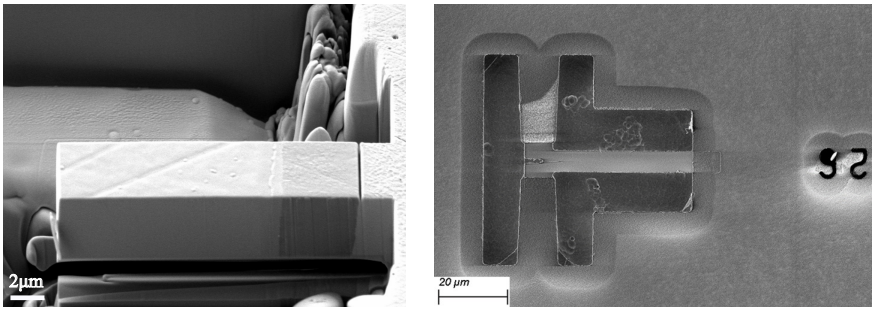

(a) (b)

FIGURE 4.27: Two examples of micromechanical tests developed to quantify fracture toughness: (a) Micro-cantilever on UO_2 / Cr interface (Courtesy of R. Henry, CEA LECA-STAR) [Henry, 2019], (b) Lab-on-chip on free-standing SiO_2 film (Courtesy of S. Jaddi, UCL) [Jaddi et al., 2021]

Fig. 4.27 shows two examples of micromechanical tests developed to quantify fracture toughness at the local scale. Fig. 4.27a corresponds to a micro-cantilever beam machined using Focused Ion Beam technique - basically an microscopic milling machine - allowing to locate the sample at an interface between UO_2 and Cr. A fine notch, also machined with FIB technique, is added at the interface to characterize fracture toughness. Note that the tests could also have been done without the initial crack, as in the section above, to quantify crack nucleation. A nanoindenter is then used to load the beam up to the critical force at which crack propagates. The critical force is then converted into fracture toughness. Fig. 4.27b corresponds to an experimental device based on the lab-on-chip technique [Pardoen et al., 2016]. Basically two layers are deposited on a substrate, one corresponding to the material studied and the other acting as the tensile machine. This layer starts pulling on the first layer as soon as the contact between the substrate is removed, due to internal stresses.

4.5 Conclusion

The experimental observations of fracture of metallic alloys presented in this chapter have highlighted some key points that are important to keep in mind when dealing with fracture mechanics, namely:

- The notions of brittle and ductile depend on the scale of the study and are therefore to be handled with care;
- A ductile failure mechanism can lead to a brittle failure on a structural scale;
- Conversely, a brittle failure mechanism may well be associated with a significant ductility at the scale of the structure;
- Testing condition such as specimen geometry and loading devices may have a strong impact on test results;
- A material can have several fracture mechanisms depending on the stress and environmental conditions.

A certain number of parameters are relevant when it comes to quantifying crack initiation and propagation, whether it is the fracture toughness K_c / fracture energy γ_c in a general way, or more specifically the notion of critical stress σ_c for brittle fracture mechanisms and that of critical strain ε_c for ductile failure mechanisms. Here again, some essential points must be kept in mind:

- The knowledge of the fracture mechanism is an essential prerequisite for the choice of the appropriate failure criterion and more generally for the modeling of the failure;
- The failure criterion used at the scale of interest must be relevant to the phenomenon of interest (initiation versus propagation).

Reader's attention is drawn on the fact that one of the richest source of information is the tested specimen itself. To analyze all the information provided, fractography analysis and post-mortem microstructural investigations have to be carried out.

All of these elements make it possible to choose the relevant mechanical test with respect to the phenomenon of interest and the desired fracture property. In other words, all mechanical tests can be fracture tests (after all, you only need to pull hard enough), but only well performed and analyzed tests on well chosen specimens can provide usable data for modeling and simulation. Some specimen geometries / test types have been presented in this chapter with examples of use. Defining the relevant fracture mechanics test for a given problem can be a challenge in itself. For standard fracture properties at the

usual engineering scales, a good way to proceed is to start by looking at standard tests (*e.g.* in ASTM or ISO standards). These standards, which are rather like recipes, allow for quality testing. Their specifications, sometimes obscure (but for good reasons), can serve as starting points for developing new tests such as the micro-mechanical tests presented in the last section.

Bibliography

[ASTM B871-01 2013] ASTM B871-01: Standard Test Method for Tear Testing of Aluminum Alloy Products / ASTM. 2013. – Technical repport

[ASTM E1820-18 2018] ASTM E1820-18: Standard Test Method for Measurement of Fracture Toughness / ASTM. 2018. – Technical repport

[ASTM E1921-22a 2022] ASTM E1921-22A: Standard Test Method for Determination of Reference Temperature, T0, for Ferritic Steels in the Transition Range / ASTM. 2022. – Technical repport

[ASTM E23-18 2018] ASTM E23-18: Standard Test Methods for Notched Bar Impact Testing of Metallic Materials / ASTM. 2018. – Technical repport

[ASTM E399-22 2022] ASTM E399-22: Standard Test Method for Linear-Elastic Plane-Strain Fracture Toughness of Metallic Materials / ASTM. 2022. – Technical repport

[Azihari 2023] Azihari, R.: *Approche micromécanique et modélisation de la rupture intergranulaire - Application à la corrosion sous contrainte assistée par l'irradiation*, Université Toulouse 3, Diss., 2023

[Benzerga and Leblond 2010] Benzerga, A. A. ; Leblond, J.-B.: Ductile Fracture by Void Growth to Coalescence. In: Aref, Hassan (Hrsg.) ; Giessen, Erik van d. (Hrsg.): *Advances in Applied Mechanics* Bd. 44. Elsevier, 2010, p. 169–305

[Bridgman 1964] Bridgman, P.W.: *The stress distribution at the neck of a tension specimen.* Cambridge, MA and London, England : Harvard University Press, 1964. – 3565–3587 S.

[Dehm et al. 2018] Dehm, G. ; Jaya, B.N. ; Raghavan, R. ; Kirchlechner, C.: Overview on micro- and nanomechanical testing: New insights in interface plasticity and fracture at small length scales. In: *Acta Materialia* 142 (2018), p. 248–282

[Griffith 1921] Griffith, A.A.: The phenomena of rupture and flow in solids. In: *Philosophical Transactions of the Royal Society A* 221 (1921), p. 582–593

[Henry 2019] Henry, R.: *Caractérisation locale des propriétés à la rupture du combustible nucléaire irradié*, Université de Lyon, Diss., 2019

[Hure et al. 2022] Hure, J. ; Courcelle, A. ; Turque, I.: A micromechanical analysis of swelling-induced embrittlement in neutron-irradiated austenitic stainless steels. In: *Journal of Nuclear Materials* 565 (2022), p. 153732

[Hure et al. 2018] Hure, J. ; Tanguy, B. ; Ritter, C. ; Bourganel, S. ; Sefta, F.: Extensive investigation of the mechanical properties of a Chooz A internal component. In: *Proceedings of Fontevraud 9: Contribution of Materials Investigations and Operating Experience to Light Water NPPs' Safety, Performance and Reliability*, 2018

[Hure et al. 2015] Hure, J. ; Vaille, C. ; Wident, P. ; Moinereau, D. ; Landron, C. ; Chapuliot, S. ; Benhamou, C. ; Tanguy, B.: Warm PreStress effect on highly irradiated reactor pressure vessel steel. In: *Journal of Nuclear Materials* 464 (2015), p. 281–293

[Inglis 1913] Inglis, C.E.: Stresses in a Plate Due to the Presence of Cracks and Sharp Corners. In: *Trans. Inst. Naval Archit.* 55 (1913), p. 219–241

[Jaddi et al. 2021] Jaddi, S. ; Raskin, J.P. ; Pardoen, T.: On-chip environmentally assisted cracking in thin freestanding SiO_2 films. In: *Journal of Materials Research* 36 (2021), p. 2479–2494

[Leblond 2003] Leblond, J.B.: *Mécanique de la rupture fragile et ductile*. Lavoisier, 2003

[Pardoen et al. 2016] Pardoen, T. ; Colla, M.S. ; Idrissi, H. ; Amin-Ahmadi, B. ; Wang, B. ; Schryvers, D. ; Bhaskar, U.K. ; Raskin, J.P.: A versatile lab-on-chip test platform to characterize elementary deformation mechanisms and electromechanical couplings in nanoscopic objects. In: *Comptes Rendus Physique* 17 (2016), Nr. 3, p. 485–495

[Petit et al. 2019] Petit, T. ; Besson, J. ; Ritter, C. ; Colas, K. ; Helfen, L. ; Morgeneyer, T. F.: Effect of hardening on toughness captured by stress-based damage nucleation in 6061 aluminum alloy. In: *Acta Materialia* 180 (2019), p. 349–365

[Petit et al. 2018] Petit, T. ; Ritter, C. ; Besson, J. ; Morgeneyer, T. F.: Impact of machine stiffness on 'pop-in' crack propagation instabilities. In: *Engineering Fracture Mechanics* 202 (2018), p. 405–422

[Petit et al. 2022] Petit, T. ; Tanguy, B. ; Wident, P. ; Parrot, A.: Application of miniature-C(T) for determination of the master curve and DBTT of a highly neutron-irradiated RPV steel. In: *Proceedings of Fontevraud 10: International Symposium on Contribution of Materials Investigations and Operating Experience to LWRs' Safety, Performance and Reliability*, 2022

[Pineau et al. 2016] Pineau, A. ; Benzerga, A.A. ; Pardoen, T.: Failure of metals I: Brittle and ductile fracture. In: *Acta Materialia* 107 (2016), p. 424–483

[Rice 1968] Rice, J.R.: A Path Independent Integral and the Approximate Analysis of Strain Concentration by Notches and Cracks. In: *Journal of Applied Mechanics* 35 (1968), p. 379–386

[Rice and Tracey 1969] Rice, J.R. ; Tracey, D.M.: On the ductile enlargement of voids in triaxial stress fields. In: *Journal of the Mechanics and Physics of Solids* 17 (1969), Nr. 3, p. 201–217

[Roth and Mohr 2016] Roth, C.C. ; Mohr, D.: Ductile fracture experiments with locally proportional loading histories. In: *International Journal of Plasticity* 79 (2016), p. 328–354

[Rudnicki and Rice 1975] Rudnicki, J.W. ; Rice, J.R.: Conditions for the localization of deformation in pressure-sensitive dilatant materials. In: *Journal of the Mechanics and Physics of Solids* 23 (1975), Nr. 6, p. 371–394

[Shokeir 2022] Shokeir, Z.: *Influence of radiation damage on fracture toughness of aluminum alloys in nuclear research reactors*, MINES Paristech, Diss., 2022

[Shokeir et al. 2022] Shokeir, Z. ; Besson, J. ; Belhadj, C. ; Petit, T. ; Madi, Y.: Edge tracing technique to study post-necking behavior and failure in Al alloys and anisotropic plasticity in line pipe steels. In: *Fatigue & Fracture of Engineering Materials & Structures* 1-16 (2022)

[Sutton et al. 2017] Sutton, M. A. ; Matta, F. ; Rizos, D. ; Ghorbani, R. ; Rajan, S. ; Mollenhauer, D. H. ; Schreier, H. W. ; Lasprilla, A. O.: Recent Progress in Digital Image Correlation: Background and Developments since the 2013 W M Murray Lecture. In: *Experimental mechanics* 57 (2017), p. 1–30

[Zhu and Joyce 2012] Zhu, X.K. ; Joyce, J.A.: Review of fracture toughness (G, K, J, CTOD, CTOA) testing and standardization. In: *Engineering Fracture Mechanics* 85 (2012), p. 1–46

5

Linear Elastic Fracture Mechanics

Véronique Lazarus

École nationale supérieure de techniques avancées (ENSTA Paris) et Institut Universitaire de France (IUF)

The aim of Linear Elastic Fracture Mechanics (LEFM) is to study the propagation of a crack assuming that the material breaks in the linear elastic regime. The center point for this discipline is that the stress field is amplified in the vicinity of defects (holes, notches, cracks, etc.). This is the equivalent of the spike effect in electromagnetism and can be visualised and measured using photoelasticity (Fig. 5.1).

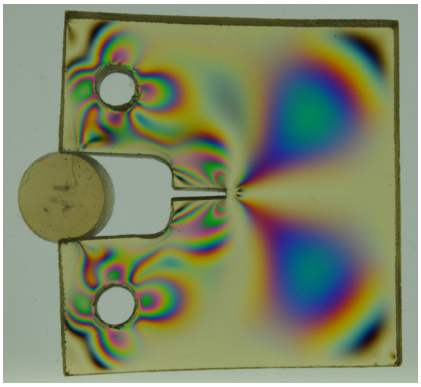

FIGURE 5.1: Visualisation of the stress field using photoelasticity. The load is applied through the introduction of a cylinder that opens the gap on the left side of the sample. Stress amplification can be seen in the vicinity of the slit extremity with the development of two symmetrical lobes that are typical for tensile cracks, but also near the two holes on the left.

This framework is currently used to assess the safety of sensitive components, as in aeronautics or in nuclear power plants. Section 5.1 aims to give the basis of LEFM, section 5.2 an overview of the methods to determine the key quantities ruling the crack advance (Stress Intensity Factors, Energy Release Rate), and section 5.3 some examples of applications. While previous sections deal with the well-establish part of the theory, in which simplified smoothed

out geometries are generally considered, section 5.4 will be an opening on works under progress about perturbation approaches that permit to deal with distorted crack geometries.

5.1 Basis of Linear Elastic Fracture Mechanics

The main ingredients and definitions of this scientific field, namely the Stress Intensity Factors (SIF) and Energy Release Rate (ERR) are given in section 5.1.1. These quantities give an indication of the load at the crack tip. They are used in the principles ruling the crack propagation that are given in section 5.1.2.

5.1.1 The ingredients

Consider a cracked isotropic linear elastic body Ω (Fig 5.2). Denote $\mathbb{K}$ the 4th order stiffness tensor, E, ν denoting the Young modulus and Poisson's ratio, λ, ν the Lamé's coefficients.

Assume here that body forces, such as weight, have a negligible effect in comparison to the load applied via the boundary conditions. Decompose the boundary $\partial\Omega$ of Ω in three parts ($\partial\Omega = \partial\Omega_c \cup \partial\Omega_T \cup \partial\Omega_d$) without any overlap, such as given external surface forces $\vec{T}^d$ apply on $\partial\Omega_T$ and given displacement $\vec{u}^d$ apply on $\partial\Omega_d$, the complementary part $\partial\Omega_c$ of the boundary of Ω being stress free. Define a crack $\mathcal{F}$ as a discontinuity surface of the displacement field, meaning that a crack is constituted by two surfaces, called *crack lips*, that are geometrically superposed in the unloaded configuration (Fig 5.2a), but no longer once the load is applied. In the deformed configuration, we suppose that the lips do not interpenetrate so that they remain traction free (Fig 5.2b). For crack problems with lip contacts, unilateral contact conditions have to be written on the crack lips [Bui, 2006; Marigo, 2016] and the linearity of the problem with the applied loads is then broken.

In 3D, the crack lips are discontinuity surfaces delimited by a line, called *crack front* (Fig 5.2c). In 2D, the crack lips reduces to 1D lines of discontinuity ending with a point, the *crack tip* (Fig 5.2a,b).

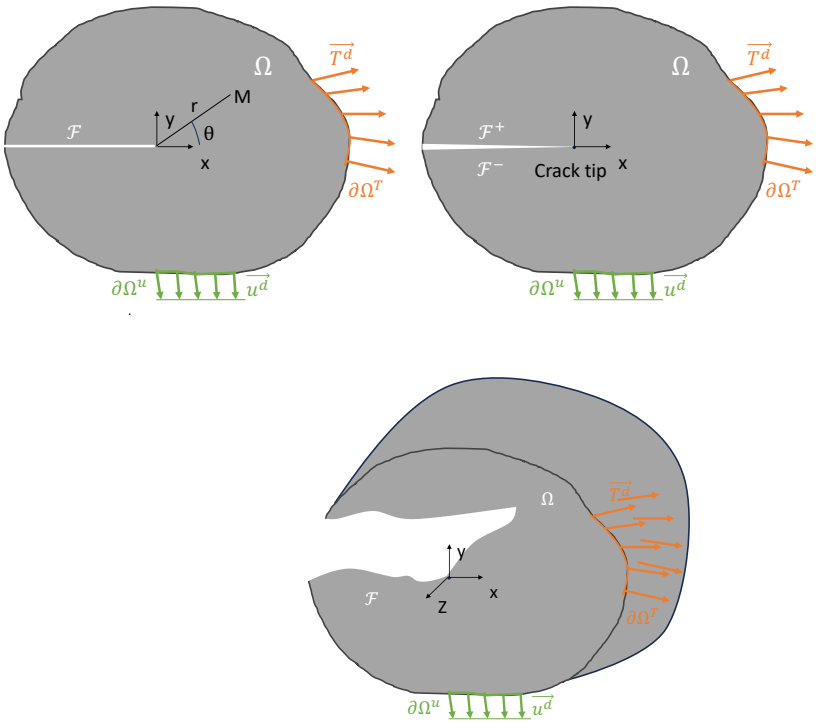

FIGURE 5.2: Linear Elastic Fracture Boundary Value Problems. a-b) a 2D problem with a straight crack. c) a 3D problem with a distorted crack (surface and front). a) The crack is closed in the initial unloaded configuration. b-c) A discontinuity of the displacement field is observed once the body is loaded.

5.1.1.1 Strong form of the linear elasticity problem

For a fixed crack geometry, displacement $\vec{u}$, strain $\boldsymbol{\epsilon}$ and stress $\boldsymbol{\sigma}$ fields constitute the unique solution[1] of the following Boundary Value Problem (BVP) defined by:

- partial differential equations at all points of Ω:

$$\left\{\begin{array}{l} \vec{\mathrm{Div}}(\boldsymbol{\sigma}) = \vec{0} \\ \boldsymbol{\sigma} = \mathbb{K}.\boldsymbol{\epsilon} = 2\mu\,\boldsymbol{\epsilon} + \lambda\,(\mathrm{tr}\boldsymbol{\epsilon})\mathbf{1} \Leftrightarrow \boldsymbol{\epsilon} = \mathbb{K}^{-1}.\boldsymbol{\sigma} = \frac{1+\nu}{E}\,\boldsymbol{\sigma} - \frac{\nu}{E}(\mathrm{tr}\boldsymbol{\sigma})\mathbf{1} \\ \boldsymbol{\epsilon}(\vec{u}) = \frac{1}{2}(\mathbf{Grad}(\vec{u}) +^T \mathbf{Grad}(\vec{u})), \end{array}\right. \tag{5.1}$$

- boundary conditions ($\partial\Omega = \partial\Omega_c \cup \partial\Omega_T \cup \partial\Omega_d$):

$$\left\{\begin{array}{l} \boldsymbol{\sigma}.\boldsymbol{n} = \vec{T}^{\,d} \text{ on } \partial\Omega_T \\ \boldsymbol{\sigma}.\boldsymbol{n} = \vec{0} \text{ on } \partial\Omega_c \cup \mathcal{F} \\ \vec{u} = \vec{u}^{\,d} \text{ on } \partial\Omega_d \end{array}\right. \tag{5.2}$$

5.1.1.2 Weak form of the linear elasticity problem

In the purpose to write the elasticity problem in the weak/variational form and to introduce notations that will be useful in this book, introduce the following spaces of kinematically admissible displacements:

$$\begin{array}{l} \mathcal{C} = \{\vec{u} \in H^1(\Omega) : \vec{u} = \vec{u}^{\,d} \text{ on } \partial\Omega_d\}, \\ \mathcal{C}_0 = \{\vec{u} \in H^1(\Omega) : \vec{u} = \vec{0} \text{ on } \partial\Omega_d\}, \end{array} \tag{5.3}$$

the density of elastic energy:

$$w(\boldsymbol{\epsilon}) = \frac{1}{2}\boldsymbol{\sigma} : \boldsymbol{\epsilon} = \frac{1}{2}\boldsymbol{\epsilon} : \mathbb{K} : \boldsymbol{\epsilon} \tag{5.4}$$

the internal energy W_{int} and the total work W_{ext} of external forces:

$$W_{int} = -\int_{\Omega/\mathcal{F}} \boldsymbol{\sigma} : \boldsymbol{\epsilon}\mathrm{d}\Omega; \quad W_{ext} = \int_{\partial\Omega} \vec{T}.\vec{u}\mathrm{d}S \tag{5.5}$$

and the potential energy:

$$\mathcal{P}(\vec{u}) = \int_{\Omega/\mathcal{F}} w(\boldsymbol{\epsilon}(\vec{u}))\mathrm{d}\Omega - \int_{\partial\Omega_T} \vec{T}^{\,d}.\vec{u}\mathrm{d}S \tag{5.6}$$

We get using equilibrium equations $W_{int} + W_{ext} = 0$ (also known as principle of virtual power):

$$\mathcal{P}(\vec{u}) = \frac{1}{2}W_{ext} - \int_{\partial\Omega_T} \vec{T}^{\,d}.\vec{u}\mathrm{d}S = \frac{1}{2}\int_{\partial\Omega_u} \vec{T}.\vec{u}^{\,d}\mathrm{d}S - \frac{1}{2}\int_{\partial\Omega_T} \vec{T}^{\,d}.\vec{u}\mathrm{d}S \tag{5.7}$$

[1] we suppose that Boundary Conditions are written in order to prevent any body rigid motion, so that the displacement solution is unique as the strain and stress solutions. It is for instance the case if all the components of the displacement are imposed on one part of the boundary.

This formula will be useful to derive the compliance formula in section 5.2.3.

The solution $\vec{u}$ of the BVP (5.1-5.2) satisfies the potential energy minimum theorem [Marigo, 2016]:

$$\vec{u} = \text{argmin}_{\vec{u}^* \in \mathcal{C}} \mathcal{P}(\vec{u}^*) \tag{5.8}$$

Notice that while in 3D, $\mathcal{P}(\vec{u})$ has the dimension of an energy, for 2D elasticity problems, Ω is a surface so that $\mathcal{P}(\vec{u})$ is an energy by unit thickness.

5.1.1.3 Definition of the Stress Intensity Factors (SIF)

Consider a 2D elasticity problem with a straight crack front (Fig 5.2a,b). Denote x, y, z a direct system of axis, such as x is in continuity with the crack surface, y is normal and z is the out of plane direction. Looking for solutions with finite elastic energy, it is possible to show [Williams, 1952] that the stress field is singular in the vicinity of the crack tip [Bui, 2006; Leblond, 2003]. More precisely,

$$\sigma_{ij}(r,\theta) = \frac{K_I}{\sqrt{2\pi r}} f_{ij}^I(\theta) + \frac{K_{II}}{\sqrt{2\pi r}} f_{ij}^{II}(\theta) + \frac{K_{III}}{\sqrt{2\pi r}} f_{ij}^{III}(\theta) + O(1) \tag{5.9}$$

when $r \to 0$, (r, θ) being the polar coordinates defined from the crack tip and the tangent to the crack lips (Fig 5.2a).

Functions $f_{ij}^p(\theta)$ are universal (in the sense they do not depend on the BVP) functions depending on θ only, given by:

$$\left\{ \begin{array}{ll} f_{xx}^I = \cos\left(\frac{\theta}{2}\right)\left(1 - \sin\left(\frac{\theta}{2}\right)\sin\left(\frac{3\theta}{2}\right)\right) & f_{xx}^{II} = -\sin\left(\frac{\theta}{2}\right)\left(2 + \cos\left(\frac{\theta}{2}\right)\cos\left(\frac{3\theta}{2}\right)\right) \\ f_{yy}^I = \cos\left(\frac{\theta}{2}\right)\left(1 + \sin\left(\frac{\theta}{2}\right)\sin\left(\frac{3\theta}{2}\right)\right) & f_{yy}^{II} = \sin\left(\frac{\theta}{2}\right)\cos\left(\frac{\theta}{2}\right)\cos\left(\frac{3\theta}{2}\right) \\ f_{xy}^I = \cos\left(\frac{\theta}{2}\right)\sin\left(\frac{\theta}{2}\right)\cos\left(\frac{3\theta}{2}\right) & f_{xy}^{II} = \cos\left(\frac{\theta}{2}\right)\left(1 - \sin\left(\frac{\theta}{2}\right)\sin\left(\frac{3\theta}{2}\right)\right) \end{array} \right. \tag{5.10}$$

and

$$\left\{ \begin{array}{l} f_{xz}^{III} = -\sin\left(\frac{\theta}{2}\right) \\ f_{yz}^{III} = \cos\left(\frac{\theta}{2}\right) \end{array} \right. \tag{5.11}$$

the other components being zero. Note that in Fig. 5.1, the load is in mode I ($K_{II} = K_{III} = 0$) and the shape of the two symmetrical lobes is associated to the shape of the functions f_{xx}^I, f_{yy}^I, f_{xy}^I.

While the elastic stresses are theoretically infinite, physically the material responds with irreversible dissipative processes (damage, plasticity...) in a zone called *Process Zone (PZ)*. If its size is small in comparison with the size of Ω and the crack size, the prefactors K_p, $p = I$, II, III are relevant to quantify the intensity of the stress in the vicinity of the crack tip, they are therefore called *Stress Intensity Factors*.

The first term of the corresponding displacement fields expansion can be obtained from Eq. 5.10-5.11 using the constitutive law to get $\boldsymbol{\epsilon}$ and further integration of the definition of $\boldsymbol{\epsilon}$ (Eq. 5.1). It gives:

$$u_i = \frac{K_p}{4\mu}\sqrt{\frac{r}{2\pi}}\xi_i^p(\theta) \tag{5.12}$$

with:

$$\begin{cases} \xi_r^I = (2\kappa-1)\cos\left(\frac{\theta}{2}\right) - \cos\left(\frac{3\theta}{2}\right) & \xi_r^{II} = -(2\kappa-1)\sin\left(\frac{\theta}{2}\right) + 3\sin\left(\frac{3\theta}{2}\right) \\ \xi_\theta^I = -(2\kappa+1)\sin\left(\frac{\theta}{2}\right) + \sin\left(\frac{3\theta}{2}\right) & \xi_\theta^{II} = -(2\kappa+1)\cos\left(\frac{\theta}{2}\right) + 3\cos\left(\frac{3\theta}{2}\right) \end{cases} \tag{5.13}$$

and

$$\xi_z^{III} = 8\sin\left(\frac{\theta}{2}\right) \tag{5.14}$$

The other components are equal to zero.

While Eq. 5.9-5.11 are valid whether in Plane Stress (PS) or Plane Strain (PE) hypotheses for the stress field, the Kolosov constant κ appearing in the expansion of the displacement is equal to $\kappa = 3 - 4\nu$ in PE and $\kappa = \frac{3-\nu}{1+\nu}$ in PS. As mentioned in Bui's book [Bui, 2006], the solution is not exact in PS as the corresponding strain field is not compatible with the existence of a displacement field. However, it has been shown to be pertinent in most of the PS problems [Bui, 2006]. A practical way to decide which is the more relevant hypothesis is given in Triclot *et al.* [Triclot et al., 2023].

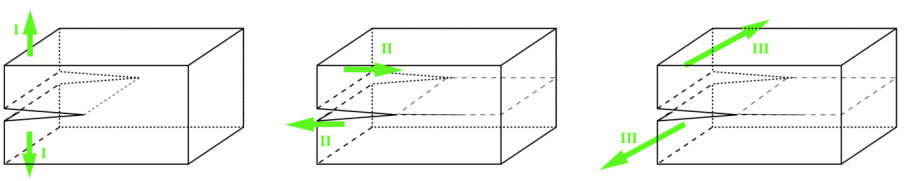

FIGURE 5.3: Three fracture modes: mode I for tensile crack, mode II for plane-shear, mode III for antiplane shear

Each SIF corresponds to one mode of discontinuity of the crack lips (Fig 5.3): mode I corresponds to symmetrical opening, mode II to plan shear, mode III to antiplane shear. Indeed, using Eq. 5.12, 5.13 and 5.14 to evaluate the displacement jump $[\![u_i]\!] \equiv u_i^+ - u_i^-$ across the crack lips, one has:

$$\begin{array}{lllll} \text{For } K_{II} = K_{III} = 0: & [\![u_x]\!] = [\![u_z]\!] = 0 & [\![u_y]\!] = \frac{K_I(1+\kappa)}{\mu}\sqrt{\frac{r}{2\pi}} \\ \text{For } K_I = K_{III} = 0: & [\![u_y]\!] = [\![u_z]\!] = 0 & [\![u_x]\!] = \frac{K_{II}(1+\kappa)}{\mu}\sqrt{\frac{r}{2\pi}} \\ \text{For } K_I = K_{II} = 0: & [\![u_x]\!] = [\![u_y]\!] = 0 & [\![u_z]\!] = \frac{4K_{III}}{\mu}\sqrt{\frac{r}{2\pi}} \end{array} \tag{5.15}$$

Let us mention that the next term (of order 1 in the development of $\vec{u}$, of order 1 in the development of $\boldsymbol{\sigma}$) in the vicinity of the crack tip involves T-stresses. They have been shown to have an impact on the selection of the crack path [Cotterell and Rice, 1980; Mesgarnejad et al., 2020; Lebihain et al., 2022; Shaikeea et al., 2022; Doitrand et al., subm].

5.1.1.4 Definition of the Energy Release Rate (ERR)

For a given body (that is material and geometry), the potential energy defined in Eq. 5.6 depends only on the crack length ℓ and the applied load $(\vec{T}^d, \vec{u}^d)$.

When the crack length increases at constant load $(\vec{T}^{\,d}, \vec{u}^{\,d})$, elastic energy is released by the creation of stress free surfaces, so that the Energy Release Rate defined by:

$$\mathcal{G} \equiv -\left.\frac{\partial \mathcal{P}}{\partial \ell}\right)_{\vec{T}^{\,d} \text{ and } \vec{u}^{\,d} \text{ constant}}, \tag{5.16}$$

is a positive quantity. Positivity of $\mathcal{G}$ can also be demonstrated rigorously using the potential energy minimum principle given in Eq. 5.8 and the increase of the set $\mathcal{C}$ (defined in Eq. 5.3) with the crack length [Marigo, 2016].

The SIF as well as the ERR can be used to quantify the loading of the crack tip. They are related by Irwin's formula [Irwin, 1958]:

$$\mathcal{G} = \frac{1}{E'}\left(K_I^2 + K_{II}^2\right) + \frac{1+\nu}{E} K_{III}^2 \tag{5.17}$$

with $E' = E$ for PS, $E' = E/(1-\nu^2)$ for PE.

5.1.2 Crack propagation rules

The aim of this section is to discuss when and how a preexisting crack propagates. Several situations will be considered. The case of a component submitted to cyclic load (fatigue crack propagation), in which the crack advance little by little at each cycle, will be presented briefly in section 5.1.2.1. For monotonous loading, the existence of a threshold below which propagation does not occur is discussed in section 5.1.2.2. The dynamics of crack propagation beyond the threshold is the topic of section 5.1.2.3. Eventually, the crack path selection is addressed in section 5.1.2.3.

5.1.2.1 Fatigue

Many industrial components are subjected to cyclic loadings (turbines, airplanes, rails...), that progressively damage the material. In the first instance, the advance rate of a crack $\frac{\mathrm{d}a}{\mathrm{d}N}$ during one cycle can be estimated by Paris' law [Erdogan and Paris, 1963]:

$$\frac{\mathrm{d}a}{\mathrm{d}N} = C(\Delta K_I)^n \tag{5.18}$$

where C, n are material constants and ΔK_I the SIF amplitude during one cycle.

In practice, the link between the advance rate and the cyclic load is often more complexe and there is a whole literature on fatigue crack propagation. We will not enter in more details here. But it is worth to be aware that many repeated cycles may growth a crack significantly until reaching the point of catastrophic failure discussed below.

5.1.2.2 Crack propagation threshold

Pull on a sheet of paper containing a crack (Fig 5.4). You will notice that below a certain force the crack doesn't propagate, meaning that there exists a

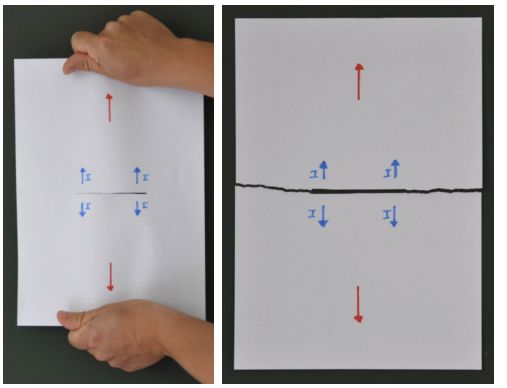

FIGURE 5.4: Paper plate containing a crack loaded in mode I, before and after fracture.

threshold below which the crack stays harmless. The seminal Griffith criteria [Griffith, 1920] states that the crack will not advance if :

$$\mathcal{G} < \mathcal{G}_c \tag{5.19}$$

where $\mathcal{G}_c$ is a material constant corresponding to the energy cost to advance the crack by unit surface. In other words, the crack cannot advance if the elastic energy released is not enough to cover the fracture costs. In the seminal work of Griffith [Griffith, 1920], $\mathcal{G}_c$ was meant as a reversible energy, in the same way as the surface tension of a liquid. But as crack propagation is irreversible, the costs linked to the dissipative processes occuring in the Process Zone have to be included in $\mathcal{G}_c$ and are generally much larger than the reversible energy required to separate two atoms [Marder, 2009].

In mode I, it is equivalent to Irwin's criterion through Eq. 5.17, that is:

$$K_I < K_{Ic} \Rightarrow \text{ no crack advance} \tag{5.20}$$

where $K_{Ic} = \sqrt{\frac{E}{1-\nu^2}\mathcal{G}_c}$ is the fracture toughness. The physical reasoning behind this criterion is that a crack cannot propagate if the tensile stress level near the crack tip, that can be quantified by the mode I SIF, is not high enough. Note that the SI unit of K_{Ic} is Pa.m$^{1/2}$ hence changing m in mm does not yield a factor of 10 but $10^{-3/2}$, so that unit errors may be difficult to perceive.

While K_I and $\mathcal{G}$ depend on the BVP, that is on the elastic constants, the load ($\vec{T}^d$, $\vec{u}^d$) and the component geometry, $\mathcal{G}_c$ and K_{Ic} are material constants. Irwin's (Eq. 5.20) and Griffith's (Eq. 5.19) criterion are thus practical ways to know if a preexisting crack has some risk to propagate or not for a given BVP. Ashby diagrams can be used to obtained typical values of the material constants depending on the kind of material [Ashby, 1989; Wegst and Ashby, 2004].

5.1.2.3 Dynamics of crack propagation

Once the propagation threshold is reached, the crack may propagate without stopping leading to catastrophic failure of the specimen. It is in particular the case in the experiments of Fig. 5.4. But in some cases, crack propagation may only occur if the load is increased (think for instance to the tearing of a sheet of paper). In this section, we aim to discuss in which case the propagation can be controlled or not.

Suppose that the load $(\vec{T}^d,\ \vec{u}^d)$ is proportional to one single parameter $t \geq 0$. For a given body (fixed geometry and material constants), the ERR and SIF depend on t and ℓ only: $\mathcal{G} = \mathcal{G}(\ell, t)$ and $K_p = K_p(\ell, t)$. By linearity of the BVP, the solution $(\vec{u},\ \boldsymbol{\epsilon},\ \boldsymbol{\sigma})$ varies linearly with the applied load, so that $K_p(\ell, t) = t\hat{K}_p(\ell)$ (use Eq. 5.15), hence $\mathcal{G}(\ell, t) = t^2\hat{\mathcal{G}}(\ell)$ (use Eq. 5.17), where $\hat{K}_p(\ell)$ and $\hat{\mathcal{G}}(\ell)$ denote the SIF and ERR for unit load ($t = 1$), hence depend on the crack length only. These notations allows to decouple the load and the crack length effects.

Start with a problem containing a crack with an initial length ℓ_0. Suppose that the load t increases and that the crack growths along a prescribed path. We aim to find the crack length $\ell(t)$ as a function of t in the quasi-static limit, i.e. so that at each t, equilibrium is satisfied. Note that t denotes an instant corresponding the load t, and not a real time. First and second thermodynamical principles then implies [Francfort and Marigo, 1998; Bourdin et al., 2008]:

$$\begin{cases} (\mathcal{G}(\ell, t) - \mathcal{G}_c)\dot{\ell}(t) = 0 & \text{(energy balance)} \\ \dot{\ell}(t) \geq 0 & \text{(irreversibility condition)} \end{cases} \tag{5.21}$$

Quasistatic crack growth ($\dot{\ell}(t) > 0$) can thus be achieved only if $t^2\hat{\mathcal{G}}(\ell(t)) - \mathcal{G}_c = 0$ for all t, hence only if $\hat{\mathcal{G}}'(\ell) < 0$ (where $\hat{\mathcal{G}}'(\ell) \equiv \frac{\mathrm{d}\hat{\mathcal{G}}}{\mathrm{d}\ell}$). Indeed taking the derivative of the equation with t yields $2t\hat{\mathcal{G}}(\ell) + t^2\hat{\mathcal{G}}'(\ell) = 0 \Rightarrow \hat{\mathcal{G}}'(\ell) = -2\hat{\mathcal{G}}(\ell)/t$ which is a negative quantity. If $\frac{\mathrm{d}\hat{\mathcal{G}}}{\mathrm{d}\ell} > 0$ then $\mathcal{G}(\ell(t+\Delta t), t+\Delta t) > \mathcal{G}_c$ at least for a short moment $\Delta t > 0$, meaning that the available elastic energy is too large to stay at equilibrium, dynamical crack propagation will occur as long as $\mathcal{G}(\ell(t + \Delta t), t + \Delta t) > \mathcal{G}_c$. This case must be avoided for sensitive components for which the rupture is life-threatening, since it may lead to catastrophic failure. If needed, you may refer to the book of Freund [Freund, 1998] about the dynamical aspects of crack propagation.

Another way of thinking about quasi-static crack evolution is to suppose that ℓ increases, instead of t as previously, and to look at the load $t(\ell)$ required to get $\mathcal{G}(\ell, t(\ell)) - \mathcal{G}_c = 0$ for all ℓ. Irreversibility and energy balance are then automatically satisfied. This implies that $t(\ell)^2\hat{\mathcal{G}}(\ell) = \mathcal{G}_c$ for all ℓ. Deriving this equation with respect to ℓ yields $t'(\ell) = -t(\ell)\frac{\hat{\mathcal{G}}'(\ell)}{2\hat{\mathcal{G}}(\ell)}$, meaning that to control quasistatic crack propagation, the load t must be decreased if $\hat{\mathcal{G}}'(\ell) > 0$ and

increased if $\hat{\mathcal{G}}'(\ell) < 0$, in line with the results obtained previously reasoning in term of increasing load t.

This point will be illustrated on the example of a Double Cantiveler Beam (DCB) in section 5.3.2.

5.1.2.4 Crack propagation direction

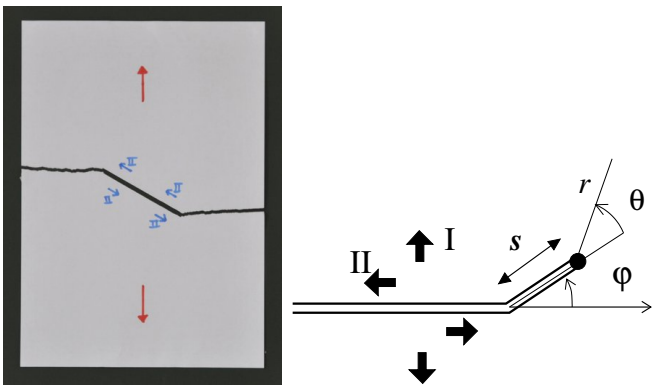

FIGURE 5.5: Left: Kinking of a crack loaded in mode I+II. Right: definition of the kink angle φ

In previous section, we supposed that the crack path was known. But as in the example of Fig. 5.5 (left), the crack may deviates from its initial plane. What about the determination of the new propagation direction φ, also called the *kink angle*, that is defined in Fig. 5.5 (right)? Several criterions have been proposed over time, notably the:

MTS Maximum Tensile Stress criterion [Erdogan and Sih, 1963]: the crack propagates in the direction where the tensile opening stress is maximum: $\dfrac{\partial \sigma_{\theta\theta}}{\partial \theta}(\varphi) = 0$

Max ERR Maximum Energy Release Rate [Erdogan and Sih, 1963] : the crack propagates in the direction where the available elastic energy is maximum, *i.e.* where it overcomes first the fracture costs $\mathcal{G}_c$: $\max_\varphi \mathcal{G}^*(\varphi)$, where $\mathcal{G}^*(\varphi)$ is the ERR when the crack propagates in the direction φ.

PLS Principal of Local Symmetry [Goldstein and Salganik, 1974]: the crack propagates in a direction where the mode II SIF is zero: $K_{II}^*(\varphi) = 0$ where $K_{II}^*(\varphi)$ is the mode II SIF for a infinetisimal small crack extension in the direction φ.

Based on different physical arguments, they have indeed been shown to

yield different values of φ using the formula that will be given in §5.2.4. However, for isotropic elasticity, they never differ more than 1.5 ° [Amestoy and Leblond, 1992], so that they can be used indifferently for practical purposes.

For anisotropic materials (composites, crystal, material printed by additive manufacturing [Corre and Lazarus, 2021]), the fracture costs $\mathcal{G}_c$ depends on the direction φ. Among the above criteria, the Max ERR can be generalized by searching for the maximum of $\mathcal{G}(\varphi) - \mathcal{G}_c(\varphi)$ [Ibarra et al., 2016].

5.1.3 3D problem

Consider the general case of a 3D problem (Figure 5.2c) with a non-planar crack surface and a curved front. Introduce a curvilinear abscissa s along the crack front and a local direct orthonormal frame $(\vec{e}_x(s), \vec{e}_y(s), \vec{e}_z(s))$ such that $\vec{e}_z(s)$ is tangent to the crack front, $\vec{e}_x(s)$ is the tangent to the crack surface orthogonal to $\vec{e}_z(s)$ pointing in the crack propagation direction, $\vec{e}_y(s) = \vec{e}_z(s) \wedge \vec{e}_x(s)$. The 2D expansions of the stress field and displacement field remain valid [Leblond, 1999] in this frame providing that the PE hypothesis is chosen in Eq. 5.13. The SIF and the ERR then depend on the point s considered along the crack front: $K_I(s)$, $K_{II}(s)$, $K_{III}(s)$, $\mathcal{G}(s)$. Irwin's, Griffith's and directional criterions can be written locally at each point s. Note that the SIF at a point of the crack front located at the surface of the body are not well defined [Bazant and Estenssoro, 1979].

5.1.4 In practice

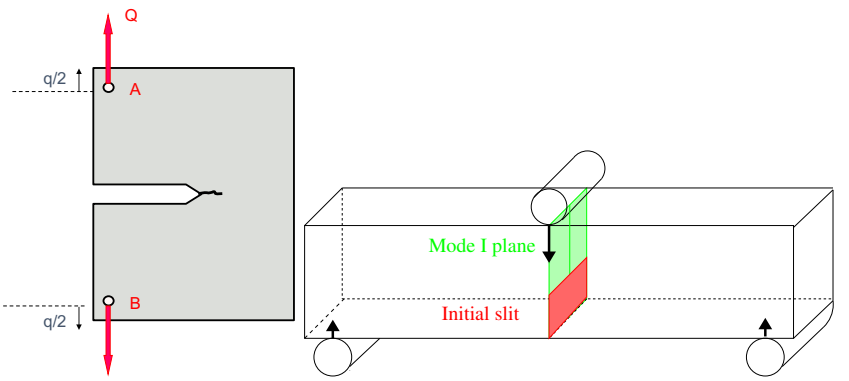

FIGURE 5.6: Compact Tensile and Three Point Bend tests

In the case of an isotropic solid, Linear Elastic Fracture Mechanics theory relies on the use of three materials constants. In addition to two elasticity constants (E, ν for instance), a third one is necessary to describe the fracture threshold (K_{Ic} or G_c). To measure K_{Ic}, standard tests, as e.g. Compact

Tensile Test specimens or Three Point Bend specimens can be used (Fig. 5.6). For these geometries, K_I is known as a function of the applied load, say Q [Tada et al., 2000]. The tests then consist to load the precracked specimens using a mechanical testing machine, until the onset of propagation. At this point, $Q = Q_c$ is measured and Irwin's criterions is satisfied. This provides a measure of K_{Ic} using $K_{Ic} = K_I(Q_c)$.

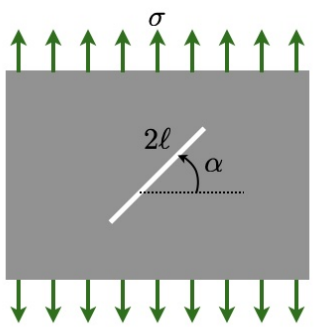

FIGURE 5.7: Plate under tension containing an inclined crack

Once E, ν and K_{Ic} are known for a given material, it is possible to use them for engineering purposes, notably to determine the maximum load or crack size that can be tolerated in a component without major risk of failure. For instance, consider the following BVP problem: a small horizontal crack of length 2ℓ is submitted remotely to a tensile stress σ (Fig. 5.7 with $\alpha = 0$). In this case, $K_I = \sqrt{\pi\ell}\sigma$. Knowing that in service, σ will always be lower than σ_{max}, a crack of length $\ell < \ell_{max}$ where $\ell_{max} \equiv K_{Ic}^2/(\sigma_{max}^2\pi)$ can be considered to be safe, since than $K_I < K_{Ic}$ which is below the propagation threshold. On the other hand, knowing that the component does not contain any crack larger than ℓ_{max}, while the stress is smaller than $\sigma_{max} \equiv K_{Ic}/\sqrt{\pi\ell_{max}}$ there is no risk of catastrophic failure. Of course, in practice, safety margins are applied.

For critical components subjected to cyclic load, whose rupture would be life-threatening, damage tolerance approach [David and Lazarus, 2022] is applied notably in the aeronautic domain. The idea, based on the fact that almost no material is perfect, is to assess that any possible defect will not cause catastrophic failure. More precisely, it consists to determine the number of load cycles N_c that are needed to drive a crack by fatigue (section 5.1.2.1) until reaching the propagation threshold (section 5.1.2.2). This pre-existing crack considered is either a detected defect or the most dangerous undetectable one.

5.2 Determination of the SIF and the ERR

To apply the propagation rules given in section 5.1.2, the SIF and the ERR have to be determined. These quantities are related to the solution ($\vec{u}$, $\boldsymbol{\epsilon}$, $\boldsymbol{\sigma}$) of the BVP (Eq. 5.1, 5.2). The aim of this section is to give an overview on the several possibilities to determine them, for more complex BVP than the one considered in section 5.1.4 above. In a first intention, the BVP is generally oversimplified to use analytical solutions (section 5.2.1). For more complex BVP geometries, Finite Element Modeling can be used (section 5.2.2). For BVP involving only one loading parameter, using the compliance formula (section 5.2.3) are useful to determine whether the crack propagation can be controlled or not, for instance to design experimental setups with controlled crack propagation. To determine the crack path, the SIF after an angular kink have to be known. This requires specific developments (section 5.2.4) as it is difficult to catch numerically with enough accuracy.

5.2.1 Analytical solutions

Analytical solutions or tabulated solutions are available for simple elasticity BVP, as for instance for an infinite plate loaded remotely (Fig. 5.7 and Eq. 5.35). Those have been listed in handbooks (e.g. [Tada et al., 2000]).

Approaches using complex number as Airy or Muskelishvili potentials [Muskhelishvili, 1953] have been used with success to obtain analytical solutions for more complex problems [Leblond, 2003; Bui, 2006]. To satisfy your eventual curiosity, feel free to look at my Ph.D report to see complex calculations using these methods [Lazarus, 1997]. Those methods can seem obsolete in light of the computational progress but stay useful to validate some numerical approach or to catch some subtil effects that cannot be obtained numerically.

5.2.2 Finite Element calculation

For more complex BVP, the elastic displacement field $\vec{u}$ can be obtained by Finite Element Methods. Several more or less accurate methods exists to extract from $\vec{u}$ the SIF and ERR values. The most straightforward one is to use interpolation near the crack tip based on William's series (Eq. 5.9), looking for the best fit in K_I, K_{II}, K_{III}. From there, the ERR can be obtained using Irwin's formula (Eq. 5.17).

Using Rice's J-integral [Rice, 1968] is another possibility:

$$\mathcal{G} = J \equiv \int_{\Gamma} (w n_x - \sigma_{ij} u_{i,x} n_j) \mathrm{d}s$$

where w is defined by Eq. 5.4, Γ is a contour encompassing the crack tip (Fig. 5.8) and $\vec{n}$ is its unit external normal. The solution is independent of

the contour Γ provided that the crack surface can be considered to be straight inside Γ [Rice, 1968; Corre et al., In p]. For a curved surface, it implies to take a contour that is close enough to the tip, so that the interior can be considered to be straight.

However, the most robust, hence used, way to proceed is to use interaction integrals [Suquet, 2005; Gosz et al., 1998] since they involve surface integrals that are less sensitive to local fluctuation through averaging effects:

$$K_p = \frac{E'}{2}\int_\Omega \left(\sigma_{ij}u^p_{j,k}\theta_{k,i} + \sigma^p_{ij}u_{j,k}\theta_{k,i} - \sigma_{ij}u^p_{i,j}\theta_{k,k}\right)\mathrm{d}\Omega \tag{5.22}$$

herein $u^p_i = \frac{1}{4\mu}\sqrt{\frac{r}{2\pi}}\xi^p_i(\theta)$ (Eq. 5.12 for unit SIF) with ξ^p_i, $p = I, II$ defined in Eq. 5.13, σ^p_{ij} defined in Eq. 5.9 with $K_q = \delta_{pq}$ and $\vec{\theta}$ is any vector field filling the following conditions:

- it is equal to zero vector outside an external contour Γ_2,
- equal to $\vec{t}$ inside an internal contour Γ, where $\vec{t}$ is a unit tangent vector to the crack surface at the crack tip,
- with a continuous connection in between, that is parallel to the crack surface along this surface.

An example of such a field is given on Fig. 5.8.

An analoguous method, called G-theta exists to obtain $\mathcal{G}$ [Destuynder and Djaoua, 1981; Bui, 2006]:

$$\mathcal{G} = -\int_\Omega {}^T\mathbf{Grad}\left(\vec{\theta}\right) : \boldsymbol{E}\mathrm{d}\Omega = -\int_\Omega \theta_{i,j}E_{ij}\mathrm{d}S \tag{5.23}$$

where the Eshelby tensor is defined by:

$$E_{ij} \quad = w\delta_{ij} - \xi_{k,i}\sigma_{kj} \tag{5.24}$$

Be aware that $\mathbf{Grad}\left(\vec{\theta}\right)$ and $\boldsymbol{E}$ are not symmetrical in general.

5.2.3 Compliance formula for one parameter loading

Using the definition of $\mathcal{G}$ (Eq. 5.16), together with (i) Eq. 5.7, (ii) the fact that Boundary Conditions are given at each point of the boundary ($\partial\Omega = \partial\Omega_T \cup \partial\Omega_u \cup \partial\Omega_c$), (iii) $\vec{T}^{\,d} = \vec{0}$ on $\partial\Omega_c$ and (iv) that the load is supposed to be constant in the definition of $\mathcal{G}$ that is $\dfrac{\partial\vec{T}^{\,d}}{\partial\ell} = \dfrac{\partial\vec{u}^{\,d}}{\partial\ell} = 0$, one gets successively:

$$\begin{aligned}\mathcal{G} = &\quad \frac{1}{2}\int_{\partial\Omega_T}\vec{T^d}.\frac{\partial\vec{u}}{\partial\ell} - \frac{1}{2}\int_{\partial\Omega_u}\frac{\partial\vec{T}}{\partial\ell}.\vec{u}^d\mathrm{d}S\\ = &\quad \frac{1}{2}\int_{\partial\Omega}\left(\vec{T}.\frac{\partial\vec{u}}{\partial\ell} - \frac{\partial\vec{T}}{\partial\ell}.\vec{u}\right)\mathrm{d}S.\end{aligned} \tag{5.25}$$

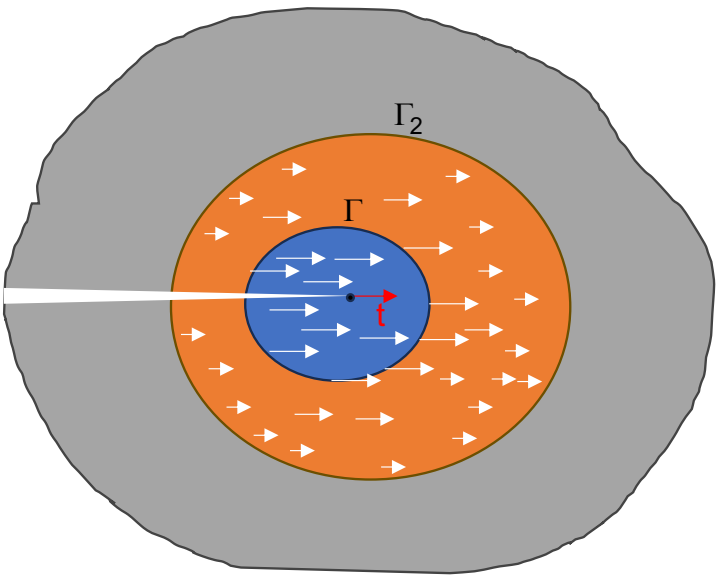

FIGURE 5.8: Example of $\vec{\theta}$ (white arrows) field used in the interaction integrals and the G-theta method.

Suppose now that we deal with a 2D BVP problem with a single parameter loading as in section 5.1.2.3, either an imposed displacement q or the conjuguate force by unit thickness Q, both being linked by $W_{ext} = Qq$ where W_{ext} is the total work of external forces by unit thickness defined in Eq. 5.5. By linearity of the BVP, it is possible to define the rigidity/stiffness $R(\ell)$ and Softness/compliance $S(\ell)$ of the sample, depending only on ℓ by:

$$Q = R(\ell)q \Leftrightarrow q = S(\ell)Q \text{ with } R = S^{-1} \tag{5.26}$$

Notice that in 2D, W_{ext} is in J/m=N, Q in N/m and q in m, so that the SI unit of R is Pa and R is in Pa^{-1}.

Using the same ingredients than above, we get

$$\mathcal{G} = \tfrac{1}{2}\left(Q.\frac{\partial q}{\partial \ell} - \frac{\partial Q}{\partial \ell}.q\right) \tag{5.27}$$

$$= -\frac{1}{2}q^2\frac{\mathrm{d}R}{\mathrm{d}\ell} \qquad \text{Stiffness formula} \tag{5.28}$$

$$= \frac{1}{2}Q^2\frac{\mathrm{d}C}{\mathrm{d}\ell} \qquad \text{Compliance formula} \tag{5.29}$$

As the rigidity of the sample decreases and the compliance increases with the crack length, $\frac{\mathrm{d}R}{\mathrm{d}\ell} < 0$ and $\frac{\mathrm{d}C}{\mathrm{d}\ell} > 0$ so that we retrieve that $\mathcal{G} > 0$. An example of application will be given in section 5.3.2.

5.2.4 Expansion of the SIF for a small kinked crack increment

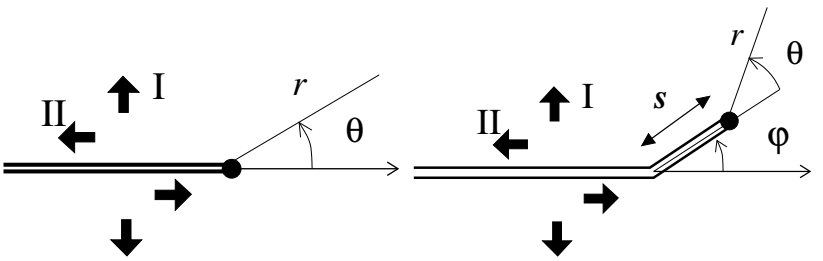

FIGURE 5.9: Crack with kinked extension in the initial (left) and final (right) configurations

Assume that the loading of the body is kept constant between the two configurations of Fig 5.9 (same configurations with or without a kinked portion of length l in the direction φ). Denote K_p the SIF before the kink, and $K_p(l,\varphi)$ the SIF defined in the same manner (that is by Eq. 5.9) taking the new tip and crack direction as references for the polar parameters (Fig 5.9).

Introduce the limit $K_p^*(\varphi)$ for $l \to 0$:

$$K_p^*(\varphi) = \lim_{l\to 0} K_p(l,\varphi) \tag{5.30}$$

J.B. Leblond (1989) has shown that:

$$K_p^*(\varphi) = F_{pq}(\varphi) K_q \tag{5.31}$$

where the functions $F_{pq}(\varphi)$ are universal functions (in the sense that they are independent of the BVP), depending on the sole value of φ. This means that knowing the values of K_q before the kink, $K_p^*(\varphi)$ can be obtained after the kink without the need to solve the entire elasticity problem. This remarkable result is valid whatever the considered BVP, for isotropic and anistropic materials [Leguillon, 1993], in 2D and 3D situations [Leblond, 1999; Leblond et al., 1999; Lazarus et al., 2001]. However, the value of $F_{pq}(\varphi)$ differs.

For an anisotropic material, they have not been determined yet, to the best of our knowledge. In the case of isotropic elasticity, the values are provided in Amestoy and Leblond [Amestoy and Leblond, 1992] for any values of φ, either under the form of some integral equations coupled with Anderson's formula (equations $(34)_1$, $(35)_1$, (36), (39) of [Amestoy and Leblond, 1992]) or of a serie (equation (66) in [Amestoy and Leblond, 1992]). For $\varphi \ll 1$ (φ being expressed in radians), the first terms are:

$$\begin{array}{lll} F_{I,I} = 1 + O(\varphi^2) & F_{I,II} = -\frac{3\varphi}{2} + O(\varphi^3) & F_{I,III} = 0 \\ F_{II,I} = \frac{\varphi}{2} + O(\varphi^3) & F_{II,II} = 1 + O(\varphi^2) & F_{I,III} = 0 \end{array} \tag{5.32}$$

Note that despite the continuity of the displacement and stress fields when $l \to 0$, $K_p^*(\varphi)$ is discontinuous crossing the kink, that is $K_p^*(\varphi) \neq K_p$ if $\varphi \neq 0$. The fact that it is discontinuous can be understood by considering an initial mode I situation ($K_{II} = 0$): while the problem is symmetrical between the top and the bottom without a kink, the symmetry is broken as soon as a small extension appears so that $K_{II}^* \neq 0$ which is different from $K_{II} = 0$.

In the same manner, we can define:

$$\mathcal{G}^*(\varphi) = \lim_{l \to 0} \mathcal{G}(l, \varphi) \tag{5.33}$$

where $\mathcal{G}(l, \varphi)$ is the energy release rate corresponding to a kinked propagation in the direction φ of length l. Using Irwin's formula [Irwin, 1957], we get when restricting to $K_{III} = 0$:

$$\mathcal{G}^*(\varphi) = \frac{1-\nu^2}{E}\left(K_I^*(\varphi)^2 + K_{II}^*(\varphi)^2\right) = \frac{1-\nu^2}{E} F_{pq}(\varphi) F_{pr}(\varphi) K_q K_r \tag{5.34}$$

Equations 5.31 and 5.34 are useful to determine the propagation direction applying the criteria Max ERR and PLS introduced in section 5.1.2.4. Indeed:

- the PSL implies: $F_{II,I}(\varphi) K_I + F_{II,II}(\varphi) K_{II} = 0$
- the Max ERR implies: $\dfrac{\partial \mathcal{G}^*}{\partial \varphi} = 0 \quad \Rightarrow \quad F_{pq}(\varphi) F'_{pr}(\varphi) K_q K_r = 0$

Hence the knowledge of $F_{pq}(\varphi)$ permits to determine φ as a function of the SIF K_I, K_{II} before propagation, that is of the applied load via the BVP. This procedure can be repeated to obtained the quasistatic crack propagation path as a function of the applied load via the successive values taken by K_p.

Moreover as the propagation in this direction requires that the elastic energy release in this direction overcomes the fracture costs, Griffith's criterion has to be written on $\mathcal{G}^*(\varphi)$ and not on the initial ERR $\mathcal{G}$, before the presence of a kink. Eq. 5.34 permits to write it as a function of the initial values of the SIF K_p and put it into practice. It will be illustrated in section 5.3.1 on a particular geometry.

5.3 Examples of application

5.3.1 Crack embedded in a plate

5.3.1.1 SIF expression

As in the case of Fig 5.4, pull on a plate containing a crack of length 2ℓ inclined with an angle α (Fig 5.7). If the size of the crack is small in comparison to

the plate size, the SIF are given by :

$$K_I = \sigma(\cos^2\alpha)\sqrt{\pi\ell}, \quad K_{II} = \sigma\sin(\alpha)\cos(\alpha)\sqrt{\pi\ell}, \quad K_{III} = 0 \tag{5.35}$$

where σ denotes the stress applied remotely. For $\alpha = 0$, one retrieves the formula given in § 5.1.4. In this case, Griffith threshold (Eq. 5.19) or equivalently Irwin's one (Eq. 5.20), yields that no propagation occurs provided that $\sigma < \frac{K_{Ic}}{\sqrt{\pi\ell}}$.

5.3.1.2 Determination of the propagation direction

For $\alpha \neq 0$, the crack is loaded in mode I+II and the propagation direction can be obtained by one of the criteria given in section 5.1.2.4. Let us consider here for simplicity the PLS $K^*_{II}(\varphi) = 0$ and that $\alpha \ll 1$ (α in radians) so that $K_I = \sigma\sqrt{\pi\ell}(1 + O(\alpha^2))$ and $K_{II} = \alpha\sigma\sqrt{\pi\ell}(1 + O(\alpha^2))$. Using Eq. 5.32 and assuming that $\varphi = O(\alpha)$, then gives: $K^*_{II} = \sigma\sqrt{\pi\ell}(\frac{\varphi}{2} + \alpha + O(\alpha^3))$, so that:

$$\varphi = -2\alpha + O(\alpha^3) \tag{5.36}$$

which justifies our assumption.

5.3.1.3 Determination of the critical load at the onset of crack propagation

Griffith threshold criterion (Eq. 5.19) has to be applied on $\mathcal{G}^*(\varphi)$ to ensure that enough energy is available to propagate in the direction φ. This gives that the propagation threshold is:

$$\sigma_c = \sqrt{\frac{EG_c}{(1-\nu^2)\pi\ell}} + O(\alpha^2) = \frac{K_{Ic}}{\sqrt{\pi\ell}} + O(\alpha^2) \tag{5.37}$$

If α is not small, the awaited kink angle to get $K^*_{II} = 0$ becomes higher and some additional terms in the expansion of $F_{pq}(\varphi)$ or the exact values of $F_{pq}(\varphi)$ provided in [Amestoy and Leblond, 1992] shall be used. We have verified that the predictions obtained in this way are conform to Erdogan and Sih experiments [Erdogan and Sih, 1963].

When the crack becomes imperceptible $\ell \to 0$, Eq. 5.37 predicts that $\sigma_c \to \infty$ which is obviously in contraction with observations. The classical stress criterion $\sigma_c = \sigma_Y$, where σ_Y is the ultimate tensile stress, takes over to get the critical load. In practice, the cut-off length is given by writing $\sigma = \sigma_c$ together with $K_I = \sigma\sqrt{\pi\ell_c} = K_{Ic}$ which gives:

$$\ell_c = \left(\frac{K_{Ic}}{\sqrt{\pi}\sigma_Y}\right)^2 \tag{5.38}$$

which is also the typical size of the process zone mentioned in section 5.1.1.3: LEFM is valid provided that the sizes of the crack and of the domain are large enough in comparison to this value. The failure stress σ_c as a function of ℓ is sketched in Fig. 5.10.

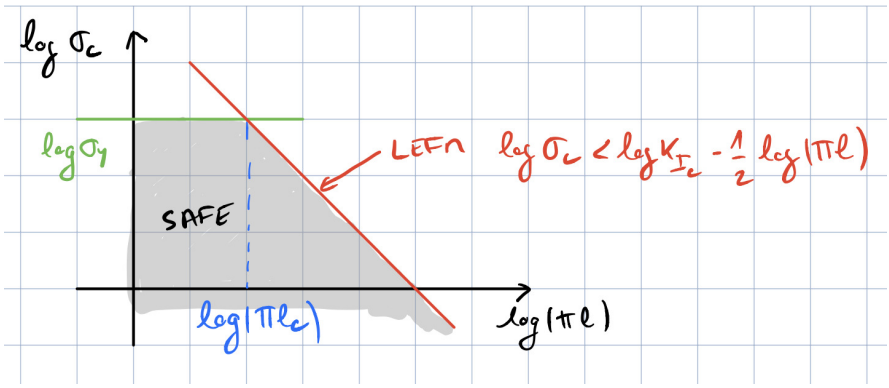

FIGURE 5.10: Sketch of the failure stress σ_c as a function of the crack size ℓ.

5.3.2 Propagation dynamics in a Double Cantilever Beam

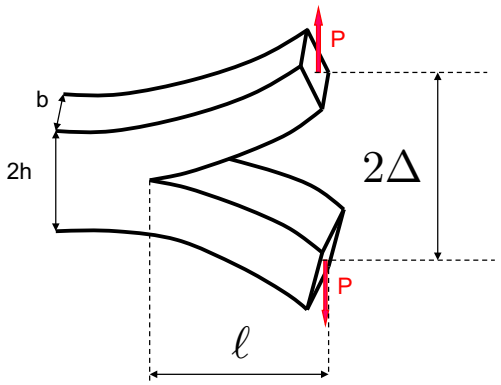

FIGURE 5.11: Double Cantilever Beam (DCB)

5.3.2.1 Determination of the ERR using compliance formula

Consider a Double Cantilever Beam (DCB) of height $2h$, thickness b containing a crack of length ℓ, loaded at the extremities by either a couple of opposite force of amplitude P, or displacement Δ (Fig 5.11). Suppose that $\ell \gg b \sim h$, then the potential energy $\mathcal{P}$ can be estimated thanks to two cantilever clamped beams of length ℓ. One has: $\Delta = 4\frac{P\ell^3}{Ebh^3}$ and $W_{ext} = 2P\Delta/b$. With the notations of section 5.2.3 and setting $Q = \frac{P}{b}$, $q = 2\Delta$ from which follows

that the compliance and the stiffness are given by:

$$S(\ell) \equiv R^{-1}(\ell) = \frac{8\ell^3}{Eh^3} \tag{5.39}$$

From there, one gets the ERR using the compliance formula (Eq. 5.29):

$$\mathcal{G} = \frac{12\ell^2 Q^2}{Eh^3} = \frac{3Eh^3 q^2}{16\ell^4} \tag{5.40}$$

that gives with the nominal notations P, Δ of the load:

$$\mathcal{G} = \frac{12\ell^2 P^2}{Eb^2 h^3} = \frac{3Eh^3 \Delta^2}{4\ell^4} \tag{5.41}$$

These last results can also be obtained directly by calculating the potential energy $\mathcal{P}$ of the set of two beams and deriving it with respect to ℓ for a fixed load.

5.3.2.2 Dynamics of crack propagation

Let us now look for the quasistatic evolution problem following Eq. 5.21. Suppose first that the load is applied by increasing the displacement ($t = \Delta$). The quasistatic evolution rules lead to two situations:

1. $\ell(t) = \ell_0$ as long as $\dot{\ell}(t) = 0 \Leftrightarrow \mathcal{G} < \mathcal{G}_c \Leftrightarrow t < t_c$ with

$$t_c = \Delta_c = \sqrt{\frac{4}{3}\mathcal{G}_c \frac{\ell_0^4}{Eh^3}} \tag{5.42}$$

2. $\ell(t)$ increases once $\dot{\ell}(t) > 0$ then $\mathcal{G} = \mathcal{G}_c$ so that:

$$\ell(t) = \ell_0 \sqrt{\frac{t}{t_c}} \tag{5.43}$$

Second, suppose that the load is applied by increasing the force $t = P$. The quasistatic evolution rules lead to two situations:

1. $\ell(t) = \ell_0$ as long as $\dot{\ell}(t) = 0 \Leftrightarrow \mathcal{G} < \mathcal{G}_c \Leftrightarrow t < t_c$ with

$$t_c = P_c = \sqrt{\frac{\mathcal{G}_c Eh^3 b^2}{12\ell_0^2}} \tag{5.44}$$

2. $\dot{\ell}(t) > 0$ then $\mathcal{G} = \mathcal{G}_c$ that implies $\ell(t) = \sqrt{\frac{\mathcal{G}_c Eh^3 b^2}{12t^2}}$ hence $\dot{\ell}(t) < 0$ in contradiction with $\dot{\ell}(t) > 0$. This means that quasistatic evolution is not possible above the threshold.

This implies that in this DCB setting, it is possible to control propagation applying increasing displacement but not increasing force.

5.3.2.3 Link between the stiffness of the sample and quasistatic propagation

Refering to section 5.1.2.3, this result is intimately related to the configuration of the problem and the sign of $\hat{\mathcal{G}}'(\ell)$ that is of $S''(\ell)$ and $R''(\ell)$ (Eq. 5.29, 5.28).

More generally, beyond the DCB example, we have that:

- It is possible to control the propagation under increasing displacement control q if and only if $R''(\ell) > 0$
- It is possible to control the propagation under increasing force control Q if and only if $S''(\ell) < 0$.

Using $R = 1/S$ and $S'(\ell) > 0$, it is straightforward to show that $S'' < 0$ implies $R'' > 0$, meaning that if the device is such as the propagation can be controlled in force, it can also be controlled in displacement. The reverse is not true however and the DCB is an example of such a setup.

5.3.2.4 Control by the crack length

As explained in section 5.1.2.3, it is also possible to look at the evolution of the load $t(\ell)$ that is required to obtain an increasing length ℓ. The quasistatic propagation rules give:

1. taking $t = q$, $-\frac{1}{2}q(\ell)^2 R'(\ell) = \mathcal{G}_c$ that is:

$$q(\ell) = \sqrt{-\frac{2\mathcal{G}_c}{R'(\ell)}} \tag{5.45}$$

   the sign of $q'(\ell)$ is equal to the sign of $R''(\ell)$
2. taking $t = Q$, $\frac{1}{2}Q(\ell)^2 S'(\ell) = \mathcal{G}_c$ that is:

$$Q(\ell) = \sqrt{\frac{2\mathcal{G}_c}{S'(\ell)}} \tag{5.46}$$

   the sign of $Q'(\ell)$ is equal to the sign of $-S''(\ell)$

This leads to three possible situations:

1. Hardening: if $S'' < 0$ (which implies $R'' > 0$), then $q' > 0$ and $Q' > 0$. The propagation can be controlled both in displacement and force control.
2. Softening: if $S'' > 0$ and $R'' > 0$, then $q' > 0$ and $Q' < 0$. The propagation can be controlled in displacement but not in force.
3. Snapback: if $R'' < 0$ (which implies $S'' > 0$), then $q' < 0$ and $Q' < 0$. The propagation can neither be controlled in displacement nor in force. It means that if the load is increased a dynamical propagation phase cannot be avoided.

For the DCB, we can easily check using Eq. 5.39, that $S'' > 0$ and $R'' > 0$ so that the configuration corresponds to the second case. Examples of other configurations corresponding to the three cases can be found in [Marigo, 2016].

5.4 Perturbed crack geometries

5.4.1 Why studying distorted/perturbed crack geometries?

Usually, the dangerousness of a crack is estimated using simplified smoothed-out geometries with planar crack faces and a regular front shape (circular, elliptical or straight in general). This raises several questions:

- are these shapes configurationally stable, in other words, what is the impact of small imperfections? Is there a risk that they amplify during propagation until the smoothed-out model becomes unrelevant or even leads to underestimation of a potential risk of catastrophic failure? Feedback from field experience, notably in aeronautics, shows that omitting small scale imperfections is efficient to avoid fatal breakdown. Use of the perturbation approaches has allowed to prove it for most engineering actual situations [Lazarus, 2011]. However, this will have to be confirmed for breakthrough materials and technologies, notably those planned to respond to the urgency of the ecological transition. For instance, the turbines envisaged in the CFM RISE project have a unprecedented size with 4 meters of diameter and an open air fan whose resistance to breakage must be guaranteed, in order that there is no risk of passengers being decapitated by a blade. Increase of the use of additive manufacturing comes also with a risk due to the inherent heterogeneities and anisotropy [Corre and Lazarus, 2021] introduced by the process and the directional printing process.
- the simplification leads to the introduction of safety coefficient to make up for our ignorance. Their overestimation while being necessary to ensure safety, has a not negligible ecological footprint. This raises the question of the possibility to find a safe tradeoff by taking into account more complexities: geometry, mixed mode load, heterogeneities, anisotropy.

After having introduced the principle of perturbation approaches (§5.4.2), we will illustrate how they can be used with these aims on two examples we have dealt with recently: crack propagation in presence of mode III (§5.4.3) and distorted crack shape in damage tolerance approaches (§5.4.4).

5.4.2 Perturbation approaches

To illustrate the idea of perturbation approaches, consider a planar crack embedded in an infinite body and loaded in mode I through some remote

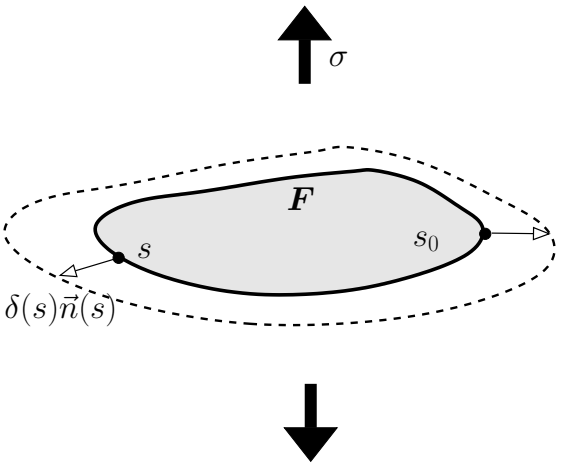

FIGURE 5.12: Planar crack loaded remotely by a remote tensile stress σ, perturbed by some coplanar propagation $\delta(s)\vec{n}(s)$.

tensile σ stress (Fig 5.12). Denote $K_I(s)$ the SIF factor at point s along the crack front, $D(s_0, s)$ the distance between two points of $\mathcal{F}$, $W(s_0, s)$ a kernel linked to the Bueckner [Bueckner, 1987] weight-functions, that is to the SIF at point s_0 when a unit doublet of point forces are applied in the vicinity of s [Lazarus, 2011].

Slightly perturbed the crack front in its plane moving each point by a small amount $\delta(s)\vec{n}(s)$ in the normal direction $\vec{n}(s)$ (Fig 5.12). To the first order in δ, the variation $\delta K_I(s_0)$ of the SIF at any point s_0 along the front is given by:

$$\delta K_I(s_0) \quad = \quad \frac{1}{2\pi}\ PV \int_{\mathcal{F}} \frac{W(s_0,s)}{D^2(s_0,s)} \cdot K(s)\,[\delta(s) - \delta(s_0)\vec{n}(s_0).\vec{n}(s)]\,\mathrm{d}s. \tag{5.47}$$

and the variation $\delta W(s_0, s_1)$ for any points s_0, s_1 of the front, by:

$$\delta W(s_0,s_1) = \frac{D^2(s_0,s_1)}{2\pi}\ PV \int_{\mathcal{F}} \frac{W(s_0,s)W(s_1,s)}{D^2(s_0,s)D^2(s_1,s)}[\delta(s) - \delta_{**}(s)]\mathrm{d}s. \tag{5.48}$$

where PV indicates that the integral are taken in the Principal Value sense, and $\delta_{**}(s)$ is a composition of a translation, a rotation and a homothetical transformation bringing s_0, s_1 to their final positions $s_0 + \delta(s_0)\vec{n}(s_0), s_1 + \delta(s_1)\vec{n}(s_1)$.

These formulas have been derived by Rice [Rice, 1989] for tensile remote loading. They have been extended to deal with shear remote load by Favier et al. [Favier et al., 2006]. They may be used to study analytically small distorsions of the crack front [Lazarus, 2011], for instance to verify if a given shape (straight or circular) is stable, that is remain keep its shape if slightly

perturbed (e.g. [Rice, 1985; Gao and Rice, 1987; Lazarus and Leblond, 2002]) or to study propagation in an heterogeneous media (e.g. [Vasoya et al., 2016; Lebihain et al., 2020, subm]). They may also be used iteratively to study numerically any large perturbations of the front (e.g. [Bower and Ortiz, 1990; Lazarus, 2003; David and Lazarus, 2022]). For the interested readers, more details about this approach initiated by Bueckner [Bueckner, 1987]-Rice[Rice, 1985] can be found in my review paper [Lazarus, 2011]. Analoguous formulas, although more complex exists for out of plane perturbations [Movchan et al., 1998; Leblond et al., 2011]. In the sequel I will illustrate on two examples how these perturbation approaches can help to meet the challenges drawn in section 5.4.1.

5.4.3 Crack propagation in presence of mode III

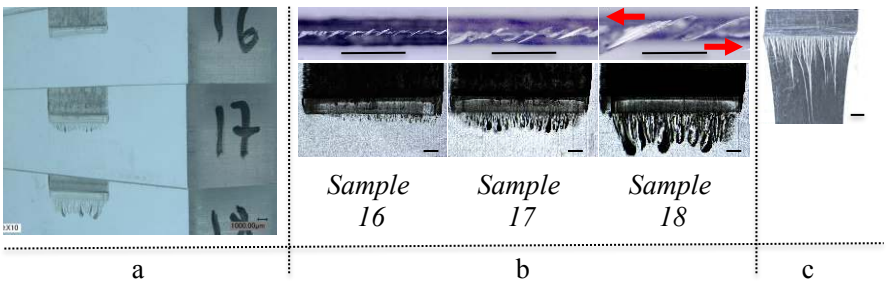

FIGURE 5.13: Facets/segments formation and coalescence as observed by transparency in fatigue bending experiments performed on PMMA [Chen et al., 2015; Cambonie et al., 2019; Lazarus et al., 2020; Hattali et al., 2021]. Columns a, b: In-situ pictures of the facets in three different samples (numbered 16, 17, 18) observed at increasing stages of the propagation outlining the facet apparition and further coalescence: (a) perspective view; (b) bottom (first row) and front views (second row). Column c: typical postmortem picture of the fracture facies; the black surface corresponds to the fracture surface left by the segments and the white lines to the ultimate fracture of the ligaments between them. The bar scales are all 1 mm.

The first is about crack propagation in presence of mode III. In this case, it is well-known [Sommer, 1969] that the propagation is not smooth but that segmentation/facetisation of the surface (Fig 5.13) usually appears. Using perturbation approach to get the variation of the SIF linked to the superposition of (i) a small in-plane wavy distorsion of the front, and (ii) a small out-of-plane wavy perturbation of the surface, we show that the trivial solution of straight propagation becomes unstable when K_{III}/K_I is larger than a threshold depending on ν [Leblond et al., 2011]. However this value appeared to be too

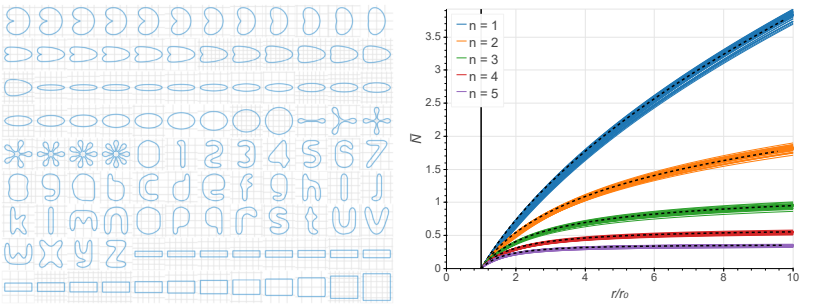

FIGURE 5.14: Left: Patchwork of the simulated shapes by the perturbation approach. Right: Evolution of the number of loading cycles with the evolution of the radius of a circular crack with the same surface area. Whatever the shape, this evolution is almost the same than for a circular crack. Therefore, a complex shape may safely be replaced by a circular crack of same area.

large in comparison with the experiments [Pham and Ravi-Chandar, 2014]. This could be explained performing calculations using phase-field method [Chen et al., 2015]: these calculations showed that (i) the instability is sub-critical, meaning that out-of-plane propagation may occur under the K_{III}/K_I threshold, being triggered by unavoidable defects, as observed in most of the experiments; (ii) the wavy perturbation grows to take the shape of facets observed experimentally. Once the facets have appeared, the crack propagation is ruled by the advance of their front. At these fronts, the SIF are lower than the ones of the initial front, due to the remaining ligaments between the facets. This induces an apparent toughening that can be quantified using a multiscale Cohesive Zone model [Leblond et al., 2015]. Comparison between this model and experiments leads to a good agreement [Hattali et al., 2021].

This example illustrates that taking into account the small scale distorsions induced by mode III using perturbation approach permits to obtain refined predictions of the fracture threshold in comparison to the ones corresponding to the smoothed out geometry.

5.4.4 Influence of distorted crack shape in damage tolerance approaches

Second example concerns damage tolerance approaches (section 5.1.4). To study the influence of distorted crack shape on lifetime prediction [David and Lazarus, 2022], we used an incremental version of the perturbation formulas (Eq. 5.47-5.48) to simulate the propagation of a huge number of crack shapes following Paris's law (Eq. 5.18). We showed that whatever the initial shape and the Paris coefficients C and n, (i) they all tend towards a circular shape, (ii) the evolution of the crack's surface area with the number of cycles is independent of the initial shape, (iii) using the surface as a measurement of crack size

yields more accurate lifetime assessments than taking the circumcircle as is done usually (Fig 5.14). Here again it illustrates that taking into account distorsion of the geometry permits to estimate accurately the induced increase of toughness.

5.5 Conclusion

Linear Elastic Fracture Mechanics is a comprehensive framework to determine when and how a crack propagates. The load applied to the structure is amplified in the vicinity of the crack tip by a stress concentration effect (Fig. 5.1). The Stress Intensity Factors and the Energy Release Rate quantify this amplification, hence are the reference quantities to determine the conditions of crack propagation. LEFM has shown its efficiency to reduce catastrophic failure of sensitive components, notably in aeronautics, thanks nevertheless to the application of safety margins. Their overestimation has a not negligible ecological footprint. This raises the question of the possibility to find a safe tradeoff by taking into account more complexities: geometry, mixed mode load, heterogeneities, anisotropy. Methods as perturbation approaches can be useful for this purpose.

Bibliography

[Amestoy and Leblond 1992] Amestoy, M. ; Leblond, J.-B.: Crack Paths in Plane Situations - II. Detailed Form of the Expansion of the Stress Intensity Factors. In: *International Journal of Solids and Structures* 29 (1992), p. 465–501

[Ashby 1989] Ashby, M.F.: Overview No. 80: On the engineering properties of materials. In: *Acta Metallurgica* 37 (1989), Nr. 5, p. 1273 – 1293. – 10.1016/0001-6160(89)90158-2

[Bazant and Estenssoro 1979] Bazant, Z.P. ; Estenssoro, L.F.: Surface singularity and crack propagation. In: *International Journal of Solids and Structures* 15 (1979), Nr. 5, p. 405–26. – 10.1016/0020-7683(79)90062-3

[Bourdin et al. 2008] Bourdin, B. ; Francfort, G. ; Marigo, J.-J.: The Variational Approach to Fracture. In: *Journal of elasticity* 91 (2008), Nr. 1, p. 5 – 148. – http://dx.doi.org/10.1007/s10659-007-9107-3

[Bower and Ortiz 1990] Bower, A.F. ; Ortiz, M.: Solution of Three-

Dimensional Crack Problems by a Finite Perturbation Method. In: *Journal of the Mechanics and Physics of Solids* 38 (1990), Nr. 4, p. 443–480

[Bueckner 1987] Bueckner, H.F.: Weight functions and fundamental fields for the penny-shaped and the half-plane crack in three-space. In: *International Journal of Solids and Structures* 23 (1987), Nr. 1, p. 57–93

[Bui 2006] Bui, H.D.: Fracture mechanics: inverse problems and solutions. Version: 2006. In: *Solid Mechanics and Its Applications* Bd. 139. Springer Dordrecht, 2006. – doi.org/10.1007/978-1-4020-4837-1

[Cambonie et al. 2019] Cambonie, T. ; Klinger, Y. ; Lazarus, V.: Similarities between mode III crack growth patterns and strike-slip faults. In: *Philosophical Transactions of the Royal Society of London A: Mathematical, Physical and Engineering Sciences* 377 (2019), Nr. 2136. – 10.1098/rsta.2017.0392 . – ISSN 1364–503X

[Chen et al. 2015] Chen, C.-H. ; Cambonie, T. ; Lazarus, V. ; Nicoli, M. ; Pons, A. J. ; Karma, A.: Crack Front Segmentation and Facet Coarsening in Mixed-Mode Fracture. In: *Physical Review Letters* 115 (2015), Nr. 26, p. 265503. – 10.1103/PhysRevLett.115.265503

[Corre et al. In p] Corre, T. ; Hild, F. ; Lazarus, V.: Determination of the Stress Intensity Factors around angular crack paths by Digital Image Correlation. (In preparation)

[Corre and Lazarus 2021] Corre, T. ; Lazarus, V.: Kinked crack paths in polycarbonate samples printed by fused deposition modelling using criss-cross patterns. In: *International Journal of Fracture* 230 (2021), Juli, Nr. 1, p. 19–31. – 10.1007/s10704-021-00518-x . – ISSN 1573–2673

[Cotterell and Rice 1980] Cotterell, B. ; Rice, J.R.: Slightly curved or kinked cracks. In: *International Journal of Fracture* 16 (1980), Nr. 2, p. 155–169

[David and Lazarus 2022] David, L. ; Lazarus, V.: On the key role of crack surface area on the lifetime of arbitrarily shaped flat cracks. In: *International Journal of Fatigue* 154 (2022), p. 106512. – 10.1016/j.ijfatigue.2021.106512 . – ISSN 0142–1123

[Destuynder and Djaoua 1981] Destuynder ; Djaoua: Sur une Interprétation Mathématique de l'Intégrale de Rice en Théorie de la Rupture Fragile. In: *Mathematical Methods in the Applied Sciences* 3 (1981), Nr. 1, p. 70–87. – 10.1002/mma.1670030106 . – ISSN 1099–1476

[Doitrand et al. subm] Doitrand, A. ; Leguillon, D. ; Molnar, G. ; Lazarus, V.: Revisiting crack front segmentation under mixed mode I+III loading with T-stress and mode-dependent fracture properties. In: *International Journal of Fracture* (submitted)

[Erdogan and Paris 1963] Erdogan, G. ; Paris, P.: A critical analysis of crack propagation laws. In: *ASME J. Basic Engng Trans.* 85 (1963), p. 528–534

[Erdogan and Sih 1963] Erdogan, G. ; Sih, G.C.: On the crack extension in plates under plane loading and transverse shear. In: *ASME J. Basic Engng* 85 (1963), p. 519–527

[Favier et al. 2006] Favier, E. ; Lazarus, V. ; Leblond, J.-B.: Coplanar propagation paths of 3D cracks in infinite bodies loaded in shear. In: *International Journal of Solids and Structures* 43 (2006), Nr. 7-8, p. 2091–2109. – 10.1016/j.ijsolstr.2005.06.041

[Francfort and Marigo 1998] Francfort, G.A. ; Marigo, J.J.: Revisiting brittle fracture as an energy minimization problem. In: *Journal of the Mechanics and Physics of Solids* 46 (1998), p. 1319–1342. – 10.1016/S0022-5096(98)00034-9

[Freund 1998] Freund, L.B. ; Batchelor, G. K. (Hrsg.) ; Wunsch, C. (Hrsg.) ; Rice, J. (Hrsg.): *Dynamic fracture mechanics.* Cambridge University press, 1998

[Gao and Rice 1987] Gao, H. ; Rice, J.R.: Somewhat circular tensile cracks. In: *International Journal of Fracture* 33 (1987), Nr. 3, p. 155–174

[Goldstein and Salganik 1974] Goldstein, R.V. ; Salganik, R.L.: Brittle Fracture of Solids with Arbitrary Cracks. In: *International Journal of Fracture* 10 (1974), p. 507–523

[Gosz et al. 1998] Gosz, M. ; Dolbow, J. ; Moran, B.: Domain integral formulation for stress intensity factor computation along curved three-dimensional interface cracks. In: *International Journal of Solids and Structures* 35 (1998), Nr. 15, p. 1763–1783. – https://doi.org/10.1016/S0020-7683(97)00132-7 . – ISSN 0020–7683

[Griffith 1920] Griffith, A.A.: The phenomena of rupture and flow in solids. In: *Philosophical Transactions of the Royal Society of London* 221 (1920), p. 163–198

[Hattali et al. 2021] Hattali, M.L. ; Cambonie, T. ; Lazarus, V.: Toughening induced by the formation of facets in mode I+III brittle fracture: Experiments versus a two-scale Cohesive Zone model. In: *Journal of the Mechanics and Physics of Solids* 156 (2021), p. 104596. – 10.1016/j.jmps.2021.104596 . – ISSN 0022–5096

[Ibarra et al. 2016] Ibarra, A. ; Roman, B. ; Melo, F.: The tearing path in a thin anisotropic sheet from two pulling points: Wulff's view. In: *Soft Matter* 12 (2016), p. 5979–5985. – 10.1039/C6SM00734A

[Irwin 1957] Irwin, G.R.: Analysis of stresses and strains near the end of a crack traversing a plate. In: *Journal of Applied Mechanics* 24 (1957), p. 361–364

[Irwin 1958] Irwin, G.R.: *Fracture. Hand. der Physik*. Bd. IV. Springer, Berlin, 1958

[Lazarus 1997] Lazarus, V.: *Quelques problèmes tridimensionnels de mécanique de la rupture fragile*, UPMC Univ Paris 6, Diss., 1997

[Lazarus 2003] Lazarus, V.: Brittle Fracture and Fatigue Propagation Paths of 3D Plane Cracks under Uniform Remote Tensile Loading. In: *International Journal of Fracture* 122 (2003), Nr. 1-2, p. 23–46. – 10.1023/B:FRAC.0000005373.73286.5d

[Lazarus 2011] Lazarus, V.: Perturbation approaches of a planar crack in Linear Elastic Fracture Mechanics: a review. In: *Journal of the Mechanics and Physics of Solids* 59 (2011), Nr. 2, p. 121–144. – 10.1016/j.jmps.2010.12.006

[Lazarus and Leblond 2002] Lazarus, V. ; Leblond, J.-B.: Crack front stability for a tunnel-crack propagating along its plane in mode 2+3. In: *Comptes Rendus de l'Académie des Sciences Paris, Serie II (Mecanique, Physique, Astronomie)* 330 (2002), Nr. 6, p. 437–443. – 10.1016/S1631-0721(02)01481-X

[Lazarus et al. 2001] Lazarus, V. ; Leblond, J.-B. ; Mouchrif, S.-E.: Crack Front Rotation and Segmentation in Mixed Mode I+III or I+II+III - Part I: Calculation of Stress Intensity Factor. In: *Journal of the Mechanics and Physics of Solids* 49 (2001), Nr. 7, p. 1399–1420. – 10.1016/S0022-5096(01)00007-2

[Lazarus et al. 2020] Lazarus, V. ; Prabel, B. ; Cambonie, T. ; Leblond, J.B.: Mode I+III multiscale cohesive zone model with facet coarsening and overlap: Solutions and applications to facet orientation and toughening. In: *Journal of the Mechanics and Physics of Solids* 141 (2020), p. 104007. – https://doi.org/10.1016/j.jmps.2020.104007 . – ISSN 0022–5096

[Lebihain et al. 2020] Lebihain, M. ; Leblond, J.-B. ; Ponson, L.: Effective toughness of periodic heterogeneous materials: the effect of out-of-plane excursions of cracks. In: *Journal of the Mechanics and Physics of Solids* 137 (2020), p. 103876. – https://doi.org/10.1016/j.jmps.2020.103876 . – ISSN 0022–5096

[Lebihain et al. 2022] Lebihain, M. ; Leblond, J.-B. ; Ponson, L.: Crack front instability in mixed-mode I+III: The influence of non-singular stresses. In: *European Journal of Mechanics - A/Solids* (2022), p. 104602. – https://doi.org/10.1016/j.euromechsol.2022.104602 . – ISSN 0997–7538

[Lebihain et al. subm] Lebihain, M. ; Vasoya, M. ; Lazarus, V.: Size effects in the toughening of brittle materials by heterogeneities: a non-linear analysis of front deformations. In: *International Journal of Solids and Structures* (submitted)

[Leblond 1989] Leblond, J.-B.: Crack Paths in Plane Situations - I. General Form of the Expansion of the Stress Intensity Factors. In: *International Journal of Solids and Structures* 25 (1989), p. 1311–1325

[Leblond 1999] Leblond, J.-B.: Crack paths in three-dimensional elastic solids. i: two-term expansion of the stress intensity factors–application to crack path stability in hydraulic fracturing. In: *International Journal of Solids and Structures* 36 (1999), Nr. 1, p. 79 – 103. – 10.1016/S0020-7683(97)00276-X

[Leblond 2003] Leblond, J.-B. ; Lavoisier (Hrsg.): *Mécanique de la rupture fragile et ductile*. Hermès sciences, 2003

[Leblond et al. 2015] Leblond, J.-B. ; Lazarus, V. ; Karma, A.: Multiscale cohesive zone model for propagation of segmented crack fronts in mode I+III fracture. In: *International Journal of Fracture (Special Invited Article Celebrating IJF at 50)* 191 (2015), February, Nr. 1, p. 167–189. – 10.1007/s10704-015-0001-x

[Leblond et al. 1999] Leblond, J.-B. ; Lazarus, V. ; Mouchrif, S.-E.: Crack paths in three-dimensional elastic solids. II. Three-term expansion of the stress intensity factors - Applications and perspectives. In: *International Journal of Solids and Structures* 36 (1999), Nr. 1, p. 105–142. – 10.1016/S0020-7683(97)00271-0

[Leblond et al. 2011] Leblond, J.B. ; Karma, A. ; Lazarus, V.: Theoretical analysis of crack front instability in mode I+III. In: *Journal of the Mechanics and Physics of Solids* 59 (2011), p. 1872–1887. – 10.1016/j.jmps.2011.05.011

[Leguillon 1993] Leguillon, D.: Asymptotic and numerical analysis of crack branching in non-isotropic materials. In: *European Journal of Mechanics A/Solids* 12 (1993), p. 33–51

[Marder 2009] Marder, M.: *Physics of fracture*. 2009

[Marigo 2016] Marigo, J.-J.: *Plasticité et Rupture*. Version: September 2016. `https://hal.science/cel-01374813`. – Lecture

[Mesgarnejad et al. 2020] Mesgarnejad, A. ; Pan, C. ; Erb, R.M. ; Shefelbine, S.J. ; Karma, A.: Crack path selection in orientationally ordered composites. In: *Physical Review E* 102 (2020), Nr. 1, p. 013004

[Movchan et al. 1998] Movchan, A.B. ; Gao, H. ; Willis, J.R.: On perturbations of plane cracks. In: *International Journal of Solids and Structures* 35 (1998), Nr. 26-27, p. 3419–3453

[Muskhelishvili 1953] Muskhelishvili, N.I.: *Some Basic Problems of the Mathematical Theory of Elasticity*. Noordhoff, Groningen, 1953

[Pham and Ravi-Chandar 2014] Pham, K.H. ; Ravi-Chandar, K.: Further examination of the criterion for crack initiation under mixed-mode I+III loading. In: *International Journal of Fracture* 189 (2014), Nr. 2, p. 121–138. – 10.1007/s10704-014-9966-0

[Rice 1968] Rice, J.R.: A Path Independent Integral and the Approximate Analysis of Strain Concentration by Notches and Cracks. In: *Journal of Applied Mechanics* 35 (1968), p. 379–386

[Rice 1985] Rice, J.R.: First-Order Variation in Elastic Fields Due to Variation in Location of a Planar Crack Front. In: *ASME Journal of Applied Mechanics* 52 (1985), Nr. 3, p. 571–579

[Rice 1989] Rice, J.R.: Weight Function Theory for Three-Dimensional Elastic Crack Analysis. In: Wei, R. P. (Hrsg.) ; Gangloff, R. P. (Hrsg.) ; American Society for Testing and Materials STP 1020 (Veranst.): *Fracture Mechanics : Perspectives and Directions (Twentieth Symposium)*. Philadelphia, USA, 1989, p. 29–57

[Shaikeea et al. 2022] Shaikeea, A.J.D. ; Cui, H. ; O'Masta, M. ; Zheng, X.R. ; Deshpande, V.S.: The toughness of mechanical metamaterials. In: *Nature Materials* 21 (2022), März, Nr. 3, p. 297–304. – 10.1038/s41563-021-01182-1 . – ISSN 1476–4660

[Sommer 1969] Sommer, E.: Formation of fracture 'lances' in glass. In: *Engineering Fracture Mechanics* 1 (1969), p. 539–546

[Suquet 2005] Suquet, P.: *Rupture et plasticité*. ENSTA/X, 2005. `http://perso.ensta-paristech.fr/~mbonnet/mec551/mec551.pdf`

[Tada et al. 2000] Tada, H. ; Paris, P.C. ; Irwin, G.R. ; Mechanical Engineers, The American S. (Hrsg.): *The Stress Analysis of Cracks Handbook*. Professional Engineering Publishing, 2000

[Triclot et al. 2023] Triclot, J. ; Corre, T. ; Gravouil, A. ; Lazarus, V.: Key role of boundary conditions for the 2D modeling of crack propagation in linear elastic Compact Tension tests. In: *Engineering Fracture Mechanics* 277 (2023), p. 109012. – 10.1016/j.engfracmech.2022.109012 . – ISSN 0013–7944

[Vasoya et al. 2016] Vasoya, M. ; Lazarus, V. ; Ponson, L.: Bridging micro to macroscale fracture properties in highly heterogeneous brittle solids: weak

pinning versus fingering. In: *Journal of the Mechanics and Physics of Solids* 95 (2016), p. 755–773. – http://dx.doi.org/10.1016/j.jmps.2016.04.022 . – ISSN 0022–5096

[Wegst and Ashby 2004] Wegst, U.G.K. ; Ashby, M.F.: The mechanical efficiency of natural materials. In: *Philosophical Magazine* 84 (2004), Nr. 21, p. 2167–2181. – 10.1080/14786430410001680935

[Williams 1952] Williams, M.L.: Stress Singularities Resulting from Various Boundary Conditions in Angular Corners of Plates in Extension. In: *Journal of Applied Mechanics* 19 (1952), p. 526

6

Global approach to fracture

Jacques Besson

Centre des Matériaux — CNRS UMR 7633 — Mines Paris PSL

The global approach to fracture allows the evaluation of the fracture properties of materials. It is based on a macroscopic evaluation of the fracture energy without trying to finely describe the physical damage processes. The methodology was initially developed to describe the brittle fracture of elastic materials. It was then extended to elastoplastic materials using the analogy between a nonlinear elastic material and a plastic material.

6.1 Introduction

The assessment of the mechanical integrity of structures that may contain cracks must be performed to ensure safety. Cracks can be detected using non-destructive techniques (NDT) such as ultrasonic testing, radiography, and visual inspection. It is often required to assume that a crack having a size smaller than the size that can be detected using NDT exists. Cracks may appear during material processing and during the manufacturing of structures. In-service loading such as fatigue and/or corrosion may also lead to crack initiation and propagation.

The so-called "global" approach to fracture may be used for the safety assessment of cracked structures. It has been developed extensively over the last decades and it is nowadays largely applied. The first section (6.2) presents the foundations of the approach in cases where plasticity is limited so that the overall behavior of the structure remains elastic. This corresponds to Linear Elastic Fracture Mechanics (LEFM). Cases, where the overall behavior is non-linear, are discussed in section 6.3. This corresponds to Non Linear Fracture Mechanics (NLFM).

Both LEFM and NLFM lead to the definition of parameters characterizing the loading at the crack tip: K_I, T, J, Q (these parameters are described below). As these parameters cannot be directly measured; they must be evaluated using techniques described in section 6.4.

Analysis of crack tip loading often assumes plane stress and plane strain

states. These hypotheses are compared with 3D simulations in the case of a CT specimen in section 6.5.

Section 6.6 describes the standardized experimental procedure used to evaluate critical values for K_I and J as well as the ductile crack growth resistance curves (J—Δa curves).

The limitations of the approach are outlined in section 6.7. In particular, the fact that these values are not material constants is evidenced.

The text will often mention test specimens such as Compact Tension (CT), Single Edge Notch Bend (SENB) or Single Edge Notch Tension (SENT) specimens. These specimens are illustrated in fig. 6.1.

CT SENT SENB

FIGURE 6.1: Examples of commonly used test specimens.

6.2 Linear fracture mechanics

Linear fracture mechanics deals with cracks in an elastic material and can be applied to cases where plastic deformation is limited to the crack tip. In that case, the overall behavior of the specimen/structure remains linear. This is, for instance, the case of ferritic steels tested at low temperatures. In the following, mode I loading (*i.e.* the loading direction is normal to the crack plane) will only be considered. Only isotropic materials are considered.

6.2.1 Stress intensity factor: crack tip stress and displacement fields

The first solution to determine stresses, strains and displacements in the vicinity of a crack tip was proposed by Williams [Williams, 1957] using complex Airy's functions. The geometry of the crack is provided in fig. 6.2. The position of a material point is given by cylindrical coordinates $(r,\, \theta)$; the origin is the crack tip. In the case of plane strain conditions, stresses are given by:

$$\sigma_{xx} = \frac{K_I}{\sqrt{2\pi r}} \cos\frac{\theta}{2}\left(1 - \sin\frac{\theta}{2}\sin\frac{3\theta}{2}\right) \tag{6.1}$$

$$\sigma_{yy} = \frac{K_I}{\sqrt{2\pi r}} \cos\frac{\theta}{2}\left(1 + \sin\frac{\theta}{2}\sin\frac{3\theta}{2}\right) \tag{6.2}$$

$$\sigma_{xy} = \frac{K_I}{\sqrt{2\pi r}} \cos\frac{\theta}{2}\sin\frac{\theta}{2}\cos\frac{3\theta}{2} \tag{6.3}$$

$$\sigma_{zz} = \nu(\sigma_{xx} + \sigma_{yy}) \tag{6.4}$$

ν is the Poisson's ratio. The plane stress case is obtained by taking $\nu = 0$. The plane strain direction corresponds to the direction of the crack front (see fig. 6.2). Displacements are given by for plane strains:

$$u_x = \frac{K_I}{2\mu}\sqrt{\frac{r}{2\pi}} \cos\frac{\theta}{2}\left(2 - 4\nu + 2\sin^2\frac{\theta}{2}\right) \tag{6.5}$$

$$u_y = \frac{K_I}{2\mu}\sqrt{\frac{r}{2\pi}} \sin\frac{\theta}{2}\left(4 - 4\nu - 2\cos^2\frac{\theta}{2}\right) \tag{6.6}$$

$$u_z = 0 \tag{6.7}$$

where μ is the shear modulus. In the above equations, K_I, referred to as the stress intensity factor, is a parameter depending on the crack length and loading.

Several remarks can be done relative to the previous sets of equations. (i) Stresses tend to ∞ very close to the crack tip. (ii) The equations are Taylor expansions only valid near the crack tip.

6.2.2 Energy release rate G

Consider an elastic structure containing a crack of length a. The structure has a stiffness k which is a function of a. A displacement u is applied to the structure so that the force is equal to $F = ku$. If the crack grows by a small amount da, the stiffness decreases. For a fixed displacement, crack advance releases energy equal to $GBda$ where G is the energy release rate (see fig. 6.3). Considering the gray area in fig. 6.3, G can be evaluated as:

$$GBda = \frac{1}{2}k(a)u^2 - \frac{1}{2}k(a+da)u^2 = -\frac{1}{2}\frac{k}{a}u^2 da \tag{6.8}$$

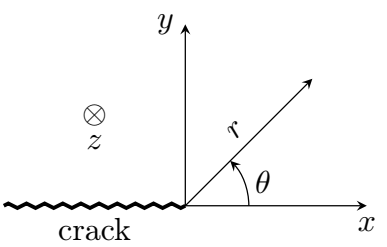

FIGURE 6.2: Description of the crack tip. ⊗ shows the plane strain direction which is along the z-direction.

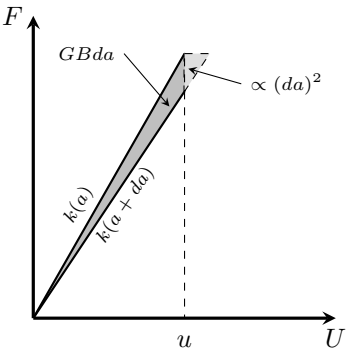

FIGURE 6.3: Energy release rate in a linear elastic structure

so that:

$$G = -\frac{1}{2B}\frac{k}{a}u^2 = -\frac{1}{2B}\frac{1}{k^2}\frac{k}{a}F^2. \tag{6.9}$$

Note that $k' = dk/da < 0$ as the stiffness of a structure decreases as the crack length increases. The same result is obtained assuming a constant force is obtained as the released energy is only increased by an amount which scales as $(da)^2$ (light gray area in fig. 6.3).

A link can be established between G and K_I. For a crack advance Δa the opening stress (σ_{yy}) (eq. 6.2) drops to 0 over a distance Δa whereas the cracks opens over the same distance following eq. 6.6. The resulting work is given by:

$$\begin{aligned}
\Delta W = G\Delta a &= B\int_0^{\Delta a} \sigma_{yy}^{\theta=0}(x)u_y^{\theta=\pi}(\Delta a - x)dx && (6.10)\\
&= \int_0^{\Delta a} \frac{K_I}{\sqrt{2\pi x}}\frac{K_I}{2\mu}\sqrt{\frac{\Delta a - x}{2\pi}}4(1-\nu)dx && (6.11)\\
&= \frac{2}{\pi}\frac{K_I^2}{E'}\int_0^{\Delta a}\sqrt{\frac{\Delta a - x}{x}}dx && (6.12)
\end{aligned}$$

Noting that the integral in the previous equation is $\frac{\pi}{2}\Delta a$, one gets Irwin's formula:

$$G = \frac{K_I^2}{E'} \tag{6.13}$$

where E' is the reduced Young's modulus: $E' = E/(1-\nu^2)$ (E: Young's modulus).

It then becomes possible to establish a link between K_I and the stiffness of the structure or test specimen. As stresses and, therefore K_I depend linearly on the applied load, one may assume that K_I can be expressed as:

$$K_I = \frac{1}{B\sqrt{W}}f_K(a/w)F \tag{6.14}$$

where W is a characteristic length of the structure (*e.g.* the width in a CT specimen). f_K is a function depending on the structure. Using eq. 6.9 together with Irwin's formula, one gets:

$$f_K = \sqrt{-\frac{1}{2}\frac{k'}{k^2}E'BW} = \sqrt{\frac{1}{2}c'E'BW} \tag{6.15}$$

where $c = 1/k$ is the compliance of the structure.

6.2.3 Plastic zone size and Irwin's correction

The von Mises stress can be evaluated using eqs 6.1 to 6.3 as:

$$\sigma_{\text{eq}} = \frac{K_I}{\sqrt{2\pi r}}\sqrt{4\nu^2 - 4\nu - \frac{3}{2}\cos(\theta) + \frac{5}{2}}\left|\cos\left(\frac{\theta}{2}\right)\right| = \frac{K_I}{\sqrt{2\pi r}}F_{\text{eq}}(\theta,\nu). \tag{6.16}$$

The limit between the elastic and plastic regions is then determined by solving $\sigma_{\text{eq}} = \sigma_0$ where σ_0 is the yield stress of the material (one assumes here perfect plasticity). This leads to the following expression for the radius at which the material is elastic:

$$r_p(\theta) = \frac{1}{2\pi}\left(\frac{K_I}{\sigma_0}\right)^2 F_{\text{eq}}^2(\theta,\nu) = r_y F_{\text{eq}}(\theta,\nu) \tag{6.17}$$

In the plane stress case ($\nu = 0$), the plastic zone size ahead of the crack ($\theta = 0$) is $r_p = r_y$ with:

$$r_y = \frac{1}{2\pi}\left(\frac{K_I}{\sigma_0}\right)^2.$$

For plane strain for the incompressible limit case mimicking plasticity ($\nu \to 1/2$), one gets $r_p = 0$. The limit between the plastic and elastic domains are displayed in fig. 6.4.

The overly simplistic above analysis neglects that stresses are changed due to plasticity and are redistributed to satisfy equilibrium. In the case of plane stresses, one assumes that the opening stress is equal to σ_0 over an unknown distance R_p. For $r > R_p$, the stress field is assumed to obey eq. 6.2 where the position of the crack tip is also unknown. These hypotheses lead to the following set of equations (where x is the position of the "virtual" crack tip with respect to R):

$$\text{equilibrium} \qquad \int_0^\infty \frac{K_I}{\sqrt{2\pi r}}\,dr = \int_0^{R_p}\sigma_0 dr + \int_{R_p}^\infty \frac{K_I}{\sqrt{2\pi(r+x)}}dr \tag{6.18}$$

$$\text{continuity} \qquad \frac{K_I}{\sqrt{2\pi(R_p+x)}} = \sigma_0 \tag{6.19}$$

One therefore assumes that the opening stress (σ_{yy}) for $0 \leq x <\leq R_p$ is equal

to the yield stress σ_0 which is consistent with the plane stress hypothesis. The solution is: $R_p = 2r_y$ and $x = -r_y$ where r_y is given in eq. 6.17. One notes that the R_p is twice as large as the uncorrected radius, *i.e.*:

$$R_p^{P\sigma} = \frac{1}{\pi}\left(\frac{K_I}{\sigma_0}\right)^2$$

The plane strain case can be treated following the same lines. One assumes that the opening stress σ_{yy} is equal to $\alpha\sigma_0$ is the plastic zone, where $\alpha > 1$ is referred to as the plasticity constraint factor. The opening stress can exceed σ_0 due to the highly triaxial stress state in the vicinity of the crack tip. One usually assumes that $\alpha = 3$ for highly constrained plane strain cases. This would imply that the plastic zone size is reduced by a factor of 9 ($= \alpha^2$) compared to the plane stress case. In a practical case, the plane strain state does not exist at the crack tip surface and the high constraint factor is only reached ahead of the blunted crack. It is generally accepted [Broek, 1982] that the plastic zone size is only 3 times smaller than in the plane stress case, *i.e.*:

$$R_p^{P\varepsilon} = \frac{1}{3\pi}\left(\frac{K_I}{\sigma_0}\right)^2$$

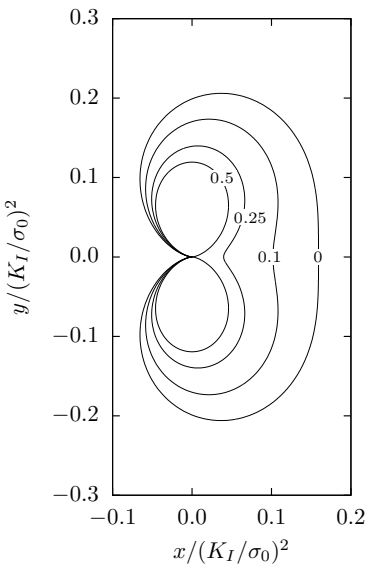

FIGURE 6.4: Plastic zone for different values of ν

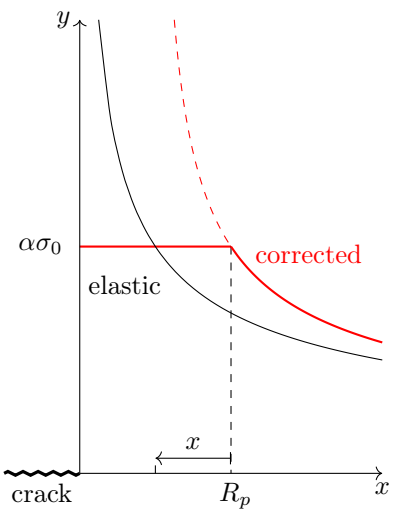

FIGURE 6.5: Irwins's correction. $\alpha = 1$ for plane stress.

6.2.4 T—stress

As mentioned above, eqs 6.1—6.3 are Taylor expansions close to the crack tip. A uniform stress in the x direction appears in the second term of the expansion [C. and Hancock, 1991]:

$$\sigma_{xx} = \frac{K_I}{\sqrt{2\pi r}} f_{xx}(\theta) + T. \tag{6.20}$$

This all induces a modification of stress in the z direction equal to νT. All other stress components are unchanged. A normalized T—stress can be defined as:

$$\beta = \frac{T\sqrt{\pi a}}{K_I} \tag{6.21}$$

This factor depends on the relative crack size (a/W) ad on the specimen type. A positive (resp. negative)β factor means that the crack tip triaxiality is increased (resp. decreased). This corresponds to a situation where brittle failure is favored (resp. potentially delayed).

6.2.5 Small scale yielding — Large scale yielding

The analysis of the stress fields around a crack tip in an elastic material shows that stresses become very high so that yielding occurs. The size of the zone where plasticity is active is proportional to $R_p \propto (K_I/\sigma_0)^2$. Small-scale yielding (SSY) corresponds to situations where R_p is much smaller than the size of the specimen or structure. In that case, the overall behavior remains linear. On the other hand, large-scale yielding (LSY) corresponds to situations where the plastic zone has reached the boundaries of the structure. In that case, the overall behavior is nonlinear. The distinction between SSY and LSY is important with respect to the modeling of fracture. Considering a 3D structure in cases where the crack reaches the outer surface of the structure, the plastic zone will indeed reach a free surface. SSY still dominates if the plastic zone size is much smaller than the thickness of the structure. In that case, plane strain conditions exist along most of the crack front.

6.3 Nonlinear fracture mechanics

In the previous section, the loading of a crack in an elastic material was described in terms of stress intensity factor and T—stress. Studying the nonlinear case is indeed more challenging. In the 60s, it was proposed to use nonlinear elasticity to mimic plastic behavior. Using this hypothesis, it also became possible to determine the stress/strain fields ahead of the crack.

6.3.1 Nonlinear elastic behavior

The nonlinear elastic behavior is described by a stress potential (w) defined to obtain strains as: $\boldsymbol{\varepsilon} = \partial w / \partial \boldsymbol{\sigma}$:

$$w(\boldsymbol{\sigma}) = \frac{1}{N+1}\varepsilon_0\sigma_0\left(\frac{\sigma_{\text{eq}}}{\sigma_0}\right)^{N+1} \quad \text{so that } \varepsilon_{ij} = \varepsilon_0\left(\frac{\sigma_{\text{eq}}}{\sigma_0}\right)^{N}\frac{3}{2}\frac{s_{ij}}{\sigma_{\text{eq}}} \tag{6.22}$$

where σ_{eq} is the von Mises stress and $\boldsymbol{s}$ the stress deviator. Such behavior is incompressible, thus corresponding to von Mises plasticity.

Eq. 6.22 describes a power-law hardening and does not allow for the initial linear behavior. It is however possible to mimic the plastic behavior for any given hardening law: $\sigma_F(p)$ where σ_F represents the flow stress and p the accumulated plastic strain. The stress tensor is given by:

$$\boldsymbol{\sigma} = \mathbb{E} : (\boldsymbol{\varepsilon} - \boldsymbol{\varepsilon}_p) \tag{6.23}$$

where $\mathbb{E}$ is the fourth order elasticity tensor and $\boldsymbol{\varepsilon}_p$ the "plastic strain" which is directly expressed as:

$$\boldsymbol{\varepsilon}_p = \frac{3}{2}p\frac{\boldsymbol{s}}{\sigma_{\text{eq}}} \tag{6.24}$$

This is equivalent to plasticity for purely radial loading (*i.e.* when $\boldsymbol{s}/\sigma_{\text{eq}}$ is constant). p is given such that:$\sigma_F(p) = \sigma_{\text{eq}}$ that is $p = \sigma_F^{-1}(\sigma_{\text{eq}})$. The following equation must therefore be numerically solved:

$$\boldsymbol{\sigma} = \mathbb{E} : \left(\boldsymbol{\varepsilon} - \frac{3}{2}\sigma_F^{-1}(\sigma_{\text{eq}})\frac{\boldsymbol{s}}{\sigma_{\text{eq}}}\right). \tag{6.25}$$

In cases where $\sigma_{\text{eq}} < \sigma_F(0)$, one gets $p = 0$ and $\boldsymbol{\sigma} = \mathbb{E} : \boldsymbol{\varepsilon}$ which corresponds to the elastic compressible behavior.

6.3.2 J integral

Path-independent integrals have been introduced into fracture mechanics by Cherepanov [Cherepanov, 1967] and Rice [Rice, 1968]. Budiansky and Rice [Budiansky and Rice, 1973] also showed that this "J-integral" is identical with the energy release rate, i.e.: $J = G$. This relation has become a common technique for calculating stress-intensity factors in linear elastic fracture mechanics (LEFM). The J-integral is defined as a contour integral around the crack tip:

$$J = \int_\Gamma \left(w dy - \vec{t}.\frac{\partial \vec{u}}{\partial x} ds\right) \tag{6.26}$$

where Γ is an arbitrary contour around the tip of the crack, $\vec{n}$ is the unit vector normal to Γ. $\vec{t}$ is the stress acting on the contour: $\vec{t} = \boldsymbol{\sigma}.\vec{n}$. Because of its path independence [Rice, 1968], the J-integral can be calculated in the remote field and also characterizes the near-tip situation. This establishes its role as a fracture parameter. However, it should be noted that the path-independence does

only hold if the following conditions are met: (i) time-independent processes, no body forces ($\sigma_{ij,j} = 0$), (ii) small strains, (iii) homogeneous hyper-elastic material, (iv) plane stress-strain field, *i.e.* no dependence on z and (v) straight and stress-free crack lips parallel to x.

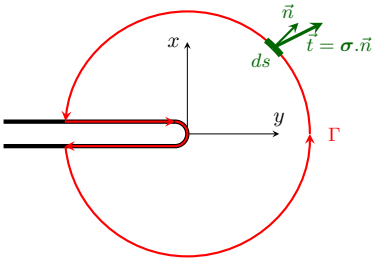

FIGURE 6.6: The J contour integral.

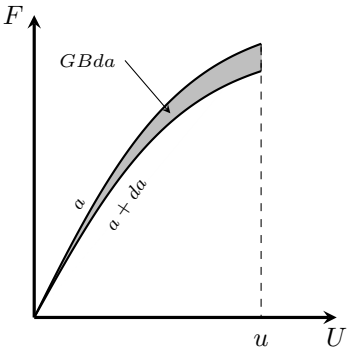

FIGURE 6.7: Energy release rate for a nonlinear material.

6.3.3 HRR fields

Using eq. 6.22, it was shown by Hutchinson [Hutchinson, 1968] and Rice & Rosengren [Rice and Rosengren, 1968] that the stress, strain, and displacement fields ahead of the crack tip can be determined[1]. The resulting fields are expressed using polar coordinates as (plane strain) [Shih, 1983]:

$$\sigma_{ij} = \sigma_0 \left(\frac{J}{\sigma_0 \varepsilon_0 I_N r} \right)^{\frac{1}{N+1}} \tilde{\sigma}_{ij}(\theta, N) \tag{6.27}$$

$$\varepsilon_{ij} = \varepsilon_0 \left(\frac{J}{\sigma_0 \varepsilon_0 I_N r} \right)^{\frac{N}{N+1}} \tilde{\varepsilon}_{ij}(\theta, N) \tag{6.28}$$

$$u_i = \varepsilon_0 r \left(\frac{J}{\sigma_0 \varepsilon_0 I_N r} \right)^{\frac{N}{N+1}} \tilde{u}_i(\theta, N) \tag{6.29}$$

The previous equations depend on J. This dependence is linked to the fact that the above solution must verify the path independence of eq. 6.26; this implies that the J integral evaluated with eq. 6.27 for a given r should not depend on r (*i.e.* path independence). The non-dimensional functions $\tilde{\sigma}_{ij}$, $\tilde{\varepsilon}_{ij}$, and $\tilde{u}_i$ are however, no longer analytical but must be tabulated [Shih, 1983]. I_n

[1] Derivations are more detailed in [Hutchinson, 1968] which can be used to implement the calculations.

is an integration constant. Fig. 6.8 displays I_N as a function of N. An example of the non-dimensional stress functions is given in fig. 6.9 for $N = 10$. Note that the analysis is still performed using a small deformation theory so that stresses still tend to ∞ as $r \to 0$.

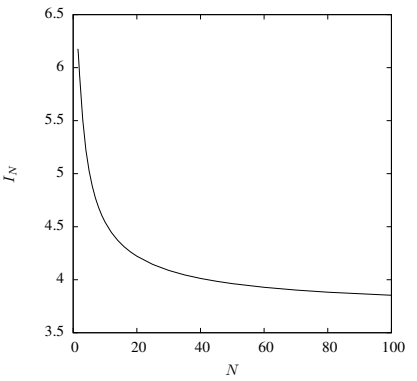

FIGURE 6.8: I_N as a function of N

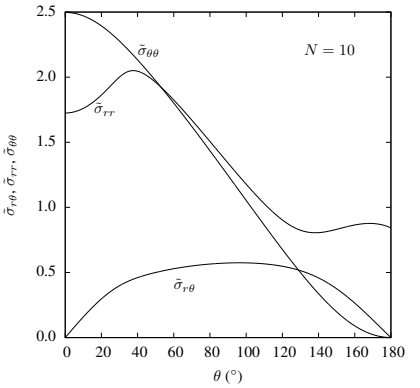

FIGURE 6.9: Functions $\tilde{\sigma}_{r\theta}$, $\tilde{\sigma}_{rr}$, $\tilde{\sigma}_{\theta\theta}$ as functions of θ for $N = 10$.

6.3.4 Crack Tip Opening Displacement (CTOD)

As the crack is loaded, it opens and blunts. The Crack Tip Opening Displacement corresponds to the local opening of the crack during loading. It can be defined (see fig. 6.10) by the distance between the points on the crack surface linked to the crack tip with lines of slope ± 1. Fig. 6.10 displays the crack profile for $N = 3$ and $N = 20$. For high values of N, the opening is almost constant along the crack. Considering eq. 6.29 for $N \to \infty$ (which corresponds to a perfectly plastic material) displacements scale as $u_i \propto J/\sigma_0$. The ratio J/σ_0 is a distance characteristic of the loading. It is representative of the "damage process zone", *i.e.* the zone where damage (brittle or ductile) is likely to develop. Following [Anderson, 2005], the CTOD can be estimated considering the opening displacement u_y evaluated for $\theta = \pi$ (eq. 6.6). One also notes that $u_x = 0$ for $\theta = \pi$. The opening displacement is then:

$$u_y(\theta = \pi) = \frac{4K_I}{E'}\sqrt{\frac{r}{2\pi}}$$

Considering Irwin's correction, one assumes an effective crack at $a + r_y$ so that CTOD can be estimated for (r_y, π): In the case of plane strain, with $r_y = R_p/2$ (with R_p given by eq. 6.2.3 or eq. 6.2.3):

$$\text{CTOD} = 2u_y(r_y, \pi) = \frac{8}{\sqrt{2k\pi}}\frac{K_I^2}{E'\sigma_0} = \frac{8}{\sqrt{2k\pi}}\frac{J}{\sigma_0} \tag{6.30}$$

with $k = 2$ for plane stress and $k = 6$ for plane strain so that CTOD $= 1.27J/\sigma_0$ in the first case and CTOD $= 0.74J/\sigma_0$ in the second case. The previous derivation does not, however, account for finite deformations at the crack tip. Other expressions for the CTOD can be found in [McMeeking, 1977] which account for the effect of hardening and finite deformations. An important aspect of the previous equation is the definition of a length $r_c = J/\sigma_0$ characterizing loading. One notes that:

$$r_c \approx \frac{K_I^2}{E'\sigma_0} \ll \frac{K_I^2}{\sigma_0^2} \approx R_p$$

as in most cases $E' \gg \sigma_0$. r_c characterizes the size of the damage process zone (*i.e.* the zone where strains, stresses and possibly damage are high) which is much smaller than the plastic zone size.

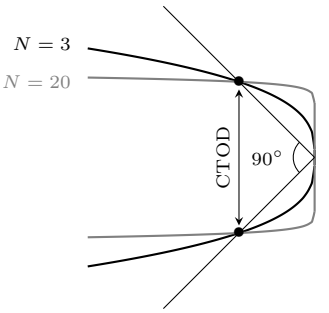

FIGURE 6.10: Crack Tip Opening Displacement (CTOD).

6.3.5 Q factor

As in the case of linear material, the stresses provided by eq. 6.27 are the first terms of a Taylor expansion. In the case of an elastoplastic material it was shown in [O'Dowd and Shih, 1991, 1992] that the stress field is shifted by constant pressure when compared to the HRR stress field:

$$\sigma_{ij} = \sigma_{ij}^{\mathrm{HRR}} + Q\sigma_0\delta_{ij} \tag{6.31}$$

where the non-dimensional factor Q depends on the specimen geometry and loading. A positive Q factor means that the crack tip is subjected to higher triaxial stresses compared to the HRR solution. This corresponds to a situation where failure (brittle or ductile) will occur earlier. On the contrary, a negative Q factor leads to lower triaxial stresses so that fracture is delayed.

6.4 Evaluation of fracture parameters: K_I, J, T and Q

In this section, the focus is put on the use of the finite element method to obtain parameters describing the stress/strain fields close to a crack tip.

6.4.1 Evaluation of K_I and J

K_I can be calculated from $J = G$ using Irwin's formula (eq. 6.13). Based on a finite element solution, using the contour integral defining J (eq. 6.26) may appear a convenient solution. However, this requires the extrapolation of stresses and strains at Gauss points to nodes on the contour [Marigo, 2012]. In practice, G is computed as volume integrals on a ring around the crack tip [de Lorenzi, 1982; SuoCombescure, 1992] using the "virtual crack extension" method.

The method is depicted in fig. 6.11. One defines a meshed ring (Ω) around the crack tip. It is bounded by an inside contour (Γ_i) and an outside contour (Γ_e). The inside contour is uniformly displaced by the quantity $\Delta\vec{a}$ (the virtual crack extension). Displacements are blocked at the outside contour. Displacements ($\Delta\vec{x}$) are linearly interpolated for FE nodes lying between both contours. G is then given by:

$$G = \frac{1}{||\Delta\vec{a}||}\int_\Omega \left(\boldsymbol{\sigma}.\frac{\partial\vec{u}}{\partial\vec{x}} - w\mathbf{1}\right).\frac{\partial\Delta\vec{x}}{\partial\vec{x}}\,d\Omega \tag{6.32}$$

where $\vec{u}$, $\boldsymbol{\sigma}$ are solutions of the FE problem. The strain energy w is computed as:

$$w = \int_{\text{history}} \boldsymbol{\sigma} : d\boldsymbol{\varepsilon}$$

in cases where w is not explicitly defined (as in eq. 6.22). The integral over Ω as well as $\partial\Delta\vec{x}/\partial\vec{x}$ are evaluated using standard FE procedures. As the virtual displacement $\Delta\vec{x}$ is proportional to $\Delta\vec{a}$, G evaluated using eq. 6.32 is independent of the selected $\Delta\vec{a}$.

Mesh independence?

The independence of the J path integral is only valid if the material is assumed to be nonlinear elastic. However, most of the time J is computed by post-processing elasto-plastic simulations. To quantify the error which is created in that case, a CT specimen is simulated using the following work-hardening law[2]:

$$\sigma_F(p) = 480 + 211(1 - \exp(-18p)) + 279(1 - \exp(-3.5p)) \quad \text{(MPa)} \tag{6.33}$$

[2]This hardening law corresponds to that of a nuclear pressure vessel and will be used for the other examples of this text.

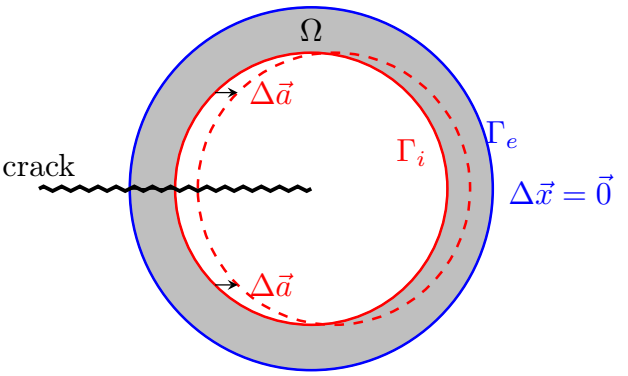

FIGURE 6.11: Virtual crack extension method to compute G.

with $E = 204\,\text{GPa}$ and $\nu = 0.3$. The J integral is computed for 10 contours around the crack tip. When using a nonlinear elastic behavior (eq. 6.25), it is verified that J does not depend on the used contour. This value of J is then used as a reference value for comparison with results obtained using von Mises plasticity. Fig. 6.12 shows the ratio of J for the i^{th} contour ($i = 1 \dots 10$) to the reference value. The plots indicate that J is not path independent in the case of an elastoplastic behavior. However, the error remains limited ($< 3\,\%$ in that case). It is also always best to use contours far from the crack tip where plasticity is limited. More details can be found in [Brocks and Scheider, 2008].

6.4.2 Evaluation of the T stress

The T stress can be evaluated following [Yang and Ravi-Chandar, 1999] and [Chen et al., 2001]. Considering eq. 6.1 and eq. 6.2, one notes that:

$$\sigma_{xx} - \sigma_{yy}|_{\theta=0} = T + O(r^{1/2}) \tag{6.34}$$

The T stress can therefore be computed by post-processing simulations (linear elastic behavior) to plot the difference between both stress components and get T. This method is however inaccurate and the method proposed in [Chen et al., 2001] provides much better results. The method relies on a contour integral given by (plane strain case):

$$I = \frac{E}{1-\nu^2} \int_\Gamma (\vec{u}.\boldsymbol{\sigma}^* - \vec{u}^*.\boldsymbol{\sigma}).\vec{n}\, dC \tag{6.35}$$

using the following values for $\boldsymbol{\sigma}^*$ and $\vec{u}^*$:

$$\sigma^*_{xx} = \frac{\cos 2\theta + \cos 4\theta}{2\pi r^2}, \quad \sigma^*_{yy} = \frac{\cos 2\theta - \cos 4\theta}{2\pi r^2}, \quad \sigma^*_{xy} = \frac{\sin 4\theta}{2\pi r^2} \tag{6.36}$$

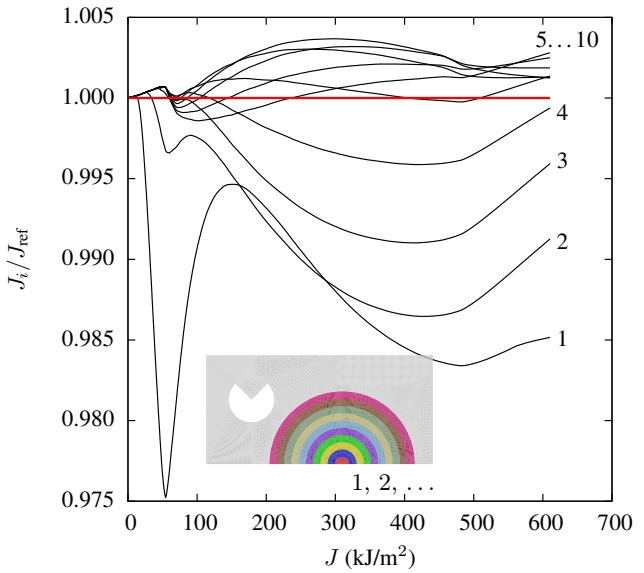

FIGURE 6.12: Ratio of J computed with an elasto-plastic behavior to the reference J computed with the corresponding nonlinear elastic behavior for various contours (shown by the image of half a CT specimen).

and

$$u_x^* = -\frac{1}{4\pi r}\frac{\kappa\cos\theta + \cos 3\theta}{2\nu}, \quad u_y^* = -\frac{1}{4\pi r}\frac{-\kappa\sin\theta + \sin\theta}{2\nu} \tag{6.37}$$

As in the case of the J integral, the computation of a contour integral in hardly suitable using the FE method. The contour integral can be replaced by a volume integral which is given by:

$$I = \frac{E}{1-\nu^2}\int_\Omega ((\vec{u}^{\,\text{FE}} - \vec{u}^{\,\text{FE}}_{\text{tip}}).\boldsymbol{\sigma}^* - \vec{u}^*.\boldsymbol{\sigma}^{\text{FE}}).\vec{\text{grad}}q\, d\Omega \tag{6.38}$$

Quantities marked as $\cdot^{\text{FE}}$ are the results of the FE simulations. $\vec{u}^{\,\text{FE}}_{\text{tip}}$ is the computed displacement of the crack tip so that there is no need to assume that it is fixed. The $\vec{q}$ field is equal to $\vec{e}_x$ on Γ_i and $\vec{0}$ on Γ_e (see fig. 6.11) and linearly interpolated in between.

T factors for CT (fig. 6.15) and MT (fig. 6.13-a) are plotted in fig. 6.13. It is observed that the simple method using the difference between σ_{xx} and σ_{yy} does not provide a constant value for the T stress along the ligament ahead of the crack tip. On the other hand, the integral method provides a constant value for T which does not depend on the selected integration ring.

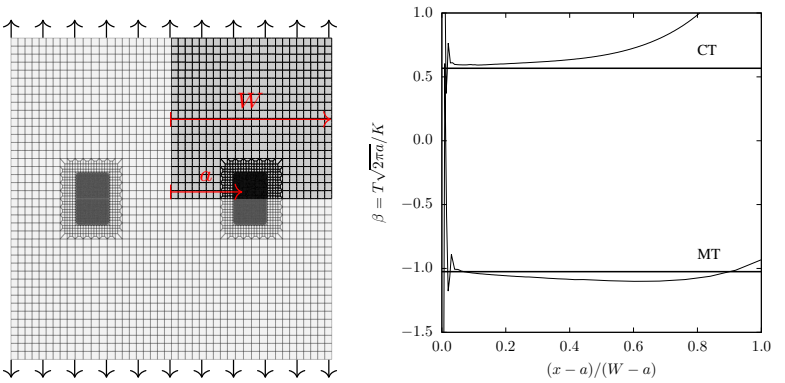

(a) (b)

FIGURE 6.13: Calculation of the T stress for CT specimens and MT specimens. (a) View of the MT specimen (only $\frac{1}{4}$ of the specimen is actually meshed.) (b) β parameter computed using eq. 6.34 as a function of the relative position in the ligament (thin lines). The thick lines represent the values obtained with the interaction integral (eq. 6.38).

6.4.3 Evaluation of the Q factor

The Q factor was introduced by O'Dowd and Shih [O'Dowd and Shih, 1991] to better describe the stress field ahead of a crack tip in the case of finite plasticity. Due to plasticity, the initially sharp crack blunts are shown in fig. 6.10 causing stress redistribution. The Q factor is difficult to evaluate as its evaluation relies on the simulation of a specimen using finite strains, the computation of the J integral and the evaluation of the HRR stress field for the evaluated J. Q is then obtained by comparing the FE stress field and the HRR stress fields. Due to blunting, both fields strongly differ close to the crack tip so that the comparison is performed at a distance equal to $2 \times J/\sigma_0$.

The first difficulty arises from the fact that the hardening law used to model the material is not always a power law required to evaluate the HRR field. In this example, the hardening law used in sec. 6.5 is employed. A power law function is fitted to match the stress-strain curve (Cauchy stress/logarithmic strain). The fit is performed for a plastic strain equal to two times the strain at the onset of necking. This leads to: $N = 6.49$, $\varepsilon_0 = 0.006$ while σ_0 was set for the yield stress (*i.e.* $480\,\mathrm{MPa}\sqrt{\mathrm{m}}$). As ε_0 and σ_0 are not independent the Q factor is evaluated at a distance from the crack tip equal to $r_c = 2J/\sigma_Y$ where σ_Y is the average of the yield stress and the ultimate tensile stress ($\sigma_Y = 584\,\mathrm{MPa}$ in the present case). Another method to evaluate the reference solution is to use a small-scale yielding model consisting of a circular region of radius $R_{\mathrm{ext}} \to \infty$ containing a crack and subjected to an increased displacement of the elastic mode I singular field applied on the far outer

boundary (eq. 6.5, 6.6). J can be computed using Irwin's formula using the applied K_I as the SSY condition prevails [McMeeking, 1977; Chen et al., 2020]. Q is then computed as:

$$Q = \left. \frac{\sigma_{yy}^{\mathrm{FE}} - \sigma_{yy}^{\mathrm{HRR}}}{\sigma_Y} \right|_{x=2r_c}$$

An example of the evaluation of Q is given in fig. 6.14 in the case of a CT specimen and a SENT specimen. The evaluation is done for $J = 294\,\mathrm{kJ/m^2}$ in both cases. In the case of the CT specimen $Q = -0.3$ which is close to 0 and indicates a highly constrained state. On the other hand, $Q = -1.16$ for the SENT specimen which is much less constrained than the CT. This clearly indicates that CT specimens are likely to fail for lower values of a failure criterion (K_{Ic} or J_c) than SENT specimens.

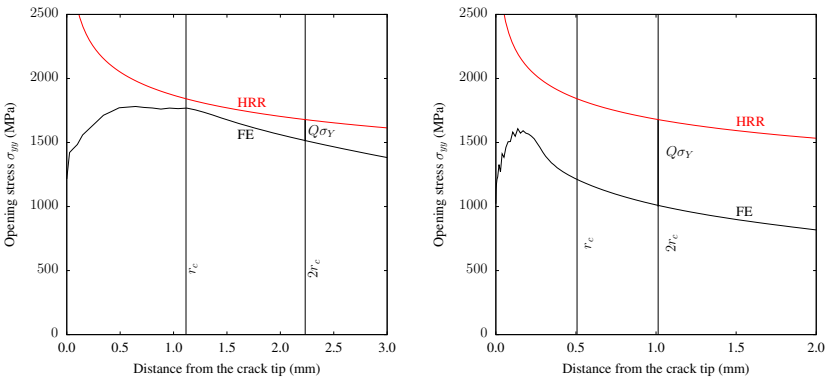

(a) CT specimen $W = 50$ mm, $a/W = 0.5$

(b) SENT specimen $W = 10$ mm, $a/W = 0.5$

FIGURE 6.14: Evaluation of the Q-factor for (a) a CT specimen and (b) a SENT specimen. $J = 294\,\mathrm{kJ/m^2}$.

6.5 Plane stress, plane strain and 3D cases

In many cases, fracture analysis is made using the assumption that the stress state corresponds to either plane stress or plane strain. These conditions are indeed impossible to meet when performing actual tests. Assuming finite strain plasticity (*i.e.* accounting for the thickness reduction due to large deformation), FE simulations under plane stress conditions lead to localized strains ahead of the crack tip within one row of elements (see below). This implies

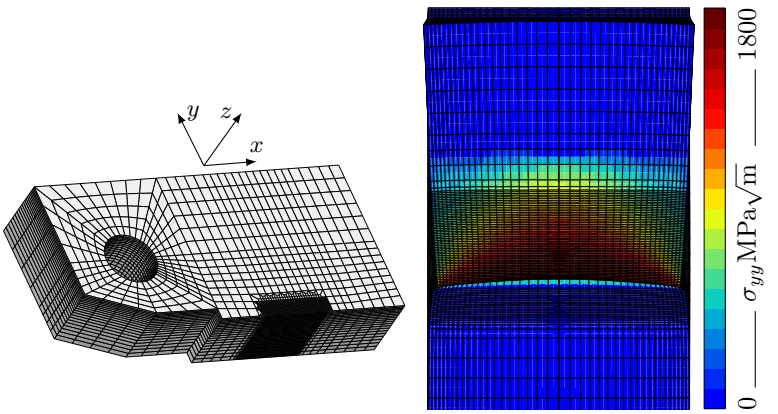

FIGURE 6.15: (a) FE mesh of the specimen using symmetries (1T). (b) Opening stress distribution.

that plane stress simulations must be limited to cases where plasticity is very limited.

To compare the stress/stain states obtained using the different assumptions, a Compact Tension specimen (CT) is simulated using finite strain plasticity.[3] The specimen corresponds to the ASTM standard [ASTM-E1820, 2008] with a width (W) equal to 50 mm and a crack length (a) equal to 25 mm. Several thicknesses are used: 25 mm (1T, which is the thickness recommended by the standard), 12.5 mm ($\frac{1}{2}$T), 6.25 mm ($\frac{1}{4}$T), and 3.125 mm ($\frac{1}{8}$T). A typical FE mesh used for the calculations is shown in fig. 6.15-(a). Symmetries are accounted for so that only $\frac{1}{4}$ of the specimen of represented. Simulations are carried out up to a Crack Mouth Opening Displacement (CMOD) equal to 4.9 mm.

The opening stress field for the CT-1T specimen is shown in fig. 6.15-(b). A significant stress gradient is observed along the crack with stresses being maximum at the center of the specimen. Plane stress conditions indeed prevail at both ends of the crack front due to the free surface as there are no stresses applied on the sample surface in the through-thickness direction. One can note that the maximum opening stress (1800 MPa) is much higher than the yield stress due to an increase in stress triaxiality in the 3D structure. This causes rapid void growth in the case of ductile failure or early failure for brittle materials.

Opening stress profiles ahead of the crack tip at the center of the specimens are plotted in fig. 6.16-(a). In all cases, one observes that the stress maximum

[3] In the text, the following hardening law is used: $\sigma_F(p) = 480 + 211(1 - \exp(-18p)) + 279(1 - \exp(-3.5p))\text{MPa}\sqrt{\text{m}}$ where σ_F is the flow stress and p the accumulated plastic strain strain. Von Mises plasticity is assumed. This hardening law corresponds to that of a nuclear pressure vessel steel at $-50\,^{\circ}$C.

is reached ahead of the crack tip. This effect is due to crack blunting, which creates a free surface at the initial crack tip. One also observes that the profile obtained for the plane strain case always differs from the 3D case (1T). When reducing the specimen thickness, the stress maximum decreases but always remains significantly higher than the stress level obtained assuming plane stress (green dashed line).

Profiles of the strain along the thickness direction (E_{zz}) are plotted in fig. 6.16-(b). The strain is relatively close to the plane strain case ($E_{zz} = 0$) for the 1T specimen but can become strongly negative as the thickness is reduced. This effect corresponds to local necking at the crack tip. The plane strain case is specific. The contour plot in fig. 6.16-(b) shows that the strain is highly localized within one row of elements. This result is made possible by the fact that E_{zz} does not derive from a continuous displacement field (*i.e.* $E_{zz} = \partial u_z / \partial z$) assuming plane stress.

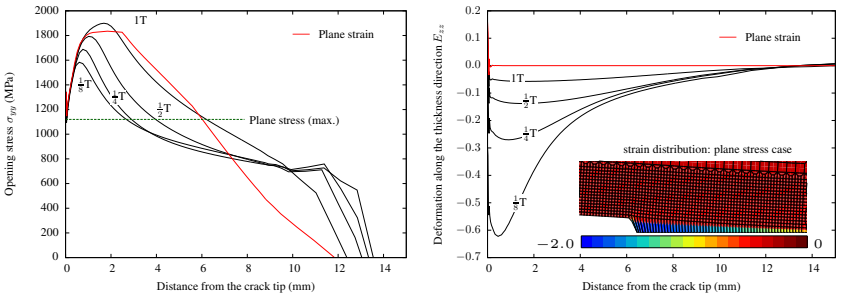

(a) (b)

FIGURE 6.16: (a) Stress profiles ahead of a crack tip (CT specimens). The maximum stress for the plane stress case is computed using the maximum flow stress that can be reached using the hardening law (Eq. 6.33) and a stress triaxiality equal to $1/\sqrt{3}$. (b) Strain profiles for different thicknesses (1T corresponds to a thickness of 25 mm). The contour plot shows the strain distribution for the plane strain case evidencing strong localization.

In order to generate a stress state corresponding more to the plane strain case, it is possible to machine side grooves (SG) on both sides of the specimens. The side groove depth is usually 10% of the thickness on both sides of the specimen. They are relatively sharp, with a radius equal to 0.1 mm. Fig. 6.17-(a) compares stress profiles at the center of the specimen for specimens with and without side grooves. It can be seen that in that case, the effect of the side grooves is limited. However (see fig. 6.17-(b)) the stress distribution in the ligament ahead of the crack is significantly modified. The highly stressed zone becomes much larger if side grooves are used. In particular, the stress drop close to the outer surface is almost suppressed. Therefore, side grooves can efficiently promote a stress/strain state close to plane strain conditions.

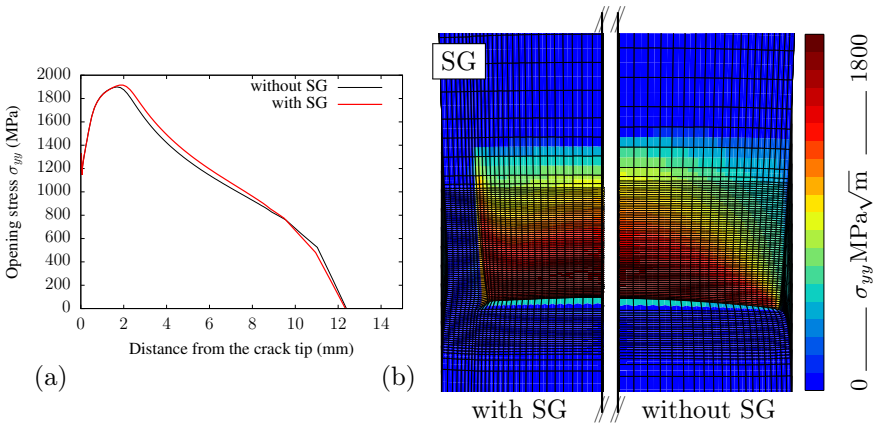

FIGURE 6.17: (a) Stress profile with and without side groove (1T). (b) Opening stress distribution with (left) and without (right) side grooves (SG).

6.6 Testing standards and fracture criteria

The global quantities (K_I, T, J and Q) introduced above can be used to derive fracture criteria. Standards exist which allow the experimental determination of K_I and J. T and Q are to be calculated when needed (see section .6.4). In the following, two standards will be briefly presented:

ASTM E399 Standard Test Method for Linear-Elastic Plane-Strain Fracture Toughness K_{Ic} of Metallic Materials

ASTM E1820 Standard Test Method for Measurement of Fracture Toughness

Other standards exist such as **ISO 12135** or **BS 7448**. They are more or less equivalent with minor differences which will not be discussed here. In the following, the details of the standards are not given and the reader should refer to the original documents to apply the methodology.

6.6.1 Linear elastic fracture — ASTM E399

Griffith's theory stipulates that fracture occurs when the energy release rate reaches a critical value, so that:

$$G = \frac{K_I^2}{E'} = 2\gamma_s \tag{6.39}$$

where γ_s is the surface energy. The factor 2 accounts for the fact that cracking corresponds to the formation of two surfaces. Therefore a "critical" stress intensity (or toughness), K_{Ic} can be evaluated as: $K_{Ic} = \sqrt{2E'\gamma_s}$. In the case of ferritic steels $\gamma_s \approx 1$ J/m^2 and $E' \approx 220$ GPa so that that the "critical" stress intensity should be about $0.6\,\mathrm{MPa}\sqrt{\mathrm{m}}$. This is fortunately not the case as plasticity around the crack significantly increases the fracture energy. Linear elastic fracture as described by ASTM 399, therefore, corresponds to fracture under SSY. In particular the standard states (section 9.1.3) TODO that

$$2.5\left(\frac{K_{Ic}}{\sigma_{YS}}\right)^2 < W - a \tag{6.40}$$

for the determined K_{Ic} value to be valid. σ_{YS} is the 0.2% offset yield stress in tension. $W - a$ corresponds to the size of the uncracked ligament. Recalling that the plane strain plastic zone size is $R_p = \frac{1}{3\pi}(K_I/\sigma_{YS})^2$ (sec. 6.2.3) the previous equation can be rewritten using R_p as:

$$R_p < \frac{1}{24}(W - a) \tag{6.41}$$

so that the plastic zone size is much smaller than the ligament size ; this condition indeed corresponds to SSY. Note that the standard tolerates some nonlinearity in the force-displacement curve.

K_I is related to the applied load by the following equation:

$$K_I = f_K(a/W)\frac{F}{B\sqrt{W}} \tag{6.42}$$

where B is the specimen thickness, a the crack length and W its width. f_K is a nondimensional parameter that depends on the test specimen geometry and which is provided by the standard. For instance in the case of the CT specimen, one gets:

$$f_K(a/W) = \frac{2 + a/W}{(1 - a/W)^{3/2}}\left(0.886 + 4.64\frac{a}{W} - 13.32\left(\frac{a}{W}\right)^2 + 14.72\left(\frac{a}{W}\right)^3 - 5.6\left(\frac{a}{W}\right)^4\right).$$

Actual formula may slightly differ from the previous equations (as in the case of bending specimens). Considering the load at which fracture is considered to initiate, K_{Ic} corresponds to the value of K_I computed using this load.

6.6.2 Nonlinear elasto-plastic fracture — ASTM E1820

The ASTM E1820 is used to determine J values from test specimens such as Compact Tension (CT), Single Edge Notch Bend (SENB) and Disk-shaped Compact Tension (DCT) specimens. The standard is designed for cases close to a plane strain state. The standard can be applied in the fully brittle regime (no ductile crack advance), in the fully ductile regime and in the transition regime where a small ductile crack advance may occur before brittle failure.

Note that the overall behavior may be nonlinear in the fully brittle regime. The standard assumes that J can be decomposed into an elastic part and a plastic part as:

$$J = J_e + J_p. \tag{6.43}$$

As shown in [Ernst et al., 1981] this decomposition is only possible if the load can be expressed as the product of a function of the plastic displacement (v_p) and a function of the crack length as:

$$F = G(a/W)H(v_p/W). \tag{6.44}$$

This decomposition has been proved experimentally in [Sharobeam and Landes, 1991, 1993] using various types of specimens (CT, SENB, CCT, SENT), different crack lengths and different materials. All specimens were machined with a blunted notch to delay crack initiation.

J_e is computed using Irwin's formula (eq. 6.13) with K_I being evaluated using eq. 6.42. This evaluation of J_p used the area under the force versus displacement curve A_p as shown in fig. 6.18. A_p represents the dissipated energy. Following [Ernst et al., 1981], J_p can then be expressed for a non-propagating crack as:

$$J_p = \eta_p \frac{A_p}{B_N(W-a)} \tag{6.45}$$

where η_p is a non-dimensional factor depending on the specimen geometry. B_N is the net specimen thickness accounting for the presence of side grooves. η_p can be derived analytically as in [Merkle and Corten, 1974] but is nowadays computed using the finite element method [Cravero and Ruggieri, 2007]. The method is then based on the following steps: (i) perform an elastoplastic simulation of a cracked specimen, (ii) evaluation J, (iii) compute J_p as $J - J_e$ (it is here assumed that f_K is known), (iv) evaluate A_p from the FE simulation, (v) plot J_p as a function of $A_p/B(W-a)$. One should then obtain a linear relation between J_p and $A_p/B(W-a)$ the slope of which corresponds to η_p.

Eq. 6.45 is only valid for a non-propagating crack. The case of a propagating crack is also described by the standard base on the work of [Ernst et al., 1981]. An incremental expression to compute J_p is used (where k represents a loading step):

$$J_p^k = \left[J_p^{k-1} + \frac{\eta_p^{k-1}}{b^{k-1} B_N} \left(A_p^k - A_p^{k-1} \right) \right] \times \left[1 + \frac{\gamma_p^{k-1}}{b^{k-1}} \left(a^k - a^{k-1} \right) \right] \tag{6.46}$$

where $b = W - a$ and γ_p is a non dimensional factor related to η_p as:

$$\gamma_p = \eta_p - 1 - \frac{b}{W} \frac{\eta_p'}{\eta_p} \tag{6.47}$$

with $\eta_p' = d\eta_p / d(a/W)$. Eq. 6.45 is retrieved if a is constant. The standard

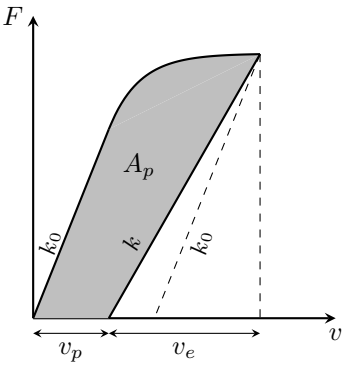

FIGURE 6.18: Definition of A_p, v_e and v_p

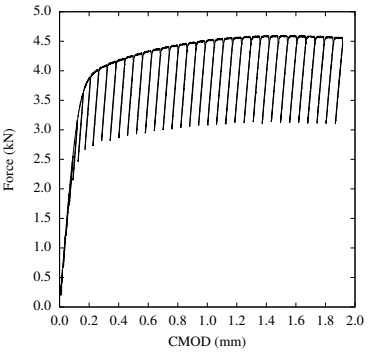

FIGURE 6.19: Experiment on a CT specimen with partial unloading

gives a simple expression for γ_p which is very close to eq. 6.47. For example, in the case of the CT specimens, one gets:

$$\eta_p = 2 + 0.522(1 - a/W), \qquad \gamma_p = 1 + 0.76(1 - a/W).$$

At this point, experimental data can be processed to obtain J provided the crack length is known. This is not an issue if brittle failure occurs in the elastoplastic regime, for instance in the case of ductile to brittle transition. In the case of a propagating crack, it is necessary to know a for each loading step. Several methods can be used and the E1820 standard provides in the case of the so-called "unloading compliance" method. The method consists in partially unloading the specimen to measure its compliance. Such a test is illustrated in fig. 6.19 in the case of highly ductile line pipe steel. The change in compliance is hardly visible and accurate extensometers must be used to measure the CMOD. As the compliance depends on the crack length a variation in compliance can be related to a variation in crack length. The main difficulty of this method is that the compliance is modified during loading due to the change in geometry. The standard accounts for the rotation on specimens such as CT or SENB. It does not account for changes due to plasticity. The corrected compliance in the unrotated configuration is then evaluated as:

$$C_c = C_m \times c \tag{6.48}$$

where c is a correction factor depending on the geometry and the opening displacement. C_c is then used to compute the following factor:

$$u = \frac{1}{1 + \sqrt{B_e E C_c}} \tag{6.49}$$

where B_e is used to account for the presence of side grooves with:

$$B_e = B - \frac{(B - B_N)^2}{B} \tag{6.50}$$

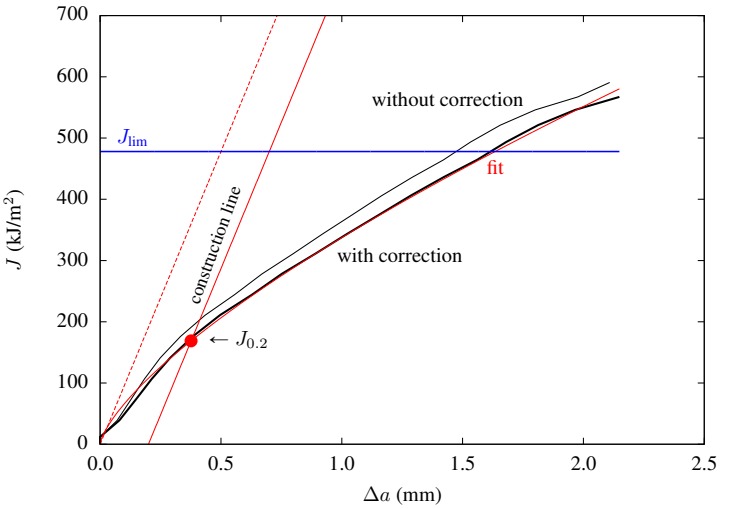

FIGURE 6.20: J—Δa curves for a vintage X52 line pipe steel. CT specimen with $B = 10$ mm and $W - a = 13$ mm.

It is important to outline that the presence of side grooves is accounted for differently in the elastic case (use B_e in eq. 6.50) or plastic case (use of B_N in eq. 6.45 and eq. 6.46). In the absence of side grooves $B = B_N = B_e$. Note also that E (and not E') is used in eq. 6.49. Finally, a/W can be expressed as a function of u. In the standard, a polynomial function is used. Processing the experimental data lead to the determination of the crack advance resistance curve J—Δa where $\Delta a = a - a_0$ is the crack advance. Such a curve is plotted in fig. 6.20. In this figure, one can observe a significant influence of the rotation correction. The standard defines a J at crack initiation ($J_{0.2}$) which corresponds to the intersection of the curve with the so-called "offset line" which has the following expression:

$$J = 2\sigma_Y(a - 0.2(\text{mm}))$$

where

$$\sigma_Y = \frac{1}{2}(\sigma_{YS} + \text{UTS})$$

where UTS is the ultimate tensile stress. The intersection can be easily determined by fitting the experimental data as $J = J_0(\Delta a/\Delta a_0)^n$ (red curve in fig. 6.20). The line $\Delta a = J/(2\sigma_Y)$ can be interpreted as the crack advance due to blunting only (red dashed line in fig. 6.20). In that case, crack advance is assumed to be half of the CTOD which is implicitly assumed to be equal to J/σ_Y. $J_{0.2}$ therefore corresponds to the value of J which the crack has actually grown by 0.2 mm. As evidenced in fig. 6.20 the initial slope of the J—Δa curve is not always equal to $2\sigma_Y$.

The standard also gives conditions for the test to be valid. In particular, the specimen dimensions should be such that:

$$B,\, W - a > 10J/\sigma_Y = 10r_c \tag{6.51}$$

which mechanics that the size of the specimen must be much smaller than the size of the damage process zone (see sec. 6.3.4 in which σ_0 is replaced by σ_Y). The maximum valid J is therefore $J_{\text{lim}} = \min(B, W-a)\sigma_Y/10$. J_{lim} is shown in fig. 6.20.

Any value of J can be converted into a fracture toughness K_J using Irwin's formula: $K_J = \sqrt{JE'}$. In particular, $K_{J_{0.2}}$ may be considered a critical value when designing structures in the ductile regime. In the case of brittle fracture, $K_{Ic} = \sqrt{J_c E'}$ is considered as the toughness where J_c is the value of J at fracture.

6.6.3 Fracture criteria?

Based on the idea that fracture corresponds to the creation of two surfaces so that $G_c \approx 2\gamma_s$, using a constant value for $K_{Ic} = \sqrt{G_c E'}$ as a failure criterion may appear reasonable. This approach appears to be working in the case of brittle material such as glass or ceramics which experiences little or no plasticity.

In the case of plastic materials, one may assume a critical value for K_J, *i.e.*K_{Jc}. In the case of brittle fracture scatter is to be expected [Beremin, 1983; Pineau et al., 2016]. This has led to the ASTM E1921 (Master curve approach).

In the case of ductile fracture, one may assume a critical value for $J_{0.2}$ (or corresponding $K_{J_{0.2}}$) to describe crack initiation. If crack growth needs to be defined, the entire J—Δa curve can be used.

6.7 Limitations of the global approach to fracture

Assuming that fracture parameters are intrinsic materials values was shown not to be correct. In the following, three examples are given which demonstrate that these parameters are not constant but depend on the specimen/structure geometry and loading history.

6.7.1 Effect of geometry: brittle fracture

Experimental studies by [Sumpter and Forbes, 1992] and [Sumpter, 1993] on SENB (Single Edge Notch Bending) and CCP (center crack panel) specimens have evidenced a strong effect of the ratio a/W on the value of the J integral

at crack initiation. The study was carried out at −50 °C on an A36 steel (brittle failure). As a/W is increased in SENB specimens, J_{1c} strongly decreases as shown on fig. 6.21. These experimental results clearly showed that using a using value for J_c as a failure criterion was not appropriate. The use of a two-parameters global failure criterion using J and Q was then proposed in [O'Dowd and Shih, 1991, 1992]. It is then possible to define a unique failure locus as shown on fig. 6.22. The observed scatter is inherent to brittle failure. The observed failure behavior can be qualitatively explained by the RKR model [Ritchie et al., 1973]. The main result is that the local stress triaxiality varies depending on the crack depth. For low values of the crack length, the Q factor is negative so that the local stress triaxiality is less than for long cracks. A higher load level (*i.e.* a higher value of J) must be applied to locally reach the critical stress, σ_c. Similar considerations explain the differences between SENB and CCP specimens. It is therefore clear that a unique value for K_{Ic} cannot be defined. Using values obtained for high values of Q (*i.e.* using CT specimens) leads to conservatism which may be detrimental (over-conservatism!). For instance, pressurized pipes are loaded in tension which corresponds to the loading applied using a SENT sample (negative Q). Values of K_{Ic} obtained using CT specimen (slightly positive Q) leads to conservatism.

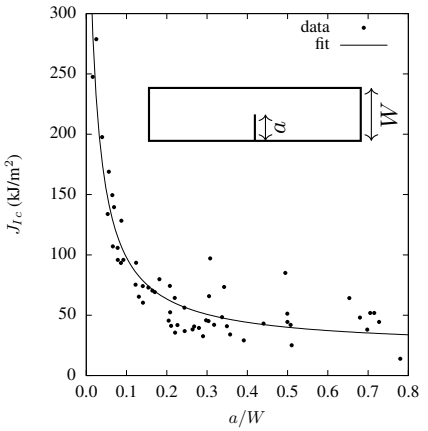

FIGURE 6.21: Evolution of J_{Ic} as a function of a/W for SENB specimens for a type A36 steel at −50 °C [Sumpter, 1993; Sumpter and Forbes, 1992].

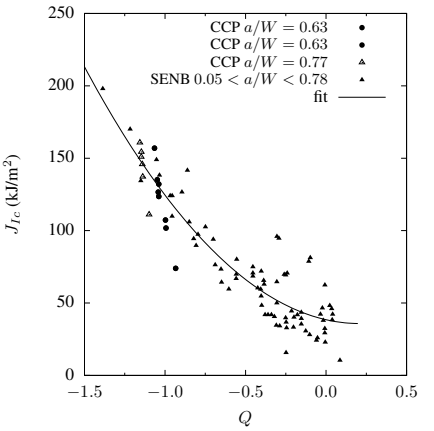

FIGURE 6.22: Evolution of J_{1c} as a function of Q for SENB and CCP specimens for a type A36 steel at −50 °C [Sumpter and Forbes, 1992; Sumpter, 1993; O'Dowd et al., 1995].

6.7.2 Effect of geometry: ductile fracture

Fig. 6.23 compares the J—Δa curves obtained on a ferritic steel for a Compact Tension (CT) specimen and Single Edge Notch Tensile (SENT) specimen [Ku-

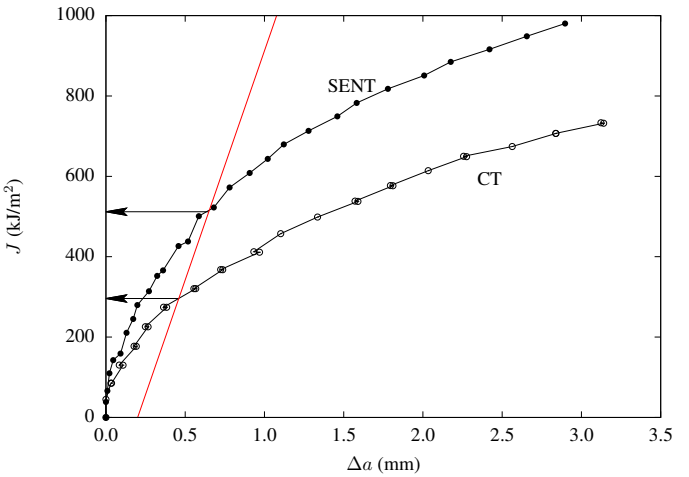

FIGURE 6.23: J—Δa curves for SENT and CT specimens (C–Mn steel [Kumar et al., 2022]).

mar et al., 2022]. It can be noticed that the SENT specimen leads to higher J values than the CT specimens. $J_{0.2}$ is equal to $512\,\mathrm{kJ/m^2}$ for the SENT specimen; it is however not valid due to the relatively small ligament of the specimen ($\simeq 7.5\,\mathrm{mm}$). $J_{0.2}$ is equal to $296\,\mathrm{kJ/m^2}$ for the CT specimen. This value is valid according to the standard. SENT specimens are interesting as they are representative of loadings experienced by pipes [Thaulow et al., 2004]. They lead to higher values for J so that conservatism in the design can be reduced. However, they are more difficult to machine as they require more material than CT specimens. Validity is more difficult to verify due to the higher toughness values.

6.7.3 Warm pre-stress effect (WPS)

The warm pre-stress effect [Roos et al., 1998; Lefevre et al., 2002; Bordet et al., 2006] plays a key role in the assessment of nuclear pressure vessel integrity during a pressurized thermal shock (PTS), for example, a loss of coolant accident (LOCA). One considers here the case of brittle fracture of a pressure vessel steel. In fig. 6.24, the gray area represents the domain where the fracture occurs when the cracked specimen is cooled down to a given temperature and then tested (red loading path). This corresponds to fracture under isothermal conditions. The domain is based on the Master Curve approach [Wallin, 1999; ASTM-E1921, 2008]. Its lower and upper limits correspond to a 5 % and a 95 % failure probability.

Two thermomechanical cycles are also shown in fig. 6.24 to illustrate the WPS effect. In both cases, a pre-cracked specimen is first loaded in the upper

shelf of the transition curve at a temperature T_1 and at values of K or J which are below that corresponding to fracture ($K_{Ic}(T_1)$ or $J_c(T_1)$). In the first type of cycle (black load path), the specimen is slowly cooled at constant load down to a lower temperature T_2 which corresponds to the lower shelf regime. The transition curve can be crossed without observing any fracture. This is simply due to the fact that plastic deformation is necessary to initiate cleavage fracture [Beremin, 1983]. As the yield strength of the material increases when the temperature is decreased no plastic deformation takes place during the cooling process, in particular when the transition curve is crossed. At temperature T_2, a higher value of the stress intensity factor has to be applied to initiate cleavage fracture. This cycle, called load–cool–fracture (LCF), produces a significant increase in the fracture toughness, compared to the value determined under isothermal conditions at the same temperature, T_2. The second type of thermomechanical loading (load–unload–cool–fracture or LUCF, blue loading path) is a little more complex since it involves a first loading, followed by unloading at temperature T_1, then the cooling step and the final test to fracture. Here again, an apparent increase of the fracture toughness is observed at temperature T_2.

It is even possible to increase K_I while decreasing temperature (dashed path in fig. 6.24). This was experimentally demonstrated in [Bordet et al., 2006]. Assuming that brittle fracture occurs only if plasticity is active and considering that the size of the plastic zone should not increase, the following condition should be respected in order to avoid fracture during the test[4]:

$$\frac{1}{K_I}\left|\frac{K_I}{T}\right| < \frac{1}{\sigma_{YS}}\left|\frac{\sigma_{YS}}{T}\right|$$

or considering the size of the damage process zone:

$$\frac{1}{K_I}\left|\frac{K_I}{T}\right| < \frac{1}{2}\left[\frac{1}{\sigma_Y}\left|\frac{\sigma_Y}{T}\right| + \frac{1}{E'}\left|\frac{E'}{T}\right|\right].$$

Needless to say, a unique value for $K_{Ic}(T)$ cannot represent the WPS effect.

6.7.4 Conclusions and need for the local approach

The above examples are evidence that a unique fracture parameter cannot describe complex situations. This can lead to conservatism *e.g.* when CT specimens are used to determine toughness which can be used for the safety assessment of structures such as pipes or pressure vessels for which the Q factor is strongly negative. Over-conservatism remains an issue if light-weight structures are assessed or when the initial material properties are reduced due to aging (temperature, irradiation,...).

To solve these issues, the local approach to fracture can be used. It uses

[4]Considering that $d\sigma_{YS}/dT < 0$, $d\sigma_Y/dT < 0$ and $dE'/dT < 0$.

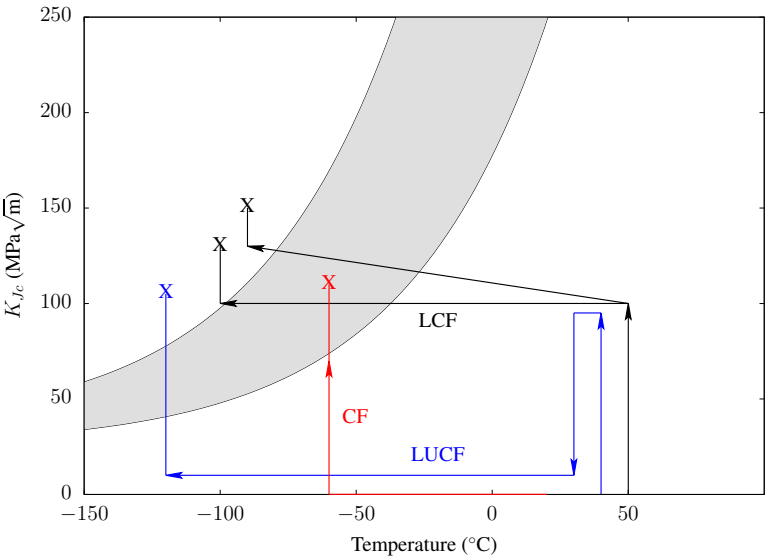

FIGURE 6.24: Loading paths used to evidence the WPS effect. CF: Cool—Load, LCF: Load—Cool—Fracture, LUCF: Load—Unload—Cool—Fracture. The gray area represents failure points obtained using the 'standard" CF path.

physically based models which can explain the observed trends (see for instance [Lefevre et al., 2002; Bordet et al., 2006] in the case of the WPS effect). The local approach to failure requires the detailed evaluation of stresses and strains in areas where fracture may initiate and cracks propagate. A precise description of the material elastoplastic behavior is therefore needed. Fracture models, which are described in this book, also require the tuning of material parameters.

Another limitation of the global approach is that it only deals with cracks and is *a priori* unable to analyze defects such as notched and crack initiation from such defects. The local approach to fracture can handle such situations.

Recommendations on how to use global fracture parameters for the safety assessment of structures are beyond the scope of this chapter. The SINTAP procedure [Steel, 1999; Ainsworth et al., 2000] can for instance be used in that case[5].

[5]ISBN 13 978-0080449470

Bibliography

[Ainsworth et al. 2000] Ainsworth, R.A. ; Bannister, A.C. ; Zerbst, U.: An overview of the European flaw assessment procedure SINTAP and its validation. In: *Int. J. of Pressure Vessels and Piping* 77 (2000), p. 869–876

[Anderson 2005] Anderson, T.L.: *Fracture Mechanics: Fundamentals and Applications*. Taylor & Francis, 2005

[ASTM-E1820 2008] ASTM-E1820: Standard Test Method for Measurement of Fracture Toughness. 2008. – Technical repport

[ASTM-E1921 2008] ASTM-E1921: Standard Test Method for Determination of Reference Temperature, T_0, for Ferritic Steels in the Transition Range. 2008. – Technical repport

[Beremin 1983] Beremin, F. M.: A local criterion for cleavage fracture of a nuclear pressure vessel steel. In: *Met. Trans.* 14A (1983), p. 2277–2287

[Bordet et al. 2006] Bordet, S. ; Tanguy, B. ; Besson, J. ; Bugat, S. ; Moinereau, D. ; Pineau, A.: Cleavage fracture of RPV steel following warm pre-stressing: micromechanical analysis and interpretation through a new model. In: *Fatigue and Fract. Engng Mater. Struct.* 29 (2006), p. 799–816

[Brocks and Scheider 2008] Brocks, W. ; Scheider, I.: Numerical Aspects of the Path-Dependence of the J-Integral in Incremental Plasticity / Institut für Werkstofforschung GKSS-Forschungszentrum Geesthacht. 2008. – Technical repport

[Broek 1982] *Kapitel* The crack tip plastic zone. In: Broek, D.: *Elementary engineering fracture mechanics*. Martinus Nijhoff Publishers, The Hague, 1982, p. 91–114

[Budiansky and Rice 1973] Budiansky, E. ; Rice, J.R.: Conservation laws and energy release rates. In: *J. Applied Mech.* 40 (1973), p. 201–203

[C. and Hancock 1991] C., Betégon ; Hancock, J.W.: Two parameter characterization of elastic–plastic crack–tip fields. In: *J. Applied Mech.* 58 (1991), p. 104–110

[Chen et al. 2001] Chen, C.S. ; Krause, R. ; Pettit, R.G. ; Banks-Sills, L. ; Ingraffea, A.R.: Numerical assessment of T–stress computation using a p–version finite element method. In: *Int. J. Frac.* 107 (2001), p. 177–199

[Chen et al. 2020] Chen, Y. ; Lorentz, E. ; Besson, J.: Properties of a nonlocal GTN model within the context of small—scale yielding. In: *Int. J. Plasticity* (2020), p. 102701

[Cherepanov 1967] Cherepanov, G.P.: Crack propagation in continuous media. In: *J. Applied Math. Mech.* 31 (1967), Nr. 3, p. 476–488

[Cravero and Ruggieri 2007] Cravero, S. ; Ruggieri, C.: Estimation procedure of J-resistance curves for SE(T) fracture specimens using unloading compliance. In: *Eng. Fract. Mech.* 74 (2007), p. 2735–2757

[Ernst et al. 1981] Ernst, H.A. ; Paris, P.C. ; Landes, J. D.: Estimations on J-integral and tearing modulus T from a single specimen test record. In: Roberts, R. (Hrsg.): *Fracture Mechanics*. ASTM STP 743, 1981, p. 476–502

[Hutchinson 1968] Hutchinson, J. W.: Singular behaviour at the end of a tensile crack in a hardening material. In: *J. Mech. Phys. Solids* 16 (1968), p. 13–31

[Kumar et al. 2022] Kumar, R. ; Besson, J. ; King, A. ; Dahl, A. ; Morgeneyer, T.F.: X-ray microtomography investigation of damage fields ahead of cracks in CT and SENT C-Mn steel samples. In: *Int. J. Frac.* (2022). – https://doi.org/10.1007/s10704-022-00674-8

[Lefevre et al. 2002] Lefevre, W. ; Barbier, G. ; Masson, R. ; Rousselier, G: A modified Beremin model to simulate the warm pre–stress effect. In: *Nucl. Eng. Des.* 216 (2002), p. 27–42

[de Lorenzi 1982] Lorenzi, H.G. de: On the energy release rate and the J–integral for 3D crack configurations. In: *Int. J. Frac.* 19 (1982), p. 183–193

[Marigo 2012] Marigo, J.-J.: *Plasticité et Rupture*. Ecole Polytechnique, 2012

[McMeeking 1977] McMeeking, R.M.: Finite deformation analysis of crack-tip opening in elastic-plastic materials and implications for fracture. In: *J. Mech. Phys. Solids* 25 (1977), p. 357–381

[Merkle and Corten 1974] Merkle, J.G. ; Corten, H.T.: A J integral analysis for the compact specimen, considering axial force as well as bending Effects. In: *Trans. ASME* (1974), p. 286–292

[O'Dowd et al. 1995] O'Dowd, N. ; Shih, C. F. ; Dodds, R. H.: The role of geometry can crack growth on constraint and implications for ductile/brittle fracture. In: *Constraint effects in fracture: theory and applications* Bd. 2, 1995, p. 134–159

[O'Dowd and Shih 1991] O'Dowd, N.P. ; Shih, C.F.: Family of crack-tip fields characterized by a triaxiality parameter—I. Structure of Fields. In: *J. Mech. Phys. Solids* 39 (1991), Nr. 8, p. 989–1015

[O'Dowd and Shih 1992] O'Dowd, N.P. ; Shih, C.F.: Family of crack-tip fields characterized by a triaxiality parameter—II. Fracture Applications. In: *J. Mech. Phys. Solids* 40 (1992), Nr. 8, p. 939–963

[Pineau et al. 2016] Pineau, A. ; Benzerga, A. A. ; Pardoen, T.: Failure of metals I: Brittle and ductile fracture. In: *Acta Mater.* 107 (2016), p. 424–483

[Rice 1968] Rice, J. R.: A path independent integral and the approximate analysis of strain concentration by notched and cracks. In: *J. Applied Mech.* 35 (1968), p. 379

[Rice and Rosengren 1968] Rice, J. R. ; Rosengren, G. F.: Plane strain deformation near a crack tip in a power-law hardening material. In: *J. Mech. Phys. Solids* 16 (1968), p. 1–12

[Ritchie et al. 1973] Ritchie, R.O. ; Knott, J.F. ; Rice, J.R.: On the relationship between critical tensile stress and fracture toughness in mild steel. In: *J. Mech. Phys. Solids* 21 (1973), p. 395–410

[Roos et al. 1998] Roos, E. ; Alsmann, U. ; Elsässer, K. ; Eisele, W. ; Seidenfuss, M.: Experiments an warm prestress effffect and their numerical simulation based on local approah. In: publishing, EMAS (Hrsg.): *Fracture from defects ECF12.* Sheffield, 14–18 Septembre, 1998, p. 939–944

[Sharobeam and Landes 1991] Sharobeam, M.H. ; Landes, J.D.: The load separation criterion and methodology in ductile fracture-mechanics. In: *Int. J. Frac.* 47 (1991), p. 81–104

[Sharobeam and Landes 1993] Sharobeam, M.H. ; Landes, J.D.: The load separation and η_{pl} development in precracked specimen test. In: *Int. J. Frac.* 59 (1993), p. 213–226

[Shih 1983] Shih, C.F.: Tables of Hutchinson–Rice–Rosengren singular field quantities / MRL E-147, Brown University. 1983. – Technical repport

[Steel 1999] Steel, British: SINTAP, Structural Integrity Assessment Procedures for European Industry. Project BE95-1426. Final Procedure, British Steel Report, Rotherham. 1999. – Technical repport

[Sumpter 1993] Sumpter, J.D.G: An experimental investigation of the T stress approach. In: *Constraint effects in fracture, ASTM STP 1171*, 1993, p. 492–502

[Sumpter and Forbes 1992] Sumpter, J.D.G. ; Forbes, A.T.: Constraint based analysis of shallow cracks in mild steel. In: *TWI/EWI/IS International conference on shallow crack fracture mechanics, Toughness Tests and applications*, 1992

[SuoCombescure 1992] SuoCombescure: On the application of G(Θ) method and its comparison with Delorenzi's approach. In: *Nucl. Eng. Des.* 135 (1992), Nr. 2, p. 207–224

[Thaulow et al. 2004] Thaulow, C. ; Østby, E. ; Nyhus, B. ; Zhang, Z.L. ; Skallerud, B.: Constraint correction of high strength steel. Selection of test specimens and application of direct calculations. In: *Eng. Fract. Mech.* 71 (2004), p. 2417–2433

[Wallin 1999] Wallin, K: The master curve method: a new concept for brittle fracture. In: *Int. J. Mater. Prod. Technol.* 14 (1999), Nr. 2-4, p. 342–354

[Williams 1957] Williams, M.L.: On the stress distribution at the base of a stationary crack. In: *J. Applied Mech.* 24 (1957), p. 101–106

[Yang and Ravi-Chandar 1999] Yang, B. ; Ravi-Chandar, K.: Evaluation of elastic T–stress by the stress difference method. In: *Eng. Fract. Mech.* 64 (1999), p. 589–605

7

Brittle fracture: physical mechanisms, mechanical assessment - Application to brittle transgranular cleavage

Anne-Françoise Gourgues-Lorenzon

Mines Paris, PSL University, Centre des Matériaux UMR CNRS 7633, BP 87, 91003 Evry cedex, France

This chapter starts with a general view of brittle fracture mechanisms. Transgranular cleavage fracture is then addressed both at the macroscopic scale (general phenomenology), then in relationship to microstructure (physical fracture mechanisms). Deterministic and probabilistic modelling approaches are then reviewed.

7.1 Introduction

Brittle fracture is generally abrupt but may result in a variety of macroscopic failure modes, as illustrated in Fig. 7.1a. Brittle-elastic fracture occurs without any sign of degradation. During quasi-brittle failure, an abnormal behavior appears well before fracture, due to the energy dissipation by some stable damage development that also affects the elastic behavior (see the decrease in stiffness in Fig. 7.1b). Brittle-plastic failure occurs after some plastic deformation, but still abruptly (Fig. 7.1c). The most favorable case of ductile fracture (Fig. 7.1d) involves a significant amount of strain and, frequently, after visible strain localization.

Brittle fracture may involve a variety of physical fracture mechanisms leading to various kinds of fracture surfaces, but with little or no macroscopic deformation (Fig. 7.2a). Fracture mechanisms of amorphous materials are still controversial and involve successive breakages of atomic bonds, in a more or less continuous manner. Brittle cracking of crystals may occur along grain boundaries (intergranular fracture, Fig. 7.2b) or across grains (transgranular cleavage fracture, Fig. 7.2c). It may depend on thermal or chemical environmental conditions. A typical example is stress corrosion cracking, where coupling a rather ductile material with a weakly-aggressive chemical environ-

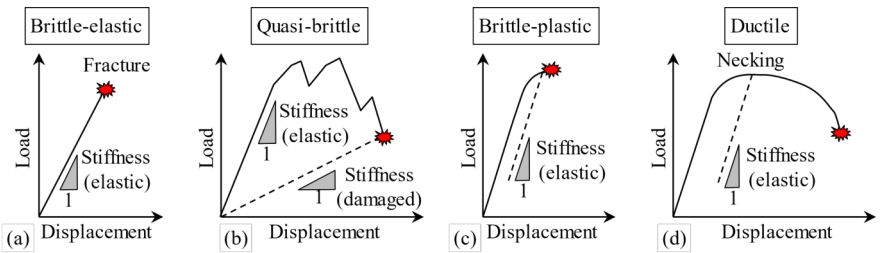

FIGURE 7.1: Macroscopic failure modes as viewed on a load vs. displacement curve.

ment and a moderate stress level may induce very brittle intergranular or transgranular fracture.

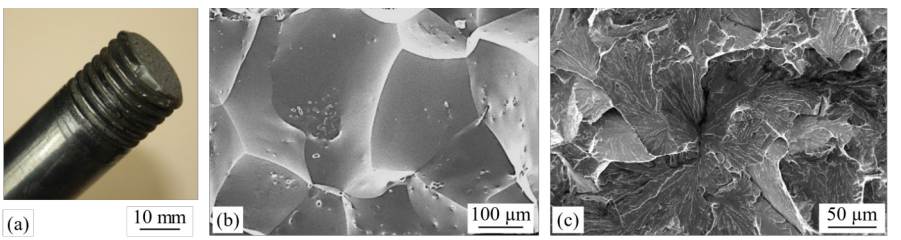

FIGURE 7.2: Brittle fracture surfaces. (a) Macroscopic view of a broken screw; (b) intergranular fracture of a zirconium alloy [Chosson, 2014]; (c) transgranular cleavage fracture of a bainitic steel.

The following of this chapter is dedicated to brittle transgranular cleavage fracture, but one must keep in mind that all physical fracture mechanisms are in competition against each other. The developed approach (Fig. 7.3) is also applied to other kinds of fracture behavior:

- Investigation of the fracture event, both at the macroscopic and at the microscopic scale to identify underlying physical mechanisms.
- Mechanical analysis and modelling to learn how to avoid this particular brittle fracture phenomenon by either changing the material or the in-service conditions. When physically based, the model includes information about the material, *i.e.*, about its microstructure, in the so-called local approach to fracture.

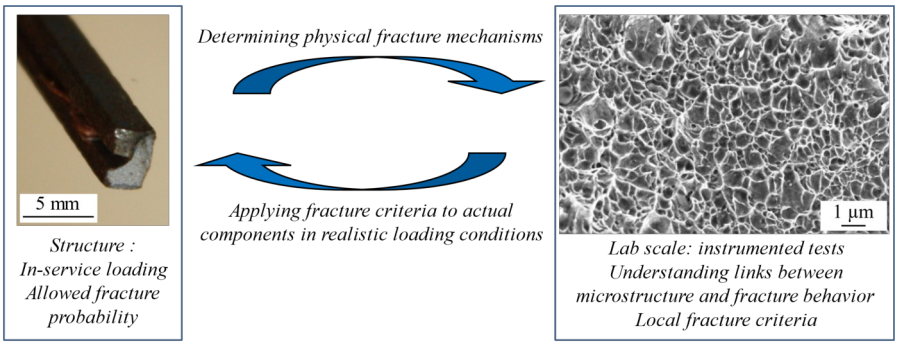

FIGURE 7.3: Principle of the local approach to fracture (here, in the case of a foil blade).

7.2 Macroscopic phenomenology of brittle cleavage transgranular fracture

7.2.1 Load vs. displacement behavior

In ceramics, cleavage fracture is generally associated with an elastic-brittle behavior. In metal alloys, plastic deformation must first occur, at least locally, in order to reach high levels of stresses that are necessary to break atomic bonds (typically, a few percent of the Young's modulus). High stress triaxiality levels close to scratches, notches, and crack tips strongly favor cleavage fracture in many materials. There are several ways to quantify the resistance to brittle fracture. The energy absorbed by the specimen (especially in impact tests, Fig. 7.4a), the fracture toughness (Fig. 7.4b) and, more simply, the fracture strain (Fig. 7.4c) are indicators of the sensitivity to brittle fracture. Nevertheless, as will be shown later in this chapter, they are not equivalent to each other. In impact tests, when the load vs. displacement curve is available (so-called "instrumented tests"), crack initiation is considered to occur at maximum load. In notched specimens, unless fracture occurs close to general yielding, stress redistribution by plastic strain often leads to a maximum in load well before crack initiation [Griffiths and Owen, 1971].

7.2.2 Macroscopic fracture mode

Macroscopic brittle failure is generally associated with fracture surfaces that are smooth and perpendicular to the maximum principal stress. The brittle part of the fracture surface frequently appears bright, which allows its area fraction (so-called "crystallinity") to be measured using a magnifier (Fig. 7.5). When zooming in, macroscopic ridges appear to spread from one or several particular locations, which are fracture initiation sites (Fig. 7.5c). If only one

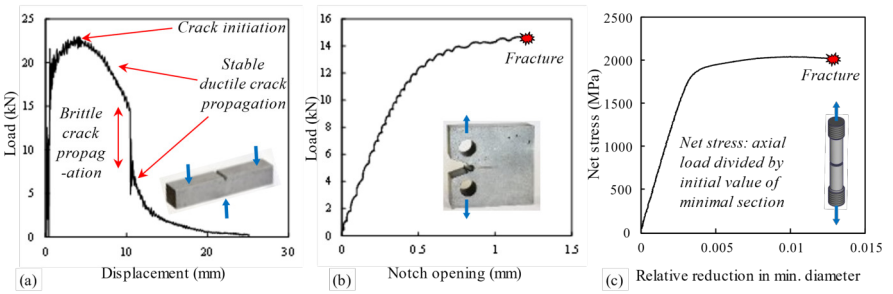

FIGURE 7.4: (a) Charpy impact toughness and (b) fracture toughness load vs. displacement curves of a low alloy ferritic steel (compact tension specimen), after [Tankoua Yinga, 2015]. (c) Net stress vs. reduction in diameter of a notched specimen, martensitic steel, after [Tioguem Teagho, 2019].

site appears (white arrow in Fig. 7.5c), fracture might be initiation controlled. If several sites appear, the fracture process was controlled by crack propagation.

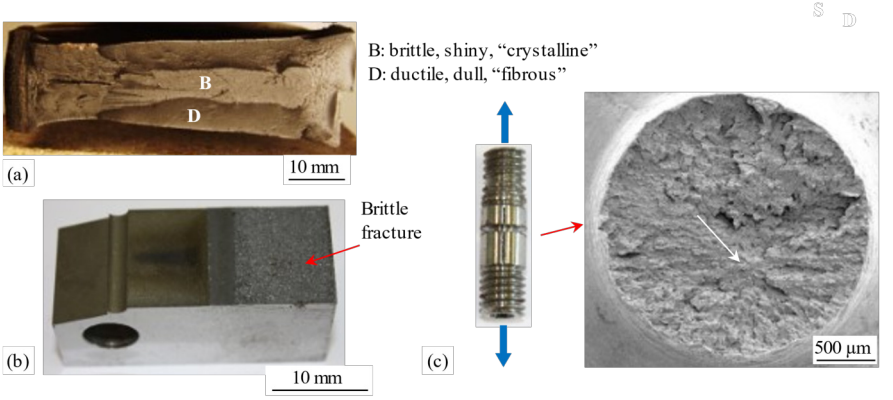

FIGURE 7.5: Macroscopic view of fracture surfaces of low alloy steels. (a) Battelle drop weight tear test specimen, low alloy steel, after [Tankoua Yinga, 2015]; (b) fracture toughness specimen; (c) axisymmetric notched specimen, after [Tankoua Yinga, 2015]. The white arrow in (c) points toward the fracture initiation site.

7.2.3 Damage development

Transgranular cleavage fracture occurs with little or no visible crack blunting, and with very low amounts of macroscopic plastic strain (*e.g.*, negligible reduction of thickness of fracture toughness specimen, as in Fig. 7.5b). When

fracture is controlled by initiation (*e.g.*, in ferritic steels at very low temperatures), no damage is observed out of the main crack, except of some crack branching; when fracture is controlled by crack propagation, arrested microcracks may be found.

7.3 Physical mechanisms of transgranular cleavage fracture

As will be detailed in this section, the cleavage fracture phenomenon occurs in three steps that are schematically represented in Fig. 7.6:

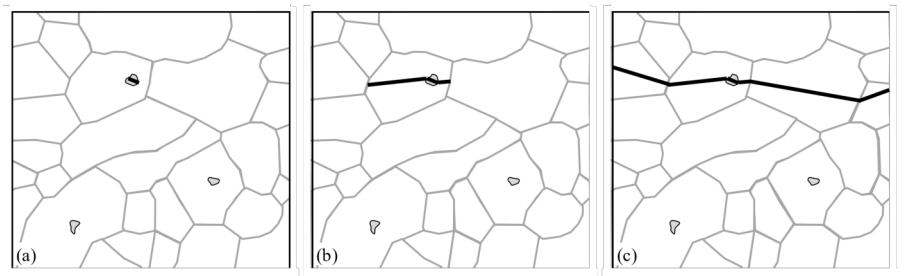

FIGURE 7.6: Brittle transgranular cleavage fracture scenario. (a) Microcrack initiation (here, by fracture of a hard particle); (b) crack propagation across the matrix and arrest at the first high-misorientation boundary; (c) propagation across that boundary and final fracture. Thin grey lines represent high-angle boundaries, and thick black lines represent the crack.

1. Initiation of a brittle crack, *e.g.*, from a particle by particle cracking or by decohesion of the particle/matrix interface (Fig. 7.6a); the phenomenon may be further assisted by local stress concentrations close to grain boundaries; in some cases, no particle can be found at the cleavage initiation site, so that cleavage is supposed to initiate from locked dislocation pile-up configurations.
2. Propagation of this microcrack into the matrix, and arrest at the first grain boundary-type obstacle (Fig. 7.6b).
3. Propagation across that grain boundary and then from grain to grain: unstable final fracture (Fig. 7.6c).

7.3.1 Crack initiation

Diffraction analysis of fracture surfaces has shown that some amount of plastic strain is necessary to trigger cleavage crack initiation, at least in steels [Newbury et al., 1974]. In many instances, yet, cleavage fracture starts from microstructural features that act as stress concentrators. These may be inclusions (Fig. 7.7a), precipitates (Fig. 7.7b), or even products from the incomplete decomposition of a parent phase (Fig. 7.7c). The crack initiation site is frequently located close to the boundary of the first cleavage facet.

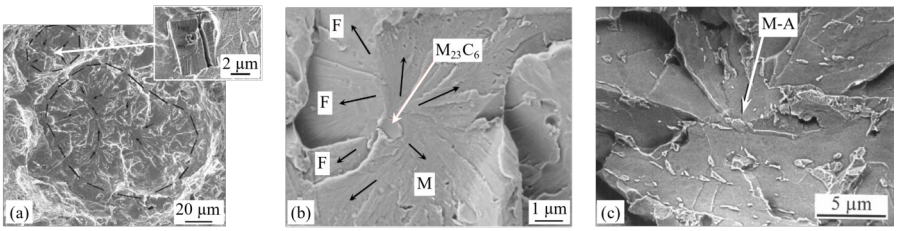

FIGURE 7.7: Cleavage crack initiation (a) from a broken TiN inclusion (inset) in a low alloy steel, after [Bilat, 2007]; (b) from a $M_{23}C_6$ carbide in a stainless steel, with propagation into ferrite (F) and martensite (M), after [Godin, 2018]; (c) from a martensite-austenite ($M-A$) constituent resulting from incomplete decomposition of austenite into bainite in a low alloy steel, after [Lambert-Perlade et al., 2004].

7.3.2 Crack propagation

Cleavage fracture occurs along preferential planes in the crystal structure, for instance, along {001} planes of ferritic iron alloys. As a consequence, cleavage fracture surfaces exhibit a number of so-called "facets". Small local crystal misorientations may result in non-planar propagation, with tiny lines within the facets that are called "rivers". The morphology of cleavage fracture surfaces is thus characterized by facets that contain rivers. In fractographic analysis, it is considered that rivers spread out from the (local) microcrack initiation point (Fig. 7.8a). These rivers may actually be steps (*e.g.*, dark features in the bright facet highlighted with an ellipse in Fig. 7.8c). They can also result from tearing of a more ductile secondary phase such as retained austenite in bainitic and martensitic steels (Fig. 7.8d).

As a consequence of the crystallographic characteristics of cleavage cracking, crack propagation across a grain boundary cannot be straight, because the geometric plane parallel to the {001} cleavage plane of one grain is generally not a {001} plane of the neighboring grains. Crack deviation is thus observed (Fig. 7.8b), making cleavage fracture surfaces rather rough at the microscopic scale. Grain boundaries are thus obstacles to cleavage crack propagation.

The strength of these obstacles depends on the grain boundary misorien-

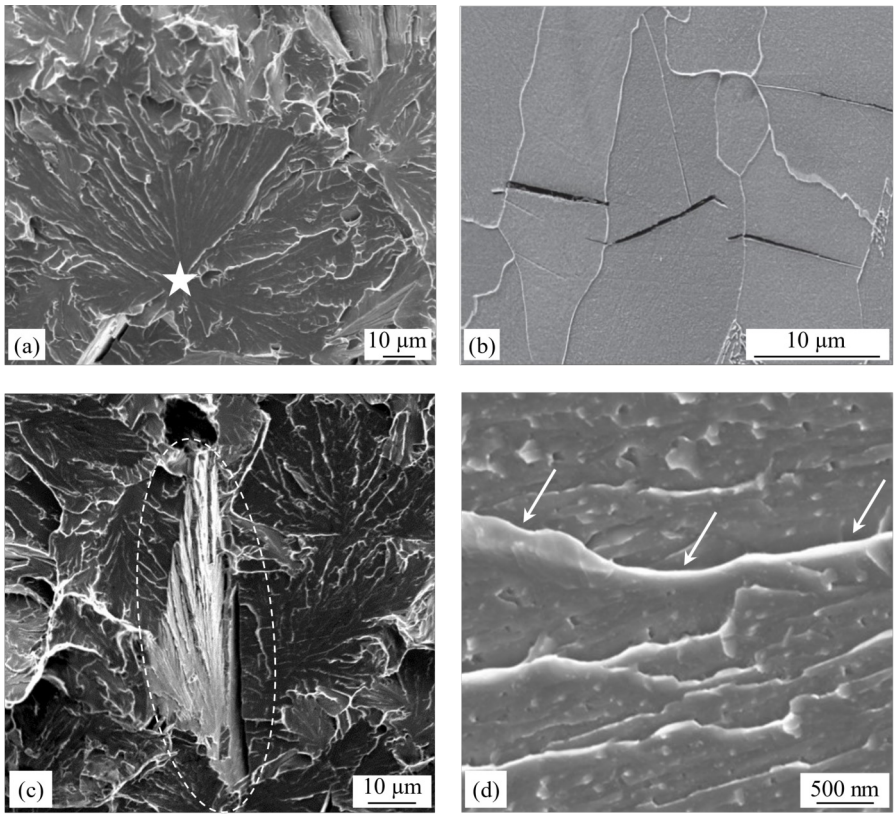

FIGURE 7.8: Propagation of cleavage fracture. (a) Cleavage facet with rivers diverging from the local microcrack nucleation site (highlighted with a star), after [Laurent, 2007]. (b) Cleavage microcracks deviated or arrested at grain boundaries: longitudinal section of an axisymmetric notched specimen of a low alloy ferritic-pearlitic steel fractured at −196 °C, after [Lambert-Perlade, 2001]. (c) Rivers resulting from final tearing of steps created by local crystal misorientations, in a facet oriented nearly parallel to the electron beam (highlighted with the dashed ellipse), after [Laurent, 2007]; (d) enlarged view of rivers resulting from ductile tearing of a secondary phase (white arrows) in a martensitic stainless steel containing retained austenite, after [Godin, 2018].

tation angle (more precisely, on the angle between the cleavage plane and the least misoriented {001} plane of the neighboring grain), but also on the local orientation of the grain boundary surface with respect to the two grains. In the so-called "tilt" configuration, crack deviation is rather easy, yet in a mixed I + II mode (Fig. 7.9a). In the so-called "pure twist" configuration, Fig. 7.9b, the crack propagation by mixed I + III mode cannot occur at once across the boundary. Either a ligament is left behind and has to be broken (this dissipates some energy), or several microcracks propagate in the next grain from the same boundary, leading to local crack branching (Fig. 7.9b). Another possibility is also local grain boundary decohesion [Gell and Smith, 1967; Lu et al., 2010]. All these phenomena significantly contribute to the dissipated energy.

Grain boundary surfaces being rarely planar, the most frequent situation is a mixed tilt + twist mode. The minimum (critical) misorientation angle that leads to microcrack arrest at a grain boundary has been measured by several authors [Gell and Smith, 1967; Qiao and Argon, 2003; Andrieu, 2013] and modelled using geometrical considerations in bicrystals [Gell and Smith, 1967; Qiao and Argon, 2003; Stec and Faleskog, 2009]. The higher the twist component, the lower the critical angle (Fig. 7.9c).

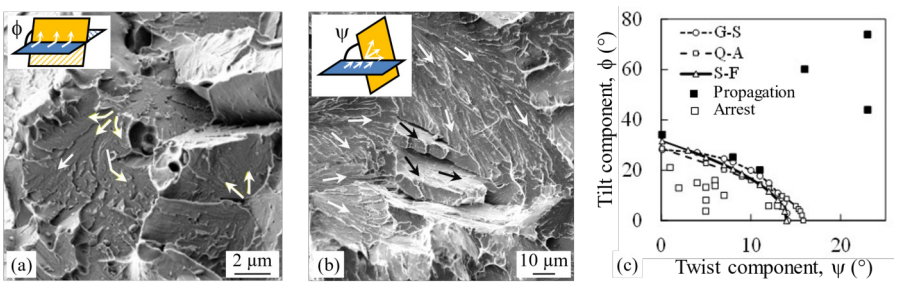

FIGURE 7.9: Propagation of a transgranular cleavage crack across a boundary in two low alloy steels. Local crack propagation directions are indicated with white arrows. (a) Tilt configuration in a martensitic steel, after [Chanh, 2022]. (b) Initiation of several parallel cleavage cracks in the same next grain (black arrows), after [Bilat, 2007]. (c) Crack propagation vs. crack arrest criterion, from topographic measurements on the fracture surface, and from Gell-Smith ($G-S$) [Gell and Smith, 1967], Qiao-Argon ($Q-A$) [Qiao and Argon, 2003], and Stec-Faleskog ($S-F$) [Stec and Faleskog, 2009] models, after [Tankoua et al., 2018].

According to the spatial distribution of grain orientations (the so-called "microtexture"), clusters of several neighboring grains, separated by boundaries that do not resist cleavage crack propagation, may be found. They have been reported as "cube grain clusters" [Ghosh et al., 2016a,b] and as "potential cleavage facets" [Tankoua et al., 2018]. They provide large cleavage facets

(Fig. 7.10a) and easy crack propagation paths, detrimental to the resistance to cleavage cracking. As they may be distributed in an anisotropic manner following manufacturing processes such as hot or cold forming, an anisotropic resistance to cleavage may occur (Fig. 7.10b-d) and brittle delamination cracks may even develop along the tensile axis of broken specimens (Fig. 7.10e). This "splitting" phenomenon tends to reduce the stress triaxiality, and thus the probability of brittle fracture normal to the loading direction; on the other hand, deviation of cleavage delamination cracks may further trigger complete brittle fracture with low amounts of absorbed energy (Fig. 7.10e) [Tankoua et al., 2018].

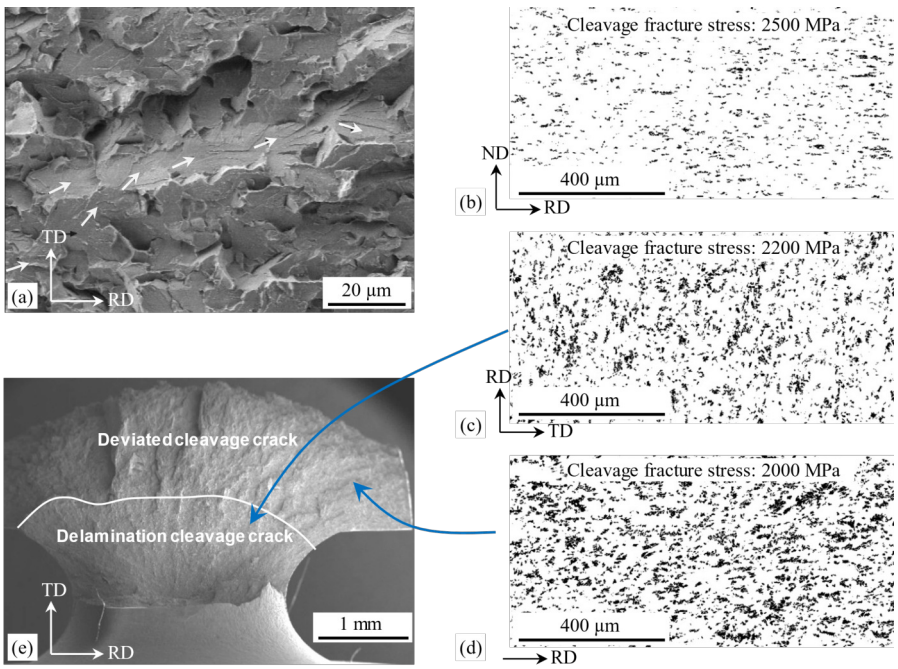

FIGURE 7.10: Effect of clusters of grains favorably oriented for easy cleavage crack propagation. (a) Easy crack propagation (white arrows) along series of cleavage facets in a low alloy steel, after [Bilat, 2007]. (b,c,d) Anisotropic resistance to cleavage cracking of a low alloy steel plate, after [Tankoua Yinga, 2015; Tankoua et al., 2018]: black regions are clusters of grains favorably oriented to fracture along the plane of the electron backscatter diffraction map; experimentally determined critical cleavage fracture stresses are indicated. (e) Broken axisymmetric notched specimen of the same steel, showing delamination by cleavage along the plane imaged in (c), followed by final fracture by cleavage crack deviation toward the tilted plane image in (d), also after [Tankoua Yinga, 2015; Tankoua et al., 2018]. RD: rolling direction, TD: transverse direction; ND: normal direction of the plate.

7.4 Experimental evaluation of the resistance to brittle fracture

There are several ways to evaluate the resistance of a given material to brittle fracture. For very brittle materials such as ceramics, glasses, very high strength fibers, and certain metal alloys (such as steels) at low temperatures, brittle fracture may occur under uniaxial tension or under bending of unnotched bars. The reduction of area at fracture ("fracture strain", ϵ_f) may be used to quantify the sensitivity to brittle fracture. In the brittle-elastic failure mode this is equivalent to considering a critical fracture stress, σ_f, as a single relationship exists between both quantities.

For materials sensitive to quasi-brittle or brittle-plastic failure, the presence of a geometric flaw, such as a notch, strongly decreases the fracture resistance. Close to the geometrical defect, the stress triaxiality is increased, so that for a given amount of plastic strain, the hydrostatic stress (and, consequently, the maximum principal stress, σ_I) is higher. The competition between ductile fracture (favored by higher amounts of plastic strain) and brittle fracture (favored by higher stress levels) is thus modified and fracture may be triggered even for low amounts of strain, *i.e.*, in a non-ductile manner. To ensure conservative design of actual components, with complex geometry or that might contain geometrical flaws, tests on notched specimens (such as the Charpy specimen shown in Fig. 7.4a) have been widely used for more than a century. The resistance of flawed specimens to brittle fracture is mainly characterized using two properties:

- Impact toughness: a specimen (generally bearing a notch) is hit by a hammer and the absorbed energy, as well as fracture surface features are determined.
- Fracture toughness: a precracked specimen is loaded (generally in a quasistatic manner) until abrupt fracture to derive the critical value of the stress intensity factor that leads to unstable crack propagation.

7.4.1 Impact toughness

In impact toughness tests, a notched specimen is hit by a hammer attached to either a pendulum (such as in the Charpy impact test, Fig. 7.11a), or to a dead weight that is allowed to fall from a given height (as in the Battelle drop weight tear test, BDWTT, Fig. 7.11b). Standardized practices are available for both kinds of tests [E28 Committee, 2022; ANSI/API (1996), 1996]. The notched test piece is loaded in three-point bending, with a given amount of impact energy that depends on the potential energy of the system just before the hammer starts falling. Typical levels of impact energy are $20 - 100\,\mathrm{kJ}$ for BDWTTs, and $300 - 750\,\mathrm{J}$ for standard Charpy impact tests.

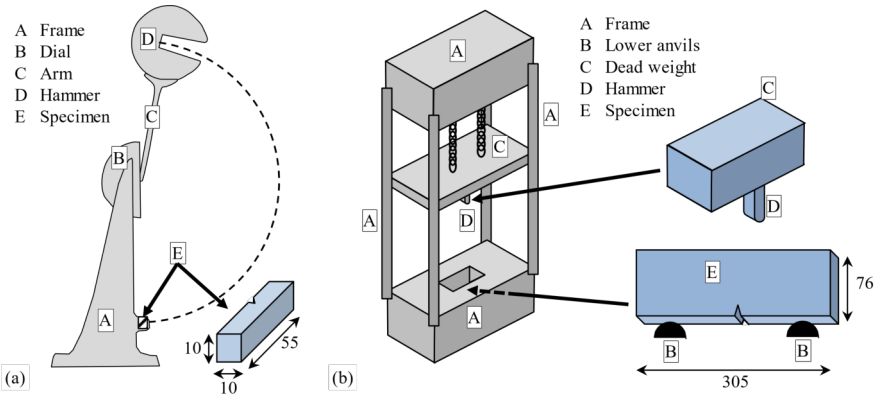

FIGURE 7.11: Impact toughness tests: (a) Charpy; (b) BDWTT. Dimensions are in mm.

Charpy tests (Fig. 7.11a) provide the total amount of energy that is absorbed by the specimen before fracture, by recording the height reached by the pendulum after hitting the specimen. Instrumented devices give access to load vs. displacement curves. In the fully brittle case, an abrupt load drop is observed well before the maximum load (Fig. 7.12a). The fracture surfaces of the specimen are then observed at low magnification (Fig. 7.12b); brittle fracture yields bright, "crystalline" fracture surfaces (Case A), whereas ductile fracture yields dull, "fibrous" surfaces (Case E). The area fraction of "bright" regions, which are attributed to brittle fracture (Case B), is estimated, this is the so-called "crystallinity" parameter. Brittle specimens show negligible deformation after fracture (Case A) whereas in ductile specimens, close to the face that is hit by the hammer (thus, loaded in compression during the bending test), the specimen width has significantly increased. The so-called "lateral expansion" on the opposite face with respect to the notch is measured there.

The total duration of an impact test is less than 0.1 s. When the specimen is not completely brittle, significant plastic deformation occurs, with a typical strain rate of a few $10^2\,\mathrm{s}^{-1}$. As a result, self-heating of the specimen close to the notch tip may go up to 150 °C for an absorbed energy of 85 J in a steel specimen, even if non-adiabatic thermal conditions prevail during the test [Tanguy et al., 2005a]. The Charpy absorbed impact energy includes contributions from both plastic deformation (if any), crack initiation, and crack propagation. The specimen preparation is easy, and the duration of the test is short, so that hundreds of specimens may be tested in an automated manner as part of production quality control procedures. The small size of Charpy specimens also allows monitoring of progressive toughness degradation under in-service conditions (*e.g.*, radiation-induced embrittlement in nuclear power plants). On the other hand, modelling of this test requires accurate knowl-

edge about the high-speed plastic flow behavior of the material and handling of contact, viscosity, and self-heating issues. For these reasons, the Charpy test is mainly used for comparison purposes, either with a reference material or with product requirements.

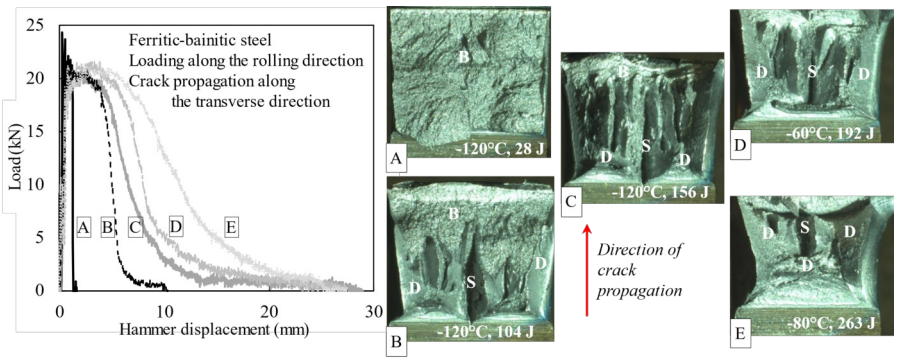

FIGURE 7.12: Instrumented Charpy impact tests. Load vs. displacement curves. Macroscopic views of fracture surfaces for various impact toughness values. B: brittle; D: ductile (shear); S; delamination split. After [Tankoua Yinga, 2015].

The BDWTT test is more severe than the Charpy test, and more representative of the ability of a material to arrest a long, propagating crack. This test involves much larger specimens (Fig. 7.11b) and the absorbed energy is generally not measured, except if an instrumented hammer is used (Fig. 7.13a). The specimen thickness, B, is the full thickness of the product (or 19 mm for thicker products). The notch is generally obtained by pressing, whereas it is machined in Charpy specimens. To avoid artefacts induced by the fabrication of the notch, the fracture surface is quantified at a distance larger than B from the notch root. It is also quantified at a distance larger than B from the face hit by the hammer (dashed box in Fig. 7.13b-c). To pass the test, the crystallinity of the fracture surface inside this region should not exceed 15 %.

Brittle fracture may appear normal to the applied stress (as in Charpy specimens). In addition, as the crack propagates over large distances (71 mm, compared to 8 mm for a standard Charpy specimen), brittle fracture may also appear along tilted planes, causing "abnormal fracture" after some ductile crack propagation (Fig. 7.13b-c). This appears in the case of an anisotropic resistance to cleavage fracture (Fig. 7.10). Cleavage crack propagation may also initiate from the compression faces (so-called "inverse fracture") or from delamination cracks (Fig. 7.13c). Such situations are less common in Charpy specimens cut from the same material, because complete fracture occurs before favorable conditions for brittle tilted cracking are met [Tankoua et al., 2018].

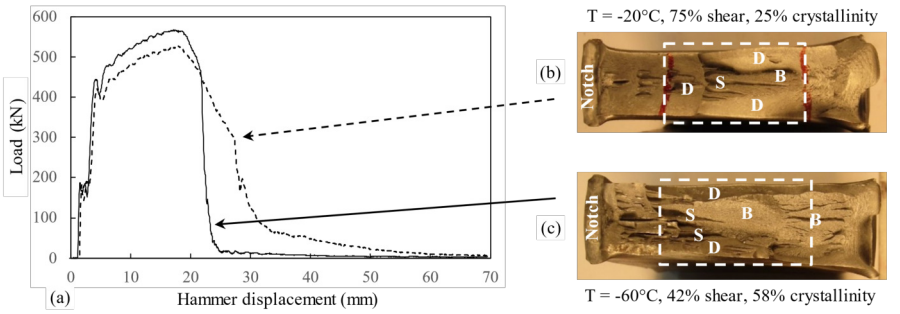

FIGURE 7.13: Instrumented BDWTT results, ferritic-bainitic steel. Load vs. displacement curves and corresponding fracture surfaces. B: brittle; D: ductile (shear); S; delamination split. The crystallinity is evaluated over the region delimited by the dashed box. After [Tankoua Yinga, 2015].

7.4.2 Fracture toughness

Fracture toughness specimens are also notched but, before the test, a sharp fatigue (pre)crack is added under conditions such that the material at the tip of that precrack is affected only over a very small distance compared to the plastic zone size expected to develop during the fracture toughness test itself. In other words, the maximum stress intensity factor, K_{max}, experienced to propagate the precrack, especially at the end of the procedure, should be well below the expected fracture toughness, K_{Ic}. Once precracked, the specimen is loaded up to fracture. There are several possible loading conditions [E08 Committee, 2022c]. Three typical specimens are shown in Fig. 7.14, namely, a three-point bending SEN(B) specimen, a compact tensile C(T) specimen, and a double cantilever tensile DC(T) specimen.

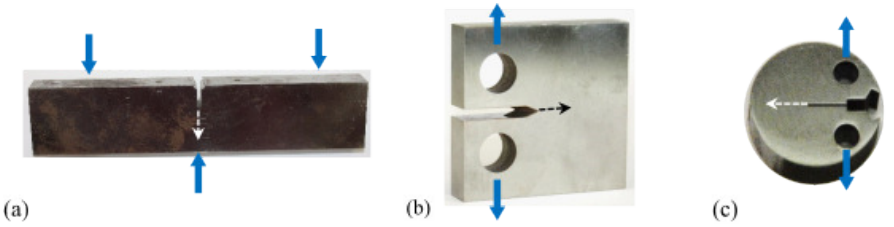

FIGURE 7.14: Typical fracture toughness specimens (untested). (a) SEN(B); (b) C(T); (c) DC(T). Thick arrows indicate the loading conditions; dashed arrows indicate the expected propagation direction of the precrack and of final fracture.

The load vs. crack mouth opening curve is recorded during the test (Fig. 7.15a). After abrupt fracture, the geometry of the precrack front is measured

(Fig. 7.15b). The fracture toughness is then determined according to formulas based on a plane strain assumption and on the linear elastic fracture mechanics (LEFM) [E08 Committee, 2022b]. For the test to be valid, plastic deformation at the tip of the precrack, as well as stable crack propagation must be very limited. The slope of a straight line, plotted between the last data point of the load vs. crack mouth opening curve and the origin, should not be lower than the stiffness of the precracked specimen by more than 5 % (Fig. 7.15a). Thus, a particularity of this test is that the validity cannot be ensured by following the procedure: a specimen may be tougher than expected, leading to an invalid determination of K_{Ic}.

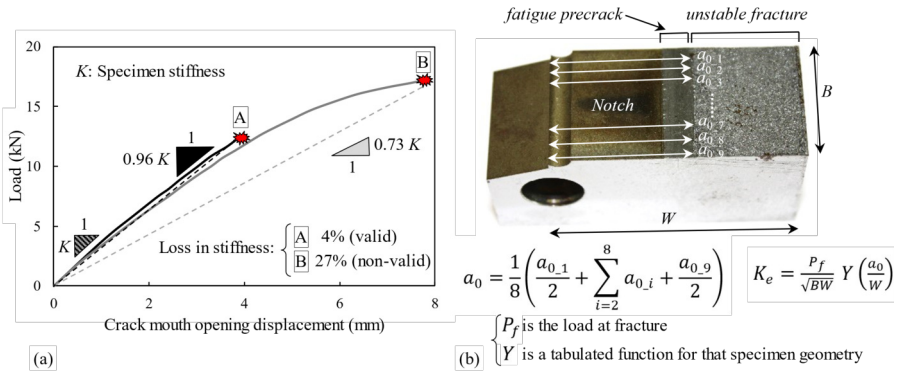

FIGURE 7.15: Fracture toughness test results. (a) Load vs. crack mouth displacement curves showing the loss-in-stiffness criterion for the test to be valid. (b) Postmortem measurement of the precrack geometry and fracture toughness calculation.

Besides analytical formulae given by LEFM, more realistic three-dimensional models, including the actual crack geometry and taking the elastic-plastic flow behavior into account, may be used. By evaluating the J-contour integral, J, and if the plastic zone size, PZS, is much smaller than any characteristic distance of the specimen (*i.e.*, the specimen thickness, B and the size of the uncracked ligament at the beginning of the test, $W - a$), an estimate of the fracture toughness, K_J, can be derived under plane strain conditions: $K_J = \sqrt{JE}$, E being the Young's modulus of the tested material. Unlike impact toughness tests (Fig. 7.16a), the loading conditions are quasistatic, self-heating of the specimen is not expected to occur (Fig. 7.16b). In addition, at least for tensile specimen geometries such as C(T) and DC(T), it is not necessary to explicitly model contact conditions between the specimen and the loading device. Numerical issues linked to the presence of a sharp crack can be overcome by using an initial crack blunting of about 15 % of the crack tip opening displacement ($CTOD$) determined at final fracture, δ_c [McMeeking, 1977].

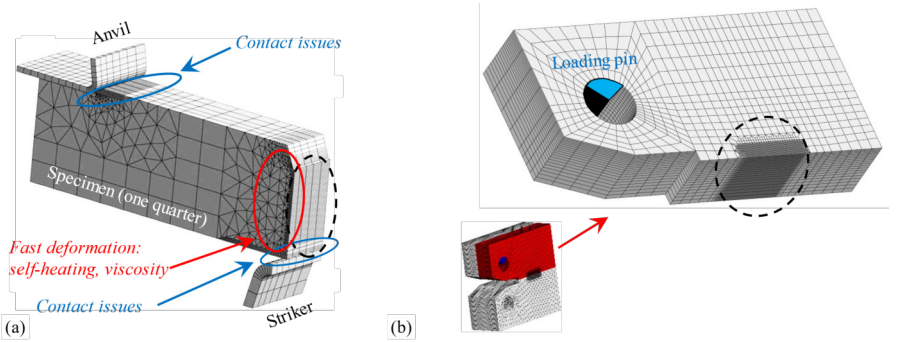

FIGURE 7.16: Comparison of impact and fracture toughness tests, based on finite element meshes of (a) one-quarter of a Charpy specimen, and (b) of one-quarter of a C(T) specimen. Continuous ellipses highlight some challenges in Charpy impact modelling. Dashed ellipses indicate the fracture process zone, with refined meshing. (a) After [Tanguy et al., 2005b], (b) after a similar mesh in the chapter on the global approach to fracture.

Brittle cleavage fracture involves crack initiation at some particular feature of the material (Fig. 7.7). Sampling effects thus lead to significant experimental scatter in fracture toughness. With increasing the specimen size, and even under plane strain conditions, the probability to find microstructural features that favor crack initiation (*e.g.*, a large brittle second phase) (Fig. 7.7a), and further unstable crack propagation (*e.g.*, a larger grain containing such a particle) (Fig. 7.6b) close to the fatigue precrack is also increased. The probability to get lower fracture toughness values thus also increases, yet with less experimental scatter than on smaller specimens. As a consequence, the experimental values of K_{Ic} depend on the specimen size, and laboratory results cannot be directly used in the brittle failure risk assessment of larger real structures.

7.4.3 Competition between fracture mechanisms: the ductile-to-brittle transition (DBT)

In many body-centered cubic metals, and in particular in the ferrite phase of iron alloys (including ferrite, bainite, and martensite microstructural constituents), the plastic flow behavior is thermally activated. At low temperatures, the yield strength is high, so that as soon as plastic flow is triggered, the critical cleavage fracture stress is reached without further significant plastic deformation; once nucleated, any microcrack instantaneously propagates in a brittle manner. This results in a brittle-plastic failure mode (left part of Fig. 7.17a). When the temperature increases, the yield strength decreases, but the critical cleavage fracture stress is much less (if any) sensitive to temperature. As a result, brittle microcracks are more easily blunted by plastic flow of the

matrix and cannot further propagate; the material is able to sustain higher load levels before being broken. Crack blunting into voids may eventually result in a ductile failure mode (right part of Fig. 7.17a). One can theoretically define a characteristic temperature, T_{GY}, below which the behavior is brittle and above which the behavior is ductile, fracture occurring after general yielding (Fig. 7.17a). In real life, however, the so-called "ductile-to-brittle transition" (DBT) occurs over a broader temperature range.

The brittle-plastic failure mode is to be avoided in structural components. To assess the sensitivity to cleavage fracture as a function of temperature, the DBT is usually characterized using impact toughness or fracture toughness tests (Fig. 7.17b). The fracture strain of notched specimens may also be used as an indicator. The crystallinity of the fracture surface decreases when the temperature increases, with two possible contributions: (i) some ductile crack advance may occur until suitable conditions for cleavage cracking, ahead of the ductile crack, are met; (ii) the cleavage crack may arrest (especially in bending tests), and final fracture may again involve ductile tearing (Fig. 7.17c).

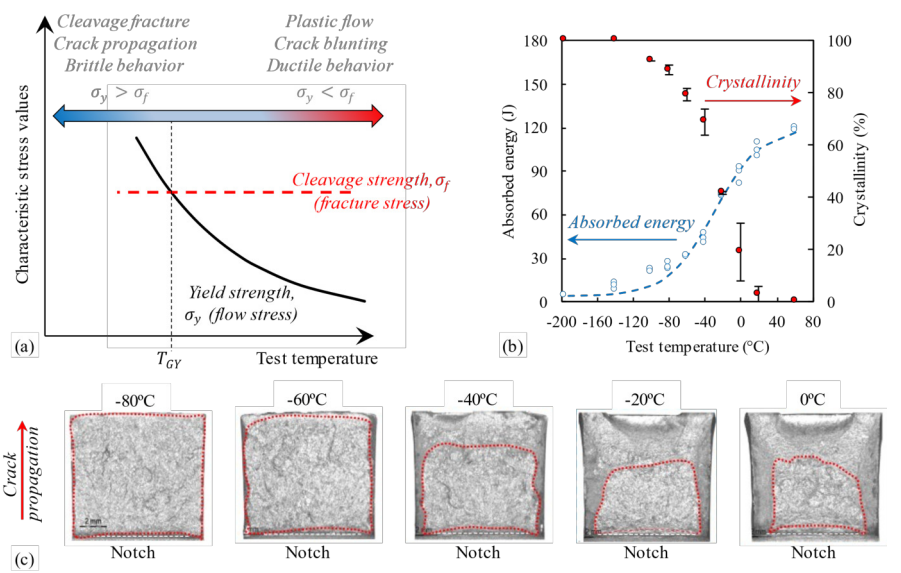

FIGURE 7.17: Ductile-to-brittle transition. (a) Schematic view of the phenomenon. (b,c) Illustration with Charpy specimens, after [Tioguem Teagho, 2019]: (b) macroscopic curves; (c) macroscopic view of fracture surfaces, with brittle regions delineated by thin continuous lines, for increasing test temperatures.

7.5 Deterministic models of brittle cleavage fracture

7.5.1 Critical cleavage fracture stress of brittle polycrystalline materials

Typical values of critical cleavage fracture stresses (a few GPa) are usually much lower than the theoretical stress required to break all atomic bonds between two crystal planes (close to one-tenth of the Young's modulus, so at least $10 - 20\,\mathrm{GPa}$ for most metals and ceramics). Stress concentration at dislocation pile-ups, in front of an obstacle such as a grain boundary, has been invoked to trigger cleavage microcrack initiation resulting in unstable fracture [Zener, 1948; Stroh, 1957] (Fig. 7.18a). Another possibility is a sessile "cracked" dislocation resulting from the reaction between dislocations from different slip systems [Cottrell, 1958] (Fig. 7.18b). In both models, triggering plastic deformation is necessary before a cleavage crack may nucleate. The microcrack stability is evaluated using an energy balance criterion initially proposed by Griffith [Griffith, 1921] for a crack of length $2c$ across the whole thickness of a plate: as soon as the elastic energy release is higher than the increase in free surface energy, crack propagation becomes unstable. The critical brittle fracture stress of a cracked plate, σ_f , was thus expressed by Griffith [Griffith, 1921] as:

$$\begin{aligned} \sigma_f &= \sqrt{\frac{2E\gamma}{\pi\nu c}} && \text{(plane stress)} \\ \sigma_f &= 2\sqrt{\frac{\mu\gamma}{\pi\nu c}} && \text{(plane strain [Griffith, 1921](1))} \end{aligned} \tag{7.1}$$

In the above equation, E is the Young's modulus, ν is the Poisson ratio, and γ is the free surface energy of the considered material. For a penny-shaped crack of diameter $2c$ in an infinite tensile-loaded body:

$$\sigma_f = 2\sqrt{\frac{\mu\gamma}{c}} \tag{7.2}$$

[Cottrell, 1958] where μ is the shear modulus of the material.

In Cottrell's model, the length of the dislocation pile-up was selected as half the grain size, D. The above Griffith-like criterion yields a value of $10\,\mathrm{J\,m^{-2}}$ for the surface energy in iron. This is ten times higher than the actual free surface energy. This so-called "effective" surface energy, now denoted as γ_p, includes the contribution of *e.g.*, tearing along rivers to form the cleavage facets (Fig. 7.8), and irreversible crack propagation across grain boundaries; in this approach, unstable cracking is propagation-controlled. Smith [Smith, 1966, 1967] represented the microcrack by a distribution of dislocations; the criterion for unstable crack propagation yielded the same result as Griffith-related criteria.

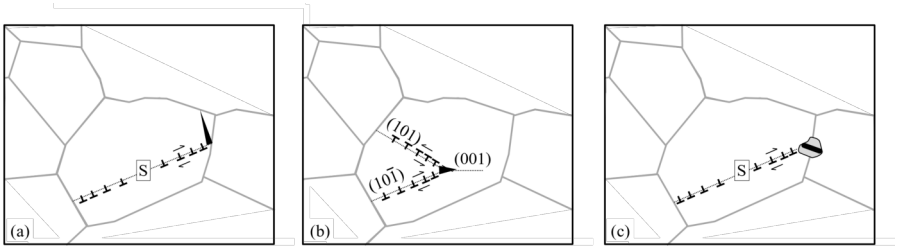

FIGURE 7.18: Schematic representation of cleavage microcrack nucleation from (a) dislocations piled up at a grain boundary; (b) the reaction between two slip systems in a cubic crystal structure; (c) dislocations piled up at a grain boundary hard particle. Note that dislocations disappear once coalesced into the crack. S is the dislocation source.

7.5.2 Influence of second phase particles on the critical cleavage fracture stress

Besides dislocation pile-ups, Mac Mahon and Cohen [McMahon and Cohen, 1965] remarked that cleavage microcracks also nucleate from intersections of twins and from stress concentration close to hard particles, such as grain boundary carbides in mild steels. This stress concentration is favored by plastic deformation. A Griffith-like criterion may thus be applied to a penny-shaped crack of the same size as the hard particle. After nucleation, either the crack immediately propagates into the surrounding grain of the matrix, or it becomes blunted by plastic deformation. After [Oates, 1968], when the cleavage crack nucleates from the intersection between a slip band (respectively, a mechanical twin) and a hard particle (Fig. 7.18c), σ_f does not depend (respectively, depends) on temperature. In both cases, the critical step is the transmission of the cleavage microcrack from the particle to the surrounding matrix grain. Plastic deformation is necessary to trigger crack nucleation at a hard particle, but a high stress level is necessary to propagate it into the matrix [Lindley et al., 1970].

Focusing on mild steels tested at $-196\,^{\circ}\mathrm{C}$, Smith [Smith, 1967, 1968] considered the nucleation of a microcrack inside a through-thickness carbide met by a twin or a slip band, with a low value of γ denoted as γ_s, *i.e.*, the free surface energy, due to the high brittleness of the carbide; for crack propagation into the matrix, he considered another, higher value of γ denoted as γ_p. If a Hall-Petch relationship is used to describe the shear stress on the dislocations, the fracture stress becomes independent of the grain size [Curry and Knott, 1979], which does not agree with experiments. Petch [Petch, 1986] extended the theory to the non-equilibrium configuration of a dislocation pile-up in front of a freshly cracked hard particle. He found an effect of both the carbide size and the grain size on the critical fracture stress. More recently, gradient plasticity associated to cohesive zone models have been applied together with

full field finite element calculations to determine a variety of crack initiation and propagation scenarios in a bicrystal containing a hard, brittle particle [Giang et al., 2018].

Critical cleavage fracture stresses were first determined using plain tensile specimens of mild steels tested at very low temperatures, then, using notched specimens tested at the temperature for which fracture occurred at the onset of general plastic yielding, T_{GY} (Fig. 7.17a). A popular example is the three-point bending specimen proposed by Griffiths and Owen [Griffiths and Owen, 1971]. Stress analysis was first conducted using the slip line theory by assuming an elastic-perfectly plastic flow behavior; by introducing linear work hardening in the constitutive behavior, Griffiths and Owen showed that the critical cleavage fracture stress, σ_f, of a Fe−Si alloy (determined at T_{GY}) was, in fact, independent of temperature.

The values of σ_f are now currently determined by finite element analysis of notched specimens, even after the onset of general yield ($T > T_{GY}$) (Fig. 7.19a), provided that the constitutive behavior is first thoroughly characterized. For each broken specimen, the fracture initiation site is determined by fractography. Then, the loading history at that point is estimated using the finite element calculations, so that a value of the critical cleavage fracture stress is determined for every specimen. It can then be plotted as a function of temperature or of some microstructural parameter. For instance, in a martensitic stainless steel, Godin [Godin, 2018] showed that the value of σ_f was independent of the cooling rate; on the other hand, the ductile-to-brittle impact toughness transition temperature was inversely proportional to the amount of austenite retained into films between martensite laths, that was dictated by the cooling rate (Fig. 7.19b,c). Retained austenite films did not influence σ_f but strongly increased the amount of plastic strain that was necessary to reach σ_f at the cleavage fracture initiation site (Fig. 7.19c).

7.5.3 Estimation of the fracture toughness from the critical cleavage fracture stress

The concept of σ_f cannot be directly applied to the LEFM analysis of precracked specimens, *i.e.*, to the determination of K_{Ic}: as soon as the specimens are loaded, the stress field becomes infinite at the crack tip, so that the value of σ_f is reached ahead of the crack front. Except for very brittle materials such as glasses, local plastic yielding occurs before cleavage fracture. This paradox is solved by considering the stochastic character of cleavage fracture: the criterion σ_f must be met over a region where the probability to find a cleavage crack initiation site is reasonably high. In the RKR model [Ritchie et al., 1973], this region is quantified by a characteristic distance, X_c, ahead of the crack tip, together with a Hutchinson-Rice-Rosengren [Hutchinson, 1968; Rice and Rosengren, 1968] stress field, using the strain hardening exponent of the material, n. According to [Ritchie et al., 1973], the value of X_c should be slightly higher than the grain size (*i.e.*, the size of a cleavage microcrack).

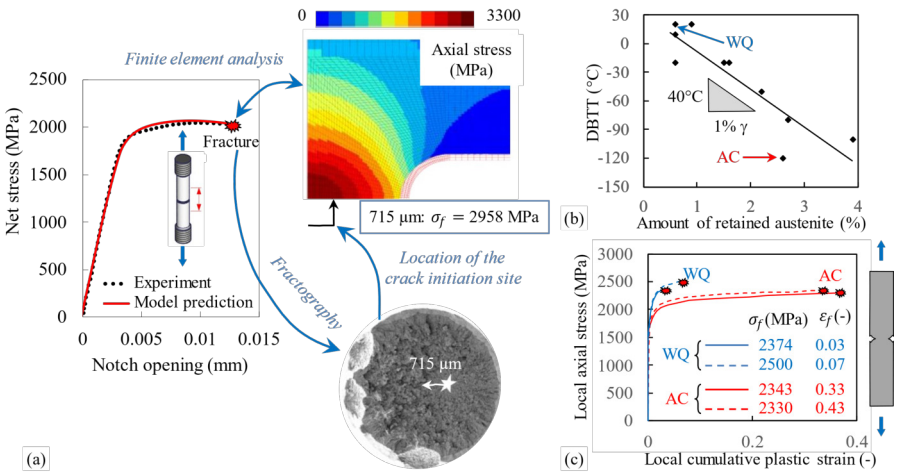

FIGURE 7.19: (a) Determination of σ_f from fractography associated to finite element analysis of notched specimens, high strength martensitic steel, after [Tioguem Teagho, 2019]. (b) DBT in impact toughness (subsized Charpy) of a martensitic stainless steel, as a function of the amount of retained austenite, and (c) typical loading history at the fracture initiation point of double edge V-notched specimens of the same material, for two amounts of retained austenite, after [Godin, 2018]. WQ: water-quenched material (little amount of retained austenite); AC: air-cooled material (higher amounts of retained austenite).

From this model, the higher the temperature, the lower the yield strength, so that to reach σ_f over the critical distance X_c, work hardening (thus higher amounts of plastic strain) must be involved, which increases the value of K_{Ic}. The opening stress reaches its maximum ahead of the elastic-plastic boundary along the ligament, again due to the necessary work hardening before cleavage fracture.

The physical meaning of the X_c parameter is still not clear. Knott [Knott, 1978] considered the influence of the grain size and of the size of carbides, in a variety of steel families. In his coarse ferritic microstructures, cleavage was initiation-controlled and started from carbides with a low value of γ_p ($14\,\mathrm{J\,m^{-2}}$). In finer ferrite microstructures, coarse carbides were rare and X_c had to be increased up to several times the grain size. In bainite and martensite, carbides were much finer, so that carbide cracking led to smaller cracks. Cleavage cracking may then be controlled by the propagation of the microcrack across the first high-angle grain boundary with the help of dislocation pile-ups, as reported experimentally [Naylor and Krahe, 1974]. This leads to higher values of γ_p ($120\,\mathrm{J\,m^{-2}}$) [Knott, 1978]. As a whole, the fracture toughness is controlled by the size of the microstructure (*i.e.*, of the unit crack path) and by the temperature-dependent yield strength and plastic flow behavior,

but σ_f only depends on the microstructure, for a given physical fracture mechanism [Bowen et al., 1986].

7.6 Probabilistic modelling of brittle cleavage fracture

To improve the resistance to cleavage fracture, especially for components with high safety requirements, the average value, but also the scatter in experimental data must be predicted by taking physical mechanisms into account. This allows identification of the most efficient microstructural actuators and their implementation in future materials processing stages. There are several sources of scatter, namely, the scattered distribution of particle and grain size (see the scenario in Fig. 7.6), and the heterogeneous nature of stress distribution in polycrystals, associated to local strain incompatibilities. To this aim, weakest link theories have been developed and applied, especially in the case of steels.

7.6.1 Criteria directly based on microstructural heterogeneity

First of all, the microstructure of the matrix itself is of prime importance in the resistance to cleavage fracture. For instance, fine martensite packets provide smaller crack paths that coarse upper bainite packets, so that the fracture toughness of mixed bainitic-martensitic steels strongly depends on the amount of bainite. Hagiwara and Knott [Hagiwara and Knott, 1982] started from Gaussian distributions of fracture toughness values for bainite and for martensite, with the same standard deviation. The fracture toughness of the mixed microstructure was modelled as a weighted average of both distributions, the weight being the bainite fraction multiplied by a cleavage sensitivity coefficient of bainite with respect to martensite, α (1.5 to 2) fitted on the experimental fracture toughness distribution; the value of α was similar to the ratio between inverse square roots of the average cleavage facet size of bainite and of martensite (1.9). For a given average fraction of bainite, the scatter in fracture toughness resulted from sampling of the microstructure by the front of the fatigue precrack (and the associated plastic zone).

Starting from the application of Smith's model to mild steels, Curry and Knott [Curry and Knott, 1978] showed that in spheroidized steels, σ_f could also be estimated from a Griffith-like criterion (penny-shaped crack, $\gamma_p = 14\,\mathrm{J\,m^{-2}}$) using the 95^{th} percentile of the carbide size distribution. Yang et al. also determined the carbide size distribution in bainitic steels; the fracture toughness was globally correlated with the size of carbides, but not with the bainite packet size. By estimating local stress fields with a finite element method, and by comparing the stress profile along the ligament with the dis-

tance between the fracture initiation site and the precrack front, they concluded that cleavage nucleation could occur under a stress between $0.85\sigma_{max}$ and σ_{max}, σ_{max} being the maximum value of the opening stress along the ligament. Tioguem [Tioguem Teagho, 2019] measured the carbide size distribution in several quenched and tempered variants of the same martensitic steel. He then calibrated the defect size in Smith's model from the actual critical opening stress estimated by finite element simulation at the experimental crack initiation site (Fig. 7.19a); the resulting value corresponded to the 98^{th} percentile of the carbide size distribution; it actually also corresponded to the size of carbides found at the cleavage nucleation sites.

7.6.2 Local approach to fracture: principle and first models

Probabilistic models aim at quantitatively relating the scatter in resistance to brittle fracture to the inhomogeneous distribution of microstructural features governing initiation and unstable propagation of cracks. To do so, the statistical distribution of microstructural features is first quantified; a number of fracture tests are carried out to quantify the scatter in macroscopic fracture resistance (*e.g.*, fracture toughness). The probabilistic models are based on a weakest-link theory; the loaded component (or laboratory specimen), hereafter the "specimen" for the sake of simplicity, is divided into a number of independent smaller regions, each of them of volume V_0 and experiencing a quasi-homogeneous stress and strain history, together with a stochastic description of microstructural features that represent potential brittle cracks. The survival probability of the specimen is the product of the survival probabilities of all these small regions. The loading history of each volume is given by a mechanical analysis of the specimen, either using available analytical solutions to two-dimensional mechanical problems [Evans, 1983; Beremin et al., 1983], or by finite element analysis of two-dimensional [Curry and Knott, 1979] and, nowadays, of three-dimensional problems.

For instance, Curry and Knott [Curry and Knott, 1979] combined available results of stress fields ahead of the crack front, in plane strain conditions, with their experimental carbide size distributions for two different steels, again with a Griffith-like fracture criterion for unstable crack propagation from broken carbides into the rest of the material.

Evans [Evans, 1983] also considered sampling of cracked carbides by the so-called "active zone" ahead of the precrack front. In their model, the shape of this active zone is defined by a heuristic function, independent of the location across the specimen thickness. The local mechanical loading is described by a HRR stress field. The "active zone" is split into independent strips, the long dimension of the strips being parallel to the crack propagation direction. The fraction of broken strips can thus be determined for any applied stress intensity factor, K, as it is equal to the fracture probability of individual strips. As soon as a given fraction (typically, 50 %) of the total number of strips is cracked, the specimen is considered to break. This enables to derive a fracture toughness

distribution from the distribution of carbide strength values, S, thanks to a Griffith criterion and a weakest-link theory for each independent strip, with:

$$\begin{aligned} G(S) &= \left(\frac{S-S_u}{S+S_0}\right)^m \qquad \text{if} \qquad S \geq S_u \\ G(S) &= 0 \qquad\qquad\quad \text{otherwise} \end{aligned} \tag{7.3}$$

In the above equation, S_u is a material parameter. Evans' model thus directly links the fracture toughness, K_{Ic}, to the statistical distribution of carbide strength, $G(S)$. Nevertheless, as the fraction of cracked strips is a fixed parameter, the statistical distribution of K_{Ic} cannot be determined.

As a whole, these first models are able to relate the toughness with relevant measurements of microstructural heterogeneity. Nevertheless, they are unable to predict the scatter of fracture toughness, as well as size effects induced by the stochastic character of cleavage fracture.

7.6.3 The Master Curve approach

From an experimental point of view, fracture toughness determination is far more expensive than impact toughness determination, so that impact toughness values are more readily available than fracture toughness values. On the other hand, using laboratory fracture toughness data to assess the behavior of real structures, while not direct, is still easier than using impact toughness data. For these reasons, correlations between impact toughness and fracture toughness values have been searched for in a variety of steels and led to the so-called "Master Curve" approach [E08 Committee, 2022a; Wallin, 1991]. The Master Curve approach assumes that the critical radius of a particle that might break depends on its size (via a Griffith criterion) but also on temperature. The distribution of particle size, r is described with the following probability density, $p(r = r_0)$:

$$p(r - r_0) = \frac{c^{a-1}}{(a-2)!}\left(\frac{r_0}{\bar{r}}\right)^{-a} \exp\left(-\frac{c}{r_0/\bar{r}}\right) \tag{7.4}$$

c, $\bar{r}$ and a being model parameters.

The effective surface energy in the Griffith criterion, γ_p, is the sum of the free surface energy, γ_s, and of a temperature-dependent term, w_p, that represents the temperature dependence of the mobility of dislocations (T being the test temperature, in Kelvin):

$$\begin{aligned} \sigma_f &= \sqrt{\frac{\pi E(\gamma_p + w_p)}{2(1-\nu^2)r_0}} \\ \text{with } w_p &= w_0 + (w_p(0) - w_0)\exp(mT) \end{aligned} \tag{7.5}$$

where w_0, $w_p(0)$ and m are model parameters.

A weakest-link assumption allows calculating the survival probability of

the specimen, $1 - p_f$, as the product of all elementary survival probabilities over the plastic zone size, PZS, by considering the total number density of particles, N_a, and the fraction F of particles that are eligible to fracture (typically, 0.1 % to 1 %):

$$1 - p_f = 1 - \prod_{X=0}^{PZS} \left(1 - p(r \geq r_0)\right)^{N_a B F dX} \tag{7.6}$$

Here, B is again the specimen thickness (Figure 7.15).

The calculations are carried out as follows. The plastic zone is modelled as a wedged region ahead of the crack tip, centered on the crack plane, of length X_p and extending over an angle θ to either side or the crack plane. For any value of the stress intensity factor, K_I, and for every distance to the crack tip, X, in the plastic zone, the local stress level is estimated from an analytical formula previously calibrated using finite element calculations results. Then, the local value of the critical radius, r_0 is calculated. By using the above equation, the fracture probability for that value of K_I is determined. By repeating the calculation over all possible values of K_I, a failure probability distribution $p_f(K_I)$ is derived. Its expectation value, K_{If}, is then compared with the average value of K_{Ic} over the experimental data base.

The above Eq. 7.6 can be approximated as follows [Wallin, 1984]:

$$p_f = \approx 1 - \exp\left(-N_a B F \sin\theta \int_{X=0}^{X_p} p(r = r_0) \cdot X dX\right) \tag{7.7}$$

In the above Eq. 7.7, θ is taken as constant. X can be further normalized by using $U = \frac{X}{(K_{Ic}/\sigma_y)^2}$. $(K_{Ic}/\sigma_y)^2$ is proportional to the plastic zone size, PZS, with σ_y the flow stress. Eq. 7.7 then becomes:

$$p_f = \approx 1 - \exp\left(-N_a B F \sin\theta \left(\frac{K_{Ic}}{\sigma_y}\right)^4 \int_{U=0}^{U_p} p(r = r_0) \cdot U dU\right) \tag{7.8}$$

with $U = \frac{X_P}{(K_{Ic}/\sigma_y)^2}$.

In [Wallin, 1984], it is further assumed that the integral term in the above Eq. 7.8 is constant (although the bounds of the integration actually depend on the fracture toughness through the definition of U). As a result, the fracture toughness probability density can be rewritten as follows (which represents a Weibull distribution with a Weibull modulus, m_1, usually taken equal to 4):

$$p_f \approx 1 - \exp\left(C \cdot K_{Ic}^{m_1}\right), \tag{7.9}$$

C being a constant.

In practice, Wallin [Wallin, 1984] assumes that below a minimum threshold

value, K_{min}, of K_I, no brittle crack propagation can occur. K_0 being a model parameter, the above Weibull distribution then becomes:

$$p_f \approx 1 - \exp\left(-\left(\frac{K_{Ic} - K_{min}}{K_0 - K_{min}}\right)^{m_1}\right). \tag{7.10}$$

The value of K_{min} is adjusted to keep $m_1 \approx 4$, which usually results in $10 - 20\,\mathrm{MPa}\sqrt{\mathrm{m}}$. In the following, it is assumed that $m_1 = 4$.

The effects of the specimen size (thickness, B) and of the testing temperature are taken into account in the K_0 parameter. A reference thickness of one inch (so-called "1T") is generally considered. At given temperature, the product $(K_{Ic}(B) - K_{min})^4\, B$ is considered as constant owing to the weakest-link assumption. Then, from the above Eq. 7.10, the fracture toughness for any specimen thickness B may be derived, provided that small scale yielding conditions are fulfilled for both values, B and $1T$, of the specimen thickness:

$$K_{Ic}(B) = K_{min} + (K_{Ic}(1T) - K_{min})\left(\frac{1T}{B}\right)^{1/4}; \tag{7.11}$$

$$p_f \approx 1 - \exp\left(-\frac{B}{1T}\left(\frac{K_{Ic} - K_{min}}{K_{0\_1T}(T) - K_{min}}\right)^4\right). \tag{7.12}$$

The value of $K_{0\_1T}(T)$ is related to the median value (*i.e.*, the 50^{th} percentile) of the probability distribution, $K_{med\_1T}(T)$, which is also a function of temperature T only, by $K_{med\_1T} \approx 1.1 K_{0\_1T}$. A simple, empirical equation (see Equation 7.13) is then used to determine the temperature dependence of K_{med_1T} and thus, the global shape of the p_f vs. T curve:

$$K_{med\_1T}(T) = 30 + 70\exp\left(0.019\cdot(T - T_0)\right) \tag{7.13}$$

with T_0 the value of temperature for which $K_{med\_1T}(T) = 100\,\mathrm{MPa}\sqrt{\mathrm{m}}$.

A heuristic relationship is then used to estimate the value of T_0 using impact toughness properties. For instance, the temperature for which the impact toughness is 28 J, T_{28J}, has been shown to be correlated to T_0 with a shifting parameter, $C(B)$, only dependent on the specimen thickness, B [E08 Committee, 2022a].

Starting from impact toughness data (Fig. 7.20a), the T_0 temperature may be estimated by using the shifting parameter, $C(B)$. Then, using Eq. 7.12 and Eq. 7.13, fracture toughness properties may be estimated as a function of temperature (Fig. 7.20b,c).

This method may work well for ferritic steels but must be empirically adapted for other steel microstructures such as bainite [Lambert-Perlade et al., 2004].

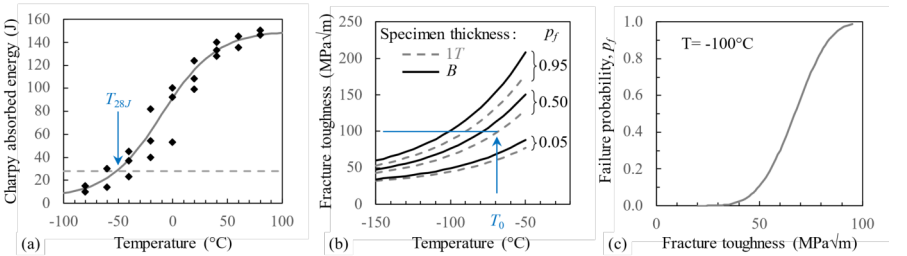

FIGURE 7.20: Schematic view: application of the "Master Curve" approach. (a) Impact toughness data (diamonds); from the fitted curve, $T_{28J} = -100\,°\mathrm{C}$. (b) After determination of $T_0 = -70\,°\mathrm{C}$ by using the empirical shifting parameter $C\,(B)$, the fracture toughness is predicted as a function of temperature, for specimen thickness $1T$ then $B = 12.5\,\mathrm{mm}$, respectively, by using Eq. 7.13 and inverting Eq. 7.12. For $T = T_0$, $K_{med\_1T} = 100\,\mathrm{MPa}\sqrt{\mathrm{m}}$. (c) For a given temperature, prediction of the statistical distribution of fracture toughness values.

7.6.4 Local approach to fracture: the Beremin model

In the Beremin model [Beremin et al., 1983], the process zone is taken as the plastic zone PZ of the considered specimen or component. The minimum amount of plastic strain used to delineate the PZ does not affect the results, as long as it remains small. The PZ is divided into N independent elementary regions, each of volume V_0 (V_0 being a model parameter). A weakest-link assumption is also made. Within each of the N elementary regions, a cleavage microcrack may initiate from microstructural defects, such as hard secondary phases. The nature of the defects is determined by fracture surface examinations. The size distribution of these defects, and thus, of resulting microcracks is described with a two-parameter power-law equation:

$$p(a) = \alpha \cdot a^{-\beta} \tag{7.14}$$

with a being now the defect size, and α and β model parameters that depend on the value of V_0. A Griffith-like criterion is used to relate the critical defect size, a_c, to the local stress level, σ, so that the fracture probability, $P(\sigma)$, under the local stress level, is given by:

$$\begin{aligned} \sigma &= \sqrt{\frac{\pi E \gamma_s}{2(1-\nu^2)a_c}} \\ \text{so that } a_c(\sigma) &= \frac{\pi E \gamma_s}{2(1-\nu^2)\sigma^2} \\ \text{and } P(\sigma) &= \int_{a_c(\sigma)}^{+\infty} p(a)da. \end{aligned} \tag{7.15}$$

Combining this probability density with the size distribution of defects yields:

$$P(\sigma) = \left(\frac{\sigma}{\sigma_u}\right)^m \tag{7.16}$$

with $m = 2\beta - 2$ and in plane strain conditions,

$$\sigma_u = \left(\frac{m}{2\alpha}\right)^{1/m} \sqrt{\frac{2}{\pi}\frac{E\gamma}{1-\nu^2}}. \tag{7.17}$$

With the plain strain assumption, the scatter in fracture probability, represented by parameter m, is thus directly related to the size distribution of defects, assumed to be uniform in space. In the more general case, m is a fitting parameter. The plastic constraint and the stress state are directly taken into account by calculating the so-called Weibull stress, σ_W, which is the $m-th$ moment of the distribution of the maximum principal stress, σ_I, over the plastic zone PZ:

$$\begin{aligned} \sigma_W &= \left[\int_{PZ} \sigma_I^m \frac{dV}{V_0}\right]^{1/m} \\ P_f &= 1 - \exp\left[-\left(\frac{\sigma_W}{\sigma_u}\right)^m\right]. \end{aligned} \tag{7.18}$$

This assumes that the individual fracture probability of each elementary volume V_0 in the PZ is, in fact, small. For a given value of V_0, the two m and σ_u parameters are adjusted on experimental results. This can be made using tensile tests on axisymmetric notched specimens (Fig. 7.21a), such as those shown in Fig. 7.4c. The effect of the specimen size and the possible loss of plastic constraint are implicitly taken into account in the model through the calculation of the Weibull stress by integration over the PZ (Fig. 7.21a). On the other hand, the maximum principal stress depends on the plastic flow behavior, which implicitly takes temperature and loading rate effects into account. Once the two model parameters are identified (Fig. 7.21b), the approach may be applied to any structural component (Fig. 7.21c). In practice, the σ_u parameter must often be rendered temperature-dependent, in order for the model to reasonably predict the DBT behavior.

For ferritic and bainitic steels with low inclusion levels, typical values of m and σ_u are close to 20 and about $2000 - 3000$ MPa, respectively [Tanguy et al., 2005b]. Lower values of the Weibull exponent m may be found (*e.g.*, around 7) by introducing a threshold value of fracture toughness, K_{min}, as in the Master Curve approach ; the consequence is that the value of σ_u becomes very high (close to 6600 MPa, [Gao et al., 2005]).

In plane strain conditions, and assuming a power-law flow hardening behavior which leads to HRR stress and strain fields, the fracture toughness predicted by the Beremin model only depends on the plastic flow behavior and on the product $K_{Ic}^4 B$ (as in the Master Curve model if $K_{min} = 0$). The

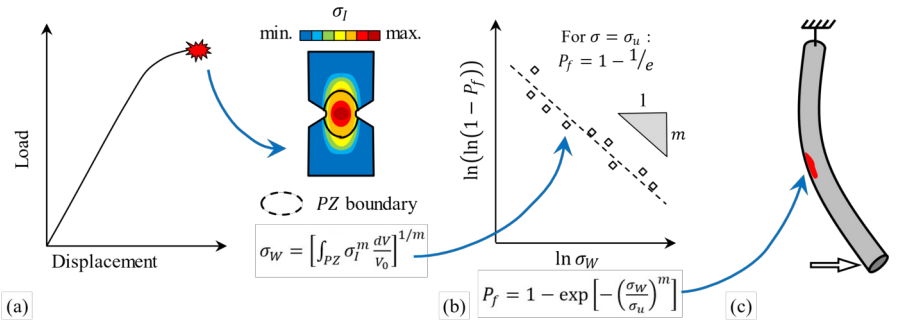

FIGURE 7.21: Principle of the Beremin model. (a, b) Calibration of the Beremin model: (a) determination of the Weibull stress; (b) calibration of the two parameters m and σ_u. (c) Application of the calibrated model to another component.

effect of temperature is driven by the evolution of the yield strength, σ_y, so that $K_{Ic}\sigma_y^{(m/4)-1}$ is constant.

The Beremin model has further been applied to brittle intergranular fracture [Kantidis et al., 1994], and to prior ductile tearing of large clusters of sulfide inclusions in the DBT [Renevey et al., 1996].

A variant of the Beremin model does not consider the maximum principal stress only, but a weighted average of the maximum principal stress and the hydrostatic stress. This aims at taking the orientation of harmful particles and of crystallographic cleavage fracture planes into account. The effect is significant in the case of short cracks and loss of plastic constraint, but not for long cracks [Boåsen et al., 2019].

In order to take the polycrystalline character of many cleavage-sensitive materials into account, full field crystal plasticity calculations have been coupled to the Beremin approach in the so-called "Microstructure informed brittle fracture" (MIBF) model [Forget et al., 2016]. In this model, additional scatter is introduced owing to heterogeneous strain incompatibility between neighboring grains. The local stress acting in each elementary volume V_0 is thus scattered around the maximum principal stress considered in the Beremin model, σ_I. This scatter is determined by adjusting a probability distribution on a set of full field crystal plasticity calculations of polycrystalline aggregates. The number density of particles, as well as the particle size distribution are determined experimentally. The only free parameter of the model is the free surface energy used in the Griffith criterion, γ. In the considered bainitic steel, a best fit yielded a very reasonable value of $8.18\,\mathrm{J\,m^{-2}}$ for γ. More details may be found in [Forget et al., 2016].

7.6.5 Effects of plastic strain on the sensitivity to cleavage fracture

The *geometric* effect of plastic strain on the sensitivity to cleavage fracture may be taken into account through the change in true stress, as in [McMahon and Cohen, 1965]. It also modifies the grain size and, in particular, the size of any crack arrested at high angle grain boundaries, see Fig. 7.6b. Under monotonous tensile loading, and assuming that plastic flow involves no volume change, a strain-corrected Weibull stress may thus be calculated as a function of the maximum principal strain, ε_I [Lambert-Perlade et al., 2004; Beremin et al., 1983; Hahn, 1984; Martín-Meizoso et al., 1994; Margolin et al., 1997]; for instance [Beremin et al., 1983]:

$$\sigma_W = \left[\int_{PZ} \sigma_I^m \frac{dV}{V_0} \exp\left(-\frac{m\varepsilon_I}{2}\right)\right]^{1/m}. \tag{7.19}$$

Another effect of plastic strain is early fracture (or interfacial decohesion) at hard second phases such as carbides. If, during that stage, the material is not brittle (*e.g.*, in ferritic steels, if the temperature is high enough), nucleated microcracks may blunt by plastic deformation, transforming into voids instead of propagating. As a result, a significant fraction of cleavage initiation sites is, in fact, no longer active in the fracture process. This is the origin of the so-called Warm Prestress (WPS) effect [McMahon and Cohen, 1965; Ripling and Baldwin Jr., 1951; Lindley, 1966, 1967; Gurland, 1972]. As a result, both the yield strength and the cleavage fracture stress increase [Margolin et al., 1997; Knott, 1967; Groom and Knott, 1975]. The change in strain hardening and, more generally, the strain history may be taken into account in the cleavage crack initiation models from inclusions [Gao et al., 2005; Ruggieri and Dodds, 2015; Bordet et al., 2005; Wallin and Laukkanen, 2006; Bernauer et al., 1999; Stöckl et al., 2000]. A review of strain history effects can be found in [Pineau, 2006].

More recently, the modification of microtexture induced by prior plastic strain (such as cold forming process, or even plastic strain developed during the fracture test itself in the DBT) has been considered. The anisotropic size and spatial distribution of clusters that are prone to give large cleavage facets, when loaded along particular tensile directions, has been shown to also affect the anisotropic sensitivity to cleavage fracture (Fig. 10) [Tankoua et al., 2018; Baldi and Buzzichelli, 1978]. This distribution may be controlled by modifications of the processing history [Tankoua et al., 2022].

7.6.6 Taking the full cleavage fracture scenario into account in the local approach to fracture

Going back to the cleavage fracture scenario of Fig. 7.6, major microstructural sources of scatter in cleavage fracture resistance are the distribution of defects that initiate cleavage microcracks, Fig. 7.6a, and the size distribution

of grains, Fig. 7.6b (or of clusters of favorably oriented grains, Fig. 7.10). Three events must occur in sequence for cleavage fracture to occur from the actual critical region: (i) onset of plastic strain, at least in that region; (ii) initiation of a microcrack by *e.g.* fracture of a hard particle, Fig. 7.6a, and propagation into the neighboring matrix grain, Fig. 7.6b; (iii) propagation across the first high-angle boundary, Fig. 6c. The so-called "double barrier" model was developed to take these successive events into account by conditional probability calculations, as follows [Lambert-Perlade et al., 2004; Martín-Meizoso et al., 1994]. In this model, the probability for a crack to initiate from a particle is a function of the local amount of plastic strain. It can be determined by knowing the fracture stress of the particles (or even its probability distribution), and by using a micromechanical model to derive the stress in the particle, σ_p, from the stress-strain field in the surrounding matrix (Fig. 7.22a). This requires experimental data that are not readily available. For instance, a Heaviside function of stress, using a threshold value σ_p^c determined from micromechanical analysis of unit cells (Fig. 7.22a), was used in [Lambert-Perlade et al., 2004]:

$$\begin{array}{ll} p_f(\sigma_p) = 1 & \text{if} \sigma_p \geq \sigma_p^c \\ p_f(\sigma_p) = 0 & \text{otherwise.} \end{array} \tag{7.20}$$

Crack propagation into the surrounding grain (Fig. 7.6b) is determined using a Griffith criterion; here, the critical size of a particle, $a_c(\sigma_I)$, under given maximum principal stress σ_I, is determined by an effective fracture toughness across the particle-matrix interface, K_{Ia}^{pm}, and a geometrical factor, $\beta' = 1.25$ that is related to a penny-shaped crack:

$$a_c(\sigma_I) = \left(\frac{\beta' K_{Ia}^{pm}}{\sigma_I} \right)^2 . \tag{7.21}$$

The probability $P_f(\sigma_I)$ to find a particle of critical size $a_c(\sigma_I)$ under the local maximal principal stress σ_I becomes:

$$P_f(\sigma_I) = \int_{a_c(\sigma_I)}^{+\infty} p(a) p_f(\sigma_p) da \tag{7.22}$$

where σ_p is a function of σ_I.

For complete fracture to occur, at least one microcrack initiated from the particle, propagated in the first grain and stopped at a high-misorientation grain boundary (Fig. 7.6b) must be able to propagate into the next grain (Fig. 7.6c). Thus, at least one grain containing a microcrack must exceed a critical size, $D_c(\sigma_I)$, again according to a Griffith-like criterion and again assuming a penny-shape microcrack morphology. With $p_g(D)$ being the grain size distribution, and $K_{Ia}^{mm}(T)$ being the temperature-dependent effective fracture toughness across the grain boundary, this becomes:

$$D_c(\sigma_I) = \left(\frac{\beta' K_{Ia}^{mm}(T)}{\sigma_I} \right)^2 . \tag{7.23}$$

As a consequence, the fracture probability $P_F(\sigma_I)$ under the local maximum principal stress σ_I becomes:

$$P_F = (\sigma_I) = \int_{D_c(\sigma_I)}^{+\infty} \left(1 - \exp\left(-N_a \frac{\pi D^3}{6} \cdot P_f(\sigma_I)\right)\right) \cdot p_g(D) dD \qquad (7.24)$$

The exponential factor accounts for the probability to find hard particles in the considered grains of size D, N_a being again the number density of hard particles. The above equation is then integrated over the plastic zone, as in the Beremin approach.

The size distributions of hard particles and of grains are determined experimentally, the only adjustable model parameters being K_{Ia}^{pm} (a constant) and $K_{Ia}^{mm}(T)$. K_{Ia}^{mm} must be temperature-dependent in order for the model to correctly predict the DBT behavior. In [Lambert-Perlade et al., 2004], the model was applied to a bainitic steel that fractured from martensite-austenite constituents (Fig. 7.7c). Acoustic emission allowed to monitor crack initiation events, even well before final fracture. In the DBT, the number of such events markedly increased with temperature, yet the minimum value (related to K_{Ia}^{pm}) being rather independent from temperature (Fig. 7.22).

7.7 Concluding remarks

Brittle fracture is an abrupt, stochastic phenomenon, associated to low toughness levels. It is to be avoided in structural components. Examination of broken specimens allow determination of physical fracture mechanisms, namely, crack initiation from plastic deformation features or from microstructural defects, crack propagation (including across microstructural barriers) followed by unstable fracture.

The resistance to brittle fracture is generally characterized using toughness properties. These properties generally depend on the experimental testing conditions, such as the specimen size and geometry, and cannot be directly transferred from laboratory specimens to actual components. On the other hand, physically informed "local approach to fracture" models relate a local critical fracture stress to fractographic and microstructural features. When using a weakest link assumption, local approach models allow predictions of the average level and of the scatter in fracture resistance. They may be used to determine the effects of in-service conditions, such as the temperature in the ductile-to-brittle transition domain, and any environmental effect such as *e.g.*, ingress of chemical species or irradiation-induced embrittlement. They provide useful information about the efficiency of microstructural improvement.

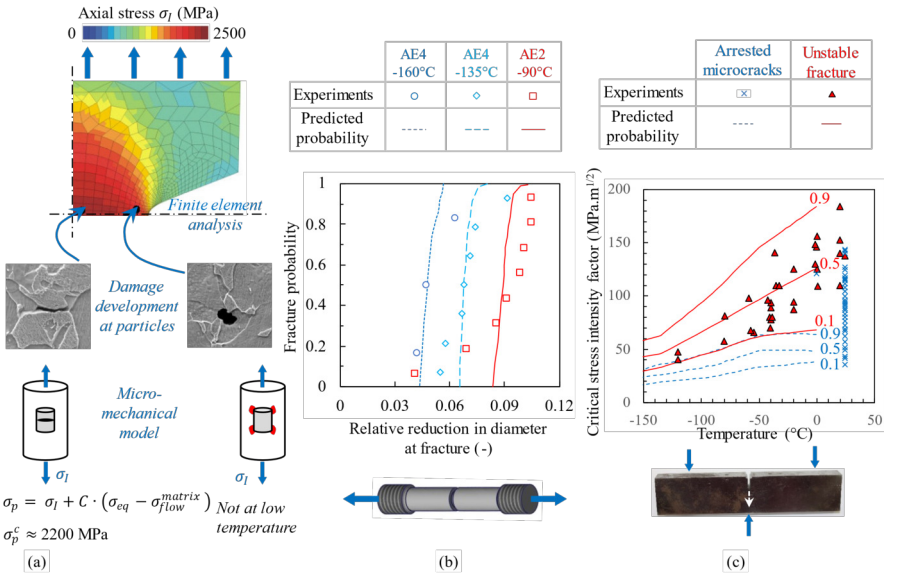

FIGURE 7.22: Calibration and application of the double-barrier model in a bainitic steel. (a) Determination of a critical fracture stress in secondary phase particles, from tests on notched specimens. Interfacial decohesion was not observed at low temperatures. (b) Calibration of the model on two types of axisymmetric specimens (AE4 and AE2, with a notch tip radius of 4 mm and 2 mm, respectively). (c) Comparison of model predictions with experimental values of stress intensity factors at crack initiation and at unstable fracture (fracture toughness), of precracked bending specimens, as a function of test temperature. After [Lambert-Perlade et al., 2004; Lambert-Perlade, 2001].

Bibliography

[Andrieu 2013] Andrieu, A.: *Mécanismes et modélisation multi-échelle de la rupture fragile trans- et inter-granulaire des aciers pour réacteurs à eau sous pression, en lien avec le vieillissement thermique*, Ecole Nationale Supérieure des Mines de Paris, PhD thesis, Juli 2013. `https://pastel.archives-ouvertes.fr/pastel-00957868`. – Issue: 2013ENMP0046

[ANSI/API (1996) 1996] ANSI/API (1996): *RP 5L3 standard. Recommended practice for conducting drop-weight tear tests on line pipe*. 1996. – Washington, DC

[Baldi and Buzzichelli 1978] Baldi, G. ; Buzzichelli, G.: Critical stress for delamination fracture in HSLA steels. In: *Metal Science* 12 (1978), Oktober, Nr. 10, p. 459–472. – 10.1179/030634578790433332 . – ISSN 0306–3453

[Beremin et al. 1983] Beremin, F.M. ; Pineau, A. ; Mudry, F. ; Devaux, J.C. ; D'Escatha, Y. ; Ledermann, P.: A local criterion for cleavage fracture of a nuclear pressure vessel steel. In: *Metallurgical Transactions A* 14 (1983), November, Nr. 11, p. 2277–2287. – 10.1007/BF02663302 . – ISSN 0360–2133, 1543–1940

[Bernauer et al. 1999] Bernauer, G. ; Brocks, W. ; Schmitt, W.: Modifications of the Beremin model for cleavage fracture in the transition region of a ferritic steel. In: *Engineering Fracture Mechanics* 64 (1999), Nr. 3, p. 305–325

[Bilat 2007] Bilat, A.-S.: *Estimation du risque de rupture fragile de soudures de pipelines en aciers à haut grade : caractérisation et modélisation*, École Nationale Supérieure des Mines de Paris, PhD thesis, Juni 2007. `https://pastel.archives-ouvertes.fr/tel-00186517`

[Bordet et al. 2005] Bordet, S.R. ; Karstensen, A.D. ; Knowles, D.M. ; Wiesner, C.S.: A new statistical local criterion for cleavage fracture in steel. Part I: model presentation. In: *Engineering Fracture Mechanics* 72 (2005), Februar, Nr. 3, p. 435–452. – 10.1016/j.engfracmech.2004.02.009 . – ISSN 00137944

[Bowen et al. 1986] Bowen, P. ; Druce, S.G. ; Knott, J.F.: Effects of microstructure on cleavage fracture in pressure vessel steel. In: *Acta Metallurgica* 34 (1986), Juni, Nr. 6, p. 1121–1131. – 10.1016/0001-6160(86)90222-1 . – ISSN 00016160

[Boåsen et al. 2019] Boåsen, M. ; Stec, M. ; Efsing, P. ; Faleskog, J.: A generalized probabilistic model for cleavage fracture with a length scale – Influence of stress state and application to surface cracked experiments. In: *Engineering Fracture Mechanics* 214 (2019), Juni, p. 590–608. – 10.1016/j.engfracmech.2019.03.041 . – ISSN 00137944

[Chanh 2022] Chanh, C.: *Analyse du lien entre microstructure, chargement mécanique et fissuration lors de la traction en croix de soudures par point par résistance d'un acier inoxydable martensitique*, Université Paris sciences et lettres, PhD thesis, Juli 2022. – Issue: 2022UPSLM022

[Chosson 2014] Chosson, R.: *Étude expérimentale et modélisation du comportement en fluage sous pression interne d'une gaine en alliage de zirconium oxydée en atmosphère vapeur*, Mines ParisTech, PhD thesis, Dezember 2014. `https://hal-mines-paristech.archives-ouvertes.fr/tel-01314559`

[Cottrell 1958] Cottrell, A.H.: Theory of brittle fracture in steel and similar metals. In: *Trans. Met. Soc. AIME* Vol: (1958), April. `https://www.osti.gov/biblio/4347093`

[Curry and Knott 1978] Curry, D.A. ; Knott, J.F.: Effects of microstructure on cleavage fracture stress in steel. In: *Metal Science* 12 (1978), November, Nr. 11, p. 511–514. – 10.1179/msc.1978.12.11.511 . – ISSN 0306–3453

[Curry and Knott 1979] Curry, D.A. ; Knott, J.F.: Effect of microstructure on cleavage fracture toughness of quenched and tempered steels. In: *Metal Science* 13 (1979), Juni, Nr. 6, p. 341–345. – 10.1179/msc.1979.13.6.341 . – ISSN 0306–3453

[E08 Committee 2022a] E08 Committee: Test Method for Determination of Reference Temperature, T_0, for Ferritic Steels in the Transition Range / ASTM International. Version: 2022. 2022. – Technical repport

[E08 Committee 2022b] E08 Committee: Test Method for Linear-Elastic Plane-Strain Fracture Toughness of Metallic Materials / ASTM International. Version: 2022. 2022. – Technical repport

[E08 Committee 2022c] E08 Committee: Test Method for Measurement of Fracture Toughness / ASTM International. Version: 2022. 2022. – Technical repport

[E28 Committee 2022] E28 Committee: Test Methods for Notched Bar Impact Testing of Metallic Materials / ASTM International. Version: 2022. 2022. – Technical repport

[Evans 1983] Evans, A.G.: Statistical aspects of cleavage fracture in steel. In: *Metallurgical Transactions A* 14 (1983), Juli, Nr. 7, p. 1349–1355. – 10.1007/BF02664818 . – ISSN 0360–2133, 1543–1940

[Forget et al. 2016] Forget, P. ; Marini, B. ; Vincent, L.: Application of local approach to fracture of an RPV steel: effect of the crystal plasticity on the critical carbide size. In: *Procedia Structural Integrity* 2 (2016), p. 1660–1667. – 10.1016/j.prostr.2016.06.210 . – ISSN 24523216

[Gao et al. 2005] Gao, X. ; Zhang, G. ; Srivatsan, T.S.: Prediction of cleavage fracture in ferritic steels: a modified Weibull stress model. In: *Materials Science and Engineering: A* 394 (2005), März, Nr. 1-2, p. 210–219. – 10.1016/j.msea.2004.11.035 . – ISSN 09215093

[Gell and Smith 1967] Gell, M. ; Smith, E.: The propagation of cracks through grain boundaries in polycrystalline 3% silicon-iron. In: *Acta Metallurgica* 15 (1967), Februar, Nr. 2, p. 253–258. – 10.1016/0001-6160(67)90200-3 . – ISSN 00016160

[Ghosh et al. 2016a] Ghosh, A. ; Modak, P. ; Dutta, R. ; Chakrabarti, D.: Effect of MnS inclusion and crystallographic texture on anisotropy in Charpy impact toughness of low carbon ferritic steel. In: *Materials Science and Engineering: A* 654 (2016), Januar, p. 298–308. – 10.1016/j.msea.2015.12.047 . – ISSN 09215093

[Ghosh et al. 2016b] Ghosh, A. ; Patra, S. ; Chatterjee, A. ; Chakrabarti, D.: Effect of Local Crystallographic Texture on the Fissure Formation During Charpy Impact Testing of Low-Carbon Steel. In: *Metallurgical and Materials Transactions A* 47 (2016), Juni, Nr. 6, p. 2755–2772. – 10.1007/s11661-016-3458-y . – ISSN 1073–5623, 1543–1940

[Giang et al. 2018] Giang, N.A. ; Seupel, A. ; Kuna, M. ; Hütter, G.: Dislocation pile-up and cleavage: effects of strain gradient plasticity on microcrack initiation in ferritic steel. In: *International Journal of Fracture* 214 (2018), November, Nr. 1, p. 1–15. – 10.1007/s10704-018-0313-8 . – ISSN 0376–9429, 1573–2673

[Godin 2018] Godin, H.: *Effet de la microstructure sur la transition ductile-fragile d'aciers inoxydables martensitiques emboutissables à chaud*, Ecole Nationale Supérieure des Mines de Paris, PhD Thesis, 2018. `http://www.theses.fr/2018PSLEM036/document`

[Griffith 1921] Griffith, A.A.: VI. The phenomena of rupture and flow in solids. In: *Philosophical Transactions of the Royal Society of London. Series A, Containing Papers of a Mathematical or Physical Character* 221 (1921), Januar, Nr. 582-593, p. 163–198. – 10.1098/rsta.1921.0006 . – ISSN 0264–3952, 2053–9258

[Griffiths and Owen 1971] Griffiths, J.R. ; Owen, D.R.J.: An elastic-plastic stress analysis for a notched bar in plane strain bending. In: *Journal of the Mechanics and Physics of Solids* 19 (1971), November, Nr. 6, p. 419–431. – 10.1016/0022-5096(71)90009-3 . – ISSN 00225096

[Groom and Knott 1975] Groom, J.D.G. ; Knott, J.F.: Cleavage Fracture in Prestrained Mild Steel. In: *Metal Science* 9 (1975), Januar, Nr. 1, p. 390–400. – 10.1179/030634575790444946 . – ISSN 0306–3453

[Gurland 1972] Gurland, J.: Observations on the fracture of cementite particles in a spheroidized 1.05% C steel deformed at room temperature. In: *Acta Metallurgica* 20 (1972), Mai, Nr. 5, p. 735–741. – 10.1016/0001-6160(72)90102-2 . – ISSN 00016160

[Hagiwara and Knott 1982] Hagiwara, Y. ; Knott, J.F.: Cleavage fracture in mixed microstructure. In: *5th International Conference on Fracture*. Oxford : Pergamon Press, 1982, p. 707–714

[Hahn 1984] Hahn, G.T.: The Influence of Microstructure on Brittle Fracture Toughness. In: *Metallurgical and Materials Transactions A* 15 (1984), Juni, Nr. 6, p. 947–959. – 10.1007/BF02644685 . – ISSN 1073–5623, 1543–1940

[Hutchinson 1968] Hutchinson, J.W.: Singular behaviour at the end of a tensile crack in a hardening material. In: *Journal of the Mechanics and Physics of Solids* 16 (1968), Januar, Nr. 1, p. 13–31. – 10.1016/0022-5096(68)90014-8 . – ISSN 00225096

[Kantidis et al. 1994] Kantidis, E. ; Marini, B. ; Pineau, A.: A CRITERION FOR INTERGRANULAR BRITTLE FRACTURE OF A LOW ALLOY STEEL. In: *Fatigue & Fracture of Engineering Materials and Structures* 17 (1994), Juni, Nr. 6, p. 619–633. – 10.1111/j.1460-2695.1994.tb00261.x . – ISSN 8756–758X, 1460–2695

[Knott 1967] Knott, J.F.: Effects of strain on notch brittleness in mild steel. In: *J. Iron Steel Inst* 205 (1967), p. 966–969

[Knott 1978] Knott, J.F.: MICRO-MECHANISMS OF FRACTURE AND THE FRACTURE TOUGHNESS OF ENGINEERING ALLOYS. Version: 1978. In: *Advances in Research on the Strength and Fracture of Materials*. Elsevier, 1978. – 10.1016/B978-0-08-022136-6.50016-0 . – ISBN 978–0–08–022136–6, p. 61–92

[Lambert-Perlade 2001] Lambert-Perlade, A.: *Rupture par clivage de microstructures d'aciers bainitiques obtenues en conditions de soudage*, École Nationale Supérieure des Mines de Paris, PhD thesis, Mai 2001. `https://pastel.archives-ouvertes.fr/tel-00005749`

[Lambert-Perlade et al. 2004] Lambert-Perlade, A. ; Sturel, T. ; Gourgues, A. F. ; Besson, J. ; Pineau, A.: Mechanisms and modeling of cleavage fracture in simulated heat-affected zone microstructures of a high-strength low alloy steel. In: *Metallurgical and Materials Transactions A* 35 (2004), März, Nr. 3, p. 1039–1053. – 10.1007/s11661-004-0030-y . – ISSN 1073–5623, 1543–1940

[Laurent 2007] Laurent, A. / Mines Paris. 2007. – Technical repport

[Lindley 1966] Lindley, T.C: The effect of pre-strain and strain-ageing on the cleavage fracture of a high-manganese steel. In: *Acta Metallurgica* 14 (1966), Nr. 12, p. 1835–1839. – https://doi.org/10.1016/0001-6160(66)90036-8 . – ISSN 0001–6160

[Lindley 1967] Lindley, T.C.: The effect of pre-strain and strain-ageing on the cleavage fracture of a low carbon steel. In: *Acta Metallurgica* 15 (1967), Februar, Nr. 2, p. 397–399. – 10.1016/0001-6160(67)90222-2 . – ISSN 00016160

[Lindley et al. 1970] Lindley, T.C. ; Oates, G. ; Richards, C.E.: A critical of carbide cracking mechanisms in ferride/carbide aggregates. In: *Acta Metallurgica* 18 (1970), November, Nr. 11, p. 1127–1136. – 10.1016/0001-6160(70)90103-3 . – ISSN 00016160

[Lu et al. 2010] Lu, W. ; Chen, J. ; Chakravarthula, S.S. ; Qiao, Y.: Resistance to cleavage cracking and subsequent shearing of high-angle grain boundary. In: *Engineering Fracture Mechanics* 77 (2010), März, Nr. 5, p. 768–775. – 10.1016/j.engfracmech.2009.12.009 . – ISSN 00137944

[Margolin et al. 1997] Margolin, B.Z. ; Shvetsova, V.A. ; Karzov, G.P.: Brittle fracture of nuclear pressure vessel steels—I. Local criterion for cleavage fracture. In: *International Journal of Pressure Vessels and Piping* 72 (1997), Juni, Nr. 1, p. 73–87. – 10.1016/S0308-0161(97)00012-4 . – ISSN 03080161

[Martín-Meizoso et al. 1994] Martín-Meizoso, A. ; Ocaña-Arizcorreta, I. ; Gil-Sevillano, J. ; Fuentes-Pérez, M.: Modelling cleavage fracture of bainitic steels. In: *Acta Metallurgica et Materialia* 42 (1994), Juni, Nr. 6, p. 2057–2068. – 10.1016/0956-7151(94)90031-0 . – ISSN 09567151

[McMahon and Cohen 1965] McMahon, C.J. ; Cohen, M.: Initiation of cleavage in polycrystalline iron. In: *Acta Metallurgica* 13 (1965), Juni, Nr. 6, p. 591–604. – 10.1016/0001-6160(65)90121-5 . – ISSN 00016160

[McMeeking 1977] McMeeking, R.M.: Finite deformation analysis of crack-tip opening in elastic-plastic materials and implications for fracture. In: *Journal of the Mechanics and Physics of Solids* 25 (1977), Oktober, Nr. 5, p. 357–381. – 10.1016/0022-5096(77)90003-5 . – ISSN 00225096

[Naylor and Krahe 1974] Naylor, J. P. ; Krahe, P. R.: The Effect of the Bainite Packet Size on Toughness. In: *Metallurgical transactions* 5 (1974), Juli, Nr. 7, p. 1699–1701. – 10.1007/BF02646352 . – ISSN 2379–0083

[Newbury et al. 1974] Newbury, D.E. ; Christ, B.W. ; Joy, D.C.: Relevance of electron channeling patterns to embrittlement studies. In: *Metall. Trans.* 5 (1974), p. 1505–1508

[Oates 1968] Oates, G.: Effect of hydrostatic stress on cleavage fracture in a mild steel and a low-carbon manganese steel. In: *J. Iron Steel Inst* 206 (1968), p. 930–935

[Petch 1986] Petch, N.J.: The influence of grain boundary carbide and grain size on the cleavage strength and impact transition temperature of steel. In: *Acta Metallurgica* 34 (1986), Juli, Nr. 7, p. 1387–1393. – 10.1016/0001-6160(86)90026-X . – ISSN 00016160

[Pineau 2006] Pineau, A.: Development of the Local Approach to Fracture over the Past 25 years: Theory and Applications. In: *International Journal of Fracture* 138 (2006), März, Nr. 1-4, p. 139–166. – 10.1007/s10704-006-0035-1 . – ISSN 0376–9429, 1573–2673

[Qiao and Argon 2003] Qiao, Y. ; Argon, A.S.: Cleavage cracking resistance of high angle grain boundaries in Fe–3%Si alloy. In: *Mechanics of Materials* 35 (2003), März, Nr. 3-6, p. 313–331. – 10.1016/S0167-6636(02)00284-3 . – ISSN 01676636

[Renevey et al. 1996] Renevey, S. ; Carassou, S. ; Marini, B. ; Eripret, C. ; Pineau, A.: Ductile - Brittle Transition of Ferritic Steels Modelled by

the Local Approach to Fracture. In: *Le Journal de Physique IV* 06 (1996), Oktober, Nr. C6, p. C6–343–C6–352. – 10.1051/jp4:1996634 . – ISSN 1155–4339

[Rice and Rosengren 1968] Rice, J.R. ; Rosengren, G.F.: Plane strain deformation near a crack tip in a power-law hardening material. In: *Journal of the Mechanics and Physics of Solids* 16 (1968), Januar, Nr. 1, p. 1–12. – 10.1016/0022-5096(68)90013-6 . – ISSN 00225096

[Ripling and Baldwin Jr. 1951] Ripling, E.J. ; Baldwin Jr., W.J.: Rheotropic embrittlement of steel. In: *Trans. ASM* 43 (1951), p. 778–805

[Ritchie et al. 1973] Ritchie, R.O. ; Knott, J.F. ; Rice, J.R.: On the relationship between critical tensile stress and fracture toughness in mild steel. In: *Journal of the Mechanics and Physics of Solids* 21 (1973), November, Nr. 6, p. 395–410. – 10.1016/0022-5096(73)90008-2 . – ISSN 00225096

[Ruggieri and Dodds 2015] Ruggieri, C. ; Dodds, R.H.: An engineering methodology for constraint corrections of elastic–plastic fracture toughness – Part I: A review on probabilistic models and exploration of plastic strain effects. In: *Engineering Fracture Mechanics* 134 (2015), Januar, p. 368–390. – 10.1016/j.engfracmech.2014.12.015 . – ISSN 00137944

[Smith 1966] Smith, E.: The formation of a cleavage crack in a crystalline solid—I. In: *Acta Metallurgica* 14 (1966), August, Nr. 8, p. 985–989. – 10.1016/0001-6160(66)90219-7 . – ISSN 00016160

[Smith 1967] Smith, E.: The nucleation and growth of cleavage microcracks in mild steel. In: *Physical basis of yield and fracture*, The Institute of Physics and Physical Society, Oxford, UK, 1967, p. 36–46

[Smith 1968] Smith, E.: Cleavage fracture in mild steel. In: *International Journal of Fracture Mechanics* 4 (1968), Juni, Nr. 2, p. 131–145. – 10.1007/BF00188940 . – ISSN 0020–7268, 1573–2673

[Stec and Faleskog 2009] Stec, M. ; Faleskog, J.: Micromechanical modeling of grain boundary resistance to cleavage crack propagation in ferritic steels. In: *International Journal of Fracture* 160 (2009), Dezember, Nr. 2, p. 151–167. – 10.1007/s10704-009-9415-7 . – ISSN 0376–9429, 1573–2673

[Stroh 1957] Stroh, A.N.: A theory of the fracture of metals. In: *Advances in Physics* 6 (1957), Oktober, Nr. 24, p. 418–465. – 10.1080/00018735700101406 . – ISSN 0001–8732, 1460–6976

[Stöckl et al. 2000] Stöckl, H. ; Böschen, R. ; Schmitt, W. ; Varfolomeyev, I. ; Chen, J.H.: Quantification of the warm prestressing effect in a shape welded 10 MnMoNi 5-5 material. In: *Engineering Fracture Mechanics* 67 (2000), September, Nr. 2, p. 119–137. – 10.1016/S0013-7944(00)00053-9 . – ISSN 00137944

[Tanguy et al. 2005a] Tanguy, B. ; Besson, J. ; Piques, R. ; Pineau, A.: Ductile to brittle transition of an A508 steel characterized by Charpy impact test - Part I: Experimental Results. In: *Engineering Fracture Mechanics* 72 (2005), Januar, Nr. 1, p. 49–72. – 10.1016/j.engfracmech.2004.03.010 . – ISSN 00137944

[Tanguy et al. 2005b] Tanguy, B. ; Besson, J. ; Piques, R. ; Pineau, A.: Ductile to brittle transition of an A508 steel characterized by Charpy impact test - Part II: modeling of the Charpy transition curve. In: *Engineering Fracture Mechanics* 72 (2005), Februar, Nr. 3, p. 413–434. – 10.1016/j.engfracmech.2004.03.011 . – ISSN 00137944

[Tankoua et al. 2018] Tankoua, F. ; Crépin, J. ; Thibaux, P. ; Cooreman, S. ; Gourgues-Lorenzon, A.-F.: Quantification and microstructural origin of the anisotropic nature of the sensitivity to brittle cleavage fracture propagation for hot-rolled pipeline steels. In: *International Journal of Fracture* 212 (2018), August, Nr. 2, p. 143–166. – 10.1007/s10704-018-0297-4 . – ISSN 0376–9429, 1573–2673

[Tankoua et al. 2022] Tankoua, F. ; Crépin, J. ; Thibaux, P. ; Cooreman, S. ; Gourgues-Lorenzon, A.-F.: Contribution of the microtexture evolution induced by plastic deformation on the resistance of a hot-rolled pipeline steel to flat cleavage fracture and to brittle delamination cracking. In: *International Journal of Fracture* 233 (2022), Februar, Nr. 2, p. 211–237. – 10.1007/s10704-022-00621-7 . – ISSN 0376–9429, 1573–2673

[Tankoua Yinga 2015] Tankoua Yinga, F.: *Transition ductile-fragile des aciers pour gazoducs : Étude quantitative des ruptures fragiles hors plan et corrélation à l'anisotropie de microtexture*, Ecole Nationale Supérieure des Mines de Paris, PhD thesis, Juli 2015. `https://pastel.archives-ouvertes.fr/tel-01212488`. – Issue: 2015ENMP0014

[Tioguem Teagho 2019] Tioguem Teagho, F.: *Lien entre microstructure et transition ductile-fragile des aciers trempés-revenus à haute résistance*, Université Paris sciences et lettres, PhD thesis, November 2019. `https://pastel.archives-ouvertes.fr/tel-02513106`. – Issue: 2019PSLEM040

[Wallin 1984] Wallin, K.: The scatter in K_{IC}-results. In: *Engineering Fracture Mechanics* 19 (1984), Januar, Nr. 6, p. 1085–1093. – 10.1016/0013-7944(84)90153-X . – ISSN 00137944

[Wallin 1991] Wallin, K.: Statistical modelling of fracture in the ductile to brittle transition region. In: Blauel, J.G. (Hrsg.) ; Schwalbe, K.H. (Hrsg.): *Defect assessment in components*. Elsevier, 1991 (EGF/ESIS Publication). – ISBN 978–0–85298–742–1, p. 415–445

[Wallin and Laukkanen 2006] Wallin, K. ; Laukkanen, A.: Aspects of cleavage fracture initiation – relative influence of stress and strain. In: *Fatigue &*

Fracture of Engineering Materials and Structures 29 (2006), September, Nr. 9-10, p. 788–798. – 10.1111/j.1460-2695.2006.01005.x . – ISSN 8756–758X, 1460–2695

[Zener 1948] Zener, C.: *Fracturing of metals.* ASM, Cleveland, OH, 1948

8

Ductile fracture in metals: mechanisms and characterization

Florent Hannard
Institute of Mechanics Materials and Civil Engineering (iMMC), Université catholique de Louvain, Belgium

Aude Simar
Institute of Mechanics Materials and Civil Engineering (iMMC), Université catholique de Louvain, Belgium

Thilo Morgeneyer
Centre des Matériaux, Mines Paris, PSL University, 91003, Evry, France

Ductile failure can be described at the macroscopic scale by indicators such as the strain to fracture that depends on the applied stress state (triaxiality, Lode parameter). In terms of mechanisms, ductile failure is the result of the nucleation, growth and coalescence of cavities. In engineering alloys, nucleation generally occurs on second phase particles. Each of these mechanisms can be modelled using analytical expressions that are also presented in this chapter. These models are presented from their simplest to their more advanced forms. The relevance of these model extensions are discussed.

The nucleated cavities can present strong spatial heterogeneities. These heterogenous effects are also discussed and examples are illustrated exploiting advanced characterization tools. The chapter closes with more a detailed description of these advanced characterization methods for ductile damage including 2D, 3D (X-ray tomography) and 4D (time resolved) imaging.

8.1 Introduction

Ductile fracture encompasses failure by plastic instability and damage driven by plastic deformation. Ductile fracture may occur as final crack propagation under monotonic loading, *e.g.* after fatigue crack propagation or after stress corrosion cracking. It can also be the result of a forming process or a crash

without the presence of a crack prior to ductile fracture. Ductile fracture takes place in most cases for cubic face centred materials, such as aluminium and copper alloys as well as austenitic steel. The main driving forces of ductile fracture are *plastic deformation* and *positive hydrostatic stress* (σ_m), *i.e.* high levels of stress triaxiality η defined as:

$$\eta = \sigma_m / \sigma_{eq} \tag{8.1}$$

where σ_m is the hydrostatic stress and σ_{eq} is the equivalent Von Mises stress.

Ductile fracture is identified here by its damage micromechanisms. The classical ductile fracture mechanisms are *(i) void nucleation, (ii) void growth and (iii) void coalescence*. The void nucleation phase occurs typically on second phase particles in engineering alloys. They have either lower strength than the ductile matrix or they are brittle and give rise to voids after some elastic or plastic deformation. The void growth is promoted by the presence of positive hydrostatic stresses in the material. Void coalescence may occur through internal necking of voids that have undergone substantial growth or by void sheeting between voids with limited growth. All these mechanisms will be detailed further in the following sections.

8.2 Modes of ductile fracture at the macro-scale

Structural metallic alloys have been continuously improved to avoid cleavage and intergranular fracture. Therefore, ductile failure has become central in structural integrity assessment, together with fatigue and corrosion [C. Tekogu, 2015]. Ductile fracture always involves void nucleation and growth due to plasticity until they eventually coalesce, forming a micro-crack and initiating failure of the specimen. These fundamental mechanisms will be described in section 8.3.

There are situations where the damage sequence and the void coalescence stage are controlling the onset of failure (see Fig. 8.1(a)). For sufficiently homogeneous materials, voids have similar sizes and are rather uniformly distributed within the microstructure. In other words, the damage evolution is rather homogeneous and an "average" description of damage evolution is possible. From a modeling perspective, ductile damage within homogeneous materials can be described using elementary models for each mechanism, and these models will be discussed in section 8.3.

However, in some other cases, ductility is tied to the onset of macroscopic plastic instability of the component as a precursor to failure (see Fig. 8.1(b)) [C. Tekogu, 2015]. One example is the formation of shear bands and necking-

type instabilities initiating failure during metal forming. Many sheet forming operations are limited by strain localization, as typically characterized by a forming limit diagram. Another example is the slant fracture mode usually observed within metallic thin sheets due to the formation of shear bands near the crack tip. These plastic instabilities can originate from multiple softening mechanisms such as thermal softening, plastic anisotropy, or kinematic hardening. In that case, damage softening is a consequence but not the cause of plastic localisation [Pineau et al., 2016]. The final material separation within the shear band still involves void nucleation, growth and coalescence, but only after the local accumulation of large plastic strains and with little evidence of any voids outside the localization band.

Nowadays, there is considerable experimental evidence that indicates that the ductile damage process is strongly affected by microstructural heterogeneities, *e.g.* due to interactions between voids concentrated into clusters (see Fig. 8.1(c)). These microstructural heterogeneity effects on ductile fracture, which is the rule rather than the exception within commercial alloys [Lecarme et al., 2014], are further discussed in section 8.4.

Finally, the particular case of ductile failure under shear loading, usually with limited void growth, will be discussed in section 8.5.

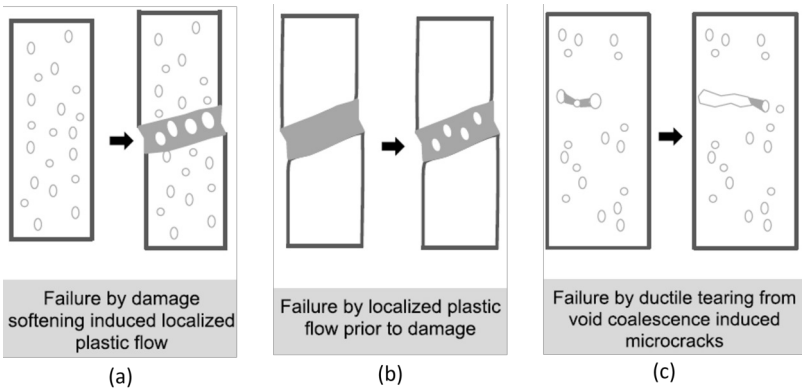

FIGURE 8.1: Schematic representation of the different modes of ductile fracture commonly observed in metals. After [C. Tekogu, 2015]

Strain to fracture and stress state effects

The effect of multi-axial tensile stress states on the yielding of metals has been studied since the early 20^{th} century by studying tubes under combinations of internal pressure, torsion and tension [Lode, 1926a]. The effect of the stress state on the failure of metals was recognized later by P.W. Bridgman, Nobel Prize in Physics in 1946. He found out that the section of a material

that fails after necking under atmospheric pressure can be reduced to a point, *i.e.* a transition from ductile failure to purely-plastic failure, by superimposing a hydrostatic pressure (see Fig. 8.2). This significant increase in ductility is explained by the high hydrostatic pressure suppressing void growth, thereby delaying damage and fracture. The effect of hydrostatic pressure, favoring high ductility, is fundamental to the large plastic strains that can be reached in forming processes such as extrusion [Hancock, 1992]. However, in the absence of superimposed hydrostatic pressure, structural applications usually involve various stress states as quantified by the stress triaxiality ratio.

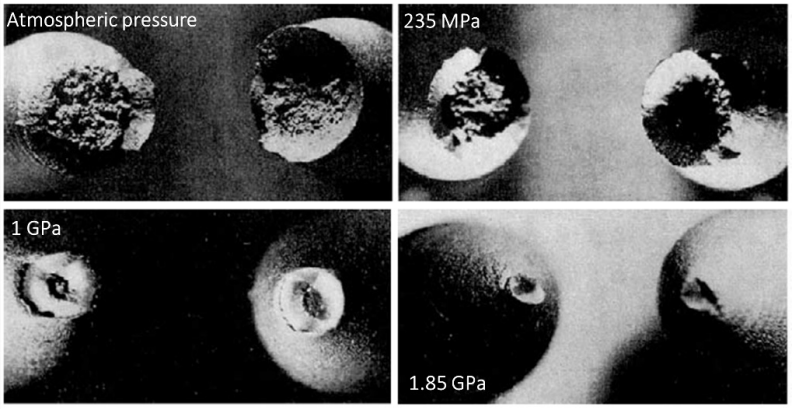

FIGURE 8.2: A series of tensile tests on mild steel specimens showing increase of fracture strain (*i.e.* reduction of area in the neck) with increased pressure. After P. W. Bridgman [Bridgman, 1964]

The effect of stress triaxiality on ductile fracture can be studied at the macroscale by varying the sample geometries and thus without an in-depth analysis of the ductile damage mechanisms. A fracture strain is determined at the critical location in the broken sample, *i.e.* where the fracture is assumed to initiate first. Failure frequently occurs within a zone of plastic deformation localization, *e.g.* in the neck of a tensile specimen involving a different triaxiality compared to the homogeneously deforming specimen. Finite Element (FE) calculations are thus usually needed to generate such curves as the local stress triaxiality must be calculated in the critical location.

Such studies can also be performed using tubular specimens to deform materials up to fracture under shear stress states combined with tensile stresses [Papasidero et al., 2015; Barsoum and Faleskog, 2007]. The advantage of such sample geometries is that they do not have a severe notch that could lead to premature crack nucleation at elevated levels of stress triaxiality. The determination and comparison of the strain to fracture can be ambiguous as it can be determined in different ways:

1. An experimental approach may be used based on digital image correlation (DIC) on the sample surface [Dunand and Mohr, 2011]. The highest strain measured at fracture is then plotted. This approach is only valid if the highest strain is reached on the sample surface. Furthermore, it strongly depends on the chosen physical subset size for the DIC correlation, especially if the strain fields are highly localized.
2. An hybrid experimental-numerical approach: experiments are conducted and 3D finite element simulations are carried out. The strain at fracture is determined for the mesoscopic strain or displacement at which the sample broke in the experiment. The local strain value is then determined inside the structure in the FE simulation [Simar et al., 2010; Mohr and Marcadet, 2015; Brünig et al., 2008]. Particular interest must lay on the mesh size for which a reliable result can be obtained.

Fig. 8.3(a) shows schematically the evolution of fracture strain as a function of stress triaxiality, from $\frac{1}{3}$ for uniaxial tension to higher stress triaxiality levels for thick and deeply notched samples. The fracture strain usually strongly decreases with increasing levels of stress triaxiality and this is well established for sufficiently large levels of triaxiality [Pineau et al., 2016].

However, Bao *et al.* [Bao and Wierzbicki, 2004] have reported "lower-than expected" fracture strains for lower positive levels of stress triaxiality η (*i.e.* below $\frac{1}{3}$ for uniaxial tension, see Fig. 8.3(b)), with a minimum fracture strain for shear ($\eta = 0$). This seminal work by Bao *et al.* has motivated numerous studies on this topic. In particular, Papasidero *et al.* [Papasidero et al., 2015] conducted a study for the same range of stress states but using a tubular sample made of nominally the same material. The relationship between strain to fracture and stress triaxiality is quite different and increases towards shear (see Fig. 8.3(b)). The discrepancy in results may be linked to the definition of fracture strain and the way in which it was obtained. The exact material production route may also have affected the result. This highlights the care that must be taken when fracture strains are compared between different studies, as mentioned above. The underlying damage mechanisms in shear fracture will be developed in section 8.5.

Bao *et al.* [Bao and Wierzbicki, 2004] also observed different fracture strains when changing the sample geometry but keeping the same level of stress triaxiality. The Lode parameter [Lode, 1926b] was identified as a suitable additional mechanical parameter to differentiate these mechanical loading conditions and, in particular, the state of generalized shear where the Lode parameter vanishes. The Lode parameter is generally calculated from the stress tensor [Papasidero et al., 2014], but it can also be applied to the strain rate

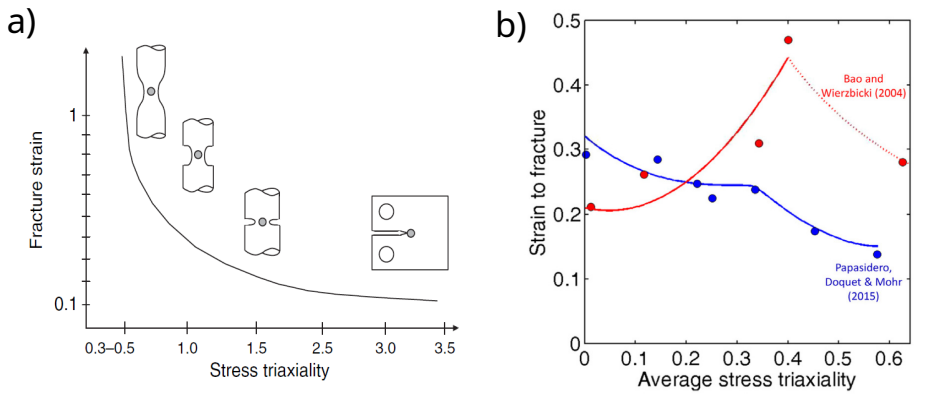

FIGURE 8.3: a) Strain to fracture versus triaxiality for critical locations in different sample geometries ranging from uniaxial tension to deeply notched samples. b) Strain to fracture versus triaxiality ranging from shear to bi-axial tension for AA2024T531. After [Papasidero et al., 2015]

tensor, as suggested in Lode's work [Lode, 1926b]. The Lode angle θ is a function of the third invariant of the deviatoric stress tensor as given in Eq.8.2:

$$cos(3\theta) = \frac{27}{2}\frac{J_3}{\sigma_{eq}^3} \tag{8.2}$$

The Lode angle θ ranges from 0 to $\frac{\pi}{3}$ and it is frequent to use the non-dimensional Lode angle parameter $\bar{\theta}$ (ranging from -1 to 1) [Papasidero et al., 2014]:

$$\bar{\theta} = 1 - \frac{6}{\pi}\theta \tag{8.3}$$

In plane stress state, the stress triaxiality and the Lode angle parameter are related in the following way:

$$\bar{\theta} = 1 - \frac{2}{\pi}\arccos(-\frac{27}{2}\eta(\eta^2 - \frac{1}{3})) \tag{8.4}$$

Rather phenomenological models predict the strain to fracture based on a fracture locus, *i.e.* a surface describing the fracture strain as a function of stress triaxiality and Lode parameter (both assumed relatively constant during straining) [Bao and Wierzbicki, 2004; Papasidero et al., 2015; Mohr and Marcadet, 2015]. For example, Fig. 8.4 depicts a fracture envelope, defined using the Hosford-Coulomb failure criterion [Papasidero et al., 2015], in the stress triaxiality and Lode parameter space. Such fracture envelope is the outcome of an extensive experimental campaign based on a variety of specimens of different geometry to quantify the effect of stress state on the onset of fracture.

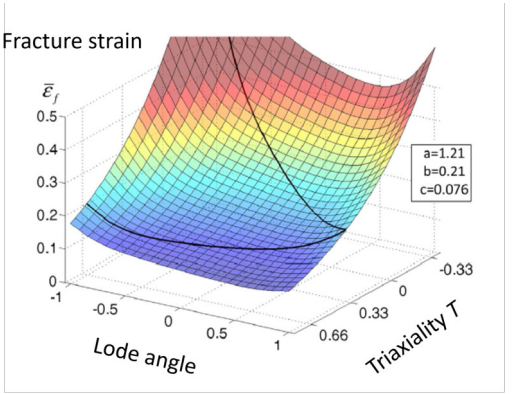

FIGURE 8.4: Hosford-Coulomb fracture envelope in the stress triaxiality and Lode parameter space for AA2024-T531, after [Papasidero et al., 2015].

8.3 Ductile damage micro-mechanisms

The classical mechanism leading to ductile failure in metals involves the void nucleation, growth and coalescence of cavities. Fig. 8.5(a) schematizes a notched tensile sample and the evolution of the damage sequence within a typical metallic microstructure containing coarse (in black) and smaller (in grey) second phase particles within the matrix (in white). Void nucleation generally occurs on these second phase particles by decohesion from the matrix or by fracture of these particles. These nucleated voids then grow with increasing plastic deformation, while new voids continue to nucleate. With increasing plastic deformation and void growth, the void spacing decreases and interactions between neighboring voids become more prevalent. The onset of void coalescence corresponds to the localization of plastic deformation and rapid void growth in the ligament connecting adjacent voids. After the onset of void coalescence, the final failure of the remaining ligament may be associated with the nucleation of a second population of voids nucleating on smaller particles, rather than localized void growth until impingement [Fabrègue and Pardoen, 2008].

With a resolution of around 1 μm, X-ray 3D microtomography is a very effective imaging tool to study ductile failure and will be further discussed in section 8.6. Fig. 8.5(b, c) illustrates the visualization during an in-situ tensile test in X-ray microtomography of the notched region of a sample made of X100 steel and with the geometry shown in Fig. 8.5(a). Fig. 8.5(b) shows the initial X-ray microtomography volume, *i.e.* before deformation, and 2D cross-sections through the volume. Initial voids are observed in blue and in black

within the volume and cross-sections, respectively. Only the outer edges of the matrix are shown for clarity in 3D, while the matrix appears in gray within the cross-sections. The evolution of the damage process is shown in Fig. 8.5(c) by imaging the same notched region of the specimen at increasing deformation steps (*i.e.* reduction of the cross-sectional areas). When comparing the first deformation step of Fig. 8.5(c) with the initial state (Fig. 8.5(b)), it is clear that the number of voids within the volume has significantly increased due to void nucleation. With further deformation, significant void growth is observed in the second step and local coalescence events are evidenced by showing interconnected voids in yellow within the 3D volume. In the last step, more generalized void coalescence initiates, resulting in microcracks forming over a length scale large enough to trigger the catastrophic failure of the specimen.

8.3.1 Nucleation

Several void nucleation mechanisms have been identified and they can act individually, competitively, or collaboratively, depending on the material and loading conditions [Noell et al., 2023]. These mechanisms can be differentiated between particle-based nucleation and particle-free nucleation. Particle-free void nucleation is associated with deformation-induced defects such as vacancies, dislocation pile-ups or deformation twins. Attention is here focused on the particle-based void nucleation mechanisms, which are most commonly observed during ductile fracture [Pineau et al., 2016]. However, many details regarding particle-free mechanisms have recently been reviewed by Noell *et al.* [Noell et al., 2023]. Void nucleation associated with particles originates from the fracture of brittle particles or decohesion of the particle-matrix interface. Grain boundary decohesion associated with precipitate-free zones (PFZs) in age-hardening alloys, *i.e.* void nucleation occurring at weaker grain boundaries, is a particular case and is further discussed in section 8.4.2.

Void nucleation has mainly been modeled with critical stress criteria or critical strain criteria. One of the first models for void nucleation by interface decohesion has been proposed by Ashby [Ashby, 1966]. In this model, the normal stress acting across the particle-matrix interface increases with plastic strain due to the accumulation of dislocations, and void nucleation occurs when the stress at the interface exceeds a critical stress. There has been a long debate as to whether or not there exists a critical strain to nucleate cavities [Goods and Brown, 1979], *i.e.* if a strain criterion is applicable or not. The stress acting inside or at the interface of the particle originates from the work-hardening of the matrix around the particle. This local work hardening being a function of the plastic strain in the material, a strain-based criterion is thus somewhat equivalent to a local critical stress condition [Goods and Brown, 1979].

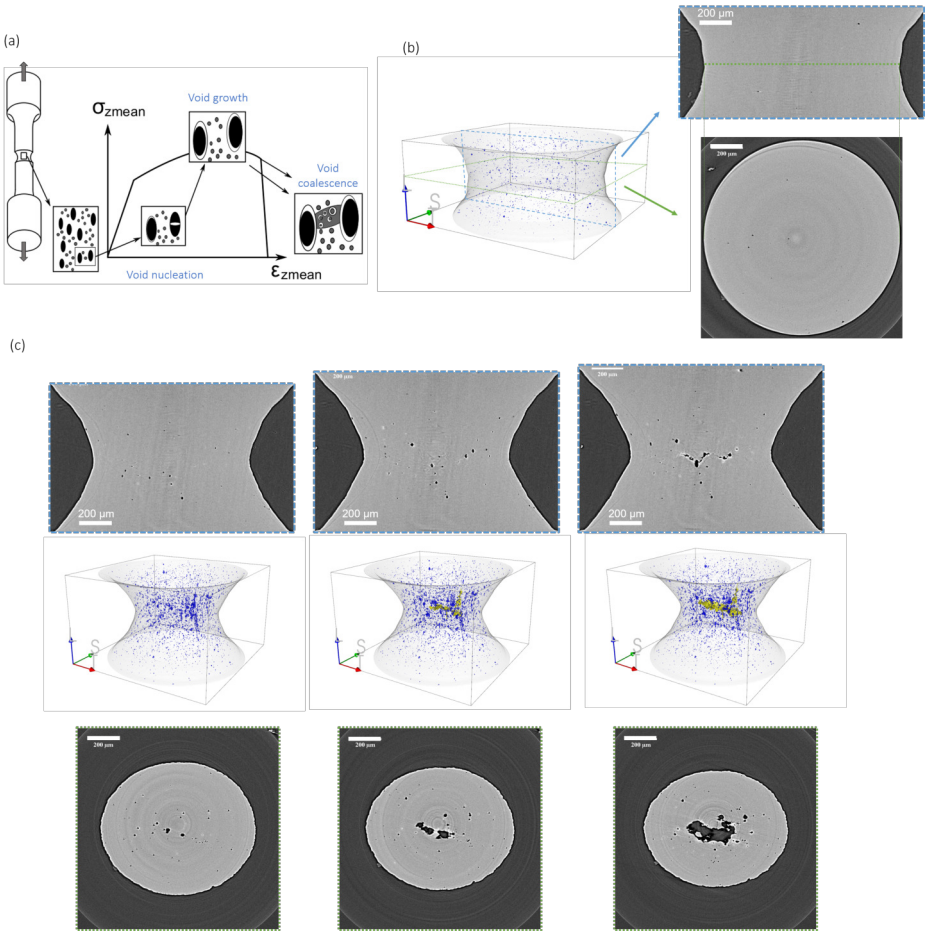

FIGURE 8.5: a) Schematic of the ductile damage sequence. b) Visualization in X-ray microtomography of the notched region of a sample made of X100 steel. c) Evolution of the damage process by imaging the same notched region of the specimen at increasing deformation steps (*i.e.* reduction of the cross-sectional areas). Adapted from [Madi et al., 2019].

Needleman [Needleman, 1987] compared a stress-controlled criterion with a strain-controlled criterion and observed quite different predictions for the onset of plastic localization. This is due to the hydrostatic tension dependence of the stress-controlled criterion which induces early flow localization. In practice, strain-controlled void nucleation laws are frequently preferred because they are more simple to implement numerically [Pineau and Pardoen, 2007]. However, strain-controlled criteria do not capture the dependence of

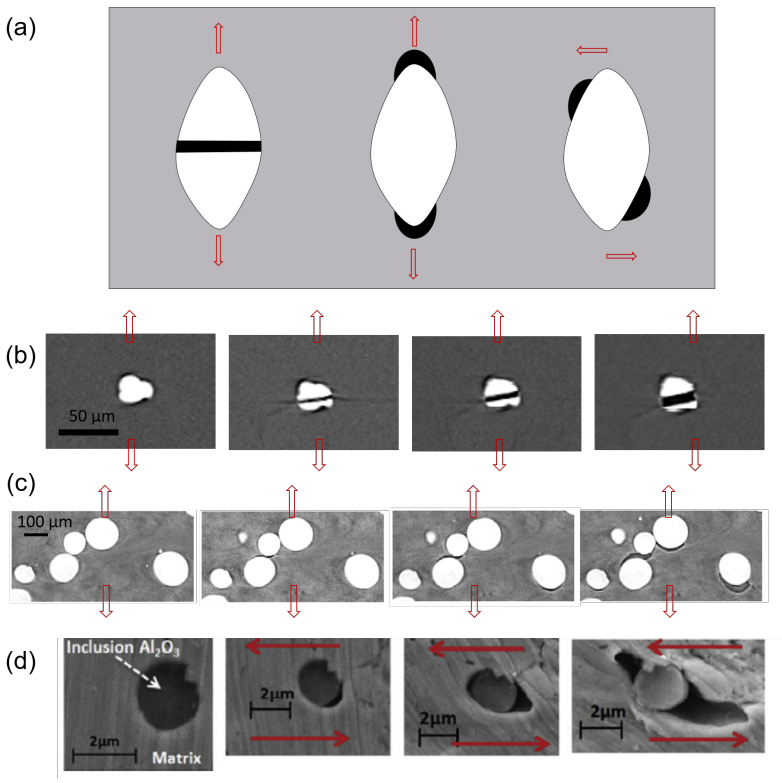

FIGURE 8.6: a) Schematic representation of the different particle-based void nucleation mechanisms: particle fracture and interface decohesion for tension or shear-dominated loading. In situ observation of these void nucleation mechanisms in (b,c) tensile loading of aluminium matrix composites [Ferre et al., 2015] and (d) in shear loading of HSLA steel [Achouri et al., 2013].

void nucleation upon stress triaxiality [Benzerga and Leblond, 2010].

Argon *et al.* [Argon, 1976] proposed a stress-based criterion for void nucleation by interface decohesion:

$$\sigma_{inh} + \sigma_m = \sigma_c \tag{8.5}$$

where σ_{inh} is the interfacial tensile stress from the strain inhomogeneity effect, σ_m is the hydrostatic stress, and σ_c is the critical stress to reach void nucleation. Argon [Argon, 1976] developed approximate expressions for σ_{inh}, expressed as $\sigma_{inh} = k_A \sigma_{eq}$, where σ_{eq} is the equivalent Von Mises stress and k_A is a geometrical factor given for a limited number of idealized cases (slender rods, platelets and round particles). Such a model for σ_{inh} does not take into account the interaction between particles. Argon [Argon et al., 1975] showed

that it is a good approximation for volume fraction lower than about 1%. It can thus be applied to clean metals with limited impurities, such as wrought Al alloys usually containing around 1% of intermetallic particles [Hannard et al., 2017]. However, particle interactions might not be negligible for a very heterogeneous distribution of particles, such as within clusters of particles that involve a larger value of the local particle volume fraction (see further discussion in section 8.4.1).

The Beremin model [Beremin, 1981] is based on the decomposition of the stress in the particle as the sum of the stress in the matrix and of an additional stress transfer arising from the deformation mismatch between the particle and the matrix [1]. Particles are treated as brittle solids and the fracture of the particle is assumed to occur when the maximum principal stress in the particle reaches a critical value :

$$\left(\sigma_{\text{princ}}^{\max}\right)^{\text{part}} = \sigma_{\text{crit}}^{\text{part}} \qquad \text{or} \qquad \left(\sigma_{\text{princ}}^{\max}\right)^{\text{int}} = \sigma_{\text{crit}}^{\text{int}} \tag{8.6}$$

Using Eshelby's theory [Eshelby, 1957] and the secant elasto-plastic modulus extension proposed by Berveiller and Zaoui [Berveiller and Zaoui, 1978] for the deforming matrix, the maximum principal stress in the particle is given by :

$$\left(\sigma_{\text{princ}}^{\max}\right)^{part} = \Sigma_{\text{princ}}^{\max} + k_b \; E_p \; \varepsilon_{eq} \tag{8.7}$$

where $\Sigma_{\text{princ}}^{\max}$ is the maximum principal stress in the matrix, k_b is a stress concentration factor which depends on the particle shape and orientation and E_p is the secant modulus of the matrix.

In order to derive this expression, it has been assumed that E_p is much smaller than the Young's modulus of the particle and the elastic strain in the particle has been neglected. The secant modulus $E_p = \sigma_{eq}/\varepsilon_{eq}$ and eq. (8.7) becomes :

$$\left(\sigma_{\text{princ}}^{\max}\right)^{part} = \Sigma_{\text{princ}}^{\max} + k_b \; \sigma_{eq} \tag{8.8}$$

For axisymmetric loadings, $\Sigma_{\text{princ}}^{\max} = \sigma_m + \frac{2}{3}\sigma_{eq}$ where σ_m is the mean stress and this gives :

$$\left(\sigma_{\text{princ}}^{\max}\right)^{part} = \sigma_m + (\frac{2}{3} + k_b)\sigma_{eq} = (T + \frac{2}{3})\sigma_{eq} + k_b\sigma_{eq} \tag{8.9}$$

In this form, eq. (8.9) is very similar to that already derived by Argon, see eq. (8.5). The factor k_b appearing in eq. (8.9) depends on the shape of the ellipsoidal particle through Eshelby's tensor [Eshelby et al., 1953]. In the seminal paper of the Beremin group [Beremin, 1981], a strong temperature dependence of $\sigma_{\text{crit}}^{\text{part}}$ was noted when comparing eq. (8.7) with experimental results

[1] F.M. Beremin is the name of a French research group founded in the early 1980s including researchers from Ecole des Mines (Paris), Framatome (Saint-Marcel) and BCCN (Dijon).

obtained at different temperatures. Thus, it was proposed to use the tangent modulus $E_t = ((\sigma_{eq} - \sigma_0)/\varepsilon_{eq})$ instead of the secant modulus $E_p = \sigma_{eq}/\varepsilon_{eq}$ since the effect of strain inhomogeneity should not include the yield stress σ_0.

Since the interaction law given in eq. (8.7) is based on Eshelby's theory, the stress field is considered as homogeneous within the particle and at the interface with the matrix. It is thus not possible to model the transition between particle cracking and interface decohesion depending on particle geometry or loading conditions. For example, Lassance *et al.* [Lassance et al., 2007] characterized the damage process of two 6xxx series Al alloys and observed that the dominant mode of nucleation is dependent on the particle configuration. Particle fracture is observed for particles elongated along the main loading direction. Interface decohesion is observed when the loading direction is perpendicular to the long dimension of the particle. The competition between particle fracture and interface decohesion depends on multiple factors, such as the flow properties of the matrix, the particle aspect ratio and the stress triaxiality. These effects have been addressed with more advanced finite element (FE) simulations [Lee and Mear, 1999; Roux et al., 2014].

Needleman [Needleman, 1987] suggested a modification of the Argon criterion. The nucleation stress is, similarly with the Beremin and the Argon criteria, a linear combination of the effective stress σ_{eq} and the hydrostatic tension σ_m, with the proportion of each term being an adjustable parameter c :

$$\sigma_{eq} + c\sigma_m = \sigma_c \tag{8.10}$$

This criterion was first shown to provide a good characterization of void nucleation by interface decohesion [Needleman, 1987] for the adjustable parameter c equal to 0.4. Later, Shabrov and Needleman [Shabrov et al., 2004] have shown that this criterion is also suitable for the case of particle cracking, but in this case, the optimal value of the parameter c was found to be 0.6.

The complexity of the nucleation process is such that the critical stress σ_c has to be identified from experiments [A. Pineau, 2007]. The experimental σ_c does not directly represent the fundamental interface cohesive strength or ideal particle strength, but rather some effective measures of strength depending on the choice of micromechanical model used to compute the stress inside the particle [Kosco and Koss, 1993; Benzerga and Leblond, 2010].

The onset of void nucleation by inclusion cracking depends on the inclusion size, with larger inclusions cracking at lower stresses [Shabrov et al., 2004; Hannard et al., 2016]. Chapter 7 explains in details brittle fracture. This is explained by the fact that larger particles have a greater probability of containing a critical volume defect [Kwon and Asaro, 1990]. Fig. 8.7(b) shows the fraction of broken particles as a function of the reconstructed particles size, obtained within Al 6056 tensile sample observed by X-ray tomography. The

analysis indicates a strong size effect on the probability of particle fracture. For example, particles smaller than 1 μm are almost never fractured, while particles larger than about 8 μm are almost always broken, see Fig. 8.7(b).

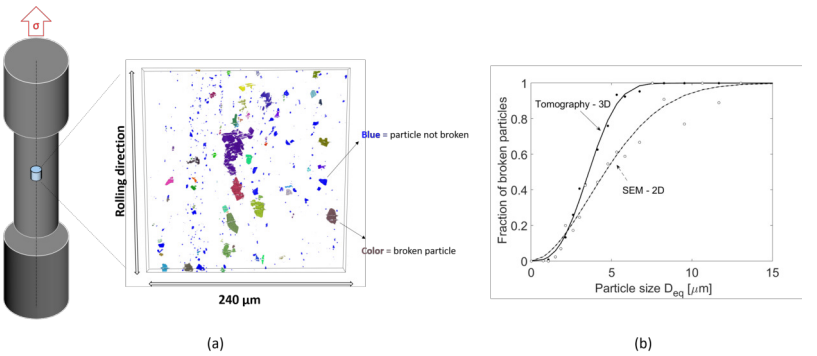

FIGURE 8.7: (a) Visualization of a sub-volume extracted from an Al 6056 tensile sample loaded along the rolling direction (T4 state, deformed up to 420 MPa), after automatized particle reconstruction. Unbroken particles are shown in blue and broken particles in other colors. (b) Fraction of broken particles as a function of the equivalent particle diameter (over 10,000 particles analyzed). See [Hannard et al., 2017] for more details.

Consequently, a statistical distribution of the critical stress for nucleation must be used in order to capture the common distribution of particle size. Such distribution of the nucleation process has usually been introduced through the application of Weibull statistics [Maire et al., 1997; Lewis and Withers, 1995; Babout et al., 2004]:

$$P(\sigma_{part}^{max}, V_{part}) = 1 - exp\left(-\frac{V_{part}}{V_0}\left(\frac{\sigma_{\text{princ}}^{\text{max,Part}}}{\sigma_w}\right)^m\right) \tag{8.11}$$

where σ_w and m are the Weibull stress and modulus, V_0 is the volume of particle for which the probability of survival is 37% at σ_w. For σ_w and V_0 fixed, void nucleation is confined in a narrower strength range when m increases. In principle, a single set of Weibull parameters (m, σ_w, V_0) should describe the probability of void nucleation within the material at all levels of straining [Lewis and Withers, 1995; Hannard et al., 2016].

Tanaka *et al.* [Tanaka et al., 1970] derived an energy-based void initiation criterion, with a particular interest in very small particles. Indeed, the elastic strain energy stored in very small particles could be insufficient compared to the corresponding energy for the creation of internal interfaces. Interfacial cracks are thus energetically favorable above a critical size and void nucleation can be modelled with a stress criterion for particles above this critical size. This critical size was initially estimated at about 25 nm [Tanaka et al., 1970] but is more likely to be above 100 nm [Benzerga and Leblond, 2010].

8.3.2 Void growth

Rice and Tracey (R&T) developed a simple void growth model [Rice and Tracey, 1969] which has been extensively applied in the literature. This model captures the effect of the stress state on the void growth that has been described at the macro scale in Fig. 8.3 and 8.4. The original version was developed for a spherical void in an infinite, rigid perfectly plastic material and under uniform remote strain and stress. The void volume change depends only on the hydrostatic stress, while the void shape evolution is dictated by the deviatoric stress component. The strain rate field is expressed in terms of the principal components $\dot{\varepsilon}_1 \geq \dot{\varepsilon}_2 \geq \dot{\varepsilon}_3$.

A version of the R&T model taking into account the aspect ratio evolution of an ellipsoidal void, with axes aligned with the principal loading directions (Σ_1,Σ_2,Σ_3), has been elaborated by Thomason [Thomason, 1990]. The rate of change of each radius (R_i, i=1,2,3) is given by:

$$\dot{R_k} = \left((1+E)\dot{\varepsilon_k} + \sqrt{\frac{2}{3}\dot{\varepsilon_l}\dot{\varepsilon_l}}D \right) R_{mean} \tag{8.12}$$

where $R_{mean} = \frac{R_1+R_2+R_3}{3}$ is used because the void is not spherical.

The dilatational factor D is given by $D = 0.558\ \sinh\left(\frac{3}{2}T\right) + 0.008\ \nu\ cosh\left(\frac{3}{2}T\right)$ for non-hardening materials and $D = 0.75T$ for linear hardening materials. The Lode variable is defined as $\nu = \frac{-3\varepsilon_2}{\varepsilon_1-\varepsilon_3}$. For axisymmetric loadings, the Lode variable ν is equal to 1 and the dilatational factor for non-hardening materials becomes :

$$D = \alpha \exp\left(\frac{3}{2}T\right) \tag{8.13}$$

The pre-exponential parameter α, equal to 0.283 in the original work of R&T, was later re-evaluated by Huang [Huang, 1991] using a more accurate numerical method :

$$\alpha = \begin{cases} 0.427\ T^{1/4} & \text{for} \quad T \leqslant 1, \\ 0.427\ T & \text{for} \quad T > 1. \end{cases} \tag{8.14}$$

The incompressible extension factor $(1 + E)$ was initially equal to $5/3$ in the original work of R&T. Later, Worswick and Pick [Worswick and Pick, 1990] proposed a more elaborated expression based on FE void cell calculations.

Using the incompressibility equation ($\dot{\varepsilon}_1 + \dot{\varepsilon}_2 + \dot{\varepsilon}_3 = 0$) and the definition of the Lode variable, integration of eq. (8.12) gives the following general

expressions for the three principal radii of an ellipsoidal void :

$$R_1 = \left(A + \frac{3+\nu}{2\sqrt{\nu^2+3}} B \right) R_0 \tag{8.15}$$

$$R_2 = \left(A - \frac{\nu}{\sqrt{\nu^2+3}} B \right) R_0 \tag{8.16}$$

$$R_3 = \left(A + \frac{\nu-3}{2\sqrt{\nu^2+3}} B \right) R_0 \tag{8.17}$$

where $A = \left(\frac{2\sqrt{\nu^2+3}}{3+\nu} D\varepsilon_1 \right)$ and $B = \frac{1+E}{D}(A-1)$. This integrated form provides useful estimates of the changes in volume and shape of the void in various plastic flow fields. However, it should be emphasized that the integration is strictly valid only when the principal axes of the strain rates ($\dot{\varepsilon}_1$,$\dot{\varepsilon}_2$,$\dot{\varepsilon}_3$) remain fixed in direction throughout the strain path [Thomason, 1990], including uniaxial tension (ν=1), pure shear (ν=0) and biaxial tension (ν=-1). Furthermore, the integrated form is only correct if the triaxiality does not change during the loading, which is not true after the onset of necking.

The R&T model has been successfully used by many authors [Marino et al., 1985; Kumar et al., 2009; Taktak et al., 2009; Pardoen and Delannay, 1998; Landron et al., 2011; Lecarme et al., 2014], provided that the pre-exponential parameter α is taken as a free parameter adjusted to account for the approximations in the model. Marini *et al.* [Marini et al., 1985] have shown that the parameter α increases with the initial void volume fraction. Indeed, the Rice and Tracey analysis describes the growth of a single void in an infinite perfectly plastic matrix. If the initial void volume fraction increases, the dilute void growth approximation becomes less accurate because the strain fields around the voids interact. This explains why the parameter α was found higher than the theoretical value when adjusting the model toward experimental measurements [Marino et al., 1985; Kumar et al., 2009; Taktak et al., 2009; Pardoen and Delannay, 1998; Landron et al., 2011; Lecarme et al., 2014; Hannard et al., 2016]. Lecarme *et al.* [Lecarme et al., 2014] have discussed several possible origins for the high value of the average factor α when compared to the one theoretically predicted by Huang (0.43).

Growth of penny-shaped void

When voids nucleate by particle cracking, voids are initially penny-shaped (R_z^0 very small along the loading direction) and the mode of deformation is dominated by opening and blunting of the void/crack tip [Tvergaard, 2011]. Based on this observation, Lassance *et al.* [D. Lassance, 2006] have proposed a simple mapping between the evolution of the void aspect ratio W_{void} and a parameter λ describing the void distribution (λ is the ratio of the average

distance along the loading direction to the one in the normal plane):

$$W_{void} = \lambda_0 \frac{exp(\varepsilon_{eq}) - 1}{exp(-\varepsilon_{eq}/2)} \tag{8.18}$$

The evolution law given in eq. (8.18) has shown good agreement with unit cell calculations [D. Lassance, 2006].

Void locking

At low triaxiality, voids elongate along the loading direction while contracting in the transverse direction. However, in the case of particle fracture, the particle fragments constrain the transverse contraction of the penny-shape void [D. Lassance, 2006; Tvergaard, 2011]. The same behavior occurs in the case of void nucleation by interface decohesion, with the particle inside the cavity hindering the transverse contraction of the void [Siruguet and Leblond, 2004; Bordreuil et al., 2003]).

For example, Tvergaard [Tvergaard, 2011] studied the effect of particle fragments on the growth of initially penny-shaped voids using axisymmetric cells (see Fig. 8.8(b)). Fig. 8.8(a) shows the evolution of the porosity for a void initially very flat (W^0_{void} =0.091) with (plain line) and without (dotted line) a cracked particle. The effect of void locking is more significant at low triaxiality (η=1/3). For stress triaxiality larger than 2/3, the void growth is unchanged with and without the cracked particle. Indeed, void locking effect is expected only in the case of void contraction in the transverse directions.

8.3.3 Coalescence

8.3.3.1 Void coalescence by ligament necking

The first stage of void growth by relatively homogeneous plastic deformation of the matrix surrounding the voids is interrupted by the localization of the plastic flow in the ligament between the voids. This localization corresponds to the onset of coalescence (Fig. 8.9). From that point on, a second mode of void growth, called void coalescence, starts, driven by plasticity localized between the primary voids. The problem is quite similar to an internal necking process at a micro-scale.

The criterion of Brown and Embury [Brown and Embury, 1973] for predicting the onset of coalescence has been widely used, mainly due to its simplicity. This criterion states that coalescence starts when two voids are close enough to be connected by microshear bands aligned at 45° to the main axis of the inter-void ligament. For a spheroidal void in the deformed configuration, this

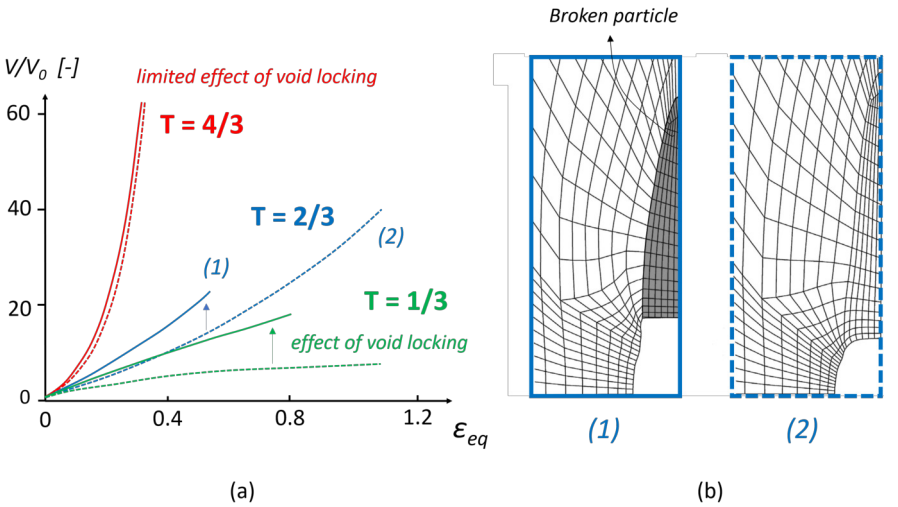

FIGURE 8.8: (*a*) Effect of particle fragments on the growth of initially penny-shaped voids based on unit cell results of Tvergaard (redrawn from [Tvergaard, 2011]). A plain/dotted line corresponds to void growth with/without void locking effect. (*b*) The unit cell, (1) with and (2) without the particle fragment. The initial void aspect ratio W^0_{void} is 0.091 and the particle aspect ratio W_p is 5.

condition is met when [Tekoğlu et al., 2012]:

$$\chi = \frac{1}{\sqrt{W^2 + 1}} \tag{8.19}$$

where W is the void aspect ratio and χ the void spacing ratio, as defined in Fig. 8.10.

Thomason [Thomason, 1990] developed a more advanced criterion based on the physical interpretation of void coalescence by internal necking, *i.e.* the competition between a stable and homogeneous deformation mode as opposed to an unstable, highly localized deformation mode in the ligament. In the early stages of deformation, the voids are small and widely spaced, *i.e.* the critical stress required to initiate localized plastic flow σ_n within the ligament is considerably larger than the macroscopic plastic flow σ_z. A localized deformation mode within the void ligaments would thus be energetically unfavorable and the diffuse flow is better predicted by a constitutive model for porous media (see Fig. 8.11), such as the Gurson model discussed in chapter 9.

With increasing plastic flow, the energy required to transition to a localized deformation mode within the void ligaments decreases due to two different

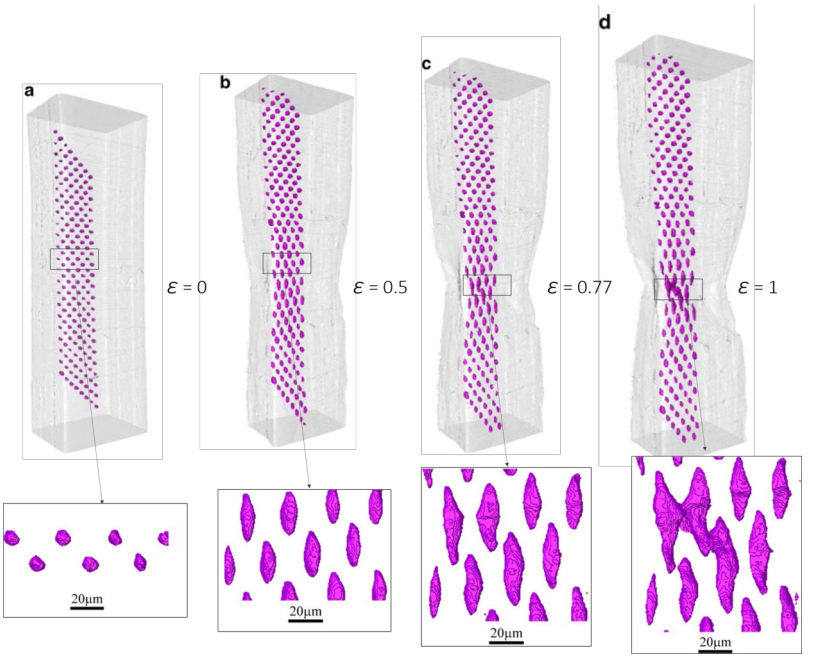

FIGURE 8.9: Tomography observations of the transition from (a,b) homogeneous growth to (c,d) internal necking of artificially and regularly inserted voids by laser-drilling copper sheets. After [Weck et al., 2008].

contributions. First, the local stress acting on the matrix ligament increases because the effective area fraction of the ligament decreases with void growth. Furthermore, the transition stress σ_n is evolving with the geometry of the voids because the ligament "neck" geometry increases the local stress triaxiality. Thomason [Thomason, 1985b] has shown that this geometrical effect can be rationalized by the use of a "plastic constraint factor", C_f, which is a function of the void aspect ratio (W_{void}) and the void spacing ratio (χ).

The plastic limit-load of the ligament, *i.e.* the transition to the localized deformation mode, is reached when the following constraint is satisfied :

$$\frac{\sigma_1}{(1-\gamma\chi^2)} \geq C_f\left(W_{void},\chi\right)\sigma_0 \tag{8.20}$$

where γ=1 for an axisymmetric unit cell and $\gamma = \pi/4$ for a cubic cell.

Thomason [Thomason, 1985b,a] has used two different unit cells, namely, a square-prismatic unit cell containing a square-prismatic void and a cylindrical symmetric unit cell containing circular-cylindrical void, in order to assess the sensitivity of the model to the detailed void shape. The matrix material was assumed to be perfectly plastic in both cases. The two different unit-cell models gave very similar dependence of the constraint factor with W_{void} and χ. In

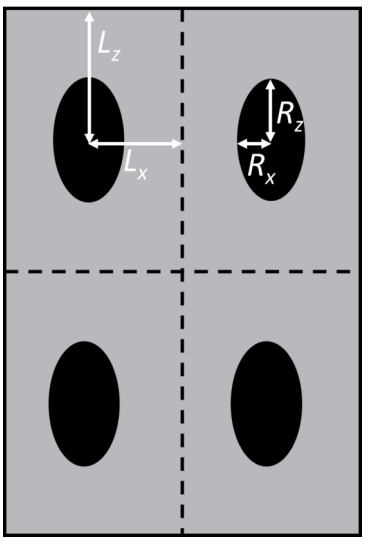

FIGURE 8.10: Idealization of axisymmetric spheroidal voids (such as classically used for unit cell-type FEM calculation) when loading along the vertical direction. The void aspect ratio W is defined as $\frac{L_z}{L_x}$ and the void spacing ratio χ as $\frac{R_x}{L_x}$.

the case of the axisymmetric cell, the following expression gives an empirical expression for C_f which is a close approximation of the upper-bound analysis [Thomason, 1985b] :

$$C_f = \left[\alpha \left(\frac{1-\chi}{\chi W_{void}}\right)^2 + \beta \frac{1}{\sqrt{\chi}}\right], \tag{8.21}$$

with α=0.1 and β=1.2. The constraint factor C_f decreases as the voids open (W_{void} increases) and get closer to each other (χ increases), see Fig. 8.12(a). From a physical point of view, this is explained by a lower ligament stress triaxiality increasing the rate of plastic deformation and favoring void coalescence.

Several variants of the plastic constraint factor C_f have been proposed in order to generalize and enhance the model, but the essence remains the same. The expression for the constraint factor C_f was improved by Pardoen and Hutchinson [Pardoen and Hutchinson, 2000] in order to incorporate material hardening. The parameter α is replaced by a function of the strain-hardening exponent n (α=0.1+0.217n+4.83n^2) and σ_0 is replaced by the current mean yield stress σ_y of the matrix.

Thomason's coalescence model does not predict any coalescence between

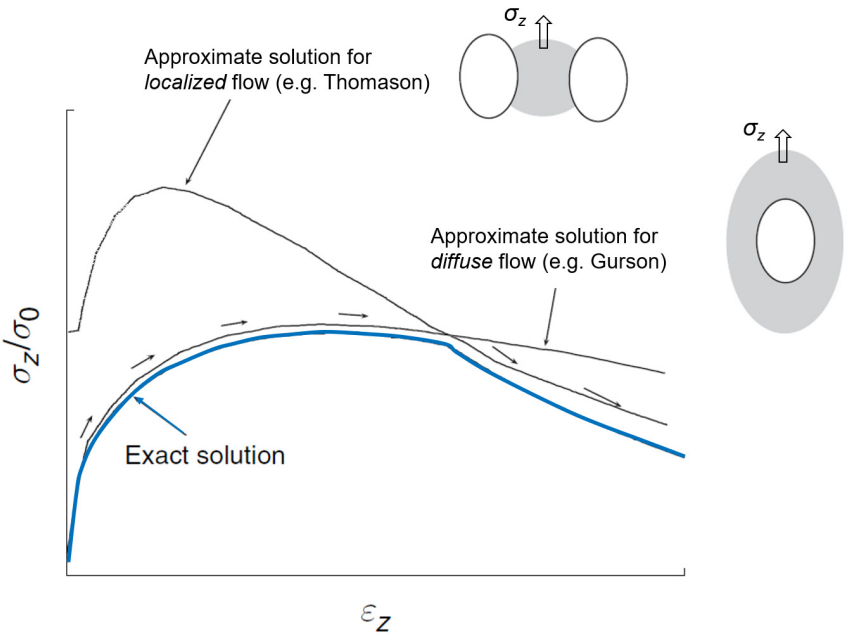

FIGURE 8.11: Schematic description of the competition between the two modes of plasticity around voids. In the early stages of deformation, the growth is stable. At some point, the deformation localized within the void ligament. Adapted from [Pineau and Pardoen, 2007].

very flat voids. Indeed, the constraint factor C_f given by eq. (8.12) goes to infinity in the limit of very flat voids, *i.e.* W_{void} approaches 0 (see Fig. 8.12(a)). This trend is explained by the axisymmetric velocity fields used by Thomason which diverge for penny-shaped cracks. In other words, eq. (8.20) will never be satisfied for very low W_{void} and Thomason's model predicts that no coalescence would occur for very flat voids. To avoid this limitation, Benzerga [Benzerga, 2000] used improved trial velocity fields in the limit-analysis procedure (see Fig. 8.12(b)) and the numerical results are shown in Fig. 8.12(a). Benzerga proposed a new form of the plastic constraint factor based on these numerical results :

$$C_f = \left[0.1\left(\frac{\chi^{-1}-1}{W^2+0.1\chi^{-1}+0.02\chi^{-2}}\right)^2 + 1.3\frac{1}{\sqrt{\chi}}\right], \tag{8.22}$$

In practice, however, the quantitative predictions obtained with the two models are very close for most cases analyzed [Benzerga and Leblond, 2010]. Indeed, penny-shaped voids rapidly open in the loading direction, become more rounded and W_{void} increases rapidly to values for which both models give

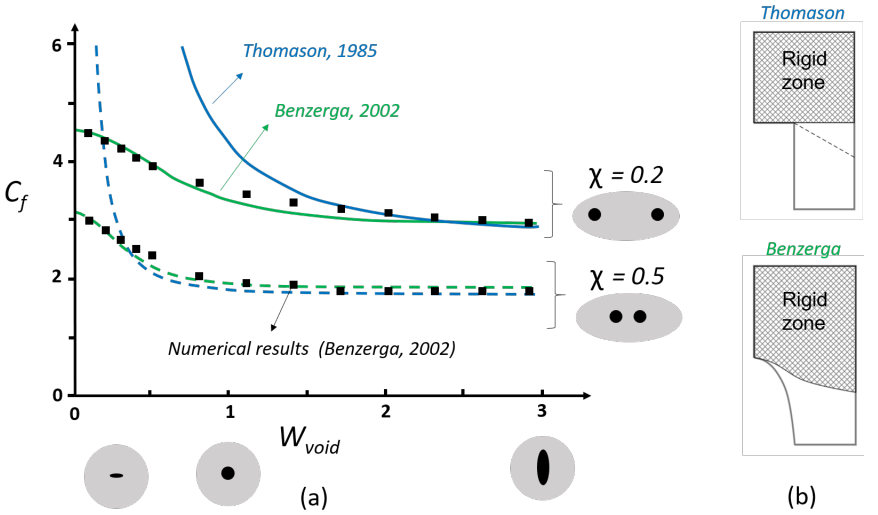

FIGURE 8.12: (*a*) Effect of the voids configuration (W_{void} and χ) on the plastic constraint factor C_f. (*b*) Unit cells used by Thomason [Thomason, 1985b,a] and by Benzerga [Benzerga, 2002].

similar results, *i.e.* W_{void} larger than about 1 (see Fig. 8.12(*a*)). Furthermore, the highly constrained and localized character of plastic flow in the inter-void ligament during void coalescence limits the effect of void shape (W_{void}) and the inter-void spacing χ is the key parameter controlling the transition to the coalescence mode [Benzerga and Leblond, 2010].

Scheyvaerts *et al.* [Scheyvaerts et al., 2011] further improved eq. (8.20) in order to account for the orientation of the inter-void ligament. Indeed, the void axes are not necessarily aligned with the principal loading directions and the ligament is not necessarily transverse to the maximum principal stress. The two voids are thus transformed into an effective configuration made of two identical voids (defined by W_{eff} and χ_{eff}) in order to allow the evaluation of the coalescence model and σ_1 is taken as the stress normal to the ligament. This extension of the coalescence criterion reduces to its original definition when the voids are aligned and have the same orientation.

In many ductile metallic alloys, the growth and coalescence of primary voids (typically larger than 1 μm) is affected by the growth of a second population of much smaller voids. For steels, the second population may be associated with small carbides or grain-size-controlling dispersoid particles in Al alloys. These secondary voids do not affect the stable growth of the primary voids but strongly accelerate the void coalescence process by softening the material in the ligament between the voids where the strains are very

large [Fabrègue and Pardoen, 2008]. The softening induced by the growth of this second population has been heuristically introduced in the coalescence criterion of eq. (8.20) by multiplying the yield stress of the matrix material by (1-f_2), with f_2 being the maximum value of the secondary void volume fraction over the ligament [Fabrègue and Pardoen, 2008].

8.3.3.2 Void coalescence by void sheeting

The second mechanism by which voids can coalesce is the so-called void sheeting mechanisms [Garrison Jr and Moody, 1987]. In this mechanism, void growth of the primary void is generally limited due to low levels of stress triaxiality. However, the strain levels, in particular locally between two voids, are high and can give rise to the nucleation of a second population of voids (as discussed in the previous section). The second population of voids is nucleated on smaller second-phase particles that are present in high density between primary nucleated voids. For example, in aluminium alloys these are generally Mn and Cr rich dispersoids of a typical size of 50-100 nm [Fabrègue and Pardoen, 2008].

Fig. 8.13(a) shows the void sheeting mechanism between two large voids in steel via a 2D metallography section [Cox and Low, 1974] and Fig. 8.13 (b) shows the void sheeting mechanism for an aluminium alloy on a tomography section of an imaged stopped crack. Fig. 8.13 (c) show the fractography for the same material with very fine dimples between the two large voids. These fine dimples belong to the void sheet. It is imagined that the nucleation, growth and coalescence of the small voids occur all at once for a very small increment of macroscopic loading and the process can even be sustained by the energy released during elastic unloading of the material at fracture.

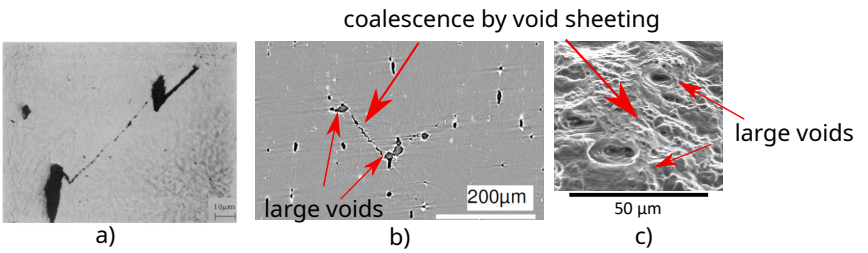

FIGURE 8.13: Coalescence by void sheeting a) in steel, after [Cox and Low, 1974] b) for a stopped crack in a AA2139 T3 alloy observed by tomography c) on the fracture surface for the same alloy, adapted after [Ueda et al., 2014]

8.4 Damage mechanisms in heterogeneous materials

As discussed in previous sections, the understanding of the micro-mechanisms leading to ductile fracture is quite advanced. Furthermore, much effort has been devoted to the prediction and numerical modeling of these mechanisms, but the development of predictive engineering models remains a challenge (see, for example, the blind predictions challenges from the Sandia National Laboratories [Boyce, 2014]).

One particularly challenging aspect of ductile damage is linked to microstructural variability, while modeling approaches always require some degree of idealization of the microstructure. For example, several micromechanical models are based on void unit cell-type FEM calculations. These models would thus provide accurate predictions for sufficiently ideal microstructures, generating very regular distributions of voids and with uniform elasto-plastic behavior, but this is the exception rather than the rule in engineering materials. Of course, these models remain useful and several calibration approaches have been developed, but major questions remain in the case of heterogeneous materials.

One difficulty associated with the introduction of an explicit representation of the microstructure in models is that it is computationally expensive, especially for heterogeneous materials which require a larger representative volume element in order to be representative of the entire microstructure. Significant efforts have gone into refining these "average" models and much progress has been made to account for heterogeneities on damage accumulation [Pardoen et al., 2010]. However, there is a natural limit to their accuracy. For example, models based on a more or less periodic void distribution cannot properly reproduce the physical mechanisms of the failure process within heterogeneous materials, *i.e.* voids growth and that will merge to form microcracks that propagate throughout the heterogeneous particles field [Z. Chen, 2013; Hannard et al., 2016].

In this section, the most common types of microstructural heterogeneities are discussed, together with experimental evidence indicating that they strongly affect the ductile damage process. The most common types of heterogeneities found in polycrystalline metals are illustrated in Fig. 8.14:

1. Type I. Heterogeneous second phase distributions: The morphology (*i.e.* size, shape and orientation) of coarse second phase particles responsible for primary void nucleation usually varies significantly within the same microstructure. Furthermore, their distribution can be spatially concentrated into clusters.
2. Type II. Distributions of initial porosities and micro-cracks: A dis-

tribution of initial porosities and micro-cracks, *i.e.* resulting from material processing and not due to void nucleation, are also usually observed in metals. For example, cast Al alloys often present large amount of porosities due to gas involved in the molten state, or micro-cracks due to heat-tearing. In wrought Al alloys, pre-existing porosity remains much smaller than in cast alloys and typically ranges between 0.001% and 1% [Pineau and Pardoen, 2007].

3. Type III. Crystallographic orientation of the grains. A crystallographic texture, as caused for instance by the preferred orientation of the grains along the rolling direction, impacts the ductile failure as void growth is driven by plastic deformation of the surrounding material.
4. Type IV. Heterogeneity within the grain-boundary regions: Precipitation-hardening alloys may exhibit heterogeneous precipitation of coarse phases at grain boundaries, inhibiting the formation of precipitates in the grain boundary region. These Precipitate Free Zones (PFZs) remain thus much softer compared to the core of the grains, which promotes strain localization and intergranular fracture.

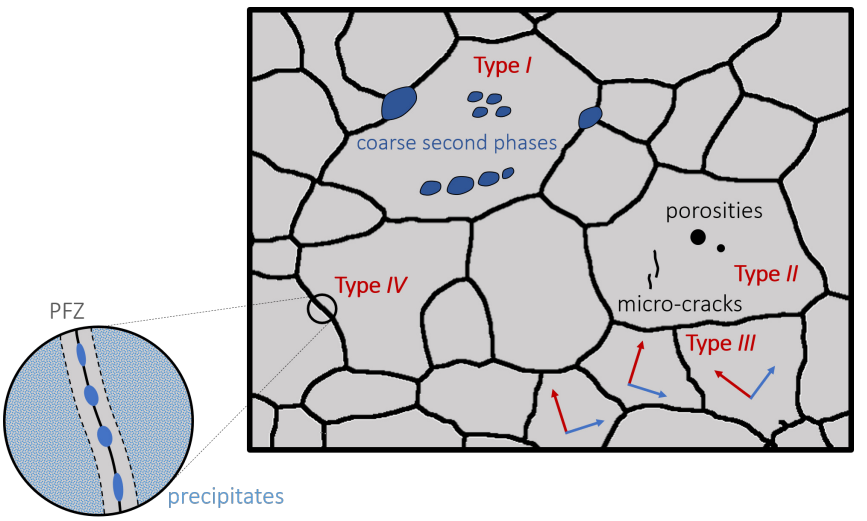

FIGURE 8.14: Various types of microstructural heterogeneities found in polycrystalline metals, as described in the text.

The microstructural heterogeneity effects usually depend on the loading direction and three types of sources of anisotropy can impact the fracture behavior [Hannard et al., 2018]:

1. Plastic anisotropy is related to the crystallographic texture and is

associated with a yield stress and a strain hardening which depend on the loading direction.

2. Morphological anisotropy originates both from the shape of the voids or from the shape of the void nucleating particles. For example, particle cracking is favored on elongated particles preferentially aligned along the loading direction [Beremin, 1981].
3. Topological anisotropy results from the spatial distribution of particles, particularly affecting void coalescence. For example, during the rolling of wrought Al alloys, brittle intermetallic particles are broken and a stringer-type particle clustering develops along the rolling direction [Pilkey et al., 1998].

8.4.1 Clustering and anisotropic distribution of particles

The spatial distribution of brittle particles, *i.e.* void nucleation sites, can significantly influence the damage process in cases of strong heterogeneity. For example, coalescence might occur early in clusters of particles (Fig. 8.15, first order clustering), regions in which void nucleation was fast and void close to one another, while other regions of the material exhibit limited damage (Fig. 8.15, homogeneous). Fig. 8.15(c) and (d) show X-Ray microtomography reconstructed images just before fracture of tensile tests performed on alloy Al 6056-T4 associated with a second-order clustering and after breaking these clusters by friction stir processing, respectively [Hannard et al., 2018]. After local redistribution and homogenization of particle distribution, the fracture strain is significantly improved, as observed by comparing the final cross-sections shown in Fig. 8.15(c) and (d).

Furthermore, the shape and distribution of the clusters themselves also influence the damage sequence. For example, a strong and anisotropic large-scale clustering of particles, *i.e.* particles clusters are much closer to each other in the rolling direction compared to the transverse direction. This proximity of clusters creates an easy percolating crack path along the rolling direction as a crack can extend along this direction throughout the material without the need to cross less-damaged matrix (Fig. 8.15, second order clustering(T)). On the opposite, the presence of a tougher matrix between these clusters strongly reduces their detrimental effect on the fracture properties by allowing a second stage of stable void growth between clusters (Fig. 8.15, second order clustering(R)).

8.4.2 Precipitate Free Zones (PFZ) and coarse precipitates

One of the main sources of ductile damage in aluminum alloys is associated with void nucleation on micron-sized intermetallic particles (see Fig. 8.16(a)),

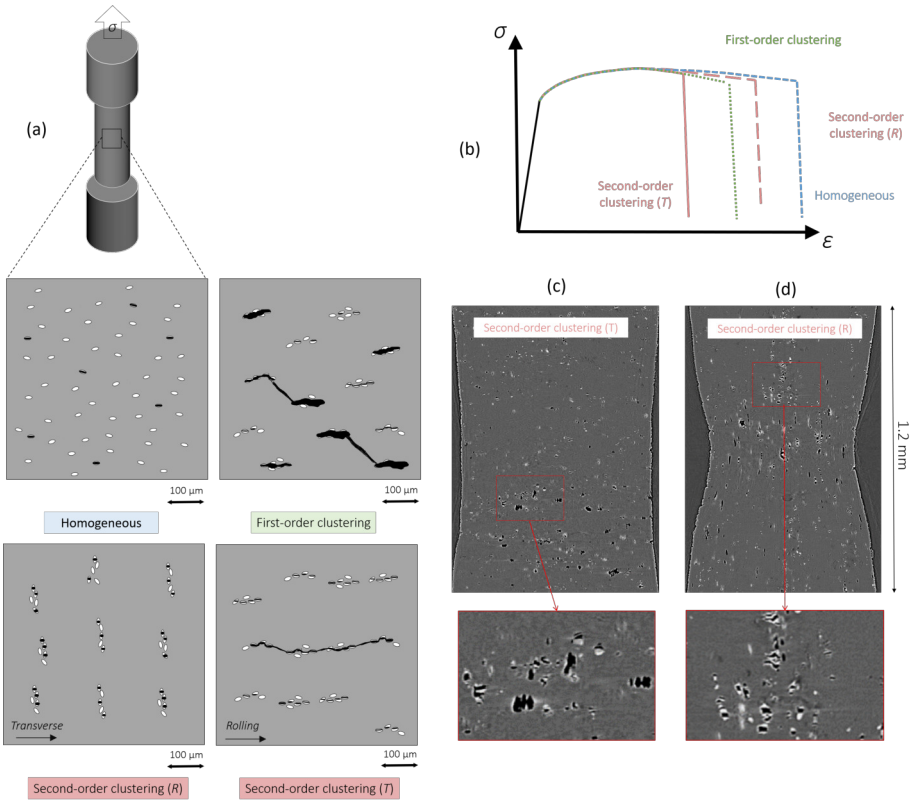

FIGURE 8.15: (a) Schematics of the damage sequence depending on the spatial distribution of void-nucleating particles and (b) corresponding tensile curves. (c) X-Ray microtomography reconstructed images just before fracture of tensile tests performed on alloy Al 6056-T4, associated with a second-order clustering and loaded along (c) the transverse direction and (d) the rolling direction. Voids appear in black in the grey matrix and IM particles appear in white. See [Hannard et al., 2018] for more details.

as discussed previously. However, in addition to these brittle particles, 7xxx Al alloys often exhibit grain boundaries surrounded by a thin layer of material softer than the grain core (see Fig. 8.16(*c*)), promoting strain localization and intergranular fracture [Lezaack et al., 2022], see Type IV in Fig. 8.14. These softer zones, called precipitate-free zones (PFZs), have been associated with heterogeneous precipitation of coarser precipitates, which are trapping the alloying elements in the vicinity of the grain boundary (GB).

Fig. 8.16 illustrates the competition between intergranular and transgranular fracture in the 7475 Al alloy [Lezaack et al., 2022]. Using friction stir

processing (FSP) and post-FSP heat treatments, microstructures with similar hardening precipitates and PFZs but with very different grain structures and intermetallic particles size distribution were generated. The formation of elongated cracks following the grain boundaries is observed within the rolled material, *i.e.* intergranular fracture (see Fig. 8.16(e)). On the opposite, fully transgranular crack propagation is observed and intergranular damage is fully inhibited after FSP due to grain refinement (see Fig. 8.16(f)). The competition between transgranular and intergranular failure is strongly affected by the microstructure or the stress state, as extensively discussed in [Kamp et al., 2002; Pardoen et al., 2010; Lezaack et al., 2022].

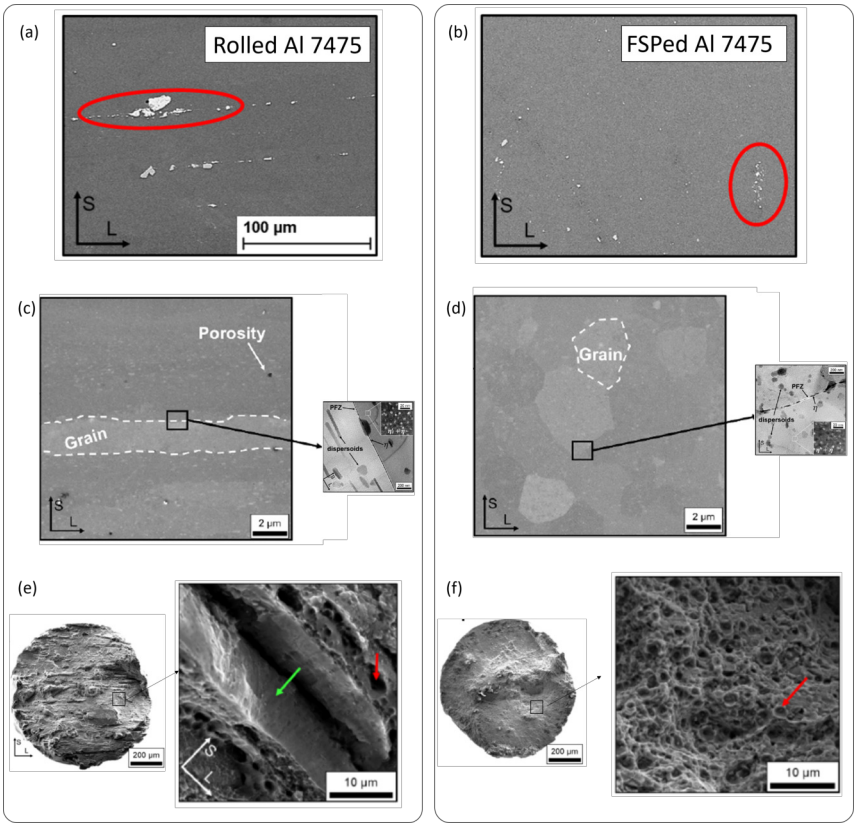

FIGURE 8.16: Metallographic observations and SEM fractography of 7475 Al specimens, (a) before and (b) after FSP. Intergranular and transgranular failure mechanisms are observed in (a) and (b), respectively. Adapted from [Lezaack et al., 2022].

The particular case of ductile damage originating from these microstruc-

tural heterogeneities under shear loading will be discussed in the following section 8.5.

8.5 Shear fracture mechanisms

Under shear loading the stress triaxiality at the continuum level is null. This driving force is thus lacking for void growth and fracture. Still, failure under shear occurs as indicated in previous sections. The study of this advanced mechanism is currently largely debated in the community [Abedini et al., 2018; Gross and Ravi-Chandar, 2016; Roth et al., 2018; Tancogne-Dejean et al., 2021; Buljac et al., 2023] and some of these results will be discussed in the present section.

Studies in steels have shown that the steel matrix may decohere from the particles normal to the maximal principal stress direction and give rise to void growth. The voids then elongate and rotate [Abedini et al., 2018; Roth et al., 2018]. This mechanism can be observed in Fig. 8.17(c) for an FB600 steel for in situ laminography data in a ligament of a flat 'smiley'-shape shear sample shown in Fig. 8.17(a). The final fracture surface for this material is given in Fig. 8.17(d) where a CaO particle may be seen in the center of the elongated void. The final fracture has taken place by the nucleation of very small voids, potentially at the ferrite bainite interface. These voids have also been sheared.

The damage mechanisms under shear loading for high-strength Al-alloys are shown in the rest of Fig. 8.17. The evolution of a pre-existing hydrogen pore is shown in Fig. 8.17(e, f). The void elongates, rotates and almost closes. The final crack passes close to the void, but the void does not seem to have a major effect on the final fracture.

Concerning intermetallic particles, they fracture normal to the direction of the maximum principal stress, see Fig. 8.17(g, h). Despite the lack of stress triaxiality the voids grow between the particle debris, as the intermetallic particles are known to be stiff.

Similar mechanisms have been observed by in situ laminography for an aluminium alloy 2198, see Fig. 8.17 (i). The particle showed a crack normal to the maximum principal stress direction. A void then grew during shearing between the two particle parts. Finally, the void fully contributed to the final crack. This highlights again the role of particles in shear fracture and the uncommon way in which voids may grow under these circumstances, *i.e.* due to the stiff particle debris that keeps the voids open.

This is consistent with findings by Tomstad *et al.* [Tomstad et al., 2022] who found that the fracture strain in shear loading is reduced when the intermetallic particle content is increased.

8.6 Experimental methods for ductile damage

Various methods to quantify ductile damage have already been introduced in the previous sections. This section provides a brief review of these methods, with a more detailed description of recent developments regarding 2D, 3D (X-ray tomography) and 4D (time resolved) imaging.

Experimental methods for assessing ductile damage can be divided into indirect and direct methods. Indirect methods involve measuring physical or mechanical properties that are affected by the presence of damage, such as density or Young's modulus. Direct methods involve direct imaging of the microstructure and damage, either directly during testing (in situ approaches), by stopping the testing of the specimens (ex situ approaches), or after the failure of the specimen (post mortem observations). This section briefly reviews direct methods, differentiating two-dimensional imaging, three-dimensional imaging, and finally four-dimensional imaging (*i.e.* 3D imaging over a period of time).

8.6.1 2D Methods

There are numerous two-dimensional approaches, including fractography and metallography (see Fig. 8.18), to study the deformation and fracture of materials.

The goal of fractography (Fig. 8.18(a)) is to characterize the damage sequence from the final fracture surface, interpreting fracture mechanisms from the surface topography and features. Réaumur (1722) already evaluated the quality of steels by observation of their fracture surfaces, identifying surfaces exhibiting "many little mirrors of irregular shape and arrangement" as an indicator of poor quality [Lynch and Moutsos, 2006]. Zappfe and Clogg used the term fractography for the first time in 1943, describing a new tool for studying fracture surfaces in metals [Zapffe and Clogg, 1945]. However, these early fractography studies were performed with high-magnification light microscopy and thus small depth of focus, hindering the investigation of rough ductile fracture topography [Azevedo and Marques, 2010]. Nowadays, scanning electron microscope (SEM) is widely used for the examination of ductile fracture surfaces facilitated by simple sample preparation and large depth of

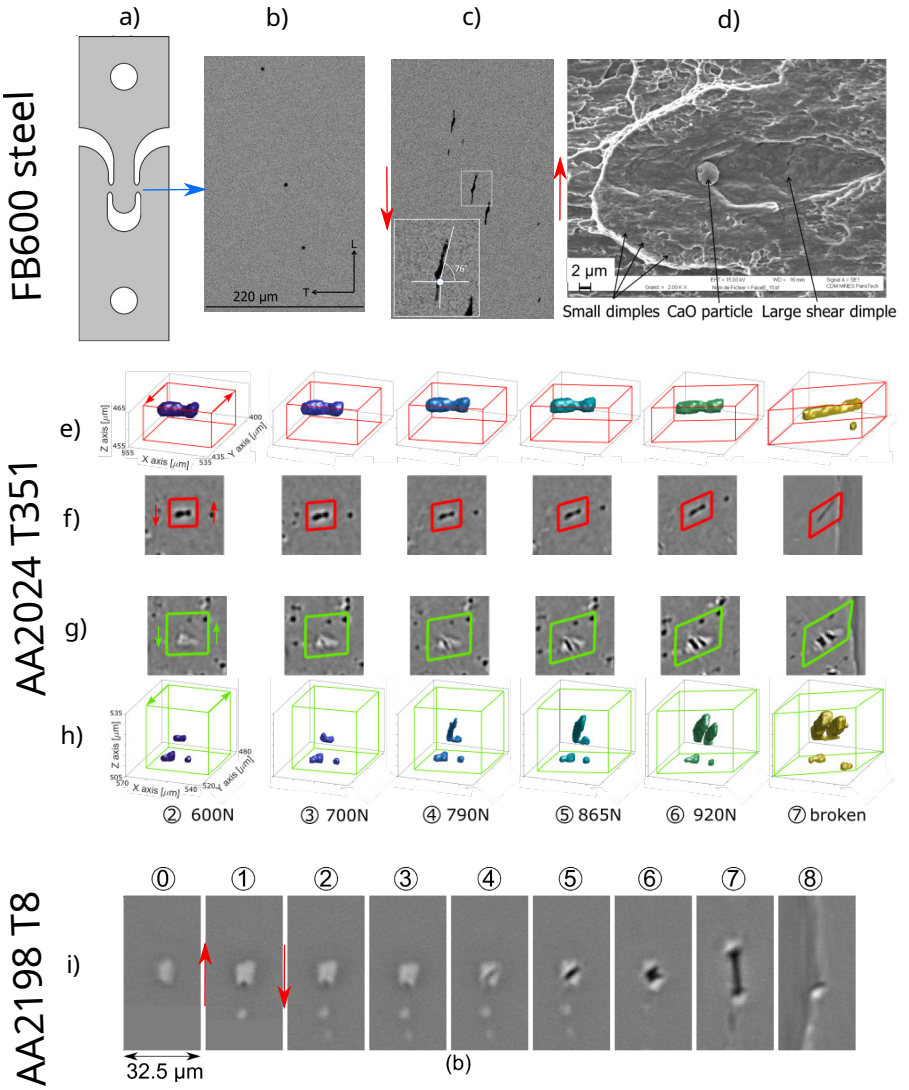

FIGURE 8.17: Damage mechanisms under shear loading a) and b) damage evolution from CaO particles observed by in situ laminography c) corresponding fractography for FB600 steel, after [Roth et al., 2018]; for AA2024 d) 3D view e) 2D laminography sections of the evolution of a void, after [Tancogne-Dejean et al., 2021]; f) 2D laminography sections g) 3D view of the evolution of a particle; h) 2D laminography sections of a particle in AA2198, after [Buljac et al., 2023]

focus (150 μm to 10mm at 100x [Azevedo and Marques, 2010]).

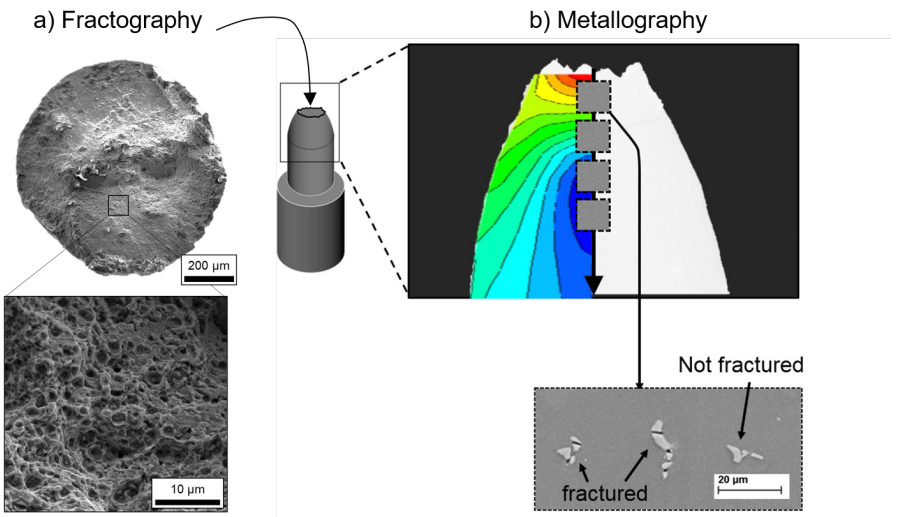

FIGURE 8.18: Schematic of a broken tensile specimen, illustrating (*a*) fractography and (*b*) metallography. Adapted from [Hannard et al., 2016].

On the other hand, metallographic sections through damaged specimens (and arrested test) or through fracture surfaces are often characterized with various imaging techniques such as optical microscopy, SEM, Transmission Electron Microscopy (TEM) or Electron backscatter diffraction (EBSD). For example, metallographic observations of broken tensile samples polished down to mid-thickness can be used to analyze the probability of fracture of intermetallic particles at various distances from the fracture surface (Fig. 8.18(*b*)). For each particle, the high magnification SEM allows to identify particle dimensions and if it is broken or not broken. This also allowed to build the result of Fig. 8.7(*b*). The color map shows the finite element simulation used to compute the strain history at the position of the particle within the sample. Metallographical observations allow characterizing multiple microstructural features that can influence the damage sequence and fracture process, such as grain structure, distribution of impurities, or segregation of alloying elements at grain boundaries. Recently, in situ TEM has also been used to study the damage sequence within copper single crystals [Ding et al., 2016]. This high resolution technique enables the investigation of the intricate interplay between dislocation sources and obstacles confined within nanoligaments during the process of necking, *i.e.* during coalescence.

8.6.2 3D Methods

The word "tomography" comes from the Greek word "tomos" meaning "slice". The technique has been initially developed for medical applications in the

1970s. Cormack [Cormack, 1973] was the first to demonstrate the feasibility to reconstruct the cross-section image of an object with a limited number of X-ray radiographs. The first Computed Tomography (CT) scanner was built later by Hounsfield [Hounsfield, 1973]. Hounsfield developed a new approach for image reconstruction using the computers available at that time. In this way, the concept of computed tomography was born [2]. Computed tomography improved with the development of digital computers [Stock, 1999] and industrial X-ray computed tomography for non-destructive materials characterization was marketed in the 1980's.

8.6.2.1 The principle of X-ray tomography

The principle of X-ray tomography basically consists of an extension of classical X-ray radiography. A series of radiographs is recorded for different angular positions of the sample, which rotates around an axis perpendicular to the beam. Each radiograph provides only a projection of the variation of X-ray absorptivity within the object. The set of radiographs (a scan) is then combined to reconstruct the three-dimensional distribution of the local attenuation coefficient of the material. The reconstructed volumetric image consists of a 3D matrix of voxels (analogous to pixels in a 2D digital image), for which the grey level of each voxel describes the X-ray attenuation at that position.

The voxel size is dependent on the field of view and the number of detector elements. Indeed, the specimen must remain in the field of view for all rotations in order to ensure a good volume reconstruction. For a fixed voxel size, the maximum specimen diameter is thus limited by the number of elements of the detector (usually between 1000 and 4000 pixels across the width for a CCD detector [Maire and Withers, 2014]) multiplied by the voxel size. Recently, commercial nanoCT systems have started to appear in research laboratories. Spatial resolutions substantially below 1 μm can be achieved, but much smaller specimen diameters than in microCT are thus required. Microtomography is usually associated with at least 50μm spatial resolution and nanotomography for spatial resolutions substantially below 1μm [Stock, 2008].

Modern laboratory projection microCT systems operate in cone beam geometry (Fig. 8.19(a)). With the use of a cone beam, the spatial resolution is changing with the source-to-object distance. Synchrotron X-ray microtomography uses a parallel beam (Fig. 8.19.(b)) where the source-to-object distance is very large (*e.g.* 145m on ID19 at the European Synchrotron Radiation Facility (ESRF) [Withers, 2007]). In this case, the spatial resolution can be tuned using different types of detectors [Babout, 2011]. The parallel beam geometry facilitates in-situ experiments since a large distance between sam-

[2] Cormack and Hounsfield, generally credited with inventing computed tomography, were awarded the Nobel Prize in Medicine in 1979.[Cierniak, 2011]

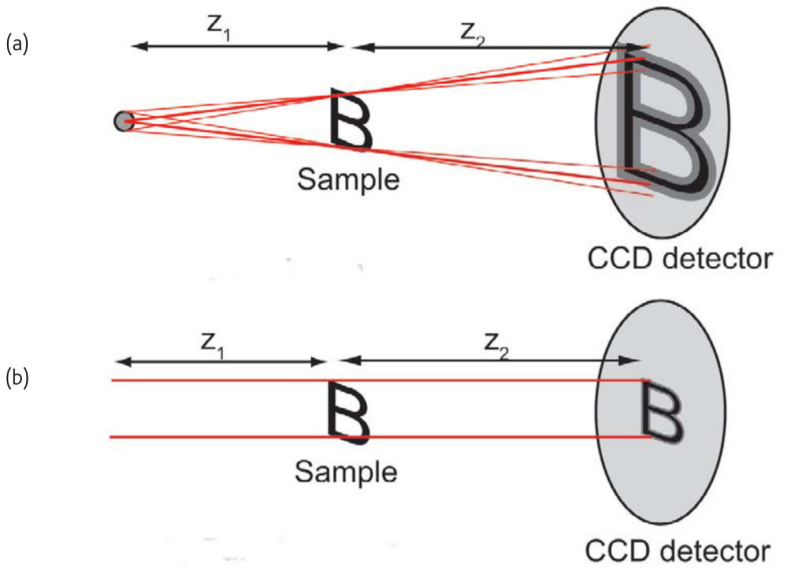

FIGURE 8.19: Schematics illustrating (*a*) cone-beam and (*b*) parallel-beam projection systems. Reproduced from [Withers, 2007].

ple and detector can be maintained without loss of intensity [R. Schurch and Withers, 2015]. Synchrotron facilities offer X-rays with high flux, and high coherence, with the ability to tune the X-ray spectrum from a broad spectrum to a monochromatic beam [R. Schurch and Withers, 2015]. The high flux also facilitates in-situ experiments as it enables rapid tomography data collection [Wu et al., 2017]. Furthermore, monochromatic X-rays are advantageous since their wavelength can be specifically tuned to achieve greater absorption contrast compared to a broad spectrum source (such as laboratory sources) [R. Schurch and Withers, 2015]. Nowadays, multiple manufacturers offer turnkey microCT systems for routine, day to day laboratory characterisation [Stock, 2008]. However, commercial laboratory microCT employs polychromatic radiation and provide thus lower contrast than synchrotron microCT with monochromatic radiation. A review of commercial laboratory microCT systems can be found in Ref. [Stock, 2008].

Recently, multi-scale correlative methods [Burnett, 2014], which involve the coordinated use of X-ray tomography combined with other characterization techniques have been developed ("coordinated" refers to the fact that all analyses are performed for the same 3D region). This type of approach allows a more complete understanding than either method could have provided separately. For example, such a 3D correlative approach has been used to pro-

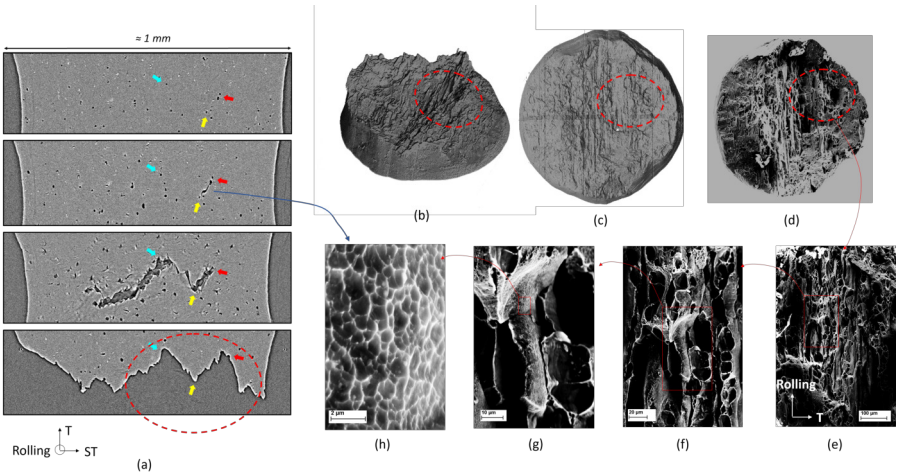

FIGURE 8.20: (a) 3D X-ray microtomography cross-sections of the damage evolution within an Al 6056 (T6 state) tensile specimen, with a voxel size of 1.06 μm^3. A few voids are tracked from scan to scan and identified by colored arrows. (b, c) 3D perspectives of the broken specimen. (d) Fracture surface observed by SEM, with the same orientation shown in (c). (e) to (h) SEM images of the fracture surface, with increasing magnification. The high magnification image in (h) shows small dimples as typically associated with a second population of voids nucleating on dispersoids in high-strength Al alloys. This region corresponds to the micro-crack observed in (a), as identified by the connecting arrow. Data from [Hannard et al., 2016].

vide greater insight into the mechanisms of ductile fracture in low alloy steel [Daly and Burnett, 2017]. An example of correlative characterization of damage by in situ X-ray tomography combined with SEM fractography is shown in Fig.8.20. The early formation of a micro-crack is observed early in the deformation process, as shown in Fig.8.20(a). By performing SEM fractography in a correlative approach, it is possible to identify the region of the fracture surface corresponding to this micro-crack, as identified by the connecting arrow (Fig.8.20(a) and (h)). In this example, in situ tomography allows identifying micro-cracks appearing early during the test. However, the voxel size of 1.06 μm^3 does not allow to observe the second population of voids that originated such micro-cracks, as identified with the population of smaller dimples on high magnification SEM images (Fig.8.20(h)).

8.6.2.2 Synchrotron laminography

Synchrotron laminography [Helfen et al., 2005] can be used for 3D imaging of local regions of interest inside sheet materials at high resolution. In cases of

scanning flat samples at high resolution, computed tomography (CT) would cause strong artifacts by projection angles close to the sample surface [Xu et al., 2012]. X-ray transmission is strongly reduced in this case. To overcome this problem, synchrotron radiation computed laminography (SRCL) is used for scanning regions of interest in flat laterally extended objects [Helfen et al., 2005, 2012]. A wide range of engineering-relevant boundary conditions and local stress-strain histories can be studied using synchrotron laminography [Kong et al., 2022]. Xu *et. al* [Xu et al., 2012] compared the image quality between CT and CL for flat samples and concluded that CL reconstructed flat structures in every direction equally well whereas structures in some directions could not be reconstructed well in CT.

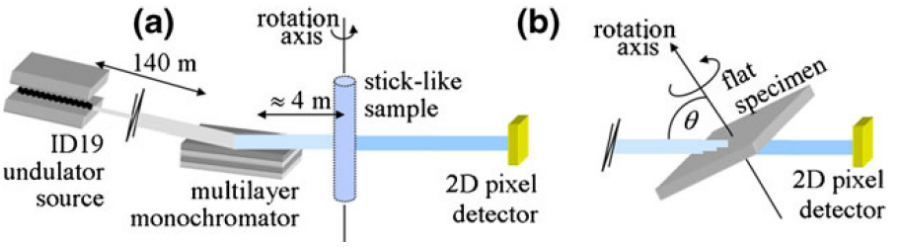

FIGURE 8.21: Schematic representation of synchrotron radiation (a) computed tomography and (b) computed laminography set-ups after [Helfen et al., 2005; Morgeneyer et al., 2013b].

Fig. 8.21 presents the typical (a) Computed Tomogaphy (CT) and (b) Computed Laminography (CL) set-ups at synchrotron facilities. Unlike the rotation axis perpendicular (θ=90°) to the beam direction in CT, the rotation axis is inclined at an angle of θ <90° with respect to the beam direction in the computed laminography. The projected images of the sample are acquired over an angular range between 180 to 360° around the rotation axis. Since the whole scan process takes few minutes, the sample usually has to stay stationary before being scanned [Morgeneyer et al., 2013b]. The stack of radiographies is then processed to reconstruct a 3D volumetric image by using a filtered-back projection algorithm [Myagotin et al., 2013].

The ductile damage mechanisms are illustrated in Fig. 8.22 during monotonic loading of a fatigue pre-cracked sample. The microstructure of the aluminium alloy 6061 (T6 state) is studied with 2D reconstructed sections of the 3D laminography data from a 1 mm thick pre-cracked specimen: iron-rich particles appear in white, while Mg_2Si particles appear in dark gray. The fatigue pre-crack is hardly visible in Fig. 8.22(a). It opens under load and the crack tip blunting can be observed in Fig. 8.22(b). Void nucleation from a Mg_2Si particle is also observed in this figure. A cavity is formed at 40 µm in front of the crack tip and 45° with respect to the loading direction. A pre-existing

void is present in the material above the crack front. The closer the cavity is to the crack, the larger the void growth rate. Simultaneous void growth for some voids and void nucleation for other particles are observed.

Two types of void coalescence can be observed in Fig. 8.22(d). First, coalescence by internal necking between voids nucleated from coarse precipitates. A second mechanism by void sheeting is also observed, with shear bands forming between voids initiated from coarse precipitates. These "void sheets" formed between larger voids are oriented at 45° from the loading direction. In these localization bands, a second population of micro-voids is initiated on smaller precipitates (dispersoids of chrome and manganese), which are not visible with the voxel size of 0.7 μm [Shen et al., 2013]. The largest stress triaxiality is expected at the mid-thickness of the specimen, which should favor void growth and coalescence by internal necking. This process is then bypassed by the formation of shear bands containing micro-voids before joining the crack. From Fig. 8.22(e), a crack has formed by voids linkages and starts to propagate perpendicular to the loading direction. As coarse precipitates are distributed on grain boundaries, the crack propagation is likely to follow an intergranular mode.

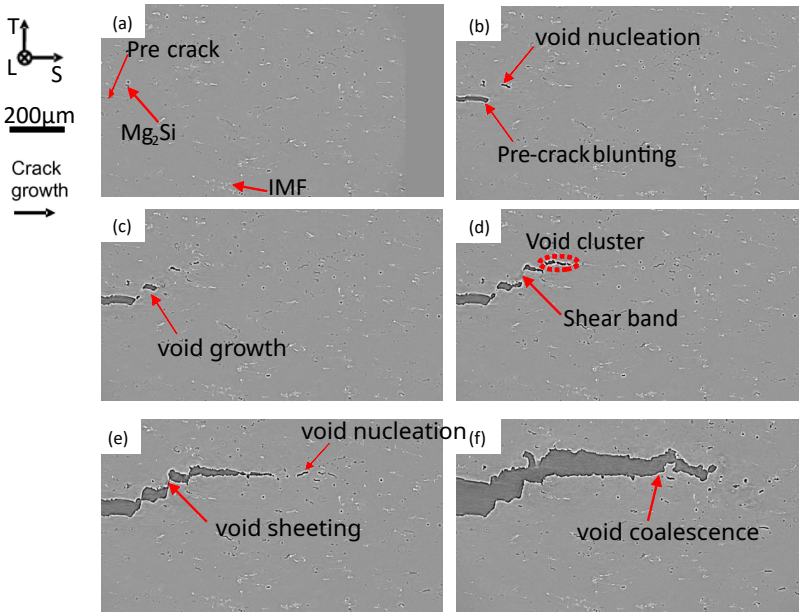

!

FIGURE 8.22: 2D sections of reconstructed 3D in situ laminography data at the center of a 1mm thick AA6061 sample, adapted after [Shen et al., 2013]

8.6.3 4D Methods and Digital Volume Correlation (DVC)

Digital volume correlation (DVC) is the extension of more classical 2D Digital Image Correlation (DIC). The principle of DVC consists in matching the gray levels f in the reference configuration x and those of the deformed volume g such that

$$f(x) = g[x + u(x)] \tag{8.23}$$

where u is the displacement field with respect to the reference volume. In real applications, the previous conservation of the gray level is not satisfied, especially in laminography where deviations appear not just due to acquisition noise but also due to reconstruction artifacts because of missing information (angles). Another difference with respect to DIC is that no artificial image contrast, as the typical spray paint speckle pattern in 2D DIC, can be exploited. A 3D image contrast of the microstructure is thus required for DVC, which is a limitation of this technique for some materials. In addition, when damage nucleates, the conservation of gray values is no longer satisfied, as damage appears as additional dark voxels. Consequently, the solution consists in minimizing the gray level residual $\rho(x) = f(x) - g[x + u(x)]$ by considering its L2-norm with respect to kinematic unknowns associated with the parametrization of the displacement field.

The residuals of the correlation, $\rho(x)$ may in some cases be used to quantify the damage evolution in the material, see *e.g.* [Buljac et al., 2018]. Digital volume correlation was successfully applied to ductile fracture of engineering materials [Morgeneyer et al., 2013a, 2014].

Fig. 8.23 shows an example of an application of DVC in ductile fracture. Here, the intermetallic particles present in the Al alloy provided the necessary image contrast with the Al-matrix to be able to perform the correlation. The strain field for the first load step given in Fig. 8.23(b). It shows a heterogeneous strain field with a localized slant band. This band remains active for the following load steps. The final fracture occurred along this strained band. The new insight gained from DVC is that this kind of heterogeneity was present from the very early loading onwards. It could not be reproduced by continuum level plasticity models [Morgeneyer et al., 2014]. Crystal plasticity effect may be at the origin of the found strain field and be the precursor of the final slant fracture [Morgeneyer et al., 2021].

8.6.4 Conclusions

These new imaging techniques have allowed significant progress in the understanding of ductile fracture. The advantage of non-destructive methods, that are significantly improving in resolution every year, is their ability to track damage while straining (4D methods). The understanding of damage mecha-

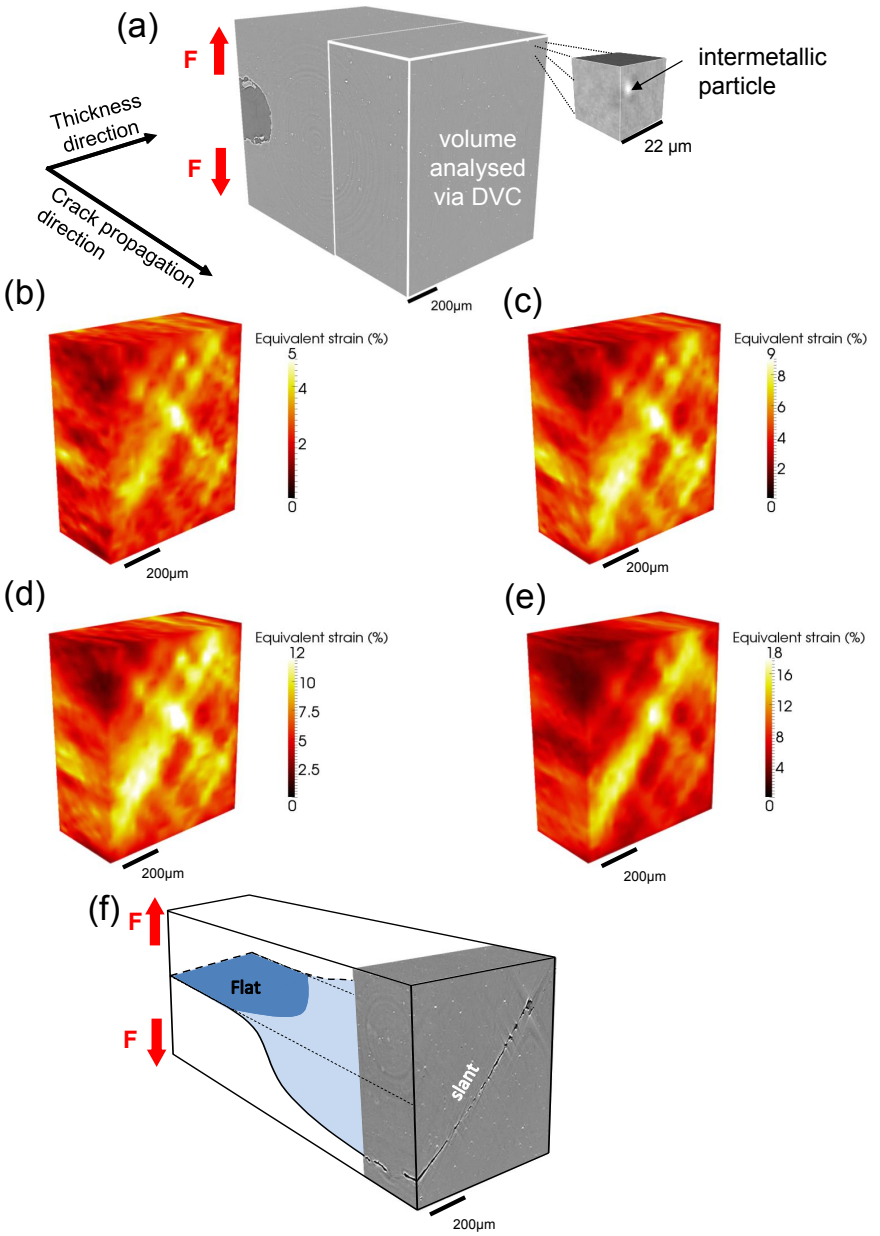

FIGURE 8.23: DVC applied to ductile fracture of an Al-alloy: a) region of interest scanned by laminography, the ROI for DVC is marked in white, b-e) cumulated equivalent strain fields for increasing macroscopic displacement f) final crack path along the former strain localization band. After [Morgeneyer et al., 2014]

nisms and the models described in section 3 have largely benefited from these new techniques for their validation and improvements.

Bibliography

[A. Pineau 2007] A. Pineau, T. P.: Failure of Metals. In: *Compr. Struct.l Integr. 2.* 2007, p. 684–797

[Abedini et al. 2018] Abedini, A. ; Butcher, C. ; Worswick, M.J.: Experimental fracture characterisation of an anisotropic magnesium alloy sheet in proportional and non-proportional loading conditions. In: *International Journal of Solids and Structures* 144-145 (2018), p. 1–19. – ISSN 0020–7683

[Achouri et al. 2013] Achouri, M. ; Germain, G. ; Dal Santo, P. ; Saidane, D.: Experimental characterization and numerical modeling of micromechanical damage under different stress states. In: *Materials & Design* 50 (2013), Nr. Supplement C, p. 207–222. – ISSN 0261–3069

[Argon 1976] Argon, A.S.: Formation of Cavities From Nondeformable Second-Phase Particles in Low Temperature Ductile Fracture. In: *Journal of Engineering Materials and Technology* 98 (1976), p. 60–68

[Argon et al. 1975] Argon, A.S. ; Im, J. ; Safoglu, R.: Cavity formation from inclusions in ductile fracture. In: *Metallurgical Transactions A* 6 (1975), p. 825–837. – ISSN 0360–2133

[Ashby 1966] Ashby, M.F.: Work hardening of dispersion-hardened crystals. In: *Philosophical Magazine* 14 (1966), Nr. 132, p. 1157–1178

[Azevedo and Marques 2010] Azevedo, C.R.F. ; Marques, E.R.: Three-dimensional analysis of fracture, corrosion and wear surfaces. In: *Engineering Failure Analysis* 17 (2010), Nr. 1, p. 286–300. – ISSN 1350–6307. – Papers presented at the 25th meeting of the Spanish Fracture Group

[Babout 2011] Babout, L.: *Study of degradation process in engineering materials using X-ray (micro)tomography and dedicated volumetric image processing and analysis.* Politechnika Lodzka, 2011

[Babout et al. 2004] Babout, L ; Brechet, Y ; Maire, E ; Fougeres, R: On the competition between particle fracture and particle decohesion in metal matrix composites. In: *Acta Materialia* 52 (2004), Nr. 15, p. 4517 – 4525

[Bao and Wierzbicki 2004] Bao, Yingbin ; Wierzbicki, Tomasz: On fracture locus in the equivalent strain and stress triaxiality space. In: *International*

Journal of Mechanical Sciences 46 (2004), Nr. 1, p. 81–98. – ISSN 0020–7403

[Barsoum and Faleskog 2007] Barsoum, Imad ; Faleskog, Jonas: Rupture mechanisms in combined tension and shear—Experiments. In: *International Journal of Solids and Structures* 44 (2007), Nr. 6, p. 1768–1786. – ISSN 0020–7683. – Physics and Mechanics of Advanced Materials

[Benzerga 2000] Benzerga, A.A.: *Rupture ductile des toles anisotropes, simulation de la propagation longitudinale dans une tole pressurisee*, Ecole des Mines de Paris, Diss., 2000

[Benzerga 2002] Benzerga, A.A.: Micromechanics of coalescence in ductile fracture. In: *J Mech Phys Solids* 50 (2002), Nr. 6, p. 1331 – 1362

[Benzerga and Leblond 2010] Benzerga, A.A. ; Leblond, J.-B.: Ductile Fracture by Void Growth to Coalescence. In: Aref, Hassan (Hrsg.) ; Giessen, Erik van d. (Hrsg.): *Advances in Applied Mechanics* Bd. 44. Elsevier, 2010. – ISSN 0065–2156, p. 169–305

[Beremin 1981] Beremin, F.M.: Cavity formation from inclusions in ductile fracture of A508 steel. In: *Metall. Mater. Trans. A* 12 A (1981), p. 723 – 731

[Berveiller and Zaoui 1978] Berveiller, M. ; Zaoui, A.: An extension of the self-consistent scheme to plastically-flowing polycrystals. In: *Journal of the Mechanics and Physics of Solids* 26 (1978), Nr. 5–6, p. 325 – 344

[Bordreuil et al. 2003] Bordreuil, Cyril ; Boyer, Jean-Claude ; Salle, Emmanuelle: On modelling the growth and the orientation changes of ellipsoidal voids in a rigid plastic matrix. In: *Modelling and Simulation in Materials Science and Engineering* 11 (2003), Nr. 3, p. 365

[Boyce 2014] Boyce, B. et a.: The Sandia Fracture Challenge: blind round robin predictions of ductile tearing. In: *International Journal of Fracture* 186 (2014), Nr. 1, p. 5–68

[Bridgman 1964] Bridgman, Percy W.: *Studies in Large Plastic Flow and Fracture, With Special Emphasis on the Effects of Hydrostatic Pressure.* Cambridge, MA and London, England : Harvard University Press, 1964. – ISBN 9780674731349

[Brown and Embury 1973] Brown, L.M. ; Embury, J.D.: Initiation and growth of voids at second-phase particles. In: *Proc. Conf. on Microstructure and Design of Alloys, Institute of Metals and Iron and Steel Insitute, London. 1973, 1,(33), 164-169*, 1973

[Brünig et al. 2008] Brünig, M. ; Chyra, O. ; Albrecht, D. ; Driemeier, L. ; Alves, M.: A ductile damage criterion at various stress triaxialities.

In: *International Journal of Plasticity* 24 (2008), Nr. 10, p. 1731–1755. – ISSN 0749–6419. – Special Issue in Honor of Jean-Louis Chaboche

[Buljac et al. 2018] Buljac, Ante ; Helfen, Lukas ; Hild, Francois ; Morgeneyer, Thilo F.: Effect of void arrangement on ductile damage mechanisms in nodular graphite cast iron: In situ 3D measurements. In: *Engineering Fracture Mechanics* 192 (2018), p. 242–261

[Buljac et al. 2023] Buljac, Ante ; Kong, Xiang ; Helfen, Lukas ; Hild, Francois ; Morgeneyer, Thilo F.: Shear loading dominated damage mechanisms and strain localization studied by in situ 3D laminography imaging and Digital Volume Correlation for AA2198-T8. In: *Mechanics of Materials* 178 (2023), p. 104558. – ISSN 0167–6636

[Burnett 2014] Burnett, T.L.: Correlative tomography. In: *Scientific reports* 4 (2014), Nr. 1, p. 4711

[C. Tekogu 2015] C. Tekogu, T. P. J.W. Hutchinson H. J.W. Hutchinson: On localization and void coalescence as a precursor to ductile fracture. In: *Philo. Trans. R. Soc. London, Ser. A* 373 (2015), Nr. 2038

[Cierniak 2011] Cierniak, R.: *Some Words about the History of Computed Tomography.* X-Ray Computed Tomography in Biomedical Engineering, 2011

[Cormack 1973] Cormack, A M.: Reconstruction of densities from their projections, with applications in radiological physics. In: *Physics in Medicine and Biology* 18 (1973), Nr. 2, p. 195

[Cox and Low 1974] Cox, T. B. ; Low, J. R.: An investigation of the plastic fracture of AISI 4340 and 18 Nickel-200 grade maraging steels. In: *Metallurgical and Materials Transactions B* 5 (1974), Jun, Nr. 6, p. 1457–1470. – ISSN 1543–1916

[D. Lassance 2006] D. Lassance, T. P. F. Scheyvaerts S. F. Scheyvaerts: Growth and coalescence of penny-shaped voids in metallic alloys. In: *Eng. Fract. Mech.* 73 (2006), Nr. 8, p. 1009–1034

[Daly and Burnett 2017] Daly, M. ; Burnett, T.L.: A multi-scale correlative investigation of ductile fracture. In: *Acta Materialia* 130 (2017), p. 56 – 68

[Ding et al. 2016] Ding, Ming-Shuai ; Du, Jun-Ping ; Wan, Liang ; Ogata, Shigenobu ; Tian, Lin ; Ma, Evan ; Han, Wei-Zhong ; Li, Ju ; Shan, Zhi-Wei: Radiation-Induced Helium Nanobubbles Enhance Ductility in Submicron-Sized Single-Crystalline Copper. In: *Nano Letters* 16 (2016), Nr. 7, p. 4118–4124

[Dunand and Mohr 2011] Dunand, Matthieu ; Mohr, Dirk: Optimized butterfly specimen for the fracture testing of sheet materials under combined

normal and shear loading. In: *Engineering Fracture Mechanics* 78 (2011), Nr. 17, p. 2919–2934. – ISSN 0013–7944

[Eshelby 1957] Eshelby, J. D.: The Determination of the Elastic Field of an Ellipsoidal Inclusion, and Related Problems. In: *Proceedings of the Royal Society of London. Series A. Mathematical and Physical Sciences* 241 (1957), Nr. 1226, p. 376–396

[Eshelby et al. 1953] Eshelby, J.D. ; Read, W.T. ; Shockley, W.: Anisotropic elasticity with applications to dislocation theory. In: *Acta Metallurgica* 1 (1953), Nr. 3, p. 251 – 259

[Fabrègue and Pardoen 2008] Fabrègue, D. ; Pardoen, T.: A constitutive model for elastoplastic solids containing primary and secondary voids. In: *Journal of the Mechanics and Physics of Solids* 56 (2008), Nr. 3, p. 719–741. – ISSN 0022–5096

[Ferre et al. 2015] Ferre, A. ; Dancette, S. ; Maire, E.: Damage characterisation in aluminium matrix composites reinforced with amorphous metal inclusions. In: *Materials Science and Technology* 31 (2015), Nr. 5, p. 579–586

[Garrison Jr and Moody 1987] Garrison Jr, WM ; Moody, NR: Ductile fracture. In: *Journal of Physics and Chemistry of Solids* 48 (1987), Nr. 11, p. 1035–1074

[Goods and Brown 1979] Goods, S.H. ; Brown, L.M.: Overview No. 1: The nucleation of cavities by plastic deformation. In: *Acta Metallurgica* 27 (1979), Nr. 1, p. 1–15. – ISSN 0001–6160

[Gross and Ravi-Chandar 2016] Gross, A. J. ; Ravi-Chandar, K.: On the deformation and failure of Al 6061-T6 at low triaxiality evaluated through in situ microscopy. In: *International Journal of Fracture* 200 (2016), p. 185–208. – ISSN 1573–2673

[Hancock 1992] Hancock, J. W. ; Argon, A. S. (Hrsg.): *Constraint and Stress State Effects in Ductile Fracture*. New York, NY : Springer New York, 1992. – 99–144 S. – ISBN 978–1–4612–2934–6

[Hannard et al. 2017] Hannard, F. ; Castin, S. ; Maire, E. ; Mokso, R. ; Pardoen, T. ; Simar, A.: Ductilization of aluminium alloy 6056 by friction stir processing. In: *Acta Materialia* 130 (2017), p. 121–136. – ISSN 1359–6454

[Hannard et al. 2016] Hannard, F. ; Pardoen, T. ; Maire, E. ; Bourlot, C. L. ; Mokso, R. ; Simar, A.: Characterization and micromechanical modelling of microstructural heterogeneity effects on ductile fracture of 6xxx aluminium alloys. In: *Acta Materialia* 103 (2016), p. 558 – 572

[Hannard et al. 2018] Hannard, F. ; Simar, A. ; Maire, E. ; Pardoen, T.: Quantitative assessment of the impact of second phase particle arrangement on damage and fracture anisotropy. In: *Acta Materialia* 148 (2018), p. 456–466. – ISSN 1359–6454

[Helfen et al. 2005] Helfen, L. ; Baumbach, T. ; Mikulík, P. ; Kiel, D. ; Pernot, P. ; Cloetens, P. ; Baruchel, J.: High-resolution three-dimensional imaging of flat objects by synchrotron-radiation computed laminography. In: *Applied Physics Letters* 86 (2005), Nr. 7, p. 071915

[Helfen et al. 2012] Helfen, Lukas ; Morgeneyer, Thilo F. ; Xu, Feng ; Mavrogordato, Mark N. ; Sinclair, Ian ; Schillinger, Burkhard ; Baumbach, Tilo: Synchrotron and neutron laminography for three-dimensional imaging of devices and flat material specimens. In: *International Journal of Materials Research* 103 (2012), Nr. 2, p. 170–173

[Hounsfield 1973] Hounsfield, G. N.: Computerized transverse axial scanning (tomography): Part 1. Description of system. In: *The British Journal of Radiology* 46 (1973), Nr. 552, p. 1016–1022

[Huang 1991] Huang, Y.: Accurate Dilatation Rates for Spherical Voids in Triaxial Stress Fields. In: *Journal of Applied Mechanics* 58 (1991), 12, Nr. 4, p. 1084–1086. – ISSN 0021–8936

[Kamp et al. 2002] Kamp, N ; Sinclair, I ; Starink, MJ: Toughness-strength relations in the overaged 7449 Al-based alloy. In: *Metallurgical and Materials Transactions A* 33 (2002), p. 1125–1136

[Kong et al. 2022] Kong, Xiang ; Helfen, Lukas ; Hurst, Mathias ; Haenschke, Daniel ; Missoum-Benziane, Djamel ; Besson, Jacques ; Baumbach, Tilo ; Morgeneyer, Thilo F.: 3D in situ study of damage during a 'shear to tension' load path change in an aluminium alloy. In: *Acta Materialia* 231 (2022), JUN 1. – ISSN 1359–6454

[Kosco and Koss 1993] Kosco, J. B. ; Koss, D. A.: Ductile fracture of mechanically alloyed iron-yttria alloys. In: *Metallurgical Transactions A* 24 (1993), Mar, Nr. 3, p. 681

[Kumar et al. 2009] Kumar, Jalaj ; Srivathsa, B. ; Kumar, Vikas: Stress triaxiality effect on fracture behavior of IMI-834 titanium alloy: A micromechanics approach. In: *Materials and Design* 30 (2009), Nr. 4, p. 1118 – 1123

[Kwon and Asaro 1990] Kwon, D. ; Asaro, R.J.: A study of void nucleation, growth, and coalescence in spheroidized 1518 steel. In: *Metall Mater Trans A* 21 (1990), p. 117–134

[Landron et al. 2011] Landron, C. ; Maire, E. ; Bouaziz, O. ; Adrien, J. ; Lecarme, L. ; Bareggi, A.: Validation of void growth models using X-ray microtomography characterization of damage in dual phase steels. In: *Acta Mater* 59 (2011), Nr. 20, p. 7564 – 7573

[Lassance et al. 2007] Lassance, D. ; Fabregue, D. ; Delannay, F. ; Pardoen, T.: Micromechanics of room and high temperature fracture in 6xxx Al alloys. In: *Prog. Mater Sci.* 52 (2007), Nr. 1, p. 62–129

[Lecarme et al. 2014] Lecarme, L. ; Maire, E. ; Kumar, A. ; De-Vleeschouwer, C. ; Jacques, L. ; Simar, A. ; Pardoen, T.: Heterogenous void growth revealed by in situ 3-D X-ray microtomography using automatic cavity tracking. In: *Acta Mater* 63 (2014), Nr. 0, p. 130 – 139

[Lee and Mear 1999] Lee, B.J. ; Mear, M.e.: Stress concentration induced by an elastic spheroidal particle in a plastically deforming solid. In: *Journal of the Mechanics and Physics of Solids* 47 (1999), Nr. 6, p. 1301 – 1336

[Lewis and Withers 1995] Lewis, C.A. ; Withers, P.J.: Weibull modelling of particle cracking in metal matrix composites. In: *Acta Metallurgica et Materialia* 43 (1995), Nr. 10, p. 3685 – 3699

[Lezaack et al. 2022] Lezaack, Matthieu B. ; Hannard, Florent ; Simar, Aude: Understanding the ductility versus toughness and bendability decoupling of large elongated and fine grained Al 7475-T6 alloy. In: *Materials Science and Engineering: A* 839 (2022), p. 142816

[Lode 1926a] Lode, W: Versuche über den Einfluß der mittleren Hauptspannung auf das Fließen der Metalle Eisen, Kupfer und Nickel. In: *Zeitschrift für Physik* 36 (1926), Nr. 11-12, p. 913–939

[Lode 1926b] Lode, W.: Versuche über den Einfluß der mittleren Hauptspannung auf das Fließen der Metalle Eisen, Kupfer und Nickel. In: *Zeitschrift für Physik* 36 (1926), p. 913–939

[Lynch and Moutsos 2006] Lynch, Stanley P. ; Moutsos, S: A brief history of fractography. In: *Journal of Failure Analysis and Prevention* 6 (2006), p. 54–69

[Madi et al. 2019] Madi, Yazid ; Garcia, J-M ; Proudhon, Henry ; Shinohara, Y ; Helfen, L ; Besson, Jacques ; Morgeneyer, Thilo F.: On the origin of the anisotropic damage of X100 line pipe steel: Part I—In situ synchrotron tomography experiments. In: *Integrating Materials and Manufacturing Innovation* 8 (2019), Nr. 4, p. 570–596

[Maire et al. 1997] Maire, E. ; Wilkinson, D.S. ; Embury, J.D. ; Fougeres, R.: Role of damage on the flow and fracture of particulate reinforced alloys and metal matrix composites. In: *Acta Materialia* 45 (1997), Nr. 12, p. 5261 – 5274

[Maire and Withers 2014] Maire, E. ; Withers, P. J.: Quantitative X-ray tomography. In: *International Materials Reviews* 59 (2014), Nr. 1, p. 1–43

[Marini et al. 1985] Marini, B. ; Mudry, F. ; Pineau, A.: Ductile rupture of A508 steel under nonradial loading. In: *Eng Fract Mech* 22 (1985), Nr. 3, p. 375 – 386

[Marino et al. 1985] Marino, B. ; Mudry, F. ; Pineau, A.: Experimental study of cavity growth in ductile rupture. In: *Engineering Fracture Mechanics* 22 (1985), Nr. 6, p. 989–996. – ISSN 0013–7944

[Mohr and Marcadet 2015] Mohr, Dirk ; Marcadet, Stephane J.: Micromechanically-motivated phenomenological Hosford–Coulomb model for predicting ductile fracture initiation at low stress triaxialities. In: *International Journal of Solids and Structures* 67-68 (2015), p. 40–55. – ISSN 0020–7683

[Morgeneyer et al. 2013a] Morgeneyer, T. F. ; Helfen, L. ; Mubarak, H. ; Hild, F.: 3D Digital Volume Correlation of Synchrotron Radiation Laminography images of ductile crack initiation: An initial feasibility study. In: *Experimental Mechanics* 53 (2013), p. 543–556

[Morgeneyer et al. 2014] Morgeneyer, T. F. ; Taillandier-Thomas, T. ; Helfen, L. ; Baumbach, T. ; Sinclair, I. ; Roux, S. ; Hild, F.: In situ 3D observation of early strain localisation during failure of thin Al alloy (2198) sheet. In: *Acta Materialia* 69 (2014), p. 78–91

[Morgeneyer et al. 2013b] Morgeneyer, T.F. ; Helfen, L. ; Mubarak, H. ; Hild, F.: 3D Digital Volume Correlation of Synchrotron Radiation Laminography images of ductile crack initiation: An initial feasibility study. In: *Experimental Mechanics* 53 (2013), p. 543–556

[Morgeneyer et al. 2021] Morgeneyer, Thilo F. ; Khadyko, Mikhail ; Buljac, Ante ; Helfen, Lukas ; Hild, Francois ; Benallal, Tore Ahmed B. Ahmed Børvik ; Hopperstad, Odd S.: On crystallographic aspects of heterogeneous plastic flow during ductile tearing: 3D measurements and crystal plasticity simulations for AA7075-T651. In: *International Journal of Plasticity* 144 (2021), p. 103028

[Myagotin et al. 2013] Myagotin, A. ; Voropaev, A. ; Helfen, L. ; Hanschke, D. ; Baumbach, T.: Efficient volume reconstruction for parallel-beam computed laminography by filtered backprojection on multi-core clusters. In: *IEEE transactions on image processing* 22 (2013), Nr. 12, p. 5348–5361

[Needleman 1987] Needleman, A.: A Continuum Model for Void Nucleation by Inclusion Debonding. In: *Journal of Applied Mechanics* 54 (1987), Nr. 3, p. 525–531

[Noell et al. 2023] Noell, Philip J. ; Sills, Ryan B. ; Benzerga, A.A. ; Boyce, Brad L.: Void Nucleation During Ductile Rupture of Metals: A

Review. In: *Progress in Materials Science* (2023), p. 101085. – ISSN 0079–6425

[Papasidero et al. 2015] Papasidero, J. ; Doquet, V. ; Mohr, D.: Ductile fracture of aluminum 2024-T351 under proportional and non-proportional multi-axial loading: Bao–Wierzbicki results revisited. In: *International Journal of Solids and Structures* 69-70 (2015), p. 459–474. – ISSN 0020–7683

[Papasidero et al. 2014] Papasidero, Jessica ; Doquet, Véronique ; Leperer, Sebastien: Multiscale investigation of ductile fracture mechanisms and strain localization under shear loading in 2024-T351 aluminum alloy and 36NiCrMo16 steel. In: *Materials Science and Engineering: A* (2014)

[Pardoen and Delannay 1998] Pardoen, T. ; Delannay, F.: Assessment of void growth models from porosity measurements in cold-drawn copper bars. In: *Metall Mater Trans A* 29 (1998), p. 1895–1909

[Pardoen and Hutchinson 2000] Pardoen, T. ; Hutchinson, J.W.: An extended model for void growth and coalescence. In: *Journal of the Mechanics and Physics of Solids* 48 (2000), Nr. 12, p. 2467–2512. – ISSN 0022–5096

[Pardoen et al. 2010] Pardoen, T. ; Scheyvaerts, F. ; Simar, A. ; Tekoglu, C. ; Onck, P.R.: Multiscale modeling of ductile failure in metallic alloys. In: *C R Phys* 11 (2010), Nr. 3-4, p. 326 – 345

[Pilkey et al. 1998] Pilkey, A.K. ; Worswick, M.J. ; Thomson, C.I.A. ; Burger, G. ; Lloyd, D.J.: Effect of second-phase particle clustering on formability of Al–Si sheet. In: *Advances in Industrial Materials. Canadian Institute of Mining, Metallurgy and Petroleum, Montreal* (1998)

[Pineau et al. 2016] Pineau, A. ; Benzerga, A.A. ; Pardoen, T.: Failure of metals I: Brittle and ductile fracture. In: *Acta Materialia* 107 (2016), p. 424–483. – ISSN 1359–6454

[Pineau and Pardoen 2007] Pineau, A. ; Pardoen, T.: 2.06 - Failure of Metals. In: Milne, I. (Hrsg.) ; Ritchie, R.O. (Hrsg.) ; Karihaloo, B. (Hrsg.): *Comprehensive Structural Integrity*. Oxford : Pergamon, 2007. – ISBN 978–0–08–043749–1, p. 684–797

[R. Schurch and Withers 2015] R. Schurch, R. B. S. Rowland R. S. Rowland ; Withers, P.: Comparison and Combination of Imaging Techniques for Three Dimensional Analysis of Electrical Trees. In: *IEEE Transactions on Dielectrics and Electrical Insulation* 22 (2015), Nr. 2, p. 709–719

[Rice and Tracey 1969] Rice, J.R. ; Tracey, D.M.: On the ductile enlargement of voids in triaxial stress fields. In: *Journal of the Mechanics and Physics of Solids* 17 (1969), Nr. 3, p. 201–217. – ISSN 0022–5096

[Roth et al. 2018] Roth, Christian C. ; Morgeneyer, Thilo F. ; Cheng, Yin ; Helfen, Lukas ; Mohr, Dirk: Ductile damage mechanism under shear-dominated loading: In-situ tomography experiments on dual phase steel and localization analysis. In: *International Journal of Plasticity* 109 (2018), p. 169–192. – ISSN 0749–6419

[Roux et al. 2014] Roux, E ; Shakoor, M ; Bernacki, M ; Bouchard, P-O: A new finite element approach for modelling ductile damage void nucleation and growth—analysis of loading path effect on damage mechanisms. In: *Modelling and Simulation in Materials Science and Engineering* 22 (2014), Nr. 7, p. 075001

[Scheyvaerts et al. 2011] Scheyvaerts, F. ; Onck, P.R. ; Tekoglu, C. ; Pardoen, T.: The growth and coalescence of ellipsoidal voids in plane strain under combined shear and tension. In: *Journal of the Mechanics and Physics of Solids* 59 (2011), Nr. 2, p. 373 – 397

[Shabrov et al. 2004] Shabrov, M.N. ; Briant, C.L. ; Needleman, A. ; Kim, S. ; Sylven, E. ; Sherman, D.H. ; Chuzhoy, L.: Void nucleation by inclusion cracking. In: *Metallurgical and Materials Transactions A* 35 (2004), Nr. 6, p. 1745–1755

[Shen et al. 2013] Shen, Y. ; Morgeneyer, T. F. ; Garnier, J. ; Allais, L. ; Helfen, L. ; Crepin, J.: Three-dimensional quantitative in-situ study of crack initiation and propagation in AA6061 Al-alloy sheets via synchrotron laminography and finite-element simulations. In: *Acta Materialia* 61 (2013), p. 2571–2582

[Simar et al. 2010] Simar, A. ; Nielsen, K.L. ; Meester, B. de ; Tvergaard, V. ; Pardoen, T.: Micro-mechanical modelling of ductile failure in 6005A aluminium using a physics based strain hardening law including stage IV. In: *Engineering Fracture Mechanics* 77 (2010), Nr. 13, p. 2491 – 2503

[Siruguet and Leblond 2004] Siruguet, Karine ; Leblond, J.-B.: Effect of void locking by inclusions upon the plastic behavior of porous ductile solids—I: theoretical modeling and numerical study of void growth. In: *International Journal of Plasticity* 20 (2004), Nr. 2, p. 225 – 254

[Stock 2008] Stock, S. R.: Recent advances in X-ray microtomography applied to materials. In: *International Materials Reviews* 53 (2008), Nr. 3, p. 129–181

[Stock 1999] Stock, S.R.: X-ray microtomography of materials. In: *International Materials Reviews* 44 (1999), Nr. 4, p. 141–164

[Taktak et al. 2009] Taktak, R. ; Benseddiq, N. ; Imad, A.: Analysis of ductile tearing using a local approach to fracture. In: *Fatigue Fract. Eng. Mater. Struct.* 32 (2009), Nr. 6, p. 525–530

[Tanaka et al. 1970] Tanaka, K. ; Mori, T. ; Nakamura, T.: Cavity formation at the interface of a spherical inclusion in a plastically deformed matrix. In: *Philosophical Magazine* 21 (1970), Nr. 170, p. 267–279

[Tancogne-Dejean et al. 2021] Tancogne-Dejean, Thomas ; Roth, Christian C. ; Morgeneyer, Thilo F. ; Helfen, Lukas ; Mohr, Dirk: Ductile Damage of AA2024-T3 under Shear Loading: Mechanism Analysis Through In-Situ Laminography. In: *Acta Materialia* (2021), p. 116556. – ISSN 1359–6454

[Tekoğlu et al. 2012] Tekoğlu, C. ; Leblond, J.-B. ; Pardoen, T.: A criterion for the onset of void coalescence under combined tension and shear. In: *Journal of the Mechanics and Physics of Solids* 60 (2012), Nr. 7, p. 1363–1381. – ISSN 0022–5096

[Thomason 1985a] Thomason, P.F.: A three-dimensional model for ductile fracture by the growth and coalescence of microvoids. In: *Acta Metall.* 33 (1985), Nr. 6, p. 1087–1095

[Thomason 1985b] Thomason, P.F.: Three-dimensional models for the plastic limit-loads at incipient failure of the intervoid matrix in ductile porous solids. In: *Acta Metall.* 33 (1985), Nr. 6, p. 1079–1085

[Thomason 1990] Thomason, P.F.: *Ductile Fracture of Metals*. Pergamon press, 1990

[Tomstad et al. 2022] Tomstad, Asle J. ; Frodal, Bjørn H. ; Børvik, Tore ; Hopperstad, Odd S.: Influence of particle content on the ductility of extruded non-recrystallized aluminium alloys subjected to shear loading. In: *Materials Science and Engineering: A* 850 (2022), p. 143409. – ISSN 0921–5093

[Tvergaard 2011] Tvergaard, V.: Void shape effects and voids starting from cracked inclusion. In: *Int J Solids Struct* 48 (2011), Nr. 7–8, p. 1101 – 1108

[Ueda et al. 2014] Ueda, T. ; Helfen, L. ; Morgeneyer, T. F.: In-situ laminography study of three-dimensional individual void shape evolution at crack initiation and comparison with GTN-type simulations. In: *Acta Materialia* 78C (2014), p. 254–270

[Weck et al. 2008] Weck, A. ; Wilkinson, D.S. ; Maire, E. ; Toda, H.: Visualization by X-ray tomography of void growth and coalescence leading to fracture in model materials. In: *Acta Materialia* 56 (2008), Nr. 12, p. 2919–2928. – ISSN 1359–6454

[Withers 2007] Withers, Philip J.: X-ray nanotomography. In: *Materials Today* 10 (2007), Nr. 12, p. 26 – 34

[Worswick and Pick 1990] Worswick, M.J. ; Pick, R.J.: Void growth and constitutive softening in a periodically voided solid. In: *J Mech Phys Solids* 38 (1990), Nr. 5, p. 601 – 625

[Wu et al. 2017] Wu, S.C. ; Xiao, T.Q. ; Withers, P.J.: The imaging of failure in structural materials by synchrotron radiation X-ray microtomography. In: *Engineering Fracture Mechanics* 182 (2017), Nr. Supplement C, p. 127 – 156

[Xu et al. 2012] Xu, Feng ; Helfen, Lukas ; Baumbach, Tilo ; Suhonen, Heikki: Comparison of image quality in computed laminography and tomography. In: *Opt. Express* 20 (2012), Jan, Nr. 2, p. 794–806

[Z. Chen 2013] Z. Chen, C. B.: *Application of the complete percolation model*. Springer Netherlands, 2013

[Zapffe and Clogg 1945] Zapffe, CA ; Clogg, M: Fractography-a new tool for metallurgical research. In: *Transactions of the American Society for Metals* 34 (1945), p. 71–107

9

Basic concepts and modeling of ductile fracture

Léo Morin

University of Bordeaux, Laboratoire I2M

Djimédo Kondo

Sorbonne University, Institut Jean Le Rond d'Alembert

This chapter aims at presenting basic concepts of modeling fracture in ductile porous materials. The approach is mainly based on the so-called local approach which relies on the use of constitutive models describing voids growth and coalescence phenomena. A prototype of such constituve law is the Gurson-Tvergaard-Needleman model which is presented in detail. For completeness, we also provide elements of some recent coalescence criteria. The chapter terminates with various extensions of the GTN models including those devoted to voids shape effects.

9.1 Introductory comments

Ductile fracture through voids nucleation, growth and coalescence is the dominant mode of failure of metallic alloys at medium and high temperatures as shown in chapter 8. This mode of failure occurs after large deformations, due to the propagation of macroscopic cracks leading to the tearing of structures.

As detailed in chapter 8, ductile failure follows three stages [Garrison and Moody, 1987] : (i) voids are nucleated at the level of inclusions or second phase particles (see for instance recent studies based on 3D tomography [Hannard et al., 2018]) by decohesion of the particle-matrix interface, or by rupture of these inclusions (see Figure 9.1a); (ii) these cavities grow and deform by plastic flow of the surrounding matrix: this is the growth phase (see Figure 9.1b); (iii) finally, in the coalescence phase, neighboring cavities eventually join to form a macroscopic crack leading to the ruin of the structure (see Figure 9.1c).

There are several approaches to model ductile fracture: uncoupled models such as the Rice-Tracey one [Rice and Tracey, 1969] (in which the porosity does not change the mechanical behavior; see chapter 8) and coupled mod-

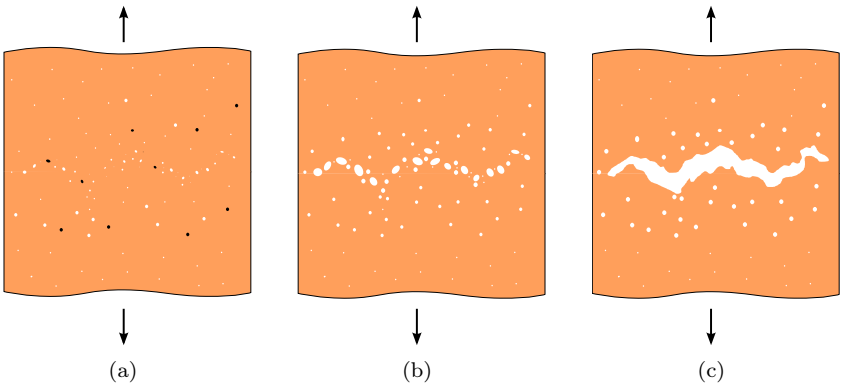

FIGURE 9.1: Three main mechanisms of ductile fracture. (a) Void nucleation, (b) Void growth and (c) Void nucleation. After Morin [2015].

els (in which the damage changes the mechanical behavior). In the coupled approach, which is often referred to as the local approach to fracture, the modeling of ductile fracture is essentially based on a detailed physical description of the local fracture process zone [Besson, 2010]. The most advanced models of ductile fracture are then based on a *micromechanical* approach with an upscaling procedure whose main objective is to define the macroscopic behavior of a plastic material containing voids.

It results a material constitutive law with a progressive softening induced by the growth of cavities [Benzerga et al., 2016]. The mechanics of ductile fracture appears therefore mainly as a problem of deriving appropriate constitutive laws for elastoplastic materials with an evolving porosity. Then, the numerical integration of the homogenized constitutive laws of ductile porous materials, in a finite element code, is necessary to proceed to a structural calculation.

Within the local approach to ductile fracture, two mathematical modeling frameworks allow the development of micromechanical models:

- The "nonlinear homogenization" approach which is based on the use of rigorous bounds for nonlinear composites for non linear composites (including voided materials) whose constituents behaviors are described by means of a single potential (in particular purely viscous materials) [Ponte Castañeda, 1991; Willis, 1991; Michel and Suquet, 1992]. This approach allows to establish expression of the macroscopic criterion of the porous material and to take into account voids shape effects [Danas and Ponte Castañeda, 2009; Danas and Aravas, 2012] and crystal anisotropy [Agoras and Ponte Castañeda, 2013; Mbiakop et al., 2015a].

- The classical limit analysis based approach, which relies on a coupling between limit analysis and Hill-Mandel type homogenization. This approach

follows the the pioneering work of Gurson [1977] (see also [Gurson, 1975]) and is generally considered to be the most suitable to describe both the growth phase and the coalescence phase in ductile fracture.

In this chapter, we will begin by presenting the main ingredients that are needed to define constitutive models of ductile failure. This will be illustrated through the Gurson model and its direct extension, the so-called Gurson-Tvergaard-Needleman (GTN) model. Then, we will focus on some developments allowing to account for voids shape effects or plastic anisotropy of the matrix. The last part of the chapter will be devoted to a presentation of various micromechanical modeling of coalescence phenomena.

9.2 Homogenization and limit-analysis

Limit-analysis combined with Hill-Mandel homogenization is a convenient framework to derive constitutive equations for porous ductile solids as it permits to effectively operate the scale transition. The objective of this section is to provide the basic ingredients which allows the derivation of the relationship between stress and strain at the macroscale, for a given description at the microscale.

Since ductile failure involves large plastic deformation, a formulation accounting for finite deformations is necessary. Therefore, we will adopt an eulerian description, with $\boldsymbol{\sigma}$ and $\boldsymbol{d}$ the Cauchy stress and the rate of deformation, respectively.

9.2.1 Hill-Mandel homogenization theory

We first recall general results of the Hill-Mandel homogenization theory [Mandel, 1964; Hill, 1967], which can be declined in two approaches depending on the boundary conditions assumed for the RVE: kinematic boundary conditions or static boundary conditions. In practice, ductile failure models are derived using the kinematic approach, we will restrict ourselves to this case.

Macroscopic stress and strain rate

We consider a representative volume element Ω containing a void ω. The porosity (volume fraction of void) is defined as

$$f = \frac{\mathrm{vol}(\omega)}{\mathrm{vol}(\Omega)}. \tag{9.1}$$

We assume that the RVE is subjected to homogeneous boundary strain rate conditions:

$$\mathbf{v}(\mathbf{x}) = \boldsymbol{D} \cdot \mathbf{x}, \quad \forall \mathbf{x} \in \partial\Omega, \tag{9.2}$$

where $\mathbf{v}$ is the microscopic velocity field and $\boldsymbol{D}$ a second-rank symmetric tensor.
By using Green's formula ($\int_{\partial\Omega} u_i n_j \, \mathrm{d}S = \int_\Omega u_{i,j} \, \mathrm{d}V$ for any vector $\mathbf{u}$) or divergence theorem and the above definition of the boundary condition (9.2), it can be shown that

$$\langle \boldsymbol{d} \rangle_\Omega = \frac{1}{\mathrm{vol}(\Omega)} \int_\Omega \boldsymbol{d} \, \mathrm{d}V = \boldsymbol{D}, \tag{9.3}$$

where the notation $\langle \cdot \rangle_\Omega$ stands for volume averaging over Ω. Therefore, $\boldsymbol{D}$ is called the macroscopic rate of deformation.
Noting that $d_{ij} = \frac{1}{2}(v_{i,j} + v_{j,i})$, the proof of (9.3) follows from the result:

$$\begin{aligned}
\int_\Omega v_{i,j} \, \mathrm{d}V &= \int_{\partial\Omega} v_i n_j \, \mathrm{d}S && \text{(Green's formula)} \\
&= \int_{\partial\Omega} D_{ik} x_k n_j \, \mathrm{d}S && \text{(boundary condition)} \\
&= D_{ik} \int_\Omega (x_k)_{,j} \, \mathrm{d}V && \text{(Green's formula)} \\
&= D_{ik} \int_\Omega (\delta_{kj}) \, \mathrm{d}V \\
&= \mathrm{vol}(\Omega) D_{ij}.
\end{aligned} \tag{9.4}$$

Knowing by analogy that $\int_\Omega v_{j,i} \, \mathrm{d}V = \mathrm{vol}(\Omega) D_{ji}$, this proves the result (9.3).

The macroscopic stress $\boldsymbol{\Sigma}$ is defined as the volume average of the microscopic stress $\boldsymbol{\sigma}$

$$\boldsymbol{\Sigma} = (1 - f) \langle \boldsymbol{\sigma} \rangle_{\Omega - \omega}, \tag{9.5}$$

where the notation $\langle \cdot \rangle_{\Omega-\omega}$ stands for volume averaging over the sound volume $\Omega - \omega$:

$$\langle \cdot \rangle_{\Omega-\omega} = \frac{1}{\mathrm{vol}(\Omega - \omega)} \int_{\Omega-\omega} (\cdot) \, \mathrm{d}V. \tag{9.6}$$

Hill-Mandel lemma

Let us consider $\mathbf{v}$ a kinematically admissible velocity field (verifying the boundary conditions (9.2)) and $\boldsymbol{\sigma}$ a statically admissible stress field (verifying $\mathrm{div}(\boldsymbol{\sigma}) = 0$ in Ω) and satisfying the conditions $\boldsymbol{\sigma}.\mathbf{n} = 0$ on $\partial\omega$.

The volume average $\langle \boldsymbol{\sigma} : \boldsymbol{d} \rangle_\Omega$ is given by

$$\begin{aligned}
\frac{1}{\mathrm{vol}(\Omega)} \int_\Omega \sigma_{ij} d_{ij} \, \mathrm{d}V &= \frac{1}{\mathrm{vol}(\Omega)} \int_{\partial\Omega} \sigma_{ij} n_j v_i \, \mathrm{d}S && \text{(principle of virtual work)} \\
&= \frac{1}{\mathrm{vol}(\Omega)} \int_{\partial\Omega} \sigma_{ij} n_j D_{ik} x_k \, \mathrm{d}S && \text{(boundary condition (9.2))} \\
&= \frac{1}{\mathrm{vol}(\Omega)} \int_\Omega \left(\sigma_{ij} D_{ik} x_k\right)_{,j} \, \mathrm{d}V && \text{(divergence theorem)} \\
&= \frac{1}{\mathrm{vol}(\Omega)} \int_\Omega \left(\sigma_{ij} D_{ik} \delta_{kj}\right) \mathrm{d}V && \text{(equilibrium)} \\
&= \Sigma_{ij} D_{ij} && \text{(definition of } \boldsymbol{\Sigma}\text{)}
\end{aligned} \tag{9.7}$$

This proves the Hill-Mandel lemma:

$$\langle \boldsymbol{\sigma} : \boldsymbol{d} \rangle_\Omega = \boldsymbol{\Sigma} : \boldsymbol{D}. \tag{9.8}$$

It should be stressed that this Lemma still holds also for uniform stress boundary conditions as well as for periodic ones.
Note also that the Hill lemma will serve as basis for the micro-macro upscaling for the porous material.

9.2.2 Limit-analysis

The derivation of the Gurson model that will be presented below is based on the theoretical framework of Limit Analysis which can be found in [Salençon, 2002]. The textbook [Leblond, 2003] also introduced the main concepts of this theory for the derivation of the macroscopic strength of ductile porous media.

Classical limit-analysis[1] considers rigid-ideal-plastic materials within a small displacement - small strain (linearized) framework. Under such assumptions the macroscopic strength locus of a porous medium can be determined using the upper-bound theorem (see e.g. [Salençon, 2002]).
The starting point is that the strength of the solid phase is characterized by a convex set of admissible stress states, $\mathcal{C}$ which in turn is defined by a convex strength criterion $\phi(\boldsymbol{\sigma}) \leq 0$. The dual definition of the strength criterion consists in introducing the support function $\pi(\boldsymbol{d})$ of $\mathcal{C}$, which is defined on the set of symmetric second order tensors $\boldsymbol{d}$ and is convex w.r.t. the microscopic Eulerian strain rate $\boldsymbol{d} = \frac{1}{2}\left(\mathbf{grad}(\mathbf{v}) + \mathbf{grad}(\mathbf{v})^{\mathrm{T}}\right)$:

$$\pi(\boldsymbol{d}) = \sup_{\boldsymbol{\sigma}^* \in \mathcal{C}} \boldsymbol{\sigma}^* : \boldsymbol{d}. \tag{9.9}$$

$\pi(\boldsymbol{d})$ represents the maximum "plastic" dissipation capacity the material (here

[1] The reader interested by the distinction between classical and sequential limit analysis can refer to the recent paper [Leblond et al., 2018])

the solid phase) can afford. Its macroscopic counterpart is defined as

$$\Pi(\boldsymbol{D}) = \inf_{\mathbf{v}\in\mathcal{K}(\boldsymbol{D})} (1-f)\langle\pi(\boldsymbol{d})\rangle_{\Omega-\omega} \quad \text{with} \quad \boldsymbol{d} = \frac{1}{2}\left(\mathbf{grad}(\mathbf{v}) + \mathbf{grad}(\mathbf{v})^{\mathrm{T}}\right). \tag{9.10}$$

In this definition the set $\mathcal{K}(\boldsymbol{D})$ consists of those velocity fields $\mathbf{v}$ which are kinematically admissible with $\boldsymbol{D}$ and plastically admissible (for instance, this leads to a traceless $\boldsymbol{d}$ in the case of incompressible plasticity).
Using the Hill-Mandel lemma, the fundamental inequality of limit-analysis reads :

$$\boldsymbol{\Sigma} : \boldsymbol{D} \ \leq \Pi(\boldsymbol{D}), \tag{9.11}$$

where $\boldsymbol{D}$ is arbitrary and independent of $\boldsymbol{\Sigma}$.

The parametric equation of the strength locus is then given by

$$\boldsymbol{\Sigma} = \frac{\partial \Pi}{\partial \boldsymbol{D}}(\boldsymbol{D}). \tag{9.12}$$

This combination of Hill-Mandel homogenization and limit-analysis will thus permit to provide a macroscopic strength criterion, a macroscopic flow rule as well as an evolution equation of the porosity.

In practice, the determination of the macroscopic yield locus is done by the following steps:

1. Choice of a RVE Ω;
2. Choice of a trial velocity field $\mathbf{v}$ kinematically admissible with $\boldsymbol{D}$;
3. Calculation of the macroscopic plastic dissipation $\Pi(\boldsymbol{D})$ (for the postulated velocity field);
4. Derivation of the macroscopic yield locus $\boldsymbol{\Sigma} = \partial\Pi(\boldsymbol{D})/\partial\boldsymbol{D}$.

9.3 The Gurson model for ductile porous materials

Gurson's model [Gurson, 1977] (see also [Gurson, 1975]) plays a central role in the modelling of ductile failure. It is considered as the most important contribution to this field since not only it explicitly accounts for the effect of the porosity on the non linear constitutive behavior of ductile porous materials, but also it paved the way to predict degradation and then failure phenomena in this class of materials.

9.3.1 Gurson's macroscopic criterion for porous materials

The original Gurson model [Gurson, 1977] is based on the derivation of a macroscopic yield criterion and normality rule, which, completed by porosity

evolution equation, define a ductile failure model. Therefore, we first present the basics of the derivation of the macroscopic plasticity criterion of the considered ductile porous material.

Gurson's approach is based on the limit-analysis of a hollow sphere made of a rigid-plastic material and subjected to an arbitrary loading, in the framework of Hill-Mandel homogenization. This choice of a spherical cell containing a spherical void can be considered as the most simple three-dimensional elementary cell representative of a ductile porous material.

Position of the problem

We consider a spherical "elementary cell" Ω of external radius b containing a concentric spherical void ω of internal radius a (see Figure 9.2). The porosity at a current time is thus defined by $f = a^3/b^3$. The spherical coordinates and associated local orthonormal basis are respectively denoted by r, θ, φ and $(\mathbf{e}_r, \mathbf{e}_\theta, \mathbf{e}_\varphi)$.

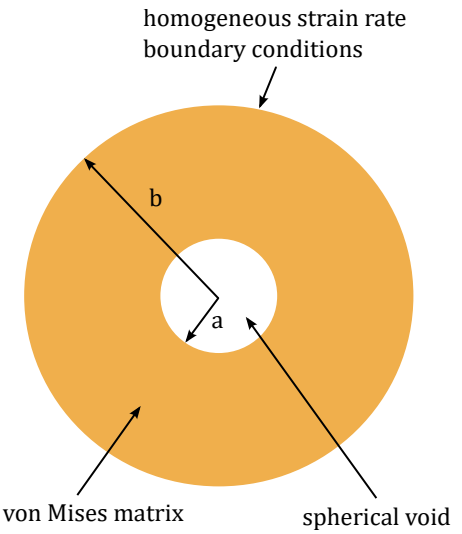

FIGURE 9.2: Spherical cell considered by Gurson

The material is assumed to be rigid-perfectly-plastic and to obey von Mises criterion

$$\phi(\boldsymbol{\sigma}(\mathbf{x})) = \sigma_{eq}^2 - \sigma_0^2 \leq 0, \qquad \forall \mathbf{x} \in \Omega - \omega, \tag{9.13}$$

where σ_0 is the yield stress (here the material strength since perfect plasticity is considered) and σ_{eq} is the equivalent von Mises stress defined by

$$\sigma_{\text{eq}} = \sqrt{\frac{3}{2}\boldsymbol{\sigma}' : \boldsymbol{\sigma}'}, \quad \boldsymbol{\sigma}' = \boldsymbol{\sigma} - \frac{1}{3}(\text{tr}\,\boldsymbol{\sigma})\,\mathbf{I}, \tag{9.14}$$

with $\mathbf{I}$ is the second-order unit tensor.

The corresponding support function (the local plastic dissipation) is obtained by applying (9.9)) for (9.13):

$$\pi(\boldsymbol{d}) = \sigma_0 d_{\text{eq}}, \tag{9.15}$$

where $\boldsymbol{d}$ is a traceless strain rate tensor and d_{eq} the equivalent strain rate defined by

$$d_{\text{eq}} = \sqrt{\frac{2}{3}\boldsymbol{d} : \boldsymbol{d}}. \tag{9.16}$$

Finally, the spherical cell is subjected to conditions of homogeneous boundary strain rate:

$$\mathbf{v}(\mathbf{x}) = \mathbf{D} \cdot \mathbf{x} \quad , \quad \forall \mathbf{x} \in \partial\Omega, \tag{9.17}$$

where $\mathbf{v}$ denotes the velocity, $\mathbf{x}$ the position-vector at current time and $\mathbf{D}$ the macroscopic strain rate tensor.

The considered trial velocity fields

In order to determine the macroscopic plastic dissipation, trial velocity fields, supposedly mimicking the local mechanisms of deformation, are required. Gurson considered two simple families of incompressible velocity fields

$$\mathbf{v}(\mathbf{x}) = \mathbf{v}^A(\mathbf{x}) + \mathbf{v}^B(\mathbf{x}) \tag{9.18}$$

defined by

$$\mathbf{v}^A(\mathbf{x}) = \frac{b^3}{r^2} D_{\text{m}} \mathbf{e}_r \quad ; \quad \mathbf{v}^B(\mathbf{x}) = \boldsymbol{D}' \cdot \mathbf{x}, \tag{9.19}$$

where $D_{\text{m}} = (\text{tr}\,\mathbf{D})/3$ denotes the mean macroscopic strain rate and $\boldsymbol{D}' = \mathbf{D} - D_{\text{m}}\,\mathbf{I}$ the deviatoric part of the macroscopic strain rate tensor. The first term $\mathbf{v}^A$ corresponds to the radial expansion of the cavity while the second term $\mathbf{v}^B$ corresponds to a homogeneous strain rate.

The associated local strain rate is given by

$$\boldsymbol{d}(\mathbf{x}) = \boldsymbol{d}^A(\mathbf{x}) + \boldsymbol{d}^B(\mathbf{x}) \tag{9.20}$$

with

$$\boldsymbol{d}^A(\mathbf{x}) = \frac{b^3}{r^3} D_{\text{m}}(-2\mathbf{e}_r \otimes \mathbf{e}_r + \mathbf{e}_\theta \otimes \mathbf{e}_\theta + \mathbf{e}_\varphi \otimes \mathbf{e}_\varphi) \quad ; \quad \boldsymbol{d}^B = \boldsymbol{D}'. \tag{9.21}$$

Macroscopic plastic dissipation

For the velocity field defined previously, the estimate Π of the macroscopic plastic dissipation (9.10) is given by

$$\Pi(\boldsymbol{D}) = \frac{1}{\text{vol}(\Omega)} \int_{\Omega - \omega} \sigma_0 d_{\text{eq}} \, \text{d}\Omega \tag{9.22}$$

$$= \frac{1}{\text{vol}(\Omega)} \int_a^b 4\pi r^2 \sigma_0 \langle d_{\text{eq}}(r) \rangle_{S(r)} \, \text{d}r, \tag{9.23}$$

where the symbol $\langle\cdot\rangle_{S(r)}$ denotes an average value over the sphere $S(r)$ of radius r. It can be shown that Π is of the form

$$\Pi(\boldsymbol{D}) = \frac{1}{\mathrm{vol}(\Omega)} \int_a^b 4\pi r^2 \sigma_0 \sqrt{D_{\mathrm{eq}}^2 + \frac{4b^6}{r^6} D_{\mathrm{m}}^2} \left\langle \sqrt{1+\eta(\mathbf{x})} \right\rangle_{S(r)} \mathrm{d}r, \tag{9.24}$$

where the function $\eta(\mathbf{x})$ is given by

$$\eta(\mathbf{x}) = \frac{\dfrac{4}{3}\boldsymbol{d}^A(\mathbf{x}) : \boldsymbol{d}^B(\mathbf{x})}{(d_{\mathrm{eq}}^A(\mathbf{x}))^2 + (d_{\mathrm{eq}}^B(\mathbf{x}))^2}. \tag{9.25}$$

In order to calculate analytically the macroscopic plastic dissipation, approximations are then introduced. Assuming that η is a small parameter, the expression $\sqrt{1+\eta(\mathbf{x})}$ can be replaced by a Taylor expansion; at the first order (which is the only case that Gurson considered) this leads to $\langle\sqrt{1+\eta(\mathbf{x})}\rangle_{S(r)} = \langle 1+\eta(\mathbf{x})/2\rangle_{S(r)} = 1$. Then, a closed-form expression of the macroscopic plastic dissipation $\Pi^{\mathrm{Gurson}}(\boldsymbol{D})$ can be obtained:

$$\Pi^{\mathrm{Gurson}}(\boldsymbol{D}) = \sigma_0 \left[\arg\sinh\left(\frac{2D_{\mathrm{m}}x}{D_{\mathrm{eq}}}\right) - \sqrt{4D_{\mathrm{m}}^2 + \frac{D_{\mathrm{eq}}^2}{x^2}} \right]_{x=1}^{x=1/f}. \tag{9.26}$$

It must be noted that higher-order expansion of the term $\sqrt{1+\eta(\mathbf{x})}$ would lead to other expressions of the macroscopic plastic dissipation [Leblond and Morin, 2014]. In particular, the third-order approximation permits to account for the effect of the third invariant of the stress tensor.

Macroscopic yield surface

The macroscopic yield surface associated with the macroscopic dissipation $\Pi^{\mathrm{Gurson}}(\boldsymbol{D})$ is defined by

$$\boldsymbol{\Sigma} = \frac{\partial \Pi^{\mathrm{Gurson}}}{\partial \boldsymbol{D}}(\boldsymbol{D}). \tag{9.27}$$

Since Π^{Gurson} depends on $\boldsymbol{D}$ only through D_{m} and D_{eq} one has

$$\boldsymbol{\Sigma} = \frac{\partial \Pi^{\mathrm{Gurson}}}{\partial D_{\mathrm{m}}} \frac{\partial D_{\mathrm{m}}}{\partial \boldsymbol{D}} + \frac{\partial \Pi^{\mathrm{Gurson}}}{\partial D_{\mathrm{eq}}} \frac{\partial D_{\mathrm{eq}}}{\partial \boldsymbol{D}} = \frac{1}{3} \frac{\partial \Pi^{\mathrm{Gurson}}}{\partial D_{\mathrm{m}}} \boldsymbol{I} + \frac{\partial \Pi^{\mathrm{Gurson}}}{\partial D_{\mathrm{eq}}} \frac{2\boldsymbol{D}'}{3D_{\mathrm{eq}}}. \tag{9.28}$$

This implies that the macroscopic mean and equivalent stresses Σ_{m} and Σ_{eq} are given by

$$\begin{cases} \Sigma_{\mathrm{m}} &= \dfrac{1}{3} \dfrac{\partial \Pi^{\mathrm{Gurson}}}{\partial D_{\mathrm{m}}} \\ \Sigma_{\mathrm{eq}} &= \left| \dfrac{\partial \Pi^{\mathrm{Gurson}}}{\partial D_{\mathrm{eq}}} \right|, \end{cases} \tag{9.29}$$

which, after calculation, reads

$$\left\{\begin{array}{ll} \Sigma_{\rm m} & = \dfrac{2\sigma_0}{3}\left(\text{arg sinh}\left(\dfrac{\lambda}{f}\right) - \text{arg sinh}(\lambda)\right) \\ \Sigma_{\rm eq} & = \sigma_0\left(\sqrt{1+\xi^2} - \sqrt{f^2+\xi^2}\right) \end{array}\right. , \quad \text{with} \quad \xi = \frac{2D_{\rm m}}{D_{\rm eq}}. \tag{9.30}$$

This is the *parametric* equation of the yield criterion. It can be written explicitly by noticing that

$$\cosh\left(\frac{3}{2}\frac{\Sigma_{\rm m}}{\sigma_0}\right) = \frac{1}{f}\left(\sqrt{f^2+\xi^2}\sqrt{1+\xi^2} - \xi^2\right) \tag{9.31}$$

and

$$\frac{\Sigma_{\rm eq}^2}{\sigma_0^2} = 1 + f^2 + 2\xi^2 - 2\sqrt{f^2+\xi^2}\sqrt{1+\xi^2}. \tag{9.32}$$

The combination of these two equations leads to the usual form of Gurson's criterion

$$\Phi^G(\boldsymbol{\Sigma}, f) = \frac{\Sigma_{\rm eq}^2}{\sigma_0^2} + 2f\cosh\left(\frac{3}{2}\frac{\Sigma_{\rm m}}{\sigma_0}\right) - 1 - f^2 = 0. \tag{9.33}$$

A remarkable point of this macroscopic criterion lies in the contribution of the mean stress $\Sigma_{\rm m}$, due to the cavity (in the case $f \neq 0$). Also, as expected, the criterion (9.33) reduces to von Mises criterion in the case $f = 0$. It is also noticeable that in the case of a purely hydrostatic loading ($\Sigma_{\rm eq} = 0$), the criterion reduces to

$$\Sigma_{\rm m} = -\frac{2}{3}\sigma_0 \log(f), \tag{9.34}$$

which is the exact solution of a rigid-plastic hollow sphere subjected to a hydrostatic loading. In the case of a purely deviatoric loading ($\Sigma_{\rm m} = 0$) the yield criterion reduces to

$$\Sigma_{\rm eq} = (1-f)\sigma_0, \tag{9.35}$$

which is only an upper estimate of the exact limit-load in this case. For completeness, it must be emphasized that the nonlinear variational homogenization model of [Ponte Castañeda, 1991] (see also [Suquet, 1995]) leads to a better upper bound $\Sigma_{\rm eq} = \sigma_0 \frac{1-f}{\sqrt{1+2f/3}}$.

The yield locus is represented in the meridian plane ($\Sigma_{\rm m}/\sigma_0$; $\Sigma_{\rm eq}/\sigma_0$) for several values of the porosity in Figure 9.3.

In the case $f = 1$, the yield criterion reduces to $\boldsymbol{\Sigma} = \mathbf{0}$, which corresponds to a complete degradation of the material which accounts for the final failure.

9.3.2 The original Gurson model

The previous macroscopic yield criterion (9.33) must then be completed in order to formulate the searched constitutive law: this is the original (primitive)

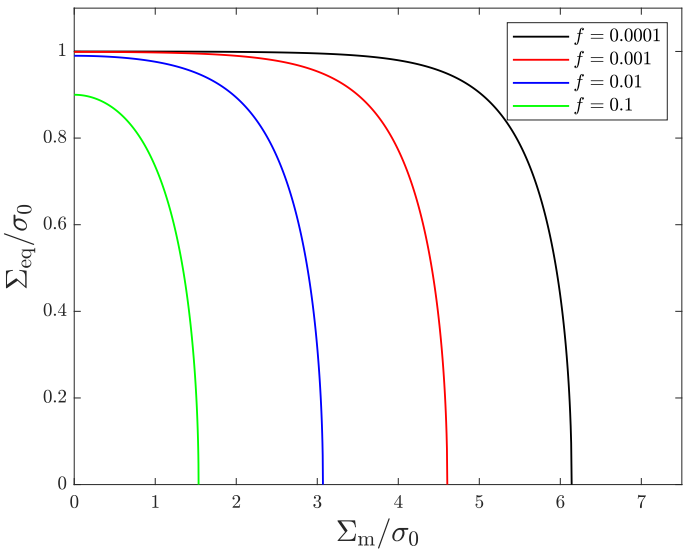

FIGURE 9.3: Yield surfaces of Gurson's model for several values of the porosity.

Gurson model which includes a macroscopic plastic flow rule, an evolution equation of the porosity and an expression for the elastic strain rate. Since ductile failure is a process involving large strains, Gurson's model is formulated in a finite deformation framework. Only the main ingredients are presented hereafter (see Chapter 3 for a detailed description of finite deformation modelling).

First, let us assume (as classically) that the total Eulerian strain rate $\boldsymbol{D}$ is given by the following decomposition

$$\boldsymbol{D} = \boldsymbol{D}^e + \boldsymbol{D}^p, \tag{9.36}$$

where $\boldsymbol{D}^e$ is the elastic strain rate and $\boldsymbol{D}^p$ is the plastic strain rate. Only the total Eulerian strain rate $\boldsymbol{D}$ is compatible and can be put of the form

$$\boldsymbol{D} = \frac{1}{2}\left(\mathbf{grad}(\mathbf{V}) + \mathbf{grad}(\mathbf{V})^{\mathrm{T}}\right), \tag{9.37}$$

where $\mathbf{V}$ is the macroscopic velocity of the material point.

The plastic strain rate $\boldsymbol{D}^p$ is given by the property of normality of the flow rule (which is preserved during the upscaling procedure, see for instance [Rice, 1971]):

$$\boldsymbol{D}^p = \dot{\Lambda}\frac{\partial \Phi^G}{\partial \boldsymbol{\Sigma}}(\boldsymbol{\Sigma}) = \dot{\Lambda}\left(\frac{f}{\sigma_0}\sinh\left(\frac{3}{2}\frac{\Sigma_m}{\sigma_0}\right)\boldsymbol{I} + 3\frac{\boldsymbol{\Sigma}'}{\sigma_0^2}\right) \tag{9.38}$$

where $\dot{\Lambda}$ is the plastic multiplier. As expected, the plastic strain rate is compressible, due to the presence of a cavity.

Then, the elastic strain rate $\boldsymbol{D}^e$ is connected to some objective time-derivative (here the so-called Jaumann derivative) of the Cauchy stress tensor using an hypoelasticity law:

$$\tilde{\boldsymbol{\Sigma}} = \dot{\boldsymbol{\Sigma}} + \boldsymbol{\Sigma}\cdot\boldsymbol{\Omega} - \boldsymbol{\Omega}\cdot\boldsymbol{\Sigma} = \lambda \mathrm{tr}(\boldsymbol{D}^e)\boldsymbol{I} + 2\mu\boldsymbol{D}^e. \tag{9.39}$$

In this equation, $\boldsymbol{\Omega}$ is an antisymetric rotation-rate tensor. In the case where

$$\boldsymbol{\Omega} = \frac{1}{2}\left(\mathbf{grad}(\mathbf{V}) - \mathbf{grad}(\mathbf{V})^{\mathrm{T}}\right). \tag{9.40}$$

For few more information about objective time-derivatives of the Cauchy stress, see for instance chapter 3. Obviously, the above coupling between elasticity and plasticity still holds under linearized strain conditions, the hypoelastic law being replaced by the classical Hooke's law.

Finally, the evolution equation of the porosity is deduced from the strain rate (in the case where nucleation is neglected). The contribution of elasticity to ductile fracture phenomena is generally small (at least under monotonic loadings), so that the rate of the porosity is supposed to depend only on the plastic strain rate. Therefore, it is directly deduced from the property of plastic incompressibility of the matrix:

$$f = \frac{\omega\Omega - \dot{\Omega}\omega}{\Omega^2} = \frac{\Omega-\omega}{\Omega}\times\frac{\dot{\Omega}}{\Omega} = (1-f)\mathrm{tr}(\boldsymbol{D}^p), \tag{9.41}$$

where the property $\omega = \Omega$ is used due to incompressibility of the matrix.

At this stage, it is interesting to note that the intrinsic dissipation for the Gurson model reads

$$\mathcal{D} = \boldsymbol{\Sigma} : \boldsymbol{D}^p \tag{9.42}$$

which corresponds to the plastic power. Despite the porosity changes (see equation (9.41)), its evolution does not contribute to the dissipation $\mathcal{D}$. Moreover, f is not related to some normality property as there is no thermodynamic force associated to it. This situation in which the porosity evolution is closely related to the plastic flow rule suggests that the Gurson model cannot be considered as a plastic-damage one in the usual sense.

9.3.3 The Gurson-Tvergaard-Needleman (GTN) model

The primitive Gurson model has been extended by Tvergaard and Needleman [1984] in order to include several important features of ductile fracture problems such as: strain hardening, void nucleation and coalescence. Overall, these modifications are heuristic but they permit to improve considerably the predictive capabilities of the primitive Gurson model.

Strain hardening

An important drawback of the Gurson model is that it is derived from classical limit-analysis which restricts by essence the behavior of the matrix to that of a rigid-perfectly-plastic material.

In order to account for strain hardening, the constant yield limit σ_0 in the criterion (9.33) is replaced by some "average yield stress" $\bar{\boldsymbol{\sigma}}$ given by:

$$\bar{\boldsymbol{\sigma}} \equiv \boldsymbol{\sigma}(\bar{\varepsilon}) \tag{9.43}$$

where $\sigma(\varepsilon)$ is a function providing the local yield limit as a function of the local accumulated plastic strain ε, and $\bar{\boldsymbol{\varepsilon}}$ represents some "average equivalent strain" in the heterogeneous, porous material. The evolution of $\bar{\boldsymbol{\varepsilon}}$ is governed by the following equation [Gurson, 1977]:

$$(1-f)\bar{\boldsymbol{\sigma}} : \dot{\bar{\boldsymbol{\varepsilon}}} = \boldsymbol{\Sigma} : \boldsymbol{D}^p \tag{9.44}$$

which expresses the heuristic assumption that the plastic dissipation in the heterogeneous porous material is equal to that in a fictitious "equivalent" homogeneous material with equivalent strain $\bar{\boldsymbol{\varepsilon}}$ and yield stress $\bar{\boldsymbol{\sigma}}$.

Void nucleation

Contrary to voids growth, voids nucleation is generally difficult to be adequately modeled. A classical description is obtained by assuming that the rate of nucleated voids depends only on the strain rate through its scalar measure $\bar{\boldsymbol{\varepsilon}}$

$$f_{\text{nucleation}} = \mathcal{A}\dot{\bar{\boldsymbol{\varepsilon}}}. \tag{9.45}$$

The parameter $\mathcal{A}$ generally depends on the equivalent strain $\bar{\boldsymbol{\varepsilon}}$ because nucleation is supposed to require important strain but it is also limited by the initial distribution of inclusions. The model of Chu and Needleman [1980] assumes that the parameter $\mathcal{A}$ follows a Gaussian distribution

$$\mathcal{A} = \frac{f_N}{s_N\sqrt{2\pi}} \exp\left[-\frac{1}{2}\left(\frac{\bar{\varepsilon}-\varepsilon_N}{s_N}\right)^2\right], \tag{9.46}$$

where f_N, ε_N and s_N respectively represent the volume fraction, average nucleation strain and standard deviation of the nucleating voids. The evolution equation of the porosity is then given by

$$\dot{f} = \dot{f}_{\text{growth}} + \dot{f}_{\text{nucleation}}. \tag{9.47}$$

It must be noted that other laws have been proposed using stress-based criterion (see for instance [Benzerga and Leblond, 2010]).

Coalescence and refinement of the RVE

A simple way to account for voids coalescence mechanism consists in replacing the porosity f in the yield criterion by an effective porosity qf^*. This allows to improve the prediction of the model with unit cell calculations (e.g. using a cubic unit-cell):

$$\Phi^{GTN}(\boldsymbol{\Sigma}, f, \bar{\boldsymbol{\sigma}}) = \frac{\Sigma_{\text{eq}}^2}{\bar{\boldsymbol{\sigma}}^2} + 2qf^*\cosh\left(\frac{3}{2}\frac{\Sigma_{\text{m}}}{\bar{\boldsymbol{\sigma}}}\right) - 1 - (qf^*)^2 = 0. \tag{9.48}$$

Indeed, it has been shown that during the void growth stage, the growth kinetics are underestimated by Gurson's which has lead to the introduction of the parameter q (also known as Tvergaard's parameter). It can also be interpreted as a heuristic coefficient which plays a role of adjustment of the porosity at failure. For instance, in the case of a cubic unit-cell, the cell loses its bearing capacity when the spherical void reaches the exterior boundary of the cube, that is for $f = \pi/6 \approx 0.52$ while the spherical Gurson cell loses its carrying capacity for $f = 1$. Therefore, to account approximately for the cell shape, this parameter q is therefore generally taken as $q \approx 1.5$. Then, this effective porosity qf is replaced by qf^* in the criterion in order to reproduce coalescence using the following (crude) modelling proposed by [Tvergaard and Needleman, 1984]:

$$f^* = \begin{cases} f & \text{if} \quad f \leq f_c \\ f_c + \delta(f - f_c) & \text{if} \quad f > f_c, \end{cases} \tag{9.49}$$

where f_c and $\delta > 1$ are material parameters. This models stipulates that if the porosity reaches a critical value f_c, it is artificially increased (as the parameter δ is greater than 1) to reproduce coalescence phenomena.

Heuristic modification of the GTN model to account for shear damage

A previous remark on the Gurson model is the absence of the third deviatoric stress invariant J_3 (or Lode angle) in the plastic criterion. However, various results from specific tests have shown that this lode angle effect can be non negligible (see experiments by [Bao and Wierzbicki, 2004] and [Barsoum and Faleskog, 2007]). In addition, in the case of pure shear loadings, Gurson's model predicts no void growth because the evolution equation of the porosity reduces to $\dot{f} = 0$. Probably, on the basis of these experimental evidences, Nahshon and Hutchinson [2008] proposed a modification of the porosity evolution equation (9.41) in which is now incorporated the effects of the third deviatoric stress ($\boldsymbol{s}$) invariant, J_3:

$$\dot{f} = (1 - f)\mathrm{tr}(\boldsymbol{D}^p) + k_\omega f \omega(\boldsymbol{\Sigma}) \frac{\Sigma'_{ij} D^p_{ij}}{\Sigma_{\mathrm{eq}}}. \tag{9.50}$$

in which $\omega(\boldsymbol{\Sigma}) = 1 - (\frac{27}{2}\frac{J_3}{\Sigma_{\mathrm{eq}}^3})^2$, with $J_3 = det\boldsymbol{s}$.
Such heuristic modification of the mass balance conservation suggests to interpret f as a (non dissipative) damage parameter and not as porosity. This very simple model has permitted to reproduce several micromechanical simulation including shear-dominated loadings [Tvergaard and Nielsen, 2010].

Predictions of the model

The predictions of the GTN model are illustrated in an evolution problem of a material point for two values of the stress triaxiality $T = \Sigma_{\mathrm{m}}/\Sigma_{\mathrm{eq}} = [1;\ 3]$, respectively in Figures 9.4 and 9.5. The case considered for this illustration

is that of a hardenable material (following a power-law isotropic hardening law) containing initial voids (with $f_0 = [0.0001;\ 0.001;\ 0.01]$) with no nucleation ($f_N = 0$) and no shear damage contribution ($k_\omega = 0$). Coalescence is accounted for by considering typical values $f_c = 0.05$ and $\delta = 5$.

For a given triaxiality, the first observation is that the initial porosity has an important influence on the overall behavior. Indeed, if the initial porosity increases, the stress level decreases and softening occurs more rapidly. This is in agreement with the dependence of the yield locus with respect to the porosity (represented in Figure 9.3).

The triaxiality is also an important parameter because, for a given initial porosity, an increase of the stress triaxiality leads more softening. This is due to void growth that is driven by stress triaxiality (see equation (9.41)): an increase of the stress triaxiality leads to an increase of the void growth rate which in turns accelerate softening (because of the direct dependence of the yield locus upon the porosity).

Finally, the influence of coalescence has been specifically highlighted because it accelerates the degradation of the material with an abrupt softening. Coalescence is thus determinant for the prediction the failure.

9.4 Some micromechanical extensions of the GTN model

Despite its important successes in reproducing several experiments of ductile fracture (including e.g. the cup and cone failure and failure of CT specimen), the Gurson and GTN approaches can be insufficient for several practical situations. Indeed, due to the hypotheses made in its derivation (spherical void, plastic isotropy of the matrix, diffuse plasticity) it cannot account for anisotropic materials, non-spherical voids, nanosized voids for instance. Furthermore, Gurson's analysis is by essence restricted to the void growth stage due to the conditions of homogeneous boundary strain rate which exclude strain localisation within the RVE: the modelling of coalescence in a micromechanical approach also requires modifications in the analysis.

The (micromechanical) extensions of Gurson's model therefore can be (mainly) divided into three categories:

1. A modification of the shape of the void to account for non-spherical voids, such as spheroidal or ellipsoidal voids;
2. A modification of the local plastic criterion to account for other matrix behavior, such as plastic anisotropy and single crystals behavior;
3. A modification of the velocity fields in order to describe strain localization in the RVE (for the modelling or coalescence) or simply improve the description of void growth.

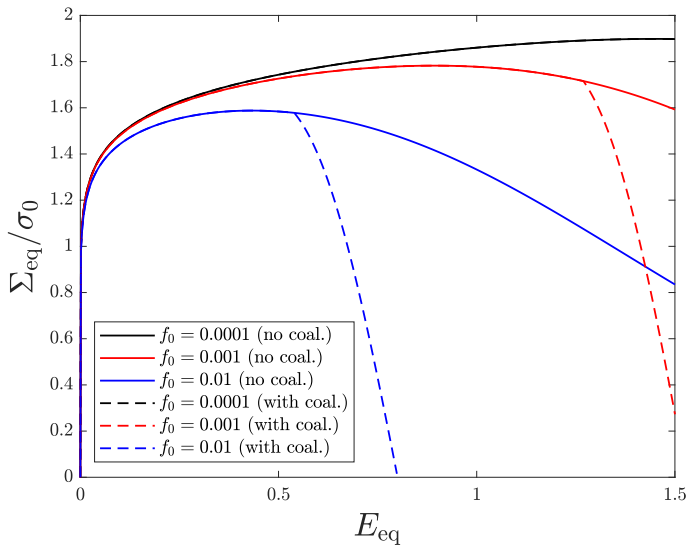

(a)

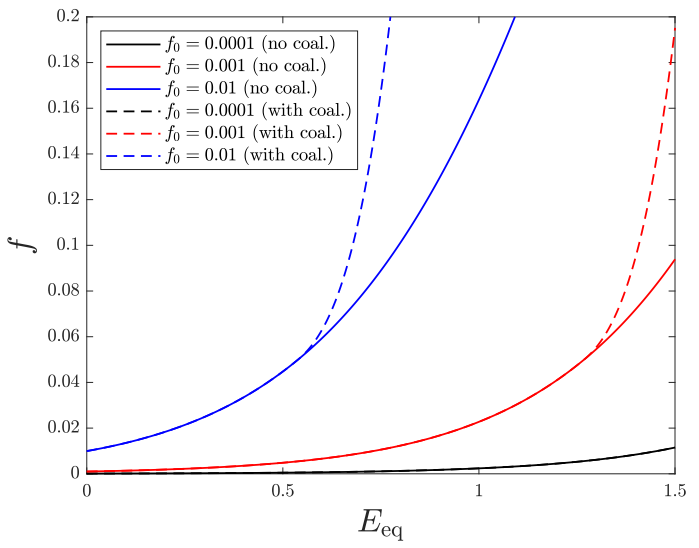

(b)

FIGURE 9.4: Predictions of the GTN model in the case $T = 1$. (a) Evolution of the normalized macroscopic stress $\Sigma_{\text{eq}}/\sigma_0$ and (b) Evolution of the porosity f. The predictions without coalescence are represented with full lines and the predictions with coalescence are represented with dotted lines.

These two first items (voids shape effects and plastic anisotropy) are an-

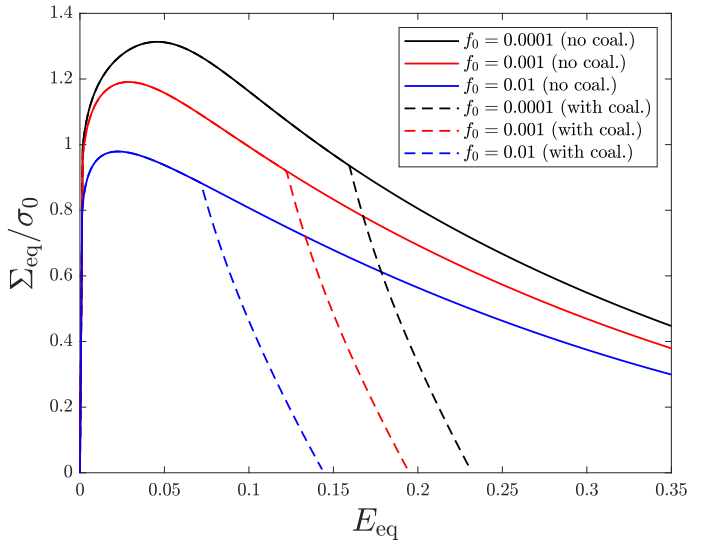

(a)

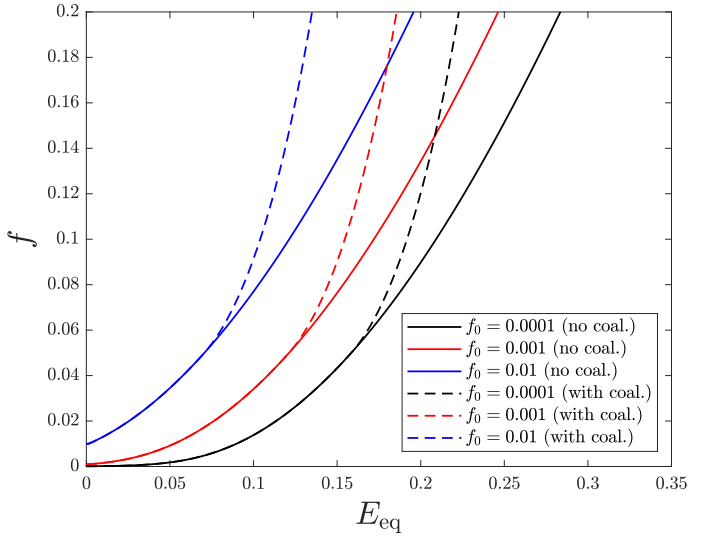

(b)

FIGURE 9.5: Predictions of the GTN model in the case $T = 3$. (a) Evolution of the normalized macroscopic stress $\Sigma_{\rm eq}/\sigma_0$ and (b) Evolution of the porosity f. The predictions without coalescence are represented with full lines and the predictions with coalescence are represented with dotted lines.

alyzed here while section 9.5 will be devoted to the modelling of coalescence phenomena.

9.4.1 Void shape effects

The most restrictive limitation of Gurson's model is the hypothesis of spherical voids. This is in practice not realistic because voids generally deform and look more like ellipsoids than spheres. Cavities possessing three different axes have been observed experimentally (see Figure 9.6(a)) using scanning electron microscopy techniques [Benzerga et al., 2004], and numerically (see Figure 9.6(b)) after the shearing of initially spherical cavities [Nielsen et al., 2012]. Taking into account the shape effects is therefore necessary to better approximate the real shape of the cavities. In particular it is essential to describe failure at low stress triaxiality because in that case, the porosity decreases but coalescence is still reached by interactions between elongated voids: void shape effects are thus important in shear-dominated loadings.

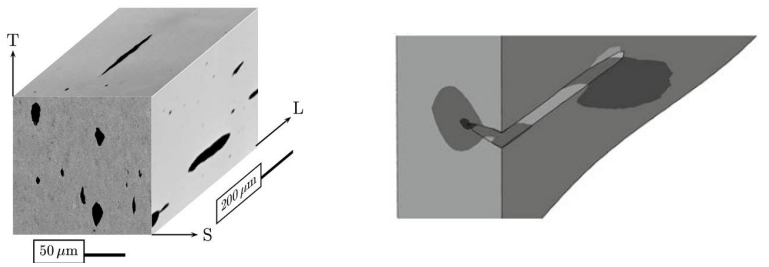

(a) (b)

FIGURE 9.6: Non-spherical cavities obeserved (a) Experimentally using SEM [Benzerga et al., 2004] and (b) Numerically during intense shearing [Nielsen et al., 2012].

The Gologanu-Leblond-Devaux (GLD) model for spheroidal voids

The GLD model is an extension of Gurson's model for spheroidal (oblate or prolate) voids. Its derivation is based on a limit-analysis of a spheroidal cell containing a confocal spheroidal cavity (and made of a von Mises matrix). The voids geometry considered is a spheroid with rotational symmetry axis Oz, half-axes a_2 and b_2, containing a confocal spheroidal void with half-axes a_1 and b_1. The porosity is given by $f = \frac{a_1 b_1^2}{a_2 b_2^2}$.

In the case of an axisymmetric loading the yield criterion is given by

$$\Phi^{GLD}(\boldsymbol{\Sigma}) = \frac{C}{\sigma_0^2}\left(\Sigma_{zz} - \Sigma_{xx} + \eta\Sigma_h\right)^2 + 2(1+g)(f+g)\cosh\left(\kappa\frac{\Sigma_h}{\sigma_0}\right) - (1+g)^2 - (f+g)^2 = 0 \tag{9.51}$$

where C, η, Σ_h, g and κ are parameters that depend on the geometry.

The Madou-Leblond model for ellipsoidal voids

Since the GLD model is restricted to spheroidal voids, it is not relevant for general loading conditions. To overcome this restriction Madou and Leblond [2012] have proposed an extension of this model to general ellipsoidal cavities. In this model, the elementary cell Ω is ellipsoidal and contains a confocal ellipsoidal cavity ω of semi-axes $a > b > c$ oriented along the (local) unit vectors $\mathbf{e}_x$, $\mathbf{e}_y$, $\mathbf{e}_z$. The cavity boundary is characterized by the quadratic form $\mathcal{P}$ defined by

$$\mathcal{P}(\mathbf{u}) \equiv \frac{(\mathbf{u}.\mathbf{e}_x)^2}{a^2} + \frac{(\mathbf{u}.\mathbf{e}_y)^2}{b^2} + \frac{(\mathbf{u}.\mathbf{e}_z)^2}{c^2}. \tag{9.52}$$

The matrix $\mathbf{P} \equiv (P_{ij})$ of the quadratic form $\mathcal{P}$ is expressed in the fixed frame $(\mathbf{e}_1, \mathbf{e}_2, \mathbf{e}_3)$ of the observer and permits to describe the orientation and semi-axes ratios of the ellipsoidal cavity; indeed its diagonalization provides the semi-axes and the local unit vectors $\mathbf{e}_x$, $\mathbf{e}_y$, $\mathbf{e}_z$ defining the orientation. A mixed analytical-numerical limit-analysis has been performed on this elementary ellipsoidal cell and led to the macroscopic yield criterion [Madou and Leblond, 2012]

$$\Phi^{ML}(\boldsymbol{\Sigma}, \mathbf{P}, f, \sigma_0) = \frac{\mathcal{Q}(\boldsymbol{\Sigma})}{\sigma_0^2} + 2(1+g)(f+g)\cosh\left[\frac{\mathcal{L}(\boldsymbol{\Sigma})}{\sigma_0}\right] - (1+g)^2 - (f+g)^2 \leq 0. \tag{9.53}$$

In equation (9.53):

- $\mathcal{Q}(\boldsymbol{\Sigma})$ is a quadratic form of the components of the Cauchy stress tensor $\boldsymbol{\Sigma}$ defined by
$$\mathcal{Q}(\boldsymbol{\Sigma}) = \boldsymbol{\Sigma} : \mathbb{Q} : \boldsymbol{\Sigma} \tag{9.54}$$
where $\mathbb{Q}(\mathbf{P}, f)$ is a fourth-order tensor which is related to classical Willis's bound for non-linear composites (see [Madou and Leblond, 2012]);

- $\mathcal{L}(\boldsymbol{\Sigma})$ is a linear form of the diagonal components of $\boldsymbol{\Sigma}$ in the basis $(\mathbf{e}_x, \mathbf{e}_y, \mathbf{e}_z)$ defined by
$$\mathcal{L}(\boldsymbol{\Sigma}) = \kappa \mathbf{H} : \boldsymbol{\Sigma} \tag{9.55}$$
where $\kappa(\mathbf{P}, f)$ is a scalar and $\mathbf{H}(\mathbf{P}, f)$ a second-order tensor of unit trace;

- $g(\mathbf{P}, f)$ is the so-called 'second' porosity. It is related to the volume fraction of a fictitious prolate spheroidal void obtained by rotating the completely flat ellipsoid confocal to the ellipsoidal cavity ω about its major axis. This parameter is null in the case of prolate voids, non-zero in the case of oblate voids, and reduces to the classical 'crack density' of Budiansky and O'Connell in the case of penny-shaped cracks. It naturally arises in the limit-analysis procedure of the ellipsoidal void and permits to account for the effect of a penny-shaped crack (having a null porosity) on the yield surface [Madou and Leblond, 2012].

The flow rule is deduced from the normality property and the evolution equation is given as in Gurson's model. The originality of this model is an evolution equation of the matrix $\mathbf{P}$ (characterizing the shape and orientation of the ellipsoidal voids) given by

$$\dot{\mathbf{P}} = -\mathbf{P}.(\boldsymbol{D}^v + \boldsymbol{\Omega}^v) - (\boldsymbol{D}^v + \boldsymbol{\Omega}^v)^T.\mathbf{P} \tag{9.56}$$

where $\boldsymbol{D}^v$ and $\boldsymbol{\Omega}^v$ are respectively the strain-rate and rotation-rate tensors of the cavity. These rates are given by:

$$\left\{ \begin{array}{ll} \boldsymbol{D}^v & = \mathbb{L} : \boldsymbol{D}^p \\ \boldsymbol{\Omega}^v & = \boldsymbol{\Omega} + \mathbb{R} : \boldsymbol{D}^p, \end{array} \right. \tag{9.57}$$

where $\boldsymbol{\Omega}$ is the rotation-rate tensor of the material (antisymmetric part of the velocity gradient). The tensors $\mathbb{L}(\mathbf{P}, f)$ and $\mathbb{R}(\mathbf{P}, f)$ are fourth-order 'localization tensors', as the tensor $\mathbb{L}$ relates the (local) void strain-rate $\boldsymbol{D}^v$ to the macroscopic strain-rate $\boldsymbol{D}$, and the tensor $\mathbb{R}$ relates the (local) void rotation-rate $\boldsymbol{\Omega}^v$ to the macroscopic rotate-rate $\boldsymbol{\Omega}$. They are based on plastic corrections of the elastic formula provided by [Ponte Castañeda and Zaidman, 1994] in the elastic case, determined by numerical analyses. The details and expressions of these tensors can be found in [Madou et al., 2013].

9.4.2 Plastic anisotropy of the matrix

Another important limitation of Gurson's model concerns the hypothesis of isotropic von Mises matrix which is not realistic in several situations including textured materials or single crystals. In the case of textured materials, the plastic behavior is no longer isotropic and there is a clear need to account for anisotropy. In the case of porous plastic single crystals, crystalline anisotropy is also necessary to describe the stress state surrounding intragranular voids.

The Benzerga-Besson model for orthotropic materials

The most common case of texture-induced anisotropy is orthotropy. In this case, the material has three planes of symmetry orthogonal to each other whose intersections correspond to the axes of anisotropy; the yield strength of the material is different along these three axes. [Hill, 1948] proposed an extension of the Gurson criterion by taking into account this orthotropy in a phenomenological way, in the form of a quadratic criterion. In this context, Benzerga and Besson [2001] proposed to replace the local von Mises criterion in the limit-analysis procedure by the local Hill's anisotropic criterion:

$$\phi(\boldsymbol{\sigma}) = \boldsymbol{\sigma} : \mathbb{A} : \boldsymbol{\sigma} - \sigma_0^2 \leq 0 \tag{9.58}$$

where $\mathbb{A}$ is Hill's matrix. Using the same velocity fields than Gurson, Benzerga and Besson [2001] have succeeded to determine the macroscopic plastic

dissipation which leads to the criterion

$$\Phi^{BB} = \frac{\boldsymbol{\Sigma} : \mathbb{A} : \boldsymbol{\Sigma}}{\sigma_0^2} + 2f\cosh\left(\frac{\kappa\Sigma_m}{\sigma_0}\right) - 1 - f^2 = 0, \quad \kappa = \frac{3}{2}\sqrt{\frac{5}{2h_1 + h_2 + 2h_3}}, \tag{9.59}$$

where the coefficients h_1, h_1 and h_1 are related to the tensor $\mathbb{H}$ defined by $\mathbb{H} : \mathbb{A} = \mathbb{A} : \mathbb{H} = \mathbb{K}$ ($\mathbb{K}$ being the deviatoric projection tensor). Naturally, this criterion allows to retrieve the Gurson one when the matrix is isotropic.

Combining voids shape and plastic anisotropy effects

The above extension which accounts for plastic anisotropy of the matrix has been followed by a series of studies that simultaneously take into account of both plastic anisotropy and voids shape effects. Among these studies, mention can be made of [Monchiet et al., 2006], [Keralavarma and Benzerga, 2008], [Monchiet et al., 2008], [Keralavarma and Benzerga, 2010] or [Morin et al., 2015b].

The successive influence of void shape and plastic anisotropy is represented in Figure 9.7, by considering Gurson's model for spherical voids within an isotropic matrix (with $f = 0.01$), the GLD model for spheroidal voids within an isotropic matrix (for a prolate cavity with an aspect ratio of 5 and $f = 0.01$), as well as the Keralavarma-Benzerga [Keralavarma and Benzerga, 2010] and the Monchiet criteria [Monchiet et al., 2008] for spheroidal voids within an anisotropic matrix (for a prolate cavity with an aspect ratio of 5 and $f = 0.01$ embbeded in an anisotropic matrix).

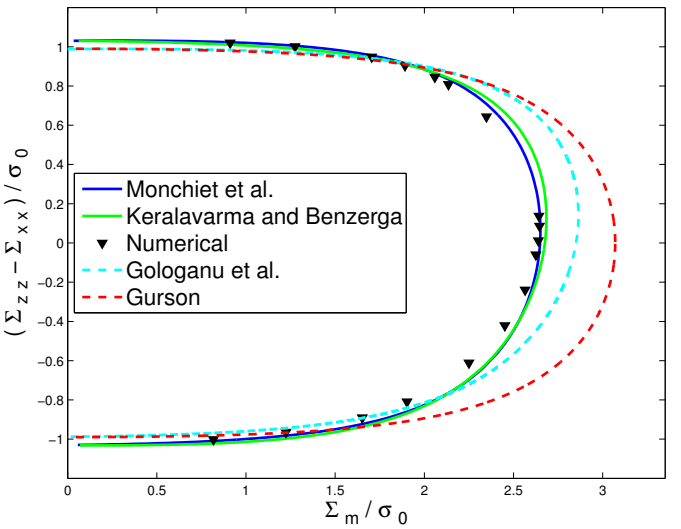

FIGURE 9.7: Influence of void shape and plastic anisotropy on the yield locus. After [Morin et al., 2014].

The case of single crystals porous materials

Comparatively to studies on polycrystals, few works have been devoted to the constitutive response of 3D plastic single crystals containing voids. However, the importance of the crystalline anisotropy to describe the stress state surrounding intragranular voids has been clearly evidenced from experimental point of view as well as analytically and numerically (see for instance [Kysar et al., 2005] [Srivastava and Needleman, 2013]). Based on the variational nonlinear homogenization method of [deBotton and Ponte Castañeda, 1995] and guided by limit-analysis results, [Han et al., 2013] have first proposed a multi yield criterion for 3D porous FCC single crystals containing spherical voids. These authors made use of the Schmid law. In the following of this work, Paux et al. [2015] have proposed a model based on limit analysis for which they considered a regularized form of the Schmid law. For completeness, it must be mentioned that [Mbiakop et al., 2015b] have developed a model for viscoplastic single crystals with ellipsoidal voids. Interestingly, these authors have also shown that these three models deliver very close estimates for rate-independent porous plasticity in the case of low plastic anisotropy (namely, face-centered cubic crystals) and spherical voids.

9.5 Micromechanical modelling of coalescence

The coalescence phase has been experimentally observed using various experimental techniques, such as scanning electron microscopy [Benzerga et al., 1999; Benzerga, 2000], computed tomography [Weck et al., 2008] or synchrotron laminography [Shen et al., 2013]. Several modes of coalescence have been observed: (i) by internal necking (Figure 9.8a), (ii) by shear (Figure 9.8b), and (iii) by columns (Figure 9.8c). During the coalescence by internal necking (or coalescence in layers), the cavities meet in a plane perpendicular to the main direction of the loading: the inter-cavity ligament contracts in a way similar to necking of a bar in tension. This mode of coalescence is the most common. During shear coalescence, the cavities meet in shear bands at 45 degrees to the main loading direction. Finally, during coalescence in columns, the cavities meet in bands parallel to the loading direction.

9.5.1 Numerical observations in unit-cell calculations

Numerical calculations on unit-cells have permitted to improve our understanding of the mechanisms of coalescence. In particular, the pioneering work of Koplik and Needleman [1988] highlighted key micromechanical aspects of coalescence by internal necking. They considered a cylindrical cell containing

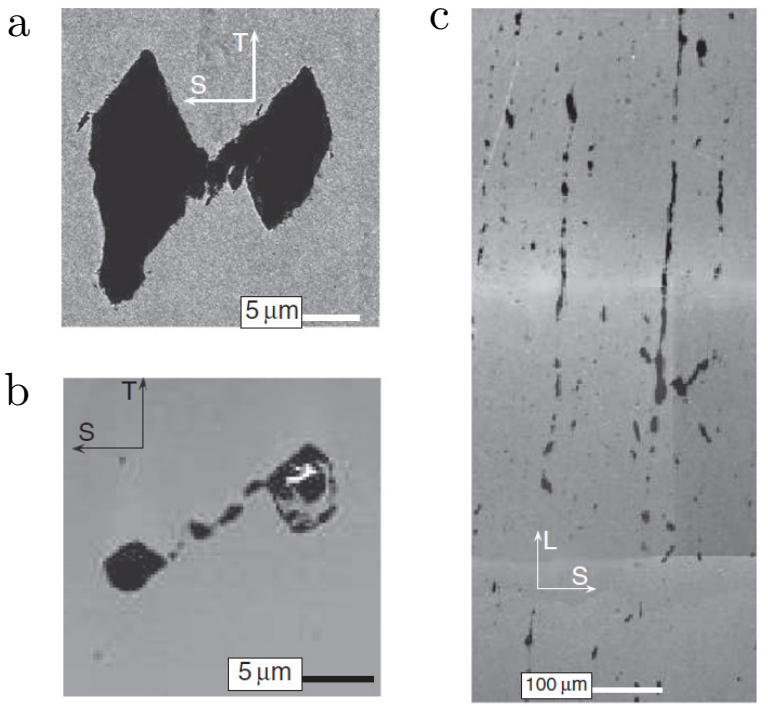

FIGURE 9.8: Three main modes of coalescence. (a) Coalescence by internal necking (also know as coalescence in layers) [Benzerga et al., 1999]. (b) Coalescence in shear [Benzerga, 2000]. (c) Necklace coalescence (also known as coalescence in columns) [Benzerga, 2000]. In the three cases considered, the loading is vertical.

a spherical void and subjected to quasi-periodic boundary conditions[2], for various proportional loading paths. We reproduce in Figure 9.9 typical results associated with these simulations, namely the evolution of equivalent stress, porosity, void aspect ratio, and radial strain [Benzerga and Leblond, 2010]. Coalescence is characterized by a transition from a triaxial state of cell deformation to a uniaxial state (pure extension in the axial direction) (Figure 9.9d). This transition corresponds to a localization of the plastic deformation in the inter-cavity ligament, involving the presence of elastic regions above and below the void, which impose quasi-nullity of the horizontal components of the overall strain rate. This localization leads to a rapid tightening of the inter-cavity ligament, which explains the very rapid growth of the porosity (Figure 9.9b) having as a direct consequence an abrupt softening of the material (Figure 9.9a).

The particularity of coalescence is therefore the localization of the defor-

[2]This modeling is an approximation of a periodic VER subjected to periodic conditions.

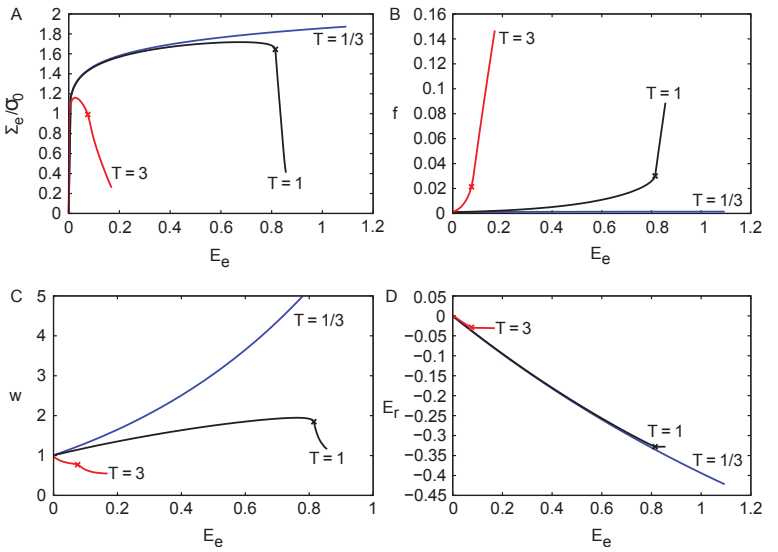

FIGURE 9.9: Micromechanical simulations results on a cylindrical cell containing an initially spherical cavity, subjected to axisymmetric macroscopic loading at fixed triaxiality. (a) Evolution of equivalent stress; (b) Evolution of porosity; (c) Evolution of void aspect ratio; (d) Evolution of radial strain. After Benzerga and Leblond [2010].

mation in the ligament between neighboring cavities: the plasticity is no longer diffuse as it was in the growth phase. The Hill-Mandel boundary conditions used in the derivation of growth models prohibit this phenomenon and are therefore not adapted to model the coalescence phase. In essence, coalescence can be viewed as a classical plasticity problem (with plastic and rigid zones), which can be solved by the limit analysis method provided that elasticity and strain hardening are neglected. The only ingredient that is required is a proper description of strain localisation in the ligament between neighboring voids.

9.5.2 The Thomason-Benzerga-Leblond model

The Thomason model

On the basis of some experimental observations, Thomason [1985] had the intuition that coalescence occurred as a result of the localization of plastic deformation in the ligament between cavities and therefore proposed velocity fields to describe this phenomenon. His model is based on a limit-analysis of a prismatic cell containing a prismatic void subjected to boundary conditions allowing a localization of the deformation in the ligament between neighboring voids; localization is implicitly taken into account by using appropriate velocity fields in the limit-analysis procedure. Nonetheless, the analytical de-

termination of the macroscopic dissipation of a prismatic voided cell being difficult, Thomason only proposed a numerical calculation of the integral giving this dissipation and then proposed an empirical criterion in order to fit his numerical results. The Thomason criterion reads

$$\Phi^T = \frac{\Sigma_{33}}{\bar{\sigma}} - (1-\chi^2)\left[0.1\left(\frac{\chi^{-1}-1}{W}\right)^2 + 1.2\sqrt{\chi^{-1}}\right] \tag{9.60}$$

where Σ_{33} is the coalescence stress supported by the porous medium (the main loading is oriented along a $\mathbf{e}_3$ axis). The value of this stress depends on the spacing between the cavities through the parameter χ (related to the porosity in the localization band) and on the shape of the cavity through the parameter W.

The Benzerga-Leblond model

Benzerga and Leblond [2014] have revisited the analysis of Thomason [1985] and succeeded in deriving a fully analytic coalescence criterion. Their analysis is based on the limit-analysis of a cylindrical cell containing a cylindrical void, characterized by the *void aspect ratio* $W \equiv h/R$, the *ligament parameter* $\chi \equiv R/L$ and the *cell aspect ratio* $\lambda \equiv H/L$ (see Figure 9.10). The local orthonormal basis associated with the cylindrical coordinates r, θ, z is denoted $(\mathbf{e}_r, \mathbf{e}_\theta, \mathbf{e}_z)$ and that associated with the Cartesian coordinates x_1, x_2, x_3 is denoted $(\mathbf{e}_1, \mathbf{e}_2, \mathbf{e}_3)$, with $\mathbf{e}_3 = \mathbf{e}_z$.

In the approach proposed by the authors, coalescence is assumed to occur in the plane $\mathbf{e}_1$–$\mathbf{e}_2$, due to a major applied stress parallel to the axis $\mathbf{e}_3$. As observed by Koplik and Needleman [1988], coalescence starts when the strain rate localizes in the horizontal ligament between neighbouring voids. The cell is consequently divided into two parts, the central one Ω_{lig} containing the plastic horizontal inter-void ligament and the void ω, and the rigid regions above and below the void denoted $\Omega - \Omega_{\text{lig}}$. Therefore, the cylindrical cell is subjected to boundary conditions of the following form:

$$\left\{\begin{array}{lcll} v_r(r=L,z) & = & 0 & -H \leq z \leq H \\ v_z(r, z=\pm H) & = & \pm D_{33} H & 0 \leq r \leq L. \end{array}\right. \tag{9.61}$$

The velocity field considered by Benzerga and Leblond [2014], verifying the property of incompressibility and the boundary conditions, is

$$\left\{\begin{array}{ll} v_r(r) = & \dfrac{HD_{33}}{2h}\left(\dfrac{L^2}{r} - r\right) \\ v_z(z) = & \dfrac{HD_{33}}{h} z \end{array}\right. \qquad (-h < z < h). \tag{9.62}$$

This velocity field, which is represented in Figure 9.10, implies that the overall horizontal strain rate components are nil. It should be noted that this velocity field introduces a tangential discontinuity at the interface between the plastic

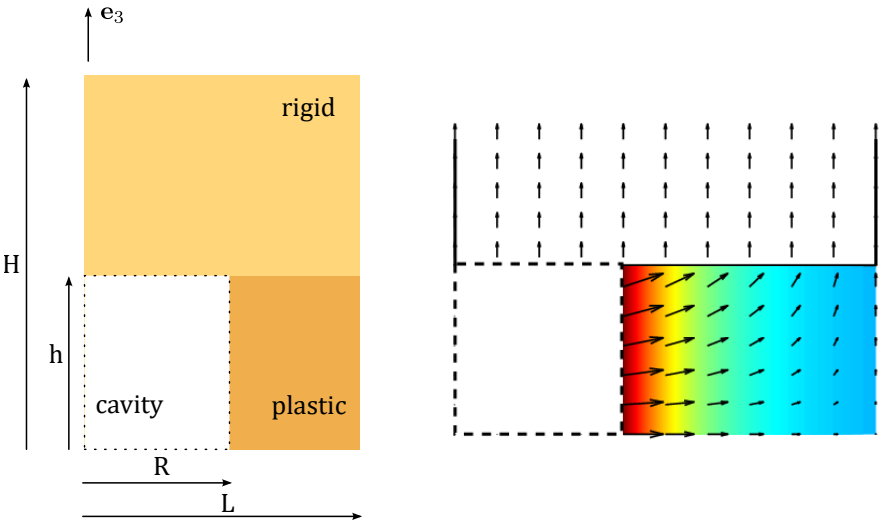

FIGURE 9.10: Cylindrical cell and velocity field considered by Benzerga and Leblond [2014]. After Morin et al. [2015a].

and rigid parts which is not physical but admissible within the limit-analysis procedure[3].

The overall (analytical) yield criterion derived from limit-analysis using this trial velocity field reads:

$$\Phi^{BL} = \frac{\Sigma_{33}}{\sigma_0} - \frac{1}{\sqrt{3}}\left[2 - \sqrt{1+3\chi^4} + \ln\frac{1+\sqrt{1+3\chi^4}}{3\chi^2} + \frac{\chi^3 - 3\chi + 2}{3\chi W}\right].$$

This model improves Thomason [1985]'s model because (i) it is analytical and (ii) it provides a tighter upper bound which makes the limit-load closer to the exact one. Owing to its analytical character, it has then been improved or extended in order to account for flat voids [Hure and Barrioz, 2016], shear loadings [Torki et al., 2015] or plastic anisotropy [Keralavarma and Chockalingam, 2016] among others.

The coalescence criterion is represented in the plane $(\Sigma_{\rm m}/\sigma_0;\ (\Sigma_{33}-\Sigma_{11})/\sigma_0)$ for several values of the ligament parameter $\chi = [0.2;\ 0.4;\ 0.6;\ 0.8]$ in Figure 9.11. In this plane, the coalescence criterion corresponds to a line because the criterion reads $\Sigma_{33} = \Sigma_{33}^{\rm coal}$. An increase of the value of the ligament parameter χ leads to a reduction of the yield loci size.

[3] In the presence of a velocity discontinuity, the plastic dissipation should be taken in the sense of distributions with a strain rate concentrated on a surface.

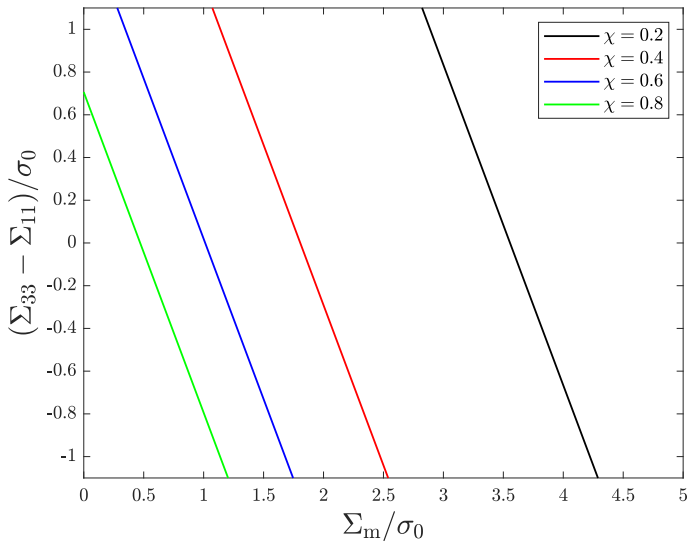

FIGURE 9.11: Yield surfaces of Benzerga-Leblond model for several values of the ligament parameter χ.

9.5.3 On the use of coalescence criterion with void growth models

The coalescence criteria presented above are then used in conjunction with the void growth criteria within a *hybrid approach* [Benzerga et al., 1999; Zhang et al., 2000; Pardoen and Hutchinson, 2000; Benzerga, 2002]: the final yield surface of a porous medium thus corresponds to the intersection between that corresponding to growth and that corresponding to coalescence: we represent in Figure 9.12a the yield surface associated with Gurson [1977] criterion for a spherical cavity of porosity $f = 0.1$ and a yield surface associated with Benzerga and Leblond [2014]'s coalescence criterion. The final (hybrid) criterion corresponds to the intersection between the two criteria (Figure 9.12b).

This hybrid approach has been successfully used to simulate crack propagation in 3D specimens and can thus be considered as a physically-based alternative to the (crude) modelling of coalescence as done in the GTN model (see Eq. 9.49). Nonetheless, in the hybrid approach, the presence of corners on the yield surface may trigger artificial plastic flow localization at the macroscopic scale.

9.5.4 Towards a unified description of void growth and coalescence

In addition to the presence of corners on the yield surface, another drawback of the hybrid approach is that growth and coalescence are described with

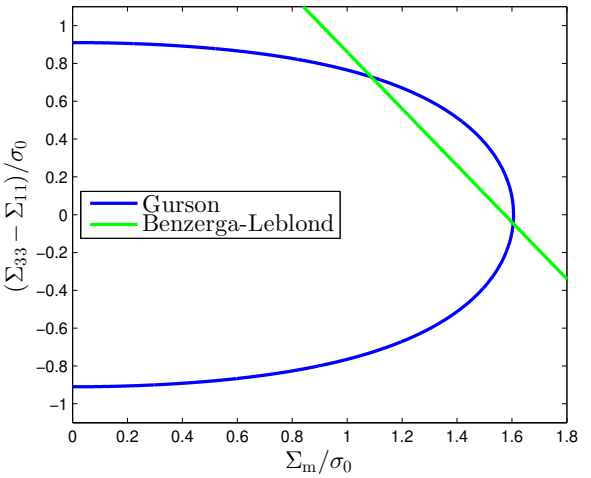

(a)

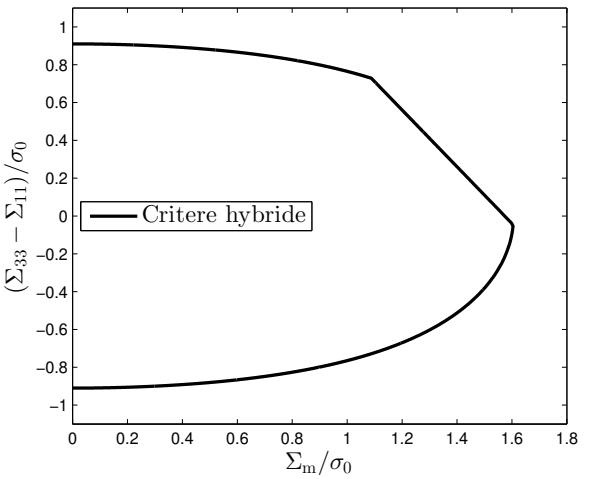

(b)

FIGURE 9.12: Practical use of a coalescence criterion with a growth criterion. The parameters are $f = 0.1$ for Gurson's model and $\chi = 0.46$ and $W = 1$ for the Benzerga-Leblond model. After [Morin, 2015].

different geometries which makes the resulting criterion only approximate. The development of a unified framework of void growth and coalescence permits to settle interrogations of this kind [Morin et al., 2016].

In contrast with the model of Benzerga and Leblond [2014] (where the

coalescence condition is enforced by $D_{11} = 0$), the cylindrical cell is now subjected to boundary conditions of the following form (see Figure 9.13):

$$\left\{ \begin{array}{lcll} v_r(r = L, z) & = & D_{11}L & -H \leq z \leq H \\ v_z(r, z = \pm H) & = & \pm D_{33}H & 0 \leq r \leq L. \end{array} \right. \tag{9.63}$$

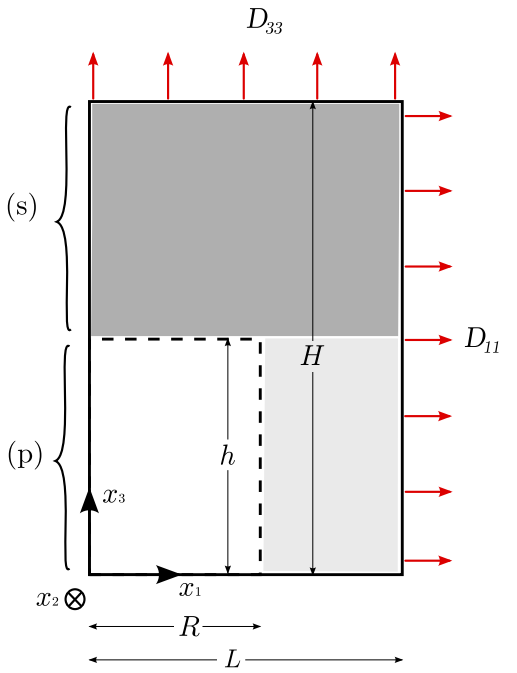

FIGURE 9.13: Cell considered to describe both growth and coalescence. After Morin et al. [2016].

In order to describe the growth of the void prior to the localization of the strain rate in the ligament, Benzerga and Leblond [2014]'s velocity field is extended by (i) dropping the condition $D_{11} = 0$ and (ii) allowing the sound region (which corresponds to the rigid region when coalescence takes place)

to deform uniformly. A velocity field satisfying these conditions is

$$0 \leq |z| \leq h \begin{cases} v_r(r) = & \frac{3}{2}\frac{H}{h} D_m \frac{L^2}{r} + \left[\frac{3}{2}\Big(1 - \frac{H}{h}\Big) D_m - \frac{D_{33}}{2}\right] r \\ v_z(z) = & \left[D_{33} - 3\Big(1 - \frac{H}{h}\Big) D_m\right] z \end{cases} \tag{9.64}$$

$$h \leq |z| \leq H \begin{cases} v_r(r) = & \frac{3D_m - D_{33}}{2} r \\ v_z(z) = & (D_{33} - 3D_m) z + 3H D_m. \end{cases} \tag{9.65}$$

The calculation of the macroscopic plastic dissipation using this velocity field leads to a yield criterion which is defined by curved and straight parts. The curved (regular) part of the yield locus is given by the criterion

$$\Phi(\mathbf{\Sigma}) = \left(\frac{\Sigma_{33} - \Sigma_{11} + A}{c\sigma_0}\right)^2 + 2\chi^2 \cosh\left(\sqrt{3}\frac{\Sigma_{11} - (1-c)\Sigma_{33} - A - cB}{c\sigma_0}\right) - 1 - \chi^4 \tag{9.66}$$

where

$$\begin{cases} A = \sigma_0 (1-c)\ \mathrm{sgn}(\mathrm{D}_{11}) \\ B = \dfrac{\sigma_0}{3\sqrt{3}} \dfrac{\chi^3 - 3\chi + 2}{W\chi}\ \mathrm{sgn}(\mathrm{D}_{\mathrm{m}}). \end{cases} \tag{9.67}$$

The straight part of the yield criterion, corresponding to the coalescence phase, is given by

$$\begin{cases} \Sigma_{33} = \dfrac{\sigma_0}{\sqrt{3}} \left[\ln\left(\dfrac{1 + \sqrt{1+3\chi^4}}{3\chi^2}\right) + 2 - \sqrt{1+3\chi^4}\right] + \dfrac{\sigma_0}{3\sqrt{3}} \dfrac{\chi^3 - 3\chi + 2}{W\chi} \\ \left|\Sigma_{33} - \Sigma_{11} - \dfrac{c\sigma_0}{\sqrt{3}}\left(2 - \sqrt{1+3\chi^4}\right)\right| \leq \sigma_0 (1-c). \end{cases} \tag{9.68}$$

In addition, using this velocity field, it can be shown that corners are absent of the yield locus in contrast with the hybrid approach.

Illustrative results for the yield locus of a cylindrical hollow cell are provided in Figure 9.14 for a void aspect ratio $W = 1$ and two values of the ligament parameter, $\chi = 0.4$ and 0.6, associated with the unified criterion, a hybrid criterion (obtained as previously by truncating Gurson's yield locus with the Benzerga-Leblond yield locus). In addition, numerical simulations of limit-analysis performed for the same exact cells using the finite element method have been plotted in order to highlight the main features of the unified approach. On the "coalescence line", the predictions of the hybrid and unified

models coincide because they are based on the same trial velocity field. The main difference is that the transition between growth and coalescence phase is smooth using the unified criterion; the absence of corners (also observed in the numerical results) may thus be one advantage of this approach.

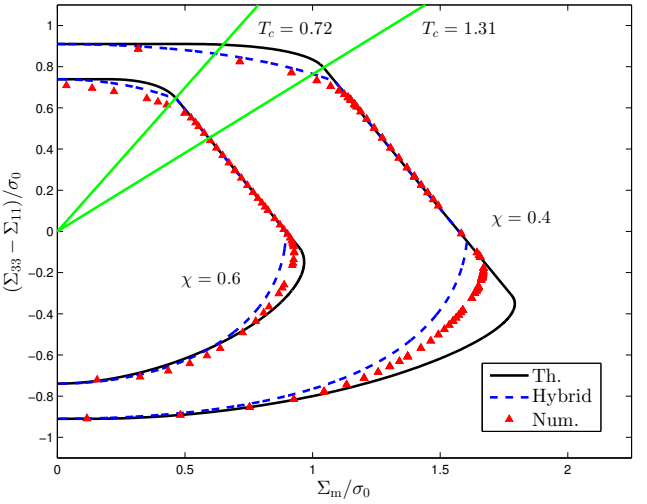

FIGURE 9.14: Comparison of the yield surfaces obtained using the hybrid approach and the unified model. After Morin et al. [2016].

This model is interesting from a theoretical point of view because it describes both growth and coalescence with a single class of velocity fields, thus emphasizing the basic unity of the two stages and the possibility of their unified description. In this approach, the yield locus has no corners, in agreement with numerical results of limit-analysis [Morin et al., 2016].

9.6 The case of sub-micron voids

Despite their great interest in practical situations involving structural materials, the above growth and coalescence models may not be suitable to describe the growth of sub-micron voids. Indeed, it is now well admitted that size effects arise when plasticity occurs at small scales related to several factors including notably the Hall-Petch effect, an increase of geometrically necessary dislocation densities in presence of high strain gradient and some patterning of dislocation cells associated to grain refinement. Mention has to be made to the work of Hure et al. [2020] who have evidenced a notable size effect on the

growth of very small voids ($\leq$ 10 nm), resulting in a reduced void deformation. The development of models for ductile porous materials with sub-micron voids has mainly followed two approaches.

Strain-gradient plasticity

The first class of models is based on a refinement of Gurson [1977]'s model by considering strain gradient plasticity model in the matrix surrounding the void. This approach is generally considered relevant for micron-sized voids for which conventional plasticity is not adapted. When the size of the cavities is comparable to or smaller than the internal length of the plastic solid a strong dependence of the yield locus with the void size is observed. In this context, Monchiet and Bonnet [2013] have considered Fleck and Hutchinson [1997]'s model, which includes a dependence of the strain gradient (double gradient of velocity) within the local plastic potential:

$$\pi(\boldsymbol{d},\boldsymbol{\eta}) = \sigma_0 \xi_{eq} = \sigma_0 \sqrt{d_{eq}^2 + l_1^2 \eta_{ijk}^{(1)} \eta_{ijk}^{(1)} + l_2^2 \eta_{ijk}^{(2)} \eta_{ijk}^{(2)} + l_3^2 \eta_{ijk}^{(3)} \eta_{ijk}^{(3)}}, \qquad (9.69)$$

where $\eta_{ijk}^{(1)}$, $\eta_{ijk}^{(2)}$, and $\eta_{ijk}^{(3)}$ are related to the invariants of the strain gradient rate $\boldsymbol{\eta}$ and l_1, l_2 and l_3 are the internal length scales of the material. After computation of the macroscopic plastic dissipation, the resulting macroscopic Gurson type yield criterion depends on the void size through the ratio a/l_1 (where a is the cavity size):

$$\Phi(\boldsymbol{\Sigma}, f) = \frac{\Sigma_{\rm eq}^2}{\sigma_0^2} + 2f\cosh\left(\frac{3}{2\beta}\frac{\Sigma_{\rm m}}{\sigma_0}\right) - 1 - f^2 = 0 \qquad (9.70)$$

in which

$$\beta = \frac{3}{\ln f}\left[\text{Arcsinh}\left(\frac{\alpha}{u}\right) - \sqrt{1+\frac{u^2}{\alpha^2}}\right]_{u=f^{1/3}}^{u=1} \quad \text{with} \quad \alpha = \frac{1}{3}\sqrt{\frac{2}{5}}\frac{a}{l_1}. \qquad (9.71)$$

This model predicts, for small voids, (i) a reduction of softening and (ii) a decrease of the growth rate. This effect is generally referred to as smaller is slower (see Figure 9.15).

Interface approach of size effects

The second approach is based on an extension of Gurson [1977]'s model by representing the cavity surface through a stress interface model, which is generally assumed to correspond to nano-sized voids. For these materials, an increase of the strength is observed, due to the presence of surface effects at the interface between the bulk material and the void. By following the limit analysis approach, [Dormieux and Kondo, 2010] has succeeded to extend the Gurson strength criterion (9.33) to the case of ductile nanoporous materials, with the

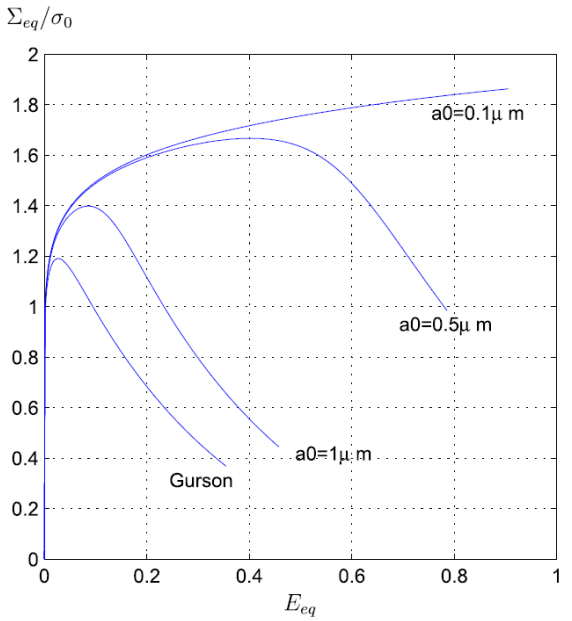

FIGURE 9.15: Influence of void size on the evolution of the normalized equivalent stress in the case $T = 3$. After Monchiet and Bonnet [2013].

aim of predicting void-size effects. The methodology proposed by these authors relies on the consideration of imperfect coherent interfaces at the cavity layer for which is performed the limit analysis based on the same velocity field as in the Gurson computation. A remarkable extension of the model related to the void-size-dependent strength criterion has been established by Gallican and Hure [2017] who have simultaneously adding coalescence modeling and plastic anisotropy in nanoporous materials.

9.7 Brief Conclusions and some current researches directions

The aim of this chapter is to introduce to basic developments of limit-analysis based models for ductile fracture. Before concluding and indicating some current research directions, it must be recalled that in addition to the textbook [Leblond, 2003], there are several reviews papers to which the reader may refer for detailed presentation of some specifics points. Among these reviews, mention has to be made of [Besson, 2010], [Benzerga and Leblond, 2010] or [Benzerga et al., 2016].

Gurson model primarily relies on the limit analysis of a hollow sphere subjected to a homogeneous macroscopic strain rate. This has led to an upper bound of a macroscopioc strength surface of the ductile porous material. This constitutes the main micromechanical component of the model which has been built by transforming the obtained strength criterion into a plasticity criterion which by normality property delivers the macroscopic flow rule of the porous material. Such flow rule is completed by the porosity evolution equation obtained by mean of mass conservation law. We have also seen the importance of a proper micromechanics-based modeling of both void growth and coalescence phenomena. The Gurson-Tvergaard-Needleman constitutes a basic prototype of ductile fracture model which can be improved. However a remaining question is the thermodynamics consistency of such model. This question raises also that of the status of the porosity f which, obviously, is not a dissipative variable since it does not enters in the intrinsic dissipation. This point requires further research development. Concerning coalescence, the unified approach, obtained by combining voids growth and coalescence criteria seems to be promising. There is probably still needs of researches in this direction. Owing to the absence of internal length in the GTN model, and to the occurrence of softening phenomena before failure, nonlocal formulations can be required. Several recent studies provide new insights on this aspects (see for instance [Zhang et al., 2018], [Tuhami et al., 2022], etc.) and this must be helpful for ductile failure prediction of structures.
At the nanoscale, void size effects are supposed to arise. Recent developed models by incorporating surface effects in a thin layer close to the void boundary allow to predict voids size effects which affect the initial yield surface and thus modifies plasticity before straining. Recent developments include the derivation of a micromechanical model for nanovoid coalescence as in [Gallican and Hure, 2017]. This paves the way for the derivation of complete models dedicated to nanovoided ductile materials.

For completeness, we provide here some comments on current research on non linear homogenization of ductile heterogeneous materials which can be useful for elastoplastic porous materials with hardenable constituents, mention has to be made of [Cheng et al., 2017] who have proposed a decoupling between reversible and dissipative phenomena approach. This has led them to obtain a macroscopic model described by an overall free energy and a macroscopic dissipation potential. In order to fully handle the coupling between reversible and dissipative phenomena such as elasto(visco)-plasticity, one may refer to incremental variational approach as introduced by Lahellec and Suquet [2007]. In this framework, the concerned non linear behaviors of constituents are described by means of two potentials, namely a free energy and a dissipation potential as it is the case for Generalized Standard Materials. The incremental variational approach has been followed and implemented with some variants by several authors among which [Brassart et al., 2012], [Agoras et al., 2016] and [Lucchetta et al., 2019] which, in principle, allow to deal with elastoplastic

porous materials without porosity evolution (this is still a matter of research). Unfortunately, although reversible and dissipative processes are coupled at small scale, the incremental variational approach does not allow to separate them at macroscopic scale. Moreover, these studies are still in a early state of development which does not allow to use them for structural computations.

Bibliography

[Agoras et al. 2016] Agoras, M. ; Avazmohammadi, R. ; Ponte Castañeda, P.: Incremental variational procedure for elasto-viscoplastic composites and application to polymer- and metal-matrix composites reinforced by spheroidal elastic particles. In: *International Journal of Solids and Structures* 97-98 (2016), Oktober, p. 668–686. – 10.1016/j.ijsolstr.2016.04.008 . – ISSN 0020–7683

[Agoras and Ponte Castañeda 2013] Agoras, M. ; Ponte Castañeda, P.: Iterated linear comparison bounds for viscoplastic porous materials with "ellipsoidal" microstructures. In: *Journal of the Mechanics and Physics of Solids* 61 (2013), März, Nr. 3, p. 701–725. – 10.1016/j.jmps.2012.11.003 . – ISSN 0022–5096

[Bao and Wierzbicki 2004] Bao, Y. ; Wierzbicki, T.: On fracture locus in the equivalent strain and stress triaxiality space. In: *International Journal of Mechanical Sciences* 46 (2004), Januar, Nr. 1, p. 81–98. – 10.1016/j.ijmecsci.2004.02.006 . – ISSN 0020–7403

[Barsoum and Faleskog 2007] Barsoum, I. ; Faleskog, J.: Rupture mechanisms in combined tension and shear—Micromechanics. In: *International Journal of Solids and Structures* 44 (2007), August, Nr. 17, p. 5481–5498. – 10.1016/j.ijsolstr.2007.01.010 . – ISSN 0020–7683

[Benzerga 2000] Benzerga, A.A.: *Rupture ductile des tôles anisotropes*, Ecole Nationale Supérieure des Mines de Paris, Diss., 2000

[Benzerga 2002] Benzerga, A.A.: Micromechanics of coalescence in ductile fracture. In: *Journal of the Mechanics and Physics of Solids* 50 (2002), Nr. 6, p. 1331–1362. – 10.1016/S0022-5096(01)00125-9

[Benzerga and Besson 2001] Benzerga, A.A. ; Besson, J.: Plastic potentials for anisotropic porous solids. In: *European Journal of Mechanics - A/Solids* 20 (2001), Mai, Nr. 3, p. 397–434. – 10.1016/S0997-7538(01)01147-0 . – ISSN 0997–7538

[Benzerga et al. 1999] Benzerga, A.A. ; Besson, J. ; Pineau, A.:

Coalescence-Controlled Anisotropic Ductile Fracture. In: *Journal of Engineering Materials and Technology* 121 (1999), April, Nr. 2, p. 221–229. – 10.1115/1.2812369 . – ISSN 0094–4289

[Benzerga et al. 2004] Benzerga, A.A. ; Besson, J. ; Pineau, A.: Anisotropic ductile fracture: Part II: theory. In: *Acta Materialia* 52 (2004), September, Nr. 15, p. 4639–4650. – 10.1016/j.actamat.2004.06.019 . – ISSN 1359–6454

[Benzerga and Leblond 2010] Benzerga, A.A. ; Leblond, J.-B.: Ductile fracture by void growth to coalescence. In: *Advances in Applied Mechanics* 44 (2010), p. 169–305. – 10.1016/S0065-2156(10)44003-X

[Benzerga and Leblond 2014] Benzerga, A.A. ; Leblond, J.-B.: Effective yield criterion accounting for microvoid coalescence. In: *Journal of Applied Mechanics* 81 (2014), Nr. 3, p. 031009. – 10.1115/1.4024908

[Benzerga et al. 2016] Benzerga, A.A. ; Leblond, J.-B. ; Needleman, A. ; Tvergaard, V.: Ductile failure modeling. In: *International Journal of Fracture* 201 (2016), Juli, Nr. 1, p. 29–80. – 10.1007/s10704-016-0142-6 . – ISSN 0376–9429, 1573–2673

[Besson 2010] Besson, J.: Continuum Models of Ductile Fracture: A Review. In: *International Journal of Damage Mechanics* 19 (2010), Januar, Nr. 1, p. 3–52. – 10.1177/1056789509103482 . – ISSN 1056–7895

[Brassart et al. 2012] Brassart, L. ; Stainier, L. ; Doghri, I. ; Delannay, L.: Homogenization of elasto-(visco) plastic composites based on an incremental variational principle. In: *International Journal of Plasticity* 36 (2012), p. 86–112

[Cheng et al. 2017] Cheng, L. ; Danas, K. ; Constantinescu, A. ; Kondo, D.: A homogenization model for porous ductile solids under cyclic loads comprising a matrix with isotropic and linear kinematic hardening. In: *International Journal of Solids and Structures* 121 (2017), August, p. 174–190. – 10.1016/j.ijsolstr.2017.05.024 . – ISSN 0020–7683

[Chu and Needleman 1980] Chu, C.C. ; Needleman, A.: Void Nucleation Effects in Biaxially Stretched Sheets. In: *Journal of Engineering Materials and Technology* 102 (1980), Juli, Nr. 3, p. 249–256. – 10.1115/1.3224807 . – ISSN 0094–4289

[Danas and Aravas 2012] Danas, K. ; Aravas, N.: Numerical modeling of elasto-plastic porous materials with void shape effects at finite deformations. In: *Composites Part B: Engineering* 43 (2012), September, Nr. 6, p. 2544–2559. – 10.1016/j.compositesb.2011.12.011 . – ISSN 1359–8368

[Danas and Ponte Castañeda 2009] Danas, K. ; Ponte Castañeda, P.: A finite-strain model for anisotropic viscoplastic porous media: I – Theory. In: *European Journal of Mechanics - A/Solids* 28 (2009), Mai, Nr. 3, p. 387–401. – 10.1016/j.euromechsol.2008.11.002 . – ISSN 0997–7538

[deBotton and Ponte Castañeda 1995] deBotton, G. ; Ponte Castañeda, P.: Variational estimates for the creep behaviour of polycrystals. In: *Proceedings of the Royal Society of London. Series A: Mathematical and Physical Sciences* 448 (1995), Januar, Nr. 1932, p. 121–142. – 10.1098/rspa.1995.0009

[Dormieux and Kondo 2010] Dormieux, L. ; Kondo, D.: An extension of Gurson model incorporating interface stresses effects. In: *International Journal of Engineering Science* 48 (2010), Juni, Nr. 6, p. 575–581. – 10.1016/j.ijengsci.2010.01.004 . – ISSN 00207225

[Fleck and Hutchinson 1997] Fleck, N.A. ; Hutchinson, J.W.: Strain Gradient Plasticity. In: *Advances in Applied Mechanics* Volume 33 (1997), p. 295–361. – 10.1016/S0065-2156(08)70388-0

[Gallican and Hure 2017] Gallican, V. ; Hure, J.: Anisotropic coalescence criterion for nanoporous materials. In: *Journal of the Mechanics and Physics of Solids* 108 (2017), November, Nr. Supplement C, p. 30–48. – 10.1016/j.jmps.2017.08.001 . – ISSN 0022–5096

[Garrison and Moody 1987] Garrison, W.M. ; Moody, N.R.: Ductile fracture. In: *Journal of Physics and Chemistry of Solids* 48 (1987), Nr. 11, p. 1035–1074. – 10.1016/0022-3697(87)90118-1 . – ISSN 0022–3697

[Gurson 1975] Gurson, A.L.: *Plastic flow and fracture behavior of ductile materials incorporating void nucleation, growth, and interaction.* Brown University, 1975

[Gurson 1977] Gurson, A.L.: Continuum theory of ductile rupture by void nucleation and growth: Part I–Yield criteria and flow rules for porous ductile media. In: *ASME Journal of Engineering Materials and Technology* 99 (1977), Januar, Nr. 1, p. 2–15. – 10.1115/1.3443401 . – ISSN 0094–4289

[Han et al. 2013] Han, X. ; Besson, J. ; Forest, S. ; Tanguy, B. ; Bugat, S.: A yield function for single crystals containing voids. In: *International Journal of Solids and Structures* 50 (2013), Juli, Nr. 14–15, p. 2115–2131. – 10.1016/j.ijsolstr.2013.02.005 . – ISSN 0020–7683

[Hannard et al. 2018] Hannard, F. ; Simar, A. ; Maire, E. ; Pardoen, T.: Quantitative assessment of the impact of second phase particle arrangement on damage and fracture anisotropy. In: *Acta Materialia* 148 (2018), April, p. 456–466. – 10.1016/j.actamat.2018.02.003 . – ISSN 1359–6454

[Hill 1948] Hill, R.: A theory of the yielding and plastic flow of anisotropic metals. In: *Proc. R. Soc. London A* 193 (1948), Mai, Nr. 1033, p. 281–297. – 10.1098/rspa.1948.0045 . – ISSN 1364–5021, 1471–2946

[Hill 1967] Hill, R.: The essential structure of constitutive laws for metal composites and polycrystals. In: *Journal of the Mechanics and Physics of*

Solids 15 (1967), März, Nr. 2, p. 79–95. – 10.1016/0022-5096(67)90018-X . – ISSN 0022–5096

[Hure and Barrioz 2016] Hure, J. ; Barrioz, P.O.: Theoretical estimates for flat voids coalescence by internal necking. In: *European Journal of Mechanics - A/Solids* 60 (2016), November, p. 217–226. – 10.1016/j.euromechsol.2016.08.001 . – ISSN 0997–7538

[Hure et al. 2020] Hure, J. ; Barrioz, P.O. ; Tanguy, B.: Assessing size effects on the deformation of nanovoids in metallic materials. In: *Scripta Materialia* 177 (2020), März, p. 54–57. – 10.1016/j.scriptamat.2019.09.005 . – ISSN 1359–6462

[Keralavarma and Benzerga 2008] Keralavarma, S.M. ; Benzerga, A.A.: An approximate yield criterion for anisotropic porous media. In: *Comptes Rendus Mécanique* 336 (2008), September, Nr. 9, p. 685–692. – 10.1016/j.crme.2008.07.008 . – ISSN 1631–0721

[Keralavarma and Benzerga 2010] Keralavarma, S.M. ; Benzerga, A.A.: A constitutive model for plastically anisotropic solids with non-spherical voids. In: *Journal of the Mechanics and Physics of Solids* 58 (2010), Juni, Nr. 6, p. 874–901. – 10.1016/j.jmps.2010.03.007 . – ISSN 00225096

[Keralavarma and Chockalingam 2016] Keralavarma, S.M. ; Chockalingam, S.: A criterion for void coalescence in anisotropic ductile materials. In: *International Journal of Plasticity* 82 (2016), Juli, p. 159–176. – 10.1016/j.ijplas.2016.03.003 . – ISSN 0749–6419

[Koplik and Needleman 1988] Koplik, J. ; Needleman, A.: Void growth and coalescence in porous plastic solids. In: *International Journal of Solids and Structures* 24 (1988), Nr. 8, p. 835–853. – ISSN 0020–7683

[Kysar et al. 2005] Kysar, J.W. ; Gan, Y.X. ; Mendez-Arzuza, G.: Cylindrical void in a rigid-ideally plastic single crystal. Part I: Anisotropic slip line theory solution for face-centered cubic crystals. In: *International Journal of Plasticity* 21 (2005), August, Nr. 8, p. 1481–1520. – 10.1016/j.ijplas.2004.07.007 . – ISSN 0749–6419

[Lahellec and Suquet 2007] Lahellec, N. ; Suquet, P.: On the effective behavior of nonlinear inelastic composites: I. Incremental variational principles. In: *Journal of the Mechanics and Physics of Solids* 55 (2007), September, Nr. 9, p. 1932–1963. – 10.1016/j.jmps.2007.02.003 . – ISSN 0022–5096

[Leblond et al. 2018] Leblond, J.-B. ; Kondo, D. ; Morin, L. ; Remmal, A.: Classical and sequential limit analysis revisited. In: *Comptes Rendus Mécanique* 346 (2018), April, Nr. 4, p. 336–349. – 10.1016/j.crme.2017.12.015 . – ISSN 1631–0721

[Leblond and Morin 2014] Leblond, J.-B. ; Morin, L.: Gurson's Criterion and Its Derivation Revisited. In: *Journal of Applied Mechanics* 81 (2014), Nr. 5, p. 051012. – 10.1115/1.4026112

[Leblond 2003] Leblond, Jean-Baptiste: *Mécanique de la rupture fragile et ductile*. 2003 (Hermes Science Publications)

[Lucchetta et al. 2019] Lucchetta, A. ; Auslender, F. ; Bornert, M. ; Kondo, D.: A double incremental variational procedure for elastoplastic composites with combined isotropic and linear kinematic hardening. In: *International Journal of Solids and Structures* 158 (2019), Februar, p. 243–267. – 10.1016/j.ijsolstr.2018.09.012 . – ISSN 0020–7683

[Madou and Leblond 2012] Madou, K. ; Leblond, J.-B.: A Gurson-type criterion for porous ductile solids containing arbitrary ellipsoidal voids—II: Determination of yield criterion parameters. In: *Journal of the Mechanics and Physics of Solids* 60 (2012), Mai, Nr. 5, p. 1037–1058. – 10.1016/j.jmps.2012.01.010 . – ISSN 0022–5096

[Madou et al. 2013] Madou, K. ; Leblond, J.-B. ; Morin, L.: Numerical studies of porous ductile materials containing arbitrary ellipsoidal voids—II: Evolution of the length and orientation of the void axes. In: *European Journal of Mechanics - A/Solids* 42 (2013), November, p. 490–507. – 10.1016/j.euromechsol.2013.06.005 . – ISSN 0997–7538

[Mandel 1964] Mandel, J.: Contribution théorique à l'etude de l'écrouissage et des lois de l'écoulement plastique. In: *Proceedings of 11th International Congress on Applied Mechanics*. Munich, 1964. – ISBN 978–3–662–27863–5 978–3–662–29364–5, p. 502–509

[Mbiakop et al. 2015a] Mbiakop, A. ; Constantinescu, A. ; Danas, K.: A model for porous single crystals with cylindrical voids of elliptical cross-section. In: *International Journal of Solids and Structures* 64-65 (2015), Juli, p. 100–119. – 10.1016/j.ijsolstr.2015.03.017 . – ISSN 0020–7683

[Mbiakop et al. 2015b] Mbiakop, A. ; Constantinescu, A. ; Danas, K.: On void shape effects of periodic elasto-plastic materials subjected to cyclic loading. In: *European Journal of Mechanics - A/Solids* 49 (2015), Januar, p. 481–499. – 10.1016/j.euromechsol.2014.09.001 . – ISSN 0997–7538

[Michel and Suquet 1992] Michel, J.C. ; Suquet, P.: The constitutive law of nonlinear viscous and porous materials. In: *Journal of the Mechanics and Physics of Solids* 40 (1992), Mai, Nr. 4, p. 783–812. – 10.1016/0022-5096(92)90004-L . – ISSN 0022–5096

[Monchiet and Bonnet 2013] Monchiet, V. ; Bonnet, G.: A Gurson-type model accounting for void size effects. In: *International Journal of Solids and Structures* 50 (2013), Januar, Nr. 2, p. 320–327. – 10.1016/j.ijsolstr.2012.09.005 . – ISSN 00207683

[Monchiet et al. 2008] Monchiet, V. ; Cazacu, O. ; Charkaluk, E. ; Kondo, D.: Macroscopic yield criteria for plastic anisotropic materials containing spheroidal voids. In: *International Journal of Plasticity* 24 (2008), Juli, Nr. 7, p. 1158–1189. – 10.1016/j.ijplas.2007.08.008 . – ISSN 0749–6419

[Monchiet et al. 2006] Monchiet, V. ; Gruescu, C. ; Charkaluk, E. ; Kondo, D.: Approximate yield criteria for anisotropic metals with prolate or oblate voids. In: *Comptes Rendus Mécanique* 334 (2006), Juli, Nr. 7, p. 431–439. – 10.1016/j.crme.2006.06.001 . – ISSN 1631–0721

[Morin 2015] Morin, L.: *Influence des effets de forme et de taille des cavités, et de l'anisotropie plastique sur la rupture ductile*, Paris 6, These de doctorat, Juli 2015. `https://www.theses.fr/2015PA066230`

[Morin et al. 2015a] Morin, L. ; Leblond, J.-B. ; Benzerga, A.A.: Coalescence of voids by internal necking: Theoretical estimates and numerical results. In: *Journal of the Mechanics and Physics of Solids* 75 (2015), Februar, p. 140–158. – 10.1016/j.jmps.2014.11.009 . – ISSN 0022–5096

[Morin et al. 2016] Morin, L. ; Leblond, J.-B. ; Benzerga, A.A. ; Kondo, D.: A unified criterion for the growth and coalescence of microvoids. In: *Journal of the Mechanics and Physics of Solids* 97 (2016), Dezember, p. 19–36. – 10.1016/j.jmps.2016.01.013 . – ISSN 0022–5096

[Morin et al. 2015b] Morin, L. ; Leblond, J.-B. ; Kondo, D.: A Gurson-type criterion for plastically anisotropic solids containing arbitrary ellipsoidal voids. In: *International Journal of Solids and Structures* 77 (2015), Dezember, p. 86–101. – 10.1016/j.ijsolstr.2015.05.021 . – ISSN 0020–7683

[Morin et al. 2014] Morin, L. ; Madou, K. ; Leblond, J.-B. ; Kondo, D.: A new technique for finite element limit-analysis of Hill materials, with an application to the assessment of criteria for anisotropic plastic porous solids. In: *International Journal of Engineering Science* 74 (2014), Januar, p. 65–79. – 10.1016/j.ijengsci.2013.08.006 . – ISSN 0020–7225

[Nahshon and Hutchinson 2008] Nahshon, K. ; Hutchinson, J.W.: Modification of the Gurson model for shear failure. In: *European Journal of Mechanics - A/Solids* 27 (2008), Januar, Nr. 1, p. 1–17. – 10.1016/j.euromechsol.2007.08.002 . – ISSN 0997–7538

[Nielsen et al. 2012] Nielsen, K.L. ; Dahl, J. ; Tvergaard, V.: Collapse and coalescence of spherical voids subject to intense shearing: studied in full 3D. In: *International Journal of Fracture* 177 (2012), Oktober, Nr. 2, p. 97–108. – 10.1007/s10704-012-9757-4 . – ISSN 0376–9429, 1573–2673

[Pardoen and Hutchinson 2000] Pardoen, T. ; Hutchinson, J.W.: An extended model for void growth and coalescence. In: *Journal of the Mechanics and Physics of Solids* 48 (2000), Nr. 12, p. 2467–2512. – 10.1016/S0022-5096(00)00019-3

[Paux et al. 2015] Paux, J. ; Morin, L. ; Brenner, R. ; Kondo, D.: An approximate yield criterion for porous single crystals. In: *European Journal of Mechanics - A/Solids* 51 (2015), Mai, p. 1–10. – 10.1016/j.euromechsol.2014.11.004 . – ISSN 0997–7538

[Ponte Castañeda 1991] Ponte Castañeda, P.: The effective mechanical properties of nonlinear isotropic composites. In: *Journal of the Mechanics and Physics of Solids* 39 (1991), Nr. 1, p. 45–71. – 10.1016/0022-5096(91)90030-R . – ISSN 0022–5096

[Ponte Castañeda and Zaidman 1994] Ponte Castañeda, P. ; Zaidman, M.: Constitutive models for porous materials with evolving microstructure. In: *Journal of the Mechanics and Physics of Solids* 42 (1994), September, Nr. 9, p. 1459–1497. – 10.1016/0022-5096(94)90005-1 . – ISSN 0022–5096

[Rice 1971] Rice, J.R.: Inelastic constitutive relations for solids: An internal-variable theory and its application to metal plasticity. In: *Journal of the Mechanics and Physics of Solids* 19 (1971), November, Nr. 6, p. 433–455. – 10.1016/0022-5096(71)90010-X . – ISSN 0022–5096

[Rice and Tracey 1969] Rice, J.R. ; Tracey, D.M.: On the ductile enlargement of voids in triaxial stress fields. In: *Journal of the Mechanics and Physics of Solids* 17 (1969), Juni, Nr. 3, p. 201–217. – 10.1016/0022-5096(69)90033-7 . – ISSN 0022–5096

[Salençon 2002] Salençon, J.: *De l'Elasto-plasticité au Calcul à la rupture*. Editions de l'Ecole Polytechnique, 2002. – 264 S. `https://hal.science/hal-00112707`

[Shen et al. 2013] Shen, Y. ; Morgeneyer, T.F. ; Garnier, J. ; Allais, L. ; Helfen, L. ; Crépin, J.: Three-dimensional quantitative in situ study of crack initiation and propagation in AA6061 aluminum alloy sheets via synchrotron laminography and finite-element simulations. In: *Acta Materialia* 61 (2013), April, Nr. 7, p. 2571–2582. – 10.1016/j.actamat.2013.01.035 . – ISSN 1359–6454

[Srivastava and Needleman 2013] Srivastava, A. ; Needleman, A.: Void growth versus void collapse in a creeping single crystal. In: *Journal of the Mechanics and Physics of Solids* 61 (2013), Mai, Nr. 5, p. 1169–1184. – 10.1016/j.jmps.2013.01.006 . – ISSN 0022–5096

[Suquet 1995] Suquet, P.: Overall properties of nonlinear composites: a modified secant moduli theory and its link with Ponte Castañeda's nonlinear variational procedure. In: *Comptes rendus de l'Académie des sciences. Série II, Mécanique, physique, chimie, astronomie* 320 (1995), Nr. 11, p. 563–571

[Thomason 1985] Thomason, P.F.: A three-dimensional model for ductile fracture by the growth and coalescence of microvoids. In: *Acta Metallurgica*

33 (1985), Juni, Nr. 6, p. 1087–1095. – 10.1016/0001-6160(85)90202-0 . – ISSN 0001–6160

[Torki et al. 2015] Torki, M.E. ; Benzerga, A.A. ; Leblond, J.-B.: On void coalescence under combined tension and shear. In: *Journal of Applied Mechanics* 82 (2015), Juli, Nr. 7, p. 071005. – 10.1115/1.4030326 . – ISSN 0021–8936

[Tuhami et al. 2022] Tuhami, A.E.O. ; Feld-Payet, S. ; Quilici, S. ; Osipov, N. ; Besson, J.: A two characteristic length nonlocal GTN model: Application to cup–cone and slant fracture. In: *Mechanics of Materials* 171 (2022), p. 104350

[Tvergaard and Needleman 1984] Tvergaard, V. ; Needleman, A.: Analysis of the cup-cone fracture in a round tensile bar. In: *Acta metallurgica* 32 (1984), Nr. 1, p. 157–169. – ISSN 0001–6160

[Tvergaard and Nielsen 2010] Tvergaard, V. ; Nielsen, K.L.: Relations between a micro-mechanical model and a damage model for ductile failure in shear. In: *Journal of the Mechanics and Physics of Solids* 58 (2010), September, Nr. 9, p. 1243–1252. – 10.1016/j.jmps.2010.06.006 . – ISSN 0022–5096

[Weck et al. 2008] Weck, A. ; Wilkinson, D.S. ; Maire, E. ; Toda, H.: Visualization by X-ray tomography of void growth and coalescence leading to fracture in model materials. In: *Acta Materialia* 56 (2008), Juli, Nr. 12, p. 2919–2928. – 10.1016/j.actamat.2008.02.027 . – ISSN 1359–6454

[Willis 1991] Willis, J.R.: On methods for bounding the overall properties of nonlinear composites. In: *Journal of the Mechanics and Physics of Solids* 39 (1991), Nr. 1, p. 73–86. – 10.1016/0022-5096(91)90031-I . – ISSN 0022–5096

[Zhang et al. 2018] Zhang, Y. ; Lorentz, E. ; Besson, J.: Ductile damage modelling with locking-free regularised GTN model. In: *International Journal for Numerical Methods in Engineering* 113 (2018), Nr. 13, p. 1871–1903

[Zhang et al. 2000] Zhang, Z.L. ; Thaulow, C. ; Ødegård, J.: A complete Gurson model approach for ductile fracture. In: *Engineering Fracture Mechanics* 67 (2000), September, Nr. 2, p. 155–168. – 10.1016/S0013-7944(00)00055-2 . – ISSN 0013–7944

10

Numerical simulations using local damage models

Thomas Helfer

CEA, DES/IRESNE/DEC/SESC/LSC, Département d'Études des Combustibles, Cadarache, France

Jérémy Hure

Université Paris-Saclay, CEA, Service d'Étude des Matériaux Irradiés, Gif-sur-Yvette, 91191, France

This chapter is dedicated to the description of issues encountered when performing numerical simulations of fracture using local damage models. First, these issues are evidenced based on a prototypical analytical example. Finite-element method is then recalled, and numerical examples are shown to lead to pathological mesh dependency. Good practices and ad-hoc solutions are finally described.

10.1 Introduction

Broadly speaking, theoretical models aiming at predicting brittle and ductile fracture presented in Chapters 4-9 can be divided into two categories. The first one, referred to as **uncoupled models**, essentially corresponds to the definition of a critical value of some variables to predict the onset of failure. Beremin (Chapter 7) and Rice & Tracey models (Chapter 8) fall into this category. These models are applied as a post-processing of analytical and / or numerical results, emphasizing the underlying assumption that damage is not coupled with the mechanical behavior, hence the name. While this approach may seem rather crude, it is relevant and efficient for a large number of applications, ranging from the prediction of brittle fracture in steels [Beremin, 1981; Andrieu et al., 2012] to the determination of the onset of ductile fracture [Marini et al., 1985; Keralavarma et al., 2020]. This chapter is focused on the second category, that can be referred to as **coupled models**, where the evolution of damage is described in the local constitutive equations (see Chapter 2). The prototypical example related to ductile fracture is the Gurson-Tvergaard-Needleman (GTN) model described in Chapter 9 in which the porosity is included in the yield criterion. Fracture is described by the progressive decrease of the stresses down to zero as the loading increases. This softening behavior at the scale of the material, although sound and consistent with the physics of fracture, leads to some issues when applied at the structural scale.

The aim of the chapter is thus to:

1. evidence these issues based on analytical and numerical examples analysed using theoretical arguments where the mathematical details are mostly hidden for simplicity. The description of those issues is important to understand why so-called non-local and variational approaches to fracture may be required (see Chapters 12 and 11).

2. present good practices when using these models in numerical simulations if non-local approaches are not required or available, both cases still being common in practice.

This chapter is organized as follows. Section 10.2 recalls some mathematical results showing that, in presence of softening behaviors, the boundary value problem is ill-posed regarding the questions of the uniqueness, existence and regularity of the solutions. These issues are illustrated with a simple analytical example. After a quick reminder of the finite element method in Section 10.3, Section 10.4 describes some practical consequences of those mathematical issues on finite element simulations. and some good practices and ad-hoc solutions are finally given in Section 10.5.

10.2 Theoretical analysis of local damage models

In this section, the mathematical conditions for which a mechanical problem has an unique regular solution are first briefly recalled. A simple example is then detailed to highlight various issues related to the use of softening behaviors in structural mechanics problem.

10.2.1 General results

The framework of standard generalized materials, introduced in Chapter 2, enables to study the mathematical properties of initial boundary value problems in damage mechanics. This framework is convenient, but it is worth highlighting that the issues exposed below are general (and generally speaking even more salient). It is also worth highlighting that this framework is also the basis of many regularization techniques (see Chapter 11) and variational approaches to fracture (Chapter 12).

Under the hypotheses of the infinitesimal strain theory and a quasi-static evolution and following [de Andrès et al., 1999; Andrieux et al., 2004; Mielke and Ortiz, 2008], the evolution of a mechanical system of standard generalized materials over a time step, from time t to time $t + \Delta\, t$, can be formally characterized by the following variational principle involving an incremental potential [Lorentz, 1999; Andrieux et al., 2004] :

$$\min_{\mathbf{u},\alpha} \quad \int_\Omega \int_t^{t+\Delta t} \left[\rho\dot{\Psi}(\boldsymbol{\epsilon}^{\mathrm{to}}(\mathbf{u})(s), \alpha(s)) + \phi\left(\dot{\alpha}(s)\right)\right] \mathrm{d}s\, \mathrm{d}V - \mathcal{P}_{\mathrm{ext}}(\mathbf{u}) \tag{10.1}$$

where $\rho\Psi$ is the free energy density which depends on a single (for simplicity here[1]) state variable α, ϕ is the dissipation pseudo-potential, $\mathbf{u}$ is the displacement field and $\mathcal{P}_{\mathrm{ext}}$ is the power of external forces.

After a backward-Euler time discretization and after removing constant terms from the global potential, one obtains the following time-discretized incremental variational principle:

$$\mathbf{u}(t+\Delta t),\ \alpha(t+\Delta t) = \underset{\mathbf{u},\alpha}{\operatorname{argmin}}\, \mathcal{L}(\mathbf{u}, \alpha) \tag{10.2}$$

where the incremental Lagrangian introduced in Chapter 2 is used:

$$\mathcal{L}(\mathbf{u}, \alpha) = \int_\Omega \left[\rho\Psi(\boldsymbol{\epsilon}^{\mathrm{to}}(\mathbf{u}), \alpha) + \Delta t \phi\left(\frac{\alpha - \alpha(t)}{\Delta t}\right)\right] \mathrm{d}V - \mathcal{W}_{\mathrm{ext}}(\mathbf{u}) \tag{10.3}$$

[1] The subsequent discussion can be generalized without any difficulty to more variables and of tensorial nature.

with $\mathcal{W}_{\text{ext}}$ denoting the work of external forces, and $\mathbf{u}(t)$ and $\alpha(t)$ stands for the known values of the displacement and internal state variable at the beginning of the time step.

Existence and uniqueness to the minimization problem (10.2) can be ensured if the incremental potential is coercive, convex and lower semi-continuous. A precise definition of those mathematical properties is out of the scope of the present text and the reader is referred to classical mathematical textbooks [Ekeland and Temam, 1974; Raviart, 1983]. It is sufficient to mention that they are not met in the context of brittle or ductile coupled fracture models and we only discuss here the consequences on several examples and give appropriate references for the interested reader.

10.2.2 A particular example

In order to highlight the consequences of dealing with softening behaviors, let us consider the simplest 1D isotropic damage behavior characterized by the following free energy :

$$\rho\Psi(\epsilon, d) = \frac{1}{2}(1-d)\,E\,\epsilon^2 \tag{10.4}$$

where E stands for the Young's modulus of the material, and $d \in [0:1]$ is a damage variable. This function is convex with respect to each variable ϵ and d taken separately [2], but not with respect to both as $\partial^2\Psi/\partial d\partial\epsilon < 0$ for $\epsilon > 0$. Hence the existence and uniqueness of the minimization problem (10.2) is not guaranteed, leading to some pathological behaviors. Following a suitable choice of the free energy, the stress - strain curve can be of the type shown on Fig. 10.1. The consequences of such behavior are detailed in the following.

[2] This point is crucial for the "alternate minimization scheme" detailed in Chapter 11.

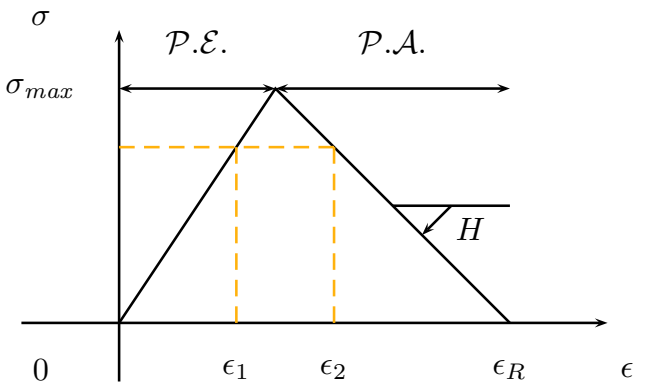

FIGURE 10.1: Prototypical softening stress-strain curve

Non-uniqueness

FIGURE 10.2: Uniaxial tensile test on a bar of length L.

Following [Forest and Lorentz, 2004], let us consider the uniaxial tensile test on a bar of length L made of a material following the behavior depicted on Figure 10.1 where a displacement U is imposed on the right part of the bar (Figure 10.2). The behavior is first elastic and the solution is unique with an homogeneous stress σ given by:

$$\sigma = E\,\epsilon \quad \text{with} \quad \epsilon = \frac{U}{L}.$$

The onset of damage is characterized by a stress peak σ_{max} and a strain σ_{max}/E. Even after this point, the stress σ is still homogeneous. According to Figure 10.1, a given stress level σ can then be reached by a strain ϵ_1 on the elastic part of the curve or by a stress ϵ_2 on the softening part of the curve. Let us now assume that the bar is split into two parts. In the first part, of length l_d, damage develops, leading the following solution:

$$\sigma = E\,\epsilon_1 = \sigma_{max} + H\left(\epsilon_2 - \frac{\sigma_{max}}{E}\right) \quad \text{and} \quad (L - l_d)\epsilon_1 + l_d\,\epsilon_2 = U.$$

This allows us to exhibit an infinite number of solutions as the length l_d is unspecified, which proves the non-uniqueness of the solutions.

However, as pointed out by Marigo [Marigo, 2000], only the solutions with

zero length, *i.e.* damage localized on points, correspond to stable minima of the Lagrangian (10.3). The solution is still not unique, as the localization of the damaging points can be chosen arbitrarily.

From a physical viewpoint, localization on specific points is related to the presence of random heterogeneities at the microscopic level that acts as preferential initiation sites. A preferential site then damages while the rest of the bar unloads elastically. From a numerical point of view, numerical instabilities can play the role of such heterogeneities.

Fracture without dissipation

The previous paragraph highlights another pathology of local damage models. The energy dissipated during the tensile test is given by:

$$S\, l_d \int_0^{\epsilon_R} \sigma\, \epsilon \, \mathrm{d}\, \epsilon \xrightarrow{l_d \to 0} 0 \tag{10.5}$$

where S is the section of the bar and ϵ_R is the strain where the material is fully damaged (see Figure 10.1). This energy thus depends on the length of the damaged region. Since the latter is null for stable solutions, such damage behavior predicts fracture with no energy dissipation, which is a physical nonsense and have a significant impact on numerical simulations, as discussed in Section 10.4.1.

Absence of solution

The uniaxial tensile test described in the previous paragraph can be changed to exhibit a trivial case where no solution exists. Consider an imposed force F rather than an imposed displacement. As the material cannot bear a stress greater than σ_{max}, no solution can be found if the imposed force is greater than $S\,\sigma_{max}$. Mathematically, the non-existence of a solution is related to the lack of coercivity of the Lagrangian (10.3).

This issue may be overcome by considering that the material cannot be fully damaged or, equivalently that a residual stiffness can be introduced, which can be done in numerical simulations [Lorentz, 2003] (see Section 10.3.3). For a damage model, one simple way of introducing a residual stiffness is to bound the damage variable to a value strictly smaller than 1 (1 corresponding in most models to a fully damaged material). Another general solution is to add a purely elastic contribution to the model with a Young's modulus much smaller than the one of the considered material. In both cases, one shall check that this residual stiffness does not impact the numerical results. This technique has also been used in [Francfort and Marigo, 1993] to perform an extensive study of the mathematical properties of a specific damage model.

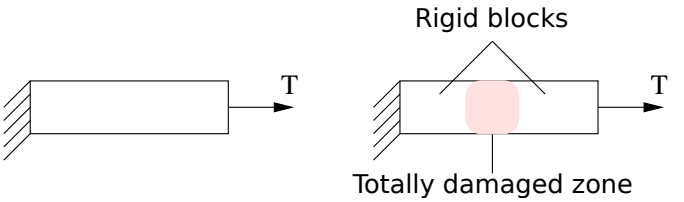

FIGURE 10.3: Bar in uniaxial tension due to an external traction force. Split of the bar in two rigid blocks.

Local or global minima

When the Lagrangian (10.3) is convex, a local minimum is also a global minimum [Céa, 1971; Demengel, 1999]. When the Lagrangian is not convex, the question of considering only global minima arises. Lorentz discusses this question by considering the previous uniaxial tensile test with an imposed force F. Due to the lack of coercivity of the Lagrangian, for any positive applied force, a global minimum corresponds to a split of the bar in two, where the right part is placed at infinity (see Figure 10.3). This is in contradiction with common sense, as one expects that the bar behaves elastically for any force below $S\,\sigma_{max}$, i.e. before damage initiation. This elastic behavior corresponds to a local minimum of the Lagrangian (10.3).

Non-existence of smooth solutions

Assuming that at least one solution to the minimization problem (10.2) exists, another issue is related to the regularity of this solution: shall we expect any property of continuity and differentiability ? The results presented in Section 10.2.2 shows that the answer is negative. In the case of an isotropic model with residual stiffness, Francfort et al. [Francfort and Marigo, 1993] established that, even with a regularized (convexified) version of the Lagrangian, natural candidates for solutions of the (global) minimization problem (10.2) are highly irregular: those candidates can be interpreted as multi-scale mixings of sound and damaged regions. Mathematically, this kind of solutions is associated with the lack of lower semi-continuity of the Lagrangian (10.3). This result has direct consequences on the numerical simulations, as discussed in Section 10.4.1.

Local damage models correspond to softening behaviors at the material scale. For such behaviors, existence and uniqueness of the solution of a mechanical problem can not be guaranteed from a theoretical point of view. In practice, it has been shown that various issues arise even in a very simple situation as the bar in tension considered here. These issues are also expected in more complex situations such as the ones solved numerically. Therefore, in

the following, the most widely used numerical method used to solve mechanical problems - finite element method FEM - is briefly presented, emphasizing the numerical parameters introduced by this method. Typical finite element simulations using a local damage model are then shown.

10.3 Brief overview of the finite element method

In this section, a brief overview of the numerical implementation of the finite element method is detailed, emphasizing the numerical aspects that may affect simulations of fracture using local damage models.

10.3.1 Principle of virtual power

Assuming that the minimization problem associated with the internal state variables $\alpha|_{t+\Delta t}$ for a given estimate of the displacement field $\mathbf{u}|_{t+\Delta t}$ is local, *i.e.*, that the internal state variables at the end of the time step can be expressed as implicit functions of the strain at the end of the time step, or equivalently, as implicit functions of the strain increment strain $\Delta\boldsymbol{\epsilon}^{\text{to}}$, the stress tensor $\boldsymbol{\sigma}$ can be considered as only a function of $\Delta\boldsymbol{\epsilon}^{\text{to}}$.

From a given state at a time t, a finite element solver determines the displacement field at the end of the time step $\mathbf{u}|_{t+\Delta t}$, using the principle of virtual power, which arises from the first variation of the Lagrangian (10.3). The principle of virtual power states that for any admissible virtual displacement $\mathbf{v}^\star$, $\mathbf{u}|_{t+\Delta t}$ must satisfy:

$$\int_\Omega \boldsymbol{\sigma}|_{t+\Delta t}\big(\Delta\boldsymbol{\epsilon}^{\text{to}}\big(\mathbf{u}|_{t+\Delta t}\big)\big) : \mathbf{Grad}(\mathbf{v}^\star) = \int_\Omega \mathbf{f}.\mathbf{v}^\star \,\mathrm{d}V + \int_{\partial\Omega_{\vec{T}}} \mathbf{t}.\mathbf{v}^\star \,\mathrm{d}S \quad (10.6)$$

where $\mathbf{f}$ and $\mathbf{t}$ correspond to imposed body force and surface force, respectively. For the sake of clarity, the notation $\boldsymbol{\sigma}|_{t+\Delta t}\big(\Delta\boldsymbol{\epsilon}^{\text{to}}\big(\mathbf{u}|_{t+\Delta t}\big)\big)$ will be simply replaced by $\boldsymbol{\sigma}$. Eq. 10.6 requires to compute $\boldsymbol{\sigma}$ from $\Delta\boldsymbol{\epsilon}^{\text{to}}$, which corresponds to the numerical integration of the constitutive equations.

10.3.2 Discretization

The finite element method is based on a discretization of the domain Ω in elements as depicted on Figure 10.4a. For some specific geometrical elements (triangles and quadrangles in $2D$, tetrahedra and hexahedra, pyramids and prisms in $3D$), it is possible to build the so-called Lagrange interpolation basis. Each basis function $\varphi^{(n)}$ is associated with a node n and has the following properties:

- $\varphi^{(n)}\left(\vec{X}_j\right) = \delta_{ij}$, where $\vec{X}_j$ denotes the coordinates of the j^{th} node.
- The support of $\varphi^{(n)}$ is limited to the elements containing the i^{th} node (Figure 10.4b). This guarantees the sparsity of the stiffness matrix (see Section 10.3.3).
- The restriction of $\varphi^{(n)}$ to an element is a polynomial.
- $\varphi^{(n)}$ is continuous at the boundary of the element.

As a consequence, the displacement is approximated by a piece-wise polynomial function. The approximation is linear if the order of all monomials of this approximation is equal to one, quadratic if the maximal order is two, etc...

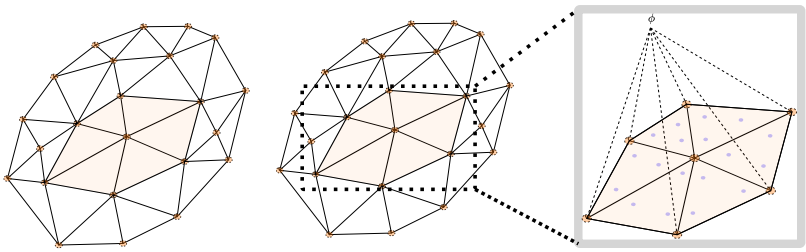

a) b)

FIGURE 10.4: a) Mesh of the domain Ω b) Basis functions and integration points

The approximation of the unknown displacement field in this finite space, still denoted $\mathbf{u}|_{t+\Delta t}$ for the sake of simplicity, and the virtual displacements can be decomposed as follows:

$$\mathbf{u}|_{t+\Delta t} = \sum_{n=1}^{N} \vec{\mathcal{U}}^{(n)\star}\, \varphi^{(n)} = \sum_{n=1}^{N} \begin{pmatrix} U_0^{(n)} \\ \vdots \\ U_d^{(n)} \end{pmatrix} \varphi^{(n)}$$

and

$$\mathbf{v}^{\star} = \sum_{n=1}^{N} \vec{\mathcal{V}}^{(n)\star}\, \varphi^{(n)} = \sum_{n=1}^{N} \begin{pmatrix} V_0^{(n)\star} \\ \vdots \\ V_d^{(n)\star} \end{pmatrix} \varphi^{(n)}, \tag{10.7}$$

where d is the space dimension. The coefficients $V_i^{(n)\star}$ defining a virtual displacement can be grouped in a vector $\vec{\mathbb{V}}^{\star}$ of $\mathbb{R}^{N\,d}$ such that:

$$\vec{\mathbb{V}}^{\star} = \begin{pmatrix} V_0^{(1)\star} & V_1^{(1)\star} & \dots & V_d^{(N)\star} \end{pmatrix}^{\mathrm{T}}$$

10.3.3 Numerical resolution

Local resolution

Evaluating Eq. 10.6 according to the discretization described in Eq. 10.7 requires to compute:

$$\vec{\mathcal{F}}_e^{(i)} = \int_{\Omega_e} \boldsymbol{\sigma} : \mathbf{Grad}\Big(\varphi^{(i)}\Big)\,\mathrm{d}\,V$$

where Ω_e is the domain of the considered element, where $\boldsymbol{\sigma}$ requires to perform the numerical integration of the constitutive equations.

Each finite element provide a quadrature rule which allows to evaluate this integral, knowing the value of the integrand at N_g specific points named integration points or Gauss points, as follows:

$$\vec{\mathcal{F}}_e^{(i)} \approx \sum_{g=1}^{N_g} w_g\, V_g\, \boldsymbol{\sigma}\Big(\vec{X}_g\Big) : \mathbf{Grad}\Big(\varphi^{(i)}\Big)\Big(\vec{X}_g\Big) \tag{10.8}$$

where w_g is the weight of the integration point, V_g is a specific volume (the jacobian of the transformation between the element and a reference element) and $\vec{X}_g$ is the position of the integration points. The choice of the quadrature rule, *i.e.*, the choice of the number of integration point N_g, their locations $\vec{X}_g$ and their weights w_g, determines the quadrature order, *i.e.*, the maximal order of the polynomials for which the Formula (10.8) is exact [Zienkiewicz, 1977; EDF, 2021].

Global resolution

The left hand side of the Principle of Virtual Power (10.6) defines a linear form on the virtual displacements $\mathbf{v}^\star$ defined by (Equation (10.7)), and by extension, a linear form on the space $\mathbb{R}^{N\,d}$ of the coefficients $\vec{\mathbb{V}}^\star$. A classical theorem on linear forms in finite dimension then states that there exists a unique vector $\vec{\mathbb{F}}_i$ of $\mathbb{R}^{N\,d}$ such that:

$$\int_\Omega \boldsymbol{\sigma} : \mathbf{Grad}(\vec{v}^\star) = \vec{\mathbb{F}}_i \cdot \vec{\mathbb{V}}^\star$$

The vector $\vec{\mathbb{F}}_i$ is called the inner forces. This vector is a function of the displacement $\mathbf{u}|_{t+\Delta\,t}$, or equivalently of the unknown coefficients $\vec{\mathbb{U}}$, through the stress tensor $\boldsymbol{\sigma}$ which is a function of the strain increment (which itself is a function of the displacement $\mathbf{u}|_{t+\Delta\,t}$).

Using the following expression of the gradient of virtual displacements,

$$\mathbf{Grad}(\vec{v}^\star) = \sum_{n=1}^{N} \vec{\mathcal{V}}^{(n)\,\star} \otimes \mathbf{Grad}\Big(\varphi^{(n)}\Big),$$

the components of the inner forces can be expressed as follows:

$$\int_\Omega \boldsymbol{\sigma} : \mathbf{Grad}(\vec{v}^\star)\,\mathrm{d}\,V = \sum_{n=1}^{N}\left(\int_\Omega \boldsymbol{\sigma} \cdot \mathbf{Grad}\left(\varphi^{(n)}\right)\mathrm{d}\,V\right) \cdot \vec{\mathcal{V}}^{(n)\star}$$
$$= \sum_{n=1}^{N} \vec{\mathcal{F}}_i^{(n)} \cdot \vec{\mathcal{V}}^{(n)\star}$$

or, equivalently:

$$\vec{\mathbb{F}}_i = \begin{pmatrix} F_{i,0}^{(1)} & F_{i,1}^{(1)} & \dots & F_{i,d}^{(N)} \end{pmatrix}^{\mathrm{T}}$$

The same reasoning allows to define the external forces $\vec{\mathbb{F}}_e$ from the right hand side of Equation (10.6). The inner and external forces thus satisfies:

$$\vec{\mathbb{F}}_i \cdot \vec{\mathbb{V}}^\star = \vec{\mathbb{F}}_e \cdot \vec{\mathbb{V}}^\star$$

This equality being true for every vector $\vec{\mathbb{V}}^\star$, another classical theorem states that the inner and external forces must be egal:

$$\vec{\mathbb{F}}_i = \vec{\mathbb{F}}_e \tag{10.9}$$

Equation (10.9) is the discrete expression of the mechanical equilibrium. In theory, Equation (10.9) allows to determine the coefficients $\vec{\mathbb{U}}$ of the unknown displacements $\mathbf{u}|_{t+\Delta t}$. In practice, as this equation is in general non linear, an iterative procedure must be used. This iterative procedure aims at determining the zero of the residual vector $\vec{\mathbb{R}}$:

$$\vec{\mathbb{R}}\left(\vec{\mathbb{U}}\right) = \vec{\mathbb{F}}_i\left(\vec{\mathbb{U}}\right) - \vec{\mathbb{F}}_e,$$

Most finite element solver relies on a more or less elaborate variant of the Newton-Raphson algorithm. Let $\vec{\mathbb{U}}^{(n)}$ be the current estimate of the solution, the next estimate is given by:

$$\vec{\mathbb{U}}^{(n+1)} = \vec{\mathbb{U}}^{(n)} + \delta\,\vec{\mathbb{U}}^{(n)} \quad \text{with} \quad \delta\,\vec{\mathbb{U}}^{(n)} = -\left.\frac{\partial \vec{\mathbb{R}}}{\partial \vec{\mathbb{U}}}^{-1}\right|_{\vec{\mathbb{U}}^{(n)}} \vec{\mathbb{R}}\left(\vec{\mathbb{U}}^{(n)}\right) \tag{10.10}$$

where

$$\mathbb{K} = \frac{\partial \vec{\mathbb{R}}}{\partial \vec{\mathbb{U}}} = \frac{\partial \vec{\mathbb{F}}_i}{\partial \vec{\mathbb{U}}}$$

denotes the stiffness matrix of the system. It can be shown that the computation of the stiffness matrix requires to compute the consistent tangent operator defined as the derivative $\dfrac{\partial \boldsymbol{\sigma}}{\partial \boldsymbol{\epsilon}^{\mathrm{to}}}$ [Feld-Payet et al., 2011]. This derivative can be computed during the behavior integration step.

The computation of the so-called Newton correction $\delta\,\vec{\mathbb{U}}^{(n)}$ requires the

resolution of a linear system (see Equation (10.10)). From a numerical point of view, sparsity of the stiffness matrix is then very desirable as specific algorithms exists for sparse matrix, both in terms of memory usage and numerical performances. Using the expression of the gradient of the displacement and the expression of the inner forces, it can be shown that the coefficient $\mathbb{K}(i,j)$ is null if the support of the basis functions $\varphi^{(i)}$ and $\varphi^{(j)}$ do not overlap.

It is worth mentioning that the standard Newton algorithm is not very robust and may fail to converge, in particular for non-convex problems as the ones encountered with local damage models. The convergence of the Newton algorithm is very sensitive to the choice of the initial estimate of the solution, which is generally either the displacement at the beginning of the time step or an extrapolation of the previous solutions. Unstable propagations in quasi-statics are thus particularly difficult to address as the evolution of the solution may be discontinuous in time [Monerie et al., 2001; Helfer, 2006]. A wide literature has been devoted to that matter, the arc-length method and other variation of the Riks algorithm being very popular solutions.

10.3.4 Synthesis of numerical parameters

This short overview of the numerical implementation of the finite element method allowed to highlight various numerical parameters involved in this method:

- **Mesh size and structure** ;
- **Order of the approximation** of the displacements, commonly linear or quadratic ;
- **Quadrature rule** for the numerical integration, commonly full (Eq. 10.8 is exact) or reduced ;

In addition, some approximations can be made regarding the computation of the term $\mathbf{Grad}\big(\varphi^{(n)}\big)$ in the computation of the inner and external forces.

The purpose of the next section is to present some numerical examples of the effect of these parameters on the results of finite element simulations using local damage models.

10.4 Numerical artifacts

The finite element method is expected to converge to the exact solution as the size of the elements decreases, under certain conditions on the quality of

the mesh and regularity of the exact solution. As detailed in Section 10.2.2, softening behaviors are not expected to lead to smooth solutions. This lack of regularity leads to various spurious numerical phenomena which are now detailed. As described by Section 10.2.2 and 10.2.2, softening leads to very irregular and strongly localized solutions of the continuous problem. In quasi-statics, this is linked to the loss of ellipticity of the boundary value problem. From a numerical point of view, after discretization of the problem thanks to the finite element formulation, this problem leads to the dependence of the results on the orientation and size of the finite element mesh, as illustrated in the next sections.

10.4.1 Dependence of the dissipated energy to the mesh size

Following the discussion of Section 10.2.2, in case of spurious localization, the dissipated energy is proportional to the element size (in the direction perpendicular to the band) and thus changes with the mesh size. In this section, some numerical examples are given to show this particular issue. The case of ductile fracture is considered as it allows exhibiting various numerical problems associated with such simulations. A Gurson-Tvergaard-Needleman model, presented in Chapter 9, is considered to describe the material behavior of the material. This model is still widely used, and relies on the following yield criterion:

$$\phi\left(\boldsymbol{\sigma}, f\right) = \left(\frac{\sigma_{\text{eq}}}{R(p)}\right)^2 + 2q_1 \cosh\left(\frac{3}{2} q_2 \frac{\sigma_m}{R(p)}\right) - 1 - \left(q_1 f\right)^2 \tag{10.11}$$

where $R(p)$ is the yield stress of the matrix material surrounding the voids. In this model, porosity f dictates the size of the yield surface and evolves under mechanical loading. Fig. 10.5 shows the typical behavior of this model regarding the evolution of both stress and porosity, for different constant stress triaxiality $T = \sigma_m/\sigma_{\text{eq}}$. In each case, a softening regime is observed after a critical applied strain where stress decreases to zero (Fig. 10.5a), representing material failure. This softening regime is induced by the increase of porosity as shown on Fig. 10.5b. Clearly, the mechanical behavior shown on Fig. 10.5 falls into the category represented in Fig. 10.1, and as discussed previously, some numerical issues are expected to arise by using such constitutive equations in finite element simulations. Two different problems can be highlighted. *For a given mesh size*, Fig. 10.6 shows the typical outputs of finite element simulations on an axisymmetric notched sample (Fig. 10.6a) and on a pre-cracked Compact Tension sample (Fig. 10.6b) for different type of finite elements. As recalled in the previous section, choosing a type of finite element means a discretization space - here linear (`4`) or quadratic (`8`) - a number of Gauss points - standard or reduced (`RI`) integration - and a mathematical relation relating displacement at nodes to strains at Gauss points - standard or BBAR method (`ICQ`). For notched sample, *i.e.*, rather smooth stress / strain gradients, the dependence to the finite element type is rather weak, at least for the onset of

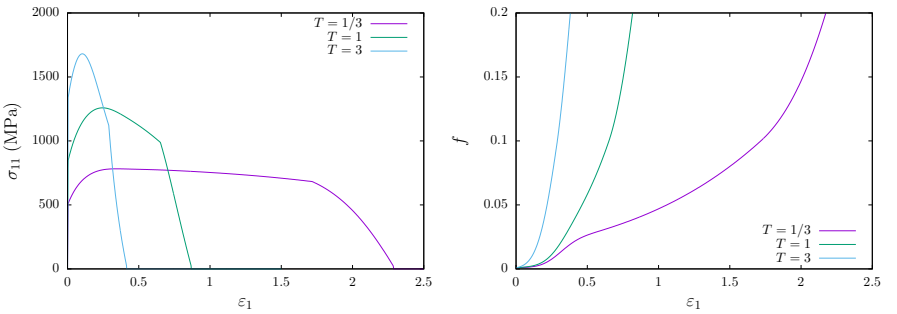

FIGURE 10.5: Typical outputs of the Gurson-Tvergaard-Needleman constitutive equations under axisymmetric loading conditions at constant stress triaxiality. Evolution of (a) stress and (b) porosity as a function of applied strain

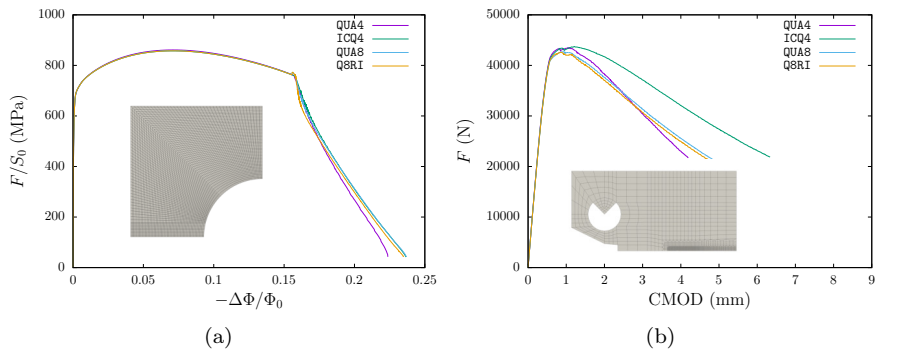

FIGURE 10.6: Typical outputs of finite element simulations on (a) axisymmetric notched sample and (b) 2D pre-cracked Compact Tension sample using Gurson-Tvergaard-Needleman (GTN) constitutive equations, for various finite elements types

failure. However, for cracked samples where strong stress / strain gradients arise at the crack tip, the choice of finite element leads to very different behaviors. The origin of this discrepancy can be traced back by looking at the local fields. Fig. 10.7 shows the values of the porosity at Gauss points for two different element types leading to differences on the load-opening curves. Two particular features can be observed. First, damage - here porosity increase - occurs at the scale of a single layer of elements (Fig. 10.7a). This observation is consistent with the general results given at the beginning of this chapter emphasizing that softening behaviors lead to localization at the smallest scale possible, here the height of the finite element. The second salient feature is that localization can in fact occurs at a scale smaller that the height of the finite element. Fig. 10.7b shows that, for that particular choice of finite element, localization occurs mainly in one layer of Gauss points. The differences

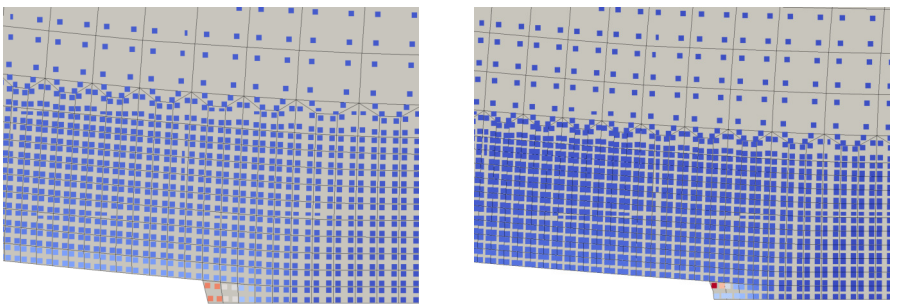

(a) (b)

FIGURE 10.7: Porosity fields at Gauss points for the finite element simulations of 2D pre-cracked Compact Tension sample, for (a) `ICQ4` and (b) `Q8RI` elements

observed in Fig. 10.7 provide a simple explanation of the differences reported in Fig. 10.6b as, broadly speaking, the energy required to propagate a crack as in Fig. 10.7a will be twice the one as for Fig. 10.7b. Besides the effect of the element type, but basically for the same reason, another problem is shown on Fig. 10.8 where the same simulations are performed *for a given element type* but this time for two different mesh size. In both cases, an effect of mesh size is observed, *i.e.*, there is no convergence of the finite element results with respect to mesh size. As for the case of the choice of the element type, the effect is rather weak, but still there, for situations involving smooth stress / strain gradients, but severe in the case of cracked samples. In the latter, a brittle behavior would emerge as mesh size is decreased to zero, which is unphysical.

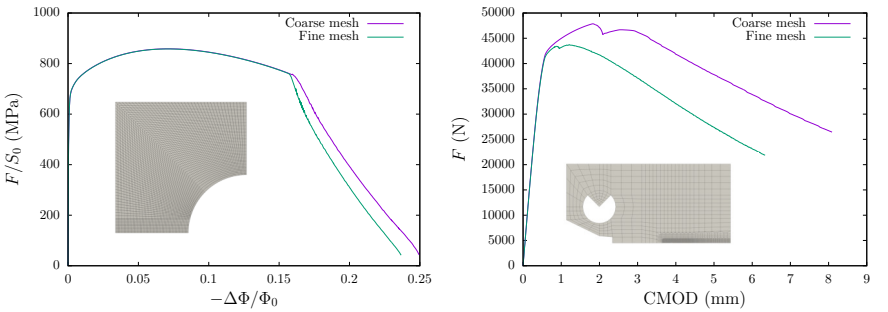

(a) (b)

FIGURE 10.8: Typical outputs of finite element simulations on (a) axisymmetric notched sample and (b) 2D pre-cracked Compact Tension sample using Gurson-Tvergaard-Needleman (GTN) constitutive equations, for different mesh size

These numerical examples have been obtained with the GTN model in the context of ductile fracture, but similar results could be shown for other models, either for brittle or ductile fracture, as soon as the constitutive equations involves a softening behavior. The key output is the pathological dependence to the mesh size and to the finite element type, which is severe for situations involving strong stress / strain gradients but moderate in other cases.

10.4.2 Dependence of the crack path to the mesh orientation

In the numerical examples given in the previous section, the effects of numerical parameters have been assessed on the macroscopic load - displacement curves. These parameters have also an effect on microscopic behavior such as crack path. Fig. 10.9 shows the output of a simulation of an axisymmetric specimen using the GTN model for a given mesh size and type but different mesh orientations. The global responses are similar for all the orientations. However, the total porosity for each mesh size at total failure shows a different crack path for each mesh orientation, which indicates mesh dependence. In both cases, the localization of the damage in a band of one element is noticeable: this corresponds to the most localised solution that can be represented by the finite element method.

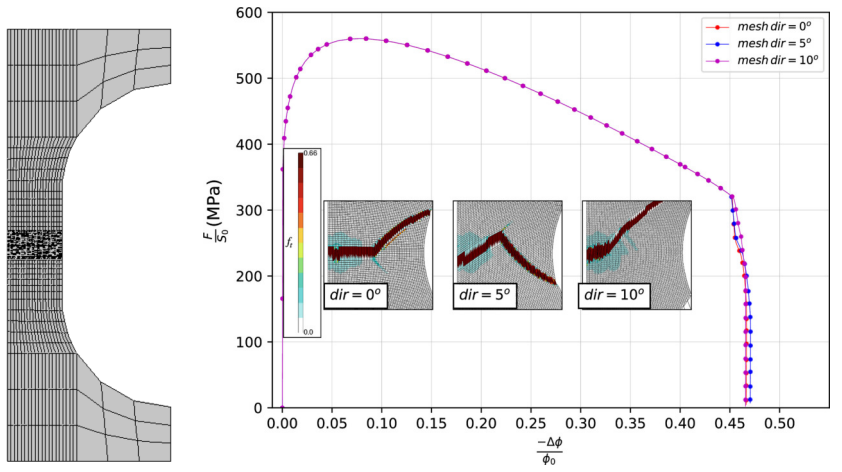

a) b)

FIGURE 10.9: Finite element simulations of an axisymmetric specimen under uniaxial loading for a given mesh size and type for different mesh orientation: (a) global mesh (b) load - displacement curves and crack paths (from [Tuhami et al., 2022]).

10.5 Good practices and ad-hoc solutions

The previous sections have shown that using local damage models / constitutive equations with a softening behavior leads theoretically to mathematical issues - non-uniqueness, no dissipation - and numerically to spurious mesh (size and type) dependencies in finite element simulations. Chapters 10 and 11 present advanced approaches to overcome the difficulties of local damage models, which are robust mathematically, physically and even numerically. However, such approaches are not always available in standard finite element solvers or are not compatible with all constitutive equations. Therefore, some good practices and ad-hoc solutions are listed below:

- **Be pragmatic**

  Depending on the problem considered, it may not be required to simulate the full crack path with a mesh-independent numerical simulations. Consider using a uncoupled fracture model that may be sufficient to predict crack initiation. Non-regularized finite element simulations may also be sufficient to predict crack initiation for situations involving weak stress / strain gradients.

- **Choose your element type carefully**

  Other problems than mesh dependency may affect finite element simulations using coupled fracture models. One particular example is related to the

large deformation involved in ductile fracture modelling, leading to volumetric locking. Here again, special finite elements have been developed to overcome this issue [Chen et al., 2020], but may not be available in standard finite element solver. Some standard finite elements behave however better than others (quadratic reduced integration, B-Bar).

- **Use mesh size as a material parameter**

Since previous examples have shown that damage localizes in a band of one (or half) element height, one may use a mesh such that the element width, denoted h, in the direction normal to the crack path is constant [Tanguy et al., 2005]. The energy dissipated is proportional to h, which allows to control the dissipated energy. This very simple strategy allows at least to compare simulations performed on different sample geometries and / or on different finite element solvers, for situations where the crack path is known. An obvious direct consequence of this strategy is that mesh convergence can not be studied.

- **Incorporate mesh size into the constitutive equations**

Another approach, proposed by Hillerborg et al. [1976], consists in incorporating the element size h in the constitutive equations such that the dissipated energy given by Equation (10.5) is independent of h. This generally results in a non-intuitive constitutive equation where the softening part of the traction curve depends on the mesh size. This technique is however still widely used for concrete in civil engineering [Fichant, 1996; Gangnant, 2016; Draup et al., 2019].

- **Consider using Cohesive Zone Model**

When the crack path is known, Cohesive Zone Models (CZM) may be a good alternative to simulate fracture, either for brittle or ductile fracture [Yoon and Allen, 1999; Monerie, 2000]. Across a given interface, cohesive zone models relate the traction forces acting on the interface to the displacement jump at the interface. The normal component of the displacement jump can be seen as the crack opening displacement. Cohesive zone models can be seen as the limit of standard constitutive models in a band of fixed size, see [Suquet et al., 1994] for details. CZM corresponds to 2D elements in 3D FEM [de Borst, 2003; Feyel, 2004]. Those elements are inserted in the mesh along the crack path when the latter is known. When the crack path is unknown, cohesive elements can be introduced at the boundaries of all finite elements [Xu and Needleman, 1995]. The reader is referred to the paper of Tijssens et al. [2000] for a critical discussion of this strategy. The fact that displacement jumps at the element boundaries is natural in Discontinuous Galerkin Methods has been exploited by Hansbo and Salomonsson [2015] to introduce cohesive zone models.

10.6 Conclusion

In this chapter, theoretical and numerical issues have been presented related to the use of local damage models, or more generally constitutive equations involving a softening behavior, for structural calculations. Existence and uniqueness of smooth solutions can not be guaranteed theoretically, which manifests itself by mesh dependence of macroscopic load - displacement curves and microscopic crack paths in finite element simulations. Some ad-hoc solutions have been proposed to limit the consequences of these issues. However, recovering fully mesh independent results requires dedicated theoretical models and numerical tools that are described in the next chapters.

Bibliography

[Andrieu et al. 2012] Andrieu, A. ; Pineau, A. ; Besson, J. ; Ryckelynck, D. ; Bouaziz, O.: Beremin model: Methodology and application to the prediction of the Euro toughness data set. In: *Engineering Fracture Mechanics* 95 (2012), p. 102–117

[Andrieux et al. 2004] Andrieux, S. ; Badel, P. ; Cano, V. ; Godard, V. ; Lorentz, É.: Analyse de modèles non locaux d'endommagement. In: *mécanismes et mécanique des matériaux et structures à longueur interne : comportement et effets d'échelles* Colloque National MECAMAT, 2004, p. 25–32

[de Andrès et al. 1999] Andrès, A. de ; Pérez, J.L. ; Ortiz, M.: Elastoplastic finite element analysis of three dimensional fatique crack growth in aluminium shafts subjected to axial loading. In: *International Journal of Solids and Structures* 36 (1999), p. 2231–2258

[Beremin 1981] Beremin, F. M.: Cavity formation from inclusions in ductile fracture of A508 steel. In: *Metallurgical Transactions A* 12A (1981), p. 723–731

[Chen et al. 2020] Chen, Youbin ; Lorentz, Eric ; Besson, Jacques: Crack initiation and propagation in small-scale yielding using a nonlocal GTN model. In: *International Journal of Plasticity* 130 (2020), p. 102701

[Céa 1971] Céa, J.: *Optimisation : théorie et algorithme*. Dunod, 1971 (Méthodes mathématiques de l'informatique)

[de Borst 2003] de Borst, R.: *Numerical aspects of cohesive-zone models*. 2003. – Engineering Fracture Mechanics

[Demengel 1999] Demengel, F.: *Introduction aux équations aux dérivées partielles elliptiques : fonctions à dérivées mesures et applications.* Diderot Multimedia-EDL, 1999

[Draup et al. 2019] Draup, Jefry ; Gangnant, Alexandre ; Colette, Gaëtan ; Doughty, Graham ; Guo, Jiansong ; Helfer, Thomas ; Torelli, Giacomo ; Mandal, Parthasarathi: Development of a Novel Damage Model for Concrete Subjected to High Temperature and Constraint. In: *Proceeding of SMIRT 25*, 2019

[EDF 2021] EDF: *Fonctions de forme et points d'intégration des éléments finis.* Version: 2021. `http://www.code-aster.org`

[Ekeland and Temam 1974] Ekeland, Ivar ; Temam, Roger: *Analyse convexe et problèmes variationnels.* Dunod, 1974. – ISBN 978–2–04–007368–8. – Google-Books-ID: GqtxQgAACAAJ

[Feld-Payet et al. 2011] Feld-Payet, Sylvia ; Besson, Jacques ; Feyel, Frédéric: Finite element analysis of damage in ductile structures using a nonlocal model combined with a three-field formulation. In: *International Journal of Damage Mechanics* 20 (2011), Nr. 5, p. 655–680

[Feyel 2004] Feyel, F.: Cohesive Zone Models. In: Besson, J. (Hrsg.): *Local approach to fracture*, École des Mines de Paris - les presses, 2004, p. 265–277

[Fichant 1996] Fichant, Stéphanie: *Endommagement et anisotropie induite du béton de structures : modélisations approchées.* 1996

[Forest and Lorentz 2004] Forest, S. ; Lorentz, É.: Localization phenomena and regularization methods. In: presses, École des Mines de Paris les (Hrsg.): *Local Approach to fracture*, 2004, p. 311–371

[Francfort and Marigo 1993] Francfort, G.A. ; Marigo, J.-J.: Stable damage evolution in a brittle continuous medium. In: *Eur. J. Mech. A/Solids* 12 (1993), Nr. 2, p. 149–189

[Gangnant 2016] Gangnant, Alexandre: *Étude de la rupture quasi-fragile d'un béton à l'échelle mésoscopique : aspects expérimentaux et modélisation.* 2016

[Hansbo and Salomonsson 2015] Hansbo, Peter ; Salomonsson, Kent: A discontinuous Galerkin method for cohesive zone modelling. In: *Finite Elements in Analysis and Design* 102-103 (2015), p. 1–6. – 10.1016/j.finel.2015.04.008

[Helfer 2006] Helfer, Thomas: *Etude de l'impact de la fissuration des combustibles nucléaires oxyde sur le comportement normal et incidentel des crayons combustible.* 2006

[Hillerborg et al. 1976] Hillerborg, A. ; Modéer, M. ; Perterson, P-E: Analysis of crack formation and crack growth in concrete by means of fracture mechanics and finite elements. In: *Cement and Concrete Research* 6 (1976), p. 779–782

[Keralavarma et al. 2020] Keralavarma, S.M. ; Reddi, D. ; Benzerga, A.A.: Ductile failure as a constitutive instability in porous plastic solids. In: *Journal of the Mechanics and Physics of Solids* 139 (2020), p. 103917

[Lorentz 1999] Lorentz, É.: *Lois de comportement à gradients de variables internes : constructions, formulation variationnelle et mise en œuvre numérique*, LMT-Cachan, Université Paris 6, Diss., 1999

[Lorentz 2003] Lorentz, É.: Loi d'endommagement d'un matériau élastique fragile / EDF-R&D/AMA. 2003 (R5.03.18-A). – Manuel de référence Code_Aster. – `http://www.code-aster.org`www.code-aster.org

[Marigo 2000] Marigo, J-J: L'endommagement et la rupture : hier, aujourd'hui et demain / IPSI : Comportements non linéaires des matériaux. 2000. – Technical repport

[Marini et al. 1985] Marini, B. ; Mudry, F. ; Pineau, A.: Ductile rupture of A508 steel under nonradial loading. In: *Engineering Fracture Mechanics* 22 (1985), Nr. 3, p. 375–386

[Mielke and Ortiz 2008] Mielke, Alexander ; Ortiz, Michael: A class of minimum principles for characterizing the trajectories and the relaxation of dissipative systems. In: *ESAIM: Control, Optimisation and Calculus of Variations* 14 (2008), Nr. 3, p. 494–516

[Monerie et al. 2001] Monerie, Y. ; Feyel, F. ; Chaboche, J.L.: Interface debonding models : a viscous regularization with a limited rate dependency. In: *International Journal of Solids and Structures* 38 (2001), p. pp. 3127–3160

[Monerie 2000] Monerie, Yann: *Fissuration des matériaux composites : rôle de l'interface fibre/matrice*. 2000

[Raviart 1983] Raviart, Pierre-Arnaud: *Introduction à l'analyse numérique des équations aux dérivées partielles*. Paris New York [etc : Masson, 1983 (Collection Mathématiques appliquées pour la maîtrise). – ISBN 978–2–225–75670–2

[Suquet et al. 1994] Suquet, P. ; Michel, J.-C. ; Thébaud, F.: Une modélisation du rôle des interfaces dans le comportement des composites à matrice métallique. In: *Revue européenne des éléments finis* 3 (1994), Nr. n 4, p. pp. 573–595

[Tanguy et al. 2005] Tanguy, B. ; Besson, J. ; Piques, R. ; Pineau, A.: Ductile to brittle transition of an A508 steel characterized by Charpy impact test: Part II: modeling of the Charpy transition curve. In: *Engineering Fracture Mechanics* 72 (2005), Nr. 3, p. 413–434

[Tijssens et al. 2000] Tijssens, M. G. A. ; Sluys, B. L. J. ; Giessen, E. van d.: Numerical simulation of quasi-brittle fracture using damaging cohesive surfaces. In: *European Journal of Mechanics - A/Solids* 19 (2000), Nr. 5, p. 761–779

[Tuhami et al. 2022] Tuhami, A El O. ; Feld-Payet, Sylvia ; Quilici, Stéphane ; Osipov, Nikolay ; Besson, Jacques: A two characteristic length nonlocal GTN model: Application to cup–cone and slant fracture. In: *Mechanics of Materials* 171 (2022), p. 104350

[Xu and Needleman 1995] Xu, X.-P. ; Needleman, A.: Numerical simulations of dynamic interfacial crack growth allowing for crack growth away from the bond line. In: *International Journal of Fracture* 74 (1995), p. 253–275

[Yoon and Allen 1999] Yoon, C. ; Allen, D. H.: *Damage dependent behavior and energy release rate for a cohesive zone in a thermoelastic solid*. 1999

[Zienkiewicz 1977] Zienkiewicz, O.C.: *The finite element method*. McGraw-Hill, 1977. – ISBN 978–0–07–084072–0

11

Overview of some nonlocal methods for regularization

Jérémy Bleyer

Ecole des Ponts ParisTech, Laboratoire Navier

Sylvia Feld-Payet

DMAS, ONERA, Université Paris Saclay, F-92322 Châtillon, France

This chapter provides a general overview of several methods which can be used to regularize problems exhibiting localization issues. All of them are characterized as being *nonlocal* in the sense that they introduce, in one way or another, a typical internal length scale which relates the state of a variable at one point with others in the neighborhood (i.e the local state principle is no longer valid). The different methods are classified depending on how such nonlocality is introduced, either by averaging, higher gradients or additional degrees of freedom.

11.1 Introduction

Apart from the pragmatic solutions discussed in chapter 10 to solve the problem of mesh dependence, it is also possible to enrich the description of the continuous medium, i.e. to introduce additional pieces of information on the internal structure of the material. This is justified, from the physical point of view, by the fact that a material point is actually associated with a relevant substructure (e.g. grains, holes,...) and the influence of the neighboring points should be taken into account during localization. This means that the local assumption of the generalized media is no longer valid for localization processes. This enrichment is often used to model size effects through the introduction of an additional internal length scale. The fact that a classical Cauchy continuum description fails to reproduce any size effect shares some strong links with the fact that softening material behaviors lead to unlimited localization. As a result, enriched continua, able to model scale effects, have also been used for the purpose of limiting the localization process when the latter is competing with the material internal length scale.

micromorphic models	gradient models	regularized models
$\rho\Psi(\boldsymbol{\epsilon}^{\mathrm{to}},\alpha)+\frac{1}{2}A\|\nabla\boldsymbol{\chi}\|^2$ $+\frac{1}{2}H_\chi\|\boldsymbol{\epsilon}^{\mathbf{to}}-\boldsymbol{\chi}\|^2$	$\rho\Psi(\boldsymbol{\epsilon}^{\mathrm{to}},\alpha)+\frac{1}{2}A\|\nabla\boldsymbol{\epsilon}^{\mathbf{to}}\|^2$	$\Psi(\boldsymbol{\epsilon}^{\mathrm{to}}_{nl},\alpha)$
	or	or
$\rho\Psi(\boldsymbol{\epsilon}^{\mathrm{to}},\alpha)+\frac{1}{2}A\|\nabla\alpha_\chi\|^2$ $+\frac{1}{2}H_\chi(\alpha-\alpha_\chi)^2$	$\rho\Psi(\boldsymbol{\epsilon}^{\mathrm{to}},\alpha)+\frac{1}{2}A\|\nabla\alpha\|^2$	$\Psi(\boldsymbol{\epsilon}^{\mathrm{to}},\alpha_{nl})$

TABLE 11.1: Enrichment principle of the most commonly used regularization methods (inspired from [Lorentz, 2019]) where α designates a damage related variable.

Enrichment of the classical continuum description can be done in various ways, notably by adding:

- regularized variables using integral or gradient-based averaging;
- higher-order gradients;
- additional kinematic degrees of freedom, e.g. with the micromorphic models.

In the following, we will give a brief review of these different methods (summarized in table 11.1), while focusing on their use as regularization strategies. In particular, local balance equations or evolution equations of state variables might be modified: this requires to modify some parts of the standard numerical solvers. Moreover, the identification of material parameters is also consequently more or less impacted by the regularization strategy. The quest for a proper material identification or for a physical microscopic origin of such additional parameters still remains a difficult challenge as of today and will not be discussed in the following. A general overview can also be found in other works, such as [Jirásek, 2008; de Borst et al., 1993; Besson et al., 2023] and their references. In particular, we suggest the work of Lorentz and Andrieux [2003] for a thorough attempt at classifying and investigating the properties and/or deficiencies of various regularization techniques.

11.2 Independently defined nonlocal variables

The first class of approaches consists in defining smoothed nonlocal mechanical fields from their local counterpart: these new nonlocal fields do not only depend on the value of their local counterpart at the considered material point, but also on their value in a certain region around this point, thus introducing the notion of *characteristic length*. Introduction of these nonlocal variables impacts the constitutive equations but not the kinematic relations or the classical equilibrium equations. Despite this attractive feature, there is still a choice to be made regarding where to replace a local variable by its

nonlocal counterpart in the constitutive equations. For a detailed discussion on this topic, we refer the reader to [Forest and Lorentz, 2004].

11.2.1 Integral models

The most intuitive manner to introduce a smoothed variable is to use a spatial average of the local variable. The use of the concept of non-local mean was introduced in the 1960s with the work of Eringen [1966c], then Kröner [1967], Kunin [1968] and Edelen [1969]; Edelen et al. [1971]; Eringen and Endelen [1972]. These works aimed at a better description of the phenomena which take place in crystals at a scale close to the one of the inter-atomic forces. The concept of non-local averaging was latter used as a localization limiter in the 1980s by Bažant et al. [1984] and Pijaudier-Cabot and Bažant [1987] in the framework of damageable elastic behavior. A synthesis of non-local approaches for plasticity and damage was proposed by Bažant and Jirásek [2002], which was completed by Jirásek and Rolshoven [2003] in the framework of plasticity.

The non-local integral approach consists, schematically, in defining the nonlocal variable at a point $\vec{x}$ as the weighted average of the local quantity of interest χ over a restricted volume Ω surrounding the point under consideration, i.e.:

$$\chi_{nl}(\vec{x}) = \frac{1}{\int_\Omega \beta(\vec{x},\vec{\xi})d\vec{\xi}} \int_\Omega \beta(\vec{x},\vec{\xi})\chi(\vec{\xi})d\vec{\xi} \tag{11.1}$$

where β is a given non-local weight function (which can be a Gaussian for example). In this case, the characteristic length scale is related to the width of the Gaussian profile.

This approach can be, in principle, applicable to any type of model. However, it raises some difficulties: e.g. choosing a suitable weight in the neighborhood of a boundary or a material interface, designing specific algorithms to build the connectivity table of integration points where χ is defined or to compute the non-local integral and its gradients [Baaser and Tvergaard, 2003].

11.2.2 Models using the gradient of an internal variable

The models using the gradient of an internal variable are considered as the differential counterpart of the integral methods. These models can be divided into two categories: explicit gradient models and implicit gradient models.

11.2.2.1 Explicit gradient models

Following the work of Aifantis on the description of the dynamics of dislocations at a microscopic scale, models using the gradient of the local variable or the thermodynamic forces are developed, notably by Zbib and Aifantis [1988]; Mühlhaus and Aifantis [1991]; de Borst and Mülhaus [1991, 1992]; Pamin [1994] and de Borst and Pamin [1996].

The principle of these models is to define explicitly the additional nonlocal

variable as a function of the local variable and its derivatives of order n:

$$\chi_{nl}(\vec{x}) = f\left(\chi(\vec{x}), \nabla^n \chi(\vec{x})\right) \tag{11.2}$$

This type of relation can be obtained by using a Taylor series expansion of the local variable χ and substituting this expansion into equation (11.1) to evaluate the integrals [Engelen et al., 2003]. Let us underline that the gradient dependence makes the stress response at a material point depend on the behavior in an infinitesimal neighborhood; the explicit gradient approximation is thus only weakly nonlocal.

Depending on the choice of the order of approximation in equation (11.2), different formulations can be considered. For example, to model ductile failure, Engelen et al. [2003] propose to disregard terms of order four and higher, leading to:

$$\chi_{nl}(\vec{x}) = \chi(\vec{x}) + \ell^2 \Delta\chi(\vec{x}) \tag{11.3}$$

with ℓ the characteristic (or internal) length introduced in the regularized model and Δ the Laplacian operator. In the case of an elastic-plastic behavior, these authors have proposed to consider, for χ, the equivalent strain measure κ and to add the Laplacian of the considered equivalent strain measure to the yield function F of the classical plasticity theory:

$$F_{nl}(\boldsymbol{\sigma}, \kappa, \Delta\kappa) = F(\boldsymbol{\sigma}, \kappa) + g\left(\kappa, \ell\right) \Delta\kappa \tag{11.4}$$

where the variable g governs the gradient influence and is a function of the characteristic length scale ℓ (e.g. $g = -h\,\ell^2$ where $h < 0$ is the softening modulus). In this study, the authors underline the drawbacks associated with the use of an explicit model, such as the impossibility to obtain a zero stress state at failure, numerical instabilities and the necessity to have rather small loading increments.

11.2.2.2 Implicit gradient models

The implicit gradient models also involve higher-order gradients, but these gradients are not directly inserted in the constitutive equations. This time, the non-local variable χ_{nl} is *implicitly* defined as the solution of a Helmholtz-type differential equation involving the local variable χ:

$$\chi_{nl} - \ell^2 \Delta\chi_{nl} = \chi \quad \text{in} \quad \Omega \tag{11.5}$$

where the Laplacian operator now acts on the non-local variable contrary to (11.3).

To uniquely define the non-local variable, the PDE (11.5) must be completed with an additional boundary condition. Since it is desirable to get $\chi_{nl} = \chi$ when χ is a constant, the following Neumann condition is generally adopted:

$$\vec{n} \cdot \mathbf{grad}(\chi_{nl}) = 0 \tag{11.6}$$

It must be noted that such implicit gradient models are equivalent to the integral ones when choosing the Green function associated with the PDE as the non-local weight function (cf [Peerlings, 1999] and [Engelen et al., 2003]).

The implicit gradient models were first developed in the context of damage with Peerlings et al. [1996], who proposed a brittle elastic model. Then Engelen et al. [2003] developed this approach for elasto-plasticity based on ductile damage in small deformations. In particular, the authors showed that, for the chosen constitutive behavior, the implicit version of the gradient model avoids a number of numerical difficulties associated with the use of the explicit version. More recently, an implicit gradient method has been used:

- in quasi-statics, within the small strain framework, to regularize a phenomenological damage model [Feld-Payet et al., 2011] with mixed nonlocal elements enabling to deal with both spurious localization and volumetric locking (see figure 11.1)
- in quasi-statics, within the large strain framework, to regularize a Gurson type damage model with two internal lengths associated to void growth and nucleation [Tuhami et al., 2022] (see figure 11.2) and simulate complex crack propagation such as cup-cone failure [Tuhami et al., 2023].
- in dynamics to regularize a Gurson type damage model and reproduce experimental results obtain on a DP450 steel [Davaze et al., 2021].
- to regularize an incremental fatigue damage model that aimed at describing fatigue crack propagation in a Ni-based superalloy [Voreux, 2022].

This method is thus very versatile but cannot be as easily applied on bounded local variables e.g. damage. Indeed, in this case, one can observe under-shoot of the nonlocal variable with respect to the upper-bound (e.g. $d = 1$) which cannot be reached.

11.3 Higher-order gradient models

Regularization strategies relying on higher-order gradients can in fact be classified into two different groups depending on which type of variable gradients are taken:

- *strain-gradient models*
- *gradient of internal variable models*

Strain gradient models refer to generalized continua where the strain gradient, or the second displacement gradient, is considered as an additional state variable. Such models result in the introduction of higher-order stresses and generalized equilibrium equations.

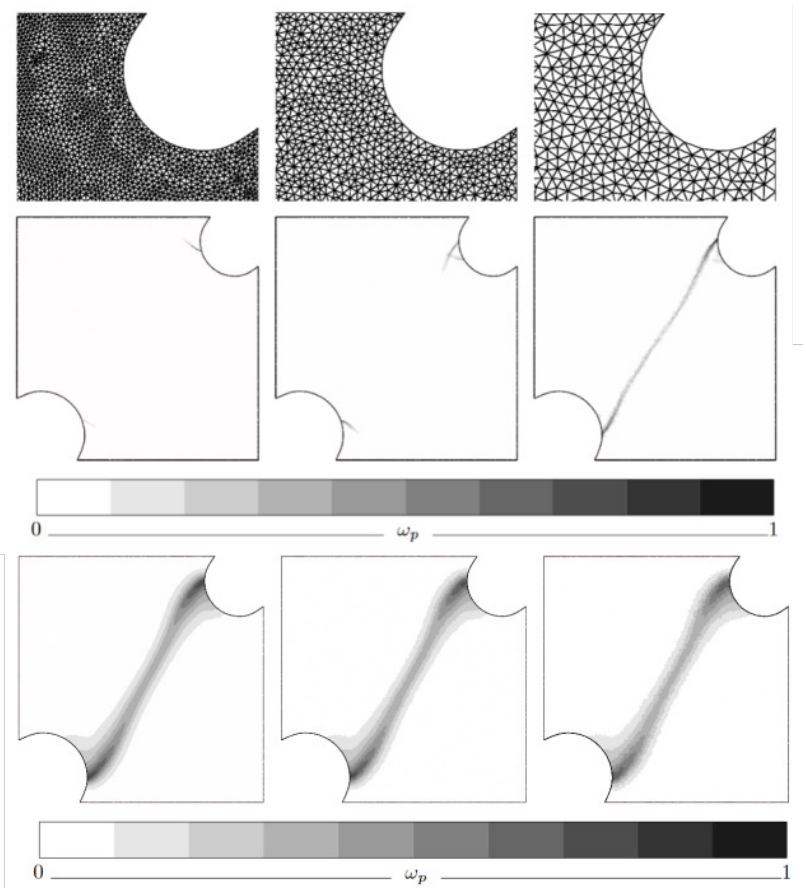

FIGURE 11.1: Damage maps for a tensile test on a double notched specimen. Top: zoom on the 3 considered meshes. Middle: maps obtained with standard finite elements [Feld-Payet, 2010]; the crack path is influenced by the finite element mesh. Bottom: maps obtained with mixed non local elements (from [Feld-Payet et al., 2011]); the crack path does not depend on the mesh size.

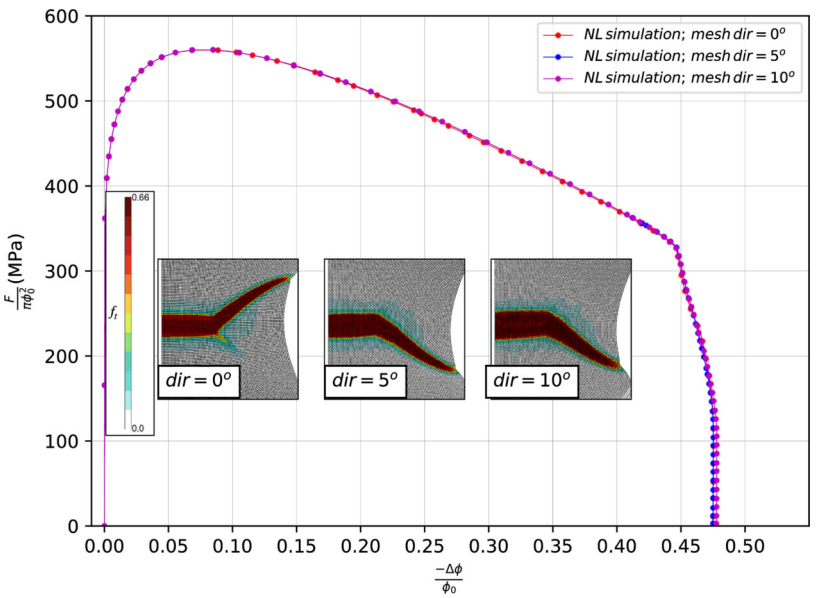

FIGURE 11.2: Same test on an axisymmetric specimen as figure 10.9, but with a regularized formulation based on the implicit gradient method with two internal lengths (from [Tuhami et al., 2022]). The crack path does not depend on the mesh orientation.

Internal variable gradients, on the other hand, lead to additional dissipative thermodynamic forces, which only affect evolution equations for the internal variables but not equilibrium equations. Consequently, the latter group modifies only the constitutive description, while the kinematic and equilibrium equations remain standard. In the following, we make the distinction with variational gradient models for which gradients of internal variables enrich the free-energy potential and/or the dissipation potential. As a consequence, the modified evolution equations are obtained as a direct consequence of the associated variational principle rather than being postulated beforehand.

11.3.1 Strain-gradient models

Some enriched continuum formulations keep the displacement field as the only independent kinematic field and improve the resolution by incorporating deformation gradients (i.e., higher-order spatial derivatives of displacements) into the constitutive equations. These theories were put forward by the works of Aero and Kuvshinskii [1960]; Grioli [1960]; Rajagopal [1960] and Truesdell and Toupin [1960] that considered only the components corresponding to the gradients of rotations. Subsequently, the gradient theory was extended to include the effects of expansion gradients (*stretch gradients* [Toupin, 1962]), second order gradient (*second strain gradient* [Mindlin, 1965]) and all order gradients [Green and Rivlin, 1964b]. This theory was then used in plasticity and led to the emergence of the so-called mechanism-based strain gradient plasticity theories [Gao et al., 1999; Huang et al., 2000; Shi et al., 2000].

Strain-gradient models consider as a state variable the strain gradient $\mathbf{grad}(\boldsymbol{\epsilon}^{\mathrm{to}}) = \mathbf{grad}(\nabla^{\mathrm{s}}\vec{u})$ in addition to the strain $\boldsymbol{\varepsilon} = \nabla^{\mathrm{s}}\vec{u}$. While the latter is associated with the Cauchy stress $\boldsymbol{\sigma}$, the former is associated with the higher-order stress $\boldsymbol{\Sigma}$ which satisfy the balance equation:

$$\vec{\mathrm{div}}\Big(\boldsymbol{\sigma} - \vec{\mathrm{div}}(\boldsymbol{\Sigma})\Big) = 0 \tag{11.7}$$

in the absence of body forces. Regarding the constitutive behavior, one generally assumes an uncoupled behavior between classical and higher-order stresses/strains and a quadratic elastic model for the higher-order part. In this context, the ratio between higher-order and classical elastic moduli defines a characteristic length scale. As stated before, the identification of higher-order moduli or their derivation from micromechanical considerations is still an important challenge at this day. Moreover, such models yield higher-order boundary conditions lacking simple physical meaning. Besides, the elastic response of these models differs from that of the classical models if the deformations are not uniform. Finally, such models require higher regularity conditions for the displacement field that standard finite-element discretizations fail to guarantee, which makes their use more difficult in practice.

Simplified versions can then be obtained by considering only specific parts

of the strain gradient such as the volume dilation $\varepsilon_V = \mathrm{tr}(\boldsymbol{\varepsilon})$, see [Fernandes et al., 2008].

Applications of strain-gradient regularization can be found in [Chambon et al., 2001] for geomaterials or in [Jouan et al., 2014] for concrete. However, Le et al. [2018] showed by studying 1D solutions that strain-gradient models cannot properly account for damage localization as they fail in reproducing the energetic equivalence of brittle fracture (mesh-independent finite and non-vanishing energy dissipation to produce a crack).

11.3.2 Variational models with gradients of internal variables

Following a similar idea as explicit and implicit gradient models, various works have proposed to limit the occurrence of large gradients of internal state variables by considering additional penalization terms to the total energy. A typical example of such kind of regularization is a quadratic expression of the gradient, such as $\frac{1}{2}A\|\nabla\alpha\|^2$, that can also be found in many *diffuse interface models* of various branches of physics, e.g. Allen-Cahn and Cahn-Hilliard models for phase separation, Ginzburg-Landau theory of supraconductors, etc.

Maugin [1990]; Frémond and Nedjar [1993, 1996] have introduced such ideas and extended the classical thermodynamic framework of internal state variables to such a setting. Doing so, it becomes possible to derive the corresponding state and evolution equations which now involve additional non-local terms. It is important to stress that such non-local constitutive equations are deduced from variational arguments as opposed to explicit/implicit gradient models in which they are directly postulated, see also [Lorentz and Andrieux, 1999; Lorentz, 1999, 2003; Lorentz and Benallal, 2005]. Finally, a more thorough analysis of such gradient damage models and their link with a regularized formulation of brittle fracture is provided in Chapter 12.

As discussed by Nguyen [2015] for instance, gradient models of standard generalized materials also benefit from the underlying variational structure obtained from the corresponding energy and dissipation potentials accounting for the additional gradient contributions. Let us thus assume that the free energy potential $\Psi(\boldsymbol{\epsilon}^{\mathrm{to}}, \alpha, \boldsymbol{g})$ is a function of the strain, an internal state variable α and its gradient $\boldsymbol{g} = \mathbf{grad}(\alpha)$. Similarly, we assume that the pseudo-dissipation potential $\phi(\dot{\alpha}, \dot{\boldsymbol{g}})$ is a function of the state variable rate $\dot{\alpha}$ and its gradient $\dot{\boldsymbol{g}}$. We now consider that the same incremental energy minimization applies in the presence of such gradient terms, that is the evolution equations at time $t + \Delta t$ from a state at time t are obtained by solving the following time-discretized variational principle:

$$\begin{aligned} \min_{\vec{u},\alpha,\boldsymbol{g}} \quad & \int_\Omega \left[\rho\Psi(\boldsymbol{\epsilon}^{\mathrm{to}}, \alpha, \boldsymbol{g}) + \Delta t \phi \left(\frac{\alpha - \alpha(t)}{\Delta t}, \frac{\boldsymbol{g} - \boldsymbol{g}(t)}{\Delta t} \right) \right] \mathrm{d}V - \mathcal{W}_{\mathrm{ext}}(u) \\ \text{s.t.} \quad & \boldsymbol{g} = \mathbf{grad}(\alpha) \end{aligned} \tag{11.8}$$

where $\mathcal{W}_{\text{ext}}$ denotes the work of external loadings. Note that we do not consider any body or surface forces associated with the state variable α or its gradient.

First, the optimality conditions with respect to the displacement field result in the standard balance of momentum for the stress field $\boldsymbol{\sigma}$. In the absence of any dependence on $\boldsymbol{g}$, the optimality conditions with respect to α result in the definition of the associated thermodynamic force and the corresponding Biot equation as follows:

$$0 = Y_{\text{nd}} + Y_{\text{d}} \tag{11.9}$$

$$0 = \frac{\partial \rho\Psi}{\partial \alpha} + \frac{\partial \phi}{\partial \dot{\alpha}} \tag{11.10}$$

where the partial derivative should be extended to the notion of sub-differentials in the non-smooth case.

In the presence of the gradient term, we can introduce the quantity $\boldsymbol{Z}$ as the Lagrange multiplier associated with the gradient constraint to obtain the following saddle point problem:

$$\begin{aligned}\max_{\boldsymbol{Z}} \min_{\vec{u},\alpha,\boldsymbol{g}} \quad & \int_\Omega \left[\rho\Psi(\boldsymbol{\epsilon}^{\text{to}}, \alpha, \boldsymbol{g}) + \Delta t \phi\left(\frac{\alpha - \alpha(t)}{\Delta t}, \frac{\boldsymbol{g} - \boldsymbol{g}(t)}{\Delta t}\right)\right. \\ & \left. - \boldsymbol{Z} \cdot (\boldsymbol{g} - \mathbf{grad}(\alpha))\right] \mathrm{d}V - \mathcal{W}_{\text{ext}}(u) \\ = & \int_\Omega \left[\rho\Psi(\boldsymbol{\epsilon}^{\text{to}}, \alpha, \boldsymbol{g}) + \Delta t \phi\left(\frac{\alpha - \alpha(t)}{\Delta t}, \frac{\boldsymbol{g} - \boldsymbol{g}(t)}{\Delta t}\right)\right. \\ & \left. - \boldsymbol{Z} \cdot \boldsymbol{g} - \vec{\mathrm{div}}(\boldsymbol{Z})\alpha\right] \mathrm{d}V - \mathcal{W}_{\text{ext}}(u) + \int_{\partial\Omega} \boldsymbol{Z} \cdot n\alpha \mathrm{d}S\end{aligned} \tag{11.11}$$

Thus we obtain for the new optimality conditions with respect to α:

$$Y_{\text{nd}} + Y_{\text{d}} - \vec{\mathrm{div}}(\boldsymbol{Z}) = \frac{\partial \rho\Psi}{\partial \alpha} + \frac{\partial \phi}{\partial \dot{\alpha}} - \vec{\mathrm{div}}(\boldsymbol{Z}) = 0 \quad \text{in } \Omega \tag{11.12}$$

$$\boldsymbol{Z} \cdot n = 0 \quad \text{on } \partial\Omega \tag{11.13}$$

and with respect to $\boldsymbol{g}$:

$$0 = \boldsymbol{Z}_{\text{nd}} + \boldsymbol{Z}_{\text{d}} - \boldsymbol{Z} \tag{11.14}$$

$$= \frac{\partial \rho\Psi}{\partial \boldsymbol{g}} + \frac{\partial \phi}{\partial \dot{\boldsymbol{g}}} - \boldsymbol{Z} \tag{11.15}$$

As a result, we obtain an additional balance equation between *local* thermodynamic forces Y and their *non-local* counterpart $\boldsymbol{Z}$. In particular, the Biot equation (see 2.68) is no longer a purely local problem characterizing the state variable evolution but a global problem involving equilibrium and boundary conditions at the structure scale.

11.3.2.1 Example: damage gradient model

As a first example, let us consider the case of a damage model with $\alpha = d$. In such cases, the standard pseudo-potential can be generally written as:

$$\phi(\dot{d}) = R(d)\dot{d}, \quad \text{with } \dot{d} \geq 0 \tag{11.16}$$

where $R(d)$ denotes the damage resistance threshold, which depends on d in general. In this case, the pseudo-potential can be explicitly integrated in time since:

$$R(d)\dot{d} = \frac{\mathrm{d}}{\mathrm{d}t} w(d) \quad \text{where } w(d) = \int_0^d R(\widehat{d})\,\mathrm{d}\widehat{d} \tag{11.17}$$

In this case, the time-continuous variational principle reads:

$$\min_{\vec{u},d} \quad \int_\Omega \left[\rho\Psi(\boldsymbol{\epsilon}^{\mathrm{to}}, d) + w(d)\right] \mathrm{d}V - \mathcal{W}_{\mathrm{ext}}(u) \tag{11.18}$$

so that we obtain a formulation equivalent to a single energy potential $\rho\Psi + w$. It must be mentioned that this specific case of GSM, where the pseudo-potential becomes a state function, corresponds to the case of simple dissipative systems introduced by Ehrlacher and Fedelich [1989].

As a result, the extension to damage gradient models can be performed by considering a damage-gradient dependent pseudo-potential, for instance:

$$\phi(\dot{d}, \dot{\boldsymbol{g}}) = R(d)\dot{d} + A\boldsymbol{g}\cdot\dot{\boldsymbol{g}} \tag{11.19}$$

where A is a positive constant. Such a model yields the variational problem

$$\min_{\vec{u},d} \quad \int_\Omega \left[\rho\Psi(\boldsymbol{\epsilon}^{\mathrm{to}}, d) + w(d) + \frac{A}{2}\mathbf{grad}(d)\cdot\mathbf{grad}(d)\right] \mathrm{d}V - \mathcal{W}_{\mathrm{ext}}(u) \tag{11.20}$$

We can observe that this extension is equivalent, at least formally, to consider the following damage-gradient dependent free-energy:

$$\rho\Psi(\boldsymbol{\epsilon}^{\mathrm{to}}, d, \mathbf{grad}(d)) = \rho\Psi(\boldsymbol{\epsilon}^{\mathrm{to}}, d) + \frac{A}{2}\mathbf{grad}(d)\cdot\mathbf{grad}(d) \tag{11.21}$$

leading to the same variational principle and evolution equations. The main difference lies in whether the additional term is considered as being part of the free energy or of the dissipation. As regards the evolution equations, we have for this example:

$$Y_{\mathrm{nd}} = \frac{\partial\rho\Psi}{\partial d} \tag{11.22}$$

$$Y_{\mathrm{d}} \leq R(d) \tag{11.23}$$

$$\boldsymbol{Z} = A\mathbf{grad}(d) \tag{11.24}$$

where the inequality stems from the irreversibility condition $\dot{d} \geq 0$, which is to be completed with the consistency condition $\dot{d}(Y_{\mathrm{d}} - R(d)) = 0$. Besides, the last equation is obtained from (11.15). Note that for the construction based on the dissipation (11.19), we have $\boldsymbol{Z}_{\mathrm{nd}} = 0$ and $\boldsymbol{Z}_{\mathrm{d}} = \boldsymbol{Z} = A\mathbf{grad}(d)$, while for the energy-based construction (11.21), we have here $\boldsymbol{Z}_{\mathrm{d}} = 0$ and $\boldsymbol{Z}_{\mathrm{nd}} = \boldsymbol{Z} = A\mathbf{grad}(d)$. In any case, the resulting damage evolution criterion

is obtained from (11.12) as:

$$Y_{\mathrm{d}} = -Y_{\mathrm{nd}} + \vec{\mathrm{div}}(\boldsymbol{Z}) \leq R(d) \tag{11.25}$$

$$-\frac{\partial \rho\Psi}{\partial d} \leq R(d) - A\Delta d \tag{11.26}$$

We can observe that the laplacian term enters the damage criterion which is no longer local. Clearly, the obtained model is different from implicit gradient models as discussed before.

11.3.2.2 Example: gradient plasticity

As a second example, let us consider the case of softening plasticity models (i.e. with negative hardening). In this case, softening-induced localization is driven by a cumulated plastic strain variable p. Therefore, the corresponding gradient model will include additional terms involving $\mathbf{grad}(p)$ in the total energy functional.

As regards the initial local model, let us assume for simplicity a von Mises elastoplastic behavior with isotropic hardening with state variables being the plastic strain $\boldsymbol{\varepsilon}^{\mathrm{p}}$ and the cumulated plastic strain p with the following potentials:

$$\rho\Psi(\boldsymbol{\epsilon}^{\mathrm{to}}, \boldsymbol{\varepsilon}^{\mathrm{p}}, p) = \frac{1}{2}(\boldsymbol{\epsilon}^{\mathrm{to}} - \boldsymbol{\varepsilon}^{\mathrm{p}}) : \mathbb{D} : (\boldsymbol{\epsilon}^{\mathrm{to}} - \boldsymbol{\varepsilon}^{\mathrm{p}}) + \rho\Psi_{\mathrm{h}}(p) \tag{11.27}$$

$$\phi(\dot{\boldsymbol{\varepsilon}^{\mathrm{p}}}, \dot{p}) = \begin{cases} \sigma_0 \dot{p} & \text{s.t.} \sqrt{2/3}\|\dot{\boldsymbol{\varepsilon}^{\mathrm{p}}}\| \leq \dot{p} \text{ and } \mathrm{tr}(\dot{\boldsymbol{\varepsilon}^{\mathrm{p}}}) = 0 \\ +\infty & \text{otherwise} \end{cases} \tag{11.28}$$

where $\rho\Psi_{\mathrm{h}}(p)$ denotes the hardening potential which is non-convex in the case of softening plasticity. For this standard material behavior, the evolution equations with respect to p yield the plastic yield criterion:

$$Y_{\mathrm{nd}} = \rho\Psi'(h) = H(p) \tag{11.29}$$

$$Y_{\mathrm{d}} \leq \sigma_0 - \sqrt{\frac{3}{2}\boldsymbol{s} : \boldsymbol{s}} \tag{11.30}$$

$$\Rightarrow \sqrt{\frac{3}{2}\boldsymbol{s} : \boldsymbol{s}} \leq \sigma_0 + H(p) \tag{11.31}$$

Let us now consider that the free energy is complemented by a quadratic potential of the plastic strain gradient:

$$\rho\Psi(\boldsymbol{\epsilon}^{\mathrm{to}}, \boldsymbol{\varepsilon}^{\mathrm{p}}, p, \mathbf{grad}(p)) = \rho\Psi_{el}(\boldsymbol{\epsilon}^{\mathrm{to}}, \boldsymbol{\varepsilon}^{\mathrm{p}}) + \rho\Psi_{\mathrm{h}}(p) + \frac{A}{2}\mathbf{grad}(p)\cdot\mathbf{grad}(p) \tag{11.32}$$

Then, $\boldsymbol{Z}_{\mathrm{nd}} = \boldsymbol{Z}_{\mathrm{d}} = A\mathbf{grad}(p)$ and we have:

$$Y_{\mathrm{nd}} = \rho\Psi'(h) = H(p) \tag{11.33}$$

$$Y_{\mathrm{d}} = -Y_{\mathrm{nd}} + \vec{\mathrm{div}}(\boldsymbol{Z}) \leq \sigma_0 - \sqrt{\frac{3}{2}\boldsymbol{s} : \boldsymbol{s}} \tag{11.34}$$

$$\Rightarrow \sqrt{\frac{3}{2}\boldsymbol{s} : \boldsymbol{s}} \leq \sigma_0 + H(p) - A\Delta p \tag{11.35}$$

Again, the plastic yield criterion is now non-local as it depends on the cumulated plastic strain laplacian, recovering the Aifantis [1987] model. Again the non-local character of the constitutive law of such models makes their numerical implementation challenging. Moreover, as discussed in various references, they possess various weaknesses such as the fact that localization bands keep on broadening after stress saturation at large strains [Jirásek and Rolshoven, 2009; Scherer et al., 2019] as in gradient-enhanced damage models [Geers et al., 1998; Simone et al., 2004].

11.4 Models with enriched kinematics

Another type of regularization method consists in adding kinematic degrees of freedom, leading to generalized Cosserat media.

11.4.1 Generalized Cosserat media

The first formulation of a generalized continuous medium was proposed by the Cosserat brothers [Cosserat and Cosserat, 1909]. It consists in considering the material particles as objects having not only degrees of freedom in translation but also in rotation. They are described by the rotation of a rigid reference frame constituted by three orthogonal unit vectors. After Günther [1958] reopened the question of a continuous oriented medium and underlined its link with the theory of dislocations, the idea of the Cosserat brothers was taken up again to lead to the emergence of generalized Cosserat theories:

- *the couple-stress elasticity* with the works of Mindlin and Tiersten [1962]; Toupin [1962, 1964] and Koiter [1964];
- The theory of elasticity with microstructure (see Mindlin);
- *the multipolar theory* with the works of Green and Rivlin [1964a]; Green [1965].
- *the micropolar and micromorphic theories* with the works of Eringen and Suhubi [1964] and Eringen [1964, 1966a,b];

All these theories characterize the motion of a solid body by additional fields which are independent of the displacement field and provide additional information about the kinematics at the lower scale. A unifying thermomechanical constitutive framework for generalized continua has been proposed by [Forest and Sievert, 2003]. Stefanou et al. [2017] studied how Cosserat elastoplastic model can be used for strain localization limitation in softening plasticity.

11.4.2 Micromorphic models

Among these higher order continua, the micromorphic continuum is one of the most general one. Its principle consists in adding to the displacement degrees of freedom, an additional degree of freedom which is typically related to a microdeformation of the underlying microstructure. Additional energy contributions are considered to penalize the difference between the macroscopic and microscopic deformation variables. In the original micromorphic model by Eringen and Suhubi [1964]; Eringen [1964], the microdeformation tensor was related to the deformation of a triad of director vectors characterizing the underlying microstructure. In the following, we rather adopt the generic approach presented in [Forest, 2009] where the microdeformation α_χ is related to a given state variable α. Again, we consider here only scalar variables for the sake of simplicity. The rationale behind the use of micromorphic models in the context of regularization is to select a state variable which is responsible for the localization process. As mentioned before, the micromorphic model is obtained by extending the free-energy with terms involving the difference $\alpha-\alpha_\chi$ and the gradient of the microdeformation $\mathbf{grad}(\alpha_\chi)$. Choosing isotropic quadratic potentials for simplicity we therefore have:

$$\rho\widetilde{\Psi}(\boldsymbol{\epsilon}^{\mathrm{to}},\alpha,\alpha_\chi,\mathbf{grad}(\alpha_\chi)) = \rho\Psi(\boldsymbol{\epsilon}^{\mathrm{to}},\alpha)+\frac{1}{2}H_\chi(\alpha-\alpha_\chi)^2+\frac{1}{2}A\mathbf{grad}(\alpha_\chi)\cdot\mathbf{grad}(\alpha_\chi) \tag{11.36}$$

where $H_\chi, A \geq 0$ are additional material parameters and $\rho\Psi$ the free-energy of the original local model. Note that, in this framework, the pseudo-potential is unchanged i.e. it is of the form $\phi(\dot{\alpha})$.

A similar variational principle as (10.1) can be considered for characterizing the evolution of the micromorphic model, it reads as:

$$\begin{aligned}\min_{\vec{u},\alpha,\alpha_\chi} \quad & \int_\Omega \left[\rho\Psi(\boldsymbol{\epsilon}^{\mathrm{to}},\alpha)+\frac{1}{2}H_\chi(\alpha-\alpha_\chi)^2+\frac{1}{2}A\mathbf{grad}(\alpha_\chi)\cdot\mathbf{grad}(\alpha_\chi)\right. \\ & \left. +\Delta t\phi\left(\frac{\alpha-\alpha(t)}{\Delta t}\right)\right]\mathrm{d}V-\mathcal{W}_{\mathrm{ext}}(\vec{u})\end{aligned} \tag{11.37}$$

The optimality condition with respect to the displacement u remain unchanged, they provide the local balance equation for the stress $\boldsymbol{\sigma} = \dfrac{\partial\rho\Psi}{\partial\boldsymbol{\epsilon}^{\mathrm{to}}}$ obtained from the local free-energy potential. The optimality conditions with

respect to α yields a similar evolution equation as (11.10):

$$0 = Y_{\mathrm{nd}} + H_\chi(\alpha - \alpha_\chi) + Y_{\mathrm{d}} \tag{11.38}$$

$$0 = \frac{\partial \rho\Psi}{\partial \alpha} + H_\chi(\alpha - \alpha_\chi) + \frac{\partial \phi}{\partial \dot{\alpha}} \tag{11.39}$$

which remains of local nature (no divergence or other differential operator) but with an additional term $H_\chi(\alpha - \alpha_\chi)$. Finally, the optimality condition for the microdeformation α_χ turns out to be the following variational problem: Find α_χ such that:

$$\int_\Omega \left[A\mathbf{grad}(\alpha_\chi) \cdot \mathbf{grad}(\beta) + H_\chi(\alpha_\chi - \alpha)\beta\right] \mathrm{d}V = 0 \quad \forall \beta \tag{11.40}$$

which is the weak form associated with:

$$\alpha_\chi - \frac{A}{H_\chi}\Delta\alpha_\chi = \alpha \quad \text{in } \Omega \tag{11.41}$$

$$\mathbf{grad}(\alpha_\chi) \cdot \vec{n} = 0 \quad \text{on } \partial\Omega \tag{11.42}$$

Note that we did not consider any Dirichlet boundary condition on the microdeformation α_χ although it is possible to do so, at least mathematically. Similarly, we did not consider any source term related with such microdeformation.

As a result, we again recover similar equations as in implicit gradient models where $\sqrt{A/H_\chi}$ can be interpreted as a regularization length scale ℓ. Note however that, in implicit gradient models, the evolution equation pertaining to the local constitutive behavior do not take into account the term $H_\chi(\alpha - \alpha_\chi)$ appearing in (11.39). Instead, the local variable is replaced with the non-local one for the next iteration.

Moreover, when considering the micromorphic modulus $H_\chi \to \infty$, the quadratic penalty term will enforce $\alpha = \alpha_\chi$ while the term $H_\chi(\alpha - \alpha_\chi)$ becomes indeterminate. However, from the weak form (11.41), we know that:

$$H_\chi(\alpha - \alpha_\chi) = -A\Delta\alpha_\chi = -A\Delta\alpha \tag{11.43}$$

As a result, we recover the expressions of the gradient of internal variable models for a quadratic gradient potential. The latter can therefore be seen as a constrained version of such micromorphic models when enforcing equality between the microdeformation α_χ and the original state variable α.

One major interest in using such micromorphic models relies in the fact that the material constitutive equations remain local and are only modified by the inclusion of an additional thermodynamic force. Let us note that it is possible to add several nonlocal variables simultaneously. One potential drawback is that the use of micromorphic models requires the identification of an additional material parameter H_χ. Even if it is expected that if H_χ is sufficiently large, the model will converge to that of the corresponding internal variable

gradient counterpart, the influence of a large yet finite value of H_χ must be assessed case by case. This method has recently been used with a dynamic explicit resolution scheme in the context of metal forming by Diamantopoulou et al. [2017] or irradiated materials by Scherer et al. [2019]. It has also been used in dynamics to regularize a Gurson type damage model and get as close as possible to experimental results obtain on a DP450 steel [Davaze, 2019] (see figure 11.3).

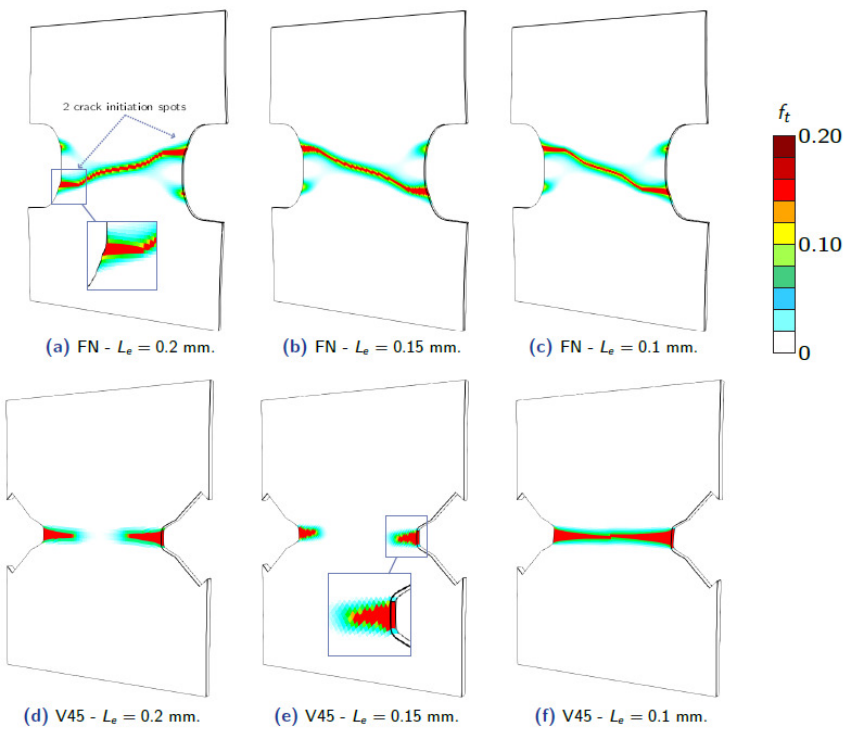

FIGURE 11.3: Load-displacement curves obtained with different meshes on FN and V45 specimens with the non-local micromorphic approach (from [Davaze, 2019]). The crack path does not depend on the mesh size.

11.4.3 Discussion

There are other less widespread methods in the literature. For example, the Thick Level Set approach to fracture [Moës et al., 2011] proposes to impose the damage distribution: minimization of the energy then aims at determining the evolution of the boundaries between the undamaged and damaged material. Different methods have also been proposed to counteract the loss of hyperbolicity of the constitutive equations in dynamics. They are known as temporal

localization limiters and encompass notably the concepts of models with delay effects [Ladevèze, 1991] and of bounded damage rate model [Allix and Deü, 1997; Allix, 2013]. However, these methods have not been as studied as the nonlocal models. In particular, Lorentz and Andrieux [2003] have tried to classify these nonlocal formulations. Their analysis of the models concluded that, usually, "effective regularization and preservation of the grounding energetic basis cannot be gained together" since "these regularization techniques are thus more pragmatic than based on physical derivations". Still from a pragmatic point of view, in our opinion, convergence of the method is a critical point. Other issues can be tackled as long as there are no major convergence issues. For example, the enlargement of the localization band that happens when introducing the gradient of a strain related quantity, can be limited by insertion of a discrete crack (see chapter14). Being able to simulate crack initiation and propagation thanks to regularized damage models opens the door to the possibility of identifying the involved parameters and, in particular, the characteristic length.

Bibliography

[Aero and Kuvshinskii 1960] Aero, E.L. ; Kuvshinskii, E.V.: Fundamental equations of the theory of elastic materials with rotationally interacting particles. In: *Fizika Tverdogo Tela* 2 (1960), p. 1399–1409

[Aifantis 1987] Aifantis, E.C.: The physics of plastic deformation. In: *International journal of plasticity* 3 (1987), Nr. 3, p. 211–247

[Allix 2013] Allix, O.: The bounded rate concept: A framework to deal with objective failure predictions in dynamic within a local constitutive model. In: *International Journal of Damage Mechanics* 22 (2013), Nr. 6, p. 808–828

[Allix and Deü 1997] Allix, O. ; Deü, J.-F.: Delayed-damage modelling for fracture prediction of laminated composites under dynamic loading. In: *Engineering transactions* 45 (1997), Nr. 1, p. 29–46

[Baaser and Tvergaard 2003] Baaser, H. ; Tvergaard, T.: A new algorithm approach treating nonlocal effects at finite rate-independent deformation using the Rousselier damage model. In: *Comput. Methods Applied Mech. Engrg.* 192 (2003), p. 107–124

[Bažant et al. 1984] Bažant, Z.P. ; Belytschko, T. ; Chang, T.-P.: Continuum model for strain softening. In: *J. Engrg. Mech.* 110 (1984), p. 1666–1692

[Bažant and Jirásek 2002] Bažant, Z.P. ; Jirásek, M.: Nonlocal integral formulations of plasticity and damage: survey of progress. In: *Journal of Engineering and Mechanics ASCE* 128 (2002), p. 1119–1149

[Besson et al. 2023] Besson, J. ; Lebon, F. ; Lorentz, E.: *Modélisation numérique en mécanique fortement non linéaire*. ISTE, 2023 (Encyclopédie Sciences. Mécanique. Modélisation numérique en mécanique)

[de Borst and Mülhaus 1991] Borst, R. de ; Mülhaus, H.B.: Continuum models for discontinuous media. In: Mier, J.G.M. van (Hrsg.) ; Rots, J.G. (Hrsg.) ; Bakker, A. (Hrsg.): *Fracture processes in Concrete, Rock and Ceramics* Bd. 2. London : E&FN Spon, 1991, p. 601–618

[de Borst and Mülhaus 1992] Borst, R. de ; Mülhaus, H.B.: Gradient-dependent plasticity: Formulation and algorithmic aspects. In: *International Journal for Numerical Methods in Engineering* 39 (1992), p. 521–539

[de Borst and Pamin 1996] Borst, R. de ; Pamin, J.: Some novel developments in finite element procedures for gradient-dependent plasticity. In: *International Journal for Numerical Methods in Engineering* 39 (1996), p. 2477–2505

[de Borst et al. 1993] Borst, R. de ; Sluys, L.J. ; Mühlhaus, H.-B. ; Pamin, J.: Fundamental issues in finite element analyses of localization of deformation. In: *Engineering Computations* 10 (1993), p. 99–121

[Chambon et al. 2001] Chambon, R. ; Caillerie, D. ; Matsuchima, T.: Plastic continuum with microstructure, local second gradient theories for geomaterials: localization studies. In: *International journal of solids and structures* 38 (2001), Nr. 46-47, p. 8503–8527

[Cosserat and Cosserat 1909] Cosserat, E. ; Cosserat, F.: *Théorie des corps déformables*. Paris, France : A. Herrman et Fils, 1909

[Davaze 2019] Davaze, V.: *Numerical modelling of crack initiation and propagation in ductile metallic sheets for crash simulations*, Université Paris sciences et lettres, Diss., 2019. – https://pastel.archives-ouvertes.fr/tel-02518318

[Davaze et al. 2021] Davaze, V. ; Vallino, N. ; Langrand, B. ; Besson, J. ; Feld-Payet, S.: A non-local damage approach compatible with dynamic explicit simulations and parallel computing. In: *International Journal of Solids and Structures* 228 (2021), p. 110999

[Diamantopoulou et al. 2017] Diamantopoulou, E. ; Liu, W. ; Labergere, C. ; Badreddine, H. ; Saanouni, K. ; Hu, P.: Micromorphic constitutive equations with damage applied to metal forming. In: *International Journal of Damage Mechanics* 26 (2017), Nr. 2, p. 314–339

[Edelen 1969] Edelen, D.G.B.: Protoelastic bodies with large deformation. In: *Archive for Rational Mechanics and Analysis* 34 (1969), p. 283–300

[Edelen et al. 1971] Edelen, D.G.B. ; Green, A.E. ; Laws, N.: Nonlocal continuum mechanics. In: *Archive for Rational Mechanics and Analysis* 43 (1971), p. 36–44

[Ehrlacher and Fedelich 1989] Ehrlacher, A. ; Fedelich, B.: Stability and bifurcation of simple dissipative systems; application to brutal damage. In: *Cracking and Damage: Strain localization and size effect* (1989), p. 217–227

[Engelen et al. 2003] Engelen, R.A.B. ; Geers, M.G.D. ; Baaijens, F.P.T.: Nonlocal implicit gradient-enhanced elasto-plasticity for the modelling of softening behaviour. In: *International Journal of Plasticity* 19 (2003), p. 403–433

[Eringen 1964] Eringen, A.C.: Simple microfluids. In: *International Journal of Engineering Science* 2 (1964), p. 205–217

[Eringen 1966a] Eringen, A.C.: Linear theory of micropolar elasticity. In: *Journal of Mathematics and Mechanics* 15 (1966), p. 909–924

[Eringen 1966b] Eringen, A.C.: Mechanics of micromorphic materials. In: *Proc. 11th International Congress of Applied Mechanics*, Springer, 1966, p. 131–138. – Berlin, Heidelberg

[Eringen 1966c] Eringen, A.C.: A unified theory of thermomechanical materials. In: *International Journal of Engineering Science* 4 (1966), p. 179–202

[Eringen and Endelen 1972] Eringen, A.C. ; Endelen, D.G.B.: On nonlocal elasticity. In: *International Journal of Engineering Science* 10 (1972), p. 233–248

[Eringen and Suhubi 1964] Eringen, A.C. ; Suhubi, E.S.: Nonlinear theory of simple microelastic solids. In: *International Journal of Engineering Science* 2 (1964), p. 189–203,398–404

[Feld-Payet 2010] Feld-Payet, S.: *Amorçage et propagation de fissures dans les milieux ductiles non locaux*, École Nationale Supérieure des Mines de Paris, Diss., 2010. – http://pastel.archives-ouvertes.fr/pastel-00583011

[Feld-Payet et al. 2011] Feld-Payet, S. ; Besson, J. ; Feyel, F.: Finite element analysis of damage in ductile structures using a non local model combined with a three-field formulation. In: *International Journal of Damage Mechanics* 20 (2011), p. 655–680

[Fernandes et al. 2008] Fernandes, R. ; Chavant, C. ; Chambon, R.: A simplified second gradient model for dilatant materials: theory and numerical implementation. In: *International Journal of Solids and Structures* 45 (2008), Nr. 20, p. 5289–5307

[Forest 2009] Forest, S.: Micromorphic approach for gradient elasticity, viscoplasticity, and damage. In: *Journal of Engineering Mechanics* 135 (2009), Nr. 3, p. 117–131

[Forest and Lorentz 2004] Forest, S. ; Lorentz, É.: Localization phenomena and regularization methods. In: presses, École des Mines de Paris les (Hrsg.): *Local Approach to fracture*, 2004, p. 311–371

[Forest and Sievert 2003] Forest, S. ; Sievert, R.: Elastoviscoplastic constitutive frameworks for generalized continua. In: *Acta Mech.* 160 (2003), p. 71–111

[Frémond and Nedjar 1993] Frémond, M. ; Nedjar, B.: Endommagement et principe des puissances virtuelles. In: *C.R. Acad. Sci.* 317, série II (1993), p. 857–864

[Frémond and Nedjar 1996] Frémond, M. ; Nedjar, B.: Damage, gradient of damage and principle of virtual power. In: *International Journal of Solids and Structures* 33 (1996), mars, Nr. 8, p. 1083–1103

[Gao et al. 1999] Gao, H. ; Huang, Y. ; Nix, W.D. ; Hutchinson, J.W.: Mechanism-based strain gradient plasticity-I. Theory. In: *Journal of the Mechanics and Physics of Solids* 47 (1999), p. 1239–1263

[Geers et al. 1998] Geers, M.G.D. ; De Borst, R. ; Brekelmans, W.A.M. ; Peerlings, R.: Strain-based transient-gradient damage model for failure analyses. In: *Computer methods in applied mechanics and engineering* 160 (1998), Nr. 1-2, p. 133–153

[Green 1965] Green, A.E.: Micro-materials and multipolar continuum mechanics. In: *International Journal of Engineering and Science* 3 (1965), p. 533–537

[Green and Rivlin 1964a] Green, A.E. ; Rivlin, R.S.: Multipolar continuum mechanics. In: *Archive for Rational Mechanics and Analysis* 17 (1964), p. 113–147

[Green and Rivlin 1964b] Green, A.E. ; Rivlin, R.S.: Simple force and stress multipole. In: *Archive for Rational Mechanics and Analysis* 16 (1964), p. 325–353

[Grioli 1960] Grioli, G.: Elasticità asimmetrica. In: *Annali di matematica pura ed applicata* 50 (1960), p. 389–417

[Günther 1958] Günther, W.: Zur Statik und Kinematik des Cosseratschen Kontinuum. In: *Abhandlungen des Braunschweigischen Wissenschaftlichen Gesellschaft* 10 (1958), p. 195–213

[Huang et al. 2000] Huang, Y. ; Gao, H. ; Nix, W.D. ; Hutchinson, J.W.: Mechanism-based strain gradient plasticity-II. Analysis. In: *Journal of the Mechanics and Physics of Solids* 48 (2000), p. 99–128

[Jirásek 2008] Jirásek, M.: *Modeling of localized inelastic deformation, Lecture Notes*. 2008. – Short course given by Milan Jirásek at the Czech Technical University in Prague, 22-26 September 2008

[Jirásek and Rolshoven 2003] Jirásek, M. ; Rolshoven, S.: Comparison of integral-type nonlocal plasticity models for strain-softening materials. In: *International Journal of Engineering Science* 41 (2003), p. 1553–1602

[Jirásek and Rolshoven 2009] Jirásek, M. ; Rolshoven, S.: Localization properties of strain-softening gradient plasticity models. Part II: Theories with gradients of internal variables. In: *International Journal of Solids and Structures* 46 (2009), Nr. 11, p. 2239–2254

[Jouan et al. 2014] Jouan, G. ; Kotronis, P. ; Collin, F.: Using a second gradient model to simulate the behaviour of concrete structural elements. In: *Finite Elements in Analysis and Design* 90 (2014), p. 50–60

[Koiter 1964] Koiter, W.T.: Couple-stresses in the theory of elasticity. In: *Proceedings Koninklijke Nederlandse Akademie van Wetenshappen, Ser. B* 67 (1964), p. 17–44

[Kröner 1967] Kröner, E.: Elasticity theory of materials with long range cohesive forces. In: *International Journal of Solids and Structures* 3 (1967), p. 731–742

[Kunin 1968] Kunin, I.A.: The theory of elastic media with microstructure and the theory of dislocations. In: Kröner, E. (Hrsg.): *Mechanics of Generalized Continua*. Springer-Verlag, 1968, p. 321–329. – Heidelberg

[Ladevèze 1991] Ladevèze, P.: *About a damage mechancs approach*. 1991. – Rapport Interne n34, Laboratoire de Mécanique et Technologies, Cachan

[Le et al. 2018] Le, D.T. ; Marigo, J.-J. ; Maurini, . ; Vidoli, S.: Strain-gradient vs damage-gradient regularizations of softening damage models. In: *Computer Methods in Applied Mechanics and Engineering* 340 (2018), p. 424–450

[Lorentz 1999] Lorentz, É.: *Lois de comportement à gradients de variables internes : constructions, formulation variationnelle et mise en œuvre numérique*, LMT-Cachan, Université Paris 6, Diss., 1999

[Lorentz 2003] Lorentz, É.: Loi d'endommagement d'un matériau élastique fragile / EDF-R&D/AMA. 2003 (R5.03.18-A). – Manuel de référence Code_Aster. – `http://www.code-aster.org`www.code-aster.org

[Lorentz 2019] Lorentz, E.: *Damage and fracture: numerical approaches at the structural scale, Lecture Notes*. 2019. – Course given by Eric Lorentz at the Mecamat seminar in Aussois, January 2019

[Lorentz and Andrieux 1999] Lorentz, É. ; Andrieux, S.: A variational formulation for non local damage models. In: *International Journal of Plasticity* 15 (1999), p. 119–138

[Lorentz and Andrieux 2003] Lorentz, E. ; Andrieux, S.: Analysis of non-local models through energetic formulations. In: *International Journal of Solids and Structures* 40 (2003), Nr. 12, p. 2905–2936. – 10.1016/S0020-7683(03)00110-0

[Lorentz and Benallal 2005] Lorentz, É. ; Benallal, A.: Gradient constitutive relations: numerical aspects and application to gradient damage. In: *Computer Methods in Applied Mechanics and Engineering* (2005). – In press

[Maugin 1990] Maugin, G.A.: *Internal variables and dissipative structures*. Walter de Gruyter, Berlin/New York Berlin, New York, 1990

[Mindlin 1965] Mindlin, R.D.: Second gradient of strain and surface tension in linear elasticity. In: *International Journal of Solids and Structures* 1 (1965), p. 417–438

[Mindlin and Tiersten 1962] Mindlin, R.D. ; Tiersten, H.F.: Effects of couple-stresses in linear elasticity. In: *Archive for Rational Mechanics and Analysis* 11 (1962), p. 415–448

[Moës et al. 2011] Moës, N. ; Stolz, C. ; Bernard, P.E. ; Chevaugeon, N.: A level set based model for crack growth: thick level set method. In: *Internat. J. Numer. Methods Engrg* 86 (2011), Nr. 3, p. 358–380

[Mühlhaus and Aifantis 1991] Mühlhaus, H.-B. ; Aifantis, E.C.: A variational principle for gradient plasticity. In: *International Journal of Solids and Structures* 28 (1991), p. 845–858

[Nguyen 2015] Nguyen, Q.-S.: Some remarks on standard gradient models and gradient plasticity. In: *Mathematics and Mechanics of Solids* 20 (2015), Nr. 6, p. 760–769

[Pamin 1994] Pamin, J.: *Gradient-dependent plasticity in numerical simulation of localization phenomena*. Delft, The Netherlands, Delft University of Technology, Diss., 1994

[Peerlings 1999] Peerlings, R.H.J.: *Enhanced damage modelling for fracture and fatigue*, Technische Universiteit Eindhoven, Diss., 1999

[Peerlings et al. 1996] Peerlings, R.H.J. ; Borst, R. de ; Brekelmans, W.A.M. ; Vree, J.H.P. de: Gradient-enhanced damage for quasi-brittle materials. In: *Int. J. Numer. Methods Engrg.* 39 (1996), p. 3391–3403

[Pijaudier-Cabot and Bažant 1987] Pijaudier-Cabot, G. ; Bažant, Z.P.: Nonlocal damage theory. In: *J. Engrg. Mech.* 113 (1987), p. 1512–1533

[Rajagopal 1960] Rajagopal, E.S.: The existence of interfacial couples in infinitesimal elasticity. In: *Annalen des Physik* 6 (1960), p. 192–201

[Scherer et al. 2019] Scherer, J.-M. ; Besson, J. ; Forest, S. ; Hure, J. ; Tanguy, B.: Strain gradient crystal plasticity with evolving length scale: Application to voided irradiated materials. In: *European Journal of Mechanics-A/Solids* 77 (2019), p. 103768

[Shi et al. 2000] Shi, M.X. ; Huang, Y. ; Hwang, K.C.: Plastic flow localization in mechanism-based strain gradient plasticity. In: *International Journal of Mechanical Sciences* 42 (2000), p. 2115–2131

[Simone et al. 2004] Simone, A. ; Askes, H. ; Sluys, L.J.: Incorrect initiation and propagation of failure in non-local and gradient-enhanced media. In: *International journal of solids and structures* 41 (2004), Nr. 2, p. 351–363

[Stefanou et al. 2017] Stefanou, I. ; Sulem, J. ; Rattez, H.: Cosserat approach to localization in geomaterials. In: *Handbook of nonlocal continuum mechanics for materials and structures. Springer* 730 (2017)

[Toupin 1962] Toupin, R.A.: Elastic materials with couple-stresses. In: *Archive for Rational Mechanics and Analysis* 11 (1962), p. 385–414

[Toupin 1964] Toupin, R.A.: Theories of elasticity with couple-stress. In: *Archive for Rational Mechanics and Analysis* 17 (1964), p. 85–112

[Truesdell and Toupin 1960] Truesdell, C. ; Toupin, R.A.: Classical field theories of mechanics. In: *Handbuch der Physik* Bd. III/1. Springer, Berlin, 1960

[Tuhami et al. 2022] Tuhami, A.E.O. ; Feld-Payet, S. ; Quilici, S. ; Osipov, N. ; Besson, J.: A two characteristic length nonlocal GTN model: Application to cup–cone and slant fracture. In: *Mechanics of Materials* 171 (2022), p. 104350

[Tuhami et al. 2023] Tuhami, A.E.O. ; Feld-Payet, S. ; Quilici, S. ; Osipov, N. ; Besson, J.: Simulations of complex crack paths using a robust and cost-efficient continuous-discontinuous approach. In: *International Journal of Solids and Structures* (2023), p. 112199

[Voreux 2022] Voreux, O.: *High temperature fatigue crack growth modeling in Nickel-based superalloys using a local approach to fracture*, université Paris-Saclay, Diss., 2022

[Zbib and Aifantis 1988] Zbib, H.M. ; Aifantis, E.C.: On the localization and postlocalization behavior of plastic deformation. In: *Res Mechanica* 23 (1988), p. 261–605

12

The variational approach to fracture and regularized fracture models

Corrado Maurini

Sorbonne Université

Abstract. This chapter provides a primer to the variational approach to fracture. After a review of the variational approach to linear elasticity, we formulate the fracture mechanics problem as an energy problem and introduce the damage models obtained as its variational approximation.

12.1 Introduction

The variational approach to fracture formulates fracture and damage mechanics as energy minimization problems. It exploits the related variational structure for the analysis of the solutions and to devise robust numerical solution strategies. The roots of this viewpoint are the works of Griffith [Griffith, 1921], Francfort, Marigo and Bourdin [Francfort and Marigo, 1993, 1998; Bourdin et al., 2000; Francfort et al., 2008], and the related mathematical literature, see *e.g.* [Ambrosio et al., 2000; Braides, 2002]. This approach led to notable progresses in the theoretical understanding of fracture mechanics and its link with damage models. It is at the basis of a game-changing numerical simulation tools of fracture through smeared damage models, which is known as "phase-field" method.

The aim of this chapter is to give a first introduction to the variational approach to damage and fracture. The exposition includes:

(i) a short review of the variational formulation for a linear elastic problem for a body with a pre-existing crack,

(ii) the introduction of variational approach to the sharp interface Griffith model of brittle fracture,

(iii) the introduction of the variational approach to gradient damage models and their link with the brittle fracture problem.

A final section will give a short overview of the open issues and current research topics in the field.

12.2 Variational formulation of the elastic problem for a body with a pre-existing crack

Before introducing the variational approach to fracture, we review the classical variational formulation of a linear elastic problem for a solid with a pre-existing crack. This preliminary step is necessary to introduce the notation and to define the potential energy of a cracked body and the energy release rate.

Let us consider a body represented by the domain $\Omega \subset \mathbb{R}^n$, including a crack set Γ in the form of a "regular" subset of co-dimension 1 of Ω, *i.e.* surfaces for $n = 3$, curves for $n = 2$, points for $n = 1$. Linear elastic fracture mechanics assumes the solid to be linear elastic in $\Omega \setminus \Gamma$ and neglects geometric nonlinearities.

The potential energy of the cracked body $\Omega_\Gamma \equiv \Omega \setminus \Gamma$ is

$$\mathcal{P}(\vec{u}, \Gamma) := \int_{\Omega\setminus\Gamma} W(\boldsymbol{\varepsilon}(\vec{u}))\,\mathrm{d}x - \mathcal{L}(\vec{u}), \tag{12.1}$$

with

$$W(\boldsymbol{\varepsilon}) := \frac{1}{2}(\mathbb{K} : \boldsymbol{\varepsilon}) : \boldsymbol{\varepsilon}, \qquad \mathcal{L}(\vec{u}) = \int_{\partial_f\Omega\setminus\Gamma} \vec{f}.\vec{u}\,\mathrm{d}s + \int_{\Omega\setminus\Gamma} \vec{b}.\vec{u}\,\mathrm{d}x$$

where $W(\boldsymbol{\varepsilon})$ is the elastic energy density, $\vec{u}$ the displacement vector, $\boldsymbol{\varepsilon}(\vec{u}) = \mathrm{sym}(\nabla\vec{u})$ the linearized strain, $\mathbb{K}$ the elastic constitutive tensor, and $\mathcal{L}(\vec{u})$ is the work of the external forces, which are assumed to be conservative. The loading is given by applied displacement $\vec{u}^d$ on the part of the boundary $\partial_u\Omega$, applied surface traction $\vec{f}$ on the part of the boundary $\partial_f\Omega \equiv \partial\Omega \setminus \partial\Omega_u$ and bulk forces $\vec{b}$ on Ω. We denote by

$$\begin{aligned} \mathcal{C}(\Gamma) &= \{\vec{u} \in H^1(\Omega \setminus \Gamma) : \quad \vec{u} = \vec{u}^d \text{ on } \partial\Omega_u \setminus \Gamma\} \\ \mathcal{C}_0(\Gamma) &= \{\vec{u} \in H^1(\Omega \setminus \Gamma) : \quad \vec{u} = \vec{0} \quad \text{on } \partial\Omega_u \setminus \Gamma\} \end{aligned}$$

the affine space of admissible displacements and the associated vector space of admissible variations, such that $\forall\vec{u} \in \mathcal{C}(\Gamma)$, $\forall\vec{v} \in \mathcal{C}_0(\Gamma)$, $\vec{u} + \vec{v} \in \mathcal{C}(\Gamma)$. The regularity requirement $\vec{u} \in H^1(\Omega\setminus\Gamma)$, where H^1 denotes the standard Sobolev space, means that the admissible displacements must have square integrable first derivatives on the uncracked domain $\Omega \setminus \Gamma$, in order to ensure a finite elastic energy: $\mathcal{P}(\vec{u}, \Gamma) < +\infty$. To simplify the presentation, let us assume that the crack set and the Dirichlet boundary conditions do not allows for rigid body modes, *i.e.* that:

$$\vec{u} \in \mathcal{C}_0(\Gamma) \quad \text{and} \quad \boldsymbol{\varepsilon}(\vec{u}) = \mathbf{0} \quad \Rightarrow \quad \vec{u} = \vec{0}. \tag{12.2}$$

Hence, we can characterize the solution of the elastic problem for a given crack set Γ as the unique solution of the following minimization problem

$$\vec{u}^* = \underset{\vec{u}\in\mathcal{C}(\Gamma)}{\operatorname{argmin}}\, \mathcal{P}(\vec{u},\Gamma), \qquad \mathcal{P}(\Gamma) := \min_{\vec{u}\in\mathcal{C}(\Gamma)} \mathcal{P}(\vec{u},\Gamma) = \mathcal{P}(\vec{u}^*,\Gamma). \tag{12.3}$$

which is also known as the *principle of minimum total potential energy*. The notation in equation (12.3) means that

$$\vec{u}^* \in \mathcal{C}: \qquad \mathcal{P}\left(\vec{u}^*\right) \leq \mathcal{P}\left(\vec{u}\right), \quad \forall \vec{u} \in \mathcal{C}(\Gamma). \tag{12.4}$$

Taking $\vec{u} = \vec{u}^* + h\,\hat{\vec{u}}$ with $h \geq 0$ and $\vec{v} \in \mathcal{C}_0$ and performing a Taylor expansion in h, the condition above writes as

$$\forall \hat{\vec{u}} \in \mathcal{C}_0: \quad 0 \leq \mathcal{P}\left(\vec{u}^* + h\,\hat{\vec{u}}\right) - \mathcal{P}\left(\vec{u}^*\right) = h\, D_{\vec{u}}\mathcal{P}(\vec{u}^*)(\hat{\vec{u}}) + o(h) \tag{12.5}$$

where

$$D_{\vec{u}}\mathcal{P}(\vec{u})(\hat{\vec{u}}) := \left.\frac{d}{dh}\mathcal{P}\left(\vec{u} + h\hat{\vec{u}}\right)\right|_{h=0} = \int_{\Omega\setminus\Gamma} \boldsymbol{\sigma}\left(\vec{u}\right) : \boldsymbol{\varepsilon}\left(\hat{\vec{u}}\right)\, \mathrm{d}\Omega - \mathcal{L}\left(\hat{\vec{u}}\right)$$

denotes the first directional derivative of the functional $\mathcal{P}$ with respect to $\vec{u}$ in the direction $\hat{\vec{u}}$ with the stress tensor defined by

$$\boldsymbol{\sigma}\left(\vec{u}\right) := \frac{\partial W}{\partial \boldsymbol{\varepsilon}}\left(\boldsymbol{\varepsilon}(\vec{u})\right) = \mathbb{K} : \boldsymbol{\varepsilon}\left(\vec{u}\right).$$

Since for any $\vec{v} \in \mathcal{C}_0$, $-\vec{v} \in \mathcal{C}_0$, the inequality implies that the solution of the minimization problem must satisfy the following first-order optimality condition:

$$\vec{u} \in \mathcal{C}: \quad D_{\vec{u}}\mathcal{P}(\vec{u})(\hat{\vec{u}}) = 0, \qquad \forall \hat{\vec{u}} \in \mathcal{C}_0, \tag{12.6}$$

which is the weak formulation of the linear elastic problem for the cracked body. Writing $\mathcal{L}\left(\hat{\vec{u}}\right)$ explicitly, eq. (12.6) can also be written as

$$\int_{\Omega\setminus\Gamma} \boldsymbol{\sigma}(\vec{u}) : \boldsymbol{\varepsilon}\left(\hat{\vec{u}}\right) = \int_{\Omega} \vec{b}\cdot\hat{\vec{u}}\,\mathrm{d}\Omega + \int_{\partial_f\Omega} \vec{f}\cdot\hat{\vec{u}}\,\mathrm{d}S = 0 \quad \forall \hat{\vec{u}} \in \mathcal{C}_0. \tag{12.7}$$

Integrating by parts and using classical arguments of the calculus of variations one can show that the weak form above implies the equilibrium equations in the strong from

$$\vec{\operatorname{div}}\,\boldsymbol{\sigma} + \vec{b} = \vec{0} \text{ in } \Omega\setminus\Gamma, \quad \boldsymbol{\sigma}.\vec{n} = \vec{f} \text{ on } \partial\Omega_f,$$

The equation above completed by the compatibility equation $\boldsymbol{\varepsilon}(\vec{u}) = \operatorname{sym}(\nabla\vec{u})$ and by the admissibility condition $\vec{u} \in \mathcal{C}(\Gamma)$ gives the full set of equation of linear elasticity.

12.3 Variational formulation of the Griffith model

Griffith [Griffith, 1921] formulated the fracture mechanics problem as the problem of minimizing the total energy of the cracked body, sum of the potential energy and the energy required to create the crack. In the simplest model, the energy required to create the crack is supposed to be proportional to its surface $\mathcal{S}(\Gamma)$ (or length in 2D). The energy per unit of surface required to create the crack is the fracture toughness G_c. Francfort and Marigo [Francfort and Marigo, 1998] provided a sound mathematical formulation of this idea. We introduce below the basics of this variational formulation to brittle fracture. We consider first the "static problem", consisting in finding the cracked state of the solid for a given load. Hence, we introduce the quasi-static evolution problem in the time-discrete setting. We start considering in the following subsection the problem of finding the crack state for a given loading, without considering an evolution.

12.3.1 Static problem: the energy release rate and the Griffith criterion

Given a preexisting crack Γ_0, the variational approach to sharp-interface Griffith fracture mechanics defines the cracked state of the solid as the solution of the following minimization problem for a total energy functional sum of the elastic energy of the cracked body and the energy required to create the crack:

$$\min_{\vec{u}\in\mathcal{C}(\Gamma),\Gamma\supseteq\Gamma_0} \mathcal{E}(\vec{u},\Gamma), \qquad \mathcal{E}(\vec{u},\Gamma) := \mathcal{P}(\vec{u},\Gamma) + G_c\,\mathcal{S}(\Gamma), \tag{12.8}$$

where the condition $\Gamma \supseteq \Gamma_0$ translates the crack irreversibility condition. This problem is extremely difficult to solve because the displacement field can jump on the crack set Γ which is itself an unknown of the problem.

We start considering the simpler case of a two-dimensional solid where the crack path Γ_s is given and the only unknown is the crack length s along this path. In this case, the energy minimization problem simplifies to

$$\min_{s\geq s_0} \mathcal{E}(s), \qquad \mathcal{E}(s) := \mathcal{P}(s) + G_c\,s \tag{12.9}$$

where

$$\mathcal{P}(s) := \min_{u\in\mathcal{C}(\Gamma_s)} \mathcal{P}(\vec{u},\Gamma_s)$$

is obtained by solving the linear elastic problem with given crack length formulated in the previous section and s_0 is the initial crack length.

As analysis illustrative example, consider the double-cantilever beam in Figure 12.1 with Young modulus E, thickness $2h$ and depth b under the plane-stress condition, with the straight crack Γ_ℓ parametrized by its length s. The

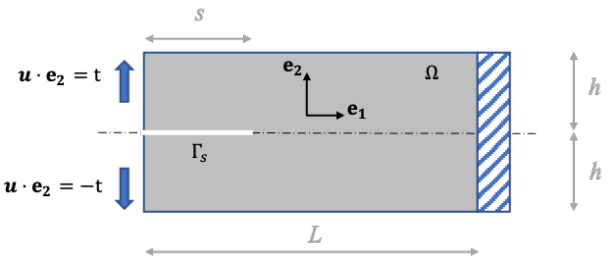

FIGURE 12.1: Double cantilever beam.

beam is loaded by an applied displacement t on the left end. A classical approximate analytical solution for this problem can be obtained using a beam model approximation, which gives:

$$\mathcal{P}(s) = \frac{Ebh^3}{4s^3}t^2.$$

A refined approximation of the potential energy can be obtained by solving the linear elastic problem at given crack length s with a finite element solver.

The optimal crack length $s^* \geq s_0$ must respect the condition

$$0 \leq \mathcal{E}(s) - \mathcal{E}(s^*) = \frac{d\mathcal{E}(s)}{ds^*}(s - s^*) + o(|s - s^*|), \quad \forall s \geq s_0$$

which, at the first order in $s - s^*$ reads as

$$s^* \geq s_0 : \quad \mathcal{E}'(s^*)(s - s^*) \geq 0, \quad \forall s \geq s_0. \tag{12.10}$$

If $s^* > s_0$, then we can take $s \geq s_0$ such that $s - s^* \geq 0$ but also $s \in (s_0, s^*)$ such that $s - s^* \leq 0$[1]. Hence, for $s^* > s_0$ the condition 12.10 implies that $\mathcal{E}'(s^*) = 0$. If $s^* = s_0$, then $s > s_0 = s^*$ implies that $s - s^* \geq 0$ and 12.10 implies only that $\mathcal{E}'(s^*) \geq 0$. Wrapping up, we have that $s^* \geq s_0$ and $\mathcal{E}'(s^*) \geq 0$. Moreover, either $s^* = s_0$ or $\mathcal{E}'(s^*) = 0$. We can synthetically write these conditions as a set of inequalities:

$$s^* - s_0 \geq 0, \qquad \mathcal{E}'(s^*) \geq 0, \qquad \mathcal{E}'(s^*)(s^* - s_0) = 0 \tag{12.11}$$

These inequalities are called Karush-Kuhn-Tucker conditions (KKT) for the unilaterally constrained optimization problem 12.9. They are *first order necessary conditions* that the solution of the minimization problem must respect. We obtain similar inequalities as soon as we have an inequality constraint. This kind of result will be used later in similar situations without explicit

[1] For example, take $s = s^* \pm (s^* - s_0)/2$)

proof.

The opposite of the derivative of the potential energy with respect to the crack length defines the energy release rate

$$G(s) := -\mathcal{E}'(s)$$

With this definition, the inequalities 12.11 write as

$$s^* \geq s_0, \qquad G(s^*) \leq G_c, \qquad (G(s^*) - G_c)\,(s^* - s_0) = 0, \tag{12.12}$$

which gives the Griffith criterion for crack propagation. It states that for the solution of the static fracture mechanics problem with a given crack path (i) the crack length cannot decrease, (ii) the energy release rate cannot exceed the fracture toughness G_c, and (iii) the crack can propagate only if $G(s^*) = G_c$. The computation of the energy release rate requires to evaluate the derivative of the potential energy of the system with respect to the crack length. In some situations, this can be done analytically, but more often G is computed numerically by solving a linear elastic problem and suitable post-processing.

The reasoning above shows that the standard Griffith criterion is a direct consequence of the energy minimization principle under an irreversibility constraint for the crack length. The variational viewpoint allows for the generalization of the model to more complex situation, including arbitrary crack patterns, anisotropic or heterogeneous media, nonlinear elasticity, cohesive fracture energy, multi-physical couplings, ...

12.3.2 Quasi-static irreversible evolutions

Let us consider the solid loaded by an imposed displacement on the boundary, whose intensity is proportional to a scalar t and monotonically increasing: $u_d(t) = t\,u_d(1)$. The loading parameter t can be assimilated with the time variable. If we assume to discretize the time variable with n steps $\{t_i\}_{i=0}^n$, knowing the crack Γ_{i-1} at the time t_{i-1}, the crack state at time t_i is found by solving the incremental minimization problem

$$(\vec{u}_i, \Gamma_i) := \underset{\vec{u}\in\mathcal{C}(\Gamma_{i-1}),\Gamma\supseteq\Gamma_{i-1}}{\operatorname{argmin}} \mathcal{E}(\vec{u}, \Gamma) \tag{12.13}$$

where $\Gamma \supseteq \Gamma_{i-1}$ translates the irreversibility condition of the crack set and implies that the surface energy $G_c\,\mathcal{S}(\Gamma)$ in 12.8 is dissipated during the evolution.

For the case of a crack on a predefined path, the first-order optimality conditions 12.11 write as:

$$s_i - s_{i-1} \geq 0, \qquad \mathcal{E}'(s_i) \geq 0, \qquad \mathcal{E}'(s_i)\,(s_i - s_{i-1}) = 0. \tag{12.14}$$

Taking the limit of 12.14 for $t_i \to t_{i-1}$, one can define a time-continuous evolution $s(t)$ that will satisfy the following evolution law at each time t:

$$\dot{s}(t) \geq 0, \qquad \mathcal{E}'(s(t)) \geq 0, \qquad \mathcal{E}'(s(t)) \cdot \dot{s}(t) = 0. \tag{12.15}$$

The "smoothness" in time is guaranteed as far as we consider evolution problems based on global energy minimality. This will not be the case when considering local minimizers. The three conditions above can be interpreted as an (i) irreversibility condition, (ii) a stability condition, and an energy balance condition (iii), typical of the theory of rate-independent evolution problems. We refer the reader to [Mielke and Roubíček, 2015] for further details on this point. In these notes, we will consider only the time-discrete version of the evolution, which is at the basis of the numerical work, see also [León Baldelli and Maurini, 2021].

12.3.3 Regularized "phase-field" variational formulation

The arbitrariness of the jump set for the displacement in eq. 12.8 renders the problem extremely complex from the theoretical and numerical standpoints. This is called a *free discontinuity problem*, for which a wealth of mathematical literature is now available [Ambrosio et al., 2000]. An efficient method for its numerical solution, initially introduced in analogue problems of image segmentation [Mumford and Shah, 1989; Ambrosio and Tortorelli, 1992], is the use of regularized formulations smearing the sharp discontinuities across bands of non-vanishing width [Braides, 1998]. Bourdin et al. [Bourdin et al., 2000] applied the Ambrosio-Tortorelli regularized formulation to the fracture mechanics problem.

This approach introduces a smooth scalar field α and the regularized energy functional

$$\mathcal{E}_\ell(\vec{u},\alpha) = \int_\Omega \left((1-\alpha)^2 + k_\ell\right) W(\boldsymbol{\varepsilon}(\vec{u}))\,\mathrm{d}x + \frac{G_c}{2}\int_\Omega \left(\frac{\alpha^2}{\ell} + \ell\,\nabla\alpha\cdot\nabla\alpha\right)\mathrm{d}x, \tag{12.16}$$

where ℓ is a scalar regularizing parameter and $k_\ell = o(\ell)$ a small residual stiffness.

The mathematical results based on the direct methods of the calculus of variations and asymptotic analysis (gamma-convergence) show that, for $\ell \to 0$, *global* minimizers of the regularized energy 12.16 tend toward *global* minimizers of the Griffith energy eq. 12.8 [Chambolle, 2003; Ambrosio and Tortorelli, 1992]. In particular, Giacomini [Giacomini, 2005] shows that the solutions of the quasi-static evolution problem eq. 12.13 may be approximated by solving at each time step the following minimization problem:

$$(\vec{u}_i,\alpha_i) \in \underset{u\in\mathcal{C}_i,\,\alpha\in\mathcal{D}(\alpha_{i-1})}{\operatorname{argmin}} \mathcal{E}(\vec{u},\alpha) \tag{12.17}$$

with

$$\mathcal{C}_i \equiv \{\vec{u}\in H^1(\Omega),\ \vec{u}=\vec{u}^d(t_i) \text{ on } \partial_u\Omega\}, \tag{12.18}$$

$$\mathcal{D}(\beta) \equiv \{\alpha\in H^1(\Omega), \alpha\geq\beta,\ \alpha=0 \text{ on } \partial_\alpha\Omega\}, \tag{12.19}$$

where we assume α to be null where Dirichlet boundary conditions on the displacement are imposed (*i.e.* $\partial_\alpha\Omega \equiv \partial_u\Omega$).

As discussed in the next section, α can be interpreted as a damage variable and the regularized energy 12.16 as the energy of a gradient damage model. The crack irreversibility translates into an *unilateral minimization* on the damage field. This model allows for the prediction of crack evolutions without *a priori* hypotheses on the crack path.

The variational approach to fracture provides a mathematical framework to study the link between damage and fracture mechanics. In this framework, the mathematical results of gamma-convergence are a cornerstone. However, direct methods of the calculus of variations and gamma-convergence give information only on global minimizers. The *global minimality* requirement is at the basis of the mathematical analysis leveraging the direct methods of the calculus of variations. Global minimality is also fundamental to retrieve crack initiation within the Griffith model and to assure the smoothness in time of the evolutions. However, *global minimality* is debatable for two reasons of opposite and complementary nature [Francfort et al., 2008]:

- In macroscopic physics, defining physically observable states as global minimizers of the energy is a too strong requirement. The common experimental evidence shows that we can observe a physical system in a meta-stable state, which is only a *local* minimum of the energy.
- The energy functional 12.16 is strongly non-convex and can have many local minima. Numerically, one can find, after space discretization, stationary points or local minimizers depending on the initial seeding point. Finding global minimizers large-scale nonlinear system with hundreds of thousand or millions of unknowns is not feasible with the current technology.

These limitations call for richer mechanical models (as cohesive fracture models or gradient damage models) and for formulations based on local energy minimality criteria, giving the interpretation of ℓ as a physical length-scale. This will be the object of the following section.

12.4 Gradient damage models and their use as a phase-field regularization of brittle fracture

We consider gradient damage models of fracture where the energy functional is in the following form

$$\mathcal{E}_\ell(\vec{u},\alpha) = \int_\Omega W(\boldsymbol{\varepsilon}(\vec{u}),\alpha)\,\mathrm{d}x + w_1 \int_\Omega \big(w(\alpha) + \ell^2\,\nabla\alpha\cdot\nabla\alpha\big)\,\mathrm{d}x - \mathcal{L}(\vec{u}), \quad (12.20)$$

with an elastic energy density in the form

$$W(\boldsymbol{\varepsilon},\alpha) = \frac{1}{2}(\mathbb{K}(\alpha):\boldsymbol{\varepsilon}):\boldsymbol{\varepsilon}, \quad \boldsymbol{\sigma} := \frac{\partial W}{\partial \boldsymbol{\varepsilon}} = \mathbb{K}(\alpha):\boldsymbol{\varepsilon}.$$

The energy functional is a slight generalization of eq. 12.16. However, we analyze here the behavior of the model for a fixed value of ℓ, and we define a solution at the time step i as an *unilateral local minimizer* of the energy above starting from the solution at the previous time step $i-1$.

$$(\vec{u}_i, \alpha_i) = \underset{(\vec{u},\alpha)\,\in\,\mathcal{C}_i\times\mathcal{D}(\alpha_{i-1})}{\arg\operatorname{loc}\min} \mathcal{E}(\hat{\vec{u}}, \hat{\alpha}), \tag{12.21}$$

where *loc min* means that the solution $(\vec{u}_i, \alpha_i) \in \mathcal{C}_i \times \mathcal{D}_i$ is such that $\forall (\vec{u}, \alpha) \in \mathcal{C}_i \times \mathcal{D}(\alpha_{i-1})$:

$$\exists \bar{h} > 0 : \quad \mathcal{E}(\vec{u}_i, \alpha_i) \leq \mathcal{E}(\vec{u}_i + h\,(\vec{u} - \vec{u}_i), \alpha_i + h\,(\alpha - \alpha_i)) \quad \forall\, h \in (0, \bar{h}). \tag{12.22}$$

Taking the first order expansion of the inequality above with respect to h one gets the first order optimality conditions:

$$\begin{cases} D_{\vec{u}}\mathcal{E}(\vec{u}_i, \alpha_i)[\vec{u} - \vec{u}_i] \geq 0, & \forall \vec{u} \in \mathcal{C}_i, \\ D_{\alpha}\mathcal{E}(\vec{u}_i, \alpha_i)[\alpha - \alpha_i] \geq 0, & \forall \alpha \in \mathcal{D}_i, \end{cases} \tag{12.23}$$

where $D_{\vec{u}}$ and D_α denote the directional derivative of the energy functional $\mathcal{E}$ with respect to the displacement and the damage, respectively, with

$$\begin{aligned} D_{\vec{u}}\mathcal{E}(\vec{u}_i, \alpha_i)[\vec{v}] &= \int_\Omega \boldsymbol{\sigma}(u) : \boldsymbol{\varepsilon}(\vec{v}) - \int_\Omega \vec{b} \cdot \vec{v}\,\mathrm{d}\Omega - \int_{\partial_f\Omega} \vec{f} \cdot \vec{v}\,\mathrm{d}S \\ D_{\alpha}\mathcal{E}(\vec{u}_i, \alpha_i)[\beta] &= \int_\Omega \left(\frac{1}{2}\left(\mathbb{K}'(\alpha) : \boldsymbol{\varepsilon}(\vec{u})\right) : \boldsymbol{\varepsilon}(\vec{u}) + w'(\alpha) \right) \beta + 2\,\ell^2 \nabla\alpha \cdot \nabla\beta\,\mathrm{d}x. \end{aligned}$$

By suitably selecting the variations $\vec{v}, \beta$ and applying standard localization arguments, one can show that, for smooth solutions, the first-order optimality condition 12.23 is equivalent to the following equilibrium equation and equilibrium boundary condition

$$\mathrm{div}\boldsymbol{\sigma} + \vec{b}_t = \vec{0} \text{ on } \Omega, \quad \boldsymbol{\sigma}.\vec{n} = \vec{f}_t \text{ on } \partial_f\Omega,$$

and to the damage criterion on the bulk Ω:

$$\alpha - \alpha_{i-1} \geq 0, \tag{12.24a}$$

$$\frac{1}{2}\mathbb{K}'(\alpha)\boldsymbol{\varepsilon}(\vec{u}) : \boldsymbol{\varepsilon}(\vec{u}) + w_1\, w'(\alpha) - 2w_1\ell^2\Delta\alpha \geq 0, \tag{12.24b}$$

$$\left(\frac{1}{2}\mathbb{K}'(\alpha)\boldsymbol{\varepsilon}(\vec{u}) : \boldsymbol{\varepsilon}(\vec{u}) + w_1\, w'(\alpha) - 2w_1\ell^2\Delta\alpha\right)(\alpha - \alpha_{i-1}) = 0, \tag{12.24c}$$

and on the boundary where the damage is not prescribed $\partial\Omega \setminus \partial_\alpha\Omega$:

$$\alpha - \alpha_{i-1} \geq 0, \quad \nabla\alpha \cdot \vec{n} \geq 0, \quad (\nabla\alpha \cdot \vec{n})(\alpha - \alpha_{i-1}) = 0 \tag{12.24d}$$

$\vec{n}$ being the outer unit normal to the boundary and $\Delta\alpha$ the Laplacian of the

damage. The equilibrium equation is obtained as for the elastic case of Section 12.2. The set of inequalities are a direct consequence of the presence of the unilateral constraint on the damage variable. They are the result of generalization to the infinite dimensional setting of the basic reasoning detailed in Section 12.3.1 for equations 12.14. For smooth-in-time solutions, equivalent conditions are obtained in a time-continuous setting as a consequence of an evolution principle based on irreversibility, energy balance, and stability. We refer the reader to [Pham and Marigo, 2010a,c; Marigo et al., 2016] for further details.

A fundamental question is to understand how the properties of the constitutive functions $\mathbb{K}(\alpha)$ and $w(\alpha)$ affect the solutions of an evolution problem. A first step is to analyze the solutions with *homogeneous damage*, which is tantamount to the analysis of the response of a material point. We focus here on the purely isotropic case where $\mathbb{K}(\alpha) = a(\alpha)\mathbb{K}_0$, where $a(\alpha)$ is an isotropic stiffness modulation. The reader can find a more general presentation in [De Lorenzis and Maurini, 2022].

Following [Pham et al., 2011b], a first important distinction is between materials showing a finite or infinite dissipation at complete failure, denoted as *weakly brittle* or *strongly brittle* materials, respectively. In *strongly brittle* materials, one can renormalize the damage variable in the interval $[0, 1]$ and assume that $a(0) = 1$, $a(1) = 1$, $w(0) = 0$, $w(1) = 1$. The constant w_1 in 12.20 can be interpreted as the energy required to fully damage a volume element, commonly denoted as *specific fracture energy* [Comi and Perego, 2001].

For homogeneous solutions with $\Delta\alpha = 0$, the damage criterion 12.24 and the stress-strain relationship imply that the domains of admissible strains and stresses are given by:

$$\begin{aligned} \mathcal{A}_{\boldsymbol{\varepsilon}}(\alpha) &= \left\{ \boldsymbol{\varepsilon} : \quad (\mathbb{K}_0\,\boldsymbol{\varepsilon}) : \boldsymbol{\varepsilon} \leq -\frac{2w_1 w'(\alpha)}{a'(\alpha)} \right\}, \\ \mathcal{A}_{\boldsymbol{\sigma}}(\alpha) &= \left\{ \boldsymbol{\sigma} : \quad \left(\mathbb{K}_0^{-1} : \boldsymbol{\sigma}\right) : \boldsymbol{\sigma} \leq \frac{2w_1 w'(\alpha)}{s'(\alpha)} \right\}, \end{aligned}$$

where $s := a^{-1}$ is the modulation of the elastic compliance. The material is said to be with

- *strain hardening* (resp. *softening*) if $\mathcal{A}_{\boldsymbol{\varepsilon}}$ is increasing (resp. *decreasing*) with α, *i.e.* if $-w'(\alpha)/a'(\alpha)$ is increasing (resp. *decreasing*),
- *stress hardening* (resp. *softening*) if $\mathcal{A}_{\boldsymbol{\sigma}}$ is increasing (resp. *decreasing*) with α, *i.e. if* $+w'(\alpha)/s'(\alpha)$ is increasing (resp. *decreasing*).

These properties are equivalent to convexity conditions of the energy density and its Legendre transform, see [Pham and Marigo, 2010b]. In [Pham et al., 2011b] and [Pham et al., 2011a], we show that to recover an energetic equivalence with Griffith brittle fracture, it is essential to use a *strongly brittle* material with *stress-softening* (see also the following Section). For stess-hardening

materials the energy (eq. 12.16) is strictly convex and the solution of the evolution problem is unique. Stress-softening is at the origin of all the interesting phenomena (and difficulties): multiple solutions, bifurcations, loss of stability. The strongly brittle behavior is necessary to obtain damage localizations with a well-defined fracture energy, assimilable to a fracture toughness.

Purely local softening damage models, corresponding to $\ell = 0$ in 12.20, are not well-posed. For a local model all the solutions are unstable in the softening regime. As shown by the gamma-convergence result, damage gradient regularization leads to a correct approximation of brittle fracture model in the limit $\ell \to 0$. This is more difficult to obtain with strain-gradient regularization. We refer the reader to [Le et al., 2018] for a specific discussion of these aspects.

The energy functional 12.16 includes as a special case the Ambrosio-Tortorellli functional 12.16 used in [Bourdin et al., 2000] to approximate the evolutions of the Griffith model 12.8. However here the *global* minimality requirement is replaced here by a *local* one. A *meta-stable* state, obtained as unilateral local minimum of the energy is accepted as stable state during an evolution. This implies that, even if global minimizers of the energy of damage models converge towards global minimizers of the Griffith energy functional 12.8, the evolutions obtained by the damage model (local minimization) and the Griffith model (global minimization) presented above may be very different. As effectively resumed by [Lancioni and Royer-Carfagni, 2009], while the original formulation of [Bourdin et al., 2000] assumes that brittle fracture is *the model* and uses the Ambrosio-Tortorelli regularisation 12.16 as *the approximation*. The damage model formulation takes the opposite viewpoint: the gradient damage model is *the model* and brittle fracture *à la* Griffith is *the approximation*.

12.4.1 Traction of a stress-softening bar: one-dimensional analysis

The study of the apparently trivial case of the traction of a one-dimensional bar discloses the basic properties of the damage models, including their ability to recover crack nucleation and their link with brittle fracture *à la* Griffith. To this end, we consider the competition of the two fundamentally different damaging modes: (i) solutions with damage *homogenous* in space, and (ii) solutions with *localized* damage. In both cases, the mechanical equilibrium imposes the stress to be constant throughout the bar. We briefly resumed below the key results and refer the reader to [Hamouche et al., 2016; Pham et al., 2011b; Le et al., 2018] for further details.

For a bar of length L with imposed end-displacements $u(0) = 0$ and $u(L) = U_t = t$, the energy 12.16 reads as

$$\mathcal{E}_\ell(u,\alpha) = \int_0^L a(\alpha) E_0 \frac{u'(x)^2}{2} \,+\, w_1 \left(w(\alpha) + \ell^2\, \alpha'(x)^2 \right) \mathrm{d}x, \tag{12.25}$$

where E_0 is the undamaged Young modulus of the material.

Repeating the passages exposed in the previous section for the case of the one-dimensional bar energy, one finds that

(i) the equilibrium equation implies that the stress

$$\sigma = E_0 a(\alpha)\,\varepsilon, \quad \varepsilon := \frac{du}{dx}$$

is a constant throughout the bar;

(ii) the damage criterion is in the form of eq. 12.24, with on $x \in (0, L)$

$$\alpha - \alpha_{i-1} \geq 0, \quad (12.26a)$$

$$\frac{E_0\, a'(\alpha)}{2}\varepsilon^2 + \left(w'(\alpha) - 2\ell^2 \frac{d^2\alpha}{dx^2}\right) w_1 \geq 0, \quad (12.26b)$$

$$\left(\frac{E_0\, a'(\alpha)}{2}\varepsilon^2 + \left(w'(\alpha) - 2\ell^2 \frac{d^2\alpha}{dx^2}\right) w_1\right)(\alpha - \alpha_{i-1}) = 0, \quad (12.26c)$$

or in terms of the stress σ

$$\alpha - \alpha_{i-1} \geq 0, \quad (12.27a)$$

$$-\frac{s'(\alpha)}{2\,E_0}\sigma^2 + \left(w'(\alpha) - 2\ell^2 \frac{d^2\alpha}{dx^2}\right) w_1 \geq 0, \quad (12.27b)$$

$$\left(-\frac{s'(\alpha)}{2\,E_0}\sigma^2 + \left(w'(\alpha) - 2\ell^2 \frac{d^2\alpha}{dx^2}\right) w_1\right)(\alpha - \alpha_{i-1}) = 0, \quad (12.27c)$$

where $s = a^{-1}$ is the compliance-modulation function.

Homogeneous solutions and their stability.

For homogeneous solutions the damage yield criterion expressed in terms of the strain or the stress σ writes as, respectively:

$$|\varepsilon| \leq \bar{\varepsilon}(\alpha) := \sqrt{\frac{w_1}{E_0}}\sqrt{\frac{-2w'(\alpha)}{a'(\alpha)}}, \qquad |\sigma| \leq \bar{\sigma}(\alpha) := \sqrt{w_1 E_0}\sqrt{\frac{2w'(\alpha)}{s'(\alpha)}}. \quad (12.28)$$

where $\bar{\varepsilon}(\alpha)$ and $\bar{\sigma}(\alpha)$ are the strain and stress limit, function of α. For a given damage level, the material is stress-hardening if $\bar{\sigma}'(\alpha) > 0$ or stress-softening if $\bar{\sigma}(\alpha) < 0$, strain-hardening if $\bar{\varepsilon}'(\alpha) > 0$ or strain-softening if $\bar{\varepsilon}(\alpha) < 0$.

Considering an evolution problem for an initially undamaged bar ($\alpha = 0$), the solution remains purely elastic until the stress reaches the *elastic limit*:

$$\sigma_e = \bar{\sigma}(0) = \sqrt{w_1 E_0}\sqrt{\frac{2w'(0)}{s'(0)}}. \quad (12.29)$$

Indeed, for smaller loading the damage criterion is verified as a strict inequality and 12.24 imposes the variations of $\alpha_i = \alpha_{i-1} = 0$. After that the elastic limit

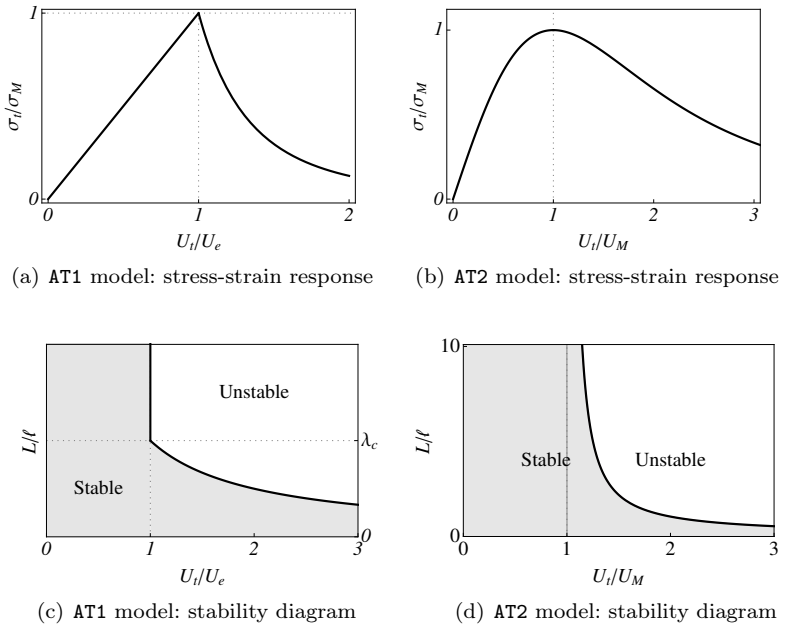

(a) `AT1` model: stress-strain response (b) `AT2` model: stress-strain response

(c) `AT1` model: stability diagram (d) `AT2` model: stability diagram

FIGURE 12.2: Response and stability of the homogenous solutions of the one-dimensional traction problem with two variants of the gradient damage model 12.25, see [Pham et al., 2011a].

is reached, the damage level is calculated by solving the damage criterion equality:

$$\alpha_{\mathrm{H}}(\varepsilon) := \bar{\varepsilon}^{-1}(\varepsilon)$$

where $\bar{\varepsilon}^{-1}$ is the inverse function of $\bar{\varepsilon}$, which is well-defined provided that the material is strain-hardening, for which $\alpha'_{\mathrm{H}}(\varepsilon) > 0$. We assume that this condition is always verified, otherwise, the homogeneous solution would be not unique. Given the damage, the stress-strain relation would be given by:

$$\sigma_{\mathrm{H}}(\varepsilon) := \bar{\sigma}(\alpha_{\mathrm{H}}(\varepsilon))$$

The maximum allowable stress in the homogeneous response is

$$\sigma_M := \max_{\varepsilon>0} \sigma_{\mathrm{H}}(\varepsilon) = \max_{0\leq\alpha\leq 1} \bar{\sigma}(\alpha). \tag{12.30}$$

Figures 12.2-top reports the homogeneous response obtained for two models used in numerical applications:

- (`AT1`): $w(\alpha) = \alpha, \quad a(\alpha) = (1-\alpha)^2$,
- (`AT2`): $w(\alpha) = \alpha^2, \quad a(\alpha) = (1-\alpha)^2$.

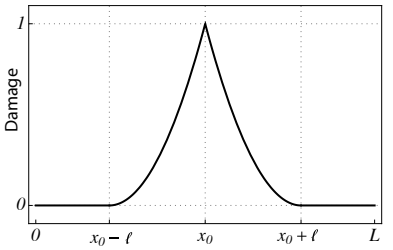

FIGURE 12.3: Localized solution with the `AT1` model: damage field along the bar.

The model (`AT2`) is particularly interesting because corresponds to the regularized approximation of Griffith proposed in [Ambrosio, 1990; Bourdin et al., 2000]. In this case, being $w'(0) = 0$, the elastic limit is null and the homogeneous response is with non-null damage for any non-vanishing loading. It show stress-hardening phase, followed by stress-softening. The model (`AT1`) has a non-null elastic limit, corresponding also to the maximal allowable stress given by $\sigma_e = \sigma_c = \sqrt{w_1 E_0}$.

The homogeneous response gives a solution to the evolution problem respecting the first order conditions 12.24. Its knowledge is important to characterize the material behavior. However the actual structural response can be different because this solution may be unstable. We analyzed point in dept in [Pham et al., 2011b], by studying for a general class of models the sign of second derivative of the energy around the homogeneous state along all admissible perturbations non-decreasing the damage. It is possible to obtain analytical expressions of the stability limits. The results for the (`AT1`) and (`AT2`) models are reported in Figures 12.2-bottom. The stability diagrams highlight a scale effect: the stability limit for the homogeneous solution depends on the ratio between the bar length L and the internal length ℓ. For short bars with ($L \ll \ell$) the homogeneous solution may be stable also in the stress-softening regime, whilst for long bars ($L \gg \ell$), it becomes unstable immediately after leaving either the elastic (`AT1`) or the stress-hardening (`AT2`) phase. We reader can find in [León Baldelli and Maurini, 2021] a numerical algorithm to perform the stability analysis of the homogeneous solution numerically and an in-depth discussion of this topic.

Localized solutions.

Localized solutions can be constructed by assuming that the damage evolves only in a segment of the bar. Because of the complementary condition in 12.24, the damage criterion must be verified as an equality in the zone where the damage evolves. In the one-dimensional case, the associated equation has a first integral and, assuming that the rest of the bar in undamaged, it reduces

to the solution of

$$-\frac{\sigma^2}{2E_0 w_1}(s(\alpha)-1)+w(\alpha)=\ell^2\alpha'^2 \tag{12.31}$$

in a segment of unknown length with $\alpha=\alpha'=0$ on the boundary. The solution of this non-linear boundary value problem gives the damage profile and the length of the damaging zone for each level of stress. The case of vanishing stress is particularly important: it is the regularized representation of a crack. For $\sigma\to 0$, the length of the localization zone, say D, and the energy dissipated in this solution, say G_c, are given by

$$D=c_{1/w}\,\ell,\qquad G_c=c_w\,w_1\,\ell. \tag{12.32}$$

where $c_{1/w}=2\int_0^1\sqrt{1/w(\alpha)}\,d\alpha$ and $c_w=4\int_0^1\sqrt{w(\alpha)}\,d\alpha$ are two dimensionless constants. Figure 12.3 reports the fully localized damage profile for the model `AT1`, for which $c_{1/w}=4$ and $c_w=8/3$. In equation 12.32 the expression for the localization length D is obtained by integrating eq. 12.31 for $\sigma=0$ on the interval $(x_0-D/2,x_0)$ where α goes from 0 to 1, where x_0 is the center of the localization zone:

$$\frac{d\alpha}{dx}=\sqrt{w(\alpha)}/\ell\Rightarrow\int_{x_0-D/2}^{x_0}\mathrm{d}x=\ell\int_0^1\frac{1}{\sqrt{w(\alpha)}}\,\mathrm{d}\alpha$$

whilst the dissipated energy is calculated with the following change of variable

$$\begin{aligned}G_c&=w_1\int_0^D w(\alpha(x))+\ell^2\alpha'(x)^2\,\mathrm{d}x=2w_1\int_0^D\ell^2\alpha'(x)^2\,\mathrm{d}x\\&=4w_1\int_{-D/2}^0\ell^2\alpha'(x)^2\,\mathrm{d}x=4w_1\int_0^1\ell^2\alpha'\,\mathrm{d}\alpha=4w_1\ell\int_0^1\sqrt{w(\alpha)}\,\mathrm{d}\alpha\end{aligned} \tag{12.33}$$

where we used that $\alpha'=\sqrt{w(\alpha)/\ell}$ for $\sigma=0$.

An explicit solution for the localization profile as a function of the stress is available for the special model with linear softening introduced in [Lorentz et al., 2012] and [Alessi et al., 2014] with

$$w(\alpha)=1-(1-\alpha)^2,\qquad a(\alpha)=\frac{1-w(\alpha)}{1+(\gamma-1)\,w(\alpha)}, \tag{12.34}$$

where $\gamma>1$ is a parameter modulating the softening response. In this model, for sufficiently long bars, the localized solution for a given stress $\sigma<\sigma_c$ has a damage field in the form, see [Alessi et al., 2014]

$$\alpha(x)=1-\sqrt{1+\left(\frac{\sigma^2}{\sigma_c^2}-1\right)\cos^2\left(\frac{x-x_0}{\ell}\right)}\qquad\text{on}\quad\left[x_0-\frac{\pi}{2}\ell;x_0+\frac{\pi}{2}\ell\right], \tag{12.35}$$

with $\sigma_c=\sqrt{2E_0w_1/\gamma}$ and $G_c=\pi w_1\ell$.

Conclusions and comparisons to Griffith.

Brittle fracture may be phenomenologically described by two key material parameters: the fracture toughness G_c, which is the energy dissipated in a crack of unit length, and the limit stress σ_c, defined as the stress level at failure in an uniaxial traction test. The results of the previous section for the traction problem show the following properties:

1. the presence of maximum admissible stress σ_M in the material response, see 12.30
2. the presence of crack-like solutions with vanishing stress and a finite dissipated energy, that can be dissipated to the fracture toughness G_c, see 12.33

A large class of models shows a similar behavior for *brittle structures* that are long enough with respect to the internal length. Our analysis concludes that the gradient damage models introduced here are good candidates to model brittle fracture if they respect three fundamental conditions: (i) *stress softening*, at least for sufficiently high damage levels, (ii) *strain hardening*, and (iii) *strongly brittle*. The existence of a non-null elastic limit ($w'(0) > 0$) is desirable for physical and computational reasons. In this sense, the model (`AT1`) is preferable over the model (`AT2`) used in [Bourdin et al., 2000]. Their response is mainly characterized by the two material parameters G_c and σ_c. For *strongly brittle materials*, the link with the Griffith's fracture model may be emphasized by replacing the volume dissipation constant w_1 with the dissipation in a localized solution G_c and rewrite the energy density in 12.20 in the form 12.16: where the internal length should be chosen to recover the correct limit stress, *i.e.* using 12.29 and 12.32 as follows:

$$\ell = \frac{2w'(0)}{s'(0)\,c_w}\frac{G_c E_0}{\sigma_c^2}. \tag{12.36}$$

For numerical applications, we often choose to retain the model (`AT1`). Indeed, it combines the simplicity of its numerical implementation with the good constitutive properties: it has an energy density quadratic with respect to α, it is strongly brittle, it has a finite elastic limit, and it shows stress-softening, and the energy is quadratic with respect to the damage variable.

Figure 12.4 reports the numerical solution for a two-dimensional version of the traction test obtained through a finite element code implementing the `AT1` model. The time history can be deduced from Figure 12.4-left, which shows the time evolution of the elastic and dissipated energy. In agreement with the analytical predictions, the solution is homogeneous and elastic for $t < t_e = t_c$. At $t = t_c$ the homogeneous solution becomes unstable and the numerical algorithm finds a new minimum of the energy corresponding to the solution with one localization (a transverse crack). For $t < t_c$ the elastic energy is a quadratic function the applied displacement (linear elasticity) and the dissipated energy is null. For $t > t_c$ the elastic energy is null and the dissipated

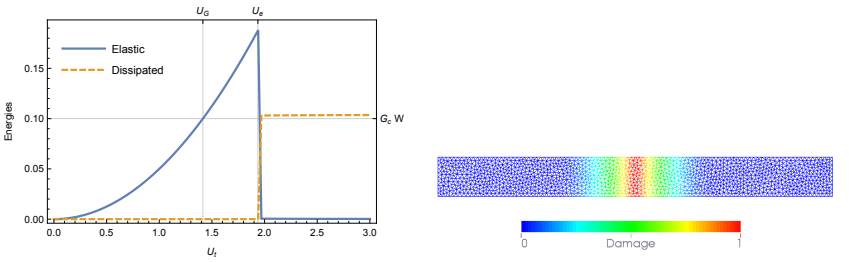

(a) Energies vs imposed displacement (b) Damage field after failure

FIGURE 12.4: Numerical simulation of the traction test using the `AT1` model ($E_0 = 1.0$, $G_c = 1.0$, $\ell = 0.1$) for a bar of length $L = 1.0$ and width $W = 0.1$. The vertical gridlines denote the analytically calculated elastic limit $t = U_e = L\sqrt{3G_c/8E_0\ell} = \sigma_c L/E_0$ and critical Griffith loading $t = U_G = \sqrt{2G_cL/E_0}$; the horizontal gridline is the dissipated energy for a transverse crack according to the Griffith model.

energy is equal to G_c times the width of the bar W, as in a Griffith model. The localization profile of Figure 12.4-right coincides with the one reported in Figure 12.3. This example is particularly useful to show that, although this kind of gradient damage models are energetically equivalent to Griffith, the evolution they predict may be different from the one given by the Griffith model. The Griffith model requires to accept global minimization as evolution law to retrieve crack nucleation. According to the global minimization criterion, the crack would appear as soon the cracked solution is energetically cheaper than the elastic solution, *i.e.* at $t_G = \sqrt{2G_cL/E_0}$ (see Figure 12.4-left). The result given by the gradient model on nucleation appears physically more acceptable because it implies the presence of limit stresses in the material. Moreover it introduces a size effect depending on the ratio between the structural size L and the internal length ℓ, which is coherent with the experimental observations. The energy of the purely elastic solution and the energy of the solution with one damage localization exactly coincide to those of the Griffith model is the internal length ℓ is sufficiently small with respect to the bar length. However, the energy barrier between the two solutions strongly depends on ℓ: the limit stress goes to infinite for $\ell \to 0$. Ignoring this energy barrier, as done in the Griffith model ruled by a global minimization principle is not acceptable.

12.4.2 Numerical implementation

In the regularized approach, the numerical solution of the quasi-static fracture/damage problem is obtained by looking for the solution of the minimization problem 12.17. This is done by an iterative method introduced in [Bourdin et al., 2000], based on the alternate minimization of the energy functional

with respect to displacement, at blocked damage field, and with respect to the damage field, at blocked displacement, until convergence, see Figure 12.5. The

Algorithm 1: Alternate minimization

Result: A stationary point of $\mathcal{E}_\ell$.
Given $(\mathbf{u}_{i-1}, \alpha_{i-1})$, the state at the previous loading step.
Set $(\mathbf{u}^{(0)}, \alpha^{(0)}) := (\mathbf{u}_{i-1}, \alpha_{i-1})$.
while *not converged* **do**
  Find $\mathbf{u}^{(p)} := \underset{\mathbf{u} \in \mathcal{C}_i}{\arg\min}\, \mathcal{E}_\ell(\mathbf{u}, \alpha^{(p-1)})$
  Find $\alpha^{(p)} := \underset{\alpha \in \mathcal{D}(\alpha_{i-1})}{\arg\min}\, \mathcal{E}_\ell(\mathbf{u}^{(p)}, \alpha)$
end
Set $(\mathbf{u}_i, \alpha_i) = (\mathbf{u}^{(p)}, \alpha^{(p)})$.

FIGURE 12.5: Alternate minimization algorithm

first sub-problem is a standard elastic problem, with the stiffness modulated by the damage field. The second sub-problem involves the minimization of a convex functional under box-constraints (the irreversibility condition on the damage field). Variational inequalities solvers are available in the open-source library PETSc [Balay et al., 2020]. For space-discretization, we employ standard finite elements with linear basis functions and uniform isotropic meshes with typical mesh size $h \sim \ell/5$. This implies the recourse to parallel computing for full-scale simulations. We refer to [Francfort et al., 2008; Farrell and Maurini, 2016] for further details and extensions of the algorithm.

12.4.3 An example of complex crack pattern: the thermal shock problem

The shrinkage of materials, induced by cooling or drying, may lead to arrays of regularly spaced cracks. Similar phenomena appearing at very different length-scales have always intrigued researchers and common people: drying of concrete, the exposure of glass or ceramics to a thermal shock, the drying of soils, or the cooling of lava fronts with the formation of columnar joints. The understanding and the predictive simulation of the morphogenesis and propagation of similar complex crack patterns is a major issue for classical fracture mechanics, which usually studies the propagation of a single pre-existing crack. Yet similar problems may be naturally tackled, theoretically and numerically, in the framework of the variational approach to damage and fracture mechanics.

We studied in [Sicsic et al., 2014; Bourdin et al., 2014] the thermal shock of a brittle slab, for which experimental results are available in [Bahr et al., 1986; Shao et al., 2010; Geyer and Nemat-Nasser, 1982]. The specimen is a thin slab, free at the boundary, composed of a homogeneous material without prestress in its initial configuration. In experiments, several slabs are stacked

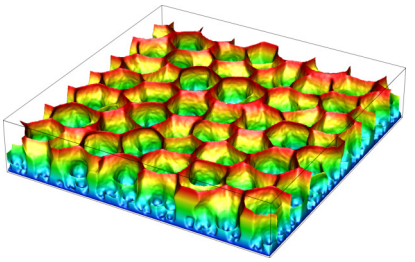

FIGURE 12.6: Complex fracture pattern for $\ell_0 = G_c/\left(EG_c\beta^2\Delta T^2\right) = 0.05\,\ell$ in a domain of size $150\ell \times 150\ell \times 20\ell$. The simulation includes 44×10^6 elements with an approximate mesh size $h = \ell/5$. To help the visualization, the crack surfaces are colored with the distance from the bottom edge, where the thermal shock is applied.

together, uniformly heated at temperature T_0 and then quenched in a cold bath inducing a temperature drop ΔT on the lateral surfaces. To include the material shrinkage induced by the thermal effects in the damage model, we consider an elastic energy density including the effect of the thermal strains:

$$W(\boldsymbol{\varepsilon}, \alpha) = \frac{a(\alpha)}{2}\left(\mathbb{K} : (\boldsymbol{\varepsilon} - \epsilon_0)\right) : (\boldsymbol{\varepsilon} - \epsilon_0) \tag{12.37}$$

where $\epsilon_0 = \beta(T_t - T_0)$ is the thermally induced inelastic deformation, β being the thermal expansion coefficient and T_t the temperature field at time t. As a first approximation, T_t is calculated as the solution of thermal evolution problem on the homogeneous undamaged solid by solving the transient heat equation. Taking a uniform temperature field T_0 as initial condition, a temperature drop ΔT is imposed on the boundary exposed to thermal shock. The dimensional analysis of the energy 12.37 highlights three characteristic lengths: the size of the domain L, the internal length ℓ, and the Griffith length $\ell_0 = G_c/\left(E\beta^2\Delta T^2\right)$. Using the material's internal length as the reference unit, the problem can be reformulated in terms of two dimensionless parameters, the size of the structure L/ℓ (a geometric parameter) and the intensity of the thermal shock ℓ_0/ℓ (a loading parameter). This is a significant departure from the classical Griffith setting where the only relevant parameter is L/ℓ_0 [Jagla, 2002; Jenkins, 2005; Bahr et al., 2010]. The time-discrete quasi-static evolution problem is solved numerically with the classical alternate minimization algorithm. Figure 12.6 shows the crack pattern generated during a three-dimensional simulation. During the simulation, a disordered pattern of small cells nucleates in the first time steps and propagates quasi-statically inside the domain with a selection mechanism that lets a more and more regular honeycomb pattern with cells of increasing diameter emerge. We refer the reader to [Sicsic et al., 2014; Bourdin et al., 2014] for further details on this problem, including comparison with experimental results and a semi-analytical treatment of the crack nucleation problem.

12.5 Extensions and current research problems

These notes give a short overview of the basic of the variational approach of fracture and damage mechanics. After [Bourdin et al., 2000], the research field has enjoyed a spectacular growth in the period between 2010 and 2020. Nowadays, the method is the largely used by the community in computational mechanics to solve complex fracture problem. A large amount of papers appeared in the last decade developed new variants of the basic model and proposed extensions of the application fields, including anisotropic materials, heterogeneous materials, viscoelasticity, large deformations, multi-physical couplings. I refrain here from giving an updated review of the literature on the topic. Instead, I provide, from a personal perspective, a list of the most important limitations of the approach presented here, pointing the reader to few references addressing the related issues:

- *Compressive loadings and multiaxial nucleation criteria.* One of the main limitation of the original Francfort-Marigo model and its regularization presented in these notes is to provide a symmetric response in traction and in compression [Amor et al., 2009; Kumar et al., 2020]. For example, reversing the sign of the loading in the traction test of Figure 12.4 would lead to the same crack evolution, but with displacements of opposite signs and the unphysical interpenetration of the crack lips. This renders the model physically admissible only for traction-cracks. This has also important implications on the crack nucleation criteria under multiaxial loading. Several models have been proposed in the literature to bypass these issues, but, to the best of my knowledge, none of them give reliable results under compressive loading. To bypass some of the difficulties of the available variational approaches, some authors propose to depart from the variational framework and formulate non-associate damage models [Kumar et al., 2020]. As a drawback they lost all the advantages of the variational theory. Vice versa, our current research effort aims at tackling the problem of crack nucleation under multiaxial loading by extending the current variational approach. We refer the reader to [Amor et al., 2009; De Lorenzis and Maurini, 2022] for a detailed discussion of this topic.

- *Coupling with plasticity and ductile fracture.* The models presented in these notes neglect plastic strains. Several models coupling plasticity and damage have been proposed in the literature [Alessi et al., 2014]. They provide interesting features and a fertile playground for further research, see also [Marigo, 2023]. The results of [Alessi et al., 2014] and [Dal Maso et al., 2016] show that the coupling between plasticity and damage provide an equivalent cohesive behavior. In our view, similar ideas can be exploited to solve the issue about nucleation under multi-axial loading within a variational framework.

- *Cohesive models.* The gradient damage models can be regarded as a smeared

version of cohesive fracture models. Eric Lorentz has shown how the modulation of the softening response of the damage model can result in the modulation of the macroscopic cohesive behavior and proposed interesting extension in this context [Lorentz et al., 2012; Lorentz, 2017].

- *Dynamics.* We assumed the evolution to be quasi-static and rate-independent, neglecting visco-elastic or inertia effects. However, this approach is not self-consistent: the solutions can be discontinuous in time, because of snap-back instabilities, like in Figure 12.4. Including inertial effects would be necessary. Extensions to dynamics have been proposed in the literature with appealing results [Bleyer and Molinari, 2017; Borden et al., 2012; Geromel fischer, 2018]. However, fundamental difficulties remain in the understanding of the properties of the solutions of the damage models when including inertial effects [Geromel fischer, 2018].

Bibliography

[Alessi et al. 2014] Alessi, R. ; Marigo, J.-J. ; Vidoli, S.: Gradient damage models coupled with plasticity: variational formulation and main properties. In: *Mechanics of Materials* (2014)

[Ambrosio 1990] Ambrosio, L.: Existence theory for a new class of varitional problems. In: *Archive for Rational Mechanics and Analysis* (1990), p. 291–322

[Ambrosio et al. 2000] Ambrosio, L. ; Fusco, N. ; Pallara, D.: *Functions of Bounded Variations and Free Discontinuity Problems*. Oxford Science Publications, 2000 (Oxford Mathematical Monographs)

[Ambrosio and Tortorelli 1992] Ambrosio, L. ; Tortorelli, V. M.: On the approximation of Free Discontinuity Problems. In: *Bollettino dell'Unione Matematica Italiana* 7 (1992), Nr. 6-B, p. 105–123

[Amor et al. 2009] Amor, H. ; Marigo, J.-J. ; Maurini, C.: Regularized formulation of the variational brittle fracture with unilateral contact: Numerical experiments. In: *Journal of the Mechanics and Physics of Solids* 57 (2009), Nr. 8, p. 1209–1229

[Bahr et al. 1986] Bahr, H.-A. ; Fischer, G. ; Weiss, H.-J.: Thermal-shock crack patterns explained by single and multiple crack propagation. In: *Journal of Materials Science* 21 (1986), p. 2716–2720

[Bahr et al. 2010] Bahr, H.-A. ; Weiss, H.-J. ; Bahr, U. ; Hoffmans, M.

; Fischer, G. ; Balke, H.: Scaling behavior of thermal shock crack patterns and tunneling cracks driven by cooling or drying. In: *Journal of the Mechanics and Physics of Solids* 58 (2010), p. 1411–1421

[Balay et al. 2020] Balay, S. ; Abhyankar, S. ; Adams, M.F. ; Brown, J. ; Brune, P. ; Buschelman, . ; Dalcin, L. ; Dener, A. ; Eijkhout, V. ; Gropp, W.D. ; Karpeyev, D. ; Kaushik, D. ; Knepley, M.G. ; May, D.A. ; McInnes, L.C. ; Mills, R.T. ; Munson, T. ; Rupp, K. ; Sanan, P. ; Smith, B.F. ; Zampini, S. ; Zhang, H. ; Zhang, H.: PETSc Users Manual / Argonne National Laboratory. 2020 (ANL-95/11 - Revision 3.13). – Technical repport

[Bleyer and Molinari 2017] Bleyer, J. ; Molinari, J.-F.: Microbranching instability in phase-field modelling of dynamic brittle fracture. In: *Applied Physics Letters* 110 (2017), Nr. 15, p. 151903

[Borden et al. 2012] Borden, Michael J. ; Verhoosel, Clemens V. ; Scott, Michael A. ; Hughes, Thomas J. ; Landis, Chad M.: A phase-field description of dynamic brittle fracture. In: *Computer Methods in Applied Mechanics and Engineering* 217-220 (2012), p. 77–95

[Bourdin et al. 2000] Bourdin, B. ; Francfort, G-A. ; Marigo, J.-J.: Numerical experiments in revisited brittle fracture. In: *Journal of the Mechanics and Physics of Solids* 48 (2000), p. 787–826

[Bourdin et al. 2014] Bourdin, B. ; Marigo, J.-J. ; Maurini, C. ; Sicsic, P.: Morphogenesis and Propagation of Complex Cracks Induced by Thermal Shocks. In: *Physical Review Letters* 112 (2014), p. 014301

[Braides 1998] Braides, A.: *Approximation of free-discontinuity problems.* Springer, 1998

[Braides 2002] Braides, A.: Γ*-convergence for beginners.* Oxford : Oxford University Press, 2002 (Oxford Lecture Series in Mathematics and its Applications **22**)

[Chambolle 2003] Chambolle, A.: A density result in two-dimensional linearized elasticity. In: *Archive for Rational Mechanics and Analysis* 167 (2003), p. 211–233

[Comi and Perego 2001] Comi, C. ; Perego, U.: Fracture energy based bidissipative damage model for concrete. In: *International Journal of Solids and Structures* 38 (2001), p. 6427–6454

[Dal Maso et al. 2016] Dal Maso, G. ; Orlando, G. ; Toader, R.: Fracture Models for Elasto-Plastic Materials as Limits of Gradient Damage Models Coupled with Plasticity: The Antiplane Case. 55 (2016), Nr. 3, p. 45

[De Lorenzis and Maurini 2022] De Lorenzis, L. ; Maurini, C.: Nucleation under multi-axial loading in variational phase-field models of brittle fracture. In: *International Journal of Fracture* 237 (2022), Nr. 1, p. 61–81

[Farrell and Maurini 2016] Farrell, P. ; Maurini, C.: Linear and nonlinear solvers for variational phase-field models of brittle fracture. In: *International Journal for Numerical Methods in Engineering* 5 (2016), Nr. 109, p. 648–667

[Francfort et al. 2008] Francfort, G.A. ; Bourdin, B. ; Marigo, J.-J.: The variational approach to fracture. In: *Journal of Elasticity* 91 (2008), Nr. 1-3, p. 5–148

[Francfort and Marigo 1993] Francfort, G.A. ; Marigo, J.-J.: Stable damage evolution in a brittle continuous medium. In: *European J. Mech. A Solids* 12 (1993), Nr. 2, p. 149–189

[Francfort and Marigo 1998] Francfort, G.A. ; Marigo, J.-J.: Revisiting brittle fracture as an energy minimization problem. In: *Journal of the Mechanics and Physics of Solids* 46 (1998), Nr. 8, p. 1319–1342

[Geromel fischer 2018] Geromel fischer, A.: *Variational approach to dynamic fracture and applications to the fragmentation of metals and ceramics*, Ecole Polytechnique, Diss., 2018

[Geyer and Nemat-Nasser 1982] Geyer, J.F. ; Nemat-Nasser, S.: Experimental Investigations of Thermally Induced Interacting Cracks in Brittle Solids. In: *International Journal of Solids and Structures* 18 (1982), Nr. 4, p. 137–356

[Giacomini 2005] Giacomini, A.: Ambrosio-Tortorelli approximation of quasi-static evolution of brittle fractures. In: *Calculus of Variations and Partial Differential Equations* 22 (2005), p. 129–172

[Griffith 1921] Griffith, A.A.: The Phenomena of Rupture and Flow in Solids. In: *Philosophical Transactions of the Royal Society A* 221 (1921), p. 163–198

[Hamouche et al. 2016] Hamouche, W. ; Maurini, C. ; Vincenti, A. ; Vidoli, S.: Basic criteria to design and produce multistable shells. In: *Meccanica* 51 (2016), p. 2305–2320

[Jagla 2002] Jagla, E.A.: Stable propagation of an ordered array of cracks during directional drying. In: *Physical Review E* (2002)

[Jenkins 2005] Jenkins, D.R.: Optimal spacing and penetration of cracks in a shrinking slab. In: *Physical Review E* (2005)

[Kumar et al. 2020] Kumar, A. ; Bourdin, B. ; Francfort, G.A. ; Lopez-Pamies, O.: Revisiting nucleation in the phase-field approach to brittle fracture. In: *Journal of the Mechanics and Physics of Solids* 142 (2020), p. 104027

[Lancioni and Royer-Carfagni 2009] Lancioni, G. ; Royer-Carfagni, G.: The Variational Approach to Fracture Mechanics. A Practical Application to the French Panthéon in Paris. In: *Journal of Elasticity* 95 (2009), p. 1–30

[Le et al. 2018] Le, D.T. ; Marigo, J.-J. ; Maurini, C. ; Vidoli, S.: Strain-gradient vs damage-gradient regularizations of softening damage models. In: *Computer Methods in Applied Mechanics and Engineering* 340 (2018), p. 424 – 450

[León Baldelli and Maurini 2021] León Baldelli, A.A. ; Maurini, C.: Numerical bifurcation and stability analysis of variational gradient-damage models for phase-field fracture. In: *Journal of the Mechanics and Physics of Solids* 152 (2021), p. 104424

[Lorentz 2017] Lorentz, E.: A nonlocal damage model for plain concrete consistent with cohesive fracture. In: *International Journal of Fracture* 207 (2017), Nr. 2, p. 123–159

[Lorentz et al. 2012] Lorentz, E. ; Cuvilliez, S. ; Kazymyrenko, K.: Modelling large crack propagation: from gradient damage to cohesive zone models. In: *International Journal of Fracture* 178 (2012), Nr. 1-2, p. 85–95

[Marigo 2023] Marigo, J.-J.: L'approche variationnelle de la rupture : un exemple de collaboration fructueuse entre mécaniciens et mathématiciens. In: *Comptes Rendus. Mécanique* (2023). – 10.5802/crmeca.170 . – Online first

[Marigo et al. 2016] Marigo, J.-J. ; Maurini, C. ; Pham, K.: An overview of the modelling of fracture by gradient damage models. In: *Meccanica* 51 (2016), dec, Nr. 12, p. 3107–3128

[Mielke and Roubíček 2015] Mielke, A. ; Roubíček, T.: *Rate-Independent Systems: Theory and Application*. Springer, 2015

[Mumford and Shah 1989] Mumford, D. ; Shah, J.: Optimal approximations by piecewise smooth functions and associated variational problems. In: *Comm. Pure and Applied Math.* 42 (1989), p. 577–685

[Pham et al. 2011a] Pham, K. ; Amor, H. ; Marigo, J.-J. ; Maurini, C.: Gradient damage models and their use to approximate brittle fracture. In: *International Journal of Damage Mechanics* 20 (2011), Nr. 4, p. 618–652

[Pham and Marigo 2010a] Pham, K. ; Marigo, J.-J.: Approche variationnelle de l'endommagement : II. Les modèles à gradient. In: *Comptes Rendus Mecanique* 338 (2010), Nr. 4, p. 199–206

[Pham and Marigo 2010b] Pham, K. ; Marigo, J.-J.: The variational approach to damage: I. The foundations [Approche variationnelle de

l'endommagement: I. Les concepts fondamentaux]. In: *Comptes Rendus Mécanique* 338 (2010), Nr. 4, p. 191–198

[Pham and Marigo 2010c] Pham, K. ; Marigo, J.-J.: The variational approach to damage: II. The gradient damage models [Approche variationnelle de l'endommagement: II. Les modèles à gradient]. In: *Comptes Rendus Mécanique* 338 (2010), Nr. 4, p. 199–206

[Pham et al. 2011b] Pham, K. ; Marigo, J.-J. ; Maurini, C.: The issues of the uniqueness and the stability of the homogeneous response in uniaxial tests with gradient damage models. In: *Journal of the Mechanics and Physics of Solids* 59 (2011), Nr. 6, p. 1163–1190

[Shao et al. 2010] Shao, Y. ; Xu, X. ; Meng, S. ; Bai, G. ; Jiang, C. ; Song, F.: Crack Patterns in Ceramic Plates after Quenching. In: *Journal of the American Ceramic Society* 93 (2010), Nr. 10, p. 3006–3008

[Sicsic et al. 2014] Sicsic, P. ; Marigo, J.-J. ; Maurini, C.: Initiation of a periodic array of cracks in the thermal shock problem: A gradient damage modeling. In: *Journal of the Mechanics and Physics of Solids* 63 (2014), Nr. 0, p. 256 – 284

13

Diffuse or sharp crack modeling?

Nicolas Moës

Ecole Centrale de Nantes et Institut Universitaire de France (IUF)

The chapter answers the above question by detailing the pros and cons of each model, both in their theoretical and computational settings. After the discussion, it is argued that the best answer is most likely in between both models. This chapter may be viewed as an argument for the next chapter devoted to the transition from a diffuse description of damage to a discrete representation of a crack.

"A continuous transition to discontinuity would be a gentle rupture" (inspired to the author by Monty Python's spirit)

13.1 Introduction

Some diffuse crack models have been discussed in detail in previous chapters. A diffuse model, often called regularized model, uses a regularization length. The regularization avoids the spurious localizations that plague purely locally models. The mathematical space in which the displacement field is sought only involves continuous fields. The displacement field exhibits however very high gradients along the crack path. The displacement has high gradient across this length to mimic a displacement discontinuity. The mesh size needs to be smaller than this length (say at least 3 to 5 elements over the regularization length). It is often thought that the introduction of a regularization length in diffuse models is governed by the sole intent to smear out the crack. It must not be forgotten that the length is also needed because the underlying bulk constitutive model is softening and requires a length to be viable theoretically and computationally. Otherwise, so-called spurious localization occurs with inadequate work dissipated values.

Contrary to diffuse crack models, sharp crack models use mathematical spaces with discontinuous displacement fields. As the crack propagates, the finite element space must adapt to allow for these discontinuities. This can be

done by meshing explicitly the crack (and adapt the mesh as cracks grow) or by keeping a fixed mesh and enrich the finite element space. The enrichment may be performed at the element level with the embedded discontinuity approach or at the nodal level with the partition of unity (extended or generalized finite element method). The displacement discontinuity may also be created in a more abrupt manner by removing elements along the crack path.

Should one use a diffuse or a sharp approach to model crack propagation? This is an interesting question for which the answer is not at all straightforward.

The chapter is organized as follows. A short bibliography on diffuse and sharp crack models is first given. This allows one to see the wide variety of existing diffuse models as well as sharp crack models. A section then discusses "Why do we compute?". This question is rather important when choosing between a diffuse or a sharp crack model. Then comes the core of the chapter : pros and cons for diffuse and sharp models. The chapter ends by the argument that the best answer lies most likely in the combination between diffuse and sharp approaches.

13.2 A short bibliography

Diffuse and sharp crack models are available in several versions.

13.2.1 Diffuse crack models

The main diffuse models are

- The non-local integral model: the evolution of the damage at a point is governed by a non-local force, calculated as the average of the local force over a certain length around the point [Bazant et al., 1984; Pijaudier-Cabot and Bazant, 1987; Lorentz and Andrieux, 2003]. Recently, a novel way to estimate this length has been proposed in the so-called eikonal approach [Rastiello et al., 2018]. A non-local integral version on the displacement field also exists [Rodríguez-Ferran et al., 2005];
- The higher order kinematic gradient model [Aifantis, 1984; Triantafyllidis and Aifantis, 1986; Schreyer and Chen, 1986] or including additional rotational degrees of freedom [Mühlhaus and Vardoulakis, 1987];
- The damage gradient model: the energy depends on the damage variable and on the damage variable and its gradient [Frémond and Nedjar, 1996; Pijaudier-Cabot and Burlion, 1996; Nguyen and Andrieux, 2005];
- Fracture was also recast in a energy minimization problem giving the so-called variational approach to fracture [Francfort and Marigo, 1998]; This

sharp model was later regularized in [Bourdin et al., 2000, 2008] using the work of Ambrosio and Tortorelli [1990];

- At about the same time, the phase-field approach was emanating from the physics community [Karma et al., 2001; Hakim and Karma, 2005, 2009] and then developed for mechanics applications [Amor et al., 2009; Miehe et al., 2010; Kuhn and Müller, 2010; Ambati et al., 2015; de Borst and Verhoosel, 2016];

- More recently, a variant to the phase-field has appeared under the name of Lip-field. The damage field needs to satisfy a Lipschitz constraint [Moës and Chevaugeon, 2021; Chevaugeon and Moës, 2021].

The gradient damage model has been compared to the non-local integral model by [Peerlings et al., 2001] and to the phase-field model by [de Borst and Verhoosel, 2016]. An energetic analysis with a comparison between different forms of regularization can also be found in [Lorentz and Andrieux, 2003]. All the above mentioned models use a length scale to regularize the local damage model. The delay damage models is an exception to this rule by making use of a regularization time. It can only be used within dynamics simulation (the regularization time gets then somehow multiplied by the wave speed to get a regularization length). The delay damage forbids damage to jump to its maximum value in a too short time. This allows damage to spread, thus creating a length effect. The delay damage was introduced in [Suffis and Combescure, 2002; Suffis et al., 2003, 2007]. It was further studied in [Zghal and Moës, 2021] showing some drawbacks of the approach.

The above presentation did concentrate on the continuum formulations. Each of them needs then to be discretized to be used by a computer. Among the models, the easiest to implement is the phase-field approach due to its variational nature. This explains its current success. A time-discretization is first performed which gives an incremental objective function. This function is then minimized using an alternate minimization. For instance, for elasto-damage models, a basic finite element solver is used to update the displacement field while another basic finite element solver updates the damage. These two solvers alternate until convergence. Then the next time-step is considered. The irreversibility of damage from one time step to the next may be taken into account by an augmented lagrangian approach [Wheeler et al., 2014] or by minimization under the proper irreversibility constraints. Another approach which is very popular is the so-called "Miehe Trick" [Miehe et al., 2010] which changes the functional to be minimized for a simpler treatment of the irrerversibility. The Miehe trick is easy to implement and this explains its success. By modifying the functional, it loses however the Gamma convergence property of the approach for the Griffith model.

13.2.2 Sharp crack models

Let us now give a short bibliography on the sharp crack models. The Griffith model [Griffith, 1920] is undoubtedly the first one chronologically speaking. A sharp crack is considered inside an elastic bulk and the crack is driven by a critical energy release rate. This energy is related to the stress intensity factors which can be used to determine the crack path.

The Griffith model was generalized later by the notion of cohesive zone which removes the crack tip singularity by spreading its effect over some length called the process zone length. The process zone is an area in front of the crack tip where the material degrades progressively. If the process zone is of non-negligible size compared to the size of the structure (and of the crack), the Griffith model is no longer valid and needs to be replaced by the cohesive zone model which introduces a characteristic length.

A cohesive model dedicated to quasi-brittle material was developed by Barenblatt [Barenblatt, 1959] and another one for ductile materials was developed by Dugdale [Dugdale, 1960]. The cohesive model is a rather simpler model than most diffuse models but yet is able to represent complex phenomena as size effect in the fracture of concrete. This led to a great popularity of the approach. It is also very much used for fragmentation analysis.

Griffith and cohesive models may be recast as energy minimization problems [Francfort and Marigo, 1998] giving the so-called variational approach to fracture. Finally, this diffuse and sharp models short bibliography needs also to mention the peridynamics approach [Silling, 2000; Javili et al., 2018] which is hard to classify since it does not rely on a continuum based model but rather on a set of points spread over the domain.

The most common numerical method to discretize the above sharp models is the finite element method (or its extensions). At some point in the past the meshless approach or the boundary element method were also popular. In the use of finite elements, there are three main possibilities.

- Keep a fixed mesh and let the crack travel along element edges by creating double nodes. This leads to a non-physical dependence between mesh orientation and crack path. This approach is however used for large simulation of fragmentation with many fragments because it is the only possible way so far to give answers in a reasonable amount of time.

- Remesh to align to the crack path. Remeshing tools have made huge progress in the past 25 years and are now able to follow complex 3D crack paths. There is however the issue of projecting the solution from one mesh to another mesh that needs to be handled with care.

- Keep the mesh fixed but let the crack enter the elements. This can be done either by the crack band model [Bazant and Oh, 1983], the embedded discontinuity approach [Simo et al., 1993] or more evolved enrichment strategy that are detailed below. Note that the crack band model is a way to implement easily cohesive zone models without creating double nodes. The crack

is assumed to run inside a layer of elements. This model is however quite sensitive to mesh orientation.

Enrichment strategies are based on the partition of unity method [Melenk and Babuska, 1996] which allows to embed extra approximation functions inside finite elements. If these functions are chosen discontinuous or singular, they can be used to represent the crack path or its tip. This leads to the extended finite element method (X-FEM) [Moës et al., 1999] or generalized finite element method (GFEM) [Duarte et al., 2001]. Another point of view on crack inside elements is given by duplicating the cut elements and providing a distinct approximation on each side [Hansbo and Hansbo, 2002, 2004; Molino et al., 2004; Burman and Hansbo, 2012; Burman et al., 2015].

Finally, still in the category of keeping the mesh fixed but the letting cracks go inside elements, the crudest approach is the kill element method which is highly mesh orientation dependent. A more evolved approach in the kill element family is the eigenerosion [Pandolfi and Ortiz, 2012].

13.3 Why do we compute ?

Choosing between diffuse and sharp crack models depends on the type of problem at stake. We detail in this section, several big families of situation for computational fracture: fatigue, dynamic loading, monotonic loading and, finally, manufacturing processes.

Fatigue

Metallic parts placed under contact in a vibrating environment will eventually be subject to crack propagation. This is a big concern for instance in bearings. The contact zone between the parts is composed of a sticking zone (no relative displacement) and a sliding zone. The crack appears in the sliding zone and propagates inside one of the parts. The number of cycles needed for a crack to appear and its afterwards path are the two main goals of fretting fatigue simulations [Baietto et al., 2013]. These simulations are still a big challenge for three main reasons. First, the sliding contact needs to be solved precisely. Then, cracks nucleate and grow under pressure. The crack faces are themselves under contact and sliding. Finally, due to the very large number of cycles, they may not be all individually computed, and "jump cycle" strategies are needed.

Another area in which contact, friction and fatigue are present is the rolling contact [Mai et al., 2017]. For instance the recurring passage of the train wheels on the rails may here and there provoke cracks.

Aside from fretting fatigue or rolling contact, fatigue on its own is already highly complex. The number of cycles needed for a crack to nucleate depends on the loading type and the material at stake. Current models recognize that a

simple stress intensity factor approach does not allow to match experiments. Realistic models need to introduce T-stress effects as well as plastic effects around the crack tip.

Fatigue is crucial in many applications where safety is an issue. Aircraft engines are subjected to fatigue loading with take-off and landing cycles which adds up to the fact that the rotor is turning. This is similar to gas turbine in nuclear plants. For these components, the importance is how often maintenance needs to be carried out. A too long period between two maintenance operations creates a hazard and too many maintenance operations is not economically viable. A trade-off needs to be built from a scientific standpoint. The main question is: how many flights (or cycles for gas turbines) are needed for a defect not initially detected to become detectable? Simulation tools are key to answer this question.

On the bright side of fatigue, small strain and displacement assumptions are usually valid and the crack paths are not too complex from the topological point of view (maybe branching but rare coalescence and a limited number of cracks).

Dynamic loading

Consider a metallic ring expanding at a given radial velocity. This velocity may for instance be created by an electromagnetic field. At some point, in the expansion, the ring will break into fragments. The higher the expansion velocity, the more fragments will be generated. When a crack appears, an unloading wave is sent out. The neighboring zones are subject to the further ring expansion as well as the incoming unloading waves. It is the combination of these two phenomena that determines the fragment sizes. Ring expansions are rather academic examples of fragmentation. Yet, they are very useful to test computational tools for fragmentation. Getting the proper number of fragments, their sizes and ejection velocities is a challenge.

A less academic example is the destruction of satellites under impact. The impact creates a huge amount of debris with different size and velocities. Knowing the space map of these debris to collect or avoid them is very important for the safety of spatial navigation.

Monotonic loading

Monotonic loading is the focus of the MEALOR II summer school. Monotonic loading, just by the name, may seem simpler to handle than the fatigue and dynamic loading case. There are however difficulties hidden behind this peaceful word. A monotonic loading means that one considers a loading that grows slowly with some given speed and "direction". Even though the loading is slow, the response may not always be quasi-static. At some point in time, kinetic energy may grow abruptly. Consider a bar stretched with an imposed displacement through a spring. The spring may be viewed as a model for the stiffness of the testing machine imposing the displacement and we can view

the bar as the specimen being tested. If the machine stiffness is higher than the bar stiffness, a quasi-static response is expected. But, if the machine stiffness is lower than the bar stiffness, the quasi-static response will be highly dynamical when rupture occurs. The reason is that the system has stored a big amount of elastic energy prior to failure and this amount is much bigger than the amount of energy needed to break the specimen. The left over energy not dissipated by failure is transformed into kinetic energy. Note that the above discussion is also connected to earthquake for which the loading is slow and gradually stores energy in the ground close to geological faults.

Manufacturing processes

We end the description with this peculiar but rather important area for fracture mechanics. A crack is not always a disappointing phenomenon. For fabrication, the crack is an ally to transform the shape of raw materials and produce parts. Blanking, piercing, boring, tool machining are processes in which cracks appear. High deformation is at stake and especially shear deformation leading to shear bands and then to fracture. What is the surface quality of the cut? What is the level of springback? How much energy is involved in the process and how can it be optimized? These are important questions in the control and optimization of manufacturing processes.

The four areas discussed above are for sure non exhaustive. We could for instance add the topic of fracture mechanics for health and biology (tissue cutting, bone fracture, kidney stone fracturing, ...).

13.4 Pros and cons

The strength of diffuse models is to handle complex crack patterns, crack nucleation and provide results rather independent on mesh orientation On the contrary, the Griffith model cannot handle crack initiation and the cohesive zone models is quite sensitive to mesh orientation if the mesh is fixed and does not adapt. However, the lack of sharp crack faces inside diffuse damage zones leads to difficulties reported in the literature. The most obvious one is the need to have fine meshes along crack paths to capture the high displacement gradients even far away from active crack fronts, leading to very high computational costs. Another limitation is related to the tension-compression asymmetric response of the damage model which is introduced in the elastic energy density. The common ones are isotropic (volumetric-deviatoric decomposition or spectral splits) and do not account for the crack orientation. As a consequence, as damage reaches its limit, the crack boundary conditions without contact (zero tension and shear) are not satisfied, leading to unphysical response [Strobl and Seelig, 2015, 2016]. Besides that, due to the limited

finite element kinematics, mesh orientation dependency appears [Strobl and Seelig, 2018]. Another important limitation of the diffuse models is the lack of access to accurate crack openings. This is problematic for instance for hydraulic fracturing in which the flow scales with the cube of the crack opening. A slight error in the opening gives a rather large error on the flow. Finally, the absence of clear discontinuity renders it difficult to impose contact and friction. Contact and friction are for examples particularly important for crack growth under rolling contact or fretting fatigue.

Following this discussion, we give a more exhaustive lists of pros and cons.

Pros for the diffuse crack models

- Ability to represent very complex crack path or networks of cracks (branching, coalescence) as well as the nucleation process.
- Simplified implementation (no jump representation).
- Ability to take into account triaxiality effects that would be complicated to do in a purely discontinuous approach.
- Ability to use complex bulk constitutive models.

Cons for the diffuse crack models

- Need to use small elements along the crack to represent the high gradients.
- Locking effects in tension-compression asymmetric models (impossibility to reach zero shear stresses).

Pros for the sharp crack models

- Natural limitation of the level of deformation and distortion in the elements (good property for ductile failure).
- Ability to coarsen the mesh.
- Gives realistic surfaces for fragmentation, cutting, machining, ...
- Direct access to the displacement jump on the crack faces (important to set up mechanical conditions such as contact, friction, hydraulic loads, ...).
- The mathematical proof of Gamma convergence is not necessary because the displacement jump is present in the formulation.

Cons for the sharp crack models

- The management of the displacement jumps clearly adds complexity to the implementation. It requires enrichment in the X-FEM/GFEM setting or remeshing in the traditional FEM setting.
- The management of branching and coalescence points is a complex issue.

13.5 The best of both worlds

We have seen in the previous section that there are pros and cons to both diffuse and sharp crack models. It would be nice to keep only the pros by combining the two models.

There are two ways to do this. One way is to create a unified model that is both diffuse and sharp, thus a model that is able to take into account softening and then be able to drive the localization to a sharp discontinuity (and tell X-FEM where to inject the jump). A model belonging to this hybrid category exists and is called the Thick Level Set approach to fracture [Moës et al., 2011]. In this model, the damage is forced to be linked to a level set field. The zero level set corresponds to the damage front and the l_c level set is the crack location where l_c is the regularizing length. Although it has theoretical advantages, the TLS model did not create breakthrough because it is rather tedious to implement and after years of studies, robustness issues have emerged. These are related to the non-convexity of the formulation with respect to the damage variable. This non convexity was first noticed by Stolz and Fremond [Frémond and Stolz, 2017].

A second way to gather the pros of both diffuse and sharp crack models is to transition from a diffuse to a sharp crack model. There has been a sustained effort in the past 20 years to introduce sharp crack faces inside diffuse damage zones, mainly in two directions. The first one is frequent remeshing to follow the crack [Feld-Payet et al., 2015; Hussein et al., 2020; Eldahshan et al., 2021]. The second one is through enrichment with discontinuous approximation functions over a fixed mesh. Early studies were performed by [Simone et al., 2003] who modeled the transition from non-local damage to sharp cracks, and by [Comi et al., 2007] who used enrichment functions in the X-FEM to facilitate the transition from a damage model to a cohesive zone model. We also mention the contribution of [Seabra et al., 2012] who placed discontinuity surfaces in plastic zones for ductile failure, as well as the works [Tamayo-Mas and Rodríguez-Ferran, 2014; Tamayo-Mas and Rodriguez-Ferran, 2015] that placed them in damage zones. More recent works may also be found in [Geelen et al., 2018; Wang and Waisman, 2016; Giovanardi et al., 2017; Muixí et al., 2021].

The next chapter discuss in details how to transition from a diffuse description of damage to ta discrete representation of a crack.

Bibliography

[Aifantis 1984] Aifantis, E.: On the structural origin of certain inelastic models. In: *Journal of Engineering Materials and Technology* 106 (1984),

p. 326–330

[Ambati et al. 2015] Ambati, M. ; Gerasimov, T. ; De Lorenzis, L.: Phase-Field Modeling of Ductile Fracture. In: *Computational Mechanics* 55 (2015), Nr. 5, p. 1017–1040. – 10.1007/s00466-015-1151-4 . – ISSN 1432–0924

[Ambrosio and Tortorelli 1990] Ambrosio, L. ; Tortorelli, V.M.: Approximation of Functional Depending on Jumps by Elliptic Functional via Gamma-Convergence. In: *Communications on Pure and Applied Mathematics* 43 (1990), Dezember, Nr. 8, p. 999–1036. – 10.1002/cpa.3160430805 . – ISSN 00103640, 10970312

[Amor et al. 2009] Amor, H. ; Marigo, J.-J. ; Maurini, C.: Regularized Formulation of the Variational Brittle Fracture with Unilateral Contact: Numerical Experiments. In: *Journal of the Mechanics and Physics of Solids* 57 (2009), Nr. 8, p. 1209–1229. – 10.1016/j.jmps.2009.04.011 . – ISSN 00225096

[Baietto et al. 2013] Baietto, M.C. ; Pierres, E. ; Gravouil, A. ; Berthel, B. ; Fouvry, S. ; Trolle, B.: Fretting fatigue crack growth simulation based on a combined experimental and XFEM strategy. In: *International Journal of Fatigue* 47 (2013), feb, p. 31–43. – 10.1016/j.ijfatigue.2012.07.007 . – ISSN 01421123

[Barenblatt 1959] Barenblatt, G.I: The Formation of Equilibrium Cracks during Brittle Fracture. General Ideas and Hypotheses. Axially-symmetric Cracks. In: *Journal of Applied Mathematics and Mechanics* 23 (1959), Januar, Nr. 3, p. 622–636. – 10.1016/0021-8928(59)90157-1 . – ISSN 00218928

[Bazant et al. 1984] Bazant, Z. ; Belytschko, T. ; Chang, T.: Continuum theory fo strain-softening. In: *Journal of Engineering Mechanics* 110 (1984), p. 1666–1692

[Bazant and Oh 1983] Bazant, Z.P. ; Oh, B.H.: Crack band theory for fracture of concrete. In: *Materials and Structures* 16 (1983), Nr. 93, p. 155–177. – ISSN 1871–6873

[de Borst and Verhoosel 2016] Borst, R. de ; Verhoosel, C.V.: Gradient damage vs phase-field approaches for fracture: Similarities and differences. In: *Computer Methods in Applied Mechanics and Engineering* 312 (2016), p. 78–94. – 10.1016/j.cma.2016.05.015 . – ISSN 00457825

[Bourdin et al. 2000] Bourdin, B. ; Francfort, G.A. ; Marigo, J.-J.: Numerical experiments in revisited brittle fracture. In: *Journal of the Mechanics and Physics of Solids* 48 (2000), April, Nr. 4, p. 797–826. – 10.1016/S0022-5096(99)00028-9 . – ISSN 00225096

[Bourdin et al. 2008] Bourdin, B. ; Francfort, G.A. ; Marigo, J.-J.: The Variational Approach to Fracture. In: *Journal of Elasticity* 91 (2008), März, p. 5–148. – 10.1007/s10659-007-9107-3 . – ISBN 1065900791

[Burman et al. 2015] Burman, E. ; Claus, S. ; Hansbo, P. ; Larson, M.G. ; Massing, E.: CutFEM: Discretizing geometry and partial differential equations. In: *International journal for numerical methods in engineering* 104 (2015), p. 472–501

[Burman and Hansbo 2012] Burman, E. ; Hansbo, P.: Fictitious domain finite element methods using cut elements: II. A stabilized Nitsche method. In: *Applied Numerical Mathematics* 62 (2012), Nr. 4, p. 328–341. – 10.1016/j.apnum.2011.01.008 . – ISSN 01689274

[Chevaugeon and Moës 2021] Chevaugeon, N. ; Moës, N.: Lipschitz regularization for fracture: the Lip-field approach. In: *Computer methods in applied mechanics and engineering* (2021), November. – 10.48550/arxiv.2111.04771 . – arXiv: 2111.04771

[Comi et al. 2007] Comi, C. ; Mariani, S. ; Perego, U.: An extended FE strategy for transition from continuum damage to mode I cohesive crack propagation. In: *International Journal for Numerical and Analytical Methods in Geomechanics* 31 (2007), Nr. 2, p. 213–238. – 10.1002/nag.537 . – ISSN 03639061

[Duarte et al. 2001] Duarte, C A. ; Hamzeh, O N. ; Liszka, T J. ; Tworzydlo, W W.: A Generalized Finite Element Method for the Simulation of Three- Dimensional Dynamic Crack Propagation. In: *Computer Methods in Applied Mechanics and Engineering* (2001)

[Dugdale 1960] Dugdale, D. S.: Yielding of Steel Sheets Containing Slits. In: *Journal of the Mechanics and Physics of Solids* 8 (1960), Mai, Nr. 2, p. 100–104. – 10.1016/0022-5096(60)90013-2 . – ISSN 0022–5096

[Eldahshan et al. 2021] Eldahshan, H. ; Alves, J. ; Bouchard, P.O. ; Perchat, E. ; Munoz, D.P.: CIPFAR: A 3D unified numerical framework for the modeling of ductile fracture based on the phase field model and adaptive remeshing. In: *Computer Methods in Applied Mechanics and Engineering* 387 (2021), p. 114171. – 10.1016/j.cma.2021.114171 . – ISSN 00457825

[Feld-Payet et al. 2015] Feld-Payet, S. ; Chiaruttini, V. ; Besson, J. ; Feyel, F.: A new marching ridges algorithm for crack path tracking in regularized media. In: *International Journal of Solids and Structures* 71 (2015), p. 57–69. – 10.1016/j.ijsolstr.2015.04.043 . – ISSN 0020–7683

[Francfort and Marigo 1998] Francfort, G.A. ; Marigo, J.-J.: Revisiting brittle fracture as an energy minimization problem. In: *Journal of the Mechanics and Physics of Solids* 46 (1998), p. 1319–1412

[Frémond and Nedjar 1996] Frémond, M. ; Nedjar, B.: Damage, gradient of damage and principle of virtual power. In: *International Journal of Solids and Structures* 33 (1996), Nr. 8, p. 1083–1103

[Frémond and Stolz 2017] Frémond, M. ; Stolz, C.: On Alternative Approaches for Graded Damage Modelling. In: Frémond, Michel (Hrsg.) ; Maceri, Franco (Hrsg.) ; Vairo, Giuseppe (Hrsg.): *Models, Simulation, and Experimental Issues in Structural Mechanics* Bd. 8. Cham : Springer International Publishing, 2017. – ISBN 978–3–319–48883–7 978–3–319–48884–4, p. 87–104

[Geelen et al. 2018] Geelen, R.J.M. ; Liu, Y. ; Dolbow, J.E. ; Rodríguez-Ferran, A.: An optimization-based phase-field method for continuous-discontinuous crack propagation. In: *International Journal for Numerical Methods in Engineering* 116 (2018), Nr. 1, p. 1–20. – 10.1002/nme.5911

[Giovanardi et al. 2017] Giovanardi, B. ; Scotti, A. ; Formaggia, L.: A hybrid XFEM –Phase field (Xfield) method for crack propagation in brittle elastic materials. In: *Computer Methods in Applied Mechanics and Engineering* 320 (2017), Nr. 41, p. 396–420. – 10.1016/j.cma.2017.03.039 . – ISSN 00457825

[Griffith 1920] Griffith, A.A.: VI. The phenomena of rupture and flow in solids. In: *Philosophical Transactions of the Royal Society of London. Series A* 221 (1920), Nr. 582-593, p. 163–198. – 10.1098/rsta.1921.0006 . – ISSN 0264–3952, 2053–9258

[Hakim and Karma 2005] Hakim, V. ; Karma, A.: Crack Path Prediction in Anisotropic Brittle Materials. In: *Physical Review Letters* 95 (2005), Dezember, Nr. 23, p. 235501. – 10.1103/PhysRevLett.95.235501 . – ISSN 0031–9007

[Hakim and Karma 2009] Hakim, V. ; Karma, A.: Laws of crack motion and phase-field models of fracture. In: *Journal of the Mechanics and Physics of Solids* 57 (2009), Februar, Nr. 2, p. 342–368. – 10.1016/j.jmps.2008.10.012 . – ISSN 00225096

[Hansbo and Hansbo 2002] Hansbo, A. ; Hansbo, P.: An unfitted finite element method, based on Nitsche's method, for elliptic interface problems. In: *Computer Methods in Applied Mechanics and Engineering* 191 (2002), 5537–5552. `http://linkinghub.elsevier.com/retrieve/pii/S0045782502005248`

[Hansbo and Hansbo 2004] Hansbo, A. ; Hansbo, P.: A finite element method for the simulation of strong and weak discontinuities in solid mechanics. In: *Computer Methods in Applied Mechanics and Engineering* 193 (2004), Nr. 33-35, p. 3523–3540. – 10.1016/j.cma.2003.12.041 . – ISSN 00457825

[Hussein et al. 2020] Hussein, A. ; Hudobivnik, B. ; Wriggers, P.: A combined adaptive phase field and discrete cutting method for the prediction of crack paths. In: *Computer Methods in Applied Mechanics and Engineering* 372 (2020), p. 113329. – 10.1016/j.cma.2020.113329 . – ISSN 00457825

[Javili et al. 2018] Javili, A. ; Morasata, R. ; Oterkus, E. ; Oterkus, S.: Peridynamics Review. In: *Mathematics and Mechanics of Solids* 24 (2018), Nr. 11, p. 3714–3739. – ISSN 1081–2865

[Karma et al. 2001] Karma, A. ; Kessler, D. ; Levine, H.: Phase-Field Model of Mode III Dynamic Fracture. In: *Physical Review Letters* 87 (2001), Juli, Nr. 4, p. 045501. – 10.1103/PhysRevLett.87.045501 . – ISSN 0031–9007

[Kuhn and Müller 2010] Kuhn, C. ; Müller, R.: A Continuum Phase Field Model for Fracture. In: *Engineering Fracture Mechanics* 77 (2010), Nr. 18, p. 3625–3634. – 10.1016/j.engfracmech.2010.08.009 . – ISSN 00137944

[Lorentz and Andrieux 2003] Lorentz, E. ; Andrieux, S.: Analysis of non-local models through energetic formulations. In: *International Journal of Solids and Structures* 40 (2003), p. 2905–2936. – 10.1016/S0020-7683(03)00110-0

[Mai et al. 2017] Mai, S. H. ; Gravouil, A. ; Nguyen-Tajan, M. L. ; Trollé, B.: Numerical simulation of rolling contact fatigue crack growth in rails with the rail bending and the frictional contact. In: *Engineering Fracture Mechanics* 174 (2017), p. 196–206. – 10.1016/j.engfracmech.2016.12.019 . – ISSN 00137944

[Melenk and Babuska 1996] Melenk, J.M. ; Babuska, I.: The partition of unity finite element method: Basic theory and applications. In: *Computer Methods in Applied Mechanics and Engineering* 139 (1996), p. 289–314

[Miehe et al. 2010] Miehe, C. ; Hofacker, M. ; Welschinger, F.: A Phase Field Model for Rate-Independent Crack Propagation: Robust Algorithmic Implementation Based on Operator Splits. In: *Computer Methods in Applied Mechanics and Engineering* 199 (2010), November, Nr. 45-48, p. 2765–2778. – 10.1016/j.cma.2010.04.011 . – ISSN 00457825

[Moës et al. 2011] Moës, N. ; Stolz, C. ; Bernard, P.-E. ; Chevaugeon, N.: A Level Set Based Model for Damage Growth: The Thick Level Set Approach. In: *International Journal for Numerical Methods in Engineering* 86 (2011), April, Nr. 3, p. 358–380. – 10.1002/nme.3069 . – ISSN 00295981

[Molino et al. 2004] Molino, N. ; Bao, Z. ; Fedkiw, R.: A virtual node algorithm for changing mesh topology during simulation. In: *ACM Transactions on Graphics (TOG)* 1 (2004), Nr. 212, 385–392. `http://portal.acm.org/citation.cfm?id=1015706.1015734`

[Moës and Chevaugeon 2021] Moës, N. ; Chevaugeon, N.: Lipschitz regularization for softening material models: the Lip-field approach. In: *Comptes Rendus Mécanique* 349 (2021), August, Nr. 2, p. 415–434. – 10.5802/crmeca.91 . – ISSN 1873–7234

[Moës et al. 1999] Moës, N. ; Dolbow, J. ; Belytschko, T.: A finite element method for crack growth without remeshing. In: *International Journal for Numerical Methods in Engineering* 46 (1999), Nr. 1, p. 131–150. – 10.1002/(SICI)1097-0207(19990910)46:1<131::AID-NME726>3.0.CO;2-J . – ISSN 1097–0207

[Mühlhaus and Vardoulakis 1987] Mühlhaus, H. B. ; Vardoulakis, L: The thickness of shear bands in granular materials. In: *Geotechnique* (1987)

[Muixí et al. 2021] Muixí, A. ; Marco, O. ; Rodríguez-Ferran, A. ; Fernández-Méndez, S.: A combined XFEM phase-field computational model for crack growth without remeshing. In: *Computational Mechanics* 67 (2021), Nr. 1, p. 231–249. – 10.1007/s00466-020-01929-8 . – ISSN 14320924

[Nguyen and Andrieux 2005] Nguyen, Q.S. ; Andrieux, S.: The non-local generalized standard approach: a consistent gradient theory. In: *Comptes rendus de l'Académie des sciences: Mécanique, physique, chimie, astronomie* 333 (2005), p. 139–145. – 10.1016/j.crme.2004.09.010

[Pandolfi and Ortiz 2012] Pandolfi, A. ; Ortiz, M.: An eigenerosion approach to brittle fracture. In: *International Journal for Numerical Methods in Engineering* 92 (2012), November, Nr. 8, p. 694–714. – 10.1002/nme.4352 . – ISSN 00295981

[Peerlings et al. 2001] Peerlings, R. ; Geers, M.G.D. ; De Borst, R. ; Brekelmans, W.A.M.: A critical comparison of nonlocal and gradient-enhanced softening continua. In: *International Journal of Solids and Structures* 38 (2001), Nr. 44-45, p. 7723–7746

[Pijaudier-Cabot and Bazant 1987] Pijaudier-Cabot, G. ; Bazant, Z.: Non local damage theory. In: *Journal of Engineering Mechanics* 113 (1987), p. 1512–1533

[Pijaudier-Cabot and Burlion 1996] Pijaudier-Cabot, G. ; Burlion, N.: Damage and localisation in elastic materials with voids. In: *Cohesive-frictional Materials* 144 (1996), p. 129–144

[Rastiello et al. 2018] Rastiello, G. ; Giry, C. ; Gatuingt, F. ; Desmorat, R.: From diffuse damage to strain localization from an Eikonal Non-Local (ENL) Continuum Damage model with evolving internal length. In: *Computer Methods in Applied Mechanics and Engineering* 331 (2018), p. 650–674. – 10.1016/j.cma.2017.12.006 . – ISSN 00457825

[Rodríguez-Ferran et al. 2005] Rodríguez-Ferran, A. ; Morata, I. ; Huerta, A.: A new damage model based on non-local displacements. In: *International Journal for Numerical and Analytical Methods in Geomechanics* 29 (2005), Nr. 5, p. 473–493. – 10.1002/nag.422 . – ISSN 03639061

[Schreyer and Chen 1986] Schreyer, HL ; Chen, Z: One-dimensional softening with localization. In: *Journal of Applied Mechanics* (1986)

[Seabra et al. 2012] Seabra, M.R.R. ; Šuštarič, P. ; Cesar de Sa, J.M.A. ; Rodič, T.: Damage driven crack initiation and propagation in ductile metals using XFEM. In: *Computational Mechanics* (2012), oct, p. 161–179. – 10.1007/s00466-012-0804-9 . – ISBN 0046601208049

[Silling 2000] Silling, S.A.: Reformulation of Elasticity Theory for Discontinuities and Long-Range Forces. In: *Journal of the Mechanics and Physics of Solids* 48 (2000), Nr. 1, p. 175–209. – 10.1016/S0022-5096(99)00029-0 . – ISSN 00225096

[Simo et al. 1993] Simo, J. C. ; Oliver, J. ; Armero, F.: An Analysis of Strong Discontinuities Induced by Strain-Softening in Rate-Independent Inelastic Solids. In: *Computational Mechanics* 12 (1993), Nr. 5, p. 277–296. – 10.1007/BF00372173 . – ISSN 0178–7675, 1432–0924

[Simone et al. 2003] Simone, A. ; Wells, G.N. ; Sluys, L.: From continuous to discontinuous failure in a gradient-enhanced continuum damage model, Comput. In: *Computer Methods in Applied Mechanics and Engineering* 192 (2003), p. 41–42

[Strobl and Seelig 2015] Strobl, M. ; Seelig, T.: A novel treatment of crack boundary conditions in phase field models of fracture. In: *Pamm* 15 (2015), Nr. 1, p. 155–156. – 10.1002/pamm.201510068

[Strobl and Seelig 2016] Strobl, M. ; Seelig, T.: On constitutive assumptions in phase field approaches to brittle fracture. In: *Procedia Structural Integrity* 2 (2016), p. 3705–3712. – 10.1016/j.prostr.2016.06.460 . – ISSN 24523216

[Strobl and Seelig 2018] Strobl, M. ; Seelig, T.: Restrictions in phase field modeling of brittle fracture. In: *Proceedings in applied mathematics and mechanics* 18 (2018), Nr. 1, p. e201800157. – 10.1002/pamm.201800157

[Suffis and Combescure 2002] Suffis, A. ; Combescure, A.: Modèle d'endommagement à effet retard: Etude numérique et analytique de l'évolution de la longueur caractéristique. In: *Revue Européenne des Éléments Finis* 11 (2002), Januar, Nr. 5, p. 593–619. – 10.3166/reef.11.593-619 . – ISSN 1250–6559

[Suffis et al. 2007] Suffis, A. ; Combescure, A. ; Chevrier, P.: A delayed damage model for the prediction of dynamic fracture experiments: Application on metallic structures. In: *European Journal of Computational Mechanics* 16 (2007), Januar, Nr. 5, p. 601–625. – 10.3166/remn.16.601-625 . – ISSN 1779–7179, 1958–5829

[Suffis et al. 2003] Suffis, A. ; Lubrecht, T.A.A. ; Combescure, A.: Damage Model with Delay Effect. In: *International Journal of Solids and*

Structures 40 (2003), Juni, Nr. 13-14, p. 3463–3476. – 10.1016/S0020-7683(03)00153-7 . – ISSN 00207683

[Tamayo-Mas and Rodríguez-Ferran 2014] Tamayo-Mas, E. ; Rodríguez-Ferran, A.: A new continuous-discontinuous damage model: Cohesive cracks via an accurate energy-transfer process. In: *Theoretical and Applied Fracture Mechanics* 69 (2014), p. 90–101. – 10.1016/j.tafmec.2013.11.009 . – ISSN 01678442

[Tamayo-Mas and Rodriguez-Ferran 2015] Tamayo-Mas, E. ; Rodriguez-Ferran, A.: A medial-axis-based model for propagating cracks in a regularised bulk. In: *International Journal For Numerical Methods in Engineering* 101 (2015), p. 489–520. – 10.1002/nme . – ISBN 978–1–4577–0079–8

[Triantafyllidis and Aifantis 1986] Triantafyllidis, N. ; Aifantis, E.: A gradient approach to localization of deformation. I. Hyperelastic materials. In: *Journal of Elasticity* 16 (1986), p. 225–237

[Wang and Waisman 2016] Wang, Y. ; Waisman, H.: From diffuse damage to sharp cohesive cracks: A coupled XFEM framework for failure analysis of quasi-brittle materials. In: *Computer Methods in Applied Mechanics and Engineering* 299 (2016), p. 57–89. – 10.1016/j.cma.2015.10.019 . – ISSN 00457825

[Wheeler et al. 2014] Wheeler, M.F. ; Wick, T. ; Wollner, W.: An Augmented-Lagrangian Method for the Phase-Field Approach for Pressurized Fractures. In: *Computer Methods in Applied Mechanics and Engineering* 271 (2014), April, p. 69–85. – 10.1016/j.cma.2013.12.005 . – ISSN 00457825

[Zghal and Moës 2021] Zghal, J. ; Moës, N.: Analysis of the Delayed Damage Model for Three One-Dimensional Loading Scenarii. In: *Comptes Rendus Physique* 21 (2021), Januar, Nr. 6, p. 527–537. – 10.5802/crphys.42 . – ISSN 1878–1535

14

From a diffuse description of damage to the discrete representation of a crack

Sylvia Feld-Payet

DMAS, ONERA, Université Paris Saclay, F-92322 Châtillon — France

The aim of this chapter is to provide the reader with guidelines to analyze and compare the different strategies in the literature designed to obtain a discrete crack representation from a diffuse damage model. To do so, these strategies are decomposed into elementary components that can be selected according to the user's requirements.

14.1 Introduction

This chapter focuses on continuous media represented by a damage model (with or without coupling with the constitutive behavior) where material degradation is represented through a scalar field, referred to as a damage field. The aim is to use this continuous damage field to build a discrete crack path. The different terms used along this chapter to describe a discrete crack path are illustrated in Figure 14.1.

As continuous-discontinuous strategies can be rather complex, it can be helpful to decompose them into elementary components. These components are the methods chosen to answer the three following questions:

- Where to insert the discontinuity?
- When to insert the discontinuity?
- How to resume computation?

The following sections tackle each of these points. The interested reader can find more details in [Feld-Payet, 2023].

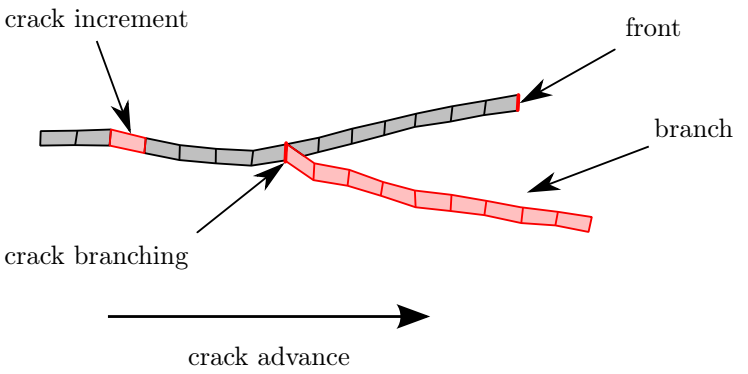

FIGURE 14.1: Illustration of the terms used to describe a discrete crack path.

14.2 Where to insert the discontinuity?

This section provides a description of the tools dedicated to define a continuous crack surface from a chosen orientation criterion. This step might not be necessary, depending on the choice of crack representation. In the case where crack is represented by a volume (in 3D or an area in 2D) without any control on its size (e.g. with the element deletion or the Thick Level Set methods), then this step is not necessary. However, if the crack is represented by a continuous band of one or several elements or by an hypersurface (i.e. a manifold of dimension $n-1$ in a space of dimension n), it is necessary to be able to define the crack surface.

14.2.1 Orientation criteria

In case of crack propagation, the crack surface corresponds to the surface where the points of the crack front are supposed to advance. From the physical point of view, this surface corresponds to the most damaged area where strains are localized. These expectations based on physics are translated into mathematical terms by orientation criteria. These criteria lead to a selection of either a set of vectors or a scalar field that will serve to define the crack surface.

14.2.1.1 Orientation criteria leading to a vector field

A first type of orientation criterion relies on local fields near the crack front to build vectors that are either tangent or normal to the crack propagation direction. These vectors are usually defined at the integration points since they are usually obtained through a tensor analysis, i.e.:

- either a bifurcation analysis, from the acoustic tensor in case of coupled damage model without any regularization as in [Belytschko et al., 2003; Song et al., 2006, 2008; Huespe et al., 2012; Crété et al., 2014; Wolf et al., 2018; Nikolakopoulos et al., 2021],
- or an analysis of the principal directions of the strain tensor [Areias and Belytschko, 2005; Dufour et al., 2012], the stress tensor [Belytschko et al., 2003; Song et al., 2006; Bobiński and Tejchman, 2016a], the damage gradient velocity [Beese et al., 2018], or the anisotropic damage tensor [Javanmardi and Maheri, 2019].

This type of analysis provides at each integration point, not one vector, but several vectors. Choosing, amongst this set of vectors, one that is consistent with the other selected vectors in the neighborhood is still a challenge since there is not a general methodology. However, several authors have followed the recommendation of Rabczuk and Belytschko [2007] and selected, for each integration point, the vector corresponding to the maximum displacement gradient or an equivalent strain.

14.2.1.2 Orientation criteria leading to a scalar field with a ridge

A second type of orientation criterion relies on local fields near the crack front to build a scalar field with maximum values where the crack should propagate. Among the different scalar fields considered in the literature, some of them also come from the exploitation of a tensor field: e.g. Wells and Sluys [2001] have proposed to consider an equivalent stress obtained from the norm of the deviatoric stress. This exploitation may require a prior spectral decomposition in order to build a function of the eigenvalues, e.g. the eigenvalues of the strain tensor for Simone et al. [2003] and Bobiński and Tejchman [2016b]. But the simplest choice is to consider directly the damage field as in [Broumand and Khoei, 2013; Seabra et al., 2013; Feld-Payet, 2010; Feld-Payet et al., 2015; Bottoni et al., 2015]. If several options are available, the best choice, as suggested by Bottoni et al. [2015] is to select a scalar field related to material degradation with the highest gradients near the crack surface.

14.2.1.3 Relation between the scalar and vector fields

Whether the considered field is a vector field or a scalar field with a ridge does not really matter, since these fields are related to the same crack surface. For the vector field, authors generally aim at providing an approximation of the normals to the scalar field iso-values, as illustrated in Figure 14.2, since the spatial evolution of their norms and directions can be helpful to determine the crack position. Besides, it should be possible to change the nature of the considered field by rather simple operations: e.g. spatial derivation of a scalar field to obtain vector fields and projection or norm calculation of vectors to obtain a scalar field.

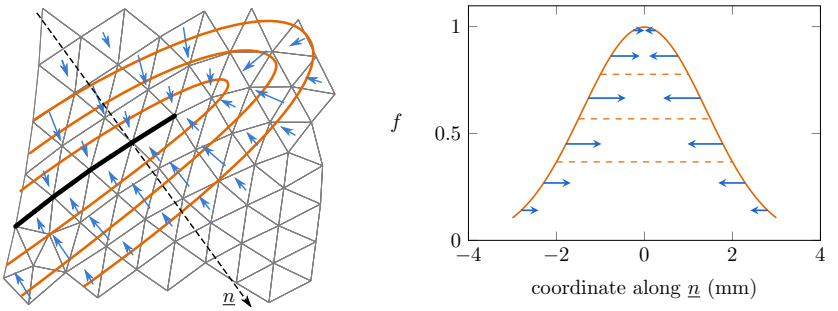

FIGURE 14.2: Relation between the vector field (in blue) and the scalar field f presenting a ridge (in orange): authors usually consider vectors corresponding to the normal components of the scalar field gradient that are thus orthogonal to the iso-values.

14.2.2 Crack path tracking

The bridge between these vector or scalar fields and the definition of a crack surface, either explicitly (i.e. with a mesh) or implicitly (i.e. with an iso-value of a locally monotonous scalar field) is crossed thanks to crack path tracking algorithms.

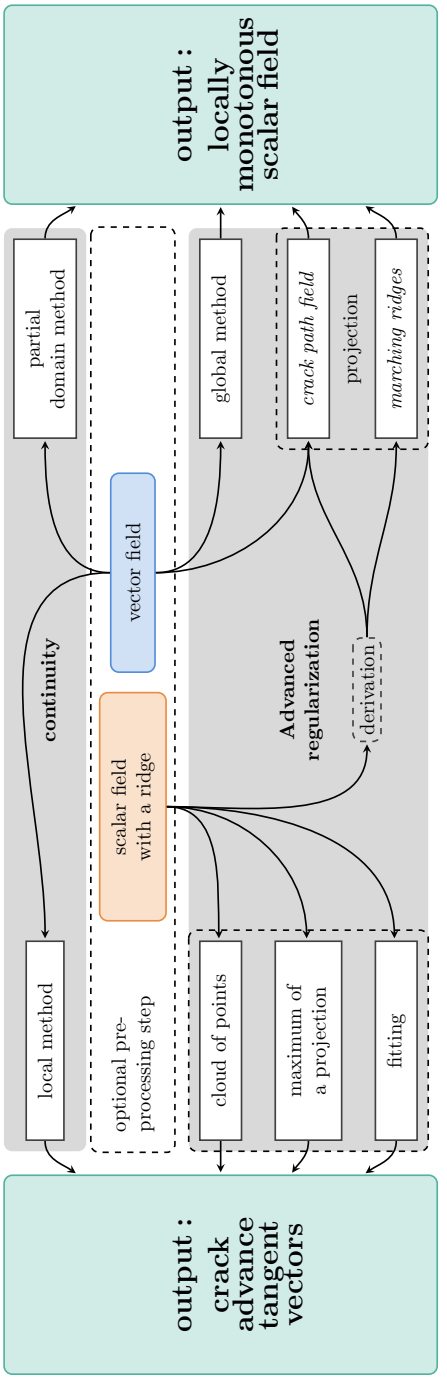

FIGURE 14.3: A classification of crack path tracking methods based on their input and output data.

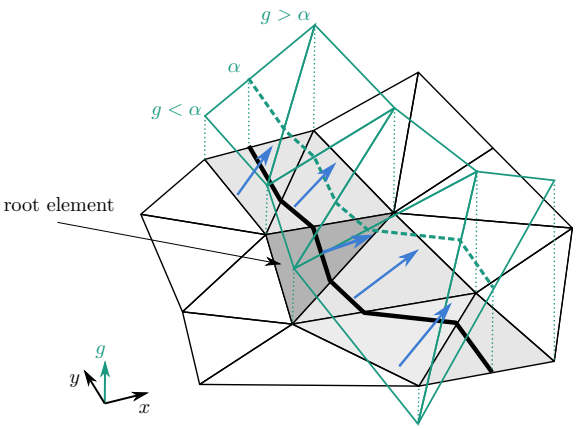

A: Partial domain method

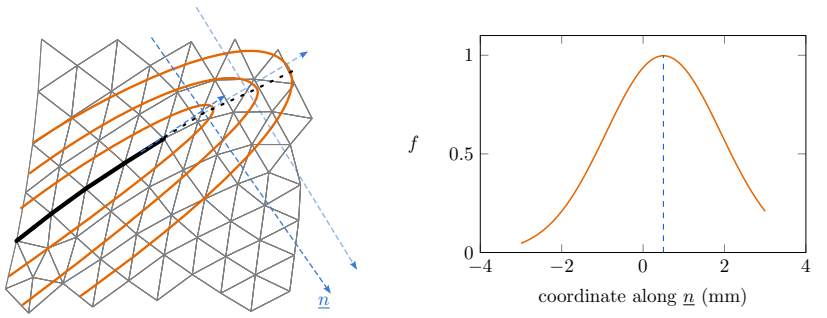

B: Search for a maximum value

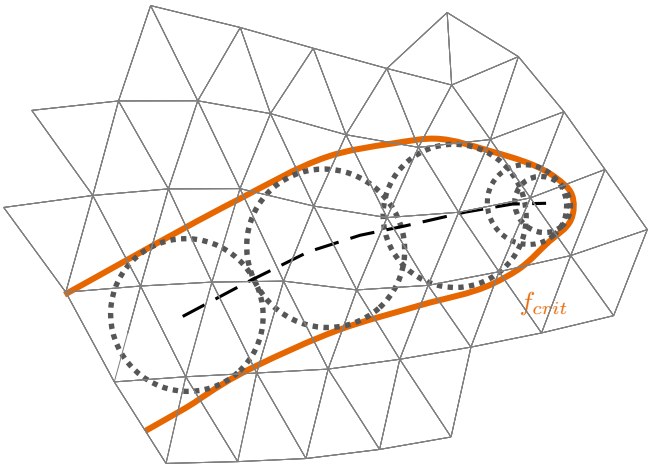

C: θ-simplified medial-axis

FIGURE 14.4: Principles of: A- the partial domain method (inspired from [Feist and Hofstetter, 2006]) with the set of considered vectors in blue and the locally monotonous scalar field in green, B- a method that looks for the maximum of a projection result (inspired from [Bottoni et al., 2015]) and C- the θ-simplified medial-axis (inspired from [Tamayo-Mas and Rodríguez-Ferran, 2015]) with the considered iso-value of f in orange.

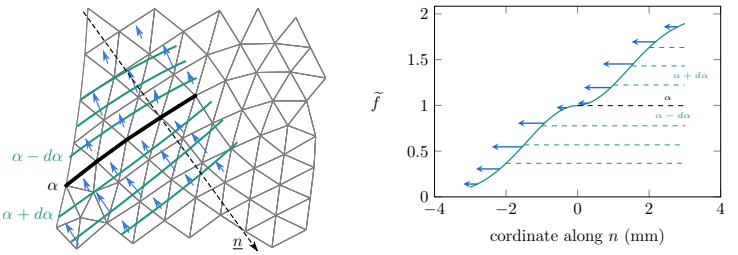

A: Global method

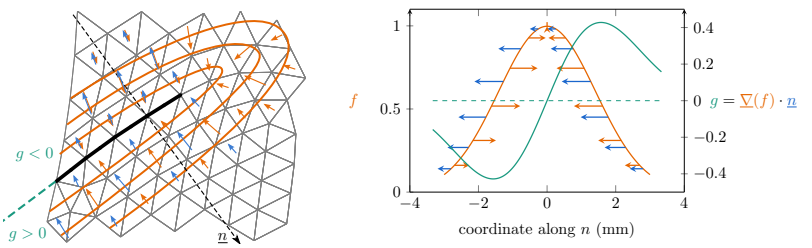

B: Crack path field method

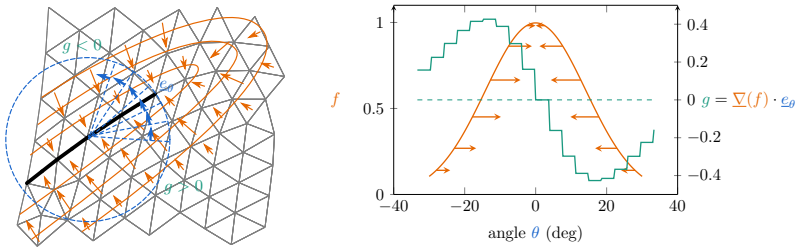

C: Marching ridges method

FIGURE 14.5: Principles of: A- the global method, B- the Crack Path Field method and C- the Marching Ridges method. The scalar field with a ridge is represented in orange, the set of considered vectors is represented in blue and the constructed field that is locally monotonous near the crack is in green.

14.2.2.1 Different types of algorithms

Originally, crack path tracking algorithms were developed to define a continuous surface from a vector field obtained from a tensor analysis and given element by element. Over time, regularity requirements have been added. Indeed, the orientation criteria (as evoked in section 14.2.1) usually lead to fields that lack regularity due to the problem's discretization. As noted by Cervera and Chiumenti [2006], this problems still remains with a finer mesh. In this respect, two types of crack path tracking algorithms can be distinguished: the first type focuses on continuity, whereas the second aims at bringing more regularity (which implies continuity). The different options are gathered in Figure 14.3. The input data are either a scalar field presenting a ridge or a set of vectors that are usually close to the normals to the scalar field iso-values. The output data are either a set of vectors that are tangent to the crack increment surface or a scalar field that is locally monotonous near the crack. With a monotonous scalar field, the crack usually corresponds to a specific iso-value and a study of the values at nodes enables to know which elements are crossed by the crack. Conversion between these two types of output data is possible, either by building tangent vectors from the intersection points between the iso-value corresponding to the crack and the elements' edges or by building a monotonous scalar field from the signed distance between any point and the closest tangent vector through projection.

14.2.2.2 Optional pre-processing step

In order to improve regularity of the crack path, a pre-processing step can be considered to improve regularity of the considered input fields. There are some quite simple methods that consist in taking into account, rather than a local value, the mechanical state in the neighborhood. Usually, the considered area is within a short distance from the crack front, i.e. the so-called *exclusion radius criterion*. Besides, for crack propagation, only the points ahead of the crack front are considered. The values for the points in the considered area are then used to perform:

- averaging techniques: e.g. Saloustros et al. [2018] have computed a stress tensor from average values at the nodes of each element;
- or smoothing techniques: e.g. Song et al. [2006] have used a mobile least square technique to smooth the stress field in dynamics; the superconvergent patch recovery technique of Zienkiewicz and Zhu [1992a,b] was used in [Feld-Payet, 2010; Feld-Payet et al., 2015] in order to build a smoothed scalar field; $L2$-projection is also a solution that has been used by Oliver et al. [2014] who referred to it as a *h-based regularization* or Eldahshan et al. [2021] who referred to is as the *Galerkin's smoothing method*.

Let us underline that the nature of the input field before and after this step remains the same.

With the same objective in mind, some authors consider non local values, such as the non local strain in [Patzák and Jirásek, 2003; Jirásek and Zimmermann, 2001] and the non local stress in [Roth et al., 2015].

14.2.2.3 Algorithms for more continuity

These approaches are meant to be used with a field of vectors defined element by element. The idea consists in building the crack surface element by element: one starts from a point in a root element and uses the normal vector in this element to define the first crack increment. Starting from the intersection point between this increment and the sides of the element, the normal vector in the next element leads to the following crack increment and so on. This procedure directly leads to a mesh of the crack surface and is designated as the *local method*. It is also possible to follow a similar procedure and to build, element by element, a monotonous scalar function with a gradient approaching the normal vector: this only requires to solve rather simple systems of equations with an arbitrary first value imposed for the root element. The crack surface then corresponds to a particular iso-value of this function. This is the *partial domain crack tracking method* proposed by Feist and Hofstetter [2006] illustrated in Figure 14.4-A. These rather cost-effective methods can however lead to implementation difficulties for the intersection management part, particularly in 3D. Indeed, if an element already has 3 intersected edges, then the normal vector of this element cannot be taken into account. Occurrence of this situation depends on the order in which the elements are processed.

14.2.2.4 Advanced algorithms for more regularity

From a vector field to a monotonous function

To the author's knowledge, the only method that uses a vector field to obtain a monotonous function is the *global method* proposed by Oliver et al. [2004]. Schematically, the idea is to start from a set of vectors that correspond to normals to the iso-values of a scalar field presenting a ridge and to build a monotonous function by orienting the normals in the same direction (instead of having different directions on each side of the crack), see Figure 14.5-A. One assumes that there is no evolution along the tangent direction. In practice, the monotonous scalar field is obtained through the resolution of a heat-conduction-like problem with adiabatic heat flux conditions at the boundary and no internal heat source. This resolution brings some issues as it involves an anisotropic conductivity-like tensor with a singular character that can be source of ill-posedness. Specific practical measures can be taken to overcome this problem (see notably [Jäger et al., 2008a,b, 2009; Annavarapu et al., 2016; Riccardi et al., 2017]). In the end, the crack surface corresponds to the iso-value of the monotonous function that intersects the current crack front. This type of approach have notably been followed by Cervera and Chiumenti

[2006]; Dufour et al. [2012]; Huespe et al. [2009, 2012] in 2D and Beese et al. [2018] in 3D.

Projection of the scalar field gradient to obtain a monotonous function

Construction of a monotonous scalar field thanks to the global method poses a certain number of difficulties due to the resolution of the auxiliary problem. Other methods have then been proposed to obtain more directly a monotonous function. They exploit the projection of a scalar field's gradient to obtain a function that is locally monotonous with an iso-zero surface corresponding to the crack increment surface. The gradient is usually projected onto a vector that could be a good approximation of the normal near the crack surface. Indeed, the scalar product then enables to focus on the gradient component that changes its sign across the crack surface. Considering all the gradient field components, as in [Eldahshan et al., 2021] with projection onto any edges, presents the risk of taking into account a non-null gradient in the direction tangent to the crack and may lead to loss of crack surface continuity.

There are two propositions that follow this principle of projecting the scalar field with a ridge onto a specific vector field. They differ notably by the choice of this specific vector field and how the projection result is exploited:

- The *Crack Path Field* method has been proposed with different vectors for the projection: in dynamics, Lloberas-Valls et al. [2016] relied on the gradient of a scalar field corresponding either to the sum or the product of the displacement components, whereas in quasi-statics, Oliver et al. [2014] and Dias et al. [2018] relied on the result of a bifurcation analysis. In any case, these vectors are selected so that they are as close as possible to the normals to the considered scalar field's iso-values. Projection onto these vectors of the scalar field gradient leads to a set of data at integration points that are used to compute, through the resolution of a linear system, a finite element approximation of the projected field at the nodes (illustrated by the green curve g in Figure 14.5-B). Analysis of the resulting nodal data indicates which elements are crossed by the iso-zero surface, i.e. the crack surface.

- The *Marching Ridges* method presents the advantage of always using the same vector field for the projection without requiring any additional analysis. Indeed, Feld-Payet [2010]; Feld-Payet et al. [2015] proposed to consider a polar grid in a plane orthogonal to the crack front and centered at the crack front. The considered vectors are then the grid's orthoradial vectors, represented in blue in Figure 14.5-C). The result of the projection is averaged over several radii for a specific direction. This averaging operation is performed for a finite number of directions, with a user controlled angular increment. Analysis of the evolution of the sign of these values (corresponding to the function g in green in Figure 14.5-C that is locally monotonous near the crack) indicates which directions correspond, in average for a given

crack increment length, to an iso-zero surface corresponding to the scalar field ridge. Let us note that an intermediate output of this method is the projection field g, which is a locally monotonous scalar field. However, this method also provides crack advance tangent vectors since it directly defines, for a given point of the crack front, the next point on the ridge: this is the point located at a distance equal to the considered crack increment length, in the selected direction. Resuming this search from the next point on the ridge thus leads to a set of tangent vectors discretizing the ridge. Although this method is based on a two-dimensional analysis, its authors proposed a general extension to 3D by considering several orthogonal planes distributed along the crack front in order to compute a set of tangent vectors.

In both cases, derivation of the scalar field necessitates prior smoothing of this field (see section 14.2.2.2) and crack branching can be captured.

From a scalar field with a ridge to a set of tangent vectors

Contrarily to methods considering vectors at the element level, methods that exploit directly a scalar field aim at inserting a straight crack increment over several elements at once. The increment starts at the current crack front and its end can be determined either by focusing on *placing the end of the crack increment* on the ridge or by focusing on an *average positioning of the increment* on the ridge. The different methods could be divided into three main categories:

- *Methods that exploit a cloud of points.* These methods consist in computing, for each considered point of the crack front, its position on the next front by averaging the positions of different integration points ahead of the front, with a weight involving the value of the considered scalar field, the distance to the current crack front and possibly the area associated with each integration point. These methods are quite popular due to their simplicity and have been used in 2D by Wells and Sluys [2001]; Simone et al. [2003]; Mediavilla Varas [2005]; Mediavilla et al. [2006]; Seabra et al. [2011]; Bobiński and Tejchman [2016b]; Wang and Waisman [2016] and in 3D by Peerlings et al. [2008]; Javani Joni [2011]; Javani et al. [2016]. As such, these methods were meant to deal with propagation of one crack only. But it is also possible to exploit a cloud of points to deal with crack initiation by fitting the first increment. For example, El Ouazani Tuhami [2022]; El Ouazani Tuhami et al. [2023] proposed to fit an ellipse based on the principal directions of the cloud after a singular value decomposition.

- *Methods that look for the maximum of a projection result.* Another type of rather simple methods consists in projecting the scalar field onto a line passing through the possible directions and choosing the direction corresponding to the maximum value along this line. This line can be a portion of circle [Broumand and Khoei, 2013; Bottoni et al., 2015] or a straight line that is orthogonal to the last crack increment [Bottoni et al., 2015], as in

Figure 14.4-B. In order to limit the effect of the finite element discretization for the evaluation along this line, the considered values are often smoothed before or after the projection: smoothing may involve a fourth-order polynomial [Comi et al., 2007], Bézier curves [Seabra et al., 2013] or a convolution product by means of a Gaussian function [Bottoni et al., 2015]. Some authors have also searched for more regularity along the direction of crack propagation by averaging the result of this evaluation for several lines located at different distances from the crack front, as in [Seabra et al., 2013]. These methods are based on a two-dimensional analysis: in 3D, it would be possible to use the strategy proposed in Feld-Payet [2010]; Feld-Payet et al. [2015] to consider several orthogonal planes distributed along the crack front in order to compute a set of tangent vectors.

- *Methods that fit a manifold of the same dimension with a symmetry hypothesis.* These methods share the same principle: to fit locally the scalar field with a manifold of the same dimension and then to assume that the ridge lies at the center of symmetry of this manifold. It is important to note that there is a symmetry assumption which may not be always suited for the considered applications. In the *simplified medial-axis approach*, Tamayo-Mas [2013]; Tamayo-Mas and Rodríguez-Ferran [2015]; Tamayo-Mas et al. [2019] have proposed to fit spheres or circles so that they are bitangent to a chosen iso-value of the scalar field, see Figure 14.4-C. Their centers are assumed to lie on the ridge. It is then possible to perform a second fitting procedure that minimizes the distance between these centers and a fixed size crack increment to determine the crack advance. In order to avoid insignificant small branches, branches with a separation angle between tangency points below a prescribed angle are discarded. One of the main advantages of this method is that it enables to capture crack branching directly. One of its main drawbacks, to this day, is that the crack can only start from a boundary. A similar strategy has been proposed by Geelen et al. [2018]. It consists in minimizing the gap between the scalar field and an auxiliary field with a symmetry axis representing the damage ridge. It provides the orientation of a series of connected, linear segments representing the crack. Crack branching can be tackled if one assumes beforehand a sufficient number of branches. For now, this method has only been applied in 2D with a phase-field damage model.

Analysis

The choice between the numerous crack path tracking methods in the literature stems from a compromise between, on the one hand, implementation and computation costs and, on the other hand, performance. The most expensive techniques are the ones that rely on a vector field (i.e. the global method and the Crack Path Field) since this field generally comes from a tensor analysis. In that case, the vectors are usually provided at each integration point. This leads to a high number of data that presents the advantage of more local

precision, but the disadvantage is a greater difficulty to bring continuity and even regularity to the resulting crack surface. On the contrary, crack path tracking methods relying on a scalar field with a ridge (or its gradient) tend to consider an average direction over several elements for each crack increment, which means less precision but more regularity and cost-effectiveness. The most cost-effective methods are the ones that exploit a cloud of points (by averaging their position or fitting an increment) and the ones that look for the maximum of a projection result. These methods may be sufficient if there is propagation of only one crack front. But, in case of branching, these methods would require additional steps. This would increase their cost and would lessen their interest compared to other techniques that are already able to directly provide several directions at once. Only a few techniques already enable to deal with crack branching. They usually all involve a separation angle which helps to distinguish real branches with numerical artifacts. This parameter corresponds to the minimum angle between two branches for them to be both taken into account: 90 to 100 degrees for Tamayo-Mas [2013]; Tamayo-Mas et al. [2019], 60 degrees for the meshless computation of Rabczuk et al. [2010], 40 degrees for Saloustros et al. [2018] and twice the angular precision, i.e. 10 to 20 degrees, for Feld-Payet [2010]; Feld-Payet et al. [2015]. The smaller the separation angle, the earlier crack branching can be captured.

14.2.3 Building a 3D discrete surface

The crack path tracking methods that lead to a three-dimensional locally monotonous scalar field defined at the nodes directly provide an implicit definition of the crack surface. However, when the output of the crack path tracking procedure is a set of tangent vectors, additional operations are necessary to obtain an implicit or explicit definition of the crack: they are described in the following, along with the different ways to switch from an implicit to an explicit definition and conversely.

14.2.3.1 From a set of tangent vectors to a mesh

There are several solutions to build the mesh of the next crack increment from a set of tangent vectors. The simplest one may be to:

1. select a finite numbers of duet points with one point on the current crack front and its counterpart on the next front (e.g. from the ends of the tangent vectors);
2. build a mesh by filling the space between the current and the next front points with triangular elements.

Some difficulties may arise, e.g.:

- when crack propagation directions overlap,
- when a point of the current crack front located on the boundary is associated

with a propagation vector oriented towards the inside of the domain (and not along the boundary),

- or when there are obstacles along the way.

Several solutions have already been proposed for some of these problems, see [Pereira et al., 2009; Chiaruttini et al., 2010; Gupta and Duarte, 2014; Garzon et al., 2014].

14.2.3.2 From a set of tangent vectors to a locally monotonous function

The tangent vectors given at different points of the current crack front can be used to update level set functions [Stolarska et al., 2001] to describe implicitly the crack. Different steps of reinitialization and reorthogonalization are then necessary: e.g. see [Duflot, 2007] for a comparison of different techniques. These operations are more complex than a simple interpolation but they also ensure more regularity for the crack surface.

14.2.3.3 Conversion between explicit and implicit representations

From an explicit representation of the crack increment surface, i.e. a mesh, it is possible to define a signed distance from this crack surface to obtain an implicit definition. Conversely, from a locally monotonous field, it is possible to study its nodal values to determine the intersection of the elements' edges with a specific iso-surface corresponding to the crack surface: this defines new surfacic elements that discretize the crack surface. Let us note that these operations do not bring more regularity to the crack surface.

14.2.4 Some challenges

To this day, there are still some difficult points with the determination of the crack path, especially for 3D problems.

14.2.4.1 Crack initiation inside the structure

Crack initiation completely inside the structure (i.e. away from any boundary) is not often tackled in the literature. Although this issue is not specific to the 3D case, it is all the more challenging in 3D.

The first step is to determine a point belonging to the crack surface. When dealing with a vector field, crack initiation starts at the level of an element and the centroid of the element can be considered as a starting point [Saloustros et al., 2018]. When dealing with a scalar field with a ridge, it is possible to choose a point that is independent of the finite element discretization since smoothing and averaging techniques are commonly used. For example, Feld-Payet et al. [2015] and Javani et al. [2016] have proposed to consider a weighted average of the points exceeding a critical damage.

Once a crack initiation point is determined, the next step consists in building the first crack increment. When dealing with a vector field, crack increments are of the size of the elements and the exhaustion method (i.e. repeating the crack increment search and insertion as many times as possible) is generally used to insert several crack increments in one time step . When dealing with a scalar field with a ridge, the crack shape and size can be more arbitrary. The main goal is to determine at least a plane for the first crack increment [Javani et al., 2016; Feld-Payet et al., 2015; El Ouazani Tuhami, 2022]. Non-planar surfaces could also be determined by first searching for the intersection of the crack surface with the three basic reference plane and then, from one intersection (e.g. the longest), performing another search in planes orthogonal to this first crack segment, as proposed by [Feld-Payet, 2010; Feld-Payet et al., 2015].

From here, the crack shape could be optimized, although this is not the usual way to proceed yet. To this day, simple crack shapes are usually considered (rectangular or elliptical). As long as the first crack increment is small enough, this is often sufficient to obtain a more realistic shape after a few crack propagation steps.

14.2.4.2 Crack branching, non planar evolution and multi-cracking

A major challenge in 3D is crack branching. Not only are they only a few crack path tracking algorithms that can directly handle crack branching, but there is also an additional difficulty to determine, from data computed along the crack front, consistent sets of directions that correspond to different branches. It can then be useful to compare the computed directions for adjacent segments along the crack front in local frames and to compare the difference with a separation angle to distinguish between two branches. If the difference between the directions for two adjacent crack front segments is close to the angular precision of the crack path tracking method, then they may correspond to the same branch. For example, if the directions for two adjacent crack front segments are less than 20 degrees apart and they were determined with the Marching Ridges method with an angular precision of 10 degree, then these directions are associated with the same branch. Thanks to these local frames, it is also possible to deal with complex evolution of the same crack front, as illustrated in figure 14.6.

Once, the directions for the different branches have been assembled, it is useful to consider each branch separately, especially for the insertion criterion (see section 14.3). The same holds for multiple cracks. Dealing with several cracks simultaneously is easier if each crack is considered independently. To do so, one can search for several potential crack initiation points. A set of elements having reached a given criterion (e.g. a minimum damage value) can be built around each computed point. If this criterion is chosen so that the selected areas do not overlap, it is then possible to consider crack initiation in each area independently.

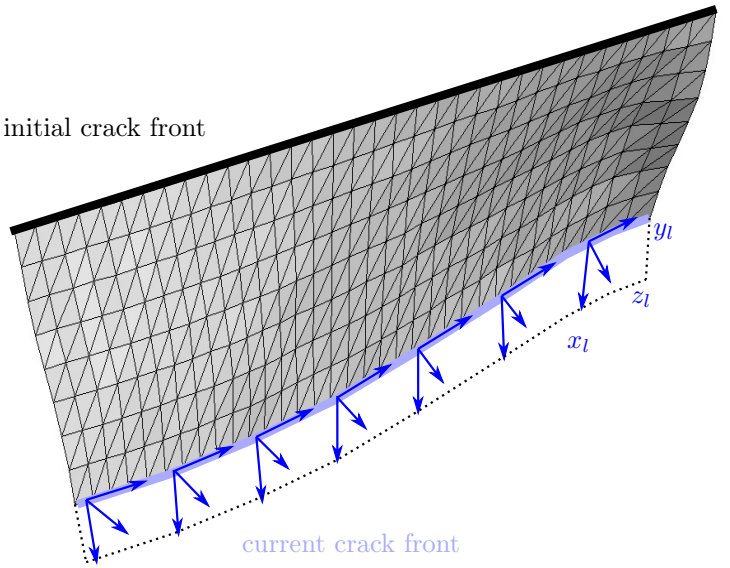

FIGURE 14.6: Some local frames used to deal with non planar evolution. Direction of unit vector $\vec{x_l}$ is the same direction as the previous crack increment. Unit vector $\vec{y_l}$ is defined based on the tangent direction of the crack front (in light blue). The dashed part corresponds to an hypothetical crack advance in the 0° direction along the x_l axis.

14.2.5 Crack merging

The last difficulty is finally the merge of the crack either with another crack or with a boundary. In such cases, there are only a few data available ahead of the crack front which may cause some trouble for the crack path tracking algorithm supposed to enforce enough regularity. It is then possible to take advantage of the knowledge of the description of the free boundary or of the other crack to guide the crack increment so that it takes the shortest path to it.

14.3 When to insert the discontinuity?

Another essential component of a continuous-discontinuous strategy is a criterion to indicate that material degradation is such that a discrete crack can appear, or in other words, that the continuous-discontinuous transition can occur. This criterion is here referred to as an *insertion* criterion.

14.3.1 Objectives of the insertion criterion

The specific meaning of the insertion criterion depends on whether the crack increment length is fixed or not.

If only cracks of fixed size are considered (as in [Feld-Payet, 2010; Feld-Payet et al., 2015; Wang and Waisman, 2016]), the insertion criterion only serves to indicate when the crack increment can be *entirely* inserted. The insertion criterion is then generally evaluated at the location of the crack increment which needs to be determined beforehand (see section 14.2).

In the case where the crack increment size is not set by the user, then the insertion criterion also serves to determine the crack increment length. This length is determined by the local state of the continuous damage field along the location of the crack path support, as illustrated in Figure 14.7 (construction of this crack support is explained in section 14.2). For 3D problems, from a crack path support determined element by element or built with constant length increments in all the directions, one can rely on the material degradation variable value to define limit points and build a contour for the crack increment from these points, e.g. by using Bezier curves as in [El Ouazani Tuhami, 2022]. This results in variable crack advance depending on the direction, which enables a more realistic crack representation.

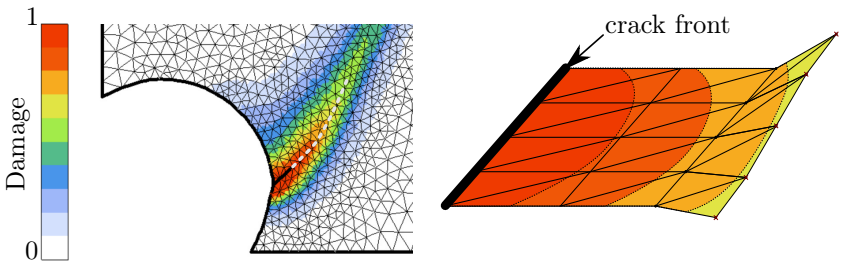

FIGURE 14.7: Crack path support where damage is evaluated represented by the dashed line in a 2D case on the left and schematically in 3D on the right.

14.3.2 Choice of the insertion criterion

General requirements for the computation are that the solution should be unique and that the evolutions of the local state should be progressive (i.e. there should not be any large perturbation). These requirements guide the choice of the insertion criterion which mainly depends on:

- the choice of the continuous damage model (regularized or standard formulation);
- whether the remaining energy in the cut area can still be dissipated after crack insertion.

One can distinguish two types of situations:

1. For standard models where damage is coupled with the constitutive behavior, the insertion criterion should enable to insert a discontinuity before loss of uniqueness of the solution. At this point, a relatively important quantity of energy is still stored within the elements lying under the inserted crack increments. This energy is then usually dissipated thanks to cohesive zone insertion or damage dissipation within a band of elements (often with a width of one element).
2. For standard uncoupled damage models or regularized coupled damage models, the choice of the insertion criterion is less constrained. In this case, the user can either choose to insert a crack when the underlying elements are fully damaged or to insert a discontinuity before complete failure, with a cohesive zone model or a band of damaging elements enabling to dissipate the remaining energy.

14.3.3 The insertion criteria

The insertion criteria mostly used in the literature are listed below. They can be used alone or combined.

14.3.3.1 Stability and uniqueness

For standard models where damage is coupled with the constitutive behavior without any regularization formulation, stability and uniqueness criteria seem the most appropriate. However, as underlined by Areias and Belytschko [2005], there is still a need for a procedure that is sufficiently robust and general. These authors however mention that in the case of elasto-plasticity, the analysis proposed by Boussaa and Aravas [2001] appears to be general enough.

14.3.3.2 Critical value of a local quantity

The most used criteria are the ones based on a critical value of a local quantity that reflects the degradation state. This quantity can be an inelastic deformation as proposed by Wells and Sluys [2001], a softening parameter as considered by Bobiński and Tejchman [2016b], or the additional deformation due to the opening of smeared cracks for Jirásek and Zimmermann [2001]; Jirásek [2004]. But most authors rely on a critical value of a damage type parameter as in [Hambli, 2001; Simone et al., 2003; Pourmodheji and Mashayekhi, 2012; Javanmardi and Maheri, 2019; Roth et al., 2015]. The associated critical values vary depending on how the remaining energy after the transition can be dissipated (notably between 0.4286 for Pourmodheji and Mashayekhi [2012] and 0.99995 for Simone et al. [2003], both considering a bounded damage variable with values between 0 and 1).

Different critical values necessarily lead to different values of force transmitted through the increment to be inserted, which are important to control during the transition. To control the transmitted force value, it is either possible to set the critical value of the chosen quantity to ensure a specific value of transmitted force if the relationship between these quantities is exactly known (as in [Wells and Sluys, 2001]) or to consider an additional criterion imposing directly a maximum value of transmitted force (e.g. 100 MPa in [Wolf et al., 2018]).

14.3.4 Challenges

The choice of the insertion criterion, especially the choice of a critical value, is also influenced by some numerical challenges.
First, the impossibility to numerically deal with a strictly null value of transmitted effort within an element may force to choose a slightly different critical value than the theoretical one (e.g. values 0.99, 0.999 or 0.99995, instead of 1, have been tested by Simone et al. [2003]).
Secondly, the locus of evaluation for the insertion criterion is also an open question. The considered quantities are all local within this context and the associated fields are more or less smooth depending on the finite element discretization. This may lead to difficulties to estimate quantities too closely from the crack front as noted by Wolf et al. [2018] and Bobiński and Tejchman [2016b]. That is why Broumand and Khoei [2013] and Bobiński and Tejchman [2016b] have proposed to evaluate the insertion criterion in a sufficiently large area ahead of the crack front. Let us note that, if the crack is represented by an hypersurface, then an evaluation along the increment to be inserted may be more relevant, as in [Feld-Payet, 2010; Feld-Payet et al., 2015].
Another challenge is to limit the disturbances associated with a discontinuity insertion within a continuous model. These disturbances are closely related to the inserted increment size, which, if not previously set, may depend on the crack insertion criterion. A compromise should be found to insert increments small enough to limit disturbance but long enough to avoid too frequent insertions and cumulating the disturbances' effects. Inserting an increment with uncontrolled length with the exhaustion method (as in [Crété et al., 2014; Wolf et al., 2018; Javanmardi and Maheri, 2019]) may indeed cause some numerical issues. Setting a fixed increment size (as in [Feld-Payet, 2010; Feld-Payet et al., 2015]) should help from a numerical point of view: if the crack increment is not long enough, a second insertion should be triggered right after the first one, and so on. This option automatically prevents the insertion of too small increments, for better or for worse. Finally, an interesting compromise might be to follow the proposition of Seabra et al. [2013] by inserting increments of variable sizes (the length being determined by a critical damage value) in several steps if necessary.

Let us note that these propositions are valid for 2D problems where the size of a crack increment is easy to define. However, for 3D problems with

different crack advances along the front, the notion of size must be re-defined. For example, El Ouazani Tuhami [2022]; El Ouazani Tuhami et al. [2023] has proposed to consider the crack surface area.

14.3.5 Prospects

The choice of an insertion criterion remains deeply motivated by numerical reasons whereas this step may be the most closely related to the physics of the failure phenomenon. This apparent contradiction may be explained by the necessity of first obtaining converged computation results before being able to compare them with experimental tests. Another explanation may also lie in the difficulty to exploit experimental tests to assess strains (by derivation of noised displacement fields, which requires the introduction of an undefined length to divide these displacements) and to detect crack initiation and propagation, especially in areas with very large deformations and in a very short time. With the development of acquisition tools (not only in 2D, but also in 3D with tomography and laminography [Bouterf et al., 2020]), of the numerical methods for image analysis and of the numerical tools to compare calculations with experiments [Feld-Payet et al., 2022], one can hope that there will be, in the near future, experimental data available to validate the proposed insertion criteria.

14.4 How to resume computation?

After inserting a discontinuity, the next step is to resume computation.

14.4.1 Challenges

The insertion of a discontinuity in a continuous model necessarily involves a change in the problem's discretization. This change is all the more drastic when there is a switch between dissipation in a volume to dissipation on a surface since the positions of the integration points are no longer the same. This is valid for mesh adaption as well as crack representation with X-FEM as reported in [Wells and Sluys, 2001; Simone et al., 2003; Broumand and Khoei, 2013; Seabra et al., 2013; Wang and Waisman, 2016; Javanmardi and Maheri, 2019]. It is then necessary to transfer the history-dependent variable fields to be able to resume computation with the new discretization. According to Perić et al. [1996], a transfer operator should:

- preserve the relations between the transferred fields (e.g. the strain tensor should be equal to the symmetric part of the displacement gradient);

- preserve global equilibrium (i.e. consistency between the stresses and the external forces);
- minimize numerical diffusion (e.g. the damage bandwidth should not be enlarged after transfer);
- enable the respect of the boundary conditions.

In practice, all these constraints cannot be respected simultaneously. Consequently, transfer involves some numerical perturbations which must be minimized. Usually, minimization of numerical diffusion prevails during transfer and specific measures are considered after transfer to restore the fields' consistency (see section 14.4.3).

14.4.2 Field transfer

To limit numerical diffusion, transfer only involves local data. Consequently, the first step of the field transfer is to determine in which element of the previous discretization the considered new point is. From here, different transfer operators are considered depending on the type of data (i.e. stored at the nodes or at the integration points). Variables stored at the nodes are usually transferred by direct interpolation from the nodal values in the previous discretization using an element's shape functions (with the rare exception of Espinosa et al. [1998] who uses an auxiliary mesh): see Figure 14.8 for an example of application. On the contrary, different options are available to transfer the data at the integration points.

Transfer using the nodes

The transfer procedure used by Lee and Bathe [1994], Perić et al. [1996], Mediavilla Varas [2005] and Khoei and Gharehbaghi [2009] after mesh adaption and Broumand and Khoei [2013] after element subdivision with X-FEM, can be decomposed into three steps:

1. extrapolation of the values at the old integration points to the nodes of the old mesh (with averaging at the nodes shared by several elements);
2. transfer the values at the nodes of the old mesh to the nodes of the new mesh;
3. interpolation of the values at the new nodes to determine the value at the new integration point.

The main problem with this procedure is the first extrapolation step that may be the source of non negligible numerical diffusion according to Mediavilla Varas [2005]. More elaborate techniques are required to limit this phenomenon like the use of a global least squares approximation proposed by Hinton and Campbell [1974] or of an iterative procedure as proposed by

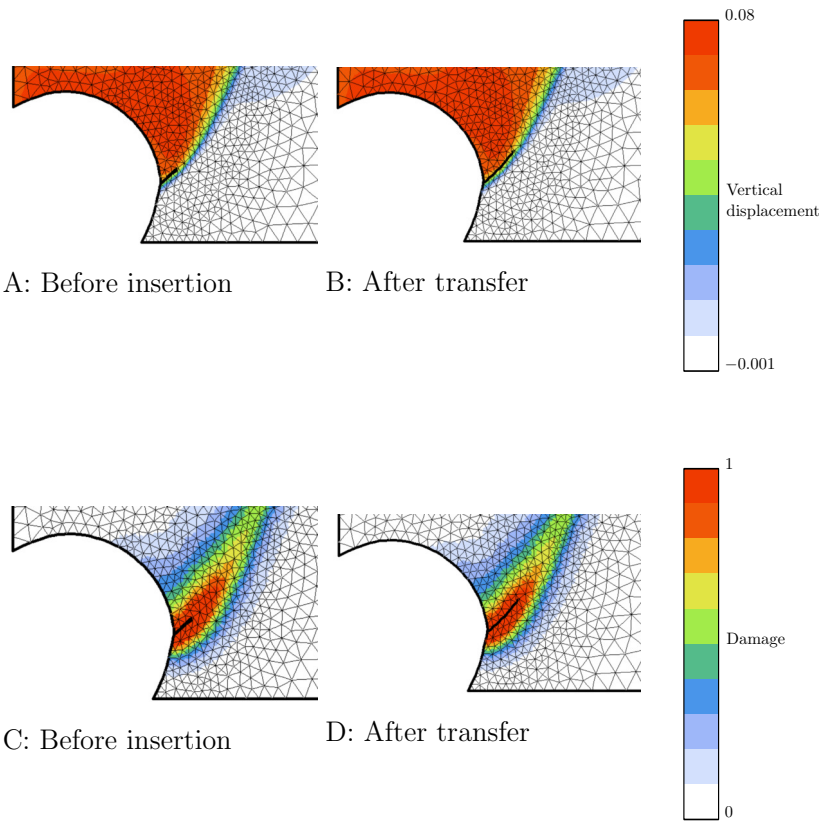

FIGURE 14.8: Maps of the vertical displacement field (stored at the nodes) and the damage field (stored at the integration point) before and after transfer, before returning to equilibrium at the next time step. Nodal interpolation was used to transfer nodal data and least square smoothing was used to transfer integration point data.

Loubignac et al. [1977]. Camacho and Ortiz [1997], inspired by the work of Ortiz and Quigley [1991], proposed to use L^2-projection to smooth the data and obtain nodal values before evaluating the values at the new integration point. However, Boroomand and Zienkiewicz [1999] underlined that, as L^2-projection is performed over the whole domain, numerical diffusion can still occur.

Transfer using a local smoothed approximation

It is also possible to provide a local smoothed approximation of the data stored at the integration points without using the nodes. For example, Wells and Sluys [2001] used, for a change of discretization due to crack insertion with X-FEM, a weighted average of the integration point data in the considered old element. A technique applicable within a more general framework is to build a local polynomial approximation of the considered field. This technique is referred to as *diffuse approximation* by Villon et al. [2002]. The polynomial coefficients can be obtained thanks to a weighted least square approximation based on values of the field to transfer at the old integration points. Once the polynomial coefficient are known, the value at the new integration point can be obtained by simple polynomial evaluation. According to Feld-Payet [2010], this method is rather efficient as long as the number of sampling points is limited (i.e. 13 integration points for 6-node triangles [Feld-Payet et al., 2015] and 30 points with quadratic thetrahedral elements): see Figure 14.8 for an example of application. See [Brancherie et al., 2006; Feld-Payet, 2010] for more details on the implementation. In a similar way, Boroomand and Zienkiewicz [1999] have proposed to consider only the data in a patch of elements around the new integration point to limit numerical diffusion.

Direct transfer without smoothing

Another type of transfer operator aims at reducing numerical diffusion by directly transferring data between integration points without any smoothing.

Contant value transfer

The simplest method is to transfer the value of the closest integration point. It is possible to limit the old integration point candidates to those in the same old element as the new point as in [Wang and Waisman, 2016]. Simone et al. [2003] choose to transfer the maximum value in the element. This type of transfer should be more appropriate if the integration point position and the element size do not vary much (e.g. for refined meshes).

Direct interpolation

Ortiz and Quigley [1991] proposed to associate shape functions to the old integration points and to use them to interpolate or extrapolate values at the new integration points belonging to the same element. However, this results

in discontinuous fields when extrapolation is used to deal with new points outside the group of old points unless specific measures for mesh subdivision are taken, as suggested by Boroomand and Zienkiewicz [1999]. This technique is thus more appropriate for a crack insertion with element sub-division for X-FEM and has, for example, been applied by Seabra et al. [2013, 2011]. Espinosa et al. [1998] proposed a similar approach based on an auxiliary mesh with 3-node triangular elements connecting the integration points in the old mesh.

Some guidelines

Patzák and Jirásek [2004] compared three transfer operators, which were based on the closest-point transfer, least-squares projection, and shape-function projection: in this study, the transfer relying on the shape-functions caused a non-negligible numerical diffusion. The closest-point transfer is obviously the most cost-effective one. However, smoothing is expected to deal better with large mesh size variations.
Whatever the choice of transfer operator is, a general recommendation could be to transfer fields when and where non-linearities are not too important and/or the energy is relatively lower. Moreover, the more local the change of discretization, the better.
Finally, let us note that the perturbations associated with transfer are also likely to highlight any instability in the problem. So it is important to deal with any source of trouble first (for example using specific measures to deal with volumetric locking) and to ensure that the problem does not depend on the discretization at the time of transfer. On the contrary, let us note that viscous effects can help to reduce the perturbations' effect.

14.4.3 Re-equilibrium

After transfer, the fields are no longer consistent and this generally causes some convergence difficulties for the next time step. It is then useful to enable time step division, as in [Boroomand and Zienkiewicz, 1999; Feld-Payet, 2010]. However, since this solution results in an increasing number of increments and thus a higher computational cost, some propositions have been made to help retrieve equilibrium more efficiently:

- transfer of only a few selected variables and exploitation of local relations to compute the remaining variables, as proposed by Camacho and Ortiz [1997]; Mediavilla Varas [2005]; Broumand and Khoei [2013].
- introduction of a relaxation step with vanishing local residual forces, as proposed by Broumand and Khoei [2013]; Javanmardi and Maheri [2019]; Seabra et al. [2013];
- introduction of an additional step with the boundary conditions of the

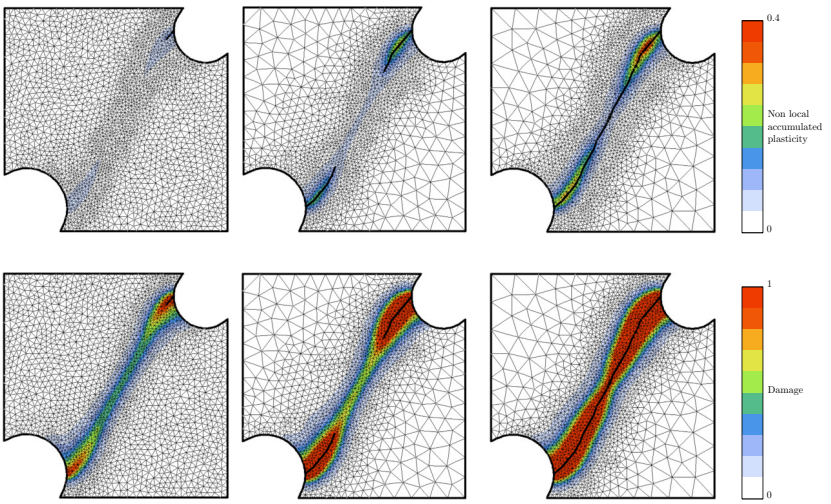

FIGURE 14.9: Illustration of a complete continuous-discontinuous strategy on the initial configuration at three different moments in the computation for a test inspired from [Mediavilla Varas, 2005] and described in [Feld-Payet et al., 2015] with crack representation through mesh adaption. The non local accumulated plasticity field (which drives damage for the considered model) was used to determine *where* to insert the crack path thanks to the Marching Ridges method. The *moment of insertion* was determined based on a critical value of the damage field. Nodal interpolation and least square smoothing were used to *transfer* data respectively at the nodes and at the integration points after crack insertion. The procedure proposed in [El Ouazani Tuhami, 2022] was used to ease the *return to equilibrium*.

current increment, either with an elastic behavior as proposed by Mediavilla Varas [2005], or with the complete constitutive behavior to also adjust plasticity and damage, as proposed by El Ouazani Tuhami [2022]; El Ouazani Tuhami et al. [2023].

14.5 Conclusion

This chapter has proposed to decompose the continuous-discontinuous strategies into elementary components:

- orientation criteria, crack path tracking algorithms and methods to build a 3D crack path to know where to insert the discontinuity;
- insertion criteria to know when to insert the discontinuity;
- transfer operators and re-equilibrium methods to resume computation.

An example of application for a ductile problem with crack represented thanks to mesh adaption is presented in Figure 14.9.
The choice of the solutions is very problem-dependent so it is important to know the advantages and limits of each option to select the most appropriate combination. This choice could be made easier if there were more numerical comparisons or benchmark tests to compare similar elementary components.

Many challenges remain from the numerical point of view, especially to deal with complex 3D crack initiation and propagation. Eventually, it is the confrontation with experimental results that will enable to validate the different choices.

Bibliography

[Annavarapu et al. 2016] Annavarapu, Chandrasekhar ; Settgast, Randolph R. ; Vitali, Efrem ; Morris, Joseph P.: A local crack-tracking strategy to model three-dimensional crack propagation with embedded methods. In: *Computer Methods in Applied Mechanics and Engineering* 311 (2016), p. 815–837

[Areias and Belytschko 2005] Areias, Pedro M. ; Belytschko, Ted: Analysis of three-dimensional crack initiation and propagation using the extended finite element method. In: *International Journal for Numerical Methods in Engineering* 63 (2005), Nr. 5, p. 760–788

[Beese et al. 2018] Beese, Steffen ; Loehnert, Stefan ; Wriggers, Peter: 3D ductile crack propagation within a polycrystalline microstructure using XFEM. In: *Computational Mechanics* 61 (2018), Feb, Nr. 1, p. 71–88. – 10.1007/s00466-017-1427-y . – ISSN 1432–0924

[Belytschko et al. 2003] Belytschko, Ted ; Chen, Hao ; Xu, Jingxiao ; Zi, Goangseup: Dynamic crack propagation based on loss of hyperbolicity and a new discontinuous enrichment. In: *International Journal for Numerical Methods in Engineering* 58 (2003), Nr. 12, p. 1873–1905

[Bobiński and Tejchman 2016a] Bobiński, Jerzy ; Tejchman, Jacek: Comparison of continuous and discontinuous constitutive models to simulate concrete behaviour under mixed-mode failure conditions. In: *International Journal for Numerical and Analytical Methods in Geomechanics* 40 (2016), Nr. 3, p. 406–435. – 10.1002/nag.2411

[Bobiński and Tejchman 2016b] Bobiński, Jerzy ; Tejchman, Jacek: A coupled constitutive model for fracture in plain concrete based on continuum theory with non-local softening and eXtended Finite Element Method. In: *Finite Elements in Analysis and Design* 114 (2016), p. 1 – 21. – 10.1016/j.finel.2016.02.001 . – ISSN 0168–874X

[Boroomand and Zienkiewicz 1999] Boroomand, B ; Zienkiewicz, OC: Recovery procedures in error estimation and adaptivity. Part II: Adaptivity in nonlinear problems of elasto-plasticity behaviour. In: *Computer methods in applied mechanics and engineering* 176 (1999), Nr. 1-4, p. 127–146

[Bottoni et al. 2015] Bottoni, Marina ; Dufour, Frédéric ; Giry, Cédric: Topological search of the crack pattern from a continuum mechanical computation. In: *Engineering Structures* 99 (2015), p. 346 – 359. – 10.1016/j.engstruct.2015.05.005 . – ISSN 0141–0296

[Boussaa and Aravas 2001] Boussaa, D. ; Aravas, N.: A numeric-symbolic approach to the problem of localization of plastic flow. In: *Computational Mechanics* 27 (2001), Apr, Nr. 4, p. 324–331. – 10.1007/s004660000227 . – ISSN 1432–0924

[Bouterf et al. 2020] Bouterf, Amine ; Buljac, Ante ; Hild, François ; Jailin, Clément ; Neggers, Jan ; Roux, Stéphane: Digital Volume Correlation of Laminographic and Tomographic Images: Results and Challenges. In: *Virtual Design and Validation*. Springer, 2020, p. 3–20

[Brancherie et al. 2006] Brancherie, Delphine ; Villon, Pierre ; Ibrahimbegović, Adnan ; Rassineux, Alain ; Breitkopf, Piotr: Transfert de champs par approximation diffuse avec conservation de l'énergie, Taylor & Francis, 2006, p. 107–118

[Broumand and Khoei 2013] Broumand, P. ; Khoei, A.R.: The extended finite element method for large deformation ductile fracture problems with a non-local damage-plasticity model. In: *Engineering Fracture Mechanics* 112-113 (2013), p. 97 – 125. – 10.1016/j.engfracmech.2013.10.002 . – ISSN 0013–7944

[Camacho and Ortiz 1997] Camacho, GT ; Ortiz, M: Adaptive Lagrangian modelling of ballistic penetration of metallic targets. In: *Computer methods in applied mechanics and engineering* 142 (1997), Nr. 3-4, p. 269–301

[Cervera and Chiumenti 2006] Cervera, M. ; Chiumenti, M.: Mesh objective tensile cracking via a local continuum damage model and a crack tracking technique. In: *Computer Methods in Applied Mechanics and Engineering* 196 (2006), Nr. 1, p. 304 – 320. – 10.1016/j.cma.2006.04.008 . – ISSN 0045–7825

[Chiaruttini et al. 2010] Chiaruttini, V ; Feyel, F ; Chaboche, JL: A robust meshing algorithm for complex 3D crack growth simulation. In: *IV European Conference on Computational Mechanics*, 2010, p. 16–21

[Comi et al. 2007] Comi, Claudia ; Mariani, Stefano ; Perego, Umberto: An extended FE strategy for transition from continuum damage to mode I cohesive crack propagation. In: *International Journal for Numerical and Analytical Methods in Geomechanics* 31 (2007), Nr. 2, p. 213–238

[Crété et al. 2014] Crété, J.P. ; Longère, P. ; Cadou, J.M.: Numerical modelling of crack propagation in ductile materials combining the GTN model and X-FEM. In: *Computer Methods in Applied Mechanics and Engineering* 275 (2014), p. 204 – 233. – 10.1016/j.cma.2014.03.007 . – ISSN 0045–7825

[Dias et al. 2018] Dias, I. F. ; Oliver, J. ; Lloberas-Valls, O.: Strain-injection and crack-path field techniques for 3D crack-propagation modelling in quasi-brittle materials. In: *International Journal of Fracture* 212 (2018), Jul, Nr. 1, p. 67–87. – 10.1007/s10704-018-0293-8 . – ISSN 1573–2673

[Duflot 2007] Duflot, Marc: A study of the representation of cracks with level sets. In: *International Journal for Numerical Methods in Engineering* 70 (2007), Nr. 11, p. 1261–1302. – 10.1002/nme.1915

[Dufour et al. 2012] Dufour, Frédéric ; Legrain, Grégory ; Pijaudier-Cabot, Gilles ; Huerta, Antonio: Estimation of crack opening from a two-dimensional continuum-based finite element computation. In: *International Journal for Numerical and Analytical Methods in Geomechanics* 36 (2012), Nr. 16, p. 1813–1830. – 10.1002/nag.1097

[El Ouazani Tuhami et al. 2023] El Ouazani Tuhami, A. ; Feld-Payet, S. ; Quilici, S. ; Osipov, N. ; Besson, J.: Simulations of complex crack

paths using a robust and cost-efficient continuous–discontinuous approach. In: *International Journal of Solids and Structures* 274 (2023), p. 112199. – 10.1016/j.ijsolstr.2023.112199 . – ISSN 0020–7683

[El Ouazani Tuhami 2022] El Ouazani Tuhami, Amar: *Simulation of ductile failure over long distances with a non–local GTN model*, Université Paris sciences et lettres, Diss., 2022. `https://pastel.archives-ouvertes.fr/tel-03869005`

[Eldahshan et al. 2021] Eldahshan, Hazem ; Alves, José ; Bouchard, Pierre-Olivier ; Perchat, Etienne ; Munoz, Daniel P.: CIPFAR: A 3D unified numerical framework for the modeling of ductile fracture based on the phase field model and adaptive remeshing. In: *Computer Methods in Applied Mechanics and Engineering* 387 (2021), p. 114171. – 10.1016/j.cma.2021.114171 . – ISSN 0045–7825

[Espinosa et al. 1998] Espinosa, Horacio D. ; Zavattieri, Pablo D. ; Emore, Gordon L.: Adaptive FEM computation of geometric and material nonlinearities with application to brittle failure. In: *Mechanics of Materials* 29 (1998), Nr. 3-4, p. 275–305

[Feist and Hofstetter 2006] Feist, C ; Hofstetter, G: An embedded strong discontinuity model for cracking of plain concrete. In: *Computer Methods in Applied Mechanics and Engineering* 195 (2006), Nr. 52, p. 7115–7138

[Feld-Payet 2010] Feld-Payet, S.: *Amorçage et propagation de fissures dans les milieux ductiles non locaux*, École Nationale Supérieure des Mines de Paris, Diss., 2010. – http://pastel.archives-ouvertes.fr/pastel-00583011

[Feld-Payet 2023] *Kapitel* Transition endommagement-fissure. In: Feld-Payet, S.: *Modélisation numérique en mécanique fortement non-linéaire: contact et rupture*. ISTE Editions Ltd, 2023. – sous la direction de J. Besson, F. Lebon, E. Lorentz

[Feld-Payet et al. 2022] Feld-Payet, S. ; Fourest, T. ; Bouda, P. ; Garaud, J.D. ; Bettonte, F. ; Tireira, A. ; Sant, Y. L. ; Besnerais, G. L. ; Belon, S.: Escale: une plateforme ouverte pour le dialogue essai-modèle-calcul. In: *Proceedings 15ème du Colloque National en Calcul des Structures CSMA*. Giens, 2022

[Feld-Payet et al. 2015] Feld-Payet, Sylvia ; Chiaruttini, Vincent ; Besson, Jacques ; Feyel, Frédéric: A new marching ridges algorithm for crack path tracking in regularized media. In: *International Journal of Solids and Structures* 71 (2015), 57-69. `https://hal-mines-paristech.archives-ouvertes.fr/hal-01199601`. – 10.1016/j.ijsolstr.2015.04.043

[Garzon et al. 2014] Garzon, J. ; O'Hara, P. ; Duarte, C. A. ; Buttlar, W. G.: Improvements of explicit crack surface representation and update

within the generalized finite element method with application to three-dimensional crack coalescence. In: *International Journal for Numerical Methods in Engineering* 97 (2014), Nr. 4, p. 231–273. – 10.1002/nme.4573

[Geelen et al. 2018] Geelen, Rudy J. ; Liu, Yingjie ; Dolbow, John E. ; Rodríguez-Ferran, Antonio: An optimization-based phase-field method for continuous-discontinuous crack propagation. In: *International Journal for Numerical Methods in Engineering* 116 (2018), Nr. 1, p. 1–20

[Gupta and Duarte 2014] Gupta, P. ; Duarte, C. A.: Simulation of non-planar three-dimensional hydraulic fracture propagation. In: *International Journal for Numerical and Analytical Methods in Geomechanics* 38 (2014), Nr. 13, p. 1397–1430. – 10.1002/nag.2305

[Hambli 2001] Hambli, Ridha: Finite element simulation of fine blanking processes using a pressure-dependent damage model. In: *Journal of Materials Processing Technology* 116 (2001), Nr. 2, p. 252 – 264. – 10.1016/S0924-0136(01)01009-3 . – ISSN 0924–0136

[Hinton and Campbell 1974] Hinton, E. ; Campbell, J. S.: Local and global smoothing of discontinuous finite element functions using a least squares method. In: *International Journal for Numerical Methods in Engineering* 8 (1974), Nr. 3, p. 461–480. – 10.1002/nme.1620080303

[Huespe et al. 2012] Huespe, Alfredo E. ; Needleman, Alan ; Oliver, Javier ; Sánchez, Pablo J.: A finite strain, finite band method for modeling ductile fracture. In: *International Journal of Plasticity* 28 (2012), Nr. 1, p. 53–69

[Huespe et al. 2009] Huespe, Alfredo E. ; Needleman, Alan ; Oliver, Javier ; Sánchez, Pedro J.: A finite thickness band method for ductile fracture analysis. In: *International Journal of Plasticity* 25 (2009), Nr. 12, p. 2349–2365

[Jäger et al. 2008a] Jäger, P ; Steinmann, P ; Kuhl, E: Modeling three-dimensional crack propagation - a comparison of crack path tracking strategies. In: *International Journal for Numerical Methods in Engineering* 76 (2008), Nr. 9, p. 1328–1352

[Jäger et al. 2008b] Jäger, Philippe ; Steinmann, Paul ; Kuhl, Ellen: On local tracking algorithms for the simulation of three-dimensional discontinuities. In: *Computational Mechanics* 42 (2008), Nr. 3, p. 395–406

[Jäger et al. 2009] Jäger, Philippe ; Steinmann, Paul ; Kuhl, Ellen: Towards the treatment of boundary conditions for global crack path tracking in three-dimensional brittle fracture. In: *Computational Mechanics* 45 (2009), Nr. 1, p. 91–107

[Javani et al. 2016] Javani, HR ; Peerlings, Ron H. ; Geers, Marc G.: Three-dimensional finite element modeling of ductile crack initiation and

propagation. In: *Advanced Modeling and Simulation in Engineering Sciences* 3 (2016), p. 1–25

[Javani Joni 2011] Javani Joni, H: *A computational damage approach towards three-dimensional ductile fracture*, Diss., 2011

[Javanmardi and Maheri 2019] Javanmardi, M.R. ; Maheri, Mahmoud R.: Extended finite element method and anisotropic damage plasticity for modelling crack propagation in concrete. In: *Finite Elements in Analysis and Design* 165 (2019), p. 1 – 20. – 10.1016/j.finel.2019.07.004 . – ISSN 0168–874X

[Jirásek 2004] Jirásek, Milan: Non-local damage mechanics with application to concrete. In: *Revue française de génie civil* 8 (2004), Nr. 5-6, p. 683–707

[Jirásek and Zimmermann 2001] Jirásek, Milan ; Zimmermann, Thomas: Embedded crack model. Part II: Combination with smeared cracks. In: *International Journal for Numerical Methods in Engineering* 50 (2001), Nr. 6, p. 1291–1305

[Khoei and Gharehbaghi 2009] Khoei, AR ; Gharehbaghi, SA: Three-dimensional data transfer operators in large plasticity deformations using modified-SPR technique. In: *Applied Mathematical Modelling* 33 (2009), Nr. 7, p. 3269–3285

[Lee and Bathe 1994] Lee, Nam-Sua ; Bathe, Klaus-Jürgen: Error indicators and adaptive remeshing in large deformation finite element analysis. In: *Finite Elements in Analysis and Design* 16 (1994), Nr. 2, p. 99–139

[Lloberas-Valls et al. 2016] Lloberas-Valls, O. ; Huespe, A.E. ; Oliver, J. ; Dias, I.F.: Strain injection techniques in dynamic fracture modeling. In: *Computer Methods in Applied Mechanics and Engineering* 308 (2016), p. 499 – 534. – 10.1016/j.cma.2016.05.023 . – ISSN 0045–7825

[Loubignac et al. 1977] Loubignac, Gilles ; Cantin, Gilles ; Touzot, Gilbert: Continuous stress fields in finite element analysis. In: *AIAA journal* 15 (1977), Nr. 11, p. 1645–1647

[Mediavilla et al. 2006] Mediavilla, J. ; Peerlings, R. H. J. ; Geers, M. G. D.: Discrete crack modelling of ductile fracture driven by non-local softening plasticity. In: *International Journal for Numerical Methods in Engineering* 66 (2006), 4, Nr. 4, p. 661–688. – 10.1002/nme.1572 . – ISSN 1097–0207

[Mediavilla Varas 2005] Mediavilla Varas, J: *Continuous and discontinuous modelling of ductile fracture*, Technische Universiteit Eindhoven, Diss., 2005

[Nikolakopoulos et al. 2021] Nikolakopoulos, Konstantinos ; Crété,

Jean-Philippe ; Longère, Patrice: Progressive failure of ductile metals: Description via a three-dimensional coupled CZM–XFEM based approach. In: *Engineering Fracture Mechanics* 243 (2021), p. 107498. – 10.1016/j.engfracmech.2020.107498 . – ISSN 0013–7944

[Oliver et al. 2014] Oliver, J. ; Dias, I.F. ; Huespe, A.E.: Crack-path field and strain-injection techniques in computational modeling of propagating material failure. In: *Computer Methods in Applied Mechanics and Engineering* 274 (2014), p. 289 – 348. – 10.1016/j.cma.2014.01.008 . – ISSN 0045–7825

[Oliver et al. 2004] Oliver, J. ; Huespe, A.E. ; Samaniego, E. ; Chaves, E.W.V.: Continuum approach to the numerical simulation of material failure in concrete. In: *International Journal for Numerical and Analytical Methods in Geomechanics* 28 (2004), p. 609–632

[Ortiz and Quigley 1991] Ortiz, M. ; Quigley, J.J.: Adaptive mesh refinement in strain localization problems. In: *Computer Methods in Applied Mechanics and Engineering* 90 (1991), Nr. 1, p. 781–804. – 10.1016/0045-7825(91)90184-8 . – ISSN 0045–7825

[Patzák and Jirásek 2004] Patzák, B. ; Jirásek, M.: Adaptive resolution of localized damage in quasi-brittle materials. In: *Journal of Engineering Mechanics, ASCE* 130 (2004), p. 720–732

[Patzák and Jirásek 2003] Patzák, Bořek ; Jirásek, Milan: Process zone resolution by extended finite elements. In: *Engineering Fracture Mechanics* 70 (2003), Nr. 7, p. 957–977. – 10.1016/S0013-7944(02)00160-1 . – ISSN 0013–7944

[Peerlings et al. 2008] Peerlings, RHJ ; Javani, HR ; Mediavilla, J ; Geers, MGD: Modelling of damage initiation and propagation in metal forming. In: *International Journal of Material Forming* 1 (2008), p. 1123–1126

[Pereira et al. 2009] Pereira, J. P. ; Duarte, C. A. ; Guoy, D. ; Jiao, X.: hp-Generalized FEM and crack surface representation for non-planar 3-D cracks. In: *International Journal for Numerical Methods in Engineering* 77 (2009), Nr. 5, p. 601–633. – 10.1002/nme.2419

[Perić et al. 1996] Perić, D ; Hochard, Ch ; Dutko, M ; Owen, DRJ: Transfer operators for evolving meshes in small strain elasto-placticity. In: *Computer Methods in Applied Mechanics and Engineering* 137 (1996), Nr. 3-4, p. 331–344. – 10.1016/S0045-7825(96)01070-5 . – ISSN 0045–7825

[Pourmodheji and Mashayekhi 2012] Pourmodheji, R. ; Mashayekhi, M.: Improvement of the extended finite element method for ductile crack growth. In: *Materials Science and Engineering: A* 551 (2012), p. 255 – 271. – 10.1016/j.msea.2012.05.014 . – ISSN 0921–5093

[Rabczuk and Belytschko 2007] Rabczuk, T. ; Belytschko, T.: A three-dimensional large deformation meshfree method for arbitrary evolving cracks. In: *Computer Methods in Applied Mechanics and Engineering* 196 (2007), Nr. 29, p. 2777 – 2799. – 10.1016/j.cma.2006.06.020 . – ISSN 0045–7825

[Rabczuk et al. 2010] Rabczuk, Timon ; Zi, Goangseup ; Bordas, Stephane ; Nguyen-Xuan, Hung: A simple and robust three-dimensional cracking-particle method without enrichment. In: *Computer Methods in Applied Mechanics and Engineering* 199 (2010), Nr. 37-40, p. 2437–2455

[Riccardi et al. 2017] Riccardi, Francesco ; Kishta, Ejona ; Richard, Benjamin: A step-by-step global crack-tracking approach in E-FEM simulations of quasi-brittle materials. In: *Engineering Fracture Mechanics* 170 (2017), p. 44–58

[Roth et al. 2015] Roth, Simon-Nicolas ; Léger, Pierre ; Soulaimani, Azzeddine: A combined XFEM-damage mechanics approach for concrete crack propagation. In: *Computer Methods in Applied Mechanics and Engineering* 283 (2015), p. 923 – 955. – 10.1016/j.cma.2014.10.043 . – ISSN 0045–7825

[Saloustros et al. 2018] Saloustros, Savvas ; Cervera, Miguel ; Pelà, Luca: Tracking multi-directional intersecting cracks in numerical modelling of masonry shear walls under cyclic loading. In: *Meccanica* 53 (2018), Nr. 7, p. 1757–1776

[Seabra et al. 2013] Seabra, Mariana R. R. ; Šuštarič, Primož ; Sa, Jose M. A. d. ; Rodič, Tomaž: Damage driven crack initiation and propagation in ductile metals using XFEM. In: *Computational Mechanics* 52 (2013), Jul, Nr. 1, p. 161–179. – 10.1007/s00466-012-0804-9 . – ISSN 1432–0924

[Seabra et al. 2011] Seabra, Mariana Rita R. ; Sa, Jose MA C. ; Andrade, Filipe X. ; Pires, Francisco F.: Continuous-discontinuous formulation for ductile fracture. In: *International journal of material forming* 4 (2011), p. 271–281

[Simone et al. 2003] Simone, Angelo ; Wells, Garth N. ; Sluys, Lambertus J.: From continuous to discontinuous failure in a gradient-enhanced continuum damage model. In: *Computer Methods in Applied Mechanics and Engineering* 192 (2003), Nr. 41-42, p. 4581–4607

[Song et al. 2006] Song, Jeong-Hoon ; Areias, Pedro M. ; Belytschko, Ted: A method for dynamic crack and shear band propagation with phantom nodes. In: *International Journal for Numerical Methods in Engineering* 67 (2006), Nr. 6, p. 868–893

[Song et al. 2008] Song, Jeong-Hoon ; Wang, Hongwu ; Belytschko, Ted: A comparative study on finite element methods for dynamic fracture. In: *Computational Mechanics* 42 (2008), Nr. 2, p. 239–250

[Stolarska et al. 2001] Stolarska, M. ; Chopp, D.L. ; Moës, N. ; Belytschko, T.: Modelling crack growth by level sets in the extended finite element method. In: *International Journal for Numerical Methods in Engineering* 51 (2001), p. 943–960

[Tamayo-Mas 2013] Tamayo-Mas, Elena: *Continuous-discontinuous modelling for quasi-brittle failure: propagating cracks in a regularised bulk*, Universitat Politècnica de Catalunya (UPC), Diss., 2013

[Tamayo-Mas et al. 2019] Tamayo-Mas, Elena ; Feliu-Fabà, Jordi ; Casado-Antolin, Montserrat ; Rodríguez-Ferran, Antonio: A continuous-discontinuous model for crack branching. In: *International Journal for Numerical Methods in Engineering* 120 (2019), Nr. 1, p. 86–104

[Tamayo-Mas and Rodríguez-Ferran 2015] Tamayo-Mas, Elena ; Rodríguez-Ferran, Antonio: A medial-axis-based model for propagating cracks in a regularised bulk. In: *International Journal for Numerical Methods in Engineering* 101 (2015), Nr. 7, p. 489–520. – 10.1002/nme.4757

[Villon et al. 2002] Villon, Pierre ; Borouchaki, Houman ; Saanouni, Khemais: Transfert de champs plastiquement admissibles. In: *Comptes Rendus Mécanique* 330 (2002), Nr. 5, p. 313–318

[Wang and Waisman 2016] Wang, Yongxiang ; Waisman, Haim: From diffuse damage to sharp cohesive cracks: A coupled XFEM framework for failure analysis of quasi-brittle materials. In: *Computer Methods in Applied Mechanics and Engineering* 299 (2016), p. 57 – 89. – 10.1016/j.cma.2015.10.019 . – ISSN 0045–7825

[Wells and Sluys 2001] Wells, G. N. ; Sluys, L. J.: A new method for modelling cohesive cracks using finite elements. In: *International Journal for Numerical Methods in Engineering* 50 (2001), Nr. 12, p. 2667–2682. – 10.1002/nme.143

[Wolf et al. 2018] Wolf, J. ; Longère, P. ; Cadou, J. M. ; Crété, J. P.: Numerical modeling of strain localization in engineering ductile materials combining cohesive models and X-FEM. In: *International Journal of Mechanics and Materials in Design* 14 (2018), Jun, Nr. 2, p. 177–193. – 10.1007/s10999-017-9370-9 . – ISSN 1573–8841

[Zienkiewicz and Zhu 1992a] Zienkiewicz, O. C. ; Zhu, J. Z.: The superconvergent patch recovery and a posteriori error estimates. Part 1: The recovery technique. In: *International Journal for Numerical Methods in Engineering* 33 (1992), Nr. 7, p. 1331–1364. – 10.1002/nme.1620330702

[Zienkiewicz and Zhu 1992b] Zienkiewicz, O. C. ; Zhu, J. Z.: The superconvergent patch recovery and a posteriori error estimates. Part 2: Error

estimates and adaptivity. In: *International Journal for Numerical Methods in Engineering* 33 (1992), Nr. 7, p. 1365–1382. – 10.1002/nme.1620330703

Modeling damage and fracture are an essential factor in ensuring control of forming processes and estimating service life expectancy. Linear fracture mechanics models proposed by Griffith (1920) and the subsequent non-linear approaches by Rice are now widely used in the industry. However, these so-called global approaches cannot account for all experimental observations and can thus lead to very conservative practices.

To overcome these limitations, so-called local approaches have been developped since the 80s. The associated models are based on an analysis of local stresses and strains. They are now implemented in numerous finite element solvers.

This collective work aims at gathering a state of the art on damage mechanics and local approaches to fracture. It was presented during the second edition of the ***MEALOR*** *summer school in Banyuls, France, from August 21st to September 1st, 2023.*